THE ASIAN MONSOON

EDITED BY: Lin Wang, Haishan Chen, Jasti S. Chowdary, Kyung-Ja Ha,
Yoshiyuki Kajikawa and Gill Martin

PUBLISHED IN: Frontiers in Earth Science and Frontiers in Environmental Science

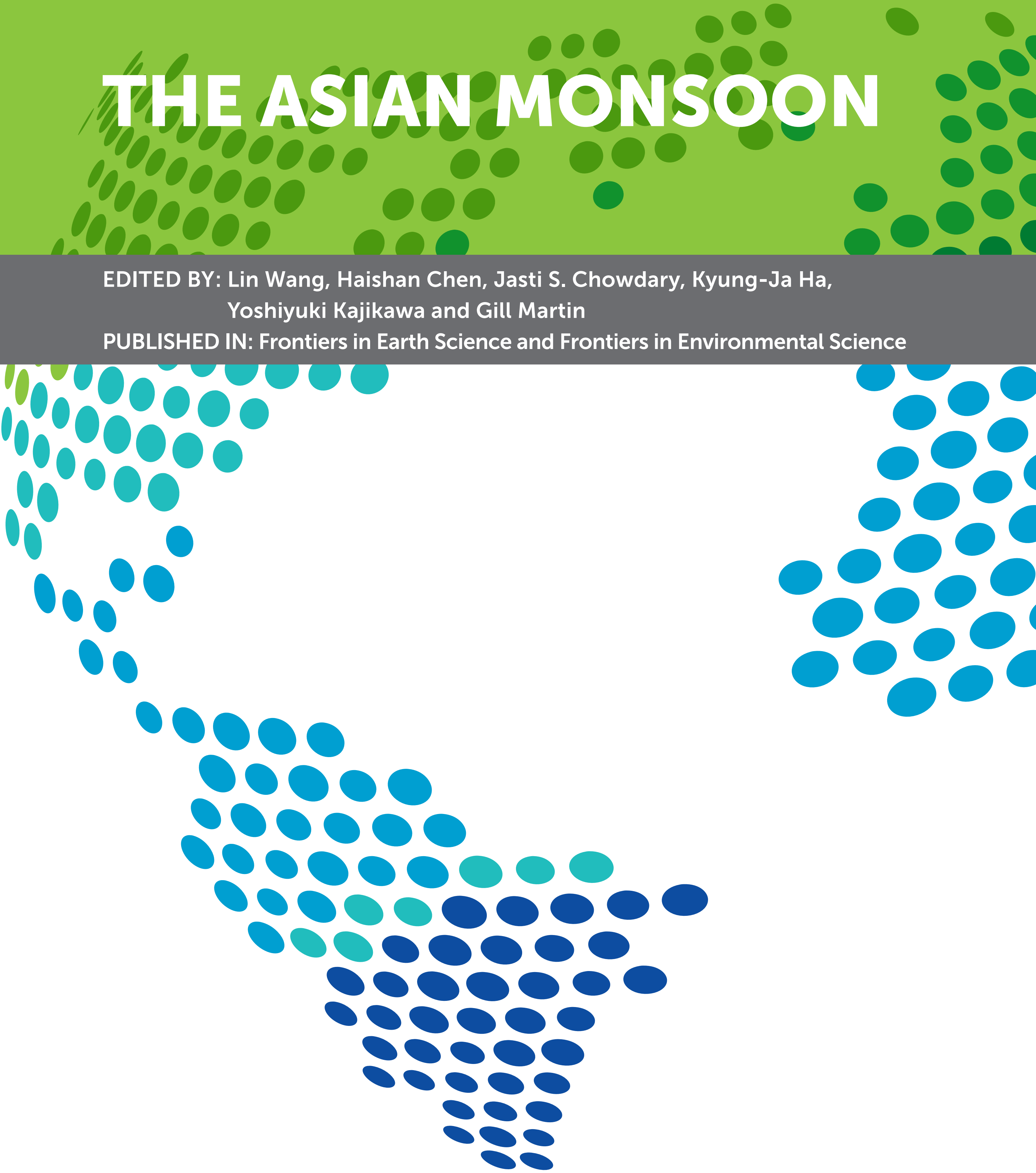

frontiers Research Topics

ISSN 1664-8714
ISBN 978-2-88971-472-8
DOI 10.3389/978-2-88971-472-8

About Frontiers

Frontiers is more than just an open-access publisher of scholarly articles: it is a pioneering approach to the world of academia, radically improving the way scholarly research is managed. The grand vision of Frontiers is a world where all people have an equal opportunity to seek, share and generate knowledge. Frontiers provides immediate and permanent online open access to all its publications, but this alone is not enough to realize our grand goals.

Frontiers Journal Series

The Frontiers Journal Series is a multi-tier and interdisciplinary set of open-access, online journals, promising a paradigm shift from the current review, selection and dissemination processes in academic publishing. All Frontiers journals are driven by researchers for researchers; therefore, they constitute a service to the scholarly community. At the same time, the Frontiers Journal Series operates on a revolutionary invention, the tiered publishing system, initially addressing specific communities of scholars, and gradually climbing up to broader public understanding, thus serving the interests of the lay society, too.

Dedication to Quality

Each Frontiers article is a landmark of the highest quality, thanks to genuinely collaborative interactions between authors and review editors, who include some of the world's best academicians. Research must be certified by peers before entering a stream of knowledge that may eventually reach the public - and shape society; therefore, Frontiers only applies the most rigorous and unbiased reviews.
Frontiers revolutionizes research publishing by freely delivering the most outstanding research, evaluated with no bias from both the academic and social point of view. By applying the most advanced information technologies, Frontiers is catapulting scholarly publishing into a new generation.

What are Frontiers Research Topics?

Frontiers Research Topics are very popular trademarks of the Frontiers Journals Series: they are collections of at least ten articles, all centered on a particular subject. With their unique mix of varied contributions from Original Research to Review Articles, Frontiers Research Topics unify the most influential researchers, the latest key findings and historical advances in a hot research area! Find out more on how to host your own Frontiers Research Topic or contribute to one as an author by contacting the Frontiers Editorial Office: frontiersin.org/about/contact

THE ASIAN MONSOON

Topic Editors:
Lin Wang, Institute of Atmospheric Physics (CAS), China
Haishan Chen, Nanjing University of Information Science and Technology, China
Jasti S. Chowdary, Indian Institute of Tropical Meteorology (IITM), India
Kyung-Ja Ha, Pusan National University, South Korea
Yoshiyuki Kajikawa, Riken Center for Computational Science, Japan
Gill Martin, Met Office Hadley Centre (MOHC), United Kingdom

Citation: Wang, L., Chen, H., Chowdary, J. S., Ha, K.-J., Kajikawa, Y., Martin, G., eds. (2022). The Asian Monsoon. Lausanne: Frontiers Media SA.
doi: 10.3389/978-2-88971-472-8

Table of Contents

frontiers in Earth Science

EDITORIAL
published: 20 August 2021
doi: 10.3389/feart.2021.748811

Editorial: The Asian Monsoon

Lin Wang[1]*, *Haishan Chen*[2], *Jasti S. Chowdary*[3], *Kyung-Ja Ha*[4], *Yoshiyuki Kajikawa*[5] and *Gill Martin*[6]

[1]Center for Monsoon System Research, Institute of Atmospheric Physics, Chinese Academy of Sciences, Beijing, China, [2]School of Atmospheric Sciences, Nanjing University of Information Science and Technology, Nanjing, China, [3]Indian Institute of Tropical Meteorology, Pune, India, [4]Center for Climate Physics, Institute for Basic Science, and Department of Atmospheric Sciences, Pusan National University, Busan, South Korea, [5]RIKEN Center for Computational Science, and Research Center for Urban Safety and Security, Kobe University, Kobe, Japan, [6]Met Office Hadley Centre, Exeter, United Kingdom

Keywords: monsoon, ENSO, interannual variability, interdecadal variability, land-atmopshere interactions, air-sea interactions

Editorial on the Research Topic

The Asian Monsoon

The Asian monsoon is an essential component of the global climate system (Trenberth et al., 2006). Its evolution and variability can significantly influence the vegetation, populations, economies, and even cultures that inhabit Asian monsoon regions, which prevails from the Indian sub-continent to Southeast and East Asia. The monsoon-related natural hazards, such as flooding, droughts, heatwaves, and blizzards, significantly impact society, and human livelihood (Wang, 2006). Therefore, it is essential to understand the variability and mechanism of *the Asian monsoon* so that skillful forecasts, predictions, and reasonable future projections can be made accordingly.

The Asian monsoon consists of both summer and winter counterparts (Ju and Slingo, 1995; Chang et al., 2006; Wang and Lu, 2017) and several sub-systems, including the Indian monsoon, the East Asian monsoon, and the western North Pacific monsoon (Wang and LinHo, 2002). These sub-systems have strong mutual linkages and vary from synoptic to multidecadal and longer time scales. They interact with the Earth's ocean, land, atmosphere, the biosphere, among others, *via* complex coupled processes (Meehl, 1994; Webster et al., 1998; Gadgil, 2003; Goswami, 2005; Yihui and Chan, 2005; Huang et al., 2007; Ha et al., 2012; Huang et al., 2012; Chen et al., 2019). It is essential to know how and why the current state-of-the-art numerical models capture these processes before making forecasts and predictions. This issue becomes increasingly crucial in light of global climate change.

In this Research Topic, the main objective was to present some recent advances and identify some remaining gaps in our knowledge on all aspects of *the Asian monsoon*. Sixteen papers were published after peer reviews. Most of them focus on the summer monsoon and discuss the role of air-sea interactions in the monsoon variability on the interannual timescale. The El Nino-Southern Oscillation (ENSO) is an essential driver for the Indian summer monsoon (ISM) precipitation (Ju and Slingo, 1995; Gadgil, 2003), and its relationship with the ISM underwent decadal weakening in the late 1970s (Kumar et al., 1999) and recovered recently (Yang and Huang, 2021; Yu et al., 2021). Bódai et al. revisit the unstable ENSO-ISM relationship and the underlying mechanism with the help of large-ensemble simulations and discuss its nonlinearity and nonergodicity. Son et al. further claim the essential role of the ISM precipitation in exciting a dominant teleconnection in boreal summer, the Silk Road pattern (SRP, Lu et al., 2002; Enomoto et al., 2003; Chowdary et al., 2019) by showing how the Rossby wave source is generated by the ISM-related diabatic heating. Although the SRP is an internal mode of the atmosphere (Yasui and Watanabe, 2010), it may be excited or amplified by atmospheric external forcing or resonance (e.g., Yasui and Watanabe, 2010; Wang et al., 2017), leading to longer atmospheric residence time over India and thereby more frequent extreme events (Lakshmi Kumar et al.).

Edited and reviewed by:
Yuqing Wang,
University of Hawaii at Manoa,
United States

****Correspondence:***
Lin Wang
wanglin@mail.iap.ac.cn

Specialty section:
This article was submitted to
Atmospheric Science,
a section of the journal
Frontiers in Earth Science

Received: 28 July 2021
Accepted: 09 August 2021
Published: 20 August 2021

Citation:
Wang L, Chen H, Chowdary JS,
Ha K-J, Kajikawa Y and Martin G
(2021) Editorial: The Asian Monsoon.
Front. Earth Sci. 9:748811.
doi: 10.3389/feart.2021.748811

The influence of ENSO on the East Asian summer monsoon (EASM) is also crucial (Xie et al., 2016; Li et al., 2017; Zhang et al., 2017). It shows significant diversity regarding the spatial patterns of ENSO (Feng et al., 2011; Yuan and Yang, 2012), the decaying speed of ENSO (Chen et al., 2012; Feng et al., 2014; Zhou et al., 2019), the background state (Feng et al., 2014), the different configurations with other oceanic signals (Xie et al., 2009; Chen et al., 2016; Feng et al., 2020), and many others. Zhang et al. further attribute this diversity to the persistence and transition speed of ENSO. Li et al. take Hong Kong as an example and link this diversity to the North Atlantic sea surface temperature. Besides ENSO, J. Xu et al. claim that the Indian Ocean dipole (Saji et al., 1999) can influence the EASM precipitation and thereby the rice yield in Jiangsu, a province in eastern China. You et al. suggest that the thermal state of the tropical western Pacific can change the meridional temperature gradient and the onset of the EASM. Huang et al. reveal that the accumulation effect of the intra-seasonal oscillation over the tropical western Pacific can change the meridional location of the western Pacific subtropical high, a crucial circulation system of the EASM. Zeng et al. suggest that the linkage between the onset dates of the ISM and the EASM strengthened after the late 1970s, which is attributed to the Indian Ocean basin warming. Liu et al. suggest that the Atlantic Multidecadal Variability and its footprint in the Indian Ocean may lead to multidecadal seesaw in the Hadley Circulation's strength between Northern and Southern Hemispheres and further to changes in land precipitation over monsoon regions. Wen et al. reveal the influences of the North Pacific Victoria Mode on the Madden-Julian Oscillation, an essential factor influencing *the Asian monsoon* on the intraseasonal timescale.

Several papers in the Research Topic discuss land-surface processes in the EASM variability, which is another essential aspect for *the Asian monsoon* (Webster et al., 1998; Xue et al., 2004; Yasunari, 2007). Wang et al. review the impacts of the soil freeze-thaw process and snow melting over the Tibetan Plateau on the EASM. Liang et al. report a decadal change in the relationship between the Tibetan Plateau temperature and summer precipitation over the South China Sea. Xu et al. identify a relationship between the Eurasian snow melting in spring and the EASM and suggest the mechanism involving the changes in the baroclinicity and transient eddy forcing. Especially, Lau et al. report a fascinating result on the role of the dust from Middle East deserts in affecting the Asian summer monsoon. They highlight that the dust-cloud-radiation-precipitation dynamical feedback on subseasonal-to-seasonal timescale can lead to anomalous diabatic heating over the Pakistan/Northwest India region and excite atmospheric Rossby waves, which shifts the whole Asian summer monsoon westward.

The Research Topic is overall successful, but it has deficiencies. For example, most of the articles focus on the air-sea interaction aspect of the monsoon on the seasonal timescale and longer. Other processes and timescales, such as the land-atmosphere interactions, internal atmospheric processes, and subseasonal variabilities or extremes, which are also essential for *the Asian monsoon*, were less discussed. There is even no paper on the Asian winter monsoon, an indispensable member of *the Asian monsoon*, and *the Asian monsoon* projection and its uncertainties, an increasing concern of both the scientific community and the public. Although this Research Topic only contains a very small sample size, it reflects the current status of the monsoon research to some extent, and a more balanced study on *the Asian monsoon* in the future is recommended.

AUTHOR CONTRIBUTIONS

All authors listed have made a substantial, direct, and intellectual contribution to the work and approved it for publication.

FUNDING

LW is supported by the National Natural Science Foundation of China (41925020, 41721004). HC is supported by the National Natural Science Foundation of China (41625019).

ACKNOWLEDGMENTS

We thank the support of the editorial office from the preparation to the publication processes of this Research Topic.

REFERENCES

Chang, C.-P., Wang, Z., and Hendon, H. (2006). "The Asian winter Monsoon," in *The Asian Monsoon*. Springer Berlin Heidelberg, 89–127.

Chen, W., Park, J.-K., Dong, B., Lu, R., and Jung, W.-S. (2012). The Relationship between El Niño and the Western North Pacific Summer Climate in a Coupled GCM: Role of the Transition of El Niño Decaying Phases. *J. Geophys. Res.* 117. doi:10.1029/2011jd017385

Chen, W., Wang, L., Feng, J., Wen, Z., Ma, T., Yang, X., et al. (2019). Recent Progress in Studies of the Variabilities and Mechanisms of the East Asian Monsoon in a Changing Climate. *Adv. Atmos. Sci.* 36, 887–901. doi:10.1007/s00376-019-8230-y

Chen, Z., Wen, Z., Wu, R., Lin, X., and Wang, J. (2016). Relative Importance of Tropical SST Anomalies in Maintaining the Western North Pacific Anomalous Anticyclone during El Niño to La Niña Transition Years. *Clim. Dyn.* 46, 1027–1041. doi:10.1007/s00382-015-2630-1

Chowdary, J. S., Hu, K., Srinivas, G., Kosaka, Y., Wang, L., and Rao, K. K. (2019). The Eurasian Jet Streams as Conduits for East Asian Monsoon Variability. *Curr. Clim. Change Rep.* 5, 233–244. doi:10.1007/s40641-019-00134-x

Enomoto, T., Hoskins, B. J., and Matsuda, Y. (2003). The Formation Mechanism of the Bonin High in August. *Q. J. R. Meteorol. Soc.* 129, 157–178. doi:10.1256/qj.01.211

Feng, J., Chen, W., Tam, C.-Y., and Zhou, W. (2011). Different Impacts of El Niño and El Niño Modoki on China Rainfall in the Decaying Phases. *Int. J. Climatol.* 31, 2091–2101. doi:10.1002/joc.2217

Feng, J., Chen, W., and Wang, X. (2020). Reintensification of the Anomalous Western North Pacific Anticyclone during the El Niño Modoki Decaying Summer: Relative Importance of Tropical Atlantic and Pacific SST Anomalies. *J. Clim.* 33, 3271–3288. doi:10.1175/jcli-d-19-0154.1

Feng, J., Wang, L., and Chen, W. (2014). How Does the East Asian Summer Monsoon Behave in the Decaying Phase of El Niño during Different PDO Phases? *J. Clim.* 27, 2682–2698. doi:10.1175/jcli-d-13-00015.1

Gadgil, S. (2003). The indianmonsoon Anditsvariability. *Annu. Rev. Earth Planet. Sci.* 31, 429–467. doi:10.1146/annurev.earth.31.100901.141251

Goswami, B. N. (2005). *South Asian Monsoon. Intraseasonal Variability in the Atmosphere-Ocean Climate System*. Editors W. K. M. Lau and D. E. Waliser (Springer Berlin Heidelberg), 19–61.

Ha, K.-J., Heo, K.-Y., Lee, S.-S., Yun, K.-S., and Jhun, J.-G. (2012). Variability in the East Asian Monsoon: a Review. *Met. Apps.* 19, 200–215. doi:10.1002/met.1320

Huang, R., Chen, J., and Huang, G. (2007). Characteristics and Variations of the East Asian Monsoon System and its Impacts on Climate Disasters in China. *Adv. Atmos. Sci.* 24, 993–1023. doi:10.1007/s00376-007-0993-x

Huang, R., Chen, J., Wang, L., and Lin, Z. (2012). Characteristics, Processes, and Causes of the Spatio-Temporal Variabilities of the East Asian Monsoon System. *Adv. Atmos. Sci.* 29, 910–942. doi:10.1007/s00376-012-2015-x

Ju, J., and Slingo, J. (1995). The Asian Summer Monsoon and ENSO. *Q.J R. Met. Soc.* 121, 1133–1168. doi:10.1002/qj.49712152509

Kumar, K. K., Rajagopalan, B., and Cane, M. A. (1999). On the Weakening Relationship between the Indian Monsoon and ENSO. *Science* 284, 2156–2159. doi:10.1126/science.284.5423.2156

Li, T., Wang, B., Wu, B., Zhou, T., Chang, C.-P., and Zhang, R. (2017). Theories on Formation of an Anomalous Anticyclone in Western North Pacific during El Niño: A Review. *J. Meteorol. Res.* 31, 987–1006. doi:10.1007/s13351-017-7147-6

Lu, R.-Y., Oh, J.-H., and Kim, B.-J. (2002). A Teleconnection Pattern in Upper-Level Meridional Wind over the North African and Eurasian Continent in Summer. *Tellus A.* 54, 44–55. doi:10.1034/j.1600-0870.2002.00248.x

Meehl, G. A. (1994). Coupled Land-Ocean-Atmosphere Processes and South Asian Monsoon Variability. *Science* 266, 263–267. doi:10.1126/science.266.5183.263

Saji, N. H., Goswami, B. N., Vinayachandran, P. N., and Yamagata, T. (1999). A Dipole Mode in the Tropical Indian Ocean. *Nature* 401, 360–363. doi:10.1038/43854

Trenberth, K. E., Hurrell, J. W., and Stepaniak, D. P. (2006). "The Asian Monsoon: Global Perspectives," in *The Asian Monsoon*. Springer Berlin Heidelberg, 67–87.

Wang, B., and LinHo (2002). Rainy Season of the Asian-Pacific Summer Monsoon*. *J. Clim.* 15, 386–398. doi:10.1175/1520-0442(2002)015<038610.1175/1520-0442(2002)015<0386:rsotap>2.0.co;2

Wang, B. (2006). *The Asian Monsoon*. Springer, 845.

Wang, L., and Lu, M.-M. (2017). "The East Asian Winter Monsoon," in *The Global Monsoon System: Research and Forecast*. 3 ed. Editors C.-P. Chang, H.-C. Kuo, N.-C. Lau, R. H. Johnson, B. Wang, and M. C. Wheeler, 51–61. doi:10.1142/9789813200913_0005

Wang, L., Xu, P., Chen, W., and Liu, Y. (2017). Interdecadal Variations of the Silk Road Pattern. *J. Clim.* 30, 9915–9932. doi:10.1175/jcli-d-17-0340.1

Webster, P. J., Magaña, V. O., Palmer, T. N., Shukla, J., Tomas, R. A., Yanai, M., et al. (1998). Monsoons: Processes, Predictability, and the Prospects for Prediction. *J. Geophys. Res.* 103, 14451–14510. doi:10.1029/97jc02719

Xie, S.-P., Hu, K., Hafner, J., Tokinaga, H., Du, Y., Huang, G., et al. (2009). Indian Ocean Capacitor Effect on Indo-Western Pacific Climate during the Summer Following El Niño. *J. Clim.* 22, 730–747. doi:10.1175/2008jcli2544.1

Xie, S.-P., Kosaka, Y., Du, Y., Hu, K., Chowdary, J. S., and Huang, G. (2016). Indo-western Pacific Ocean Capacitor and Coherent Climate Anomalies in post-ENSO Summer: a Review. *Adv. Atmos. Sci.* 33, 411–432. doi:10.1007/s00376-015-5192-6

Xue, Y., Juang, H.-M. H., Li, W.-P., Prince, S., DeFries, R., Jiao, Y., et al. (2004). Role of Land Surface Processes in Monsoon Development: East Asia and West Africa. *J. Geophys. Res.* 109. doi:10.1029/2003jd003556

Yang, X., and Huang, P. (2021). Restored Relationship between ENSO and Indian Summer Monsoon Rainfall Around 1999/2000. *The Innovation* 2, 100102. doi:10.1016/j.xinn.2021.100102

Yasui, S., and Watanabe, M. (2010). Forcing Processes of the Summertime Circumglobal Teleconnection Pattern in a Dry AGCM. *J. Clim.* 23, 2093–2114. doi:10.1175/2009jcli3323.1

Yasunari, T. (2007). Role of Land-Atmosphere Interaction on Asian Monsoon Climate. *J. Meteorol. Soc. Jpn.* 85B, 55–75. doi:10.2151/jmsj.85B.55

Yihui, D., and Chan, J. C. L. (2005). The East Asian Summer Monsoon: an Overview. *Meteorol. Atmos. Phys.* 89, 117–142. doi:10.1007/s00703-005-0125-z

Yu, S. Y., Fan, L., Zhang, Y., Zheng, X. T., and Li, Z. (2021). Reexamining the Indian Summer Monsoon Rainfall-ENSO Relationship from its Recovery in the 21 St Century: Role of the Indian Ocean SST Anomaly Associated with Types of ENSO Evolution. *Geophys. Res. Lett.* 48, e2021GL092873. doi:10.1029/2021gl092873

Yuan, Y., and Yang, S. (2012). Impacts of Different Types of El Niño on the East Asian Climate: Focus on ENSO Cycles. *J. Clim.* 25, 7702–7722. doi:10.1175/jcli-d-11-00576.1

Zhang, R., Min, Q., and Su, J. (2017). Impact of El Niño on Atmospheric Circulations over East Asia and Rainfall in China: Role of the Anomalous Western North Pacific Anticyclone. *Sci. China Earth Sci.* 60, 1124–1132. doi:10.1007/s11430-016-9026-x

Zhou, X., Liu, F., Wang, B., Xiang, B., Xing, C., and Wang, H. (2019). Different Responses of East Asian Summer Rainfall to El Niño Decays. *Clim. Dyn.* 53, 1497–1515. doi:10.1007/s00382-019-04684-6

Conflict of Interest: The authors declare that the research was conducted in the absence of any commercial or financial relationships that could be construed as a potential conflict of interest.

frontiers
in Earth Science

REVIEW
published: 02 June 2020
doi: 10.3389/feart.2020.00133

Impacts of Soil Freeze–Thaw Process and Snow Melting Over Tibetan Plateau on Asian Summer Monsoon System: A Review and Perspective

Chenghai Wang[1,2]*, ***Kai Yang***[1,2] ***and Feimin Zhang***[1,2]

[1] Research and Development Center of Earth System Model (RDCM), College of Atmospheric Sciences, Lanzhou University, Lanzhou, China, [2] Key Laboratory of Arid Climate Change and Disaster Reduction of Gansu Province, Lanzhou, China

Surface diabatic heating over the Tibetan Plateau (TP) is crucial for the onset and development of Asian summer monsoon (ASM), which is closely connected with the snow melting and freeze–thaw (SM-FT) processes in spring. This study reviews the recent processes about studies on the effects of SM-FT on the climate system over the ASM region. This review has shown that SM-FT in spring plays a dominant role in seasonal and inter-annual variations of surface diabatic heating over TP, which also have a significant relationship with the ASM activity. Moreover, the anomalies of SM-FT over TP significantly affect summer precipitation in Eastern China (EC). SM-FT in spring over TP would be a robust factor in the ASM system. The possible mechanism associated with the impacts of SM-FT on the summer general circulation in East Asia is also discussed. Under the climate change background, variations in regimes of frozen soil and snow have great potential effects on the climate in East Asia and around the globe. However, great uncertainties in the estimation of diabatic heating over TP (especially over the western TP) during spring still confine our understanding about the effects of TP thermal forcing on the ASM activity. It is suggested that improvement in the simulation of the SM-FT process in models is an effective approach for reducing the biases of climate projection in future.

Keywords: Tibetan Plateau, Asian summer monsoon, diabatic heating, freeze–thaw process, snow melting

Edited by:
Wen Chen,
Institute of Atmospheric Physics (CAS), China

Reviewed by:
Haishan Chen,
Nanjing University of Information Science and Technology, China
Yaocun Zhang,
Nanjing University, China

****Correspondence:***
Chenghai Wang
wch@lzu.edu.cn

Specialty section:
This article was submitted to Atmospheric Science, a section of the journal Frontiers in Earth Science

Received: *02 March 2020*
Accepted: *07 April 2020*
Published: *02 June 2020*

Citation:
Wang C, Yang K and Zhang F (2020) Impacts of Soil Freeze–Thaw Process and Snow Melting Over Tibetan Plateau on Asian Summer Monsoon System: A Review and Perspective. Front. Earth Sci. 8:133. doi: 10.3389/feart.2020.00133

INTRODUCTION

Monsoon is a product of the distribution of ocean, land, and special topography; its onset and development are mainly attributed to the thermal contrast between ocean and land (Meehl, 1994; Webster, 1998). Asian summer monsoon (ASM) dominates the summer precipitation belt in South and East Asia. The thermal and terrain effects of the Tibetan Plateau (TP) are important factors in the ASM climate system (e.g., Ye et al., 1957; Ye and Gao, 1979; Wu and Zhang, 1998; Ye and Wu, 1998; Wang et al., 2003; Duan et al., 2005; Wu et al., 2012a). A distinct symbol of ASM onset is the easterly arriving on the southern sides of TP and South Asia High has a jump over TP in June, and Hadley cell is replaced by the monsoon cell (Ye and Gao, 1979). Since Ye et al. (1957) found that TP is a heat source for atmospheric dynamics, researches on the dynamic and thermal forcing of TP have received much attention in the past decades (e.g., Qian et al., 2003a; Wang et al., 2003; Ding et al., 2008, 2009; Wu et al., 2012a; Duan et al., 2013; Wang C. et al., 2017). Wu et al. (2012a) demonstrated that surface sensible heating over TP forms and maintains the atmospheric circulation in the ASM regions in summer; surface sensible heating over TP acts as a pump in middle troposphere to change the atmospheric circulation around TP (Wu, 1984; Wu and Liu, 2000).

Both statistical analyses and model simulations have shown that strong TP surface diabatic heating (i.e., surface sensible and latent heat fluxes) favors an early monsoon onset and a strong ASM circulation, corresponding to a northward extent of the precipitation belt in East China (e.g., Zhao and Chen, 2001; Wang B. et al., 2008; Liu et al., 2012; Duan et al., 2013). Surface diabatic heating depends on the land surface processes (Wang C. et al., 2008, 2017; Wang et al., 2009b). An evident characteristic of TP land surface is the existence of a large amount of frozen ground and snow. The snow melting and freeze–thaw (SM-FT) process in spring strongly influences the surface sensible and latent heat fluxes in surface energy balance (Chow et al., 2008; Yang and Wang, 2019b). Although there are many available different land surface datasets over TP (**Table 1**), because of the model uncertainties and the lack of observation data, especially on the shortage of high spatiotemporal soil moisture and land surface heat flux data, some debates still exist on how the thermal effects of TP influence the ASM (Wu et al., 2012b, 2014).

There is no doubt that the land–atmosphere interaction over TP acts a crucial role in the ASM climate system. However, some issues that still remain should be further investigated. For instance, whether ASM onset is prior to or lags behind the increase of diabatic heating caused by surface status changes (e.g., SM-FT) over TP. In other words, is the changing of surface diabatic heating over TP a result of the establishment of ASM or do the changes of surface diabatic heating promote the development of ASM and its northward advance? How and why do surface diabatic heating anomalies over TP affect the ASM system anomalies? Answering these issues can be beneficial to deeply understand the characteristics of the ASM activity and its mechanism. In this study, we aim to review recent progresses about the relation between surface diabatic heating anomalies over TP as induced by the SM-FT process and the activities of ASM and attempt to answer some issues.

The structure of this study is organized as follows: section “Characteristics of Surface Diabatic Heating and Land Surface Process Over TP” reviews the variations of surface diabatic heating over TP and their relations with the land surface processes (i.e., SM-FT) during spring. Section “Connections Between SM-FT Over TP and ASM Activity” discusses the relationship between the ASM activity (e.g., summer precipitation anomalies in EC) and surface diabatic heating of TP. Section “Possible Mechanisms Associated With the Climatic Effects of SM-FT Process” discusses the possible mechanisms by which SM-FT anomalies over TP influence the summer atmospheric circulation in East Asia. The summary and possible prospects are given in section “Summary and Prospects.”

CHARACTERISTICS OF SURFACE DIABATIC HEATING AND LAND SURFACE PROCESS OVER TP

Surface Diabatic Heating and Land Surface Process Over TP

The TP, which is an immense topography crossing the east–west direction at the middle and the lower latitude in the Northern Hemisphere, not only blocks meridional airflows and the northward transportation of water vapor but also remarkably influences energy and water vapor exchange between the land surface over TP and the surrounding atmosphere. The TP thermal forcing is suggested to dominate the ASM systems, whereas large-scale orographically mechanical forcing is not essential (Wu et al., 2012a).

The estimation of TP diabatic heating is a basic problem. However, the magnitudes of surface sensible heat (SH) flux and latent heat (LH) flux have great discrepancies in different datasets (Cui and Wang, 2009; Shi and Liang, 2014; Xie et al., 2018; Yang Y. et al., 2019). The early works by Ye et al. (1957) and Flohn (1957) suggested that TP is a heat source for the surrounding atmosphere. The results of Flohn (1960) further indicated that SH is dominant prior to the monsoon onset, but LH becomes more important when the rainy season over TP arrives. Ye and Gao (1979) examined the diabatic heating over TP based on surface temperature from *in situ* observations. They concluded that TP is a heat source during summer and a heat sink in winter. Later studies further confirmed this finding (e.g., Luo and Yanai, 1983; Wu and Zhang, 1998; Duan and Wu, 2005). According to the results of Duan and Wu (2008), the SH reaches its maximum in May and June in the eastern and the western TP, respectively, and the mean SH in the western TP is larger than that in the eastern TP. The latent heat released to the atmosphere by precipitation reaches its maximum in summer (i.e., July) and is dominant in the eastern TP (**Figure 1A**). The SH presents a decreasing trend over TP (**Figure 1B**).

Changes of surface diabatic heating are closely related to the land surface processes (Yang et al., 2002; Wang C. et al., 2008; Wang et al., 2009b), such as the SM-FT process. A study showed that the magnitude of SH trend increases with elevation (Zhu et al., 2018), and the elevation dependency of the SH trend is related to the declining trend of snow depth in the recent decades, which is contributed by the strengthening of the difference between surface and air temperature (T_s-T_a). The soil moisture content over eastern TP shows a decreasing trend (Gao et al., 2015; Meng et al., 2018); this might be related to the freeze–thaw process, lead to the decline of land evapotranspiration (Jung et al., 2010), and affect surface diabatic heating consequently. The vegetation activity anomalies (e.g., NDVI) over TP caused by frozen ground changes can also affect the surface energy balance and result in surface diabatic heating anomalies (Zhang, 2005; Cuo et al., 2013).

TABLE 1 | Summary of current land surface datasets used in studies about the impacts of soil freeze–thaw and snow-melting.

	Description	Category	Coverage	Period	References
Soil moisture dataset	Measurements in agricultural meteorological stations collected by the China Meteorological Administration (CMA)	*In situ* data	China	1992–2010	/
	Global Land Data Assimilation System (GLDAS) products	Assimilation data	Globe	1949–present	Rodell et al., 2004
	Advanced Microwave Scanning Radiometer-Earth Observing System (AMSR-E) products	Satellite data	Globe	1979–2014	Njoku et al., 2003
	ERA-Interim, CPC are consist with the interannual variation of GLDAS2.0	Reanalysis data	Globe	1979–2010	Yang et al., 2016
Snow dataset	Monthly snow depth observations from CMA	*In situ* data	China	1981–2010	/
	Daily snow depth dataset derived from SMMR, SSM/I, and AMSR-E passive microwave remote sensing data	Microwave satellite data	China	1980– 2014	Che et al., 2008
	Snow cover fraction from MODIS	Satellite data	Globe	2001–2016	Pu et al., 2007
	Daily snow cover from the Interactive Multi-Sensor Snow and Ice Mapping System (IMS)	Derivation from a variety of data products including satellite imagery and *in situ* data	Globe	1997–present	Helfrich et al., 2007
	Comparing with ERA-Interim and ERA5, MERRA-2, and JRA55 have the best performance for snow depth	Reanalysis data	Globe	/	Orsolini et al., 2019
Surface sensible heat and latent heat dataset	Calculation from routine meteorological observations	/	Tibetan Plateau (TP)	1961–2003	Duan and Wu, 2008
	GAME/Tibet observations	*In situ*	TP	1994–2005	Li and Koike, 2003
	Among the CFSR, MERRA, ERA-Interim, and JRA-25, the RMSEs are larger than 10 W/m^2	Reanalysis data	TP	1979–2012	Shi and Liang, 2014

Relation Between Land Surface Processes and SM-FT

Due to the distinct characteristics of the land surface over TP, there being a large amount of frozen soil and extensive snow over TP (Qin et al., 2006; Che et al., 2008; Yang M. et al., 2019), their anomalies and changes must strongly influence the land surface processes (Wang et al., 2009b; Bao et al., 2017; Wang C. et al., 2017). For example, the runoff over TP increased due to snow melting and glacier retreating (Yao et al., 2007; Wang Z. et al., 2017; Gao et al., 2018). The SM-FT has significant impacts on the difference between surface and air temperature (T_s-T_a) before the onset of the East Asian summer monsoon (EASM) (Wang and Cui, 2011), which further leads to the surface diabatic heating anomalies. Studies showed that the energy and water exchanges between atmosphere and land are different between soil frozen and unfrozen periods (Wang and Shang, 2007; Wang et al., 2009b; Wang and Cui, 2011; Ge et al., 2016; Li et al., 2018). For example, the simulation conducted by Wang C. et al. (2008) over the western TP showed that soil water content increases with soil thawing (the LH increases), which has a considerable magnitude with SH in spring. The results from observations further confirmed this feature (Ge et al., 2016).

A distinct feature of the soil freeze–thaw (FT) process is the soil water phase change, which is distinguished from the unfrozen soil. As the soils freeze and their liquid water content decreases, a strong gradient in the matric potential develops, which drives the water toward the freezing front (Zhang et al., 2007; Swenson et al., 2012); while the soil is completely frozen, a small amount of soil liquid water, called "supercooled water," exists (Niu and Yang, 2007), with the soil thawing rapidly in spring as the soil moisture increases. A recent study from observations and model simulations over TP suggested that the soil FT process has a water storage effect. The storage index (SI), which is defined as the ratio between soil moisture after soil thawing and soil moisture before soil freezing, is used to quantify the water storage capability of soil during the FT process. It can reach up to 0.95 over TP (Yang and Wang, 2019b). Missing the soil FT process could result in drier soil (the loss of soil moisture is about 10%) because of the enhanced evaporation in the after-thaw (AT) period (i.e., spring). The land surface processes (i.e., land–atmosphere energy exchange) in cases of frozen soil and unfrozen soil are remarkably different. Variations of soil temperature and soil moisture further influence the surface diabatic heating status. A model simulation showed that, without the FT process, the mean surface latent heat flux and surface sensible heat flux over the whole TP can decrease by -1.07 W m^{-2} and increased by 4.72 W m^{-2}, respectively (**Figure 2**). Overall, the influence of the FT process on the soil moisture in spring is achieved through the water storage effect of FT.

Along with the soil FT process, the soil moisture, the soil temperature, and the surface diabatic heating vary dramatically. **Figure 3A** shows the evolution of soil moisture, precipitation, and surface SH flux and surface LH flux based on the daily *in situ* observation data in Maqu, with the thawing of frozen ground, soil moisture content, and LH increase. In particular, the increase of LH has a considerable magnitude with SH in spring;

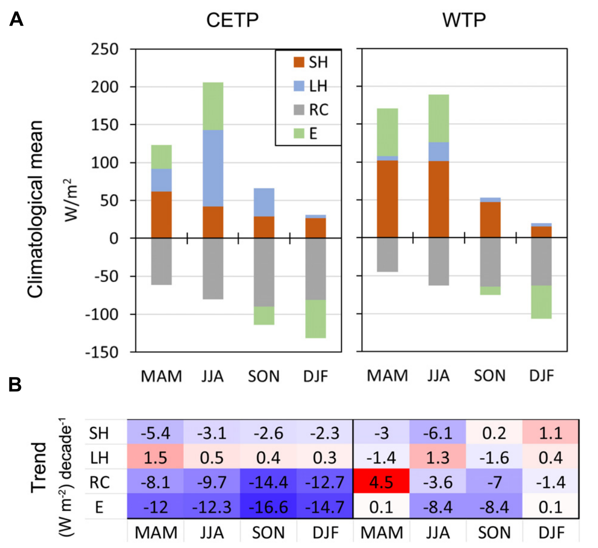

	MAM	JJA	SON	DJF	MAM	JJA	SON	DJF
SH	-5.4	-3.1	-2.6	-2.3	-3	-6.1	0.2	1.1
LH	1.5	0.5	0.4	0.3	-1.4	1.3	-1.6	0.4
RC	-8.1	-9.7	-14.4	-12.7	4.5	-3.6	-7	-1.4
E	-12	-12.3	-16.6	-14.7	0.1	-8.4	-8.4	0.1

FIGURE 1 | Characteristics of diabatic heating over Tibetan Plateau (TP). **(A)** Climatological mean (1984–2003) of surface sensible heat (SH), latent heat (LH) released to the atmosphere by precipitation, net radiation flux (RC) of the air column, and atmospheric heat source/sink (E) over the central and eastern TP and western TP. **(B)** Trend of atmospheric heat source/sink and its components. This figure is based on the data from Duan and Wu (2008).

about a month later, the LH continues to increase and becomes dominant, while the SH decreases, which is related to the coming of the rainy season over the eastern TP. Studies (e.g., Yang et al., 2002; Wang and Shang, 2007) suggested that the increase of soil moisture caused by the thawing of frozen ground about 20 days ago results in the onset of the subsequent rainy season of TP (**Figure 3B**) due to the supplement of abundant water vapor from surface evaporation. This implies that the thawing of frozen ground has an important role in the transition from dry season to wet season as well as the seasonal variations of surface diabatic heating over TP. The impacts of SM-FT on the coming of the wet season over TP can also be seen from the features of the clouds and the convection during the pre-onset periods of ASM. For instance, the results of Wang and Wang (2016) suggested that the frequency of a deep convective cloud increases rapidly after onset of the South Asian summer monsoon (SASM), which is attributed to the SM-FT process and the increase of surface diabatic heating (Wang et al., 2009a).

Snow over TP is a dominant factor that influences the surface diabatic heating through its albedo effect and hydrological effect (Barnett et al., 1989). The snow cover over TP has evident spatial and temporal variations (Wang et al., 2009c; Wang Z. et al., 2017; Bo et al., 2015). Studies suggested that variations in the spatial distribution of snow cover over TP induce the change of energy and water exchanges between land and atmosphere,

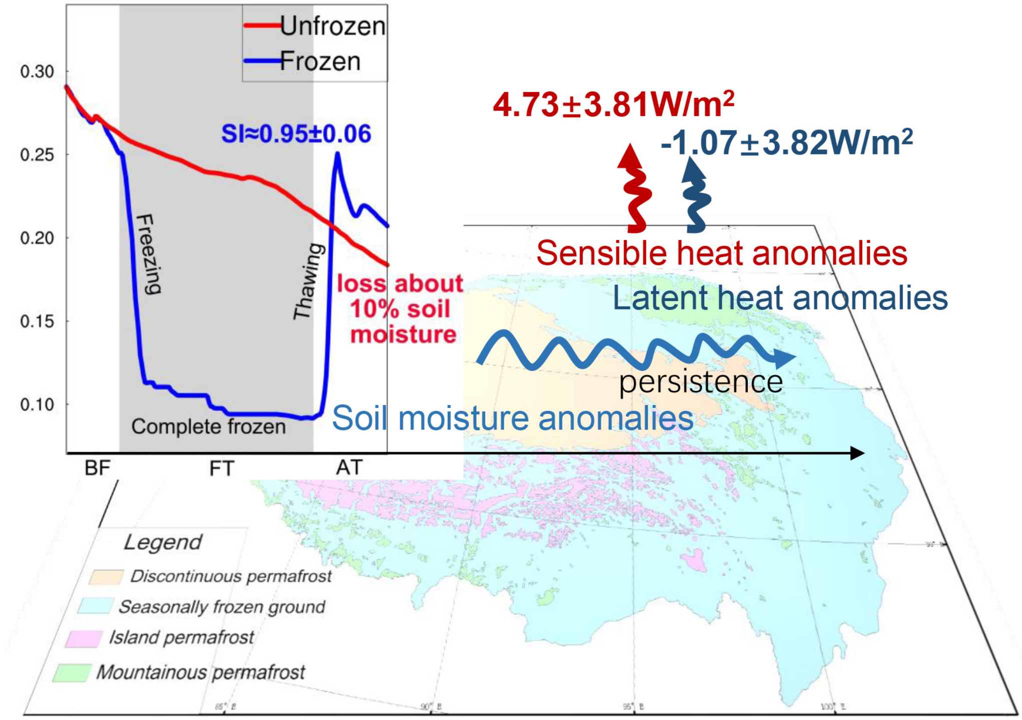

FIGURE 2 | Schematic diagram summarizing the impacts of soil freeze–thaw (FT) process on surface diabatic heating over Tibetan Plateau (TP). This diagram illustrates that soil moisture varies before freeze, FT, and after thaw (AT) periods, soil FT process has a water storage effect, and the storage index (SI) can reach 0.95 ± 0.06 at surface soil layer. Without the soil frozen process, the loss of soil moisture during AT period would be 10%, which further leads to anomalies of surface sensible heat by 4.73 ± 3.81 W/m^2 and anomalies of surface latent heat by –1.07 ± 3.82 W/m^2 through persistent soil moisture anomalies (Yang and Wang, 2019b). The map of the frozen soil over TP, including permafrost and seasonally frozen ground, comes from Li and Cheng (1996).

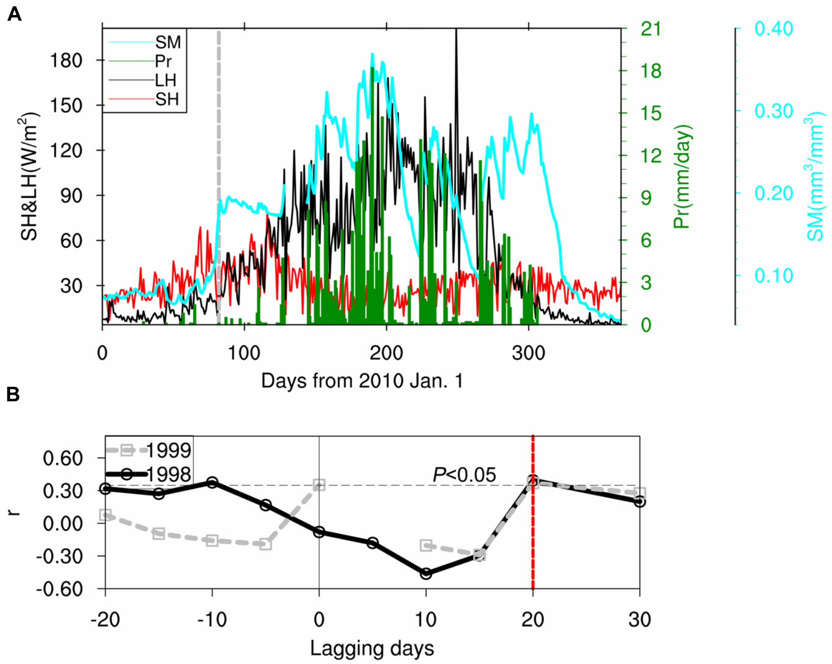

FIGURE 3 | (A) Evolution of the *in situ* observation of soil moisture (SM), precipitation (Pr), surface sensible heat (SH), and surface latent heat (LH) in Maqu; the gray dashed line indicates the date of soil complete thaw (days = 82). **(B)** Lagging correlations (*r*) between soil moisture and precipitation in TTH during spring in year 1998 (black solid line) and 1999 (gray dash line); the red dashed line represents the lagging days (=20) by which *r* in both 1998 and 1999 passes the Student *t* significant test ($p < 0.05$). This figure is based on the data in Wang and Shang (2007).

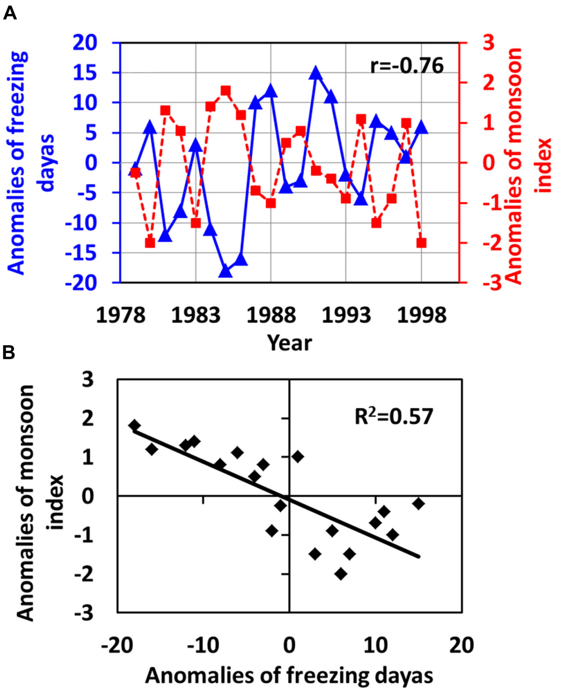

FIGURE 4 | (A) Changes in the anomalies of soil freezing days (blue solid line) and South China Sea summer monsoon index (red dashed line).
(B) Correlation between the anomalies of soil freezing days and the anomalies of South China Sea summer monsoon index (Shang and Wang, 2006).

thereby affecting surface diabatic heating and changing thermal forcing of TP to the atmosphere (Zhang and Tao, 2001; Zhu and Ding, 2007). Wang and Cui (2011) suggested that due to the cooling effect of snow cover over TP by albedo, the difference between surface and air temperature (T_s-T_a) presents a decreasing trend in April. The stronger winter–spring snow cover over TP would lead to the colder anomalies of surface temperature due to the increase of albedo; both the SH and the LH decrease before the snow is completely melted. Studies suggested that the hydrological effects are dominant and far more important than the direct thermal or albedo effect (Barnett et al., 2005; Xu and Dirmeyer, 2012). The snow melting favors the increase of soil moisture and results in the increase of latent heat flux, the decrease of sensible heat flux, and cooler surface; the surface diabatic heating anomalies persistently affect the atmospheric circulation until the summer (Barnett et al., 1989; Yasunari et al., 1991; Qian et al., 2003a; Wang C. et al., 2017).

CONNECTIONS BETWEEN SM-FT OVER TP AND ASM ACTIVITY

Many studies have emphasized on the contribution of TP thermal forcing to ASM (e.g., Ye et al., 1957; Ye and Gao, 1979; Wu and Zhang, 1998; Ye and Wu, 1998; Duan et al., 2005; Wu et al., 2012b; Cui et al., 2017). The changes of TP thermal forcing depend on the complex land surface process (e.g., SM-FT), which could influence the energy and water exchanges between land and

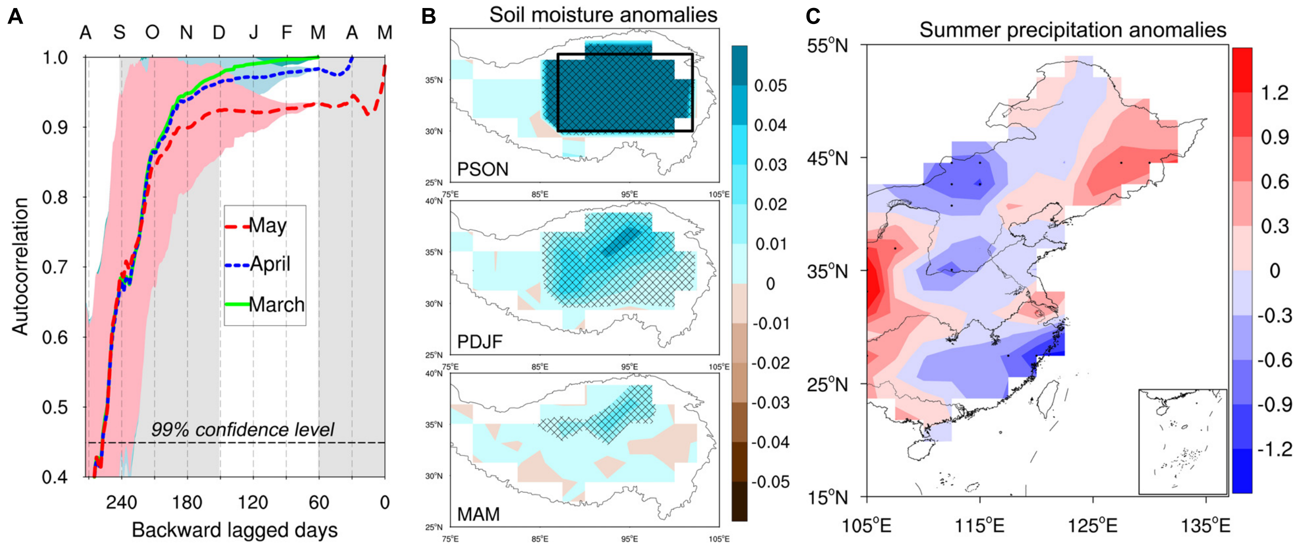

FIGURE 5 | Seasonal persistence of soil moisture anomalies and its impacts on summer precipitation in Eastern China (EC) (Yang and Wang, 2019a). **(A)** Soil moisture memory, which is defined as the lagged days when the autocorrelation of soil moisture does not pass significant test at 0.01. **(B)** Patterns of soil moisture anomalies during preceding autumn (PSON), preceding winter (PDJF), and spring (MAM), when soil moisture is increased over the eastern region of the Tibetan Plateau (rectangular box). **(C)** Corresponding pattern of summer precipitation anomalies (mm/day) in EC to the soil moisture anomalies in panel **(B)**.

atmosphere. There should be a connection between the SM-FT process over TP and the ASM activity.

An earlier study (Wang et al., 2003) suggested that the FT process over TP has significant impacts on the surrounding atmospheric circulations and is closely related with the summer precipitation in EC. As shown in **Figure 4**, the variation of the South China Sea summer monsoon is negatively correlated with the anomalies of soil frozen periods over TP (Shang and Wang, 2006). For instance, when the soil frozen period persists longer, the South China Sea Summer Monsoon would be weaker. Recent studies (Yang and Wang, 2019b,a) also indicated that the soil moisture memory calculated by the backward lagged correlation can reach up to 240 days (**Figure 5A**). This means that the soil moisture over TP during the preceding autumn (PSON) can persist up to spring (MAM), which is related to the soil FT process; the model simulation can also reproduce this persistence (**Figure 5B**). Similar as the spring soil moisture, the wetter soil moisture anomalies during PSON can lead to more precipitation over the Yangtze River Basin (YRB) and northeast China and less precipitation in south China and the Yellow River basin (**Figure 5B**); this corresponds to weak EASM. According to the water storage effect of the FT process, the mechanism associated with the impacts of the FT process over TP on EASM can be explained as follows: when the soil frozen periods are longer, more soil moisture anomalies can persist up to spring and favor the wetter anomalies of spring soil moisture; this would lead to weaker EASM. These results are consistent with the patterns of summer precipitation anomalies corresponding to the wetter spring soil moisture over TP (Wang et al., 2000, 2003; Chow et al., 2008; Li and Wang, 2016; Yang and Wang, 2019a).

The relationship between the anomalies of snow cover over TP and the ASM activity has been demonstrated by many studies (e.g., Chen, 1997, 1998, 2001; Chen and Wu, 2000; Qian et al., 2003a; Wu and Qian, 2003; Zhang et al., 2004; Wang et al., 2015). Many studies have demonstrated that there is a close relationship between snow cover over TP and EASM activity (Luo, 1995; Chen and Wu, 2000; Zhang and Tao, 2001; Xiao and Duan, 2016; Duan et al., 2018; You et al., 2020). For example, a heavier snow cover over TP can lead to a late onset of EASM and weaken the intensity of EASM. As a result, summer precipitation is less in south China and summer precipitation is more in the YRB (e.g., the flood occurs in YRB in 1998). The SASM is also a significant part of the ASM system, which has long been recognized to be influenced by snow cover over TP (Blanford, 1884; Chen and Wu, 2000; Fasullo, 2004; Brown and Mote, 2009; Dugam et al., 2009; Duan et al., 2014, 2018).

To explore the spatiotemporal variations of snow over TP and its relationship with ASM, **Figure 6** shows the distribution of standard deviation and climatological mean of snow depth in the cold season and the evaluations of a standardized series of snow depth averaged over southern TP (STP) and northern TP (NTP) based on a dataset derived from SMMR, SSM/I, and AMSR-E passive microwave remote sensing data (Che et al., 2008). The snow over TP distributes mainly over southeastern TP, Himalaya, Kunlun, and Qilian Mountains. The standard deviations (interannual variations) of snow depth over the whole TP are considerable (**Figure 6A**). The seasonal variations of winter–spring snow cover over TP contain the snow melting to some extent. Soil moisture anomalies may contain the information of snow anomalies in the preceding winter and spring through the snow melting process (Barnett et al., 1989; Yasunari et al., 1991; Qian et al., 2003a). Due to the complex underlying land surface (e.g., topography and vegetation type), there should be a

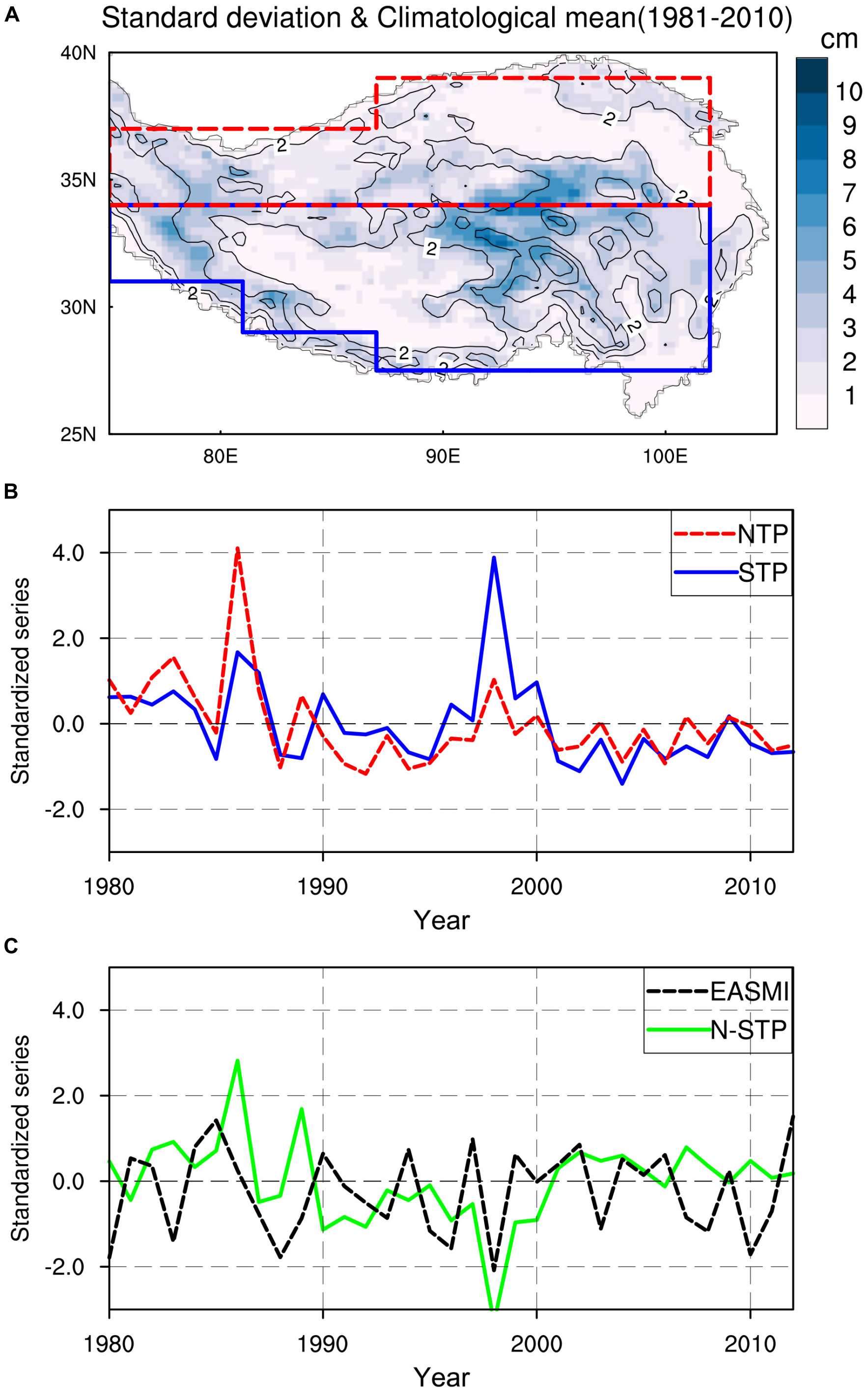

FIGURE 6 | (A) Distribution of stand deviation (color) and climatological mean (1981–2010; contour, interval is 4 cm) of snow depth over the Tibetan Plateau (TP) in the cold season (defined as the duration from November to April in the next year), regions surrounded by the blue dashed lines and red solid lines indicate the southern TP (STP) and northern TP (NTP), respectively. **(B)** Evaluations of standardized series of snow depth averaged over STP and NTP. **(C)** Evaluations of standardized series of snow depth differences between STP and NTP (N-STP) and East Asian summer monsoon index (EASMI) [defined by Li and Zeng (2001)]. The snow depth dataset is derived from SMMR, SSM/I, and AMSR-E passive microwave remote sensing data (Che et al., 2008).

great difference in spatial variations of snow cover. As shown in **Figure 6B**, the interannual and interdecadal variations of snow depth over STP and NTP have distinct differences (**Figure 6B**). The difference of snow depth between NTP and STP has a significant correlation with the East Asian Summer Monsoon Index. This indicates that the impacts of the

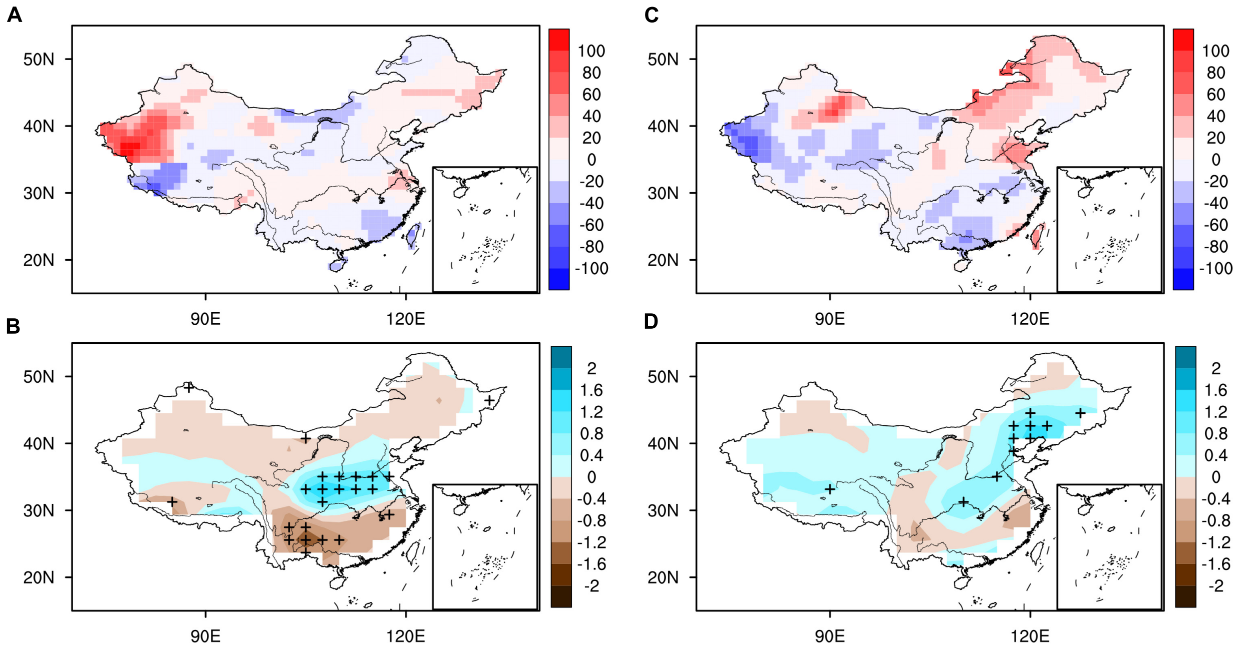

FIGURE 7 | The percentage distributions of precipitation anomalies (%; compared to 1981–2010 climatology) based on the daily precipitation data collected from 756 observation stations of the Chinese Meteorological Administration in a typical year of the Tibetan Plateau (TP) heavier snow cover in **(A)** southern TP (1987, which corresponds to weak Asian summer monsoon) and **(C)** northern TP (1990, which corresponds to strong Asian summer monsoon). The patterns of summer precipitation anomalies (sensitive experiments minus control experiment; mm/day) in Eastern China (EC) from a **(B)** sensitive experiment with heavier snow in southern TP and a **(D)** sensitive experiment with heavier snow in northern TP. The anomalies over the region with black crosses are statistically significant at 90% level under Student's *t* test (Wang C. et al., 2017).

spatiotemporal anomalies of snow over TP on the ASM system are significant.

Observations and numerical simulations have suggested that there is a strong positive correlation between winter snow cover and subsequent summer precipitation over the middle and the lower reaches of the Yangtze River valley (Chen, 1998, 2001; Wu and Qian, 2003). Recent studies (Wang C. et al., 2017; Yang et al., 2017) showed that the heavier snow cover during spring–winter over STP and NTP can lead to different patterns of summer precipitation in EC. **Figure 7** shows the percentage distributions of precipitation anomalies based on the daily precipitation data collected from 756 observation stations of the Chinese Meteorological Administration in a typical year of TP winter–spring heavier snow cover in STP and NST and the corresponding model simulations of summer precipitation anomalies by increasing surface albedo in STP and NTP during the period from November to March of the next year (Wang C. et al., 2017), with heavier snow cover in the southern TP corresponding to the weakened ASM and the stronger summer precipitation in the Yangtze River basin, but less summer precipitation in south China (**Figure 7A**); when snow is heavier in the northern TP, the ASM is enhanced. The summer precipitations in the YRB and north China become less and more, respectively, along with the northward shift of the rain belt (**Figure 7C**). Numerical simulations further confirm these patterns of summer precipitation anomalies in EC (**Figures 7B,D**). Results about the relation between winter–spring snow cover over TP and summer precipitation in EC have been applied in the operational summer climate prediction in China in the past years (Wang and Geng, 2012) and have achieved much success.

POSSIBLE MECHANISMS ASSOCIATED WITH THE CLIMATIC EFFECTS OF THE SM-FT PROCESS

Many studies have explored the physical mechanism by which TP thermal forcing affects the atmospheric circulation in East Asia (e.g., Wu and Qian, 2003; Wang B. et al., 2008; Wu et al., 2012a; Duan et al., 2014). For example, rising TP temperatures can trigger two distinct Rossby wave trains along the upper-level westerly jet and the low-level monsoon westerly, respectively, which propagate toward the downstream regions and enhance the low-level anticyclonic ridge (Wang B. et al., 2008). Wang et al. (2009a) indicated that surface diabatic heating over TP can enhance the low-frequency waves and force these to move northward and southward from TP. Li and Mao (2018) showed that the intra-seasonal Rossby wave train along the Asian westerly jet presents as the anomalous anticyclone over TP, which is located between anomalous cyclones in the upstream and the downstream areas, tending to trigger another reversed vertical–meridional cell with updraft over the south of the middle and the lower reaches of the Yangtze

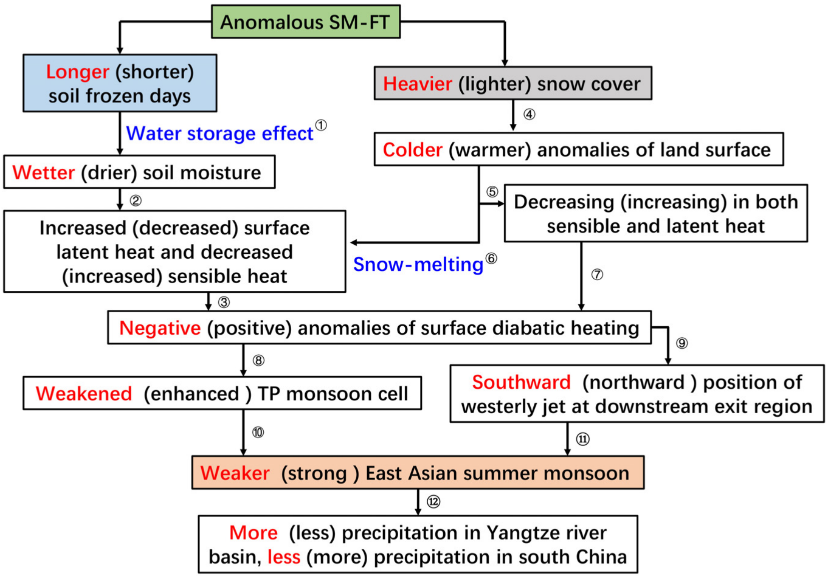

FIGURE 8 | Schematic diagram of the physical mechanism associated with the impacts of surface diabatic heating anomalies induced by snow melting and freeze–thaw anomalies on East Asian summer monsoon. This is a summary graphic derived from previous studies (i.e., ①: Wang and Shang, 2007; Yang and Wang, 2019a; ②, ③: Seneviratne et al., 2010; Zhang and Zuo, 2011; Yang and Wang, 2019b; ④, ⑤, ⑥, ⑦: Zhang and Tao, 2001; Qian et al., 2003a,b; Xiao and Duan, 2016; Wang C. et al., 2017; Duan et al., 2018; ⑧, ⑨: Yanai et al., 1992; Zhang et al., 2004; Zhu and Ding, 2007; Wang C. et al., 2017; ⑩, ⑪, ⑫: Qian et al., 2003a; Wang et al., 2003; Wu and Qian, 2003; Zhang et al., 2004; Shang and Wang, 2006; Zhu and Ding, 2007; You et al., 2020.

River valley (SMLY) and downdraft to the north through vorticity advection.

The thermal forcing anomalies of TP have direct impacts on the atmospheric circulation over TP and its surrounding regions, for instance, the vertical monsoon cell around TP and the westerly winds at the northern TP, which are the important systems of ASM (e.g., Ye and Wu, 1998; Schiemann et al., 2009). Recent studies (Wang C. et al., 2017; Yang et al., 2017) suggested that the negative anomalies of surface diabatic heating over TP induced by a heavier snow cover lead to the weakening of the ascent of the monsoon cell, the meridional temperature gradient over the northern TP and the mid-latitude westerlies. In addition, the position of the westerly jet at the downstream exit region also shifts southward because of the negative anomalies of surface diabatic heating over TP, which corresponds to low-level anomalous anticyclone over South China Sea and changes the water vapor transport in EC. When soil moisture anomalies induced by the FT process are wetter over TP, the physical mechanism explained by the anomalies of mid-latitude westerlies is also consistent (Yang and Wang, 2019a). By reviewing the previous studies (e.g., Yanai et al., 1992; Zhang and Tao, 2001; Qian et al., 2003a,b; Wang et al., 2003; Wu and Qian, 2003; Zhang et al., 2004; Shang and Wang, 2006; Wang and Shang, 2007; Zhu and Ding, 2007; Zhang and Zuo, 2011; Xiao and Duan, 2016; Wang C. et al., 2017; Yang and Wang, 2019b,a; You et al., 2020), the schematic diagram of the physical mechanism associated with the impacts of surface diabatic heating anomalies induced by the SM-FT process anomalies on EASM is depicted in **Figure 8**.

SUMMARY AND PROSPECTS

In this review, the robust roles of surface diabatic heating anomalies induced by the SM-FT process over TP in the activities of the ASM system are summarized. The variations of surface diabatic heating over TP are closely related to the SM-FT processes and play prior role in the formation of TP heat source of the atmosphere in spring and summer. The soil freeze–thaw process affects surface diabatic heating through water storage effect, which could result in about 10% change of the soil moisture content and up to 10 W m^{-2} anomalies of surface SH and LH. Winter–spring snow cover anomalies over TP lead to the surface diabatic heating anomalies through its albedo cooling effect and hydrological effects. The surface SH over TP shows a decreasing trend, which might be related to the changes of the SM-FT process under the warming background.

The SM-FT process over TP has a significant relation with the ASM activity. There is a negative correlation between the anomalies of soil frozen periods and South China Sea summer monsoon. The impacts of soil FT process over TP on the surrounding atmospheric circulation are through its effects on soil moisture anomalies. The winter–spring snow cover over TP has a significant negative relationship with the onset of ASM; the spatiotemporal anomalies of snow cover over the northern TP and the southern TP have distinct different impacts on ASM system, which is an effective signal in the seasonal prediction of summer precipitation in EC.

The possible physical mechanism associated with the impacts of the SM-FT process on the atmospheric circulation in East Asia is summarized as follows: the positive (negative) anomalies of surface diabatic heating over TP induced by the anomalous SM-FT could weaken (enhance) the ascent of the TP monsoon cell and lead to the southward (northward) position of the westerly jet at the downstream exit region. These further influence the belt of summer precipitation in EC. The TP thermal forcing anomalies affect the atmospheric circulation over the downstream region through the anomalous Rossby wave propagation.

The impacts of the soil freeze–thaw process and snow melting over TP on the ASM system have achieved much progress in the past decades. However, the uncertainties of surface diabatic heating estimation over TP still restrict our understanding on the thermal forcing effects of TP, especially over the western TP where the *in situ* observations are sparse and satellite retrievals are unreliable. Currently, the parameterization of the SM-FT processes in a numerical model still has great uncertainties, which partly results in the disagreement in model simulations of climate over TP and East Asia. How to accurately estimate the surface diabatic heating of TP by reasonably depicting the SM-FT processes is still the challenge in a future study.

AUTHOR CONTRIBUTIONS

CW designed the study, contributed to the idea, and completed the manuscript writing. KY contributed to the data analysis and manuscript writing. FZ contributed to the manuscript review.

FUNDING

This work was supported by the project "Changes in the Land–Atmosphere Coupling System on the Tibetan Plateau and Its Global Climate Effects," funded by the National Natural Science Foundation of China (91837205), and the National Natural Science Foundation of China (41661144017, 41801015, and 41805032).

REFERENCES

Bao, H. Y., Yang, K., and Wang, C. (2017). Characteristics of GLDAS soil-moisture data on the Tibet Plateau. *Sci. Cold Arid. Reg.* 9, 127–141.

Barnett, T. P., Adam, J. C., and Lettenmaier, D. P. (2005). Potential impacts of a warming climate on water availability in snow-dominated regions. *Nature* 438, 303–309. doi: 10.1038/nature04141

Barnett, T. P., Dümenil, L., Schlese, U., Roeckneg, E., and Latif, M. (1989). The effect of Eurasian snow cover on regional and global climate variations. *J. Atmos. Sci.* 46, 661–686. doi: 10.1126/science.239.4839.504

Blanford, H. F. (1884). On the connexion of the Himalaya snowfall with dry winds and seasons of drought in India. *Proc. Roy. Soc. Lond.* 37, 1–23.

Bo, Y., Li, X., and Wang, C. (2015). Seasonal characteristics of the interannual variations centre of the Tibetan Plateau snow cover. *J. Glaciol. Geocryol.* 36, 1353–1362.

Brown, R. D., and Mote, P. W. (2009). The response of Northern hemisphere snow cover to a changing climate. *J. Clim.* 22, 2124–2145. doi: 10.1175/2008jcli2665.1

Che, T., Li, X., Jin, R., Armstrong, R., and Zhang, T. (2008). Snow depth derived from passive microwave remote-sensing data in China. *Ann. Glaciol.* 49, 145–154. doi: 10.3189/172756408787814690

Chen, L. (1997). "The influence ofwinter–spring snowcover over Tibetan Plateau on atmospheric circulation and flood season precipitation in south China," in *Middle and Long-Term Water Temperature Forecast Corpus*, Vol. 1, (Beijing: China Waterpower Press*), 194–195.

Chen, L. (1998). Test and application of the relationship between anomalous snow cover in winter-spring over Qinghai-Xizang Plateau and the first summer precipitation in South China. *Q. J. Appl. Meteor.* 9, 1–32.

Chen, L. (2001). The role of the anomalous snow cover over the Qinghai-Xizang Plateau and ENSO in the great floods of 1998 in the Changjiang River valley. *Chin. J. Atmos. Sci.* 25, 184–192.

Chen, L., and Wu, R. (2000). Interannual and decadal variations of snow cover over Qinghai-Xizang Plateau and their relationships to summer monsoon rainfall in China. *Adv. Atmos. Sci.* 17, 18–30. doi: 10.1007/s00376-000-0040-7

Chow, K. C., Chan, J. C. L., Shi, X., Liu, Y., and Ding, Y. (2008). Time-lagged effects of spring Tibetan Plateau soil moisture on the monsoon over China in early summer. *Int. J. Climatol.* 28, 55–67. doi: 10.1002/joc.1511

Cui, Y., Chang, Z., Yu, L., and Wang, C. (2017). Effects of Qinghai-Xizang Plateau's spring surface diabatic heating anomalies on the East Asian summer monsoon intensity. *J. Arid Meteor.* 35, 1–11.

Cui, Y., and Wang, C. (2009). Comparison of sensible and latent heat fluxes from reanalysis datasets during the transition season over the western Tibetan Plateau. *Prog. Nat. Sci.* 19, 719–726. doi: 10.1016/j.pnsc.2008.11.001

Cuo, L., Zhang, Y., Wang, Q., Zhang, L., Zhou, B., Hao, Z., et al. (2013). Climate change on the northern Tibetan Plateau during 1957–2009: Spatial patterns and possible mechanisms. *J. Clim.* 26, 85–109. doi: 10.1175/jcli-d-11-00738.1

Ding, Y., Sun, Y., Wang, Z., Zhu, Y., and Song, Y. (2009). Inter-decadal variation of the summer precipitation in China and its association with decreasing Asian summer monsoon Part II: possible causes. *Int. J. Climatol.* 29, 1926–1944. doi: 10.1002/joc.1759

Ding, Y., Wang, Z., and Sun, Y. (2008). Inter-decadal variation of the summer precipitation in East China and its association with decreasing Asian summer monsoon. Part I: observed evidences. *Int. J. Climatol.* 28, 1139–1161. doi: 10.1002/joc.1615

Duan, A., Liu, Y., and Wu, G. (2005). Heating status of the Tibetan Plateau from April to June and rainfall and atmospheric circulation anomaly over East Asia in midsummer. *Sci. China Ser. D-Earth Sci.* 48, 250–257.

Duan, A., Wang, M., Lei, Y., and Cui, Y. (2013). Trends in summer rainfall over China associated with the Tibetan Plateau sensible heat source during 1980–2008. *J. Clim.* 26, 261–275. doi: 10.1175/jcli-d-11-00669.1

Duan, A., and Wu, G. (2005). Role of the Tibetan Plateau thermal forcing in the summer climate patterns over subtropical Asia. *Clim. Dyn.* 24, 793–807. doi: 10.1007/s00382-004-0488-8

Duan, A., and Wu, G. (2008). Weakening trend in the atmospheric heat source over the Tibetan Plateau during recent decades. Part I: observations. *J. Clim.* 21, 3149–3164. doi: 10.1175/2007jcli1912.1

Duan, A., Xiao, Z., and Wang, Z. (2018). Impacts of the Tibetan Plateau winter/spring snow depth and surface heat source on Asian summer monsoon: a review. *Chin. J. Atmos. Sci.* 42, 755–766.

Duan, A., Xiao, Z., Wu, G., and Wang, M. (2014). Study progress of the influence of the Tibetan Plateau winter and spring snow depth on Asian summer monsoon. *Meteorol. Environ. Sci.* 37, 94–101.

Dugam, S. S., Bansod, S. D., and Kakade, S. B. (2009). Pre-monsoon zonal wind Index over Tibetan Plateau and sub-seasonal Indian summer monsoon rainfall variability. *Geophys. Res. Lett.* 36:L11809.

Fasullo, J. (2004). A stratified diagnosis of the Indian Monsoon—Eurasian snow cover relationship. *J. Clim.* 17, 1110–1122. doi: 10.1175/1520-0442(2004)017<1110:asdoti>2.0.co;2

Flohn, H. (1957). Large-scale aspects of the "summer monsoon" in south and east Asia. *J. Meteor. Soc. Jpn.* 75, 180–186. doi: 10.2151/jmsj1923.35a.0_180

Flohn, H. (1960). "Recent investigations on the mechanism of the "summer monsoon" of southern and eastern Asia," *Paper Presented at Proceedings of the Symposium Monsoon of the World*, New Delhi.

Gao, B., Yang, D., Qin, Y., Wang, Y., Li, H., Zhang, Y., et al. (2018). Change in frozen soils and its effect on regional hydrology, upper Heihe basin, northeastern Qinghai–Tibetan Plateau. *Cryosphere* 12, 657–673. doi: 10.5194/tc-12-657-2018

Gao, Y., Li, X., Leung, L. R., Chen, D., and Xu, J. (2015). Aridity changes in the Tibetan Plateau in a warming climate. *Environ. Res. Lett.* 10, 34013–34024. doi: 10.1007/s00248-017-1098-4

Ge, J., Yu, Y., Li, Z., Xie, J., Liu, C., and Zan, B. (2016). Impacts of freeze/thaw processes on land surface energy fluxes in the permafrost region of Qinghai-Xizang Plateau. *Plateau Meteorol.* 35, 608–620.

Helfrich, S. R., Mcnamara, D., Ramsay, B. H., Baldwin, T., and Kasheta, T. (2007). Enhancements to, and forthcoming developments in the Interactive Multisensor Snow and Ice Mapping System (IMS). *Hydrol. Process.* 21, 1576–1586. doi: 10.5194/amt-11-2983-2018

Jung, M., Reichstein, M., Ciais, P., Seneviratne, S., Sheffield, J., Goulden, M., et al. (2010). Recent decline in the global land evapotranspiration trend due to limited moisture supply. *Nature* 467, 951–954. doi: 10.1038/nature09396 doi: 10.1038/nature09396

Li, D., and Wang, C. (2016). The relation between soil moisture over the Tibetan Plateau in spring and summer precipitation in the eastern China. *J. Glaciol. Geocryol.* 38, 89–99.

Li, J., and Mao, J. (2018). The impact of interactions between tropical and midlatitude intraseasonal oscillations around the Tibetan Plateau on the 1998 Yangtze floods. *Q. J. R. Meteorol. Soc.* 144, 1123–1139. doi: 10.1002/qj.3279 doi: 10.1002/qj.3279

Li, J., and Zeng, Q. (2001). A unified monsoon index. *Geophys. Res. Lett.* 29:1274. doi: 10.1029/2001GL013874

Li, S., and Cheng, G. (1996). *Frozen ground map of the Qinghai-Tibet Plateau*. Lanzhou: Gansu Culture Press.

Li, S., Yang, K., and Wang, C. (2018). Bias characteristics of land surface model (CLM4.5) over Tibetan Plateau during soil freezing-thawing period and its causes. *J. Glaciol. Geocryol.* 40, 322–334.

Li, X., and Koike, T. (2003). Frozen soil parameterization in SiB2 and its validation with GAME-Tibet observations. *Cold Reg. Sci. Technol.* 36, 165–182. doi: 10.1016/s0165-232x(03)00009-0

Liu, Y., Wu, G., Hong, J., Dong, B., Duan, A., Bao, Q., et al. (2012). Revisiting Asian monsoon formation and changes associated with Tibetan Plateau forcing: II. *Change Clim. Dyn.* 39, 1183–1195. doi: 10.1007/s00382-012-1335-y

Luo, H., and Yanai, M. (1983). The large-scale circulation and heat sources over the Tibetan Plateau and surrounding areas during the early summer of 1979. Part I: precipitation and kinematic analyses. *Mon. Wea. Rev.* 111, 922–944. doi: 10.1175/1520-0493(1983)111<0922:tlscah>2.0.co;2

Luo, Y. (1995). Studies on the effect of snow cover over the Qinghai-Xizang Plateau in winter and spring on general circulation over east Asia in summer. *Plateau Meteorol.* 14, 505–512.

Meehl, G. A. (1994). Coupled ocean-atmosphere-land processes and South Asian monsoon variability. *Science* 265, 263–267. doi: 10.1126/science.266.5183.263

Meng, X., Li, R., Luan, L., Lyu, S., Zhang, T., Ao, Y., et al. (2018). Detecting hydrological consistency between soil moisture and precipitation and changes of soil moisture in summer over the Tibetan Plateau. *Clim. Dyn.* 51, 4157–4168. doi: 10.1007/s00382-017-3646-5

Niu, G., and Yang, Z.-L. (2007). Effects of frozen soil on snowmelt runoff and soil water storage at a continental scale. *J. Hydrometeorol.* 7, 937–952. doi: 10.1175/jhm538.1

Njoku, E., Jackson, T., Lakshmi, V., Chan, T., and Nghiem, S. (2003). Soil moisture retrieval from AMSR-E. *IEEE Trans. Geosci. Remote Sens.* 41, 215–229. doi: 10.1109/TGRS.2002.808243

Orsolini, Y., Wegmann, M., Dutra, E., Liu, B., Balsamo, G., Yang, K., et al. (2019). Evaluation of snow depth and snow cover over the Tibetan Plateau in global reanalyses using in situ and satellite remote sensing observations. *Cryosphere* 13, 2221–2239. doi: 10.5194/tc-13-2221-2019

Pu, Z., Xu, L., and Salomonson, V. V. (2007). MODIS/Terra observed seasonal variations of snow cover over the Tibetan Plateau. *Geophys. Res. Lett.* 34:L06706.

Qian, Y., Zhang, Y., and Zheng, Y. Q. (2003a). Impacts of the Tibetan Plateau snow anomaly in winter and spring on precipitation in China in spring and summer. *J. Arid Meteor.* 21, 1–7.

Qian, Y., Zheng, Y., Zhang, Y., and Miao, M. (2003b). Responses of China's summer monsoon climate to snow anomaly over the Tibetan Plateau. *Int. J. Climatol.* 23, 593–613. doi: 10.1002/joc.901

Qin, D., Liu, S. Y., and Li, P. J. (2006). Snow cover distribution, variability, and response to climate change in western China. *J. Clim.* 19, 1820–1833. doi: 10.1175/jcli3694.1

Rodell, M., et al. (2004). The Global Land Data Assimilation System. *Bull. Amer. Meteor. Soc.* 85, 381–394.

Schiemann, R., Lüthi, D., and Schär, C. (2009). Seasonality and interannual variability of the westerly jet in the Tibetan Plateau region. *J. Clim.* 22, 2940–2957. doi: 10.1175/2008jcli2625.1

Seneviratne, S. I., Corti, T., Davin, E. L., Hirschi, M., Jaeger, E. B., Lehner, I., et al. (2010). Investigating soil moisture–climate interactions in a changing climate: a review. *Earth. Sci. Rev.* 99, 125–161. doi: 10.1016/j.earscirev.2010.02.004

Shang, D., and Wang, C. (2006). The effect of the frozen-thaw process in Tibetan Plateau on summer monsoon over Eastern Asia. *J. Arid Meteor.* 24, 19–22.

Shi, Q., and Liang, S. (2014). Surface-sensible and latent heat fluxes over the Tibetan Plateau from ground measurements, reanalysis, and satellite data. *Atmos. Chem. Phys.* 14, 5659–5677. doi: 10.5194/acp-14-5659-2014

Swenson, S. C., Lawrence, D. M., and Lee, H. (2012). Improved simulation of the terrestrial hydrological cycle in permafrost regions by the Community land model. *J. Adv. Model. Earth Syst.* 4:M08002. doi: 10.1029/2012MS000165

Wang, B., Bao, Q., Hoskins, B., Wu, G., and Liu, Y. (2008). Tibetan Plateau warming and precipitation changes in East Asia. *Geophys. Res. Lett.* 35:L14702. doi: 10.1029/2008GL034330

Wang, C., Shi, R., and Zuo, H. (2008). Analysis on simulation of characteristic of land surface in western Qinghai-Xizang Plateau during frozen and thawing. *Plateau Meteorol.* 27, 239–248.

Wang, C., and Cui, Y. (2011). Characteristics of the difference of temperature between surface and atmosphere over the Tibetan Plateau in the early stage of East Asian summer monsoon onset. *Clim. Environ. Res.* 16, 586–596.

Wang, C., Dong, A., Wang, S., and Yang, D. (2000). The correlation between precipitation in Northwest China during spring and snow depth in the Tibetan Plateau. *J. Glaciol. Geocryol.* 22, 340–346.

Wang, C., Dong, W., and Wei, Z. (2003). Study on relationship between the frozen-thaw process in Qinghai-Xizang Plateau and circulation in East-Asia. *Chin. J. Geophys.* 46, 309–316.

Wang, C., and Geng, L. (2012). Researching and application of the singular spectrum analysis combined with multi-regression in prediction of summer precipitation over China. *Meteorol. Mon.* 38, 41–46.

Wang, C., Li, Y., and Wang, Y. (2015). The impacts of interdecadal variability of circulation and Winter Monsoon on Winter Snowfall over the Tibetan Plateau. *Clim. Environ. Res.* 20, 421–432.

Wang, C., and Shang, D. (2007). Effect of the variation of the soil temperature and moisture in the transition from dry-season to wet-season over Northern Tibet Plateau. *Plateau Meteorol.* 26, 677–685.

Wang, C., Cui, Y., Jin, S., and Yan, Q. (2009a). Characteristics of Low Frequency Oscillation of spring atmospheric circulation over Qinghai-Xizang Plateau during strong and weak year of the South China Sea summer monsoon. *Prog. Nat. Sci.* 11, 1194–1202.

Wang, C., Shi, R., and Cui, Y. (2009b). Simulation analysis on characteristics of land surface over western Qinghai-Xizang Plateau during freezing–thawing period. *Sci. Cold Arid Reg.* 1, 329–340.

Wang, C., Wang, Z. L., and Cui, Y. (2009c). Spatial distributions and interannual variations of snow cover over China in the last 40 years. *Sci. Clod Arid. Reg.* 1, 509–518.

Wang, C., Yang, K., Li, Y., Wu, D., and Bo, Y. (2017). Impacts of Spatiotemporal Anomalies of Tibetan Plateau Snow Cover on Summer Precipitation in Eastern China. *J. Clim.* 30, 885–903. doi: 10.1175/jcli-d-16-0041.1

Wang, Z., Wu, R., and Huang, G. (2017). Low-frequency snow changes over the Tibetan Plateau. *Int. J. Climatol.* 38, 949–963.doi: 10.1002/joc.5221

Wang, Y., and Wang, C. (2016). Features of clouds and convection during the pre- and post-onset periods of the Asian summer monsoon. *Theor. Appl. Climatol.* 123, 551–564. doi: 10.1007/s00704-015-1372-7

Webster, P. J. (1998). Monsoons: processes, predictability and the prospects for prediction. *J. Geophys. Res.* 103, 14451–14510. doi: 10.1029/97jc02719

Wu, G. (1984). The nonlinear response of the atmosphere to largescale mechanical and thermal forcing. *J. Atmos. Sci.* 41, 2456–2476. doi: 10.1175/1520-0469(1984)041<2456:tnrota>2.0.co;2

Wu, G., Duan, A., Liu, Y., Mao, J., Ren, R., Bao, Q., et al. (2014). Tibetan Plateau climate dynamics: recent research progress and outlook. *Natl. Sci. Rev.* 2, 100–116. doi: 10.1093/nsr/nwu045

Wu, G., and Liu, Y. (2000). Thermal adaptation, overshooting, dispersion, and subtropical high. Part I: thermal adaptation and overshooting. *Chin. J. Atmos. Sci.* 24, 433–436.

Wu, G., Liu, Y., Dong, B., Liang, X., Duan, A., Bao, Q., et al. (2012a). Revisiting Asian monsoon formation and change associated with Tibetan Plateau forcing: I. Formation. *Clim. Dyn.* 39, 1169–1181. doi: 10.1007/s00382-012-1334-z

Wu, G., Liu, Y., He, B., Bao, Q., Duan, A., and Jin, F.-F. (2012b). Thermal controls on the Asian Summer Monsoon. *Sci. Rep.* 2:65. doi: 10.1038/srep00404

Wu, G., and Zhang, Y. (1998). Tibetan Plateau forcing and the timing of the monsoon onset over South Asia and the South China Sea. *Mon. Wea. Rev.* 126, 913–927. doi: 10.1175/1520-0493(1998)126<0913:tpfatt>2.0.co;2

Wu, T., and Qian, Z. (2003). The relation between the Tibetan winter snow and the Asian summer monsoon and rainfall: an observational investigation. *J. Clim.* 16, 2038–2051. doi: 10.1175/1520-0442(2003)016<2038:trbttw>2.0.co;2

Xiao, Z., and Duan, A. (2016). Impacts of Tibetan Plateau Snow Cover on the Interannual variability of the East Asian Summer Monsoon. *J. Clim.* 29, 8495–8514. doi: 10.1175/JCLI-D-16-0029.1

Xie, J., Yu, Y., Li, J., Ge, J., and Liu, C. (2018). Comparison of surface sensible and latent heat fluxes over the Tibetan Plateau from reanalysis and observations. *Meteorol. Atmos. Phys.* 131, 567–584. doi: 10.1007/s00703-018-0595-4

Xu, L., and Dirmeyer, P. (2012). Snow–atmosphere coupling strength. Part II: Albedo effect versus hydrological effect. *J. Hydrometeorol.* 14, 404–418. doi: 10.1175/jhm-d-11-0103.1

Yanai, M., Li, C., and Song, Z. (1992). Seasonal heating of the Tibetan Plateau and its effects on the evolution of the Asian summer monsoon. *J. Meteor. Soc. Jpn.* 70, 319–351. doi: 10.2151/jmsj1965.70.1b_319

Yang, K., Hu, T., and Wang, C. (2017). A numerical study on the relationship between the spring–winter snow cover anomalies over the northern and southern Tibetan Plateau and summer precipitation in East China. *Chin. J. Atmos. Sci.* 41, 345–356. doi: 10.3878/j.issn.1006-9895.1604.16119

Yang, K., and Wang, C. (2019a). Water storage effect of soil freeze-thaw process and its impacts on soil hydro-thermal regime variations. *Agric. For. Meteorol.* 265, 280–294. doi: 10.1016/j.agrformet.2018.11.011

Yang, K., and Wang, C. (2019b). Seasonal persistence of soil moisture anomalies related to freeze–thaw over the Tibetan Plateau and prediction signal of summer precipitation in eastern China. *Clim. Dyn.* 53, 2411–2424. doi: 10.1007/s00382-019-04867-1

Yang, K., Wang, C., and Bao, H. (2016). Contribution of soil moisture variability to summer precipitation in the Northern Hemisphere. *J. Geophys. Res. Atmos.* 121, 108–124.

Yang, M., Wang, X., Pang, G., Wan, G., and Liu, Z. (2019). The Tibetan Plateau cryosphere: observations and model simulations for current status and recent changes. *Earth. Sci. Rev.* 190, 353–369. doi: 10.1016/j.earscirev.2018.12.018

Yang, Y., Liu, Y., Li, M., Hu, Z., and Ding, Z. (2019). Assessment of reanalysis flux products based on eddy covariance observations over the Tibetan Plateau. *Theor. Appl. Climatol.* 138, 275–292. doi: 10.1007/s00704-019-02811-1

Yang, M., Yao, T., He, Y., Zhang, X., and Ma, Y. (2002). The water cycles between land surface and atmosphere in northern part of Tibetan Plateau. *Sci. Geogr. Sin.* 22, 29–33.

Yao, T., Pu, J., Lu, A., Wang, Y., and Yu, W. (2007). Recent glacial retreat and its impact on hydrological processes on the Tibetan Plateau. China, and surrounding regions. *Arct. Antarct. Alp. Res.* 39, 642–650. doi: 10.1657/1523-0430(07-510)[yao]2.0.co;2

Yasunari, T., Kitoh, A., and Tokioka, T. (1991). Local and remote responses to excessive snow mass over Eurasia appearing in the Northern spring and summer climate-a study with the MRI GCM. *J. Meteorol. Soc. Jpn.* 69, 473–487. doi: 10.2151/jmsj1965.69.4_473

Ye, D., and Gao, Y. (1979). *Meteorology of the Qinghai-Xizang Plateau*. Beijing: Chinese Science Press.

Ye, D., Luo, S., and Chu, P. (1957). The wind structure and heat balance in the lower troposphere over Tibetan Plateau and its surrounding. *Acta Meteor. Sin.* 28, 20–33.

Ye, D., and Wu, G. (1998). The role of the heat source of the Tibetan Plateau in the general circulation. *Meteorol. Atmos. Phys.* 67, 181–198. doi: 10.1007/bf01277509

You, Q., Wu, T., Shen, L., Pepin, N., Zhang, L., Jiang, Z., et al. (2020). Review of snow cover variation over the Tibetan Plateau and its influence on the broad climate system. *Earth. Sci. Rev.* 201:103043. doi: 10.1016/j.earscirev.2019.103043

Zhang, R., and Zuo, Z. (2011). Impact of spring soil moisture on surface energy balance and summer monsoon circulation over East Asia and precipitation in East China. *J. Clim.* 24, 3309–3322. doi: 10.1175/2011jcli4084.1

Zhang, S., and Tao, S. (2001). Influences of snow cover over the Tibetan Plateau on Asian summer monsoon. *Chin. J. Atmos. Sci.* 25, 372–390.

Zhang, T. (2005). Influence of the seasonal snow cover on the ground thermal regime: an overview. *Rev. Geophys.* 43:RG4002.

Zhang, X., Sun, S., and Xue, Y. (2007). Development and testing of a frozen soil parameterization for cold region studies. *J. Hydrometeorol.* 8, 852–861.

Zhang, Y., Li, T., and Wang, B. (2004). Decadal change of the spring snow depth over the Tibetan Plateau: the associated circulation and influence on the east Asian summer monsoon. *J. Clim.* 17, 2780–2793. doi: 10.1175/1520-0442(2004)017<2780:dcotss>2.0.co;2

Zhao, P., and Chen, L. (2001). Climatic features of atmospheric heat source/sink over the Qinghai-Xizang Plateau in 35 years and its relation to rainfall in China. *Sci. China Ser. D-Earth Sci.* 44, 858–864. doi: 10.1007/bf02907098

Zhu, L., Huang, G., Fan, G., Qü, X., Wang, Z., and Hua, W. (2018). Elevation-dependent sensible heat flux trend over the Tibetan Plateau and its possible causes. *Clim. Dyn.* 52, 3997–3400.

Zhu, Y., and Ding, Y. (2007). Influences of snow cover over Tibetan Plateau on weather and climate: advances and problems. *Meteorol. Sci. Technol.* 35, 1–8.

Conflict of Interest: The authors declare that the research was conducted in the absence of any commercial or financial relationships that could be construed as a potential conflict of interest.

frontiers
in Earth Science

ORIGINAL RESEARCH
published: 19 June 2020
doi: 10.3389/feart.2020.00226

Impact of Dust-Cloud-Radiation-Precipitation Dynamical Feedback on Subseasonal-to-Seasonal Variability of the Asian Summer Monsoon in Global Variable-Resolution Simulations With MPAS-CAM5

William K. M. Lau[1], Kyu-Myong Kim[2], Chun Zhao[3,4], L. Ruby Leung[5] and Sang-Hun Park[6]*

[1] Earth System Science Interdisciplinary Center, University of Maryland, College Park, MD, United States, [2] NASA Laboratory for Atmospheric Sciences, Goddard Space Flight Center, Greenbelt, MD, United States, [3] School of Earth and Space Sciences, University of Science and Technology of China, Hefei, China, [4] CAS Center for Excellence in Comparative Planetology, University of Science and Technology of China, Hefei, China, [5] Pacific Northwest National Laboratory, Richland, WA, United States, [6] Department of Atmospheric Sciences, Yonsei University, Seoul, South Korea

Edited by:
Kyung-Ja Ha,
Pusan National University,
South Korea

Reviewed by:
Renguang Wu,
Institute of Atmospheric Physics (CAS), China
Wen Chen,
Institute of Atmospheric Physics (CAS), China

***Correspondence:**
William K. M. Lau
wkmlau@umd.edu

Specialty section:
This article was submitted to Atmospheric Science, a section of the journal Frontiers in Earth Science

Received: *29 April 2020*
Accepted: *27 May 2020*
Published: *19 June 2020*

Citation:
Lau WKM, Kim K-M, Zhao C, Leung LR and Park S-H (2020) Impact of Dust-Cloud-Radiation-Precipitation Dynamical Feedback on Subseasonal-to-Seasonal Variability of the Asian Summer Monsoon in Global Variable-Resolution Simulations With MPAS-CAM5. Front. Earth Sci. 8:226. doi: 10.3389/feart.2020.00226

In this study, we investigate the effects of increased dust emission from the Middle East deserts on subseasonal-to-seasonal (S2S) variability of the Asian summer monsoon (ASM). Numerical experiments are performed using the Model for Prediction Across Scales (MPAS) coupled with the Community Atmosphere Model (CAM5) physics, with regional refinement at 30 km grid resolution over South Asia and the surrounding regions. Result shows that increased dust emission and transport from the Middle East/West Asia region induces a strong dust-cloud-radiation-precipitation-circulation feedback, resulting in a colder surface over the desert regions and the western Tibetan Plateau, but warmer and moister troposphere with enhanced cloudiness and precipitation over the Pakistan/Northwest India (PNWI) region. The latter changes are amplified by the dust aerosol induced Elevated Heat Pump (EHP) mechanism along the West Himalayas/Iranian Plateau foothill regions, most pronounced during May-June. During July-August, cloud radiation feedback further enhances the warming of the upper troposphere, and cooling of the land surface over the PNWI and adjacent regions over West Asia. The upper tropospheric heating and increased precipitation over PNWI spur a large-scale anomalous Rossby wavetrain and a northward displacement of the subtropical jetstream, manifesting in a contraction of the South Asian High and westward shift of the Western Pacific Subtropical High. As a result, the entire ASM precipitation-cloud system is displaced westward. Precipitation and cloudiness are intensified over northwest and western India and west Asia, but suppressed over southern and central East Asia. Analyses of the S2S variability of the upper level vorticity balance suggests that heating by Middle East dust plays an important role in exciting, and anchoring a teleconnection pattern through interactions among dust-cloud radiation, precipitation heating over the PNWI, the development of an upper level Rossby wavetrain, and the northward shift of the boreal summer jetstream over Eurasia.

Keywords: Asian summer monsoon, Middle East dust, Tibetan Plateau, aerosol-cloud radiative feedback, elevated heat pump, Rossby wavetrain, jetstream displacement, subseasonal-to-seasonal variability

INTRODUCTION

Light absorbing aerosols (LAA) consisting mainly of dust, black carbon (BC), organic carbon (OC) are well known to have strong impact on climate change in Asian summer monsoon (ASM) regions (Ramanathan et al., 2005; Lau et al., 2006, 2008, 2010; Meehl et al., 2008; Rosenfeld et al., 2008; Satheesh et al., 2008; Wang et al., 2009a,b; Bollasina et al., 2011; Sanap and Pandithurai, 2015; Li et al., 2016; Wu et al., 2016; Chu et al., 2018). From May through August, increasing monsoon southwesterlies transport large quantities of desert dusts from the Middle East across the Arabian Sea to the Indian subcontinent (Satheesh and Srinivasan, 2002; Deepshikha et al., 2005; Satheesh et al., 2006; Gautam et al., 2009a,b; Badarinath et al., 2010; and many others). Additionally, frequent outbreak of wildfires and the burning of agricultural waste also contribute to increased loading of LAA over South Asia during the pre-monsoon dry season (Zhang et al., 2020). As a result, abundant quantities of LAAs from both anthropogenic (industry, domestic consumption, and agricultural burning), and natural sources (dust and wildfires) build up to a thick and expansive layer over the Himalayas-Gangetic Plain during April-August (Gautam et al., 2010, 2011). The thick LAA layer provides an effective radiative heat source, which can trigger dynamical feedback through increased moisture and dust transport, enhanced latent heating, leading to a strengthened early monsoon via the so-called Elevated Heat Pump (EHP) feedback mechanism (Lau et al., 2006, 2008). Airborne LAA eventually falls back to the earth surface by dry and wet deposition. LAA in snow reduces the surface albedo and increases absorption of solar radiation, leading to accelerated snowmelt and warming of the surface, i.e., the snow-darkening effect. Deposition of LAAs on snow over the Himalayas-Tibetan Plateau is found to have strong impacts on the warming of the Tibetan Plateau, affecting the strength, and evolution of the ASM (Flanner and Zender, 2005; Flanner et al., 2007; Qian et al., 2009, 2015; Lau and Kim, 2018; Zhang et al., 2020).

During pre- and early monsoon, dust is by far the most dominant contributor to the atmospheric loading of LAAs affecting the Indian summer monsoon (ISM). The heating of the atmosphere by dust absorption of solar radiation over the North Arabian Sea, and Northwestern India is substantial (1–2.5 Kday^{-1}) during March-June, exceeding by as much as 1.5–2 times the forcing due to anthropogenic aerosols during the boreal winter (Ramachandran, 2005; Moorthy et al., 2007; Pandithurai et al., 2008; Satheesh et al., 2008; Das et al., 2015). More recently, observational and modeling studies have revealed significant impacts on variability of ISM induced by Middle East dust radiative forcing (Gautam et al., 2009a; Jin et al., 2014, 2016; Lau, 2014; Vinoj et al., 2014; Wei and Yang, 2014; Kim et al., 2015; Solmon et al., 2015). For monsoon dynamical feedback, Middle East dust is critically important because of (a) abundant transport by monsoon southwesterlies, (b) strong absorptive power due to its high content of iron-oxide (Sokolik and Toon, 1999; Alfaro et al., 2004), and (c) increased SW absorption due to coating by fine BC particles during passage over the densely populated regions of the ASM (Chandra et al., 2004; Prasad and Singh, 2007; Giles et al., 2012). Given the abundance of natural LAA, and their strong interactions with monsoon dynamics, it has been argued that LAA from natural sources should be considered an intrinsic component of the ASM climate system, contributing substantially to the subseasonal-to-seasonal (S2S) variability of the ASM (Lau, 2016; Li et al., 2016). Because the real climate interacts with ambient aerosols regardless of their sources, unraveling the intrinsic interactions of natural aerosol and climate is a prerequisite for better understanding of the impacts of anthropogenic aerosols on ASM. Yet, the mechanisms of interaction of LAA, in particular desert dust, with clouds, precipitation, and monsoon dynamics on S2S time scales are not well understood, and under-explored. The objective of this study is to delineate the fundamental processes that govern the interactions of LAA and ASM dynamics, from emission, transport, and radiative forcing to interactions with clouds, precipitation, convection, moisture transport, and the large-scale circulation, focusing on S2S variability of the ASM.

MODEL DESCRIPTION AND EXPERIMENTAL DESIGN

Global climate model (GCM) has been an essential tool for advancing understanding of aerosol-monsoon processes. For better simulations of climatic impacts of aerosol-precipitation-convection-circulation interactions in monsoon regions, the effects of complex topographic features such as the Himalayas-Tibetan Plateau are critically important and require high resolution, ensemble simulations at refined scales (30 km or less). Yet, up to now, most GCM experiments of aerosol-monsoon climate studies have been conducted with low-to-moderate resolution (>100–200 km) GCMs, because of the prohibitive computational resources needed for high-resolution (<30 km) GCM simulations. As a result, the effects of complex topography such as the Himalayas foothills and Tibetan Plateau region on aerosol-precipitation-convection-circulation interactions are not adequately represented in previous studies. Regional climate models (RCMs) with higher resolutions have also been used in downscaling studies, providing more realistic simulations of orographic effects on convective processes and extreme weather conditions in the ASM (Leung et al., 2003; Evans, 2011). However, RCMs are generally confined to a selected limited domain, not the entire ASM and influence regions, and are also hampered by their inability to simulate two-way interactions between the regional monsoon and the global circulation. As a result, global influence of the ASM cannot be studied using RCMs.

The global variable resolution Model for Predication Across Scales (MPAS) for the atmosphere has been designed to mitigate the aforementioned shortcomings associated with GCMs and RCMs (Skamarock et al., 2012). Through the use of regional refinement enabled by the unstructured grid, MPAS has been shown to produce high resolution regional climate and weather features comparable to those simulated by the model with global quasi-uniform high resolution mesh, but at a much smaller fraction of the computational cost (Sakaguchi et al., 2015; Zhao et al., 2019). Regional refinement also allows the regional climate simulated inside the refined mesh to exert remote influences outside the high-resolution region (Sakaguchi et al., 2016). In this study, we use the non-hydrostatic version of MPAS coupled with the physics package of Community Atmosphere Model version 5 (CAM5; Neale et al., 2012). Zhao et al. (2016) compared this non-hydrostatic MPAS-CAM5 with the hydrostatic MPAS-CAM4 used in Sakaguchi et al. (2015, 2016) in a hierarchy of aqua-planet simulations (Leung et al., 2013) and reported reduced sensitivity of the non-hydrostatic MPAS-CAM5 to model resolution compared to the hydrostatic MPAS-CAM4. A variable resolution mesh has been configured for this study similar to Zhao et al. (2016). The target high resolution (30 km) domain is centered over the complex terrain of the Middle East/Himalayas-Tibetan Plateau/South Asian monsoon region, transitioning to a low-resolution (120 km) domain covering the rest of the globe (**Figure 1**).

In the CAM5 physics package coupled in MPAS, cloud microphysics is represented by the Morrison and Gettelman (2008) scheme with prognostic cloud liquid and cloud ice and cloud droplet number. For cloud macrophysics, the total cloud fraction is calculated as the sum of the stratiform and convective cloud fractions. Cumulus convection is based on the Zhang and McFarlane (1995) scheme. Shallow convection and planetary boundary layer turbulence are based on a plume dilution model and a turbulence kinetic energy scheme described in Bretherton and Park (2009). The three-mode version of the modal aerosol scheme (MAM3) used in this study features Aitken, accumulation, and coarse modes. Aerosol components are internally mixed in each mode and the mass and number concentrations in each mode are updated during the simulation (Liu et al., 2012). The model includes important processes that influence the dust life cycle such as emission, dry and wet deposition. The Community Land Model, version 4.0 (CLM4) is used in this study and the CLM4 default data for soil properties, defined on a 1.9° × 2.5° mesh, is used for on-line calculation of dust emission fluxes. The Rapid Radiative Transfer Model for GCMs (RRTMG) is used for long-wave and shortwave radiative transfer (Iacono et al., 2000; Mlawer et al., 2016). Aerosol optical properties are calculated following Ghan and Zaveri (2007). The real component of dust refractive index varies only slightly in near-IR wavelengths (∼1.53), while its imaginary component varies between -0.004i and -0.03i. Aerosol influence on stratiform cloud microphysics droplet activation and ice nucleation are based Abdul-Razzak and Ghan (2002) and Liu et al. (2007).

Except for desert dust emissions, which are controlled by internal dynamics of the atmospheric surface and boundary layer processes, as well as land surface properties and states, emissions of BC, OC, and different types of natural and anthropogenic aerosols, and GHG gases are based on the present-day emission inventory from IPCC AR5 estimates (Lamarque et al., 2010). As a first step to tease out the roles of LAAs among the many control factors [sea surface temperature (SST), teleconnections, land use and change, emissions of diverse type of aerosols, and greenhouse gases] that are known to contribute to ASM climate variability and change, we carried out AMIP-type control integration with prescribed SST for the 10-year period (2000–2009), with full (both natural and anthropogenic) emission of LAAs (FEM). An identical experiment, except with the total LAA emissions cut by half (HEM) was carried out. The impacts of LAAs on ASM climate will be evaluated based on differences of key quantities between FEM and HEM (FEM-minus-HEM), hereafter referred to as "anomalies." Thus, the anomalies reflect the impact of increased LAA emissions and loading.

RESULTS

To begin our analysis, we examine the MPAS simulated aerosol and monsoon climatology, compared to observations. The simulated June-July-August (JJA) mean rainfall and 850 hPa winds show a reasonable distribution compared to MERRA2 reanalysis and TRMM, respectively, (**Figures 2A,B**), showing strong cross-equatorial Somali jet, prevailing southwesterlies over India/Southeast Asia, and southerlies over China. The model rainfall for the ISM shows fine structure associated with topography, including maximum rainfall over the western Ghats, the Himalaya foothills, and northeastern India. However, MPAS rainfall over the Bay of Bengal is deficient compared to TRMM. For the East Asian summer monsoon (EASM), both model and observation show that the seasonal mean rainfall is much weaker and less regionally confined compared to ISM, due to the strong influence of the subtropical jet, and larger variability in the locations of the EASM *Mei-yu* rain belt (Lau and Li, 1984; Lau et al., 2000; Ding and Chan, 2005; Wang, 2006; Zhang et al., 2006; Wang, 2009). Compared to TRMM, the model EASM rainfall is also under-estimated. For AOD, the model shows excessive dust loading over the source region near Middle East/northern Arabian Sea, northwestern Asia/eastern Eurasia, and the Taklamakan desert, compared to MODIS (**Figures 2C,D**). Over the Indian subcontinent, the Bay of Bengal/Southeast Asia, and Indo-Pacific oceanic regions, the model AOD is much weaker than MODIS. These suggest a more regional confined aerosol distribution in MPAS-CAM5 compared to MODIS, probably related to inadequate resolution of dust size distributions, and/or excessive dry and wet removal of aerosols, commonly found in numerous state-of-the-art climate models (Zender et al., 2003; Huneeus et al., 2011; Kok, 2011; Evan et al., 2014; Pan et al.,

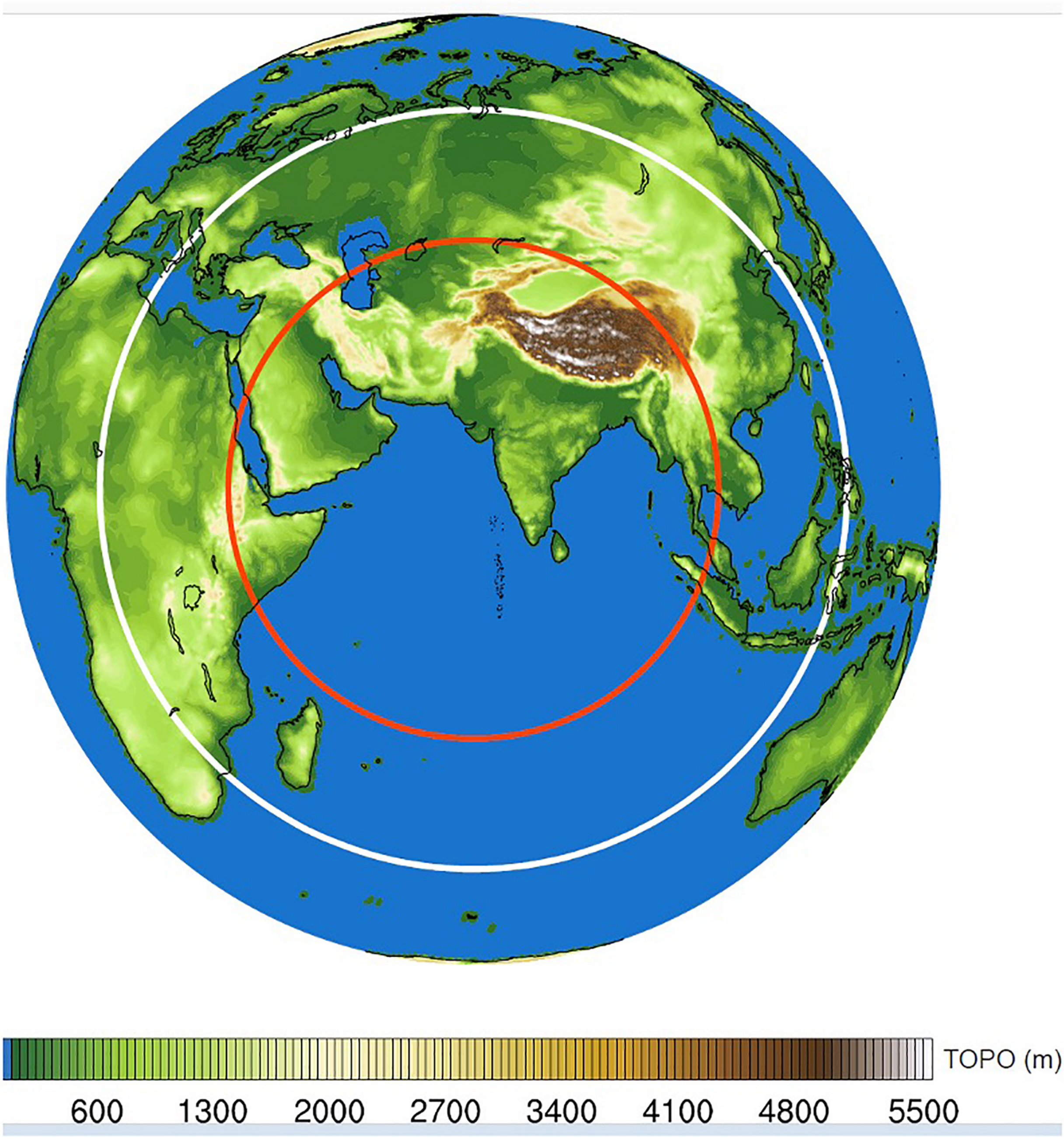

FIGURE 1 | Variable domain configuration in the MPAS experiments, with the highest resolution (25 km) centered over the target region of the Middle East desert and Indian monsoon region (inside red circle), transition via a buffer zone (between red and white circles) to the global domain with 110 km coarse resolution (outside the white circle).

2015). Possible implications of these model biases on the results are discussed in the "Conclusion" section.

AOD, Clouds, Precipitation and Circulation Changes

In this subsection, we examine the mean JJA anomaly patterns of AOD, temperature, moisture, clouds, and the large-scale circulation, respectively, over the desert-ASM domain, induced by the change in emissions of LAAs, based on the differences (FEM-minus-HEM) of these quantities. The AOD anomaly pattern (**Figure 3A**) shows clearly the dominance of dust forcing, featuring increased AOD over the Middle East desert regions, and the Taklamakan Desert over northwestern China, consistent with the experimental design (see section "Model description and experimental design"). In response, the land

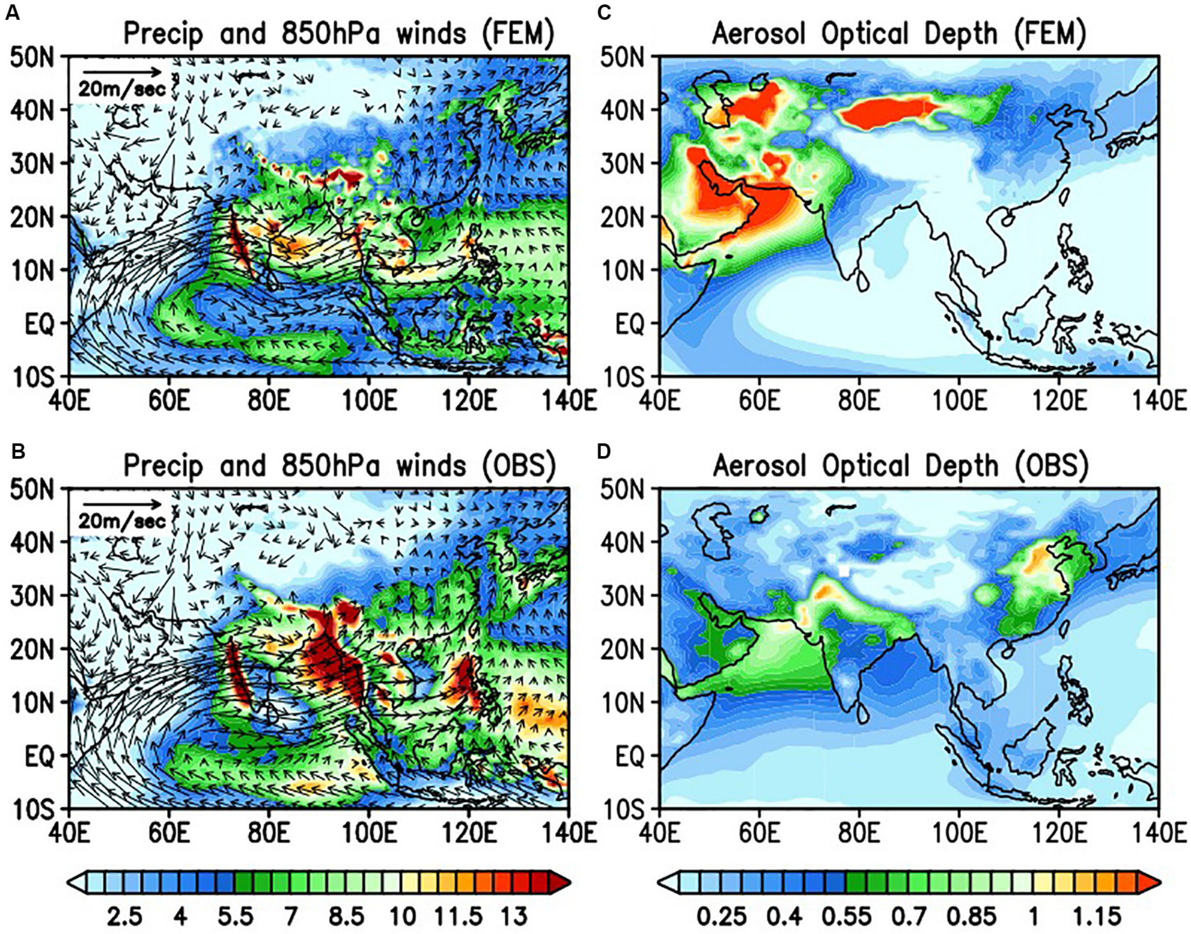

FIGURE 2 | Climatological distribution of precipitation (mm day^{-1}) and 850 hPa winds (ms^{-1}) for **(A)** MPAS simulations based on present-day aerosol emission inventory and full dust emission (FEM), with prescribed sea surface temperature (2001–2010), and **(B)** observations from TRMM and MERRA2 reanalysis (2001–2010). **(C,D)** Shows respectively AOD simulated by MPAS, and from MODIS satellite retrievals.

surface is cooled over the Middle East desert, the Tibetan Plateau, and northwestern India, and warmed over northern, and eastern Asia (**Figure 3B**). Anomalous warming of the lower and mid-troposphere is found over the desert and arid regions, centered around the Iran/Pakistan/West Himalayas region (**Figure 3C**). The tropospheric warming is mostly zonally oriented, spanning eastern Europe, central Asia to northeastern East Asia and appears to be coupled to an extensive zonally oriented cooling region over southern East Asia. Significant increase in cloudiness is found over the West Asia/Middle East region, the climatological arid region of Central Asia, and PNWI, accompanied by decreased cloudiness over East Asia and northwestern China (**Figure 3D**).

Seasonal mean (JJA) precipitation is increased over PNWI, in conjunction with the development of a cyclonic circulation cell over northwestern India, coupled to an anticyclonic cell over southern India and the Indian Ocean (**Figure 4A**). This circulation couplet strengthens the westerly moisture transport from the Arabian Sea to northwestern and western India and increases northward moisture transport from the North Arabian Sea to PNWI. As will be shown later (see **Figure 5**), the increased moisture transport to the PNWI leads to enhanced moisture convergence and cloudiness, which in turn increases shielding of solar radiation, and thus reduces the land surface temperature locally (see **Figure 3B**). Anomalous low-level easterlies are found near 15–25°N, spanning the western Pacific/South China Sea across Indo-China and PNWI. This curtails the climatological southwesterly moisture transport from the Bay of Bengal and northern India, to East Asia, resulting in suppressed precipitation and reduced cloudiness over central and southern China. The changes in precipitation, clouds and low-level winds are associated with the development of an upper tropospheric Rossby wavetrain spanning the subtropics and mid-latitudes of Eurasia, the Tibetan Plateau and East Asia. The wavetrain is likely the result of interaction of the upper tropospheric mean flow and a Rossby wave generated by the increased latent heating over PNWI region, and interaction with the jetstream (Rodwell and Hoskins, 1995). Here an elongated dipole anomaly in zonal winds at 200 hPa is found signaling a poleward shift of the jetstream that spans the Middle East, eastern Europe/central

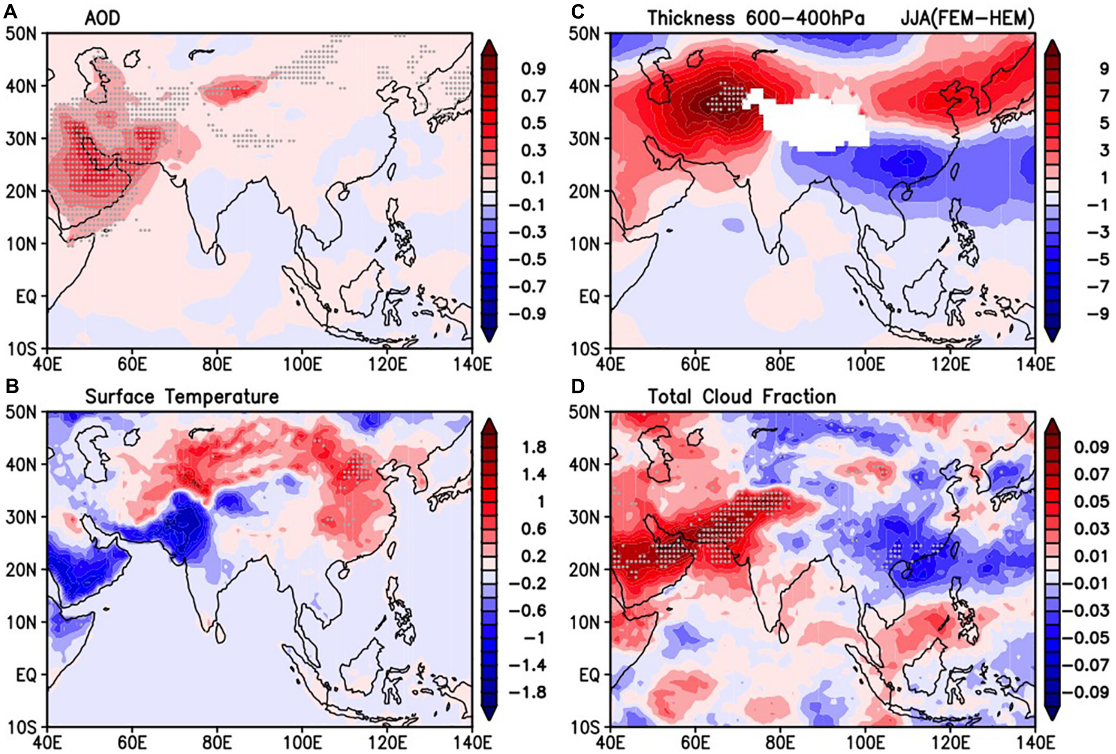

FIGURE 3 | MPAS simulated JJA anomalies in **(A)** AOD, **(B)** surface temperature (°C), **(C)** 600–400 hPa (gpm) thickness, and **(D)** cloud fraction. Anomalies are defined as the difference between FEM (full LAA emission) and HEM (half LAA emission).

Asia and East Asian regions, coupled to increased westerlies (reduced climatological upper level easterlies) over the southeast Asia/western Pacific region (**Figure 4C**). **Figure 4D** shows that the circulation changes reflect, in part, a westward shift of the West Pacific Subtropical High (WPSH), and a slightly weakened and contracted climatological South Asian High (SAH) consistent with reduced precipitation over southern and central East Asia (Lau and Li, 1984; Ding and Chan, 2005; Wang, 2006). Summing up, it can be inferred from results presented so far that increased LAA emission can lead to changes in major large-scale controls of the ASM, i.e., the WPSH, the SAH and the upper level jetstream spanning eastern Europe and East Asia.

Aerosol-Cloud Radiation, and Circulation Feedback

The roles of radiative forcing by LAAs and induced dynamical feedback of the coupled desert-ASM system are examined in this subsection. Over the desert and semi-arid regions (15–35°N, 40–70°E), the model LAAs consist of mostly dust (**Figure 5A**). Note that the concentration of dust by mass is in units of mg/kg, three order of magnitude more abundant than BC (μg/kg). The dust concentration is highest near the surface, but with significant concentration extending to the lower troposphere (∼600 hPa) and above. Over the desert and ISM region, the land surface and atmospheric boundary layer are cooled due to the blocking of downward SW by dust and BC, i.e., the solar dimming effect (Ramanathan et al., 2005). On the other hand, above the boundary layer, the troposphere is warmed by the SW absorption by dust. The warm above/cool below anomaly profile increases *local* atmospheric stability, i.e., the semi-direct effect (Hansen et al., 1997; Lohmann and Feichter, 2001), which tends to suppress convection. However, the warmer dust layer increases the low-to-mid troposphere meridional temperature gradient between the desert and the Arabian Sea to the south, thus enhancing the northward and westward transport of moisture from the North Arabian Sea to the land regions to the north (see **Figure 4A**). This can be seen in the deep layer of moist (high specific humidity) air over the desert/PNWI region (60–80E; **Figure 5C**). Together with the warming, this means a large increase in moist static energy ($C_pT + Lq$) and convective potential (**Figure 5B**). As the monsoon season advances, the increase in convective potential eventually overcomes the *local* solar dimming and semi-direct stabilizing effects through LAA induced dynamical feedback, resulting in increased latent heating over the desert and semi-arid regions (**Figure 5C**), most pronounced over the foothills of PNWI (70–80°E), and reduced latent heating over East Asia (100–120°E). For energy balance, large-scale circulation adjustments take place, with anomalous rising motions (adiabatic cooling) over the desert regions and sinking motions (adiabatic warming) connecting the desert/ISM and the EASM domain. The anomalous circulation redistributes clouds and precipitation over the entire desert-monsoon system, resulting in a warmer/wetter/more cloud desert and western

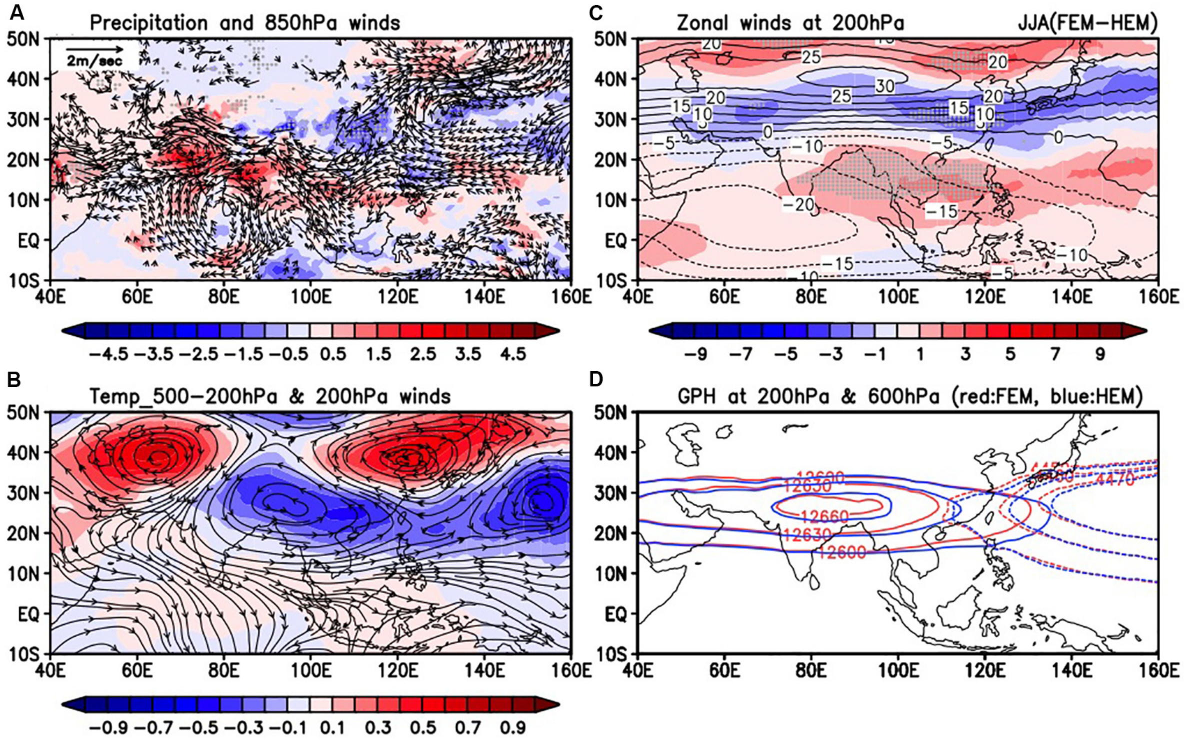

FIGURE 4 | MPAS simulated JJA anomalies in **(A)** precipitation (mm day^{-1}) and 850 hPa winds (ms^{-1}), **(B)** average temperature between 500 and 200 hPa (K), and 200 hPa winds (stremalines), **(C)** 200 hPa anomalous (colored) and climatological zonal winds (contoured), and **(D)** geopotential heights contours showing displacement of the SAH (200 hPa), and the North Pacific Subtropical High (600 hPa) due to changes in LAA radiative forcing from HEM (blue) to FEM(red).

ISM, and colder upper troposphere over the Tibetan Plateau (**Figure 5B**), coupled to a cooler/drier/less cloudy EASM. Over the desert/ISM domain, the meridional wind profile shows northerlies (negative anomalies) at upper levels in regions of increased high clouds, and southerlies (positive anomalies) in the lower troposphere, coupled to anomalies of opposite signs over the EASM domain (**Figure 5D**). These features represent regional manifestations of a contraction of the SAH and westward displacement of the WPSH (see **Figure 4D**), that are consistent with approximate vorticity balance governing thermally driven Rossby wave, circulation divergence, and zonal mean flow in a β-plane (Gill, 1980; Lau and Lim, 1982; Lau et al., 2000). Further discussion of Rossby wave-mean flow interaction is provided in section “Wavetrain-jetstream interactions.”

Since the increase in moisture over the desert/PNWI region (**Figure 5B**) is instrumental to the enhanced diabatic heating (**Figure 5C**) and subsequent changes in circulation and cloud fraction over an expansive region reaching East Asia, it is important to elaborate on the role of dust radiative forcing and cloud feedback in establishing the anomalous profile of temperature and moisture in the desert/PNWI region shown in **Figure 5B**. The strong radiative forcing by desert dust can be seen in the anomalous clear sky radiative forcing, indicating strong TOA radiative warming of the atmosphere-land system, over the Middle East, and PNWI region (**Figure 6A**) due to increased dust emission. Overall the atmosphere is warmed, and the surface is cooled (**Figures 6B,C**), due to the semi-direct effect. However, in the Middle East and PNWI (**Figure 6C**), the land surface is also warmed due to downwelling longwave radiation, as well as multiple reflection of sunlight by dust (Solmon et al., 2008; Xia and Zong, 2009; Gautam et al., 2010; di Sarra et al., 2011). The all-sky radiative forcing shows that cloud feedback plays an important role in expanding the regions of TOA radiative forcing over East Asia (**Figure 6D**, compared to **6A**), enhancing and expanding regions of atmospheric heating and cooling (**Figure 6E**, compared to **6B**). Notice that cloud radiative forcing has the largest effect at the surface, enhancing and expanding the surface cooling over the Middle East desert regions, and surface warming over East Asia (**Figure 6F** compared to **6E**) due to reduced cloudiness (see also **Figures 3B,D**).

A breakdown of the clear-sky radiative forcing over land regions of the western domain (40–75°E, 10–35°N) that includes the Middle East desert and PNWI, into shortwave (SW) and longwave (LW) radiation at TOA, ATM, and SFC (**Table 1A**), indicates that strong heating of the atmosphere (+7.6 Wm^{-2}), and cooling (−8.1 Wm^{-2}) of the surface due to SW semi-direct effect. However, while dust cools the atmosphere by LW radiation, it also contributes to land surface warming by downward longwave radiation (Huang et al., 2009; Zhao et al., 2016). As a result, the net effect of LAAs, as evident in the clear-sky total radiative (SW + LW) forcing is to warm *both* the atmosphere (2.9 Wm^{-2}), and the land surface

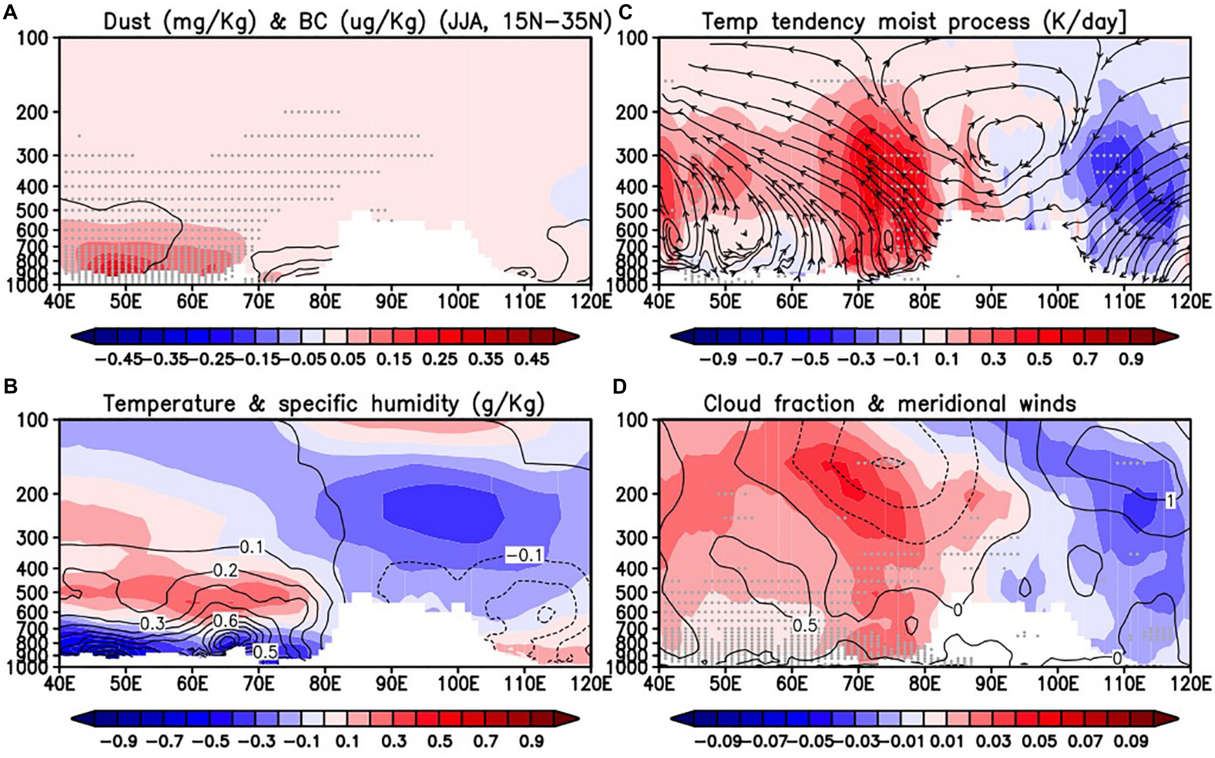

FIGURE 5 | MPAS simulated JJA anomalies in height-longitude profiles averaged over (15–35°N), across the desert-ASM domain (40–120°E) for **(A)** dust and BC loading, **(B)** temperature and specific humidity, **(C)** diabatic heating from moist processes, and streamline flow, and **(D)** cloudiness (color shading) and anomalies meridional winds (contours), with negative values denoting northerly winds (ms^{-1}).

(1.5 Wm^{-2}). These suggest that, in spite of the semi-direct effect cooling the surface, and increasing stability in the pre-monsoon season, enhanced radiative warming of the dust layer in lower troposphere over the desert region due to more dust emission is instrumental in increasing the meridional temperature gradient in the lower troposphere, and eventually leads to enhanced moisture transport, moisture convergence and precipitation over the northern PNWI.

In the presence of cloud feedback, as shown in the all-sky radiative forcing, the SW surface cooling is strongly enhanced (−13.4 Wm^{-2}) due to shielding by the increased cloudiness over the region (see **Figure 3D**). However, LW cooling of the atmosphere is much reduced (−1.6 Wm^{-2}) from the clear-sky values (−4.7 Wm^{-2}) due to trapping of LW by increased water vapor and clouds. This results in a net radiative heating of the atmosphere (+5.7 Wm^{-2}), almost double the clear-sky value (+2.9 Wm^{-2}), while inducing a net cooling (-3.2 Wm^{-2}) at the land surface, due to increased cloud shielding. This is the underlying reason for the presence of the shallow cooling air layer over land, overlain by a warmer tropospheric layer above (see **Figure 5B**). The increased heating of the dust layer enhances the meridional thermal gradient of the lower troposphere between the desert and the North Arabian Sea, facilitating the northward transport of moisture. The enhanced moisture near the surface, and in the planetary boundary layer increases the moist static energy, allowing convection to eventually break through the stability constraint by the local semi-direct effect, as the monsoon season advances. Hence clouds play an important role in enhancing the radiative heating in the dust layer, promoting moisture transport into the dust region, which further amplifies the cloud response in a cloud feedback loop.

Over the eastern domain (20–40°N, 75–120°E) which covers most the EASM region, the clear-sky radiative forcing is much smaller (<1 Wm^{-2}), and less consequential, compared to the western domain. This is consistent with the much lower model AOD over the region (**Figure 1C**). Here, the reduced cloudiness (see **Figure 3D**) consistent with the suppressed precipitation (see **Figure 4A**) contributes to the warming of the land, by increasing surface downward SW (+2.2 Wm^{-2}), resulting in a net radiative warming of the surface (+1.7 Wm^{-2}). Given the much smaller values of the clear sky SW and LW forcing over the eastern compared to the western domain, it may be inferred that strong aerosol radiative forcing is restricted to the western (desert) domain, and that changes in EASM rainfall are due largely to dynamically induced circulation-cloud radiation feedback processes.

S2S Variability

The physical processes governing the atmospheric loading and radiative forcing of LAAs are strongly dependent on winds and precipitation and are therefore closely linked to intrinsic monsoon S2S variability. Here the monthly evolution of various

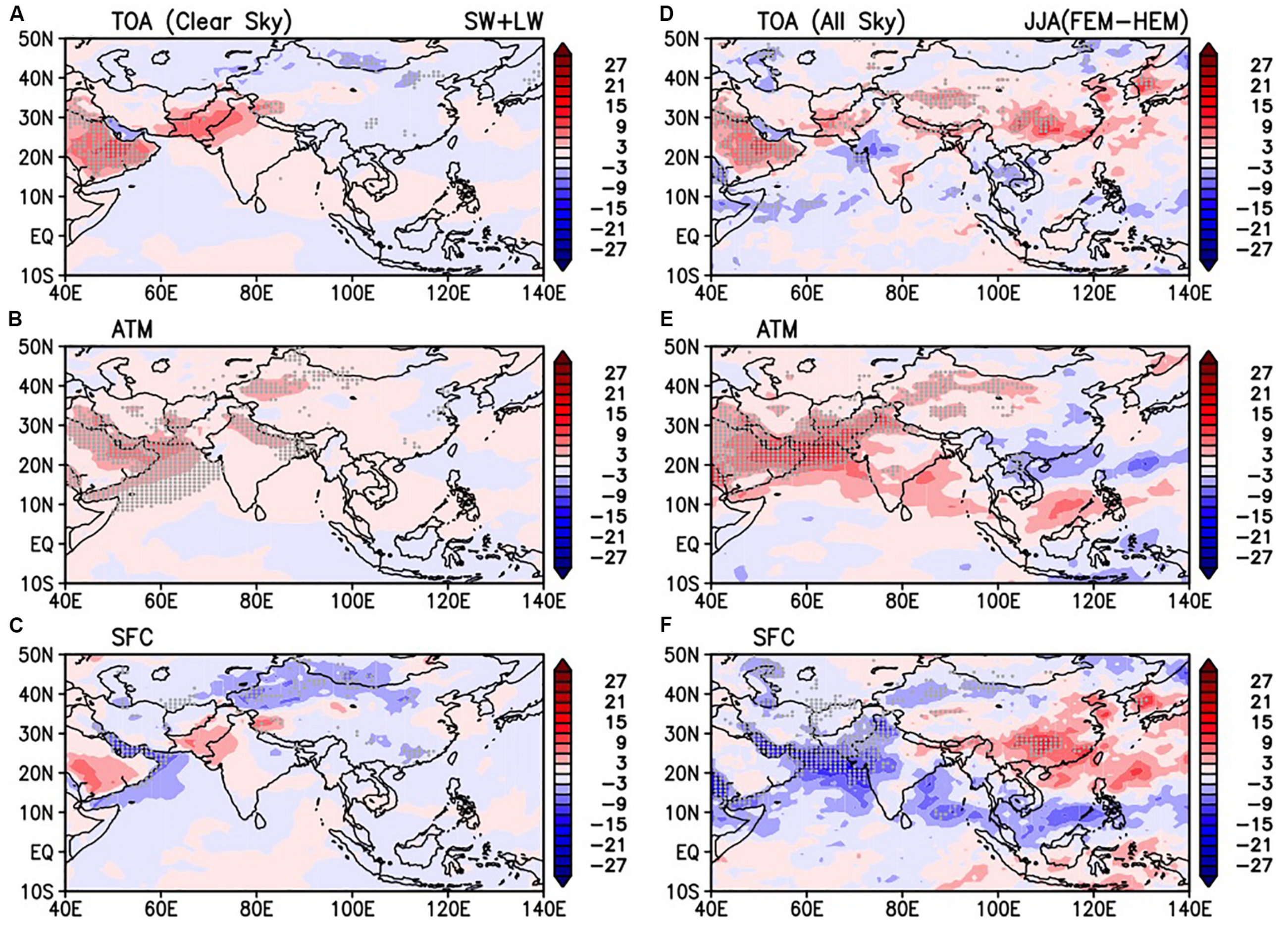

FIGURE 6 | MPAS simulated JJA anomalies in clear-sky radiation (SW + LW) for **(A)** top-of-the-atmosphere (TOA), **(B)** atmosphere (ATM), and **(C)** surface (SFC). **(D–F)** Are the same for **(A–C)**, except for All-Sky radiation. Unit in Wm^{-2}.

TABLE 1 | Clear sky, and all-Sky radiation anomalies (Wm^{-2}) for JJA, at top of the atmosphere (TOA), over the atmospheric column (ATM), and at the surface (SFC) for the land regions of **(A)** the western domain (40–75°E, 10–35°N) that include the Middle East desert, western India, and **(B)** the eastern domain (75–120°E, 20–40°E) covering northeastern India and the East Asian region. JJA (Land only).

	Clear sky			**All sky**		
	SW	**LW**	**SW + LW**	**SW**	**LW**	**SW + LW**
(A) West Domain (40–75 E, 10–35 N)						
TOA	−0.5 ± 0.70	4.8 ± 0.87	4.4 ± 1.52	−6.0 ± 1.12	8.6 ± 2.21	2.6 ± 1.14
SFC	7.6 ± 0.57	−4.7 ± 0.56	2.9 ± 0.80	7.4 ± 0.54	−1.6 ± 0.83	5.7 ± 0.85
ATM	−8.1 ± 1.09	9.5 ± 1.33	1.5 ± 2.17	−13.41 ± 1.14	10.2 ± 1.59	−3.2 ± 0.91
(B) East Domain (75–120 E, 20–40 N)						
TOA	−0.1 ± 0.36	−0.1 ± 0.48	−0.2 ± 0.79	3.0 ± 211	−0.8 ± 1.54	2.2 ± 0.76
ATM	1.1 ± 0.27	−0.1 ± 0.47	1.0 ± 0.43	0.8 ± 0.35	−0.2 ± 0.61	0.6 ± 017
SFC	−1.1 ± 0.46	−0.0 ± 0.81	−1.1 ± 1.11	2.2 ± 2.38	−0.5 ± 1.25	1.7 ± 120

changes induced by LAAs is investigated. During April-May, AOD is substantially increased over the Middle East deserts due to the doubling of emissions, from the experimental design. Over the Indo-Gangetic Plain and northern India, AOD is increased (**Figure 7A**, for May) stemming from the transport by the strengthening monsoon seasonal southwesterlies. At this time, the land surface of the desert and Indian subcontinent is cooled due to AOD SW shielding, while SW absorption by the dust layer heats the lower troposphere (see **Figure 8C**, later). This increases atmospheric stability, i.e., the semi-direct effect, resulting in reduced vertical heat transport from the boundary layer to the free atmosphere, and anomalous cooling of the mid-troposphere (**Figure 7E**), as well as reduced precipitation over the desert, the Indian subcontinent, and adjacent oceanic regions (**Figure 7I**).

As the monsoon season advances, AOD loading remains strong over Middle East deserts and downstream regions from June-August due to enhanced dust emission, and transport by the strengthening seasonal westerly low-level winds. However, the AOD increase is mostly confined to the deserts and PNWI, but less pronounced over the rest of the India subcontinent and adjacent oceans during (**Figures 7B–D**), due to removal by wet deposition and washout from increased precipitation (**Figures 7J–L**). During June, the troposphere over the land regions north of the Arabian Sea is anomalously warmer compared to regions to the south (**Figure 7F**) due to induced dust-cloud-radiation-circulation feedback (see later discussion for **Figure 8** for details). This leads to the development of a low-level cyclone over PNWI, and increased precipitation across northwest and central India, with increased low-level westerlies, transporting moisture from the Arabian Sea, and the equatorial Indian Ocean to the Indian subcontinent (**Figure 7J**). The tropospheric warming over the land north of the Arabian Sea maximizes over the western Himalayas//Iranian Plateau (WHIP) region in July and August (**Figures 7G,H**). In July, the PNWI cyclone is somewhat weakened, with increased precipitation spread over central India and the southern Bay of Bengal, and increased low level westerlies is confined to southern Arabian Sea (**Figure 7K**). In August (**Figure 7L**), the cyclonic cell is re-established, and precipitation is re-invigorated over PNWI. These reflects enhanced S2S variability of the ISM.

The topography of the WHIP region (25–35°N, 60–75°E) plays an important role in the aforementioned dust-induced dynamical feedback processes. During May-June, dust aerosols from local emission and transported from the Middle East deserts accumulate over the southern slopes of the WHIP and land region to the south, and get lofted to the mid- and upper troposphere, by orographically forced ascent and local convection (**Figures 8A,B,E,F**). BC from prescribed local emission is also increased (doubled by the experimental design) in the southern foothills of WHIP. Strong SW heating (0.2–0.4 K day^{-1}) is found in the lower and mid-troposphere over the WHIP foothills, and northern Arabian Sea, near 10–35°N (**Figures 8C,G**). Judging from the similar spatial distributions of the SW heating and dust burden, it is evident that the SW heating is due mostly to dust. This is so even though BC is highly absorbing, due to its much lower atmospheric burden compared with dust, and limited spatial distribution. During May-June, the dust SW heating induces a dynamical feedback that increases the tropospheric thermal land-sea contrast, strengthening the early monsoon, consistent with EHP effect (Lau et al., 2006, 2008). The time-delayed effect of EHP, i.e., building up of convective potential against the local stabilizing effect of dust, and eventually breaking out of deep convection, is evident in the transition from reduced precipitation in May to increased precipitation in June over the region (**Figures 8D,H**). An analysis of the daily accumulated rainfall shows that the EHP feedback advances the monsoon rainy season for ISM by about 1–2 weeks and slightly delays that for EASM by approximately 1 week (**Supplementary Figure S1**).

As the monsoon matures during July-August, the anomalous warming of WHIP in the mid- and upper troposphere intensifies, further enhancing the tropospheric meridional thermal gradient, and ascent near 20–30°N (**Figures 8I,M**). At this time, accumulation and loading of dust and BC and associated SW heating over WHIP foothills are substantially reduced (**Figures 8J,N**) due to wet removal by increased precipitation (**Figures 8L,P**). Enhanced SW heating is found in the upper troposphere (**Figures 8K,O**), stemming from absorption by increased high clouds associated with enhanced deep convection and ice-phase precipitation (see **Supplementary Figure S2**). The increased high clouds also cause strong SW cooling near the surface and the lower troposphere in August (**Figure 8O**), due to SW cloud shielding effects (Ramanathan and Collins, 1991; Lau et al., 2019). Essentially, the tropospheric temperature contrast forced by dust radiative heating during the early monsoon season is amplified and sustained through cloud radiation-precipitation-circulation feedback, affecting the entire ASM monsoon. However, as noted in the month-to-month variations of precipitation over PNWI (**Figures 8D,H,L,P**), and related quantities, the changes are not monotonic, but rather exhibiting amplitude modulation from May through August.

Wavetrain-Jetstream Interactions

In this section, we examine the roles of dust radiative-precipitation-circulation feedback processes in modulating the wavetrain-jetstream interactions affecting S2S variability of the ASM. The interaction of diabatic heating, Rossby wavetrain and jetstream, giving rise to characteristic planetary scale features in the upper troposphere are well known (Hoskins and Ambrizzi, 1993; Rodwell and Hoskins, 1995; Enomoto et al., 2003; Sato and Takahashi, 2003). Previous observational studies have unveiled a family of upper tropospheric teleconnection patterns with different flavors that can affect the boreal summer regional ASM variability from subseasonal to interdacadal time scales. These include among others, the Asian-North American (ANA) pattern, the Europe-Asia (EA) pattern, the Silk Road Pattern (SRP), the jet meridional displacement (JMD), and the circumglobal teleconnection (CGT; Lau and Weng, 2002; Lu et al., 2002; Enomoto, 2004; Wakabayashi and Kawamura, 2004; Ding and Wang, 2005, 2007; Song et al., 2013; Du et al., 2016; Hong and Lu, 2016; Wang et al., 2017; Stephan et al., 2018; Xue and Chen, 2019; and others).

In the extended domain (**Figure 9A**), the Rossby wavetrain at 200 hPa is clearly seen in the anomalous winds spanning the entire boreal summer jetstream region from Central to East Asia and the western Pacific (25–45°N, 40–160°E). The western portion of the wavetrain (C_1-A_1-C_1) is oriented in a NW-SE direction, across the jet axis (~40°N) from eastern Europe to northern India, while the eastern portion (A_2-C_2)

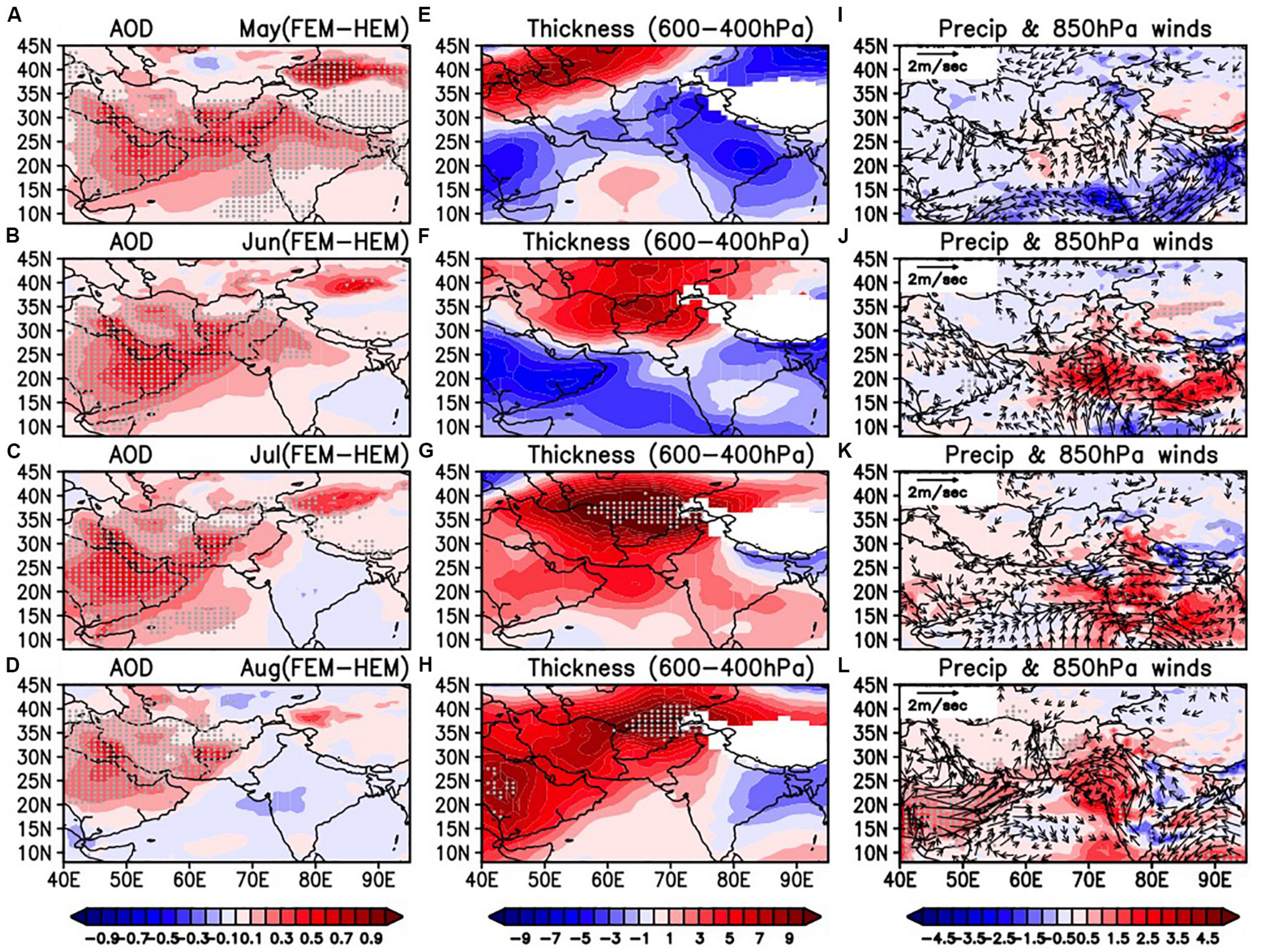

FIGURE 7 | Simulated monthly variation over the desert-ISM domain for anomalous AOD in **(A)** May, **(B)** June, **(C)** July, and **(D)** August. Panels **(E)**, **(F)**, **(G)**, and **(H)** are the same as **(A)**, **(B)**, **(C)**, and **(D)**, except for 600–400 hPa geopotential thickness (gpm). Same for Panels **(I)**, **(J)**, **(K)**, and **(L)**, except for precipitation (mm day^{-1}) and 850 hPa winds (ms^{-1}).

appears to be oriented along and slightly south of the jet axis. Most prominent are two anomalous anticyclone-cyclone pairs found near the jet entrance and exit regions, respectively. For the former, the anticyclone (A_1) is located northwest of the maximum precipitation heating over PNWI, consistent with thermally forced upper level Rossby wave by latent heating (Gill, 1980). Likewise, the cyclone (C_1) over the Tibetan Plateau is dynamically consistent with cooling of the upper troposphere over the Tibetan Plateau (see **Figure 5B**) the contraction of the SAH, and reduction in precipitation over central and southern East Asia noted earlier (see **Figures 4A,D**). Over eastern East Asia and the western Pacific, the anticyclone-cyclone pair (A_2-C_2) reflects the signature of upper level wave-mean flow interaction, associated with the northward shift of the jetstream, and westward displacement of the WPSH.

In conjunction with the Rossby wavetrain development, there is a northward shift of the jetstream (**Figure 9B**, see also **Figure 4C**). Here, we also note that the jetstream shift is associated with east-west elongated bands of surface cooling of the Middle East desert/PNWI, warming of Central Asia/Western China, and cooling further north. This anomalous surface temperature pattern is consistent with thermal wind balance, related to changes in zonal wind vertical shear (Holton, 1993). The surface cooling (warming) pattern corresponds to increased (decreased) cloudiness, and reduced (increased) net surface SW (**Figures 9C,D**), across the entire domain, indicating the importance of the cloud shielding effect in modulating the land surface temperature anomalies, and jetstream wind changes. The strong anomalous upper level northerlies near (25–35°N, 70–80°E), and southerlies at (25–35°N, 90–110°E) in **Figure 9A**, correspond to the anomalous upper level meridional winds in the vertical wind profiles, respectively, over the Middle East-West India, and the East Asian domain, and cooling over Tibetan Plateau associated with the contraction of the SAH, and the westward displacement of the WPSH (see discussion for **Figures 5C,D**). An analyses of the interaction

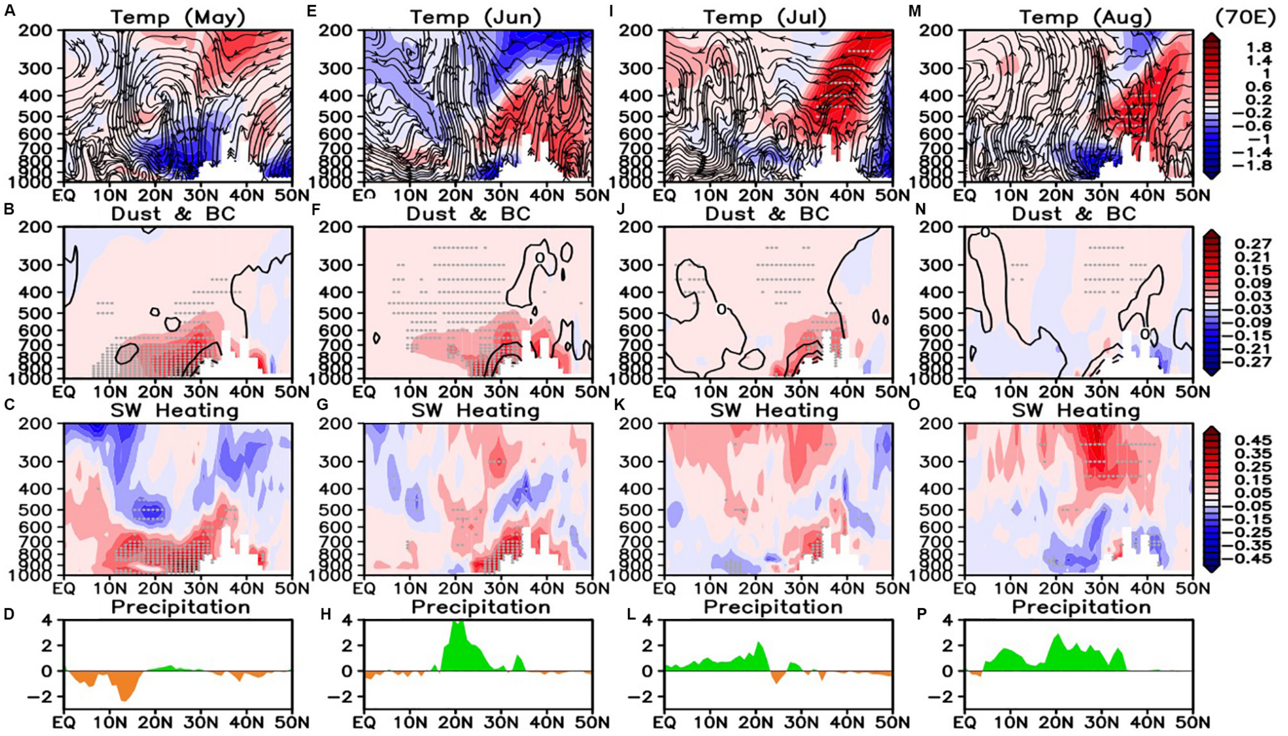

FIGURE 8 | Simulated vertical-latitude cross-sections at 70 E for anomalies in **(A)** tropospheric temperature and v-w streamlines, **(B)** atmospheric loading of dust (color shading) in mg/kg and BC (contour) um/Kg, **(C)** shortwave heating (°C day^{-1}), and corresponding changes in **(D)** anomalous precipitation (mm day^{-1}). Panels **(E)**, **(F)**, **(G)**, and **(H)** are the same as **(A)**, **(B)**, **(C)**, **(D)**, and except for June. Likewise, panels **(I)**, **(J)**, **(K)**, and **(L)** are for July, and **(M)**, **(N)**, **(O)**, and **(P)** for August.

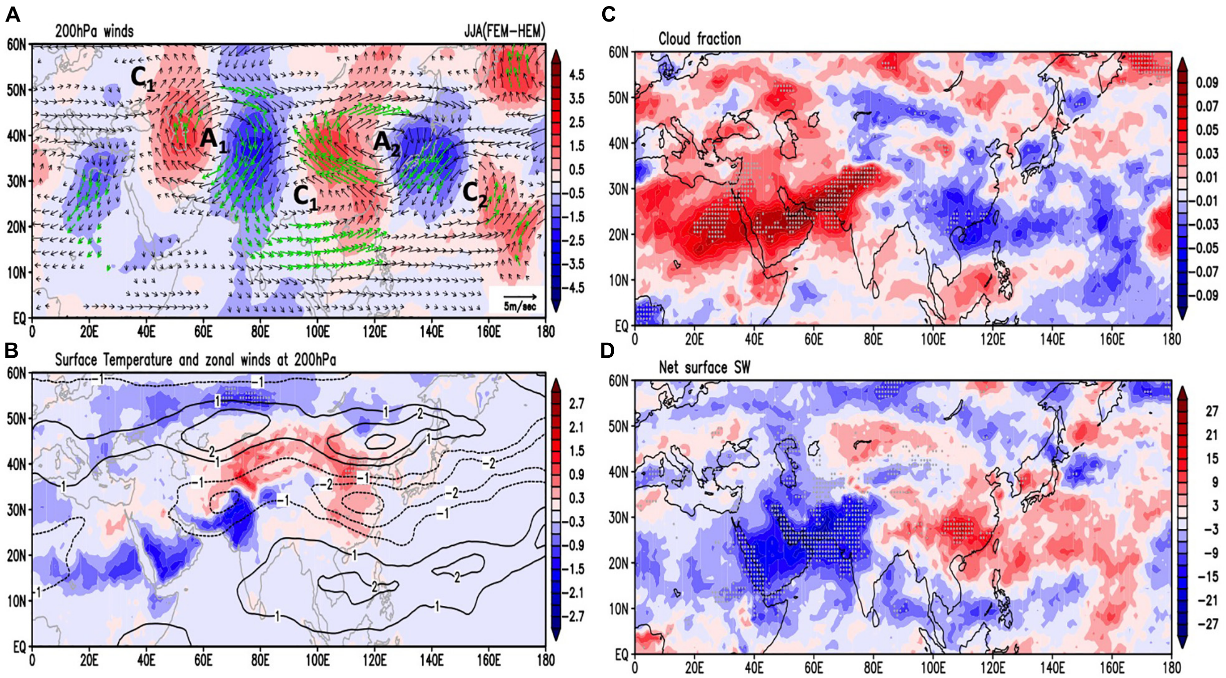

FIGURE 9 | Simulated JJA anomalies in **(A)** 200 hPa wind vectors, with northerly (southerly) merdional winds indicted by blue (red) shading, **(B)** 200 hPa zonal winds (ms^{-1}) and surface temperature (color shaded), **(C)** cloud fraction, and **(D)** surface net downward shortwave radiation (Wm^{-2}).

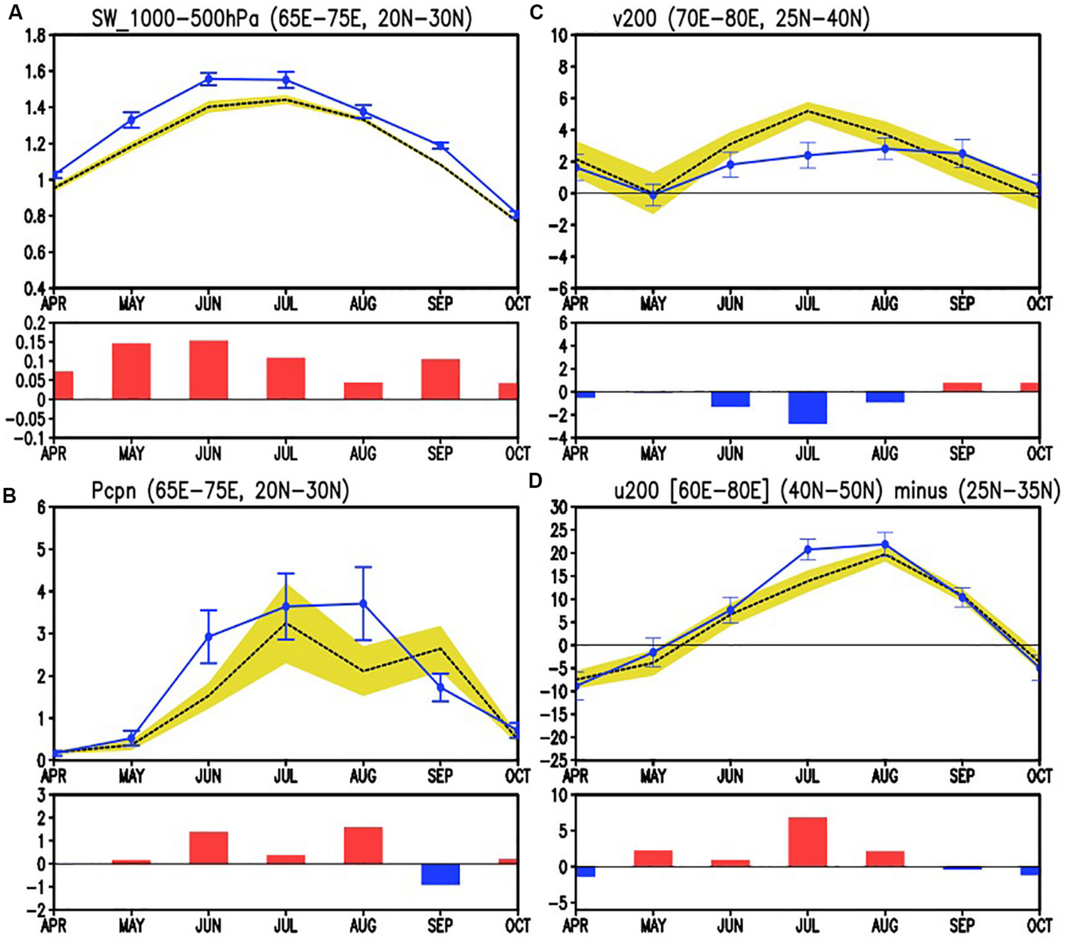

FIGURE 10 | Monthly (April through October) time series for FEM (blue line) and HEM (dotted line) showing S2S variation of **(A)** SW heating (Wm^{-2}) of the lower troposphere (1000–500 hPa) over PNWI, **(B)** precipitation (mm day^{-1}) over PNWI, **(C)** upper troposphere Rossby wave strength, represented by strength of the 200 hPa anomalous southerlies (ms^{-1}) overlying PNWI, and **(D)** zonal wind changes (ms^{-1}) indicating the northward migration and strengthening of the Middle-East jetstream. Sample 1–σ deviations are indicated by error bars for FEM, and yellow shading for HEM. Anomalies (FEM-HEM) are indicated by colored bars.

between the wavetrain and jetstream, based on vorticity balance is presented next.

Following Lau et al. (2000), over the ASM region (20–50°N, 60–140°E), the 200 hPa vorticity is governed approximately by:

$$\underbrace{\bar{V} \cdot \nabla\zeta'}_{[\text{VAM}]} + \underbrace{(\bar{\zeta} + \mathrm{f})\, \nabla \cdot V'}_{[\text{DIV}]} = -\beta v', \tag{1}$$

where ζ is the vorticity, f the Coriolis parameter, **V,** the vector winds, v, meridional wind, and the overbar represents monthly climatology, and ()' the anomalies. Notably, from Eq. (1), the anomalous meridional flow of the Rossby wave is governed approximately by contribution from the first term, i.e., vorticity advection by the mean flow [VAM], and the second term, which represents the effect of divergence [DIV] of the anomalous flow associated with precipitation heating. At 200 hPa, because of the much stronger zonal compared to meridional winds, VAM is dominated by the mean zonal wind advection. DIV is generally positive in regions of increased precipitation, contributing to a northerly (negative) meridional anomalous v'. The magnitude of DIV is also dependent on the seasonal variation of the mean vorticity $\bar{\zeta}$, mainly contributed by the zonal wind gradient term ($-\frac{\partial \bar{u}}{\partial y}$). In the tropics, away from the jet core region, VAM is small, the magnitude of upper level meridional southerly wind can be used as a measure of the strength of the Rossby anticyclone forced by DIV due to increased latent heating from enhanced precipitation (Gill, 1980; Lau and Lim, 1982).

Here, because the higher latitude location of the maximum precipitation over PNWI (25–35°N) and proximity to the jetstream, both VAM, and DIV contribute to the strength of the Rossby anticyclone, A_1. This can be seen in the month-to-month variations of key quantities and the anomalies (FEM minus HEM; vertical bars in **Figure 10**) affecting the vorticity balance of the upper troposphere. The shortwave heating in lower troposphere over the PNWI region increases steadily from April through June, as the dust loading increases due to the prescribed doubling of emission rate from HEM to FEM

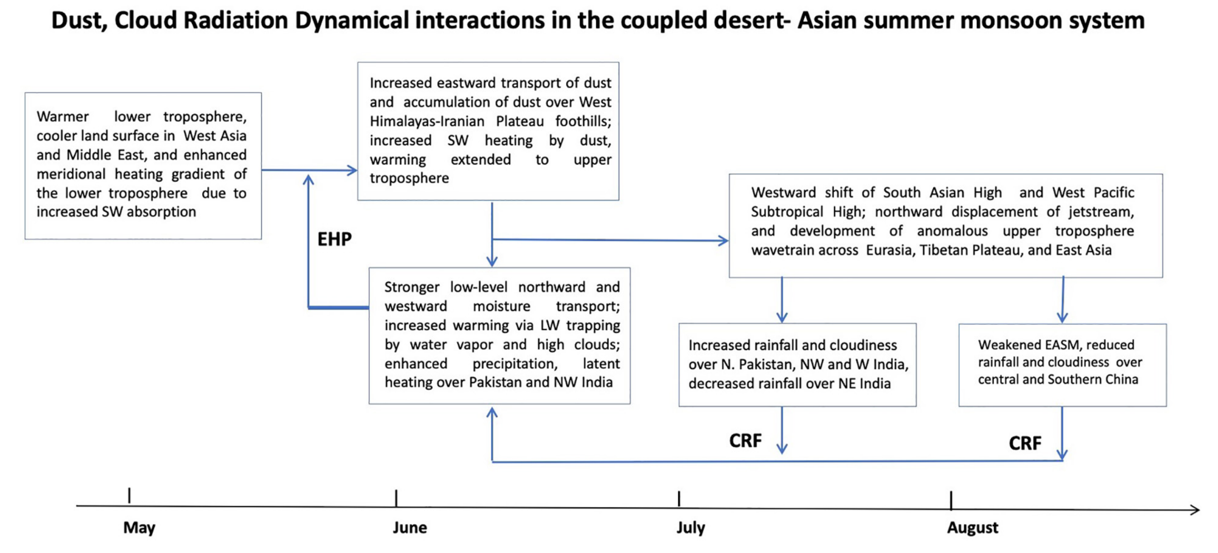

FIGURE 11 | Schematic showing key features of the dust-cloud-radiation-precipitation-circulation feedback and dynamical adjustment processes, triggered by Middle East dust radiation perturbations affecting the coupled desert-ASM system. EHP and CRF denotes, respectively, the aerosol "Elevated Heap Pump" effect, and Cloud-Radiation Feedback.

(**Figure 10A**), followed by a slow decline in July-August as a result of wash-out by the increasing monsoon seasonal precipitation (**Figure 10B**). Overall, positive anomalous precipitation is found over the PNWI, signaling an intensification and advance of the monsoon rainy season over the region. Note that the increase is not monotonic, but rather shows a high-low-high variation from June through August (anomalies in **Figure 10B**). The 200 hPa anomalous meridional winds (**Figure 10C**) are generally negative (more northerly in FEM) in June through August, consistent with the presence of an upper anticyclone, anchored by increased precipitation over PNWI via the DIV effect. However, the strength of the Rossby wavetrain, as indicated by the anomalous 200 hPa meridional winds exhibit a low-high-low magnitude variation from June to August, more in phase with the northward shift and variation of the strength of the jetstream (**Figure 10D**), indicating strong amplitude modulation by VAM. A separate calculation for the anticyclone A_2 yields similar results indicating large contribution by VAM, and strong jetstream-Rossby wave interaction affecting EASM rainfall (**Supplementary Figure S3**). These results reflect the intrinsic S2S internal dynamics that governs the interaction of monsoon precipitation, quasi-stationary Rossby wavetrain and the jetstream in the monsoon-desert coupled system. More in-depth understanding of the dynamics of the interaction, and the roles of cloud radiation feedback requires the decomposition into dominant spatial-temporal modes of monsoon intraseasonal oscillations (MISO), which is outside the scope of this study.

CONCLUSION

In this study, we have investigated the impact of desert dust on S2S variability of the ASM system, based on numerical experiments using the non-hydrostatic MPAS atmosphere model coupled with the CAM5 physics. Overall, we find that radiative perturbation from increased dust emission and transport from the Middle East/West Asia desert and arid regions induces a strong dust-cloud-radiation-precipitation-circulation feedback, resulting in a cooler land surface over the Middle East desert/West Asia region and the western Tibetan Plateau, but a warmer overlying middle and upper troposphere, with increased moistening, enhanced cloudiness and precipitation over the PNWI region. These changes are accompanied by a northward shift of the upper level jetstream over eastern Europe and the Middle East, in conjunction with an advance of the monsoon rainy season over northwestern and western India. The dust-induced dynamical feedback is underscored by large-scale dynamical adjustment processes, impacting the S2S variability of the Middle East/West Asia desert-monsoon system, illustrated schematically in **Figure 11**. Specifically, key features include:

1. In May, increased emission of dust over the Middle East desert and West Asia arid regions heats the elevated dust layer in the lower troposphere by absorption of solar radiation, and cools the land surface of the deserts of West Asia and Middle East by shortwave shielding, leading to increasing atmospheric stability through the semi-direct effect. However, the enhanced heating of the dust layer increases the meridional temperature gradient in the lower and mid-troposphere between West Asia land and the North Arabian Sea to the south, facilitating anomalous northward transport of moisture from ocean to the land in the lower troposphere.
2. In June, the meridional heating gradient in the lower troposphere continues to increase, as the advancing monsoon low-level southwesterlies transport more

dust and moisture over the PNWI region, resulting in anomalous warming and moistening of the lower troposphere over the West Himalayas-Iranian Plateau foothills regions. Eventually, the dust heating overcomes the semi-direct stability effect, and deep convection breaks out above the cooler surface layer. Amplified by the EHP dynamical feedback, the increased convection results in enhanced precipitation over PNWI. The latent heating from precipitation spawns an upper level Rossby wavetrain, with a large-scale anticyclone anchored to the northwest of the precipitation center over PNWI.

3. In July-August, the EHP effect continues, but weakened due to removal of dust aerosol by increasing precipitation washout. However increased precipitation over PNWI continues to evolve due to cloud radiation dynamical feedback, enhancing the meridional surface temperature contrast across the jetstream. This promotes a northward migration of the jetstream which further modulates the magnitude and phase of the upper level Rossby wavertrain, and strength of the monsoon meridional circulation. The net result is a weakening and contraction of the SAH and a westward displacement the WPSH, with reduced low-level southwesterly transport of moisture from India to East Asia, resulting in reduced precipitation over central and southern East Asia.
4. Both the circulation divergence (DIV) associated with increased latent heating from enhanced precipitation over PNWI and vorticity advection by the mean flow (VAM) contribute to the strength and variability of the upper level Rossby wavetrain. In June, when the Middle East jetstream is relatively weak, DIV effect is stronger. In July-August, as the jet migrates northward and strengthens, VAM becomes more dominant.

It is important to note that while our results are based on a state-of-the-art GCM, i.e., MPAS-CAM5, they are from a singular model simulation, and therefore could be dependent on model representation of physical processes. As discussed in section "Results," MPAS-CAM5 has substantial discrepancies in the climatological regional distributions of ASM precipitation and AOD compared to observations. It overestimates the AOD over the desert region, and underestimates that over East Asia, the Indian Ocean, and the western Pacific compared to observations. These could be due to lack of resolution in the dust size distribution, and excessive wet deposition commonly found in climate models, resulting in deficient remote transport of fine dust particles from the source regions (Huneeus et al., 2011). As a result of the excessive AOD, model radiative effects of dust on precipitation may be too strong over the desert and PNWI region, but too weak over East Asia compared to reality. The aforementioned MPAS-CAM5 climatological biases also raise uncertainty regarding the relative importance of dust aerosol vs. cloud feedback processes affecting the ISM vs. EASM. Hence, conclusions in our study need to be treated only qualitatively, and with caution. Further inter-comparison studies with other state-of-the-art climate models, and validation with observations are required.

Last but not least, our findings suggest that the desert and ASM subsystems are intrinsically coupled, through radiation-precipitation-circulation feedback processes, affecting many aspects of S2S variability of the desert-monsoon climate system. The upper tropospheric wavetrain and meridional displacement of the Middle-East/East Asian jetstream unveiled in our study are reminiscent of a host of upper troposphere teleconnection patterns, e.g., ANA, SRP, JMD, and CGT, known to have strong impacts on boreal summer regional S2S variability, and on longer time scales, over Eurasia and Asia, reported in many previous studies cited in section "Wavetrain-jetstream interactions." Of particular relevance is the recent observational study (Xue and Chen, 2019) which showed a distinct north-SAH teleconnection pattern associated with a northward shift of the ASM jetstream, consistent with the weakened and contracted SAH due to increased dust emission from the Middle East desert found in this study. Our results suggest that such teleconnection pattern could be excited through internal feedback mechanisms within the desert-monsoon climate system, without the need for external forcing. How these teleconnection patterns are modulated by additional external forcing such as anomalous SST, anthropogenic emissions of aerosols and greenhouse gases need to be further investigated.

DATA AVAILABILITY STATEMENT

Data sources used for this work are available from (https://ladsweb.modaps.eosdis.nasa.gov/) for MODIS AOD, (https://disc.gsfc.nasa.gov/) for MERRA2, and (https://disc.gsfc.nasa.gov/datasets/TRMM_3B43_7/summary) for TRMM 3B43 Version 7 monthly rainfall. The raw data supporting the conclusions of this article will be made available by the authors, without undue reservation, to any qualified researcher.

AUTHOR CONTRIBUTIONS

WL precieved the idea, came up with the experimental design, oversaw the entire research project, and wrote the manuscript. K-MK carried out the analyses, processed the data, plotted the figures, and provided inputs to the manuscript writing. CZ carried out the model simulation experiments, processed the model outputs for analyses, and provided inputs to the manuscript writing. LL provided technical advice, facilitated computational resources, provided revisions to the initial and final draft of the manuscript. S-HP provided technical details on the computational efficiency of variable MPAS model grid, and physic package, and suggested revisions on various drafts of the manuscript. All authors contributed to the article and approved the submitted version.

FUNDING

This work was supported by the U.S. Department of Energy (DOE), Office of Science, Biological and Environmental Research as part of the Regional and Global Modeling and Analysis program area, including Grant Award #300426-00001 to U. of Maryland from the Pacific Northwest National Laboratory (PNNL). PNNL is operated for DOE, by Battelle Memorial Institute under contract DE-AC05-76RL01830. CZ was supported by the Fundamental Research Funds for the Central Universities of China and the National Natural Science Foundation of China (grant 41775146). Most of this work was completed while he was a research scientist at PNNL.

SUPPLEMENTARY MATERIAL

The Supplementary Material for this article can be found online at: https://www.frontiersin.org/articles/10.3389/feart.2020.00226/full#supplementary-material

REFERENCES

Abdul-Razzak, H., and Ghan, S. J. (2002). A parameterization of aerosol activation, 3, Sectional representation. *J. Geophys. Res.* 107, AAC 1-1–AAC 1-6. doi: 10.1029/2001JD000483

Alfaro, S. C., Lafo, S., Rajot, J. L., Formenti, P., Gaudichet, A., and Maillé, M. (2004). Iron oxides and light absorption by pure desert dust: an experimental study. *J. Geophys. Res.* 109:D08208. doi: 10.1029/2003JD004374

Badarinath, K. V. S., Kharol, S. K., Kaskaoutis, D. G., Sharma, A. R., Ramaswamy, V., and Kambezidis, H. D. (2010). Long range transport of dust aerosols over the Arabian Sea and Indian region – A case study using satellite data and ground based measurements. *Glob. Planet. Change* 72, 164–181. doi: 10.1016/j.gloplacha.2010.02.003

Bollasina, M., Ming, Y., and Ramaswamy, V. (2011). Anthropogenic aerosols and the weakening of the Asian summer monsoon. *Science* 334, 502–505. doi: 10.1126/science.1204994

Bretherton, C. S., and Park, S. (2009). A new moist turbulence parameterization in community atmosphere model. *J. Clim.* 22, 3422–3448. doi: 10.1175/2008JCLI2556.1

Chandra, S., Satheesh, S. K., and Srinivasan, J. (2004). Can the state of mixing of black carbon aerosols explain the mystery of 'excess atmospheric absorption? *Geophys. Res. Lett.* 31:L19109. doi: 10.1029/2004GL020662

Chu, J.-E., Kim, K.-M., Lau, W. K. M., and Ha, K.-J. (2018). How light absorbing properties of organic aerosol modify the Asian summer monsoon rainfall? *J. Geophys. Res. Atmos.* 123, 2244–2255. doi: 10.1002/2017JD027642

Das, S., Dey, S., Dash, S. K., Giuliani, G., and Solmon, F. (2015). Dust aerosol feedback on the Indian summer monsoon: sensitivity to absorption property. *J. Geophys. Res. Atmos.* 120, 9642–9652. doi: 10.1002/2015JD023589

Deepshikha, S., Satheesh, S. K., and Srinivasan, J. (2005). Regional distribution of absorbing efficiency of dust aerosols over India and adjacent continents inferred using satellite remote sensing. *Geophys. Res. Lett.* 32:L03811. doi: 10.1029/2004GL022091

di Sarra, A., Di Biagio, C., Meloni, D., Monteleone, F., Pace, G., Pugnaghi, S., et al. (2011). Shortwave and longwave radiative effects of the intense Saharan dust event of 25–26 March 2010 at Lampedusa (Mediterranean Sea). *J. Geophys. Res.* 116:D23209. doi: 10.1029/2011JD016238

Ding, Q. H., and Wang, B. (2005). Circumglobal teleconnection in the Northern Hemisphere summer. *J. Clim.* 18, 3483–3505. doi: 10.1175/JCLI3473.1

Ding, Q. H., and Wang, B. (2007). Intraseasonal teleconnection between the summer Eurasian wavetrain, and the Indian monsoon. *J. Clim.* 20, 3751–3776. doi: 10.1175/JCLI4221.1

Ding, Y., and Chan, J. (2005). The East Asian summer monsoon: an overview. *Meteorol. Atmos. Phys.* 89, 117–142. doi: 10.1007/s00703-005-0125-z

Du, Y., Li, T., Xie, Z., and Zhu, Z. (2016). Interannual variability of the Asian subtropical westerly jet in boreal summer and associated with circulation and SST anomalies. *Clim. Dyn.* 46, 2673–2688. doi: 10.1007/s00382-015-2723-x

Enomoto, T. (2004). Interannual variability of the Bonin high associated with the propagation of Rossby waves along the Asian jet. *J. Meteor. Soc. Japan* 82, 1019–1034. doi: 10.2151/jmsj.2004.1019

Enomoto, T., Hoskins, B. J., and Matsuda, Y. (2003). The formation mechanism of the Bonin high in August. *Q. J. R. Meteorl. Soc.* 129, 157–178. doi: 10.1256/qj.01.211

Evan, A. T., Flamant, C., Fiedler, S., and Doherty, O. (2014). An analysis of aeolian dust in climate models. *Geophys. Res. Lett.* 41, 5996–6001. doi: 10.1002/2014GL060545

Evans, J. P. (2011). "CORDEX – An international climate downscaling initiative," in *Proceedings of the 19th International Congress on Modelling and Simulation*, Perth.

Flanner, M., and Zender, C. S. (2005). Snowpack radiative heating: influence on Tibetan Plateau climate. *Geophys. Res. Lett.* 32:L06501. doi: 10.1029/2004gl022076

Flanner, M., Zender, C. S., Randerson, T. J., and Rasch, P. J. (2007). Present-day climate forcing and response from black carbon in snow. *J. Geophys. Res.* 112:D11202. doi: 10.1029/2006JD008003

Gautam, R., Hsu, C., and Lau, K. M. (2010). Pre-monsoon characterization and radiative effects over the Indo-Gangetic plain: implications for regional climate warming. *J. Geophys. Res.* 115:D17208. doi: 10.1029/2010JD0

Gautam, R., Hsu, N. C., Lau, K. M., and Kafatos, M. (2009a). Aerosol and rainfall variability over the Indian monsoon region: distributions, trends and coupling. *Ann. Geophys.* 27, 3691–3703. doi: 10.5194/angeo-27-3691-2009

Gautam, R., Liu, Z., Singh, R. P., and Hsu, N. C. (2009b). Two contrasting dust-dominant periods over India observed from MODIS and CALIPSO data. *Geophys. Res. Lett.* 36:L06813. doi: 10.1029/2008GL036967

Gautam, R., Hsu, N. C., Tsay, S. C., Lau, K. M., Holben, B., Bell, S., et al. (2011). Accumulation of aerosols over the Indo-Gangetic plains and southern slopes of the Himalayas: distribution, properties and radiative effects during the 2009 pre-monsoon season. *Atmos. Chem. Phys.* 11, 12841–12863. doi: 10.5194/acp-11-12841-2011

Ghan, S. J., and Zaveri, R. A. (2007). Parameterization of optical properties for hydrated internally mixed aerosol. *J. Geophys. Res.* 112:D10201. doi: 10.1029/2006JD007927

Giles, D. M., Holben, B. N., Eck, T. F., Sinyuk, A., Smirnov, A., Slutsker, I., et al. (2012). An analysis of AERONET aerosol absorption properties and classifications representative of aerosol source regions. *J. Geophys. Res.* 117:D17203. doi: 10.1029/2012JD018127

Gill, A. E. (1980). Some simple solutions for heat-induced tropical circulation. *Q. J. R. Meteorol. Soc.* 106, 447–462. doi: 10.1002/qj.49710644905

Hansen, J., Sato, M., and Ruedy, R. (1997). Radiative forcing and climate response. *J. Geophys. Res.* 102, 6831–6864. doi: 10.1029/96jd03436

Holton, J. R. (1993). *An Introduction to Dynamic Meteorology, 3rd Edition, 48, International Geophysics Series*. Cambridge, MA: Academic Press.

Hong, X., and Lu, R. (2016). The meridional displacement of the summer Asian Jet, Silk Road Pattern, and tropical SST anomalies. *J. Clim.* 29, 3753–3766. doi: 10.1175/JCLI-D-15-0541.1

Hoskins, B. J., and Ambrizzi, T. (1993). Rossby wave propagation on a realistic longitudinally varying flow. *J. Atmos. Sci.* 50, 1661–1671. doi: 10.1175/1520-0469(1993)050<1661:rwpoar>2.0.co;2

Huang, J., Fu, Q., Su, J., Tang, Q., Minnis, P., Hu, Y., et al. (2009). Taklimakan dust aerosol radiative heating derived from CALIPSO observations using the Fu-Liou radiation model with CERES constraints. *Atmos. Chem. Phys.* 9, 4011–4021. doi: 10.5194/acp-9-4011-2009

Huneeus, N., Schulz, M., Balkanski, Y., Griesfeller, J., Prospero, M., Kinne, S., et al. (2011). Global dust model intercomparison in AeroCom phase I. *Atmos. Chem. Phys.* 11, 7781–7816. doi: 10.5194/acp-11-7881-2011

Iacono, M. J., Mlawer, E. J., Clough, S. A., and Morcrette, J. J. (2000). Impact of an improved longwave radiation model, RRTM, on the energy budget and thermodynamic properties of the NCAR community climate model, CCM3. *J. Geophys. Res.* 105, 14873–14890. doi: 10.1029/2000JD900091

Jin, Q., Wei, J., and Yang, Z. L. (2014). Positive response of Indian summer rainfall to Middle East dust. *Geophys. Res. Lett.* 41, 4068–4074. doi: 10.1002/2014GL059980

Jin, Q., Yang, Z., and Wei, J. (2016). Seasonal responses of indian summer monsoon to dust aerosols in the Middle East, India, and China. *J. Clim.* 29, 6329–6349. doi: 10.1175/JCLI-D-15-0622.1

Kim, M. K., Lau, W. K. M., Kim, K., Sang, J., Kim, Y., and Lee, W. (2015). Amplification of ENSO effects on Indian summer monsoon by absorbing aerosols. *Clim. Dyn.* 46:2657. doi: 10.1007/s00382-015-2722-y

Kok, J. F. (2011). A scaling theory for the size distribution of emitted dust aerosols suggests climate models underestimate the size of the global dust cycle. *Proc. National Acad. Sci. U.S.A.* 108, 1016–1021. doi: 10.1073/pnas.1014798108

Lamarque, J. F., Bond, T. C., Eyring, V., Granier, C., Heil, A., Klimont, Z., et al. (2010). Historical (1850–2000) gridded anthropogenic and biomass burning emissions of reactive gases and aerosols: methodology and application. *Atmos. Chem. Phys. Eur. Geosci. Union* 10, 7017–7039. doi: 10.5194/acp-10-7017-2010

Lau, K. M., Kim, K. M., and Kim, M. K. (2006). Asian summer monsoon anomalies induced by aerosol direct forcing: the role of the Tibetan Plateau. *Clim. Dyn.* 26, 855–864. doi: 10.1007/s00382-006-0114-z

Lau, K. M., Kim, K. M., and Yang, S. (2000). Dynamical and boundary forcing characteristics of regional components of the asian summer monsoon. *J. Clim.* 13, 2461–2482. doi: 10.1175/1520-0442(2000)013<2461:dabfco>2.0.co;2

Lau, K. M., Kim, M. K., Kim, K. M., and Lee, W. (2010). Enhanced surface warming and accelerated snow melt in the Himalayas and Tibetan Plateau induced by absorbing aerosols. *Environ. Res. Lett.* 5:025204. doi: 10.1088/1748-9326/5/2/025204

Lau, K. M., and Li, M. T. (1984). The monsoon of east-asia - a survey. *Bull. Am. Meteorl. Soc.* 65, 114–125.

Lau, K. M., and Lim, H. (1982). Thermally driven motions in an equatorial β-plane: hadley and Walker circulations during the winter monsoon. *Mon. Wea. Rev.* 110, 1372–1388.

Lau, K. M., Ramanathan, V., Wu, G.-X., Li, Z., Tsay, S. C., and Hsu, C. (2008). The joint aerosol-monsoon experiment: a new challenge for monsoon climate research. *Bull. Am. Meteorol. Soc.* 89, 369–383. doi: 10.1175/BAMS-89-3-369

Lau, K. M., and Weng, H. (2002). Recurrent teleconnection patterns linking summer monsoon variability over East Asia and North America. *J. Meteor. Soc. Japan* 80, 1309–1324. doi: 10.2151/jmsj.80.1309

Lau, W. K. M. (2014). Desert dust and monsoon rain. *Nat. Geosci.* 7, 255–256. doi: 10.1038/ngeo2115

Lau, W. K. M. (2016). The aerosol-monsoon climate system of asia: a new paradigm. *J. Meteorl. Res.* 29, 1–11. doi: 10.1007/s13351-015-5999-1

Lau, W. K. M., and Kim, K. M. (2018). Impacts of snow-darkening by deposition of light-absorbing aerosols on snowcover over the Himalayas-Tibetan-Plateau, and influences on the Asian summer monsoon: a possible mechanism for the Blanford Hypothesis. *Atmosphere* 9:438. doi: 10.3390/atmos9110438

Lau, W. K. M., Kim, K. M., Chern, J., Tao, W. K., and Leung, R. (2019). Structural change and variability of the ITCZ induced by radiation-cloud-convection-circulation interactions: inferences from the Goddard Multi-Model Framework (GMMF) experiments. *Clim. Dyn.* 54, 211–229. doi: 10.1007/s00382-019-05000-y

Leung, L. R., Mearns, L. O., Giorgi, F., and Wilby, R. L. (2003). Regional climate research. *Bull. Am. Meteorol. Soc.* 84, 89–95.

Leung, L. R., Ringler, T. D., Collins, W. D., and Ashfaq, M. (2013). A hierarchical evaluation of regional climate simulations. *EOS Trans. AGU* 94, 297–298. doi: 10.1002/2013eo340001

Li, Z., Lau, W. K. M., Ramanathan, V., Wu, G., Ding, Y., Manoj, M. G., et al. (2016). Aerosol and Monsoon Climate Interactions over Asia. *Rev. Geophys.* 54, 866–929.

Liu, X., Easter, R. C., Ghan, S. J., Zaveri, R., Rasch, P., Shi, X., et al. (2012). Toward a minimal representation of aerosols in climate models: description and evaluation in the Community Atmosphere Model CAM5. *Geosci. Model Dev.* 5, 709–739. doi: 10.5194/gmd-5-709-2012

Liu, X., Pennerc, J. E., Ghan, S. J., and Wang, M. (2007). Inclusion of ice microphysics in the NCAR community atmospheric model version 3 (CAM3). *J. Clim.* 20, 4526–4547. doi: 10.1175/JCLI4264.1

Lohmann, U., and Feichter, J. (2001). Can the direct and semi-direct aerosol effect compete with the indirect effect on a global scale? *Geophys. Res. Lett.* 28, 159–161. doi: 10.1029/2000GL012051

Lu, R., Oh, J. H., and Kim, B. J. (2002). A teleconnection pattern in upper-level meridional wind over the North African and Eurasian continent in summer. *Tellus* 54A, 44–55. doi: 10.1034/j.1600-0870.2002.00248.x

Meehl, G. A., Arblaster, J., and Collins, W. (2008). Effects of black carbon aerosols on the Indian monsoon. *J. Clim.* 21, 2869–2882. doi: 10.1175/2007JCLI1777.1

Mlawer, E. J., Iacono, M. J., Pincus, R., Barker, H. W., Oreopoulos, L., and Mitchell, D. L. (2016). Contributions of the ARM program to radiative transfer modeling for climate and weather applications. *Meteorol. Monogr.* 57, 15.1–15.19. doi: 10.1175/AMSMONOGRAPHS-D-15-0041.1

Moorthy, K. K., Babu, S. S., Satheesh, S. K., Srinivasan, J., and Dutt, C. B. S. (2007). Dust absorption over the "Great Indian Desert" inferred using ground-based and satellite remote sensing. *J. Geophys. Res.* 112:D09206. doi: 10.1029/2006JD007690

Morrison, H., and Gettelman, A. (2008). A new two-moment bulk stratiform cloud microphysics scheme in the community atmosphere model, Version 3 (CAM3). Part I: description and numerical tests. *J. Clim.* 21, 3642–3659. doi: 10.1175/2008JCLI2105.1

Neale, R. B., Richter, J. H., Conley, A. J., Park, S., Lauritzen, P. H., Gettelman, A., et al. (2012). *Description of the NCAR Community Atmosphere Model (CAM5.0).* NCAR Technical Note, NCAR/TN-486+STR, National Center for Atmospheric Research, 274. Available online at: http://www.cesm.ucar.edu/models/cesm1.0/cam/docs/description/cam5_desc.pdf

Pan, X., Chin, M., Gautam, R., Bian, H., Kim, D., Colarco, P., et al. (2015). A multi-model evaluation of aerosols over South Asia: common problems and possible causes. *Atmos. Chem. Phys.* 15, 5903–5928. doi: 10.5194/acp-15-5903-2015

Pandithurai, G., Dipu, S., Dani, K. K., Tiwari, S., Bisht, D. S., Devara, P. C. S., et al. (2008). Aerosol radiative forcing during dust events over New Delhi, India. *J. Geophys. Res.* 113:D13209. doi: 10.1029/2008JD009804

Prasad, A. K., and Singh, R. P. (2007). Changes in aerosol parameters during major dust storm events (2001–2005) over the indo-gangetic plains using AERONET and MODIS data. *J. Geophys. Res.* 112:D09208. doi: 10.1029/2006JD007778

Qian, Y., Gustafson, W. I., Leung, L. R., and Ghan, S. J. (2009). Effects of soot-induced snow albedo change on snowpack and hydrological cycle in western United States based on Weather Research and Forecasting chemistry and regional climate simulations. *J. Geophys. Res.* 114:D03108. doi: 10.1029/2008JD011039

Qian, Y., Yasunari, T. J., Doherty, S. J., Flanner, M. G., Lau, W. K. M., Ming, J., et al. (2015). Light-absorbing particles in snow and ice: measurement and modeling of climatic and hydrological impact. *Adv. Atmos. Sci.* 32, 64–91. doi: 10.1007/s00376-014-0010-0

Ramachandran, S. (2005). Pre-monsoon shortwave aerosol radiative forcing over the Arabian Sea and tropical Indian Ocean: yearly and monthly mean variabilities. *J. Geophys. Res.* 110:D07207. doi: 10.1029/2004JD005563

Ramanathan, V., Chung, C., Kim, D., Bettge, T., Buja, L., Kiehl, T. J., et al. (2005). Atmospheric brown clouds: impacts on South Asian climate and hydrological cycle. *Proc. Natl. Acad. Sci. U.S.A.* 102, 5326–5333. doi: 10.1073/pnas.0500656102

Ramanathan, V., and Collins, W. (1991). Thermodynamic regulation of ocean warming by cirrus clouds deduced from observations of the 1987 El Niño. *Nature* 351, 27–32. doi: 10.1038/351027a0

Rodwell, M. J., and Hoskins, B. J. (1995). A model for the Asian summer monsoon. Part II: cross-equatorial flow and PV behavior. *J. Atmos. Sci.* 52, 1341–1356. doi: 10.1175/1520-0469(1995)052<1341:amotas>2.0.co;2

Rosenfeld, D., Lohmann, U., Raga, G. B., O'Dowd, C. D., Kulmala, Fuzzi, M. S., et al. (2008). Flood or drought: how do aerosols affect precipitation? *Science* 321, 1309–1313. doi: 10.1126/science.1160606

Sakaguchi, K., Leung, L. R., Zhao, C., Yang, Q., Lu, J., Hagos, S. M., et al. (2015). Exploring a multi-resolution approach using AMIP simulations. *J. Clim.* 28, 5549–5574. doi: 10.1175/JCLI-D-14-00729.1

Sakaguchi, K., Lu, J., Leung, L. R., Zhao, C., Li, Y., and Hagos, S. (2016). Sources and pathways of the upscale effects on the Southern Hemisphere jet in MPAS-CAM4 variable-resolution simulations. *J. Adv. Model. Earth Syst.* 8, 1786–1805. doi: 10.1002/2016MS000743

Sanap, S. D., and Pandithurai, G. (2015). The effect of absorbing aerosol on Indian monsoon circulation and rainfall: a review. *Atmos. Res.* 16, 318–327. doi: 10.1016/j.atmosres.2015.06.002

Satheesh, S., Krishna Moorthy, K., Kaufman, Y., Kaufman, J., and Takemura, T. (2006). Aerosol optical depth, physical properties, and radiative forcing over the Arabian Sea. *Meteorol. Atmos. Phys.* 91:45. doi: 10.1007/s00703-004-0097-4

Satheesh, S. K., Krishna Moorthy, K., Babu, S. S., Vinoj, V., and Dutt, C. B. C. (2008). Climate implications of large warming by elevated aerosol over India. *Geophys. Res. Lett.* 35:L19809. doi: 10.1029/2008GL034944

Satheesh, S. K., and Srinivasan, J. (2002). Enhanced aerosol loading over Arabian Sea during the pre-monsoon season: natural or anthropogenic? *Geophys. Res. Lett.* 29:1874. doi: 10.1029/2002GL015687

Sato, N., and Takahashi, M. (2003). Formation mechanism of vorticity anomalies on the subtropical jet in the midsummer Northern Hemisphere. *Appl. Mech. Jpn.* 52, 109–115. doi: 10.11345/nctam.52.109

Skamarock, W. C., Klemp, J. B., Fowler, L. D., Duda, M. G., Park, S. H., and Ringler, T. D. (2012). A multiscale nonhydrostatic atmospheric model using centroidal Voronoi tesselations and C-grid staggering, Mon. *Weather Rev*. 140, 3090–3105. doi: 10.1175/MWR-D-11-00215.1

Sokolik, I. N., and Toon, O. B. (1999). Incorporation of mineralogical composition into models of the radiative properties of mineral aerosol from UV to IR wavelengths. *J. Geophys. Res.* 104, 9423–9444. doi: 10.1029/1998jd200048

Solmon, F., Mallet, F., Elguindi, N., Giorgi, F., Zakey, A., and Konaré, A. (2008). Dust aerosol impact on regional precipitation over western Africa, mechanisms and sensitivity to absorption properties. *Geophys. Res. Lett.* 35:L24705. doi: 10.1029/2008GL035900

Solmon, F., Nair, V. S., and Mallet, M. (2015). Increasing Arabia dust activity and the Indian summer monsoon. *Atmos. Chem. Phys.* 15, 8051–8064. doi: 10.5194/acp-12-8051-2015

Song, F., Zhou, T., and Wang, L. (2013). Two modes of the Silk Road pattern and their interannual variability simulated by LASG/IAP AGCM SAMIL2.0. *Adv. Atmos. Sci.* 30, 908–921. doi: 10.1007/s00376-012-2145-1

Stephan, C. C., Klingman, N. P., and Turner, A. G. (2018). A mechanism for the recently increased interdecadal variability of the Silk Road Pattern. *J. Clim.* 32, 717–736. doi: 10.1175/Jc:I-D18-0405.1

Vinoj, V., Rasch, P. J., Wang, H., Yoon, J., Ma, P., Landu, K., et al. (2014). Short-term modulation of Indian summer monsoon rainfall by West Asian dust. *Nat. Geosci.* 7, 308–313. doi: 10.1038/ngeo2107

Wakabayashi, S., and Kawamura, R. (2004). Extraction of major teleconnection patterns possibly associated with the anomalous summer climate in Japan. *J. Meteor. Soc. Jpn.* 82, 1577–1588. doi: 10.2151/jmsj.82.1577

Wang, B. (2006). *The Asian Monsoon, Editor, Wang B*. Chichester: Springer-Praxis Ltd.

Wang, B. (2009). Distinct principal modes of early and late summer rainfall anomalies in East Asia. *J. Clim.* 22, 3864–3875. doi: 10.1175/2009jcli2850.1

Wang, C., Jeong, G. R., and Mahowald, N. (2009a). Particulate absorption of solar radiation: anthropogenic aerosols vs. dust. *Atmos. Chem. Phys.* 9, 3935–3945. doi: 10.5194/acp-9-3935-2009

Wang, C., Kim, D., Ekman, M. L., Barth, M. C., and Rasch, P. J. (2009b). Impact of anthropogenic aerosols on Indian summer monsoon. *Geophys. Res. Lett.* 36:L21704. doi: 10.1029/2009GL040114

Wang, L., Xu, P., Chen, W., and Liu, Y. (2017). Interdecadal variations of the silk road pattern. *J. Clim.* 30, 9915–9932. doi: 10.1175/JCLI-D-17-0340.1

Wei, Q. J., and Yang, Z. L. (2014). Positive response of Indian summer rainfall to Middle East dust. *Geophys. Res. Lett.* 41, 4068–4074 .

Wu, G., Li, Z., Fu, C., Zhang, X., Zhang, R., Zhang, R., et al. (2016). Advances in studying interaction of aerosol and monsoon in China. *Sci. China Earth Sci.* 59:1. doi: 10.1007/s11430-015-5198-z

Xia, X., and Zong, X. (2009). Shortwave versus longwave direct radiative forcing by Taklimakan dust aerosols. *Geophys. Res. Lett.* 36:L07803. doi: 10.1029/2009GL037237

Xue, X., and Chen, W. (2019). Distinguishing interannual variations and possible impacted factors for the northern and southern mode of South Asia High. *Clim. Dyn.* 53, 4937–4959. doi: 10.1007/s00382-019-04837-7

Zender, C. S., Bian, H., and Newman, D. (2003). Mineral dust entrainment and deposition (DEAD) model: description and 1990s dust climatology. *J. Geophys. Res.* 108:4416.

Zhang, G. J., and McFarlane, N. A. (1995). Sensitivity of climate simulations to the parameterization of cumulus convection in the Canadian climate center general circulation model. *Atmos. Ocean* 33, 407–446. doi: 10.1080/07055900.1995.9649539

Zhang, M., Zhao, C., Cong, Z., Du, Q., Xu, M., Chen, Y., et al. (2020). Impact of topography on black carbon transport to the southern Tibetan Plateau during pre-monsoon season and its climatic implication. *Atmos. Chem. Phys.* 19, 5529–5541. doi: 10.5194/acp-2019-905

Zhang, Y., Kuang, X., Guo, W., and Zhou, T. (2006). Seasonal evolution of the upper-tropospheric westerly jet core over East Asia. *Geophys. Res. Lett.* 33:L11708. doi: 10.1029/2006GL026377

Zhao, C., Leung, L. R., Park, S. H., Hagos, S., Lu, J., Sakaguchi, K., et al. (2016). Exploring the impacts of physics and resolution on aqua-planet simulations from a non-hydrostatic global variable-resolution modeling framework. *J. Adv. Model. Earth Syst.* 8, 1751–1768. doi: 10.1002/2016MS000727

Zhao, C., Xu, M., Wang, Y., Zhang, M., Guo, J., Leung, R. L., et al. (2019). Modeling extreme precipitation over East China with a global variable-resolution modelling framework (MPASv5.2). *Geosci. Model Dev.* 12, 2707–2726. doi: 10.5194/gmd-12-2707-2019

Conflict of Interest: The authors declare that the research was conducted in the absence of any commercial or financial relationships that could be construed as a potential conflict of interest.

frontiers
in Earth Science

ORIGINAL RESEARCH
published: 29 October 2020
doi: 10.3389/feart.2020.580457

Multidecadal Seesaw in Hadley Circulation Strength Between the Two Hemispheres Caused by the Atlantic Multidecadal Variability

***Yusen Liu*[1], *Zhanqiu Gong*[1], *Cheng Sun*[1]*, *Jianping Li*[2,3] and *Lin Wang*[4]**

[1]College of Global Change and Earth System Science (GCESS), Beijing Normal University, Beijing, China, [2]Frontiers Science Center for Deep Ocean Multispheres and Earth System (FDOMES), Key Laboratory of Physical Oceanography, Institute for Advanced Ocean Studies, Ocean University of China, Qingdao, China, [3]Laboratory for Ocean Dynamics and Climate, Pilot National Laboratory for Marine Science and Technology (Qingdao), Qingdao, China, [4]Center for Monsoon System Research, Institute of Atmospheric Physics, Chinese Academy of Sciences, Beijing, China

Multidecadal variations in Hadley circulation (HC) strength have been observed during the historical period, which have significant implications for global and regional climate. However, the relationship between HC intensities in the two hemispheres remains unclear. In this study, we identify an interhemispheric seesaw in the annual HC strength at multidecadal timescales. This seesaw pattern physically corresponds to the meridional movement of the ascending branch of annual HC, leading to strengthened HC in one hemisphere and weakened HC in the other. The HC strength seesaw strongly correlates with the tropical land surface precipitation at multidecadal timescales, particularly for the monsoonal land regions. Further analyses link the HC strength seesaw to the Atlantic multidecadal variability (AMV). A suite of Atlantic Pacemaker experiments successfully reproduces the multidecadal HC strength seesaw and its relation to the AMV. The Northern Hemisphere SST warming associated with the positive AMV phase induces a northward shift of the upward branch of HC, and the Southern Hemispheric HC is strengthened in contrast to the weakened Northern Hemispheric HC. Comparisons of the North Atlantic SST forced HC changes between the coupled air–sea model and stand-alone atmospheric model suggest an important and non-negligible role of the SST footprint of AMV over the Indo-Pacific basins. The AMV and its Indo-Pacific SST footprint make a comparable contribution to the SST changes in the Northern Hemisphere, which control the movement of the HC ascending branch and thereby the interhemispheric seesaw in HC strength.

Keywords: Atlantic multidecadal variability, Hadley circulation, monsoon precipitation, Indo-Pacific air–sea coupling, interhemispheric teleconnection

Edited by:
Raquel Nieto,
University of Vigo, Spain

Reviewed by:
Pedro Miguel Sousa,
University of Lisbon, Portugal
Yipeng Guo,
Nanjing Normal University, China

****Correspondence:***
Cheng Sun
scheng@bnu.edu.cn

Specialty section:
This article was submitted to
Atmospheric Science,
a section of the journal
Frontiers in Earth Science

Received: *06 July 2020*
Accepted: *05 October 2020*
Published: *29 October 2020*

Citation:
Liu Y, Gong Z, Sun C, Li J and Wang L (2020) Multidecadal Seesaw in Hadley Circulation Strength Between the Two Hemispheres Caused by the Atlantic Multidecadal Variability.
Front. Earth Sci. 8:580457.
doi: 10.3389/feart.2020.580457

INTRODUCTION

The Hadley circulation (HC) is one of the most important atmospheric circulations and plays a dominant role in the transportation of momentum, heat, and water vapor (Trenberth and Stepaniak, 2003), which is much greater than that of the transient and stationary eddies. The HC thus is of great importance to the tropical weather and climate. The HC bridges the tropic and extratropic via transporting momentum and heat from tropics to the subtropical and higher latitudes (Diaz and Bradley, 2004), thus it is also important to the extratropical weather and climate (Lindzen, 1994;

Chang, 1995; Hou, 1998). As an important large-scale circulation in the low latitude atmosphere, the variations in HC are closely linked to the global atmospheric circulation variability and also impact on the global weather and climate change. Therefore, studying the multidecadal variability in HC is significant in understanding and researching the changes in the global climate system and regional climates as well.

The long-term HC variability has received considerable attention in recent years with the abundance of observational datasets. These studies mainly focus on the horizontal scale, width and strength of the HC (Hu and Zhou, 2010). Various studies based on different observational and reanalysis datasets have consistently pointed out that the HC exhibits an obvious trend of poleward expansion at the quantified speeds (different observational datasets during 1979–2005 show a −0.5° to 3°/decade widening in the HC poleward expansion) (Hudson et al., 2006; Frierson et al., 2007; Lu et al., 2007; Seidel et al., 2008; Johanson and Fu, 2009). A couple of factors that cause the HC expansions, including anthropogenic greenhouse gas emissions, aerosols, stratospheric ozone and natural climate variabilities (Staten et al., 2018). For instance, the warm phase of Pacific Decadal Oscillation (PDO) enhances tropical warming and leads to a contraction of the HC, and vice versa. However, whether the Atlantic climate modes played a role remains elusive. In addition, other observational and modeling studies (Tao et al., 2016; Watt-Meyer et al., 2019; Grise and Davis, 2020) have indicated an asymmetrical expansion of the HC due to multiple reasons, like greenhouse gas and ozone depletion, but their impacts vary in seasons. In general, the poleward expansion of the HC in the Northern Hemisphere (NH) is larger than the Southern Hemisphere (SH) and the expansion in the summer (JJA) and autumn (SON) is faster than the spring (MAM) and winter (DJF) (Lu et al., 2007). As to the HC strength, observational datasets have shown a strengthening trend in the annual HC since the 1990s (Chen et al., 2002; Wielicki et al., 2002). It is suggested that consistent evidence has been found for intensification in the NH winter HC since 1950, but the summer HC strength appears to be no significant change (Quan et al., 2004). However, whether the HC has intensified is still under debate (Trenberth, 2002; Held and Soden, 2006; Stachnik and Schumacher, 2011). Previous observational and reanalysis studies also analyzed the changes in HC strength and suggested its pronounced decadal variability. The previous study (Zhou and Wang, 2006) has indicated that the winter NH HC strength exhibits remarkably interannual and interdecadal variability, but the summer SH HC strength exhibits decadal variations instead. However, the connection of HC strength between the NH and SH has not been fully understood and the decadal variability of HC strength in the two hemispheres is still unclear.

In addition to the HC strength and width, empirical orthogonal function analysis has been used to detect the temporal and spatial characteristics of the HC, and its variability has also received attention. The previous study (Dima and Wallace, 2003) suggested that the annual cycle of the HC consists of two components: an equatorially symmetric mode during the boreal spring and autumn, and an equatorially asymmetric component during the boreal winter and summer. A similar result also indicates that the boreal summer HC mainly includes the equatorially asymmetric mode and equatorially symmetric mode (Feng et al., 2011). The former study mainly focuses on the interdecadal variability, while the latter corresponds to the interannual variability. It has been shown that the variation of the asymmetric mode is connected to the sea surface temperature (SST) over the tropical Indian and western Pacific oceans (Ma and Li, 2008; Feng et al., 2011; Feng et al., 2013; Quan et al., 2014). The previous study (Guo et al., 2016) also demonstrates that the asymmetric mode in boreal autumn is closely linked to the Atlantic multidecadal variability (AMV). The previous findings have focused on the year-to-year variability of seasonal HC, but the decadal-scale relationship between the annual HC strength in the two hemispheres has not been fully understood. Meanwhile, many studies suggest the SSTs over the Atlantic Ocean have impacts on the Indo-Pacific SST variability (Sun et al., 2017; Xue et al., 2018), but whether these impacts contribute to the variability of HC strength remains unclear and the relative importance of the Atlantic and Indo-Pacific SSTs for the multidecadal variations in annual HC strength has not been investigated.

In this study, we investigate the interhemispheric relationship of the HC strength at multidecadal time scales and link it to the AMV using multiple datasets. And, considering the great impact of the HC on tropical precipitation, we also analyze the relationship between the HC strength seesaw and tropical rainfalls. A mechanism is then proposed to explain how the AMV influences interhemispheric seesaw in HC strength. Statistical analyses and a suite of Atlantic Pacemaker experiments are performed to identify the Indo-Pacific effects on the HC strength decadal variability associated with the AMV signal.

DATA AND METHODS

Data and Index Definitions

Atmospheric data sets are derived from the ECMWF Atmospheric Reanalysis of the 20th Century (ERA-20C) data set (Stickler et al., 2014) and 20th century reanalysis (20CR) data (Compo et al., 2011) for the period 1900–2010. National Centers for Environmental Prediction (NCEP) data set (Kalnay et al., 1996) is for the period 1948–2014. They are used to reveal the spatial and temporal characteristics of the HC. The precipitation data from Climate Research Unit (CRU TS 4.03) (Harris, 2014) is used to investigate the relationship between HC strength and tropical rainfall in the two hemispheres for the period 1901–2010. The main results are also validated by other SST (e.g., HadSST3 and COBE-SST2) and precipitation (e.g., GPCC) observational datasets (as shown in **Supplementary Material**). The PDO index is derived from the Japan Meteorological Agency which is defined as the projections of monthly mean SST anomalies, that subtract globally averaged monthly mean SST anomalies, onto their first empirical orthogonal function vectors in the North Pacific (north of 20°N) for the period 1900–2010. All the analyses are based on annual means.

The AMV index is defined as the area-weighted average of SST anomalies over the North Atlantic region (0°–60°N, 80°W–0°). The SST data is derived from the Extended Reconstruction SST version 3 (ERSST v3b) data set (Smith et al., 2008) for the period 1900–2010.

The Hadley circulation is characterized by the mean meridional mass stream function (MMS), which is computed by vertically integrating the zonal mean meridional wind $[v]$ (Holton, 1973):

$$\psi(p, \phi) = \frac{2\pi a \cos\phi}{g} \int_0^p [v] \mathrm{d}p,$$

where ϕ is the latitude, p is the pressure, a is the Earth radius, and g is the gravitational acceleration. The locations of poleward edges of the Hadley circulation are identified as the latitudes where MMS equals $0\,\mathrm{kg{\cdot}s^{-1}}$.

The hemispheric HC strength index is calculated as the maximum value of the MMS in the tropics (Oort and Yienger, 1996). And the HC strength seesaw index is defined as the difference between the NH and the SH HC strength indices.

Statistical Methods

We confine our analysis to the post-1900 period for the data sets due to large uncertainties and less reliability in surface observations before 1900 (Folland et al., 2001). To better isolate and highlight the signal of decadal to multidecadal variability, we tend to remove the centennial-scale trends by using the removal of long-term linear trends in the variables for the post-1900 period, and the data are smoothed with a low-pass filter (11-year running means).

A two-tailed Student's t-test is used to determine the statistical significance of the linear regression and correlation between two autocorrelated time series. We use the effective number of degrees of freedom (N^{eff}), which is given by the following approximation:

$$\frac{1}{N^{\mathrm{eff}}} \approx \frac{1}{N} + \frac{2}{N} \sum_{j=1}^{N} \frac{N-j}{N} \rho_{XX}(j) \rho_{YY}(j) \tag{1}$$

where N is the sample size and $\rho_{XX}(j)$ and $\rho_{YY}(j)$ are the autocorrelations of two sampled time series X and Y, respectively, at a time lag j (Li et al., 2013; Sun et al., 2015). In order to test the significance for a correlation map (e.g., figures in the main text), we first calculate the corresponding N^{eff} for each individual grid cell (based on the time series at each grid cell) using **Eq. (1)** and then estimate the correlation values required to meet the significance level.

Model and Experiments

The model we employed in this study is the International Centre for Theoretical Physics AGCM (ICTPAGCM, version 41) coupled to a slab ocean thermodynamic mixed-layer model (SOM). The intermediate ICTPAGCM contains eight vertical levels with a horizontal resolution of T30 (3.75° × 3.75° grid). In the observation, the climatological annual-averaged mixed layer depth is geographically-varying, generally shallow in the tropics and deep in mid-high latitudes. Thus, in the SOM experiment in this study, we adopt a geographically-varying mixed layer depth for the slab ocean model. The mixed layer depth varies from 40 m in the tropics to 60 m in the extra-tropics and is constant throughout the whole simulation period. Mixed-layer temperature variation is derived from the net surface heat fluxes into the ocean (i.e., the sum of shortwave and longwave radiation and sensible and latent heat fluxes) (Kucharski et al., 2016; Sun et al., 2017).

In this study, the Atlantic is defined as the entire Atlantic basin (60°S–60°N, 70°W–20°E) and the other basins out of the Atlantic are called the Indo-Pacific region. We perform two experiments to investigate the Indo-Pacific contribution to the HC strength under the AMV forcing. The first experiment is referred to as ATL_VARMIX (Atlantic Pacemaker experiment), which is run with the ICTPAGCM coupled to the SOM in the Indo-Pacific region and with raw observational monthly-varying SSTs (with the linear trend of SST maintained) from the HadISST data prescribed over the Atlantic basin. A buffer zone with a spatial range of 7.5° is set for preventing the instability between the prescribed-SST regions and the slab ocean in which the SST is calculated from the weighted average of the modeled and prescribed SSTs. The weighting values are one in the prescribed-SST domain and linearly reduced to zero in the buffer zone. The ATL_VARMIX experiment considers the effects of not only Atlantic SST variability, but also the atmosphere-ocean coupling over the Indo-Pacific region. We also conduct a similar experiment but with climatological monthly SSTs prescribed in the Indo-Pacific region, referred to as ATL_VARAGCM. It is to examine the direct impacts of the Atlantic forcing on the Indo-Pacific atmospheric circulation without the atmosphere-ocean coupling.

The simulations of ATL_VARMIX and ATL_VARAGCM experiments are integrated from 1872 to 2013 and contain five ensemble members generated by restarting the model with small initial perturbations. The first 28 years of all simulations are taken as spin up, and the results from the rest of the period during 1900–2013 are analyzed.

RESULTS

Interhemispheric Seesaw in Hadley Circulation Strength on the Decadal Scale

The time series of the hemispheric HC strength indices suggest that the HC strength in one hemisphere generally exhibits opposite phase to the other and its decadal variability can be found in both datasets but with some differences. The hemispheric HC strength index based on NCEP data (**Figure 1A**) exhibits significant multidecadal variability and interhemispheric connection as the correlation coefficient between the hemispheres reaches −0.80 for the period 1948–2013. The HC strength in the NH shows an increasing trend in the 1950s and 1960s with a phase shift that occurred around 1970. The HC strength in the SH exhibits an opposite trend during the same period with a phase shift that occurred around 1970, indicating that a seesaw pattern in HC strength may exist between the two hemispheres. We extend our analyzed

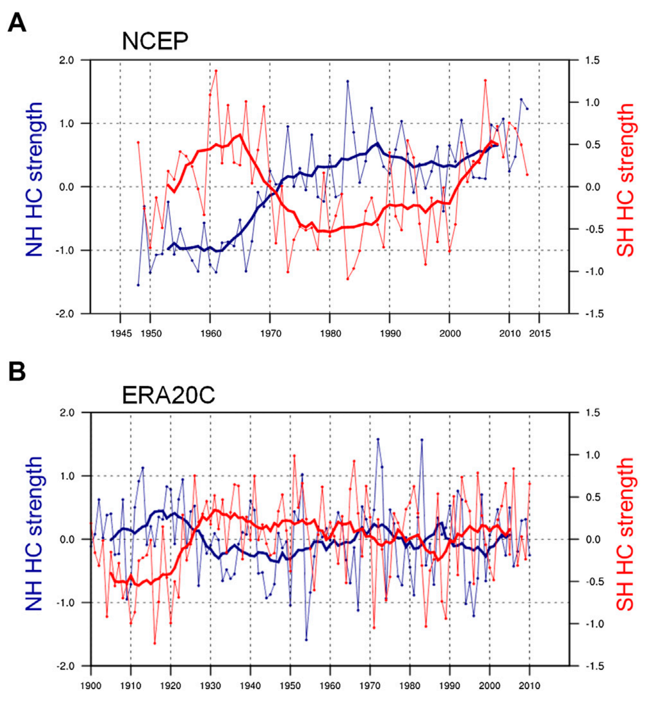

FIGURE 1 | Time series of the raw data (thin lines) and 11-year running averages (decadal component) (thick lines) of the HC strength (10^9 kg s^{-1}) indices in the NH (blue lines) and SH (red lines) derived from the **(A)** NCEP data set for 1948–2013 and from the **(B)** ERA20C data set for 1900–2010.

period from 1900 to 2010 using the ERA20C dataset (**Figure 1B**). It shows clear decadal variability before 1950. Similarly, the HC strength in the NH is also negatively correlated (−0.70) with that in the SH using the ERA20C reanalysis data set. For the overlapping period (1948–2010), the time series of hemispheric Hadley circulation strength indices depicted by the two reanalysis data are somewhat similar, as their correlation coefficients reach 0.61 and 0.68 for the Northern Hemisphere (NH) and Southern Hemisphere (SH), respectively. Also, the lead–lag relationship (**Supplementary Figure S1**) from both data sets suggests that the HC strength in the two hemispheres is negatively correlated and statistically significant within a temporal lag/lead of about 5 years (lag −1 to lag 5 for the NCEP and lag −5 to lag 0 for the ERA), which are consistent with the HC strength interhemispheric seesaw.

We then examine the time series using 20CR data for the period 1900–2010 (**Supplementary Figure S2**). It indicates that the HC strength index is also negatively correlated (−0.48) between the two hemispheres which is consistent but weaker than that in the ERA20 (−0.74) (**Supplementary Figure S3**), probably due to that the 20CR only assimilates surface variables (surface pressure, SSTs, and sea ice) but the upper-level observations are excluded (Stachnik and Schumacher, 2011). It must note that current reanalysis datasets depict the Hadley circulation with slight differences due to some systematic errors and inevitable data uncertainties (Mitas, 2005; Nguyen et al., 2013), which are beyond the current study. Albeit the decadal variabilities shown in those datasets are not completely the same, all of them have suggested a clear reversed relationship between the two hemispheres, indicating that the seesaw pattern in HC strength is valid and independent of datasets.

Relationship Between the Hadley Circulation Strength Seesaw and Atlantic Multidecadal Variability

Since the seesaw in HC strength between the two hemispheres is revealed by observational datasets, we define the HC seesaw index using the strength index in the NH minus the strength index in the SH. The difference between the NH and SH HC strength indicates that when the NH HC strength is relatively stronger (weaker) than the SH, the HC seesaw index turns to positive (negative). Thus, it depicts the interhemispheric seesaw in HC strength directly. In **Figure 2**, the time series based on NCEP and ERA20C datasets exhibit consistent multidecadal variability in HC strength seesaw index. Consistent with the above findings, the decadal variability in the HC strength seesaw index is somewhat significant and shows two turning signs in the 1960s and around 2000 in the NCEP and ERA20C data sets. For the period 1948–2010, the correlation coefficient of the strength seesaw index between the two datasets is also statistically significant and reaches 0.7, indicating that the multidecadal variations are generally in phase in different data sets. The extended time series in ERA20C suggests that the HC seesaw index turns to negative around 1925. These particular points in time highly resemble the moments when the phase changes in the AMV index in the 1920s,

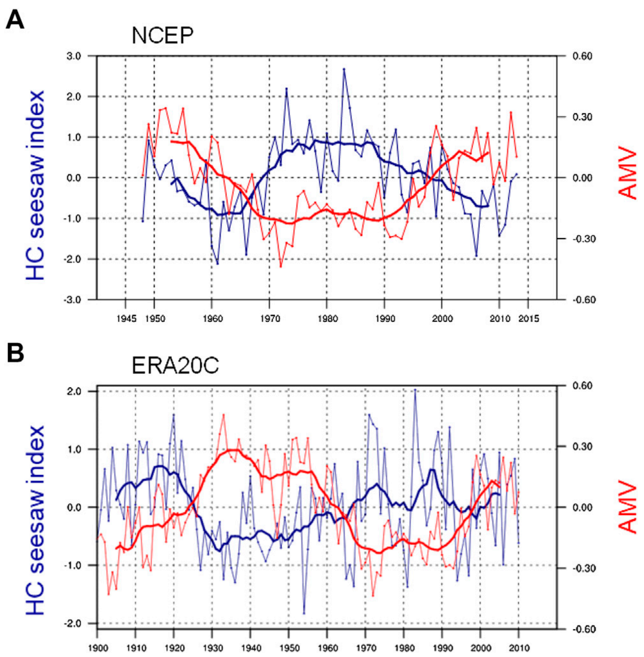

FIGURE 2 | (A) Time series of the normalized HC seesaw index (NH minus SH; blue lines) and AMV index (K) (red lines) for 1948–2013. The raw data (thin lines) and the decadal component (thick lines) are derived from the NCEP data set. **(B)** Same as in **(A)**, but for 1900–2010 based on the ERA20C data set.

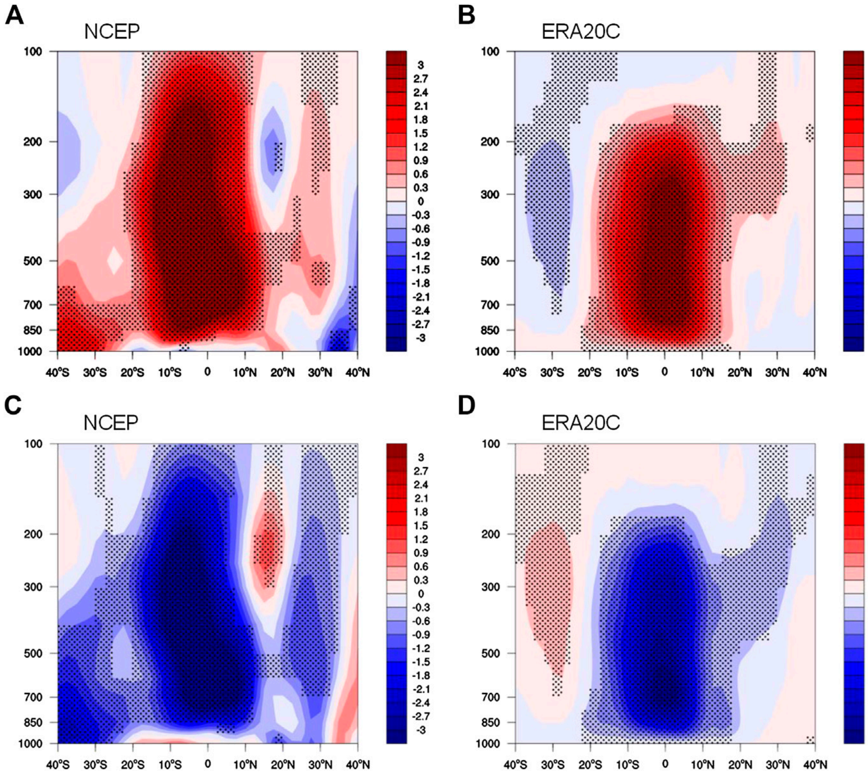

FIGURE 3 | The Hadley circulation mass stream function (10^8 kg s^{-1}) regressed on the normalized HC strength seesaw index derived from the **(A)** NCEP data set from 1948 to 2013, and **(B)** ERA20C data set from 1900 to 2010. The Hadley circulation mass stream function (10^8 kg s^{-1}) regressed on the normalized AMV index derived from the **(C)** NCEP data set and **(D)** ERA20C data set. Dotted shading indicates the regression coefficients significant at the 95% confidence level.

1960s, and around 2000. Interestingly, the AMV index exhibits reversed phases compared to the HC strength seesaw index, indicating the potential linkage between the AMV and HC strength. Then, we calculate the simultaneous correlation between the AMV and HC strength seesaw index. The correlation coefficient in the NCEP data (−0.71) is smaller than that in the ERA20C data (−0.79), but the overall relationship is consistent and statistically significant at the 90% confidence level, suggesting that the simultaneous relationship between HC strength seesaw index and the AMV is also strong and robust. We also examined the relationship between the 20CR-based HC strength seesaw index and the AMV series (**Supplementary Figure S4**). It is suggested that the strength seesaw index is negatively correlated with the AMV with the correlation coefficient reaches −0.74, consistent with the aforementioned results in the ERA20C and NCEP data. In addition, we also provide the results of AMV-HC strength seesaw correlations based on the unfiltered data (r = 0.4 and r = 0.39 for the NCEP and ERA20C data sets, respectively, both are significant at the 95% confidence level), and the correlations between AMV and HC strength seesaw show qualitatively consistent results with those based on the smoothed data. Therefore, this relationship is robust and independent of datasets.

In **Figure 3A**, it shows the spatial regression map between the Hadley circulation and the HC strength seesaw index in NCEP data. The Hadley circulation exhibits uniformly positive regression to the seesaw index from top to bottom of the troposphere. The most significant regressed zone is limited between 20°S and 20°N, but it is not symmetrical to the equator, consistent with the spatial distribution of the Hadley circulation suggested in the previous studies. However, the physical response of the Hadley circulation to the HC strength seesaw index varies in hemispheres. The Hadley circulation is positive (negative) in the NH (SH), corresponding to its definition (see *Data and Methods*). The anomalous positive response to the HC seesaw index indicates the strengthened NH HC and the weakened SH HC, referred to as the interhemispheric strength seesaw. Thus, the HC strength seesaw index defined in this study corresponds well to the spatial pattern of the interhemispheric seesaw. The regression map based on ERA20C data (**Figure 3B**) exhibits a consistent pattern, although the regression is relatively weak and insignificant above 200 hPa, and the equatorially asymmetric mode is not as remarkable as that in the NCEP data. In **Figure 3C** (NCEP) and **Figure 3D** (ERA20C), the Hadley circulation exhibits consistent negative regression with the AMV index, but the responses should be separately evaluated in the two hemispheres. The Hadley circulation in the SH is negatively regressed onto the AMV index, corresponding to the intensification in the SH HC under the AMV forcing. However, the negative regression over the NH indicates that the AMV has an opposite impact on the Hadley circulation, resulting in the

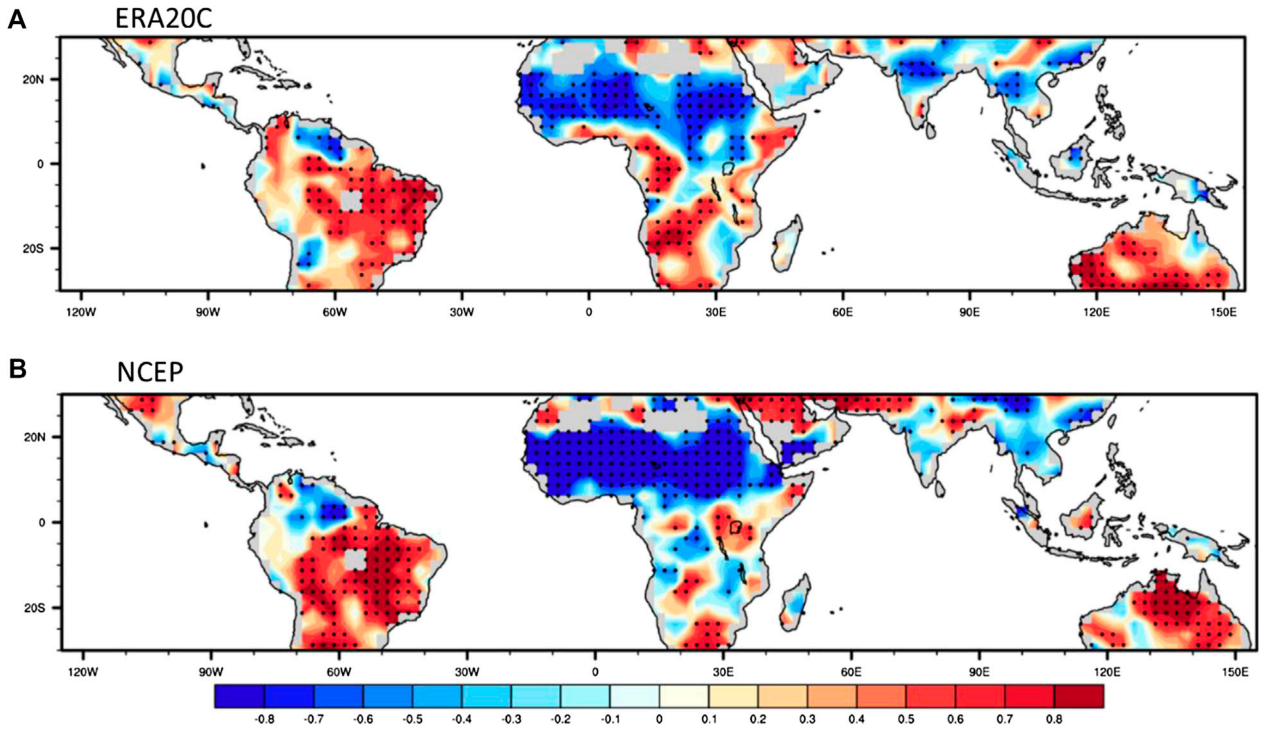

FIGURE 4 | Correlation map between the decadal component of the HC strength seesaw index and the tropical precipitation (30°S–30°N). The HC strength seesaw index is derived from **(A)** ERA20C for the period 1901–2010 and **(B)** NCEP data for the period 1948–2013. The precipitation data is derived from CRU data from 1901 to 2013. The long-term linear trends were removed before the analysis. Dotted shading indicates the correlation coefficients significant at the 95% confidence level.

weakening in circulation strength. Thus, we can conclude that the AMV is capable of modulating the HC strength in the two hemispheres at decadal time scales and contributes to the interhemispheric seesaw. The regression maps in the two datasets show an identical response to the AMV, although there are some discrepancies over upper-level troposphere and extra-tropics. In addition, the regression exhibits an equatorially asymmetric structure in NCEP data, but it is not significant in ERA20C data. Based on the analysis above, it indicates that the interhemispheric seesaw in Hadley circulation strength is closely related to the AMV index as well as the HC strength seesaw index, further validating the negative correlation between the seesaw index and the AMV as is shown in **Figure 2**.

Footprint of the Hadley Circulation Strength Seesaw on the Monsoon Precipitation

The Hadley circulation plays an important role in modulating the tropical precipitation through the meridional migration of its ascending branch which is associated with the intertropical convergence zone (ITCZ). We calculate the correlations between the tropical precipitation and the HC strength seesaw index using the ERA20C and NCEP for the period 1901–2010 and 1948–2013, respectively. For the ERA20C data set (**Figure 4A**), the correlation map exhibits a clear dipole pattern, with the positive correlations located mainly in the Southern Hemisphere, while the negative correlations located in the Northern Hemisphere, consistent with those in the NCEP reanalysis data (**Figure 4B**) and GPCC observational data (**Supplementary Figure S5**). The positive correlation is strong and significant in South America, West Africa, and Australia in the Southern Hemisphere, but the correlation changes in reverse polarity across the equator and exhibits strong negative response in the Sahel, India, Indochina Peninsula, and East Asia. Interestingly, those areas where they exhibit the most prominent responses to the HC strength seesaw largely correspond with the most active monsoon regions. Previous studies have revealed the influences of the Hadley circulation/ITCZ on the East Asian and African monsoon system (Zhou et al., 2017; Geen et al., 2018; Nicholson, 2018). The meridional movement of the ascending branch in the HC influences the global monsoon in response to the remote North Atlantic forcing, resulting in an anti-phase interhemispheric variability in monsoon strength at decadal time scales (Han et al., 2019; Xu et al., 2019), which resembles our results. Thus, it is evident that the meridional movement of the ITCZ associated with the HC ascending branch modulates the monsoon precipitation and consequently leads to the contrasting responses in the two hemispheres. Such connection can be well explained by the interhemispheric seesaw in HC strength.

It is important to note that the HC strength seesaw physically corresponds with the meridional migration of the ascending branch in the HC. The positive (negative) strength seesaw index represents the Hadley circulation in the Northern

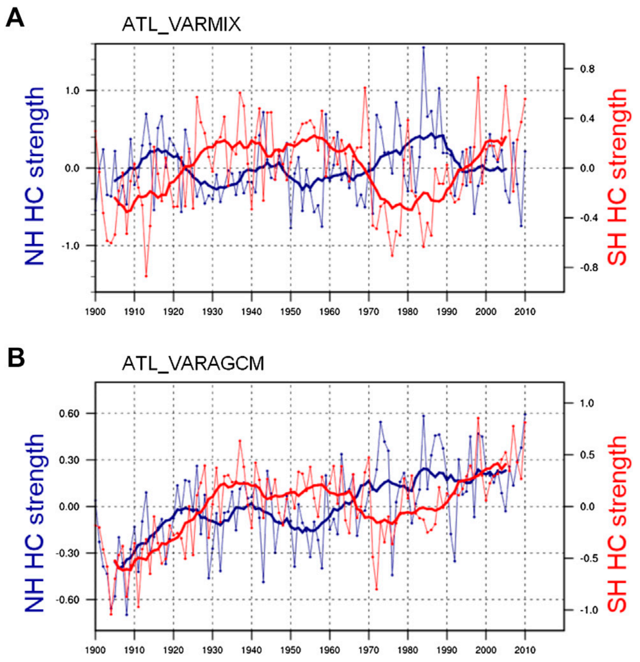

FIGURE 5 | Time series of the raw (thin lines) and decadal component (thick lines) of the HC strength indices (10^9 kg s^{-1}) in the NH (blue lines) and SH (red lines) from the **(A)** ATL_VARMIX and the **(B)** ATL_VARAGCM experiment for 1900–2010.

(Southern) Hemisphere is stronger than the other, corresponding to the southward shift (northward shift) of the ascending branch and consequently leads to a favorable condition for producing more precipitation in the Southern (Northern) Hemisphere tropical areas. Thus, the corresponding across-equatorial winds and the meridional migration of the HC ascending branch together contribute to the increased monsoon precipitation. In this study, the HC strength seesaw plays an intermedia role in connecting the monsoon systems in the two hemispheres and it provides additional evidence for the impacts of the Hadley circulation on the tropical monsoon rainfall. The previous study (Levine et al., 2018) has noted that the AMV plays a major role in impacting the ITCZ-driven precipitation across Africa and South America. Since the location of the ITCZ is associated with the Hadley circulation ascending branch, the contrasting responses of tropical precipitation to the HC strength seesaw index in the two hemispheres may be rooted in the remote AMV signal. Thus, the physical mechanism between the interhemispheric seesaw in HC strength and AMV at decadal time scales needs further investigation.

Model Evidence for Atlantic Multidecadal Variability-Hadley Circulation Strength Connection Mechanism

The observational data suggest that the multidecadal variability in the interhemispheric HC strength seesaw is evident. The regression between the Hadley circulation and the AMV index suggests that the AMV is closely related with such strength seesaw at decadal time scales. How does the AMV influence the HC strength? In this study, we propose two possible mechanisms that may be responsible for the HC strength decadal variability: one is a direct atmospheric response to the AMV-induced North Atlantic warming simulated in ATL_VARAGCM experiment; the other is the air–sea coupling process over the Indo-Pacific basins with the remote AMV forcing included, referring to as ATL_VARMIX experiment (see *Data and Methods*).

In **Figure 5**, we first examine the simulated time series of the NH and SH HC strength index for the period 1900–2010. In the ATL_VARMIX experiment (**Figure 5A**), the simulated time series exhibits obvious decadal variability through the whole analyzed period, and the strength index in one hemisphere is opposite to the other, indicating an identical interhemispheric seesaw pattern in observation. Interestingly, the simulated time series before 1950 is consistent with the ERA20C dataset, which only shows decadal variability in this period with a turning sign that occurs in the 1920s. However, the simulated time series is similar to that in the NCEP dataset after 1950, which exhibits strong decadal variability with a change of sign around 1970. Overall, the time series of the HC strength indices in the two hemispheres are successfully reproduced in the ATL_VARMIX experiment, and their decadal variabilities are significant over the whole simulation period. Consistent with the observation, the correlation coefficient of the HC strength between the two hemispheres reaches −0.80 and is statistically significant at the 95% confidence level, providing model evidence for the interhemispheric strength seesaw. Furthermore, the HC strength seesaw index simulated in the ATL_VARMIX experiment is also negatively correlated (−0.82) with the AMV index, suggesting the HC strength interhemispheric seesaw and its relation to the AMV are robust consistent with the observation. For the time series in the ATL_VARAGCM, it also exhibits decadal variability, but it is far too weak, comparing to the ATL_VARMIX and observational data. The HC strength index in the two hemispheres (**Figure 5B**) shows a generally consistent tendency toward intensification from 1900 to 2010. The opposite trends between the NH and SH HC index are not obvious in this case, especially for the period before the 1920s. Despite these discrepancies exist between the ATL_VARMIX and ATL_VARAGCM, there are some notable features that should be highlighted. The former experiment mainly depicts the decadal variability before 2000, but the recent intensification in the SH HC strength is underestimated. However, the latter experiment successfully reproduces such a trend in the 2000s, consistent with the NCEP data. Thus, we may conclude that the air–sea coupling effect over the Indo-Pacific basins contributes to the decadal variability in HC strength seesaw significantly and may amplify the direct response of the atmosphere to the remote AMV forcing. The recent HC intensification shown in the observation and ATL_VARAGCM indicates that the direct atmospheric response to the AMV also plays a role in modulating the HC strength. The HC strength index exhibits three major changes of sign in the 1920s, 1960s, and 1990s and corresponds to the three turning signs observed in the AMV index, indicating the AMV has a

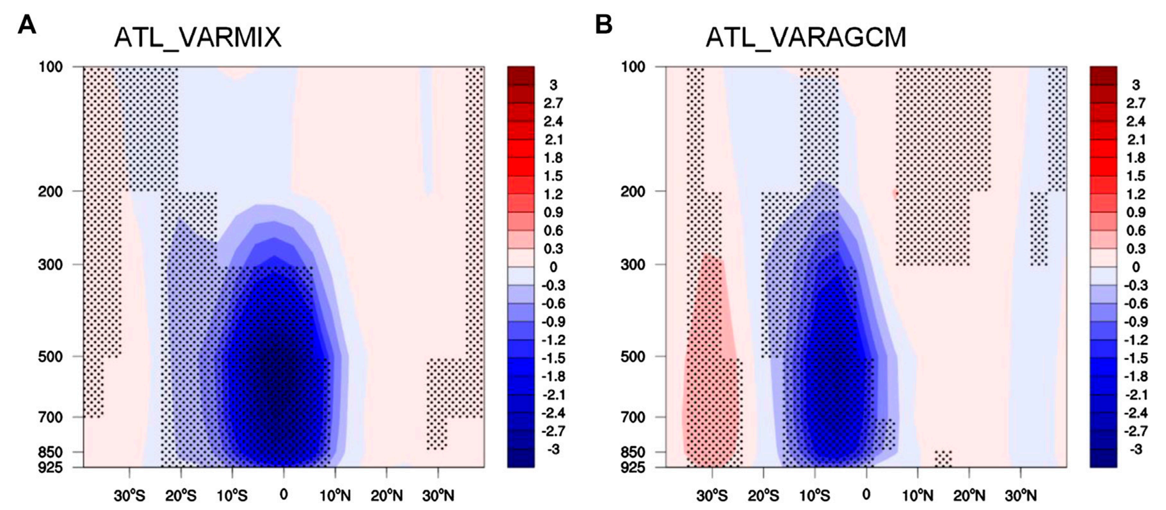

FIGURE 6 | The Hadley circulation mass stream function (10^8 kg s^{-1}) regressed on the normalized AMV index in the **(A)** ATL_VARMIX and the **(B)** ATL_VARAGCM for 1900–2013. Dotted shading indicates the regression coefficients significant at the 95% confidence level.

profound influence on the HC strength through both direct atmospheric feedback and Indo-Pacific air–sea coupling, but the latter effect is of great significance.

We then examine the Hadley circulation response to the AMV forcing in ATL_VARMIX and ATL_VARAGCM experiment. The regression map in ATL_VARMIX simulation (**Figure 6A**) suggests that the Hadley circulation is negatively regressed onto the AMV index between 15°S and 15°N, corresponding to the spatial distribution of the Hadley circulation. The simulated pattern is consistent with the observational results, but the responses over upper-level troposphere and extra-tropics are missing in the ATL_VARMIX experiment. Despite the discrepancy between observation and model simulation, the negative response is captured by the model and most significant over the tropical region. As discussed in the observation, the overall negative regression indicates an intensification in the SH HC strength and the weakening in the NH HC with respect to the remote AMV forcing. Thus, it provides model evidence for the close relationship between the interhemispheric strength seesaw and the AMV, and the non-negligible role of Indo-Pacific air–sea coupling. In **Figure 6B**, the regression map in ATL_VARAGCM also exhibits notable negative regression, indicating the direct atmospheric response to the AMV over the NH also plays a role in modulating the Hadley circulation but has limited contribution. Comparing with the simulated pattern in the ATL_VARMIX experiment, the Hadley circulation in the NH tropics (0°–10°N) shows little response to the AMV in ATL_VARAGCM experiment. The SH HC is significantly intensified by the AMV-related atmospheric feedback, but the NH HC strength does not change with it. Thus the seesaw pattern is missing without considering the Indo-Pacific air–sea coupling effect in response to the AMV.

As suggested in the above discussion, the AMV index is negatively correlated with the seesaw index in HC strength, indicating the AMV could be a potential driver of the interhemispheric strength seesaw. Thus, we calculate the zonally averaged meridional wind regressed onto the AMV index to investigate the relationship between the AMV and atmospheric circulation changes. In **Figures 7A,B**, the critical feature of the regression map is clearly shown in the two data sets, despite some discrepancies that can be found over the middle troposphere and extra-tropics. It exhibits a consistent pattern that the lower level tropical region (20°S–20°N) is governed by anomalous cross-equatorial southerlies associated with the northward shift of the ascending branch of the HC, while the overturning northerlies over upper-level troposphere form a closed atmospheric circulation across the equator. It is suggested that the AMV can induce an anomalous anticlockwise circulation over the tropical region, and its impact on the Hadley circulation is equatorially asymmetric, resulting in intensification in the SH HC strength. In the ATL_VARMIX experiment (**Figure 7C**), the regression map exhibits a consistent pattern in the ERA20C data, but it has "filtered" some of the responses outside the tropics. The lower level response is weaker than the observed, but the anomalous southerlies are still significant. Although the magnitude and strength are underestimated by the model, the experiment still reveals the equatorially asymmetric circulation anomalies, considering Indo-Pacific air–sea coupling under the AMV forcing. In the ATL_VARAGCM experiment (**Figure 7D**), it also exhibits an anomalous anticlockwise circulation in association with the AMV, but the strength is rather weak, compared with the observation. In addition, the simulated lower level wind anomalies at the north of the equator have limited response to the AMV, corresponding to the weak anomalous anticlockwise circulation. Thus, the interhemispheric seesaw is not significant in this case. We may conclude that the anomalous anticlockwise circulation over the tropics is closely related to the AMV forcing and significantly intensifies the Hadley circulation over the Southern Hemisphere.

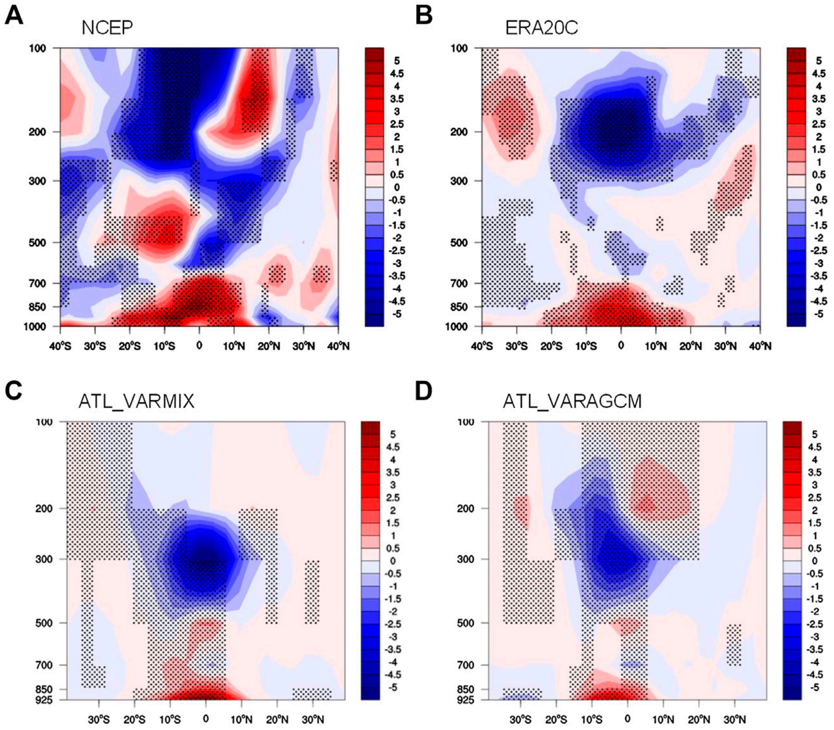

FIGURE 7 | The zonal mean meridional wind (10^{-2} m s^{-1}) regressed on the normalized AMV index derived from the observational datasets: **(A)** NCEP data set from 1948 to 2013, **(B)** ERA20C data set from 1900 to 2010, and experiments: **(C)** ATL_VARMIX, and **(D)** ATL_VARAGCM for the period 1900–2013. Dotted shading indicates the regression coefficients significant at the 95% confidence level.

The simulated pattern in ATL_VARMIX differs from the ATL_VARAGCM experiment in the anomalous cross-equatorial winds. The Indo-pacific air–sea coupling contributes a lot to the northward extension of the cross-equatorial winds, which leads to an intensification in the SH HC strength and the NH HC weakening. In conclusion, the interhemispheric seesaw in HC strength can be largely explained by the anomalous cross-equatorial winds induced by the Indo-Pacific air–sea coupling effects associated with the AMV forcing while the direct atmospheric feedback also plays a role.

In order to explain the formation of the anomalous cross-equatorial winds from an air–sea coupling perspective, we further analyze the footprints of the AMV on the NH SSTs. As shown in **Figure 8A**, the North Atlantic exhibits a uniformly warming response to the AMV signal. Previous studies (Rong and Delworth, 2007) have suggested that the AMV can influence the North Pacific climate through atmospheric teleconnection and ocean dynamics. In this study, the North Pacific SST shows a positive response to the AMV, and it is more significant over the mid-latitudes (20°N–60°N) and western North Pacific, while the eastern tropical Pacific Ocean exhibits slightly negative response. The Indian Ocean SST also shows warming response to the AMV, but it is not significant. Consistent regression patterns can be found in the HadSST3 (**Supplementary Figure S6**) and COBE SST (**Supplementary Figure S7**) data sets as well. The zonal mean SST anomalies in response to the AMV (**Figure 8C**) suggest consistent warming over the Northern Hemisphere, but the warming response is more intense over the mid-latitudes than the tropics. The SST anomalies with latitude over the Indo-Pacific is identical to the Northern Hemisphere, indicating the Indo-Pacific SST warming associated with the AMV can explain a large portion of the SST warming over the entire NH. In the ATL_VARMIX experiment (**Figures 8B,D**), the simulated regression pattern is generally consistent with the observation but discrepancies still exist. In response to the warm phase of AMV, the model shows a warming response over a large part of the North Pacific basin and negligible warming along the west coast of North America. By contrast, the SST warming along the west coast of North America is prominent in observations. These discrepancies may possibly be attributed to the role of ocean dynamics role, which is important for the SST variability over the Northeast Pacific (Chhak and Di Lorenzo, 2007; Di Lorenzo et al., 2008). Also, the model reproduces the overall warming response in the Indo-Pacific region, indicating the AMV and regional air–sea coupling together contribute to the SST warming. The zonal mean SST anomalies are also identical to the observed one, suggesting the AMV-induced warming is evident over the Northern Hemisphere. More specifically, the tropical oceans over the North Atlantic and Indo-Pacific are significantly heated through the AMV-related atmospheric and air–sea coupling processes, further inducing a northward shift of the ascending branch in the Hadley circulation. Thus, the anomalous cross-equatorial winds corresponded to the meridional movement of the ascending motions intensifies the SH HC

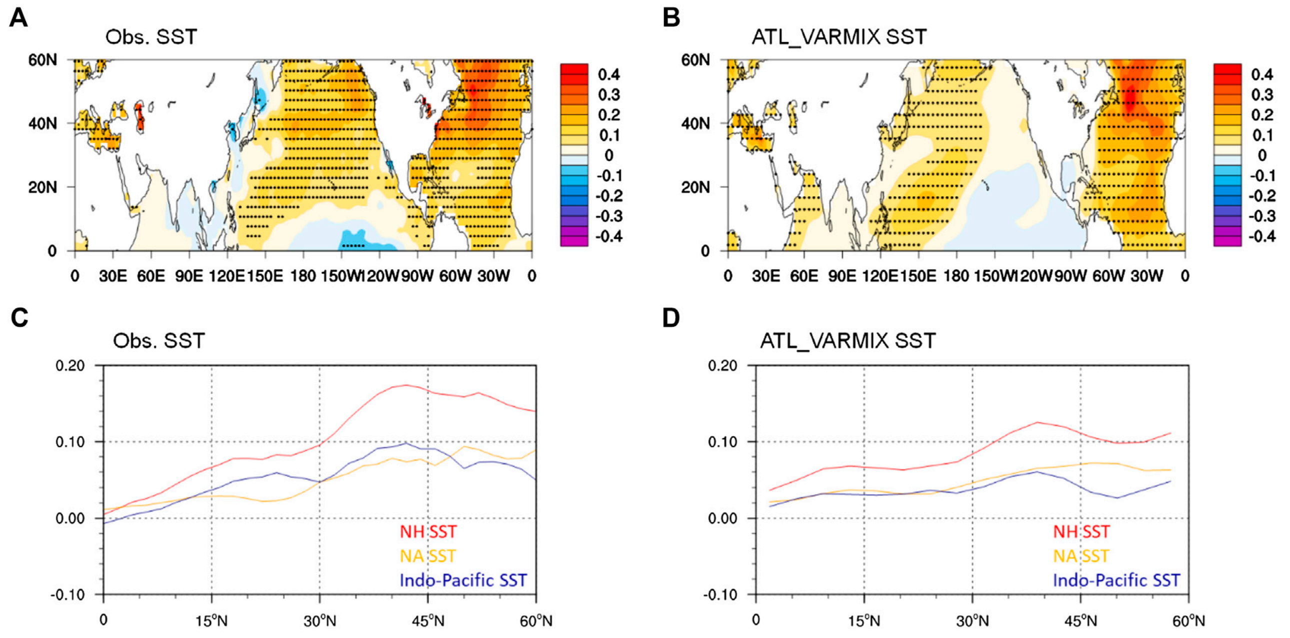

FIGURE 8 | The anomalous SST (K) regressed on the normalized AMV index derived from the **(A)** ERSST dataset and the **(B)** ATL_VARMIX experiment for the period 1900–2013. The SST over the North Atlantic is prescribed with monthly-varying SSTs from the HadISST data. Dotted shading in **(A)** and **(B)** indicates the regression coefficients significant at the 95% confidence level. The zonal mean SST anomalies (K) of the Northern Hemisphere (red lines), North Atlantic (yellow lines), and Indo-Pacific (blue lines) are derived from the **(C)** ERSST dataset and the **(D)** ATL_VARMIX experiment.

strength and weakens the HC strength in the NH, referring to the HC strength interhemispheric seesaw. These results indicate that the AMV is a global climate mode influencing not only the Atlantic-surrounded areas but also the Pacific basin, and the Pacific multidecadal SST anomalies also play a role in the interhemispheric seesaw in the HC strength through the SST footprint of AMV over the North Pacific basin.

On the other hand, whether the Indo-Pacific SST itself drives the anomalous Atlantic SST and the HC strength seesaw remain elusive. We then conduct a similar experiment but with monthly-varying observed SSTs from the HadISST data prescribed over the northern Indo-Pacific basin (30°E–90°W, 0°–60°N) while running the ICTPAGCM coupled to the SOM in the Atlantic and other basins, referring to the Indo-Pacific pacemaker experiment. The regression map (**Supplementary Figure S8A**) between the simulated SST anomalies and the AMV index is analyzed. Compared with the results from the observations (**Figure 8A**) and Atlantic pacemaker experiment (**Figure 8B**), the SST footprint of AMV over the northern Indo-Pacific basin remains, as the observed northern Indo-Pacific SST anomalies are prescribed. However, the anomalous SST responses to the observed Indo-Pacific SST forcings over the North Atlantic are rather weak, and a weak warming response is only confined to the mid-latitude North Atlantic. The North Atlantic SST response to Indo-Pacific SST forcing does not show the AMV-like basin-wide coherent pattern, indicating that the Indo-Pacific alone is not capable of reproducing the AMV signal and thus would have a limited impact on the HC interhemispheric strength seesaw. The regression pattern of the HC mass stream function on the AMV index (**Supplementary Figure S8B**) also supports the above conclusion that the Indo-Pacific SSTs are incapable of reproducing the interhemispheric HC strength seesaw, due to the absence of North Atlantic AMV-like SST anomalies in the Indo-Pacific Pacemaker simulations. Contrary to the observation and ATL_VARMIX experiment, the simulated HC anomaly pattern in response to the Indo-Pacific SST forcing experiment only exhibits a weakening in the strength in Northern Hemisphere and no significant response in Southern Hemisphere. The comparison between the results from observations, Atlantic and Indo-Pacific Pacemaker experiments confirms the critical role of AMV and suggests that the Indo-Pacific SST itself is not a driver of the AMV or the HC strength seesaw, but shows significant responses to the AMV and plays an intermediate role in the driving influence of the AMV on the HC strength seesaw.

Besides the AMV, the Pacific Decadal Oscillation is another important mode of decadal SST variability. The PDO is recognized as a dominant pattern of the North Pacific SST multidecadal variability which integrates a couple of modes of climate variability, influencing the weather patterns over the downstream regions (Newman et al., 2016). Therefore, we also investigate the relationship between the HC strength seesaw and the PDO. The filtered PDO series (**Supplementary Figure S9**) exhibits significant decadal variability with four major phase changes in the 1920s, 1940s, 1970s, and 2000s. The "warm phase" PDO is for the periods 1920–1945 and 1980–2000, while its "cool phase" lasts for about thirty years during 1945–1975. Unlike the PDO index, the HC strength seesaw index is positive before the 1920s, then turns to its negative phase till the 1960s. It is clear that the phase shifts in the PDO do not correspond with those in the HC strength seesaw. During the period 1920–1950, the opposite phase can be seen between the PDO and HC strength seesaw, whereas for the period 1950–1980, the PDO is basically in phase with the HC strength seesaw. Also, the correlation coefficient between these two time series is small and insignificant (close to zero), further indicating the relationship between them is rather too weak. **Supplementary Figure S10** shows the SST anomaly pattern of the PDO. The PDO related SST anomalies show an equatorially symmetric structure centered over the eastern tropical Pacific. Therefore, the anomalous interhemispheric meridional SST gradient for the PDO SST mode is weak and thus the effects of PDO on the tropical cross-equatorial winds are consequently weak. This may be the reason for the weak relationship between the PDO and interhemispheric seesaw in HC strength.

CONCLUSIONS AND DISCUSSIONS

In this study, we identify the multidecadal variability in the hemispheric Hadley circulation strength using NCEP and ERA20C data. The Hadley circulation strength between the two hemispheres is significantly correlated (above −0.8) at decadal time scales. It is suggested that the intensification in one hemisphere accompanies with the weakening in the other, resulting in an interhemispheric seesaw in Hadley circulation strength. The HC strength seesaw index, which represents the relative strength in each hemisphere, is negatively correlated with the AMV index. The spatial regression exhibits a strong negative response of the Hadley circulation to the AMV and leads to the strengthened HC in one hemisphere and weakened in the other, corresponding to the interhemispheric seesaw in HC strength. It is also evident that the AMV can influence the global precipitation by modulating the decadal movement of the ascending branch of the Hadley circulation and leads to an interhemispheric dipole in tropical precipitation. A suit of Atlantic Pacemaker experiments successfully reproduces the close relation between the HC strength seesaw and the AMV, consistent with observation. The ATL_VARMIX experiment indicates that the warm phase AMV and its footprints on the Indo-Pacific SST warming lead to the northward shift of the HC ascending branch and the corresponded cross-equatorial wind anomalies. Thus, the anticlockwise circulation induced by the AMV imposes onto the Hadley circulation, resulting in the strengthened SH HC and weakened in the NH. The strength seesaw is attributed to the air–sea coupling effect over the Indo-Pacific oceans in association with the AMV-induced warming (AMV footprint), while the direct atmospheric response to the AMV plays a minor role.

The Hadley Cell is one of the most important atmospheric circulations in the world. It profoundly influences the climate over the tropics and remote regions. Our study identifies the multidecadal variation in the Hadley circulation strength interhemispheric seesaw, further connecting its impact on tropical monsoonal precipitation with the remote AMV signal. In this study, the critical features of the HC strength seesaw are well captured by the two data, but observational uncertainty still exists. For example, the lead–lag relation of the interhemispheric HC strength between the current two reanalysis data sets is not quite the same (the correlation maximizes when the NH leads the SH in the NCEP, but lags the SH in the ERA20C). In addition, the experiment's performance is limited by the model resolution. The coarse grid in the model may not be enough to simulate the complex processes over the tropics and upper-level troposphere. Thus, a more reliable observation and advanced coupled model are needed in future works. As we have suggested a clear interhemispheric dipole in tropical precipitation associated with the HC strength seesaw, it is important to investigate their physical connections and the HC strength seesaw may be a valuable indicator for tropical monsoon prediction.

Our work mainly focuses on the interhemispheric differences in HC strength but other features of the Hadley circulation like the recent poleward expansion have also received considerable attention. Although the relationship between the PDO and HC strength seesaw is weak, previous studies have indicated an important role of the natural variability (PDO) in modulating the HC width (Grassi et al., 2012; Allen and Kovilakam, 2017; Staten et al., 2018). The role of the Atlantic decadal SST variability (AMV) in the HC expansion remains a future avenue of investigation.

DATA AVAILABILITY STATEMENT

The raw data supporting the conclusions of this article will be made available by the authors, without undue reservation.

AUTHOR CONTRIBUTIONS

CS designed the research. YL, CS, and GZ performed the data analysis, prepared all figures and led the writing of the manuscript. All the authors discussed the results and commented on the manuscript.

ACKNOWLEDGMENTS

We would like to thank the reviewers for their constructive comments that helped improve our manuscript. This work was jointly supported by the National Natural Science Foundation of China (41975082, 41775038, and 41790474), and National Key Research and Development Program of China (2016YFA0601801).

SUPPLEMENTARY MATERIAL

The Supplementary Material for this article can be found online at: https://www.frontiersin.org/articles/10.3389/feart.2020.580457/full#supplementary-material

REFERENCES

Allen, R. J., and Kovilakam, M. (2017). The role of natural climate variability in recent tropical expansion. *J. Clim.* 30 (16), 6329–6350. doi:10.1175/jcli-d-16-0735.1.

Chang, E. K. M. (1995). The influence of Hadley circulation intensity changes on extratropical climate in an idealized model. *J. Atmos. Sci.* 52 (11), 2006–2024. doi:10.1175/1520-0469(1995)052<2006:tiohci>2.0.co;2

Chen, J., Carlson, B. E., and Del Genio, A. D. (2002). Evidence for strengthening of the tropical general circulation in the 1990s. *Science* 295 (5556), 838–841. doi:10.1126/science.1065835

Chhak, K., and Di Lorenzo, E. (2007). Decadal variations in the California Current upwelling cells. *Geophys. Res. Lett.* 34 (14), L14604. doi:10.1029/2007gl030203

Compo, G. P., Whitaker, J. S., Sardeshmukh, P. D., Matsui, N., Allan, R. J., Yin, X., et al. (2011). The twentieth century reanalysis project. *Q. J. R. Meteorol. Soc.* 137, 1–28. doi:10.1002/qj.776

Di Lorenzo, E., Schneider, N., Cobb, K. M., Franks, P. J. S., Chhak, K., Miller, A. J., et al. (2008). North Pacific Gyre Oscillation links ocean climate and ecosystem change. *Geophys. Res. Lett.* 35 (8), 1–6. doi:10.1029/2007gl032838

Diaz, H. F., and Bradley, R. S. (2004). “The Hadley circulation: present, past, and future,” in *The Hadley circulation: present, past and future*. Berlin: Springer, 1–5.

Dima, I. M., and Wallace, J. M. (2003). On the seasonality of the Hadley cell. *J. Atmos. Sci.* 60 (12), 1522–1527. doi:10.1175/1520-0469(2003)060<1522:otsoth>2.0.co;2

Feng, J., Li, J., and Xie, F. (2013). Long-term variation of the principal mode of boreal spring Hadley circulation linked to SST over the Indo-Pacific warm pool. *J. Clim.* 26 (2), 532–544. doi:10.1175/jcli-d-12-00066.1

Feng, R., Li, J., and Wang, J. (2011). Regime change of the boreal summer Hadley circulation and its connection with the tropical SST. *J. Clim.* 24 (15), 3867–3877. doi:10.1175/2011jcli3959.1

Folland, C. K., Rayner, N. A., Brown, S. J., Smith, T. M., Shen, S. S. P., Parker, D. E., et al. (2001). Global temperature change and its uncertainties since 1861. *Geophys. Res. Lett.* 28 (13), 2621–2624. doi:10.1029/2001gl012877

Frierson, D. M., Lu, J., and Chen, G. (2007). Width of the Hadley cell in simple and comprehensive general circulation models. *Geophys. Res. Lett.* 34 (18), 19–24. doi:10.1029/2007gl031115

Geen, R., Lambert, F. H., and Vallis, G. K. (2018). Regime change behavior during Asian monsoon onset. *J. Clim.* 31 (8), 3327–3348. doi:10.1175/jcli-d-17-0118.1

Grassi, B., Redaelli, G., Canziani, P. O., and Visconti, G. (2012). Effects of the PDO phase on the tropical belt width. *J. Clim.* 25 (9), 3282–3290. doi:10.1175/jcli-d-11-00244.1

Grise, K. M., and Davis, S. M. (2020). Hadley cell expansion in CMIP6 models. *Atmos. Chem. Phys.* 20 (9), 5249–5268. doi:10.5194/acp-20-5249-2020

Guo, Y.-P., Li, J.-P., and Feng, J. (2016). Climatology and interannual variability of the annual mean Hadley circulation in CMIP5 models. *Adv. Clim. Change Res.* 7 (1–2), 35–45. doi:10.1016/j.accre.2016.04.005

Han, T., Yu, K., Yan, H., Yan, H., Tao, S., Zhang, H., et al. (2019). The decadal variability of the global monsoon links to the north Atlantic climate since 1851. *Geophys. Res. Lett.* 46 (15), 9054–9063. doi:10.1029/2019gl081907

Harris, I., Jones, P. D., Osborn, T. J., and Lister, D. H. (2014). Updated high-resolution grids of monthly climatic observations–the CRU TS3. 10 Dataset. *Int. J. Climatol.* 34 (33), 623–642. doi:10.1002/joc.3711

Held, I. M., and Soden, B. J. (2006). Robust responses of the hydrological cycle to global warming. *J. Clim.* 19 (21), 5686–5699. doi:10.1175/jcli3990.1

Holton, J. R., and Staley, D. O. (1973). An introduction to dynamic meteorology. *Am. J. Phys.* 41 (5), 752–754. doi:10.1119/1.1987371

Hou, A. Y. (1998). Hadley circulation as a modulator of the extratropical climate. *J. Atmos. Sci.* 55 (14), 2437–2457. doi:10.1175/1520-0469(1998)055<2437:hcaamo>2.0.co;2

Hu, Y., and Zhou, C. (2010). “Decadal changes in the Hadley circulation,” in *Advances in geosciences: Vol. 16: Atmospheric Science (AS)*. Singapore: World Scientific, 61–74.

Hudson, R., Andrade, M., Follette, M., and Frolov, A. (2006). The total ozone field separated into meteorological regimes. Part II: northern Hemisphere mid-latitude total ozone trends. *Atmos. Chem. Phys. Discuss.* 6 (12), 6183–6209. doi:10.5194/acpd-6-6183-2006

Johanson, C. M., and Fu, Q. (2009). Hadley cell widening: model simulations versus observations. *J. Clim.* 22 (10), 2713–2725. doi:10.1175/2008jcli2620.1

Kalnay, E., Kanamitsu, M., Kistler, R., Collins, W., Deaven, D., Gandin, L., et al. (1996). The NCEP/NCAR 40-year reanalysis project. *Bull. Am. Meteorol. Soc.* 77 (3), 437–471. doi:10.1175/1520-0477(1996)077<0437:tnyrp>2.0.co;2

Kucharski, F., Parvin, A., Rodriguez-Fonseca, B., Farneti, R., Martin-Rey, M., Polo, I., et al. (2016). The teleconnection of the tropical Atlantic to Indo-Pacific sea surface temperatures on inter-annual to centennial time scales: a review of recent findings. *Atmosphere* 7 (2), 29. doi:10.3390/atmos7020029

Levine, A. F. Z., Frierson, D. M. W., and McPhaden, M. J. (2018). AMO forcing of multidecadal Pacific ITCZ variability. *J. Clim.* 31 (14), 5749–5764. doi:10.1175/jcli-d-17-0810.1

Li, J., Sun, C., and Jin, F.-F. (2013). NAO implicated as a predictor of Northern Hemisphere mean temperature multidecadal variability. *Geophys. Res. Lett.* 40 (20), 5497–5502. doi:10.1002/2013gl057877

Lindzen, R. S. (1994). Climate dynamics and global change. *Annu. Rev. Fluid Mech.* 26 (1), 353–378. doi:10.1146/annurev.fl.26.010194.002033

Lu, J., Vecchi, G. A., and Reichler, T. (2007). Expansion of the Hadley cell under global warming. *Geophys. Res. Lett.* 34 (6), L06805. doi:10.1029/2007gl030931

Ma, J., and Li, J. (2008). The principal modes of variability of the boreal winter Hadley cell. *Geophys. Res. Lett.* 35 (1), L01808. doi:10.1029/2007gl031883

Mitas, C. M. (2005). Has the Hadley cell been strengthening in recent decades? *Geophys. Res. Lett.* 32 (3), L03809. doi:10.1029/2004gl021765

Newman, M., Alexander, M. A., Ault, T. R., Cobb, K. M., Deser, C., Di Lorenzo, E., et al. (2016). The pacific decadal oscillation, revisited. *J. Clim.* 29 (12), 4399–4427. doi:10.1175/jcli-d-15-0508.1

Nguyen, H., Evans, A., Lucas, C., Smith, I., and Timbal, B. (2013). The Hadley circulation in reanalyses: climatology, variability, and change. *J. Clim.* 26 (10), 3357–3376. doi:10.1175/jcli-d-12-00224.1

Nicholson, S. E. (2018). The ITCZ and the seasonal cycle over equatorial Africa. *Bull. Am. Meteorol. Soc.* 99 (2), 337–348. doi:10.1175/bams-d-16-0287.1

Oort, A. H., and Yienger, J. J. (1996). Observed interannual variability in the Hadley circulation and its connection to ENSO. *J. Clim.* 9 (11), 2751–2767. doi:10.1175/1520-0442(1996)009<2751:oivith>2.0.co;2

Quan, X.-W., Diaz, H. F., and Hoerling, M. P. (2004). “Change in the tropical Hadley cell since 1950, in *The Hadley circulation: present, past and future*. Berlin: Springer, 85–120.

Quan, X.-W., Hoerling, M. P., Perlwitz, J., Diaz, H. F., and Xu, T. (2014). How fast are the tropics expanding? *J. Clim.* 27 (5), 1999–2013. doi:10.1175/jcli-d-13-00287.1

Rong, Z., and Delworth, T. L. (2007). Impact of the Atlantic multidecadal oscillation on North Pacific climate variability. *Geophys. Res. Lett.* 34, 24–32. doi:10.1029/2007GL031601

Seidel, D. J., Fu, Q., Randel, W. J., and Reichler, T. J. (2008). Widening of the tropical belt in a changing climate. *Nat. Geosci.* 1 (1), 21. doi:10.1038/ngeo.2007.38

Smith, T. M., Reynolds, R. W., Peterson, T. C., and Lawrimore, J. (2008). Improvements to NOAA’s historical merged land-ocean surface temperature analysis (1880–2006). *J. Clim.* 21 (10), 2283–2296. doi:10.1175/2007jcli2100.1

Stachnik, J. P., and Schumacher, C. (2011). A comparison of the Hadley circulation in modern reanalyses. *J. Geophys. Res. Atmos.* 116 (D22), 19–27. doi:10.1029/2011jd016677

Staten, P. W., Lu, J., Grise, K. M., Davis, S. M., and Birner, T. (2018). Re-examining tropical expansion. *Nat. Clim. Change.* 8 (9), 768–775. doi:10.1038/s41558-018-0246-2.

Stickler, A., Brönnimann, S., Valente, M. A., Bethke, J., Sterin, A., Jourdain, S., et al. (2014). ERA-CLIM: historical surface and upper-air data for future reanalyses. *Bull. Am. Meteorol. Soc.* 95 (9), 1419–1430. doi:10.1175/bams-d-13-00147.1

Sun, C., Kucharski, F., Li, J., Jin, F.-F., Kang, I.-S., and Ding, R. (2017). Western tropical Pacific multidecadal variability forced by the Atlantic multidecadal oscillation. *Nat. Commun.* 8 (1), 1–10. doi:10.1038/ncomms15998

Sun, C., Li, J., and Zhao, S. (2015). Remote influence of Atlantic multidecadal variability on Siberian warm season precipitation. *Sci. Rep.* 5, 16853. doi:10.1038/srep16853

Tao, L., Hu, Y., and Liu, J. (2016). Anthropogenic forcing on the Hadley circulation in CMIP5 simulations. *Clim. Dynam.* 46 (9–10), 3337–3350. doi:10.1007/s00382-015-2772-1

Trenberth, K. E. (2002). Changes in tropical clouds and radiation. *Science* 296 (5576), 2095. doi:10.1126/science.296.5576.2095a

Trenberth, K. E., and Stepaniak, D. P. (2003). Seamless poleward atmospheric energy transports and implications for the Hadley circulation. *J. Clim.* 16 (22), 3706–3722. doi:10.1175/1520-0442(2003)016<3706:spaeta>2.0.co;2

Watt-Meyer, O., Frierson, D. M. W., and Fu, Q. (2019). Hemispheric asymmetry of tropical expansion under CO2 forcing. *Geophys. Res. Lett.* 46 (15), 9231–9240. doi:10.1029/2019gl083695

Wielicki, B. A., Wong, T., Allan, R. P., Slingo, A., Kiehl, J. T., Soden, B. J., et al. (2002). Evidence for large decadal variability in the tropical mean radiative energy budget. *Science* 295 (5556), 841–844. doi:10.1126/science.1065837

Xu, H., Song, Y., Goldsmith, Y., and Lang, Y. (2019). Meridional ITCZ shifts modulate tropical/subtropical Asian monsoon rainfall. *Sci. Bull.* 64 (23), 1737–1739. doi:10.1016/j.scib.2019.09.025

Xue, J., Sun, C., Li, J., and Mao, J. (2018). South Atlantic forced multidecadal teleconnection to the midlatitude south Indian Ocean. *Geophys. Res. Lett.* 45 (16), 8480–8489. doi:10.1029/2018gl078990

Zhou, B.-T., and Wang, H.-J. (2006). Interannual and interdecadal variations of the Hadley circulation and its connection with tropical sea surface temperature. *Chin. J. Geophys.* 49 (5), 1147–1154. doi:10.1002/cjg2.939

Zhou, B., Wang, Z., and Shi, Y. (2017). Possible role of Hadley circulation strengthening in interdecadal intensification of Snowfalls over Northeastern China under climate change. *J. Geophys. Res. Atmos.* 122 (21), 11638–11650. doi:10.1002/2017jd027574

Conflict of Interest: The authors declare that the research was conducted in the absence of any commercial or financial relationships that could be construed as a potential conflict of interest.

frontiers in Earth Science

ORIGINAL RESEARCH
published: 23 November 2020
doi: 10.3389/feart.2020.584001

Influence of the North Pacific Victoria Mode on the Madden–Julian Oscillation

Tao Wen[1], Quanliang Chen[2], Jianping Li[3], Ruiqiang Ding[4], Yu-heng Tseng[5], Zhaolu Hou[3] and Xumin Li[6]*

[1]State Key Laboratory of Earth Surface Processes and Resource Ecology, Beijing Normal University, Beijing, China, [2]Plateau Atmosphere and Environment Key Laboratory of Sichuan Province, Chengdu University of Information Technology, Chengdu, China, [3]Laboratory for Regional Oceanography and Numerical Modeling, Qingdao National Laboratory for Marine Science and Technology, Qingdao, China, [4]State Key Laboratory of Earth Surface Processes and Resource Ecology, Beijing Normal University, Beijing, China, [5]Institute of Oceanography, National Taiwan University, Taipei, Taiwan, [6]CIC-FEMD/ILCEC, Key Laboratory of Meteorological Disaster of Ministry of Education, School of Atmospheric Sciences, Nanjing University of Information Science and Technology, Nanjing, China

Using the observational data and the Coupled Model Intercomparison Project phase 5 (CMIP5) models this study examined the influence of the North Pacific Victoria mode (VM) on the Madden–Julian Oscillation (MJO). The results show that the February–April VM had a significant influence on the development and propagation of the MJO over the equatorial central-western Pacific (ECWP) during spring (March-May) between 1979 and 2017. Specifically, MJO development was favored more by positive VM events than negative VM events. These complicated connections could have been caused by the SST gradient anomalies associated with positive VM events, enhancing the convergence of low-level over the ECWP. When this is combined with warm SST anomalies in the equatorial central Pacific it could have led to a boost in the Kelvin wave anomalies, resulting in enhanced MJO activity over the ECWP. These conclusions indicate that the VM is an important factor in MJO diversity.

Keywords: Madden Julian oscillation, Victoria mode, air-sea coupling, barrier effect, coupled model intercomparison project phase 5

Edited by:
Jasti S. Chowdary,
Indian Institute of Tropical Meteorology (IITM), India

Reviewed by:
Maoqiu Jian,
Sun Yat-sen University, China
Kaiming Hu,
Institute of Atmospheric Physics (CAS), China

****Correspondence:***
Ruiqiang Ding
drq@bnu.edu.cn

Specialty section:
This article was submitted to Atmospheric Science, a section of the journal Frontiers in Earth Science

Received: *16 July 2020*
Accepted: *12 October 2020*
Published: *23 November 2020*

Citation:
Wen T, Chen Q, Li J, Ding R, Tseng Y, Hou Z and Li X (2020) Influence of the North Pacific Victoria Mode on the Madden–Julian Oscillation. Front. Earth Sci. 8:584001. doi: 10.3389/feart.2020.584001

INTRODUCTION

As one of the most important modes of intraseasonal variability in the tropics, the Madden–Julian oscillation (MJO; Hendon et al., 2007; Madden and Julian, 1971; Madden and Julian, 1972) has momentous academic value, due to its influence on short-term weather and climate phenomena globally (Lau and Chan, 1986). Many previous theoretical studies on MJO have indicated a few obvious natures, including its large-scale convective disturbance, the time scale between a month and a season, and the eastward propagation at ~5 m/s (Weickmann, 1983). Although it has been the subject of comprehensive investigation in recent decades, accurate mode simulation and prediction of the MJO remain elusive (Adames and Wallace, 2014).

Previous studies have found that there are important modes that affect tropical climate variability, such as El Niño–Southern Oscillation (ENSO) and the Indian Ocean Dipole (IOD) can modulate the MJO (Woolnough et al., 2000; Jones et al., 2004; Hendon et al., 2007; Pohl and Matthews, 2007; Moon et al., 2011; DeMott et al., 2015; Zheng and Zhang, 2018). ENSO exerts a

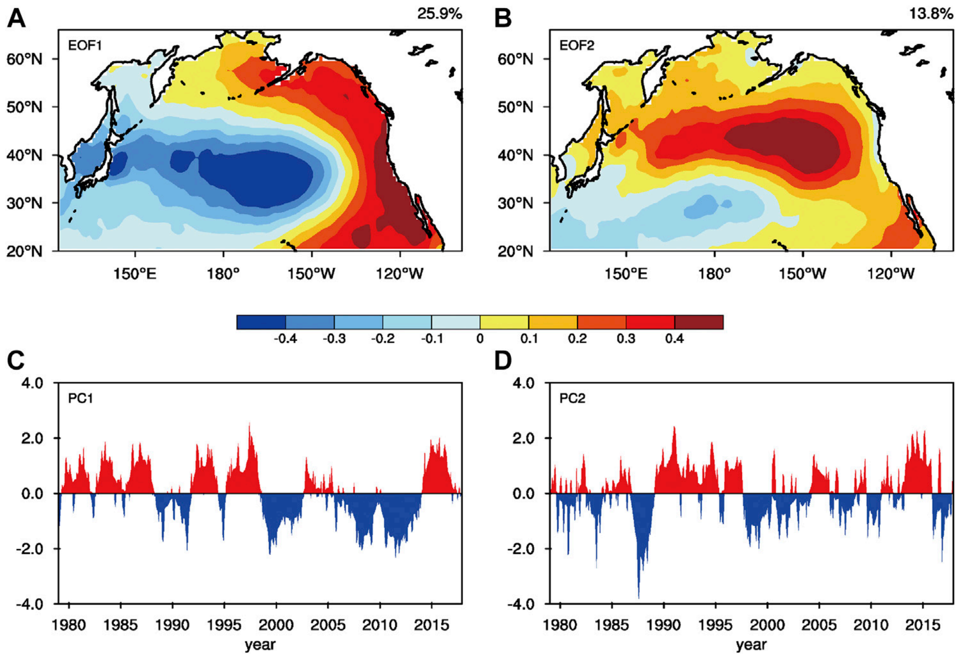

FIGURE 1 | Spatial patterns and corresponding PCs of the first two leading EOF modes of FMA SST anomalies over the North Pacific poleward of 20°N (after removing the global mean SSTA).

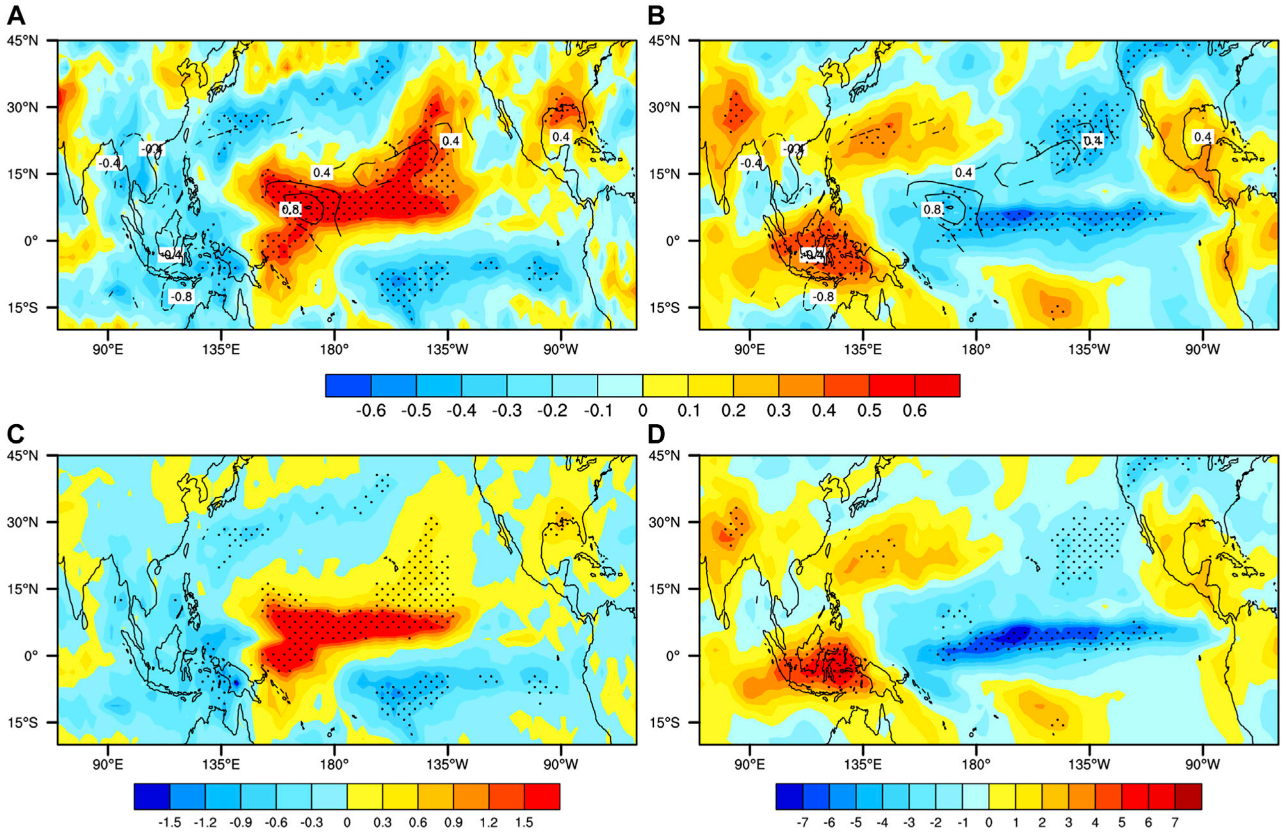

FIGURE 2 | (A) Correlation map of the FMA VMI with the following spring precipitation (shaded) and specific humidity (contours) anomalies. **(B)** As **(A)** but for the correlations between the FMA VMI and the following spring OLR (specific humidity) anomalies. **(C)** MAM precipitation anomalies regressed on the FMA VMI. **(D)** As **(C)** but for the regressions between the FMA VMI and the MAM OLR anomalies. Only anomalies exceeding 95% significance, based on a two-tailed Student's t test, are shown.

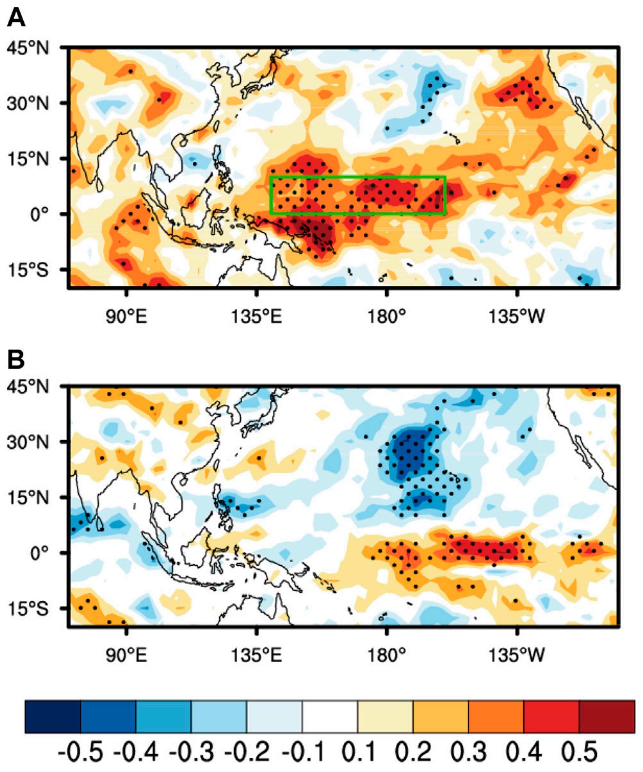

FIGURE 3 | (A) Correlation between 30 and 90 days OLR variance and the VMI. **(B)** Correlation between 30 and 90 days OLR variance and the winter (DJF) Niño3.4 index. Correlations that exceed the 95% confidence level are stippled, based on a two-tailed Student's t test.

substantial influence on all stages of MJO: the initiation, maintenance, and propagation. MJO events are more frequent during El Niño episodes than under La Niña conditions (Jones et al., 2004), and have briefer periods (Pohl and Matthews, 2007; DeMott et al., 2015), and transmit further east of the Pacific (Tam and Lau, 2005). The warm water eastward development during El Niño events expedites the expanded eastward spread of the MJO (Woolnough et al., 2000; DeMott et al., 2015). In addition, Shinoda and Han (2005) and Wilson et al. (2013) showed that the IOD plays a role in MJO activity. During negative IOD events, the MJO activity of the eastern Indian Ocean is more frequent than that of the western Indian Ocean. This is due to warm sea surface temperature anomalies (SSTAs) of the eastern but gets cold in the western Indian Ocean. Homoplastically, the reverse is true for positive IOD events.

In addition to tropical climate modes, some extratropical climate modes such as the North Atlantic Oscillation and the Arctic Oscillation play a pivotal role in the extratropical zone (Ambaum et al., 2001; Wallace and Thompson, 2002; Vecchi et al, 2004, Zhou and Miller 2005; Lin et al., 2009). These can have important modulation effects on the MJO activity in the tropics. Lin et al. (2009) mentioned that MJO activity in tropical regions may be affected by changes in the zonal wind of the troposphere over the North Atlantic. Moreover, Yoo et al. (2011), Yoo et al. (2012) have pointed out that the poleward wave train associated with the surface air temperature over the Arctic is closely related to the MJO activity in the tropics.

Recent studies have named the second empirical orthogonal function mode (EOF2) of the SSTAs found north of 20°N in the North Pacific as the Victoria mode (VM; Bond et al., 2003), which has a significant impact on convection and precipitation over that part of the tropics during the coming summer (Ding et al., 2015a). Given that during the evolution and propagation of the MJO, the convection in the equatorial central Pacific makes a momentous contribution (Pohl and Matthews, 2007), and there may be a close connection between the February-April (FMA) and MJO activity. However, there is little research on the connection and influence between VM and MJO. The primary purpose of this study was to investigate the connection between the FMA VM and MJO activity the following spring. This study examined whether there is a fundamental connection between the FMA VM over the extratropical region following MJO activity and if there is, asking how this connection is established and exploring how it works.

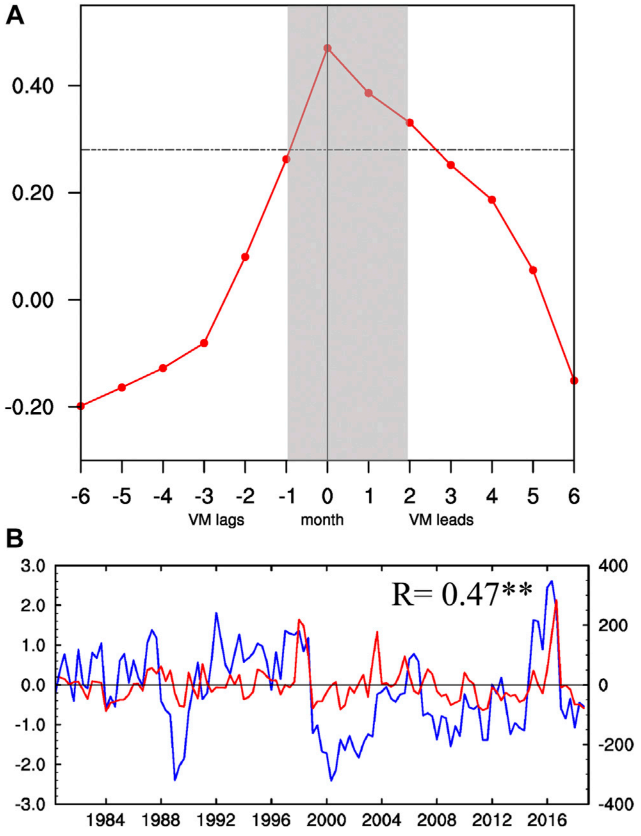

FIGURE 4 | (A) Lead–lag correlation coefficients between the FMA VMI and the OLR variance area-averaged over ECWP. The horizontal dashed line indicates the 95% significance level. **(B)** Time series of the FMA VMI (blue line) and the OLR variance area-averaged over ECWP (red line) for the period 1979–2017.

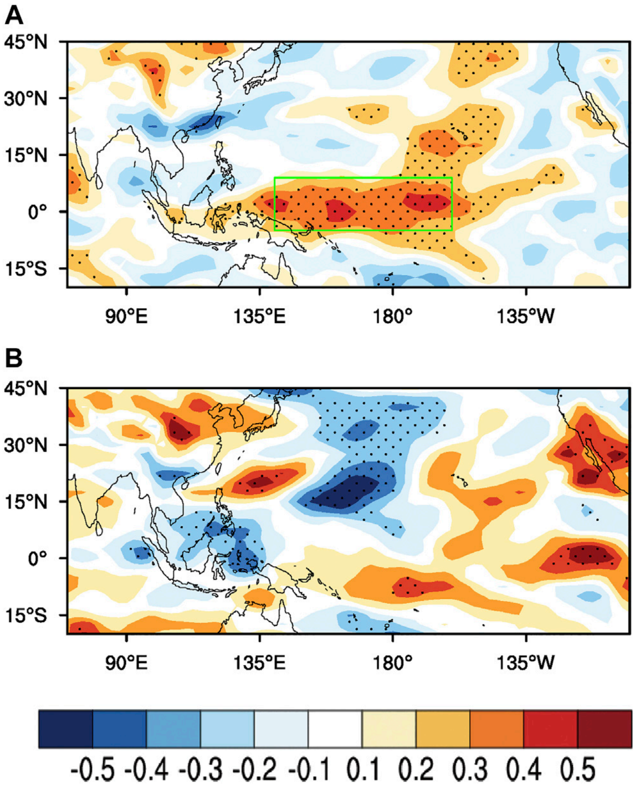

FIGURE 5 | As **Figure 3** but for 30–90 days 850 hPa zonal wind variance.

DATA AND METHODOLOGY

Observational Data

This study used data from several observational, reconstructed, and reanalysis data sets. The monthly mean SST data set was drawn from the Hadley Center global sea ice and sea surface temperature (HadISST) dataset (Rayner et al., 2006). Specific humidity, u-wind, and v-wind data were sourced from the National Centers for Environmental Prediction (NCEP) reanalysis dataset (Kalnay et al., 1996). The Outgoing Longwave Radiation (OLR) data and precipitation data were sourced from the Climate Prediction Center Merged Analysis of Precipitation dataset (Xie and Arkin, 1997) and the NCEP/NOAA (Liebmann and Smith, 1996), respectively. Data were analyzed on a 2.5° × 2.5° spatial grid over the period January 1, 1979, to December 31, 2017, except for the monthly mean SST data set, which had a spatial resolution of 1° × 1.

Daily anomalies were calculated with the time series of each grid point by removing the linear trend, which was obtained using the least square fit, and by eliminating daily climatology, which was the average of each day. Then, using the 30–90°days bandpass Lanczos filter with 401 weights, we processed the daily anomalies (Duchon, 1979). The variability of the intraseasonal timescale was obtained by diagnosing these calculated daily anomalies. We calculated the monthly anomalies by removing the linear trend and climatological monthly means, to investigate variability at the interannual timescale.

Model Datasets

To account for the difference between the effect of FMA VM and ENSO on the precipitation patterns over the equatorial central-western Pacific regions (ECWP), we used the Geophysical Fluid Dynamics Laboratory global Atmospheric Model version 2.1 (AM2.1) at a horizontal resolution of 2.5°longitude × 2°latitude. The seasonal varying climatological SSTs were used to obtain the climatological state (CTRL). Two sensitivity experiments were conducted with the composite SSTAs of the VM (5°S–60°N, 105°E–110°W) and El Niño region (15°S–15°N, 150°E–70°W) over the tropical Pacific from February to April. SSTAs outside the forcing area were set to zero and only positive loading in the region was used. Each run was integrated for 40 years and the output from the last 30 years of the integration was averaged to reduce the possible impact of the internal variability.

To evaluate whether the FMA VM over the extratropical region can affect the subsequent MJO in the tropics, we reproduced activity using current coupled models. The study used daily and monthly outputs from control experiments from two coupled atmosphere-ocean models that participated in CMIP5 (Coupled Model Intercomparison Project, phase 5). The variables we analyzed were daily OLR and monthly SST, u-wind, v-wind, specific humidity, and precipitation. For ease of comparison and the ensemble mean computation, we transformed all variables from the CMIP5 output into a horizontal resolution of 2.5° × 2.5.

Definition of Indices

This study used the RMM index, a generally used MJO index, to select MJO events. The RMM index was constituted on the multivariate EOF analysis of the united fields of OLR, 850- and 200 hPa zonal wind anomalies (Wheeler and Hendon, 2004; Zheng and Zhang, 2018). Because of the convection and circulation change characteristics of the MJO, the RMM index was an effective way to reflect the MJO's multiple structures. The RMM index is commonly used in MJO diagnostics and assessments of operational MJO forecast skill (Seo et al., 2009). Following convention, strong MJO activity was defined as occurring when the RMM amplitude exceeded 1 (i.e., $\sqrt{\text{RMM1}^2 + \text{RMM2}^2} > 1$). We recorded daily RMM values through the regularly updated online website resources of the Australian Bureau of Meteorology (Wheeler and Hendon, 2004, 2017).

Previous studies have reported that unlike the Pacific Decadal Oscillation (Ding et al., 2015a; Mantua et al., 1997), which coincides to the EOF1 of SSTAs found north of 20°N over the North Pacific, the VM is pushed by the North Pacific Oscillation like atmospheric variability through variation in heat fluxes of surface, and demonstrates a triple texture over the North Pacific (Alexander et al., 2010; Ding et al., 2015b; DeMott et al., 2015). As the VM shows the maximum variance between February and April (FMA), due to a lagging response to the affecting of North Pacific oscillation (Ding et al., 2015b), this study performed the EOF analysis method to the SSTA field of the FMA averaged in the North Pacific (100°E–100.5°W, 20.5°N–65.5°N; **Figure 1**). Hereafter, we define Pacific decadal oscillation as SSTA EOF1

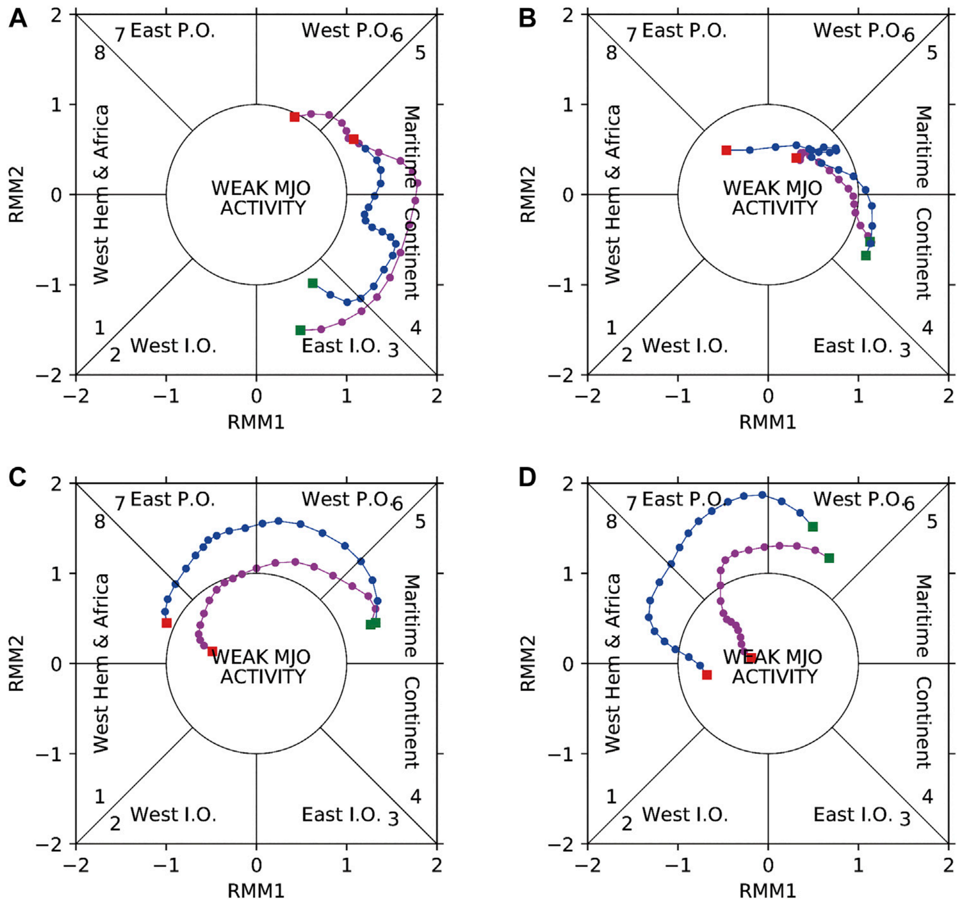

FIGURE 6 | Composite trajectories in RMM phase space for MJO events that occurred during positive and negative VM events. **(A)–(D)** The evolution of MJO events as they enter RMM phases 3 through 6. The blue and magenta lines represent MJO events that occurred during positive and negative VM events. Green boxes represent where the MJO events begin in each phase, and red boxes show their locations 20 days later. We defined weak MJO activity as having RMM amplitude <1.

mode, and the EOF2 mode is named VM. This study applies the second principal component (PC2) of time series, which is linked to the VM pattern to characterize the VM index (VMI; Ding et al., 2015a).

We filtered strongly negative and strongly positive VM events by the value of VMI. When the VMI in a certain year is greater than a positive standard deviation, we defined this year as a positive VM event, and vice versa. Therefore, we identified six positive VM events (1986, 1991, 1996, 1997, 2014, and 2015) and eight negative VM events (1988, 1998, 1999, 2000, 2001, 2007, 2008, and 2010) in the 39 years from 1979 to 2017.

Statistical Methods

Other statistical methods were used in this study, such as correlation analysis, linear regression, and partial correlation analysis. A statistical significance test of these statistical methods was undertaken, using a two-sided Student’s t test, where the amount of effective degrees of freedom (Neff) was calculated as described by Bretherton et al. (1999):

$$N^{\mathrm{eff}} \approx N\frac{1 - r_x r_y}{1 + r_x r_y},$$

where the N stands for the amount of effective time steps. The lag one autocorrelations of variables x and y are represented by r_x and r_y, respectively.

RESULTS

The Link Between the Victoria Mode and Intraseasonal Variability

Previous research results have shown that the FMA VM usually reaches a peak, but the seasonality of the MJO is out of sync with that of the VM. The MJO is usually the most active in boreal winter but it starts to weaken in the spring and the barrier effect on MJO propagation in the Maritime Continent is the most serious in spring (Salby and Hendon 1994; Ding et al., 2015a; Ding et al., 2015b). Taking this into account, this study aimed to verify whether there a possible delayed effect between the VM and

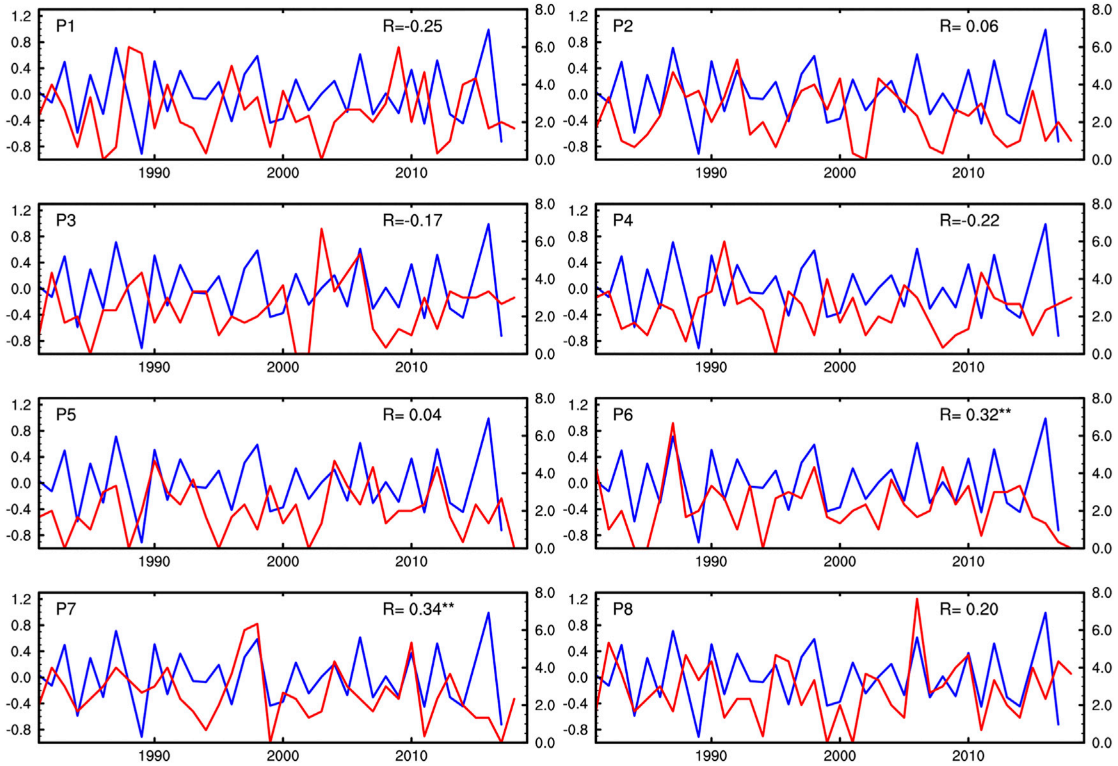

FIGURE 7 | Time series of the occurrence frequency of the eight MJO phases (day; blue lines) and the revised VMI (red lines) during MAM from 1979 to 2017 based on NCEP–NCAR reanalysis data. The correlation coefficient between these two linearly detrended time series is shown in the top-right corner of each panel and the phase label in the top-left. Two asterisks indicate that the correlation coefficient is significant at the 95% confidence level based on the Student's t test.

MJO. We first investigated the connection between the FMA VM and MJO in the coming spring (March–April–May: MAM).

The calculation of a correlation analysis method is used between the FMA VMI and the tropical precipitation, OLR, and specific humidity anomalies in the following MAM (**Figure 2**). Use the average from 850 to 200 hPa as the specific humidity for this study. The distribution of precipitation correlation is not uniform in space, but it is a notable dipole type (**Figure 2A**). Over the west of the Maritime Continent, there are significant negative correlations, whereas positive correlations are found in the eastern Maritime Continent and the equatorial central-western Pacific regions (ECWP). Over the ECWP, the correlations of the OLR (humidity) anomalies are almost inconsistent (consistent) with those of precipitation anomalies. The regressions of the MAM precipitation and OLR anomalies onto the FMA VMI (**Figures 2C,D**) show a well-defined dipole structure over the ECWP, which is consistent with the correlation patterns. The above results point out that over the ECWP the FMA VM is closely connected to convection activity and precipitation intensity in the following MAM, which is coherent with the conclusions of Ding et al. (2015a). As convection activity and precipitation intensity over the ECWP make an important contribution to the propagation of MJO events, we hypothesize that the VM has an intimate relationship with MJO activity in the following spring.

Next, we investigated the connection between the intraseasonal activity and VM over the ECWP. To facilitate this analysis, we used the variance sequence of the 30–90 days filtered OLR and 850-hPa zonal wind anomalies as surrogates for intraseasonal activity signals. A three-month moving window was used to calculate the variance of the filtered anomalies. The correlation coefficients of the FMA VMI with the filtered OLR variance sequence from the following MAM is shown in **Figure 3A**. There is one significantly correlated center between the FMA VM and the intraseasonal variability of OLR over the ECWP (0°–10°N, 140°E–160°W). The OLR intraseasonal variability was enhanced over the ECWP during positive VM events, but suppressed during negative VM events. We then investigated the connection between the FMA VMI and the coming spring (MAM) area-averaged OLR variance sequence anomalies over the ECWP (**Figure 4B**). As shown in **Figure 4B**, the correlation coefficients are 0.47 passing the 99% significant test. Furthermore, we calculated the lead-lag correlations between the FMA VMI and monthly OLR variance sequence anomalies area-averaged over the ECWP (**Figure 4A**). As shown in **Figure 4A**, the correlation over the ECWP is high when the FMA VMI leads the OLR variance by 1–2 months ($R > 0.27$), and pass the 95% significant test. Conversely, when the FMA VMI lags the OLR variance by one month, the correlation is weak. These results indicate that, over the ECWP, there is a notable lag relationship between the VM and the intraseasonal OLR variability.

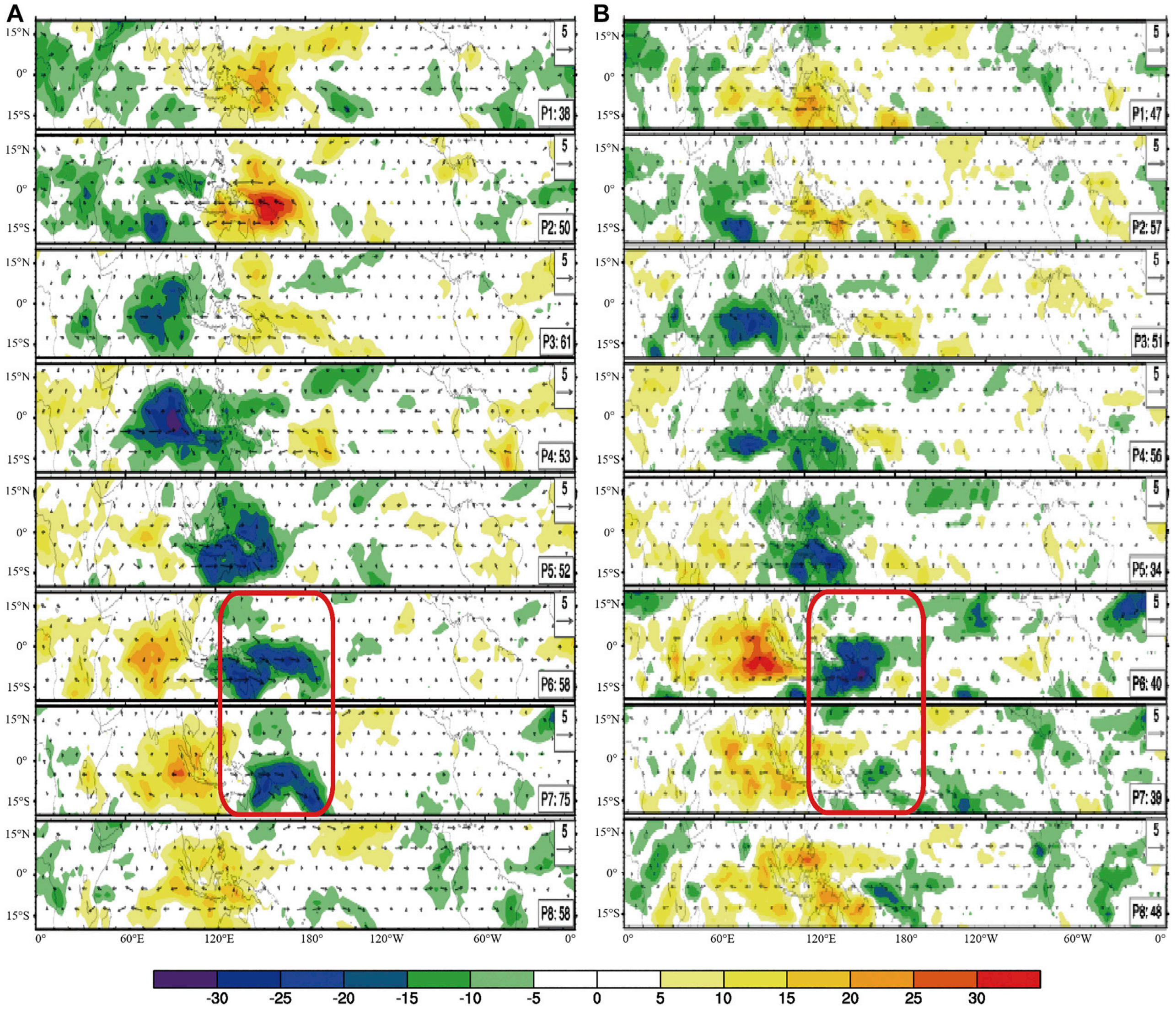

FIGURE 8 | Composite OLR (color shading: W/m^2) and 850 hPa wind vector (m/s) anomalies during the eight MJO phases in the boreal later spring (MAM) for (left) positive VM events and (right) negative VM events. MJO phases were defined using the RMM index. Only days with MJO amplitude >1 were used. OLR and 850 hPa wind vector anomalies were calculated by removing the daily seasonal cycle and then applying a 100 days high-pass digital filter to the daily time series. The size of the reference anomaly wind vector is in the upper right. Phases 1–8 are indicated as P1–P8, respectively, and the number of days used to create the composite are displayed on the lower right.

As ENSO is a strong signal in the tropics and influences MJO activity, we examined whether the VM influence on the intraseasonal OLR variability over the ECWP is independent of ENSO. We calculated the correlation coefficient between the winter DJF (December–February) Niño3.4 index and the coming MAM filtered OLR variance sequence (**Figure 3B**). We note that there are relatively weak correlations between the ENSO and intraseasonal OLR variability over the ECWP. In other words, the VM and intraseasonal OLR variability have a significant connection over the ECWP, even after removing the ENSO effect. From these results, we can conclude that the VM influence on the intraseasonal OLR variability over the ECWP is relatively independent of ENSO.

In addition to the intraseasonal OLR variability, we calculated the analogous correlation coefficients of the FMA VMI with the filtered 850 hPa zonal wind variance sequence from the following MAM (**Figure 5A**). There is a momentous connection between the VM and intraseasonal zonal wind variability across the tropical Pacific. However, there is almost no relationship between the winter DJF Niño3.4 index and the filtered 850 hPa zonal winds variance sequence from the coming MAM (**Figure 5B**).

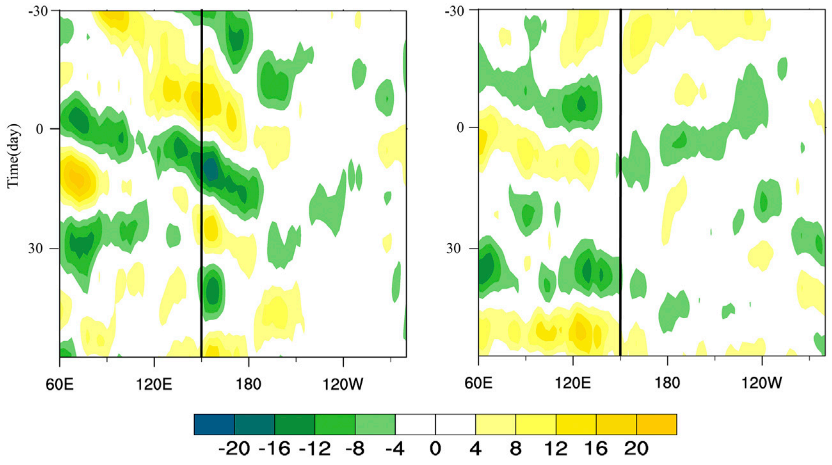

FIGURE 9 | Time-longitude diagrams of 20–90 days filtered OLR anomalies averaged over 10°S–10°N (W/m2). Time 0 is when an MJO track crosses 150°E (the solid vertical lines), which marks the eastern boundary of the Maritime Continent.

Victoria Mode Influence on Madden–Julian Oscillation Activity

In previous studies, composite anomalies of OLR and winds are often used to describe the MJO events (Wheeler and Hendon, 2004; DeMott et al., 2015). To better grasp the characteristics of spring MJO events, this study defined an event in which RMM amplitude was >1 for at least five days as an MJO event. Next, using the processed RMM index to screen the relevant RMM phase. For example, if we focus on MJO activities over WP, we will pay attention to RMM phase 6. To obtain the MJO events assigning to RMM phase 6, we slid the 10 days moving average to the RMM index to find the particular with RMM index amplitude >1 for at least 5 days. In particular, to avoid repeat filters of an MJO event, the period separating the individual MJO events must be more than 30 days, which is the lowest time required for a whole MJO cycle (Wheeler et al., 1999). This procedure was then repeated for the other RMM phases.

Figure 6 shows the composite trace of MJO events during negative VM events and positive VM events, described by the magenta and blue lines, respectively. The beginning and end of the MJO events in each phase are indicated by green and red boxes, respectively. The activity instances of MJO under different VM conditions are characterized by different trajectories. Hence, by considering them, we can better recognize the connection between the VM and MJO activity.

The propagation of MJO was weaker during negative VM events in most cases. This is most apparent in **Figures 6C,D**, in which convection is mainly gathered in the ECWP. **Figures 6C,D** show that during negative VM events, most MJO events weaken and even fade away almost immediately over the ECWP. In contrast, during positive VM events, the MJO events were comparably strong during RMM phase 6 and enhanced as the center of convective activity moved to the equatorial central Pacific. Taken together, **Figures 6C,D** suggest that during the positive (negative) VM events that the ECWP is more (less) conducive to MJO activity. These results are consistent with the intraseasonal activity anomaly patterns shown in **Figures 3**, **5**.

To further verify the above relationship, we show two time series between 1979 and 2017 together, one for the FMA VMI and the other for the spring (MAM) occurrence frequency of the eight MJO phases (**Figure 7**). The total frequency of particular MJO phases in each year was obtained by adding the frequency of days in each phase in the spring of that year. In addition, the MJO amplitude must be greater than one for each calculated day. In order to highlight the interannual variation of the FMA VM, high-pass filtering is needed before computing the average time. We found that there was a stable correlation between the FMA VMI and the MAM occurrence frequency of MJO phases 6 and 7, in which correlation coefficients were 0.32 and 0.34, respectively, and both passed the 95% significant test (**Figures 7F,G**). The above results indicate that the FMA VM may have a positive effect on the increase of the spring (MAM) occurrence frequency of MJO phase 6 (7). These correlations are consistent with the FMA VM forcing response (**Figure 2**) and its coupling to the convection over the ECWP (**Figures 3**, **6**).

To verify the independence of the underlying connection between the FMA VM and the MAM occurrence frequency of MJO phases, we also selected MJO amplitudes of different sizes (1.25 and 1.50) for calculation (not shown). The results show that the relationship between the two is not affected by the selection of the MJO amplitude threshold.

Next, we looked into the impact of VM on the MJO activity by observing the OLR and wind vector fields directly. The composited OLR (shading) and wind vector anomalies during the eight MJO phases for positive (left) and negative (right) VM events in spring (MAM) are shown in **Figure 8**. From both the left and right panels, we see that a typical MJO event is a process that involves the convective anomaly spreading eastward from the tropical western Indian Ocean astride the Maritime Continent to the equatorial central Pacific. The patterns of convection anomalies during MJO phases 6 and 7 with positive and negative VM events are disparate (**Figure 8**). The tropical convection during the positive VM events is stronger than during the negative VM events over the ECWP, especially over

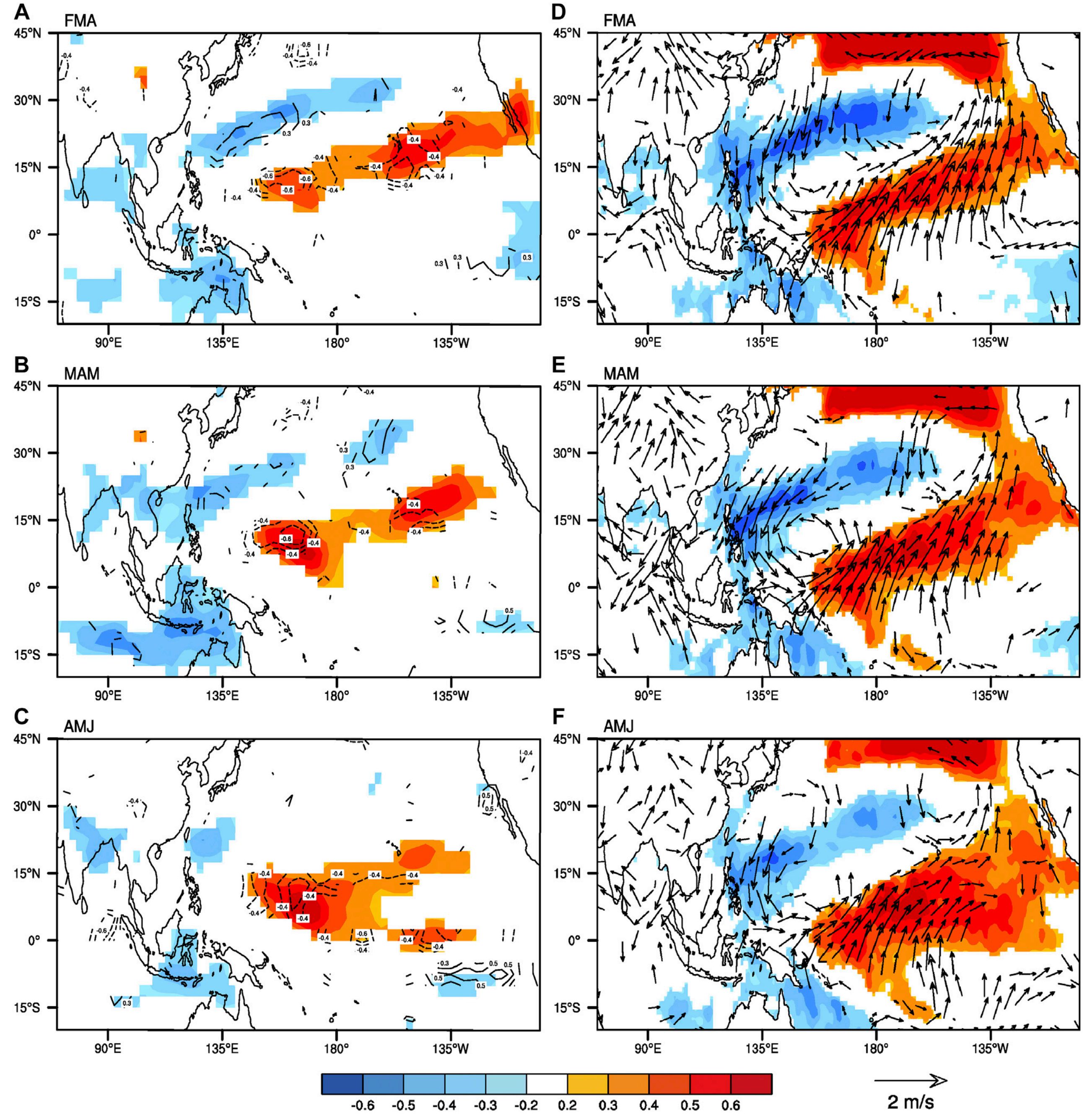

FIGURE 10 | Correlation maps of the three-month 850 hPa specific humidity (g/kg; shading), vertical velocity (10^{-2} Pa s^{-1}; contours) (left) and averaged SST (°C; shading), surface wind (m/s; vectors) (right) anomalies with the VMI from FMA season for simultaneous (FMA) and several lead times (MAM, AMJ). For vertical velocity, solid indicates positive anomalies, and dotted indicates negative anomalies. Only specific humidity, SST, and surface wind anomalies significant at the 90% confidence level are shown.

the Maritime Continent, which is one of the key areas of MJO propagating (Zhang et al., 2005, 2013; Zhang and Ling 2017). This result can be obtained not only from the OLR anomalies but also from the wind vector anomalies.

To reveal the potential MJO propagation differences associated with positive and negative VM events, we show Hovmöller charts for the 20–90 days filtered OLR anomalies averaged at 10°S–10°N from March to May between 1979 and 2017 (**Figure 9**). The composite may not represent all MJO events perfectly, but it can effectively grasp the overall difference between positive and negative VM events in MJO propagation. It is of note that the MJO exhibits a systematic eastward propagation from the tropical Indian Ocean across the Maritime Continent to the tropical eastern Pacific during

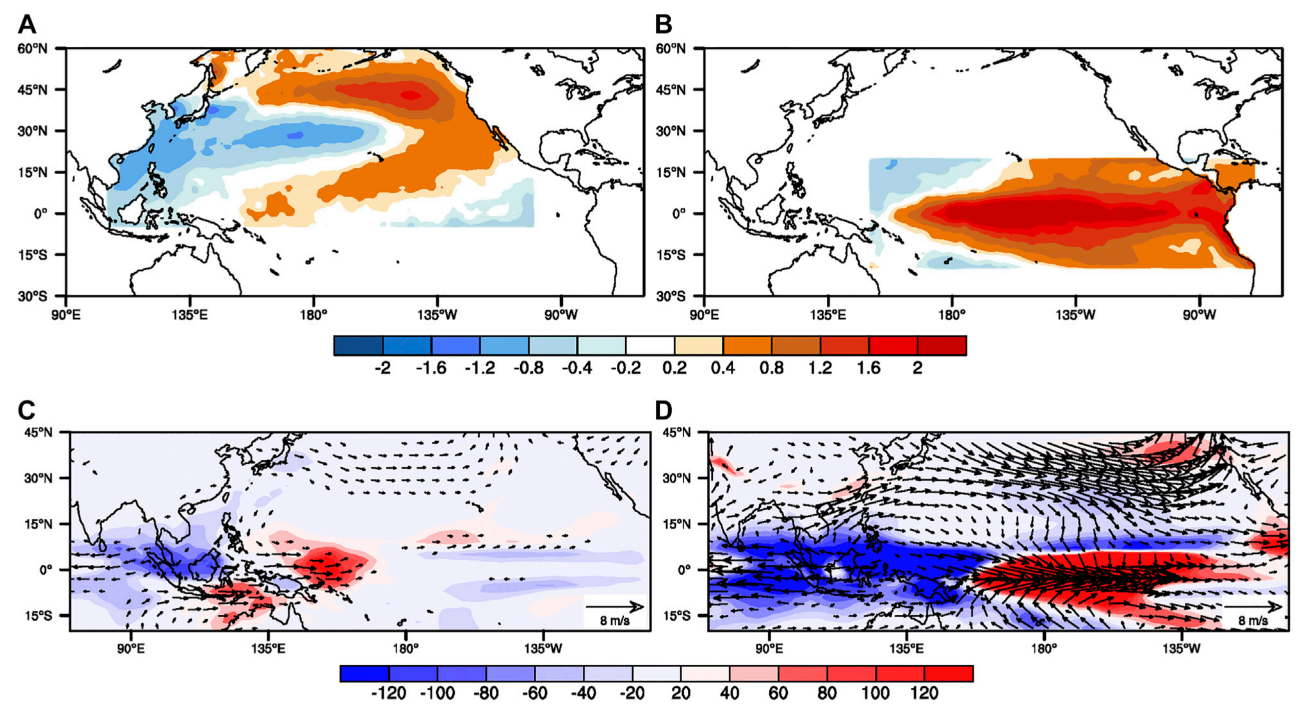

FIGURE 11 | (A), (B) Averaged SST anomaly patterns specified in **(A)** the VM run and **(B)** the El Niño run from February to April **(C), (D)** Ensemble-mean FMA response of 850 hPa wind (vectors; m/s) and precipitation (shading; mm/month) to the tropical Pacific SST forcings in **(A), (B)**, respectively.

TABLE 1 | Models used in this study.

Number	Model	Institute	Spatial resolution (Lon × lat, degree)
1	CanESM2	CCCma, Canada	2.81 × 2.79
2	MIROC5	AORI, NIES, JAMSTEC, Japan	1.41 × 1.40

positive VM events (**Figure 9A**), whereas it is difficult for convective anomalies to propagate eastward over the ECWP during negative VM events due to the suppressed convection (**Figure 9B**), which can also be seen as the Maritime Continent "barrier", an interruption to the MJO propagation. Wang et al. (2019) used cluster analysis to divide MJO propagation patterns into four prototypes of clusters, named standing, jumping, slow eastward propagation, and fast eastward propagation, respectively. Our results demonstrate that MJO propagation exhibits a slow eastward propagation pattern during positive VM events, but a jumping pattern during negative VM events. Therefore, we conclude that the VM may be an important factor in MJO diversity.

Possible Mechanisms

The above results demonstrate that the FMA VM can influence MJO activity in the following spring over the ECWP. But how the VM affects MJO activity over the ECWP has yet to be determined. To identify the reasons that the VM affects the MJO, future studies will investigate the evolutionary features of vertical velocity, humidity, surface wind, and SSTAs linked to the VM.

Furthermore, we calculate the simultaneous correlation and lag correlation of the three-month average SSTAs and surface wind anomalies with the FMA VMI, respectively (**Figure 10**). During the FMA, a well-defined tripole-like SST type is evident in the North Pacific (**Figure 10A**). As a result, positive SSTAs in the central tropical Pacific, combined with negative SSTAs in the northwest North Pacific, increase the SST gradient and span the western to central tropical Pacific. The enhanced SST gradient, in turn, tends to advance the accumulation of the low-level humidity over the northwest Pacific by affecting SST-modulated heat fluxes (Blade and Hartmann, 1993; Hsu and Li, 2012; Sugiyama et al. 2009a,b), thereby leading to the convergence of the low-level humidity in the northwest Pacific, where the development of MJO convection in the lower layer is affected by the effect of moisture accumulation in the troposphere (Wang et al., 2018). Furthermore, as a response to anomalous southwesterly associated with the FMA VM in the low-level wind field (**Figure 10D**), the northeasterly trade winds weaken and consequently reduce the upward latent heat flux (not shown), warming the ocean from the northeastern Pacific to the ECWP and therefore leading to positive wind-evaporation-SST (WES) feedback (Xie and Philander, 1994; Sooraj et al., 2009). Finally, the positive WES feedback has an obvious amplification effect on the SSTAs near the equator, which leads to the evolution and persistence of anomalous low-level humidity and vertical velocity over the ECWP during MAM, even during April–May–June (AMJ) (**Figure 10B**). The above results prove

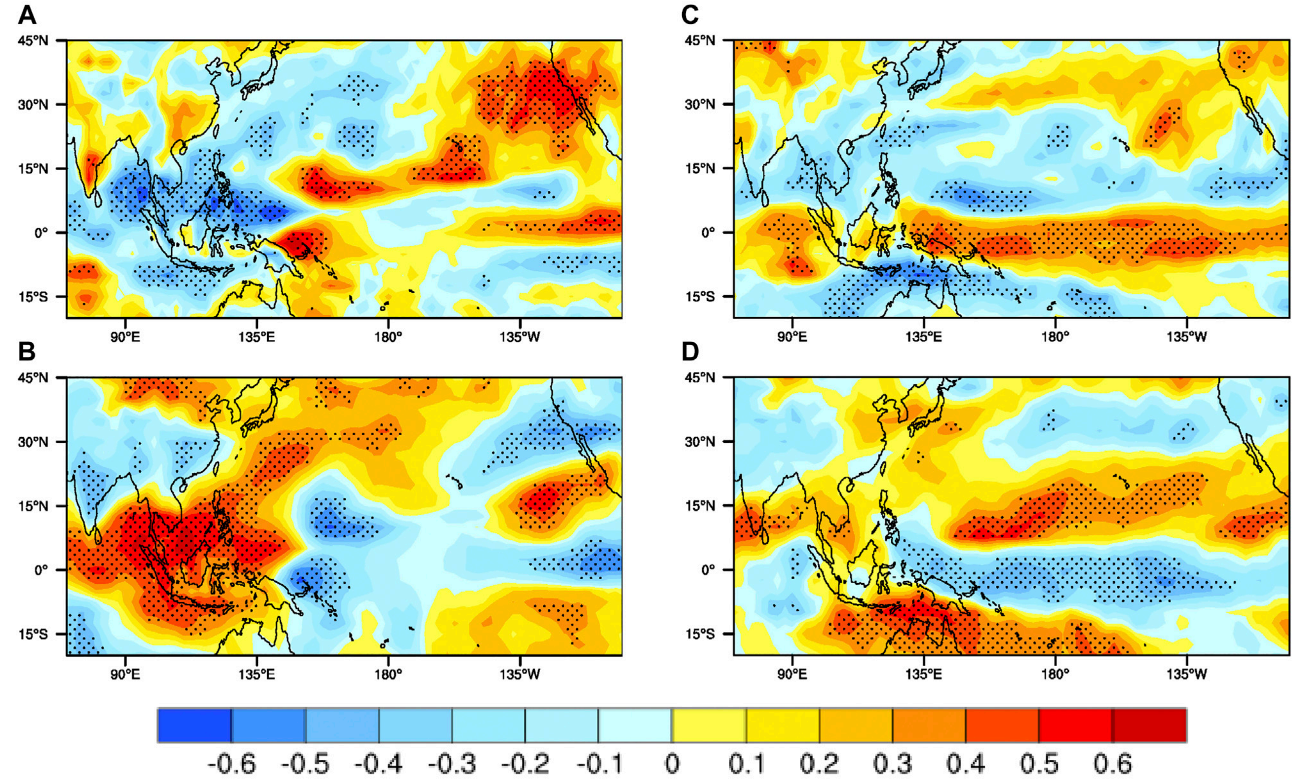

FIGURE 12 | (A) Correlation map of the FMA VMI with the following spring precipitation anomalies by the output data of the CanESM2. **(B)** As **(A)** but for the correlations between the FMA VMI and the following spring OLR anomalies. **(C)** As **(A)** but for the MIROC5. **(D)** As **(B)** but for the MIROC5. Only anomalies exceeding 95% significance, based on a two-tailed Student's t test, are shown.

the hypothesis that the VM affects MJO activity over the ECWP by positive WES feedback, enhancing the SST gradient, and increasing low-level humidity over the ECWP.

In addition to significant humidity anomalies over the ECWP, which are linked to the MJO, recent studies have noticed that MJO activity is associated with the equatorial moist Kelvin wave anomalies. (Salby and Hendon, 1994; Matthews, 2000; Wang et al., 1998, 2018). Wang et al. (2018) reported that the tropical central Pacific SSTAs can modulate MJO activity by adjusting the Kelvin wave response and its coupling to MJO convection. Our study has shown that positive VM events cause positive FMA SSTAs in the tropical central Pacific to persist until AMJ (**Figure 10**). Therefore, the SST anomaly (SSTA) forcing in the northwest Pacific, associated with positive VM events seems to be a favorable situation for the development of the MJO via the enhancement of Kelvin wave anomalies. Conversely, we can reach the homologous conclusion that the negative VM events will have an unfavorable effect on the MJO.

Model Simulations

To further confirm the difference between the effect of the VM and the ENSO (**Figures 11A,B**) on precipitation pattern over the ECWP, two sensitivity experiments were conducted (see experimental designs in *Data and Methodology*). **Figures 11C,D** show differences in low-level wind and precipitation in the FMA VM and El Niño runs relative to the CTRL run. The results of the two sensitivity experiments both show that there are two centers of positive and negative wind and precipitation anomalies in the equatorial region. In the FMA VM experiment, two precipitation centers of positive and negative are forced over the ECWP and west of MC (**Figure 11C**), which matches the effect of VM on the precipitation pattern in the equatorial obtained from the reanalysis data in **Figure 2**. In contrast, the El Niño associated SSTAs in the tropical Pacific, can affect a wider range of precipitation over the equatorial region but the center of the positive and negative precipitation it produces is more easterly (**Figure 11D**). The difference in the impact of the two sensitivity experiments on precipitation may be caused by the difference in the wind. In the FMA VM experiment, an anomalous anticyclone is forced over the western North Pacific but an anomalous cyclonic circulation has been produced in the El Niño experiments. The extratropical Pacific SST forcing can simulate the observed responses of precipitation over ECWP well, which further confirms that the influence of the VM and ENSO on the precipitation over ECWP are independent. The above results are also consistent with those of Ding et al. (2015), who conclude that there is a difference in the influence of ENSO and VM on the location of precipitation over the tropical Pacific.

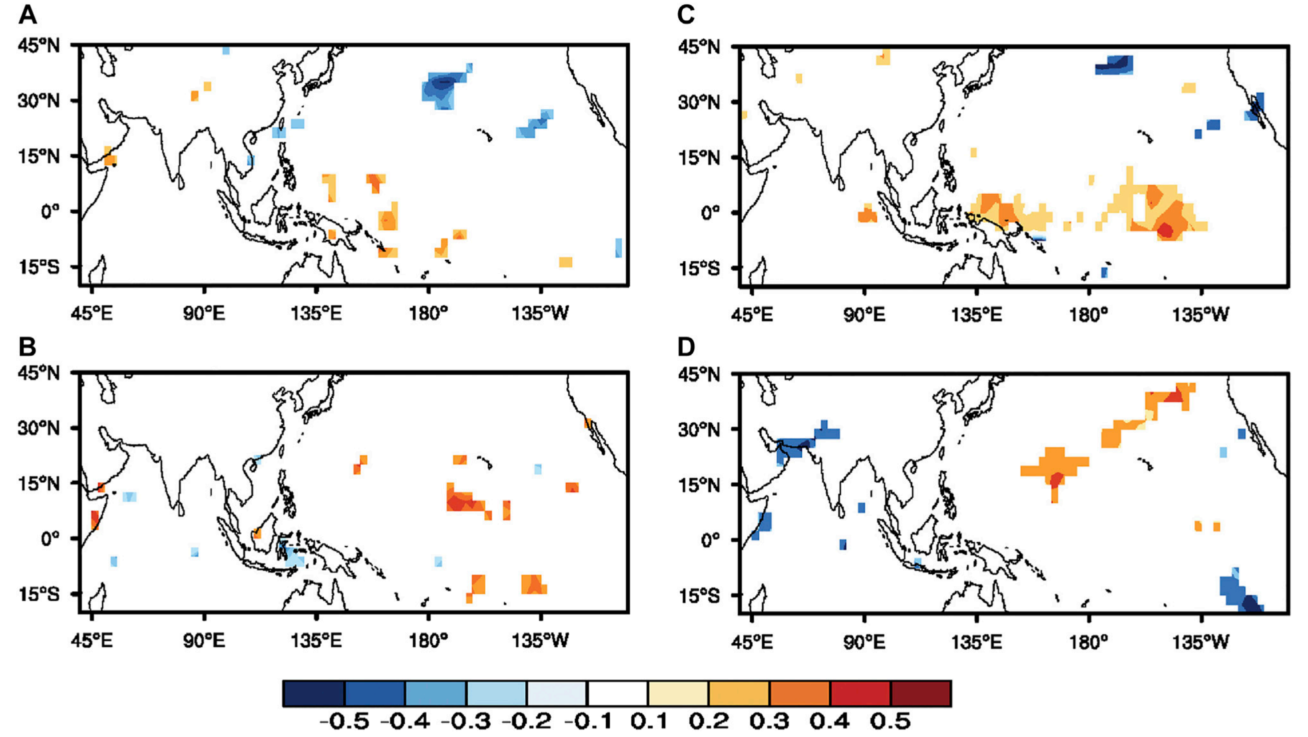

FIGURE 13 | (A) Correlation between 30 and 90 days OLR variance and the VMI by the output data of the MRIOC5. **(B)** Correlation between 30 and 90 days OLR variance and the winter (DJF) Niño3.4 index by the output data of the MRIOC5. **(C)** as **(A)**, **(D)** as **(B)** but for by the CanESM2. Correlation coefficients are significant at the 95% confidence level.

To further confirm that there is a fundamental connection between the FMA VM over the extratropical region and following MJO activity in the tropics over the ECWP, we analyzed individual models from CMIP5. It should be noted that the simulation results of VM and MJO in the CMIP5 (Chen et al., 2020) are not perfectly in the same mode. Therefore, the following two modes, which can certainly simulate MJO and VM, are selected in this study (**Table 1**).

First, we used the monthly output data of SST by the CanESM2 to calculate the VMI. A correlation analysis method was then used between the FMA VMI and the tropical precipitation and OLR anomalies in the following MAM (**Figures 12A,B**). The distribution of precipitation and OLR correlation is not uniform in space by CanESM2, but it is a notable dipole type like observational data. Over the equatorial Pacific, there are significant positive correlations. Especially, the correlations of the OLR anomalies are almost inconsistent with those of precipitation anomalies over the ECWP. In the output data by the MIROC5, a conclusion similar to **Figure 12** can also be obtained (**Figures 13C,D**). Therefore, the above results indicate that the strong correlation between FMA VMI and convection (precipitation) over the ECWP in the following MAM can be reproduced in partly CMIP5 models.

Next, we investigated the connection between the intraseasonal activity and VM over the ECWP from the partly CMIP5 models. To facilitate this analysis, we used the variance sequence of the 30–90-days filtered OLR anomalies as surrogates for intraseasonal activity signal. The correlation coefficients of the FMA VMI with the filtered OLR variance sequence from the following MAM calculated by the output data of partly CMIP5 are shown in **Figures 13A,C**. There are also two significantly correlated centers between the FMA VM and the intraseasonal variability of OLR over the ECWP. Then, we calculated the correlation coefficients between the winter DJF (December–February) Niño3.4 index and the coming MAM filtered OLR variance sequence (**Figures 13B,D**). We noted that there were relatively weak correlations between the ENSO and intraseasonal OLR variability over the ECWP. From these results, we can conclude that the relationship between the VM and the intraseasonal OLR variability over the ECWP can be reproduced in partly CMIP5 models and that they are relatively independent of ENSO.

Furthermore, we calculated the simultaneous correlation and lag correlation of the three-month average SSTAs and surface wind anomalies with the FMA VMI by the output data of CanESM2, respectively (**Figure 14**). It can be seen from **Figure 14** that the results obtained by the model data are generally consistent with the observation data. The VM affects MJO activity over the ECWP by enhancing the SST gradient and increasing low-level humidity and changing the enhancement of Kelvin wave anomalies.

SUMMARY AND DISCUSSION

This study has examined the connection between the FMA VM and ensuing MAM MJO activity over the ECWP by using

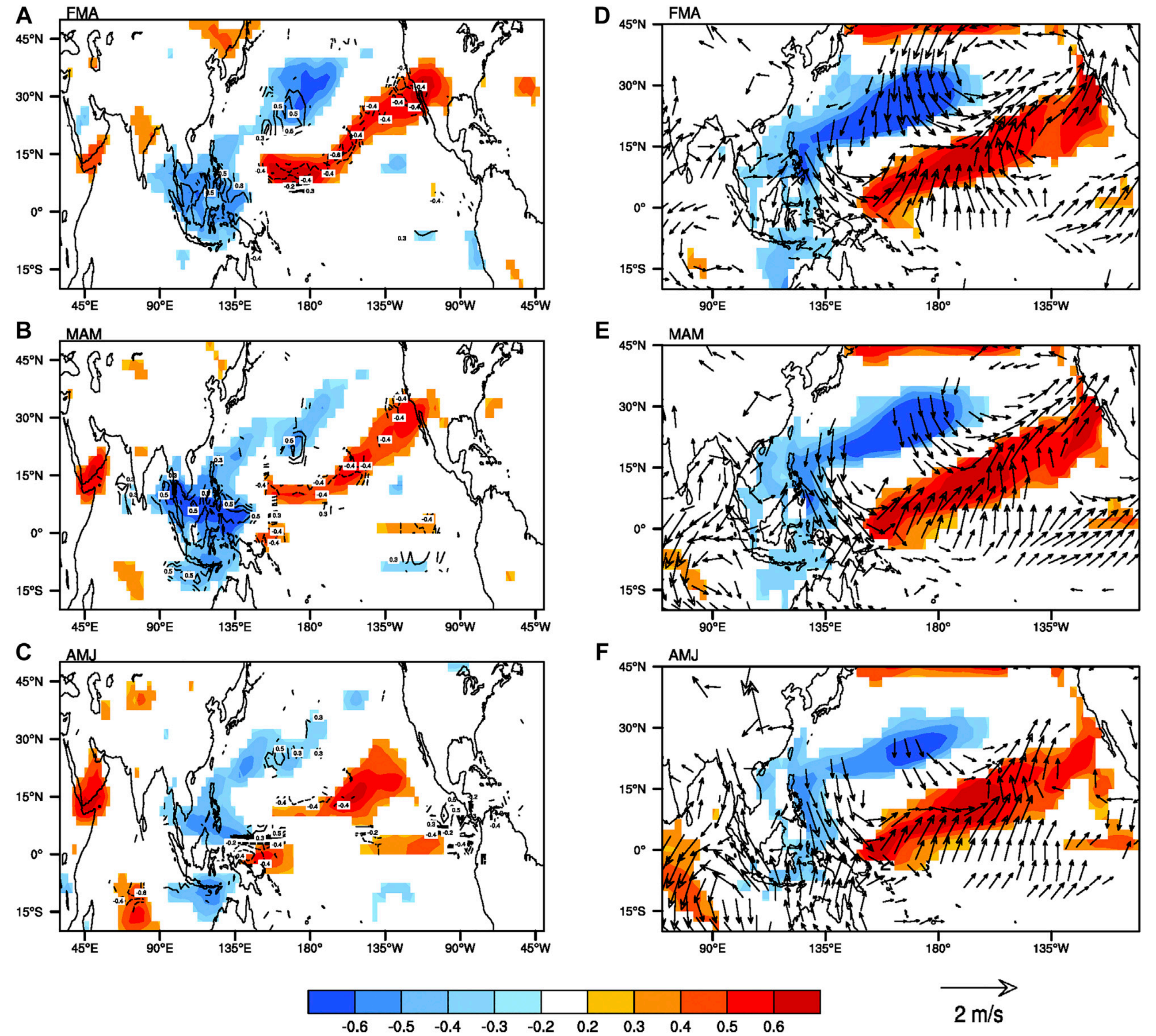

FIGURE 14 | Correlation maps of the three-month 850 hPa specific humidity (g/kg; shading), vertical velocity (10^{-2} Pa s^{-1}; contours) (left) and averaged SST (°C; shading), surface wind (m/s; vectors) (right) anomalies with the VMI from FMA season for simultaneous (FMA) and several lead times (MAM, AMJ) by the output data of the CanESM2. For vertical velocity, solid indicates positive anomalies and dotted indicates negative anomalies. Only specific humidity, SST and surface wind anomalies significant at the 90% confidence level are shown.

observational data and partly CMIP5 models. This study has shown that the atmospheric variations related to the VM may be significant factors in affecting MJO activity. The ECWP appears to be more beneficial for MJO propagation during positive VM events than during negative VM events. During positive VM events, the evolution and persistence of MJO are stronger over the ECWP, while negative VM propagates are the opposite (**Figures 6**, **8**, **9**), which proves this conclusion. This result is not surprising given that preceding studies have also reported on convection activity and precipitation intensity increases over the central-eastern Pacific ITCZ region during positive VM events (Ding et al., 2015a). It is also supported by our modeling experiments in which we examined composite SSTAs of the FMA VM (5°S-60°N, 105°E-110°W) and the preceding DJF Niño3.4 region over the tropical Pacific from February to April. The observed precipitation pattern differences in the ECWP that are associated with FMA VM and preceding ENSO are effectively simulated by these modeling experiments. Wang et al. (2018) also showed that the eastward propagation of the MJO over the CP may be affected by the background SSTAs in that region.

We also found that the VM may be an important factor that is responsible for MJO diversity. Wang et al. (2018) used cluster analysis to divide MJO propagation patterns into four prototypes

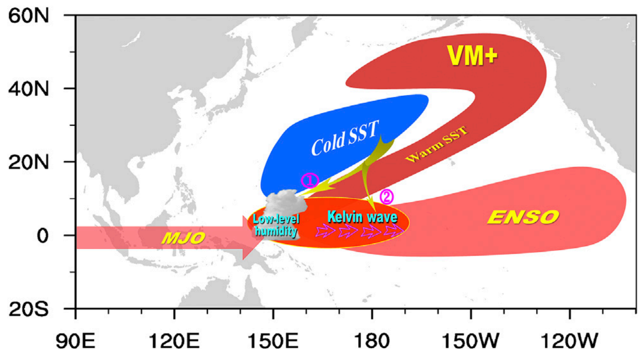

FIGURE 15 | Schematic representation of the thermodynamic ocean-atmosphere coupling between the MJO and SSTAs associated with the VM. The VM possibly influences the MJO activity through two dominant processes: one is the SST gradient anomalies associated with positive VM events that enhance low-level convergence over the equatorial central-western Pacific (ECWP), and the other is warm SST anomalies in the equatorial central Pacific that increase Kelvin wave anomalies. Therefore, the VM enhances MJO activity over the ECWP.

of clusters, and named them standing, jumping, slow eastward propagation, and fast eastward propagation, respectively. Our results demonstrate that MJO propagation exhibits a slow eastward propagation pattern during positive VM events, but a jumping pattern during negative VM events.

The schematic model in **Figure 15** shows the processes by which the FMA VM might affect the following MAM MJO activity. One possible description for these connections is that the SST gradient anomalies associated with positive VM events enhance low-level convergence over the ECWP. Meanwhile, SSTA forcing in the CP enhances the Kelvin wave anomalies. As a result, MJO development is favored in this region. This hypothesis is further supported by other MJO theories, such as wave-CISK (Wang and Rui, 1990; DeMott et al., 2015), and MJO moisture mode theories (Sobel et al., 2010, 2013), which point out that the MJO is strongly dependent on the accumulation of moisture in the low-level.

Other factors may also play a role in influencing the connection between VM on MJO activity. For example, Pu and Chen (2019) argue that the FMA VM exhibits a strong connection with tropical cyclone frequency in the following summer over the western North Pacific. It is necessary to investigate the influence of tropical cyclones on MJO development during VM events. This may further reveal the role of extratropical signals in the development and propagation of MJO.

DATA AVAILABILITY STATEMENT

The raw data supporting the conclusions of this article will be made available by the authors, without undue reservation.

AUTHOR CONTRIBUTIONS

All authors listed have made a substantial, direct and intellectual contribution to the work, and approved it for publication

FUNDING

This work was jointly supported by the National Program on Global Change and Air-Sea Interaction (GASI-IPOVAI-03, GASI-IPOVAI-06). Thanks to the UK Met Office Hadley Center, NCEP/NCAR, NASA, and Australian Bureau of Meteorology for data and support.

ACKNOWLEDGMENTS

The numerical calculations in this paper have been done on the supercomputing system in the Supercomputing Center of Nanjing University of Information Science and Technology.

REFERENCES

Adames, A. F., and Wallace, J. M. (2014). Three-dimensional structure and evolution of the MJO and its relation to the mean flow. *J. Atmos. Sci.* 71, 2007–2026. 10.1175/JAS-D-13-0254.1

Alexander, M. A., Vimont, D. J., Chang, P., and Scott, J. D. (2010). The impact of extratropical atmospheric variability on ENSO: testing the seasonal footprinting mechanism using coupled model experiments. *J. Clim.* 23, 2885–2901. 10.1175/2010JCLI3205.1

Ambaum, M. H. P., Hoskins, B. J., and Stephenson, D. B. (2001). Arctic oscillation or North Atlantic oscillation? *J. Clim.* 14, 3495–3507. 10.1175/1520-0442(2001)014<3495:AOONAO>2.0.CO;2

Blade, I., and Hartmann, D. L. (1993). Tropical intraseasonal oscillations in a simple nonlinear model. *J. Atmos. Sci.* 50, 2922–2939. 10.1175/1520-0469(1993)050<2922:TIOIAS>2.0.CO;2

Bond, N. A., Overland, J. E., Spillane, M., and Stabeno, P. (2003). Recent shifts in the state of the north pacific. *Geophys. Res. Lett.* 30, 2183. 10.1029/2003GL018597

Bretherton, C. S., Widmann, M., Dymnikov, V. P., Wallace, J. M., and Bladé, I. (1999). The effective number of spatial degrees of freedom of a time-varying field. *J. Clim.* 12, 1990–2009. 10.1175/1520-0442(1999)012<1990:TENOSD>2.0.CO;2

Chen, G., Ling, J., Li, C., Zhang, Y., and Zhang, C. (2020). Barrier effect of the indo-pacific Maritime continent on MJO propagation in observations and CMIP5 models. *J. Clim.* 33, 5173–5193. 10.1175/JCLI-D-19-0771.1

DeMott, C. A., Klingaman, N. P., and Woolnough, S. P. (2015). Atmosphere-ocean coupled processes in the Madden-Julian oscillation. *Rev. Geophys.* 53, 1099–1154. 10.1002/2014RG000478

Ding, R. Q., Li, J. P., Tseng, Y. H., and Ruan, C. Q. (2015a). Influence of the north pacific Victoria mode on the pacific ITCZ summer precipitation. *J. Geophys. Res. Atmos.* 120, 964–979. 10.1002/2014JD022364

Ding, R. Q., Li, J. P., Tseng, Y. H., Sun, C., and Guo, Y. P. (2015b). The Victoria mode in the North Pacific linking extratropical sea level pressure variations to ENSO. *J. Geophys. Res. Atmos.* 120, 27–45. 10.1002/2014JD022221

Duchon, C. (1979). Lanczos filtering in one and two dimensions. *J. Appl. Meteorol.* 18, 1016–1022. 10.1175/1520-0450(1979)018<1016:LFIOAT>2.0.CO;2

Hendon, H. H., Wheeler, M. C., and Zhang, C. (2007). Seasonal dependence of the MJO–ENSO relationship. *J. Clim.* 20, 531–543. 10.1175/JCLI4003.1

Hsu, P. C., and Li, T. (2012). Role of the boundary layer moisture asymmetry in causing the eastward propagation of the madden-julian oscillation. *J. Clim.* 25, 4914–4931. 10.1175/JCLI-D-11-00310.1

Jones, C., Waliser, D. E., Lau, K. M., and Stern, W. (2004). Global occurrences of extreme precipitation and the Madden-Julian oscillation: observations and predictability. *J. Clim.* 17, 4575–4589. 10.1175/3238.1

Kalnay, E., Tisu, M. K., Kistler, R., Collins, W. G., Deaven, D., and Gandin, L. S. (1996). The NCEP/NCAR 40-year reanalysis project. *Bull. Am. Meteorol. Soc.* 77, 437–471. 10.1175/1520-0477(1996)077<0437:TNYRP>2.0.CO;2

Liebmann, B., and Smith, C. A. (1996). Description of a complete (interpolated) outgoing longwave radiation dataset. *Bull. Am. Meteorol. Soc.* 77, 1275–1277.

Lin, H., Brunet, G., and Derome, J. (2009). An observed connection between the North Atlantic oscillation and the Madden–Julian oscillation. *J. Clim.* 22, 364–380. doi:10.1175/2008JCLI2515.1

Madden, R. A., and Julian, P. R. (1972). Description of global scale circulation cells in the Tropics with a 40–50 day period. *J. Atmos. Sci.* 29, 1109–1123. 10.1175/1520-0469(1972)029<1109:DOGSCC>2.0.CO;2

Madden, R. A., and Julian, P. R. (1971). Detection of a 40–50 day oscillation in the zonal wind in the tropical Pacific. *J. Atmos. Sci.* 28, 702–708. 10.1175/1520-0469(1971)028<0702:DOADOI>2.0.CO;2

Mantua, N. J., Hare, S. R., Zhang, Y., Wallace, J. M., and Francis, R. M. (1997). A Pacific interdecadal climate oscillation with impacts on salmon production. *Bull. Am. Meteorol. Soc.* 78, 1069–1079. 10.1175/1520-0477(1997)078<1069:APICOW>2.0.CO;2

Matthews, A. J. (2000). Propagation mechanisms for the madden-julian oscillation. *Q. J. R. Meteorol. Soc.* 126, 2637–2651. 10.1002/qj.49712656902

Moon, J., Wang, B., and Ha, K. (2011). ENSO regulation of MJO teleconnection. *Clim. Dynam.* 37, 1133–1149. 10.1007/s00382-010-0902-3

Pohl, B., and Matthews, A. J. (2007). Observed changes in the lifetime and amplitude of the Madden-Julian oscillation associated with interannual ENSO sea surface temperature anomalies. *J. Clim.* 20, 2659–2674. 10.1175/JCLI4230.1

Pu, X. S., Chen, Q. L., Zhong, Q. J., Ding, R. Q., and Liu, T. (2019). Influence of the north pacific Victoria mode on western North pacific tropical cyclone genesis. *Clim. Dynam.* 52, 245–256. doi:10.1007/s00382-018-4129-z10.1007/s00382-018-4129-z |

Rayner, N. A., Brohan, P., Parker, D. E., Folland, C. E., Kennedy, J. J., Vanicek, M., et al. (2006). Improved analyses of changes and uncertainties in sea surface temperature measured *in situ* since the mid-nineteenth century: the HadSST2 dataset. *J. Clim.* 19, 446–469. 10.1175/JCLI3637.1

Salby, M. L., and Hendon, H. H. (1994). Intraseasonal behavior of clouds, temperature, and motion in the tropics. *J. Atmos. Sci.* 51, 2207–2224. 10.1175/1520-0469(1994)051<2207:IBOCTA>2.0.CO;2

Seo, K. H., Wang, W. Q., Gottschalck, J., Zhang, Q., Schemm, J. K. E., Higgins, W. R., et al. (2009). Evaluation of MJO forecast skill from several statistical and dynamical forecast models. *J. Clim.* 22, 2372–2388. 10.1175/2008JCLI2421.1

Shinoda, T., and Han, W. Q. (2005). Influence of the Indian Ocean dipole on atmospheric subseasonal variability. *J. Clim.* 18, 3891–3909. 10.1175/JCLI3510.1

Sobel, A., and Maloney, E. (2013). Moisture modes and the eastward propagation of the MJO. *J. Atmos. Sci.* 70, 187–192. 10.1175/JAS-D-12-0189.1

Sobel, A. H., Maloney, E. D., Bellon, G., and Frierson, D. M. (2010). Surface fluxes and tropical intraseasonal variability: a reassessment. *J. Adv. Model. Earth Syst.* 2, 27. doi:10.3894/JAMES.2010.2.2

Sooraj, K. P., Kim, D., Kug, J. S., Yeh, S. W., Jin, F. F., and Kang, I. S. (2009). Effects of the low-frequency zonal wind variation on the high frequency atmospheric variability over the tropics. *Clim. Dynam.* 33, 495–507. 10.1007/s00382-008-0483-6

Sreekala, P. P., Rao, S. V. B., Rajeevan, K., and Arunachalam, M. S. (2018). Combined effect of MJO, ENSO and IOD on the intraseasonal variability of northeast monsoon rainfall over south peninsular India. *Clim. Dynam.* 51, 3865–3882. 10.1007/s00382-018-4117-3

Sugiyama, M. (2009a). The moisture mode in the Quasi-equilibrium tropical circulation model. Part I: analysis based on the weak temperature gradient approximation. *J. Atmos. Sci.* 66, 1507–1523. 10.1175/2008JAS2690.1

Sugiyama, M. (2009b). The moisture mode in the Quasi-equilibrium tropical circulation model. Part II: nonlinear behavior on an equatorial beta plane. *J. Atmos. Sci.* 66, 1525–1542. 10.1175/2008JAS2691.1

Tam, C. Y., and Lau, N. C. (2005). Modulation of the Madden-Julian oscillation by ENSO: inferences from observations and GCM simulations. *J. Meteorol. Soc. Jpn.* 83, 727–743. 10.2151/jmsj.83.727

Vecchi, G. A. (2004). The Madden-Julian Oscillation (MJO) and northern high latitude wintertime surface air temperatures. *Geophys. Res. Lett.* 31, L04104. 10.2151/jmsj.83.727

Wallace, J. M., and Thompson, D. W. J. (2002). The Pacific center of action of the Northern Hemisphere annular mode: real or artifact? *J. Clim.* 15, 1987–1991. 10.1175/1520-0442(2002)015<1987:TPCOAO>2.0.CO;2

Wang, B. (1988). Dynamics of tropical low-frequency waves - an analysis of the moist Kelvin wave. *J. Atmos. Sci.* 45, 2051–2065. 10.1175/1520-0469(1988)045<2051:DOTLFW>2.0.CO;2

Wang, B., Chen, G. S., and Liu, F. (2019). Diversity of the madden-julian oscillation. *Sci. Adv.* 5, eaax0220. doi:10.1126/sciadv.aax0220

Wang, B., and Rui, H. (1990). Dynamics of the coupled moist Kelvin-rossby wave on an equatorial beta-plane. *J. Atmos. Sci.* 47, 397–413. 10.1175/1520-0469(1990)047<0397:DOTCMK>2.0.CO;2

Wang, F., Tian, W., Xie, F., Zhang, J., and Han, Y. (2018). Effect of madden–julian oscillation occurrence frequency on the interannual variability of northern Hemisphere stratospheric wave activity in winter. *J. Clim.* 31, 5031–5049. 10.1175/JCLI-D-17-0476.1

Webster, P. J., Moore, A. M., Loschnigg, J. P., and Leben, R. R. (1999). Coupled ocean-atmosphere dynamics in the Indian Ocean during 1997–98. *Nature* 401, 356–360. 10.1038/43848

Weickmann, K. M. (1983). Intraseasonal circulation and outgoing longwave radiation modes during northern Hemisphere winter. *Mon. Weather Rev.* 111, 1838–1858. 10.1175/1520-0493(1983)111<1838:ICAOLR>2.0.CO;2

Wheeler, M. C., and Hendon, H. H. (2004). An all-season real-time multivariate MJO index: development of an index for monitoring and prediction. *Mon. Weather Rev.* 132, 1917–1932. 10.1175/1520-0493(2004)132<1917:AARMMI>2.0.CO;2

Wheeler, M. C., and Hendon, H. H. (2017). An all-season real-time multivariate MJO index: development of an index for monitoring and prediction. *Mon. Weather Rev.* 145.

Wilson, E. A., Gordon, A. L., and Kim, D. (2013). Observations of the madden julian oscillation during Indian Ocean Dipole events. *J. Geophys. Res. Atmos.* 118, 2588–2599. doi:10.1002/jgrd.50241

Woolnough, S. J., Slingo, J. M., and Hoskins, B. J. (2000). The relationship between convection and sea surface temperature on intraseasonal timescales. *J. Clim.* 13, 2086–2104. 10.1175/1520-0442(2000)013<2086:TRBCAS>2.0.CO;2

Xie, P. P., and Arkin, P. A. (1997). Global precipitation: a 17-year monthly analysis based on gauge observations, satellite estimates, and numerical model outputs. *Bull. Am. Meteorol. Soc.* 78, 2539–2558. 10.1175/1520-0477(1997)078<2539:GPAYMA>2.0.CO;2

Yoo, C., Feldstein, S., and Lee, S. (2011). The impact of the Madden-Julian Oscillation trend on the Arctic amplification of surface air temperature during the 1979-2008 boreal winter. *Geophys. Res. Lett.* 38, L24804. doi:10.1029/2011GL049881

Yoo, C., Lee, S., and Feldstein, S. B. (2012). Mechanisms of arctic surface air temperature change in response to the madden-julian oscillation. *J. Clim.* 25, 5777–5790. 10.1175/JCLI-D-11-00566.1

Zhang, C., and Zhang, B. (2018). QBO-MJO connection. *J. Geophys. Res. Atmos.* 123, 2957–2967. doi:10.1002/2017JD028171

Zhang, C., and Ling, J. (2017). Barrier effect of the indo-pacific Maritime continent on the MJO: perspectives from tracking MJO precipitation. *J. Clim.* 30, 3439–3459. 10.1175/JCLI-D-16-0614.1

Zhang, C. (2005). Madden-julian oscillation. *Rev. Geophys.* 43, 36. doi:10.1029/2004RG000158

Zhou, S. T., and Miller, A. J. (2005). The interaction of the Madden-Julian oscillation and the arctic oscillation. *J. Clim.* 18, 143–159. 10.1175/JCLI3251.1

Conflict of Interest: The authors declare that the research was conducted in the absence of any commercial or financial relationships that could be construed as a potential conflict of interest.

frontiers
in Environmental Science

ORIGINAL RESEARCH
published: 26 November 2020
doi: 10.3389/fenvs.2020.583466

Changing Relationship Between Tibetan Plateau Temperature and South China Sea Summer Monsoon Precipitation

Mei Liang[1,2], Jianjun Xu[1]*, Johnny C. L. Chan[2], Liguang Wu[3] and Xiangde Xu[4]

[1] South China Sea Institute of Marine Meteorology and College of Ocean and Meteorology, Guangdong Ocean University, Zhanjiang, China, [2] School of Energy and Environment, City University of Hong Kong, Hong Kong, China, [3] Department of Atmospheric and Oceanic Sciences and Institute of Atmospheric Sciences, Fudan University, Shanghai, China, [4] State Key Laboratory of Disastrous Weather, China Academy of Meteorological Sciences, Beijing, China

The present study documents the changes in the relationship between the Tibetan Plateau summer surface temperature (TPST) and the South China Sea summer monsoon precipitation (SCSSMP). A stepwise regression model is used to exclude the signals of global warming, El Niño–Southern Oscillation (ENSO), western North Pacific Subtropical High (WNPSH), Atlantic Multidecadal Oscillation (AMO) and Pacific Decadal Oscillation (PDO). The results indicate that the relationship between TPST–SCSSMP changes with time, going from a negative correlation during the period of 1980–1994 to an obvious positive correlation during 1998–2016 in the South China Sea. Meanwhile, the negative correlation between TPST and the East Asia subtropical front (Meiyu) is enhanced during 1998–2016. This change in the TPST–SCSSMP relationship is associated with the change of the atmospheric circulation, which is mainly due to TPST interdecadal variation. A wave–like structure at the low latitude moves eastward along the low–level monsoon flow, and a strong cyclonic circulation is apparent in the southwestern part of the Plateau, including the Indochina Peninsula, South China Sea, and the ocean to the east of the Philippines, which is consistent with the negative correlation between TPST and Outgoing Longwave Radiation (OLR). The increase in water–vapor convergence and more favorable convection conditions lead to more precipitation in the region after the late 1990s. The present results suggest that, in a changing climate, we should be cautious when using predictor with interdecadal variations.

Keywords: interdecadal variations, South China Sea summer monsoon, Tibetan Plateau, changing relationship, warming amplification

Edited by:
Haishan Chen,
Nanjing University of Information Science and Technology, China

Reviewed by:
Anmin Duan,
Institute of Atmospheric Physics (CAS), China
Wen Zhou,
City University of Hong Kong, Hong Kong

***Correspondence:**
Jianjun Xu
jxu@gdou.edu.cn

Specialty section:
This article was submitted to Atmospheric Science, a section of the journal Frontiers in Environmental Science

Received: *15 July 2020*
Accepted: *26 October 2020*
Published: *26 November 2020*

Citation:
Liang M, Xu J, Chan JCL, Wu L and Xu X (2020) Changing Relationship Between Tibetan Plateau Temperature and South China Sea Summer Monsoon Precipitation. Front. Environ. Sci. 8:583466. doi: 10.3389/fenvs.2020.583466

INTRODUCTION

Warming rate is found amplification with elevation in high–altitude region in recent years, especially the Tibetan Plateau (Beniston et al., 1997; Liu and Chen, 2000; Beniston, 2003; Seidel and Free, 2003; Pepin and Lundquist, 2008; Liu et al., 2009, 2012; Wang et al., 2014; Pepin et al., 2015; Wu et al., 2017; Zhu and Fan, 2018; Gao et al., 2019). Large evidences show that variations in Tibetan Plateau summer surface temperature (TPST) could greatly affect the interannual and interdecadal variations in the South China Sea summer monsoon by the records (Ye et al., 1957; Ye and Gao, 1979, 1992; Ding, 1992; Yanai et al., 1992; Ye and Wu, 1998; Xu et al., 2002, 2010, 2015, 2018; Zhao et al., 2003; Duan and Wu, 2005, 2008; Lu et al., 2005; Zhou et al., 2009; Duan et al., 2011, 2012, 2013; Liu et al., 2012; Wu et al., 2012a,b, 2014; Boos and Kuang, 2013).

However, in a changing climate, the Tibetan Plateau and South China Sea summer monsoon precipitation (SCSSMP) relationships would change and the understanding of them still need to research. Zhang et al. (2004) and Ding et al. (2009) described that decadal variations existed in the relationship between winter–spring snow over the Tibetan Plateau and SCSSMP in 1960s—1990s. Si and Ding (2013) suggested that the relationship between the Tibetan Plateau winter snow and the SCSSMP changed in 1999. The correlation between them changed from the positive to a strong positive. On the whole, the robustness of this relationship in a changing climate remains unclear.

There are many factors affect the SCSSMP, but these factors are not independent. For example, El Niño–Southern Oscillation (ENSO) together with the Atlantic Multidecadal Oscillation (AMO) leaded to an anomalous cyclone (anticyclone) over the western North Pacific Subtropical High (WNPSH) that persisted from the ENSO mature winter to the ENSO decaying summer, strengthening (weakening) the SCSSMP (Wu et al., 2003; Fan et al., 2018). In addition, ENSO was strongly modulated by the Pacific Decadal Oscillation (PDO), which furtherly affected on the SCSSMP (Lee et al., 2013; Feng et al., 2014; Song and Zhou, 2015; Bollasina Massimo and Gabriele, 2018). In addition, Annamalai et al. (2013) showed that global warming shifted the monsoon circulation and dried South Asia. Overall, global warming and interdecadal variability in climate systems, such as the WNPSH, ENSO, AMO, and PDO influence the change of summer rainfall in this area. It is therefore necessary to exclude these factors so as to isolate the contributions of Tibetan Plateau warming to the TPST–monsoon relationship as well as explore the robustness of the relationship in a changing climate. The present study aims to explore the evolving relationship of TPST–SCSSMP by employing a stepwise regression model to exclude the influence of these other factors.

Datasets and methods are described in section 2. In section 3, the constructed stepwise regression model and the changing relationship of TPST–SCSSMP are documented. Section 4 examines the influence of the interdecadal variation of the TPST on atmospheric circulation. In section 5, conclusions and discussions are provided.

DATASETS AND METHODS

Datasets

In this study, observational dataset and three reanalysis datasets are used to avoid the inadequate observation of Tibetan Plateau temperature at the high altitudes (Beniston et al., 1997; Ohmura, 2012; Rangwala and Miller, 2012; Wu et al., 2017). Observations used are mainly from the China Meteorological Science Data Network. The Japanese 55–year Reanalysis (JRA—55) is also used, which is a high–quality homogeneous climate dataset from 1980 to recent (Kobayashi and Iwasaki, 2016). ERA5 (the fifth generation of European Centre for Medium–Range Weather Forecasts atmospheric reanalyses of the global climate) is also used, which is a high-resolution dataset from 1950 to present (Malardel et al., 2015). An earlier version, ERA–Interim (Berrisford et al., 2011), is also used for comparisons. The Tibetan Plateau surface temperatures are therefore determined from the observation data and the 2–m surface temperature in these reanalysis datasets.

The observational dataset, with 693 national–level basic stations in China, is also used for precipitation, during the 38–year period of 1980–2016. The Global Precipitation Climatology Project (GPCP) can capture the SCSSMP precipitation well (Adler et al., 2003), therefor it is used to analysis the changes of the SCSSMP from 1980 to 2016. The Outgoing Longwave Radiation (OLR) dataset is also used. Global surface temperatures are extracted from the 2–m surface temperatures in the JRA55 reanalysis data. The ENSO index used here is the Oceanic Nino Index, obtained from https://www.cpc.ncep.noaa.gov/products/. The WNPSH index is loaded from China Meteorological Standardization Network. The AMO index is acquired from the Earth System Research Laboratory (ESRL) of National Oceanic and Atmospheric Administration (NOAA). The PDO index is downloaded from the National Centers for Environmental Information (NCEI) by using the NOAA's Extended Reconstruction of Sea Surface Temperature (ERSST Version 4).

For the download websites and resolutions of all above datasets, please see **Table 1** for detail. To reduce the error, all reanalysis datasets are interpolated to the resolution of 1.25° latitude × 1.25° longitude. Summer here is defined as June, July, and August.

Methods

The Vertically–integrated moisture flux (VIMF) is calculated using the monthly variables of specific humidity, sea–level pressure, meridional wind (v), zonal wind (u), and air temperatures data, which is integrated from low–level (1000 hPa) to mid–level (500 hPa). The amount of water vapor is mainly concentrated from surface to 500 hPa (Strong et al., 2002). The VIMF calculating equation is as follow.

$$VIMF = \frac{1}{g} \cdot \int_{pt}^{ps} V \cdot q dp$$

Where ps is surface pressure, pt 500 hPa, V the wind vector, q specific humidity and g an acceleration of gravity.

It was hardly explored the region that higher than 5,000 m above sea level (Lawrimore et al., 2011), and to obtain suitable sample sizes for Tibetan Plateau. In this study, it is quite reasonable that sites with an elevation higher than 2,000 m are selected, and we think an altitude of 2,000 m is still higher than the surrounding area and also representative. Previous studies also selected sites higher than 2,000 m. For example, Su et al. (2017) chose the grids above 2,000 m from the reanalysis datasets to quantitatively analyze the warming amplification over the

TABLE 1 | The various datasets and indexes used in this study and the corresponding Websites.

Data or index	Horizontal resolution (latitude × longitude)	Website
The daily climate dataset (version 3.0)	824 stations in China	CMA (http://data.cma.cn)
JRA-55 ERA5 ERA-Interim	1.25° × 1.25° 0.25° × 0.25° 0.25° × 0.25°	JMA (https://jra.kishou.go.jp/JRA-55/index_en.html#jra-55) ECMWF (https://rda.ucar.edu/datasets/) ECMWF (https://rda.ucar.edu/datasets/)
GPCP	2.5° × 2.5°	NOAA (https://www.esrl.noaa.gov/psd/data/gridded/)
OLR	2.5° × 2.5°	NOAA (https://www.esrl.noaa.gov/psd/data/gridded/data.interp_OLR.html)
ENSO index		NOAA (https://www.cpc.ncep.noaa.gov/products)
WNPSH index AMO index		CMA (http://www.cmastd.cn/) NOAA ESRL, (https://www.esrl.noaa.gov/psd/data/timeseries/AMO/)
PDO index		ERSST Version 4 (https://www.ncdc.noaa.gov/teleconnections/pdo/)

Tibetan Plateau. Finally, 61 stations in the eastern part of the Tibetan Plateau are selected to study in our study.

The Mann–Kendall (M–K) trend test and Theil–Sen estimator are both used to check the reliability of trend. The M–K test is a non–parametric test for detecting the presence of linear or non–linear trends in time series data. The stepwise regression is a widely–used method for fitting regression models. In this study, we use it to select predictive variables to construct a multiple regression model. Firstly, we employ it to select the significant predictive variables from global warming, ENSO, WNPSH, PDO, and AMO. Secondly, we construct a multiple regression model by using the significant predictive variables. Then we only analyze the standardized partial regression coefficients between the TPST and precipitation, as well as evaluating the relative contributions to precipitation. The significance of the results obtained by the regression method and climate mean analysis are all determined by using the standard two–tailed Student's t–test method. F test is used to test the significance of the regression equation.

TPST–SCSSMP RELATIONSHIP

Temperature Change Over the Tibetan Plateau

Since most of the stations are located in the eastern Tibetan Plateau (25°−40°N, 90°−105°E) except for six stations located outside the region, those concentrated in the east areas are selected to represent the Tibetan Plateau to avoid the effect of interpolation. A coherent warming pattern is found in the eastern Tibetan Plateau during 1980 to 2016 (**Figure 1**), where 92% of stations trends pass the 95% statistically significant (solid red dots in **Figure 1**). The trends exceeded 0.5°C/decade are all distributed over the southwest and northeast sides of the Tibetan Plateau.

To test the reliability of the reanalysis data in reflecting the TPST change, we compare it with the station data at the same region (eastern Tibetan Plateau; purple box in **Figure 1**). The interannual variation of TPST exhibits a consistent significantly increasing trend in all the datasets, although the variability is higher after 2005 (**Figure 2**). All of the datasets well reflect the annual variability of the TPST. The Mann–Kendall and Theil–Sen estimator are both used to check whether the trend is robust. The values of the trends differ slightly among the data sets, but both methods detected consistent increasing trends ($P < 0.01$). The trend is therefore reliable and robust, despite the annual variability after 2005. The 2–m global surface temperature from JRA55 is also analyzed to compare this trend with that of global warming. It is found that the global–average surface temperature increases at a relative lower rate (0.15°C/decade, $P < 0.05$) during 1980–2016. Those previous studies (Liu and Chen, 2000; Wang et al., 2008, 2014; Liu et al., 2009) were also pointed out that warming was amplified in the TPST compared with the globe and other plain regions.

The Mann–Kendall method is also employed to investigate whether a shift occurred in the temperature on the eastern Tibetan Plateau. The results show that a dramatic shift is found during 1980–2016 ($P < 0.05$) in all datasets (**Figure 3A**). The year of abrupt change in TPST may occur either in 1995 (**Figure 3D**), 1996 (**Figure 3B**), or 1997 (**Figures 3C,E**), depending on the dataset, being 1996 in the observation station, 1995 in the ERA5, but 1997 in the JRA55 and ERA–Interim. Combining all datasets, the time series is separated into two periods, 1980–1994 and 1998–2016. The temperature anomalies are $\sim$-0.37°C to −0.46°C during 1980–1994, but increase up to 0.29°C to 0.37°C during 1998–2016 ($P < 0.05$). The results verify the conclusion that the TPST warming is greater than that of the globe and a dramatic shift occurs around 1996. The snow–albedo feedback mechanism is generally used to explain Tibetan Plateau warming (Giorgi et al., 1997; Pepin and Lundquist, 2008; Liu et al., 2009; Ceppi et al., 2010). In addition, the cloud–radiation effects on water vapor and radiative fluxes (Rangwala, 2013), are also responsible too. In the present study, we are interested in the evolving relationship between the TPST and SCSSMP. It would seem reasonable to hypothesize that this interdecadal variation of the TPST may change the atmospheric circulation and water vapor conditions, which further impact the SCSSMP in the downstream area of the Plateau. The question is whether the interdecadal variation on the Tibetan Plateau warming affects TPST–SCSSMP relationship and how robust such a relationship is in a changing climate.

The Changing Relationship of TPST–SCSSMP

The reliability of the GPCP precipitation dataset is examined by comparing it with the observed precipitation dataset

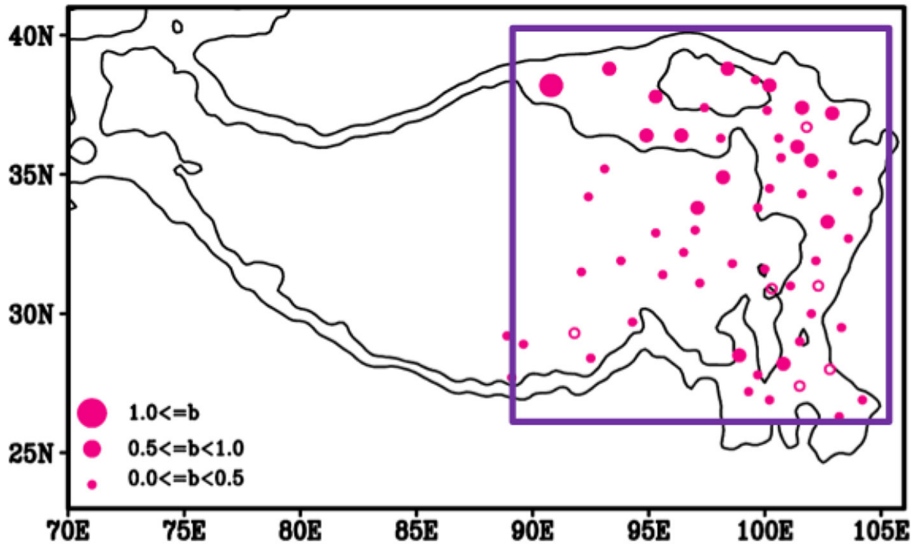

FIGURE 1 | Temperature changes at stations higher than 2,000 m above mean sea level in the eastern Tibetan Plateau during the summers of 1980–2016 (units: °C/decade; solid black lines represent the 2,000 m and 3,000 m height above mean sea level; the solid points indicate significant differences above the 95% confidence level). The purple area (27–40°N, 90–105°E) is selected as the research region for JRA55, ERA5 and ERA-Interim reanalysis temperature data at 2 m.

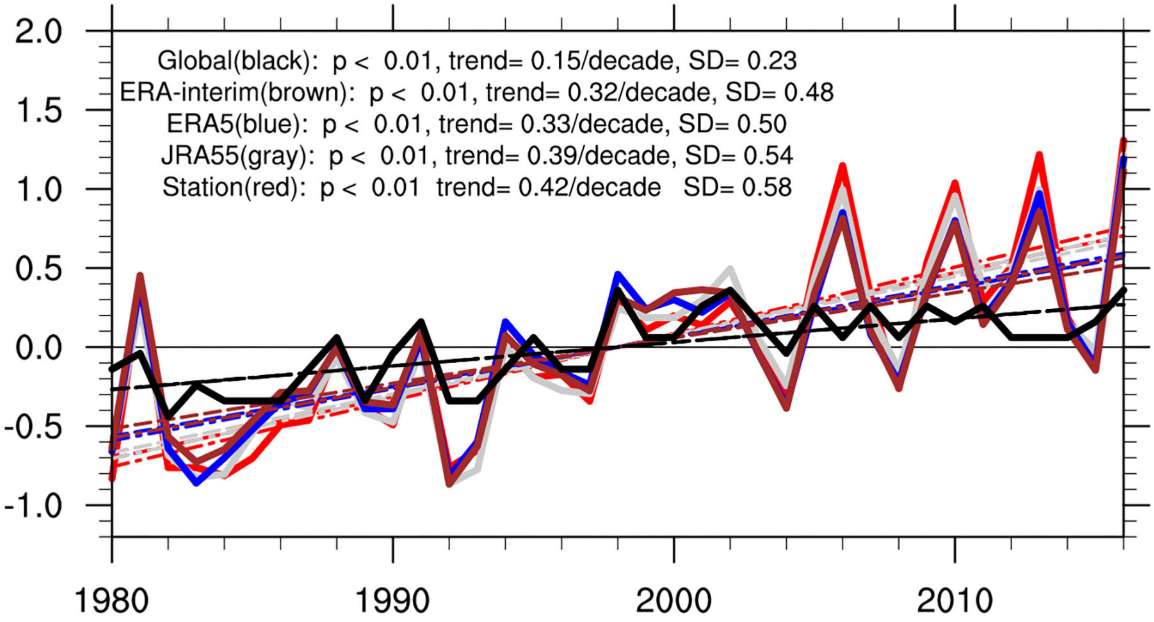

FIGURE 2 | Interannual changes in summer temperature averaged by the Tibetan Plateau and globe (black) for *in situ* stations (red), JRA55 (gray), ERA5 (blue), ERA–Interim (brown), and globe (black, JRA55) (units: °C). Significances of the trends are assessed using the Mann–Kendall test and Theil–Sen estimator. $P < 0.01$ indicates a significant difference above the 99% confidence level.

(**Figures 4A,B**). Similar spatial distribution patterns of precipitation change are found in these two describes and these spatial distribution patterns are consistent with those results from previous studies (Burke and Stott, 2017; Stanley, 2017; Xu et al., 2018). Precipitation is generally higher in the south of the Yangtze River, such as the South China, and lower in the north of the Yellow River and Southwest China. The lower precipitation in southwestern China is more obvious over the North China Plain. The similarity precipitation distribution patterns between these two datasets confirm that the GPCP precipitation data well reflects the precipitation in China and even

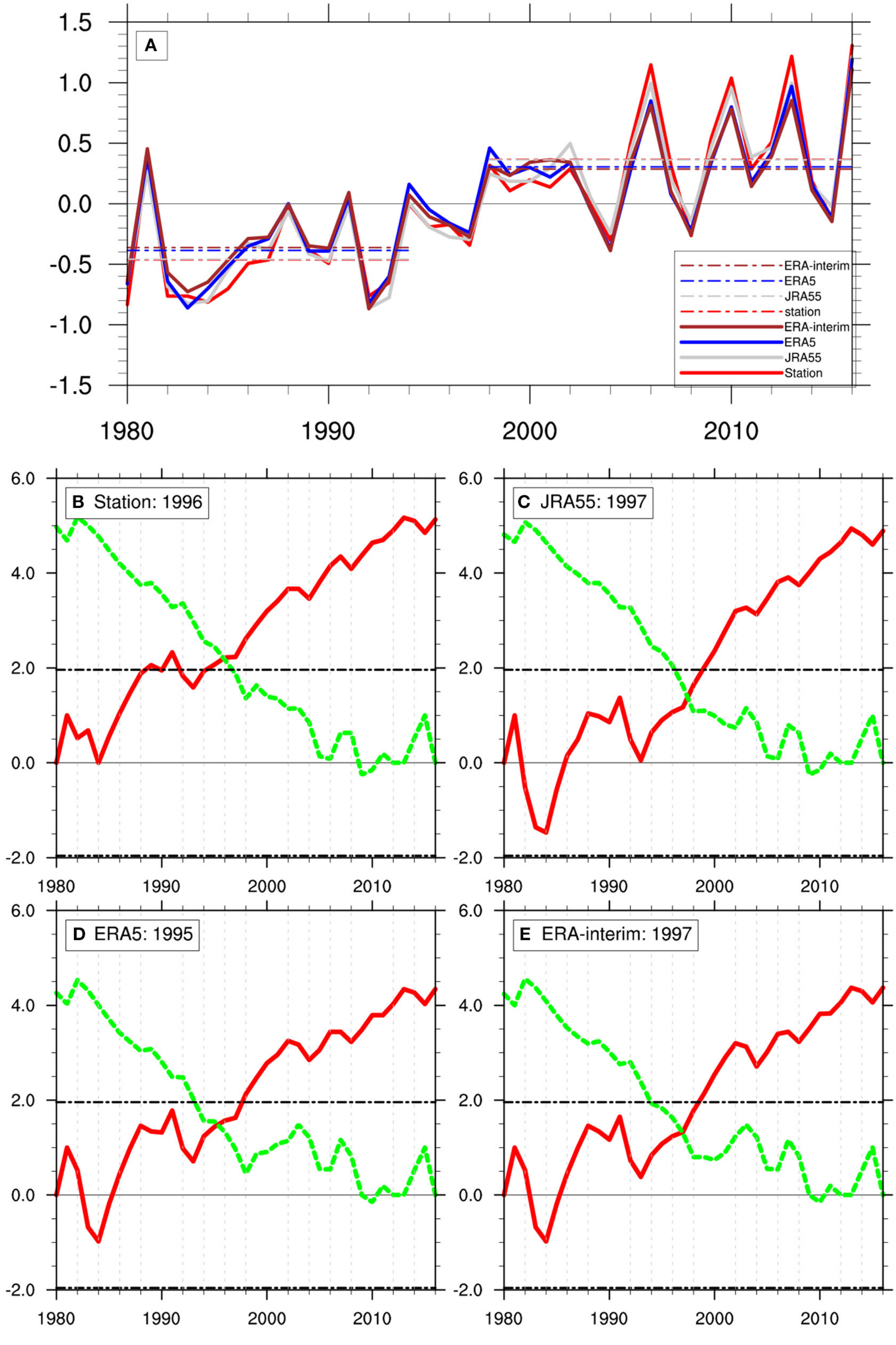

FIGURE 3 | (A) Temperature change in summer over the eastern part of the Tibetan Plateau region for 1980–1994 and 1998–2016. The solid lines are time series of Tibetan Plateau summer temperature during 1980–2016 for different datasets. The dashed lines represent the mean TPST for 1980–1994 and 1998–2016, respectively. Mann–Kendall regime shift test of the temperature over the eastern part of the Tibetan Plateau for **(B)** station, **(C)** JRA55, **(D)** ERA5, and **(E)** ERA–Interim. Red line represents the forward line; Green line represents the back line. All of them are statistically significant at the 95% confidence level.

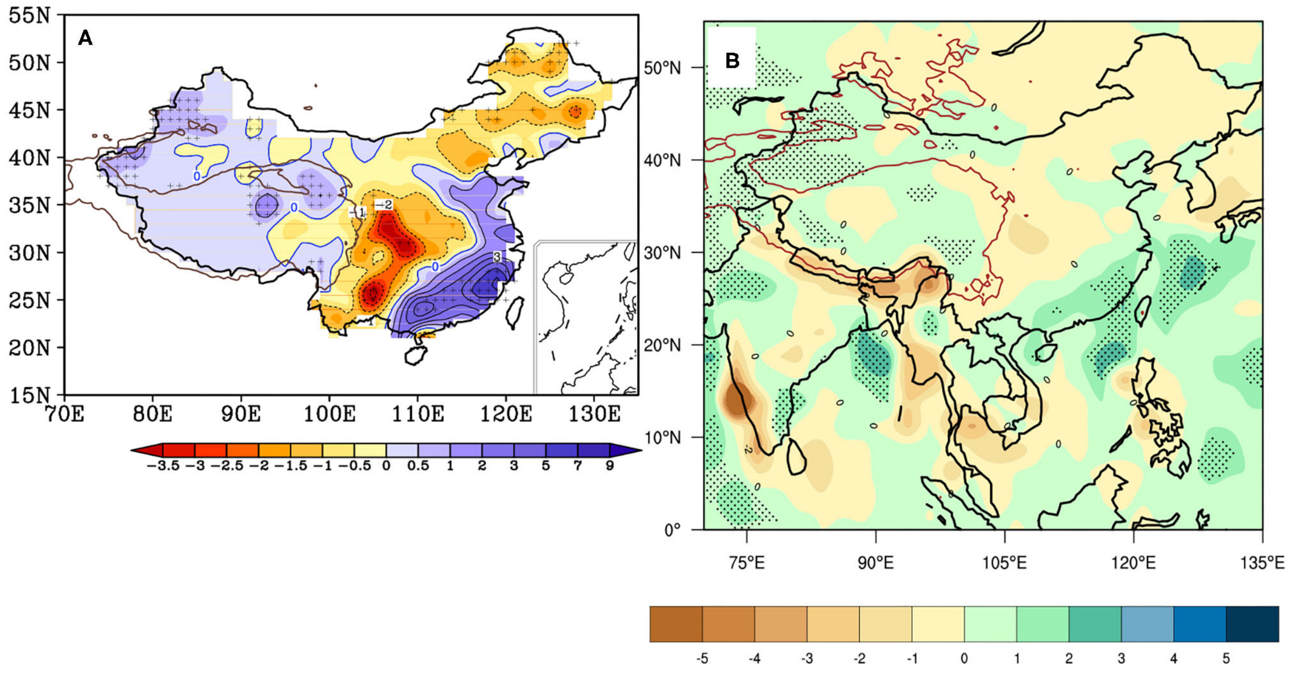

FIGURE 4 | Spatial distribution of precipitation trends in **(A)** China (based on observations) and **(B)** East Asia (based on GPCP data; brown contour delineates an altitude of 2,000 m) in the summers of 1980–2016 (units: mm/decade; cross symbols indicate statistical significance above the 95% confidence level).

in East Asia. In the subsequent analyses, we therefore use GPCP precipitation data to examine the changeable TPST–SCSSMP relationship.

In addition to TPST, global warming, interannual, and interdecadal variability, such as WNPSH, ENSO, PDO, and AMO, can also influence the summer rainfall in this area. But these factors are not independent. ENSO together with the AMO caused the WNPSH anomalous cyclone (anticyclone), strengthening (weakening) the SCSSMP (Wu et al., 2003; Fan et al., 2018). In addition, ENSO was significantly modulated by the PDO, which furtherly affected on the SCSSMP (Lee et al., 2013; Feng et al., 2014; Song and Zhou, 2015; Bollasina Massimo and Gabriele, 2018). Furthermore, Annamalai et al. (2013) showed that the warming of globe shifted the monsoon circulation and dried South Asia. This introduces a question of which factors are more important and which are less important under the interaction of these factors. How should we select the predictive variables and construct a complete and realistic regression model? In this study, a stepwise regression model is conducted to explore this question. In each step, the variable with the smallest p values which <0.1 is added to the model. The process finally terminates when no additional available variable can be removed or added to this model (Efroymson, 1960; Draper and Smith, 1981).

The variable selection procedure is shown in **Table 2**. The SCSSMP at four datasets is the variable being predicted and Tibetan Plateau, and global warming, PDO, AMO, ENSO, and WNPSH are the predictors. Firstly, we assume all the variables are predictive variables and we construct a multiple regression model. The regression equation is significance ($F > F_{0.1}$). Obviously, the predictive variables of TPST and WNPSH are both significant ($P < 0.1$), but the regression coefficients between WNPSH and SCSSMP are larger than that of TPST at four datasets. We therefore choose the WNPSH as the first predictor. According to this method, we then select the factors of TPST and global warming as the second and third predictors. After selecting three variables, it should begin to consider remove the insignificant predictor among them. Note that the last variable adds into the model, it cannot be deleted immediately. We can see that the factors of TPST, WNPSH, and are still significant. We add the variables of PDO, ENSO, and AMO by one after another. But none of the added variables and regression equation is significantly when each of variable is added, which means that PDO, ENSO, and AMO are not important predictors. Overall, TPST, global warming and WNPSH, are the three most important factors that affect the change of summer rainfall in this area. As a result, we stop adding variables. Finally, we establish a multiple regression model with the SCSSMP, TPST, global warming, and WNPSH (**Table 3**). In the following discussion, the standardized partial regression coefficient between the TPST and SCSSMP is considered as the isolated statistical relationship between them.

To examine the TPST–SCSSMP relationship after the regime shift in TPST, we calculate the standardized partial regression coefficients for period 1980–1994, 1998–2016, 1980–2016, respectively (**Figure 5**). For the entire study period (1980–2016, **Figures 5C1–C4**), we find a strong correlation between the TPST and east Asian summer monsoon rainfall (June to August), where the regression pattern resembles a "sandwich."

TABLE 2 | Picking out the main factors affected SCSSM precipitation by using stepwise regression method.

Being predicted	Predictors						
Y (SCSSMP)	**b0**	**b1(X_1, TP)**	**b2(X_2, GW)**	**b3(X_3, PDO)**	**b4(X_4, AMO)**	**b5(X_5, ENSO)**	**b6(X_6, WNPSH)**
Station	0	0.581*	−0.434	−0.309	0.030	0.230	**_−0.558*_**
JRA55	0	0.551*	−0.393	−0.323	0.029	0.198	**_−0.552*_**
ERA5	0	0.471*	−0.356	−0.316	0.053	0.186	**_−0.532*_**
ERA-I	0	0.449*	−0.384	−0.315	0.054	0.196	**_−0.522*_**

(1) Y (SCSSMP) = b0 + b1(X_6, WNPSH) ($F>F_{0.1}$)

Y (SCSSMP)	**b0**	**b1(X_1, TP)**	**b2(X_2, GW)**	**b3(X_3, PDO)**	**b4(X_4, AMO)**	**b5(X_5, ENSO)**
Station	0	**_0.505*_**	−0.369	−0.316	−202	−0.152
JRA55	0	**_0.522*_**	−0.401	−0.305	−0.202	−0.127
ERA5	0	**_0.636*_**	−0.338	−0.310	−0.173	−0.150
ERA-I	0	**_0.474*_**	−0.369	−0.308	−0.172	−0.135

(2) Y (SCSSMP) =b0 + b1(X_6, WNPSH) + b2(X_1, TP) ($F>F_{0.1}$)

Y (SCSSMP)	**b0**	**b2(X_2, GW)**	**b3(X_3, PDO)**	**b4(X_4, AMO)**	**b5(X_5, ENSO)**
Station	0	**_0.522*_**	−0.429*	−0.409*	−0.238
JRA55	0	**_0.551*_**	−0.459*	−0.379*	−0.234
ERA5	0	**_0.458*_**	−0.399	−0.401*	−0.209
ERA-I	0	**_0.499*_**	−0.427	−0.388*	−0.204

(3) Y (SCSSMP) = b0 + b1(X_6,WNPSH) + b2(X_1, TP) + b3(X_2, GW) ($F>F_{0.1}$)

Y (SCSSMP)	**b0**	**b1(X_6, WNPSH)**	**b2(X_1, TP)**	**b3(X_2, GW)**
Station	0	**_-0.496*_**	**_0.593*_**	**_-0.275*_**
JRA55	0	**_-0.470*_**	**_0.619*_**	**_-0.289*_**
ERA5	0	**_-0.472*_**	**_0.532*_**	**_-0.263*_**
ERA-I	0	**_-0.453*_**	**_0.555*_**	**_-0.278*_**

(4) Y (SCSSMP) = b0 + b1(X_6, WNPSH) + b2(X_1, TP) + b3(X_2, GW) ($F>F_{0.1}$)

*GW means the global warming. (*indicate statistical significance above the 95% confidence level; The red italics indicate the important factors for the selection of this step;* $F > F_{0.1}$ *indicate the function are statistical significance above the 90% confidence level).*

TABLE 3 | The final constructed multiple regression equations between the SCSSM precipitation and Tibetan Plateau summer surface temperature (TPST), WNPSH, global warming (GW) at four datasets.

Datasets	**Equations**
Station	Y(SCSSMP) = −0.496X_1 (WNPSH) + 0.593X_2 (TP)–0.275X_3 (GW)
JRA55	Y(SCSSMP) = −0.470X_1 (WNPSH) + 0.619X_2 (TP)–0.289X_3 (GW)
ERA5	Y(SCSSMP) = −0.472X_1 (WNPSH) + 0.532X_2 (TP)–0.263X_3 (GW)
ERA-I	Y(SCSSMP) = −0.453X_1 (WNPSH) + 0.555X_2 (TP)–0.278X_3 (GW)

A positive relationship is found in South China, Indochina Peninsula, SCS, and the western north Pacific Ocean (WNP), as well as the North China and Northeast China. At the same time, the negative relationship between them is also obvious, extending from the southern of Tibetan Plateau across the mid–lower reaches of the Yangtze River to the Korean Peninsula and Japan along the south–northeast trend, which is generally dominated by the Meiyu front. This spatial pattern is fairly consistent with those results of Hsu and Liu (2003) and Wang et al. (2008). However, comparisons with the period of 1980–1994 and 1998–2016 (**Figures 5A1–A4, B1–B4**) show that the TPST–SCSSMP relationship changes, when the shift start around 1996. It is obviously found that the TPST–SCSSMP relationship is negative during 1980–1994 but positive for 1998–2016 in the South China Sea and the negative correlation along the Meiyu front is enhanced during 1998–2016. The observation dataset and three reanalysis datasets show the same phenomenon, which demonstrates that the recent changes relationship of TPST–SCSSMP responded to TPST shift over the last 20 years is a real phenomenon but not an artifact.

We also determine to identify whether the change relationship exist in other season (spring (MAM), summer (JJA), fall (SON), winter (DJF) by calculating the standard partial regression coefficients of TPST–SCSSMP during 1980–1994 and 1998–2016. A comparison of the results for these four seasons (not showed) shows that such a changing relationship of TPST–SCSSMP only is found in the summer season. In addition, the maximum value of the partial regression coefficient during the summer can reach 0.5 and−0.6, which is larger than that in the other seasons. We therefore consider that Tibetan Plateau temperature changes in the summer season are mainly responsible for those in the circulation and rainfall patterns in downstream regions.

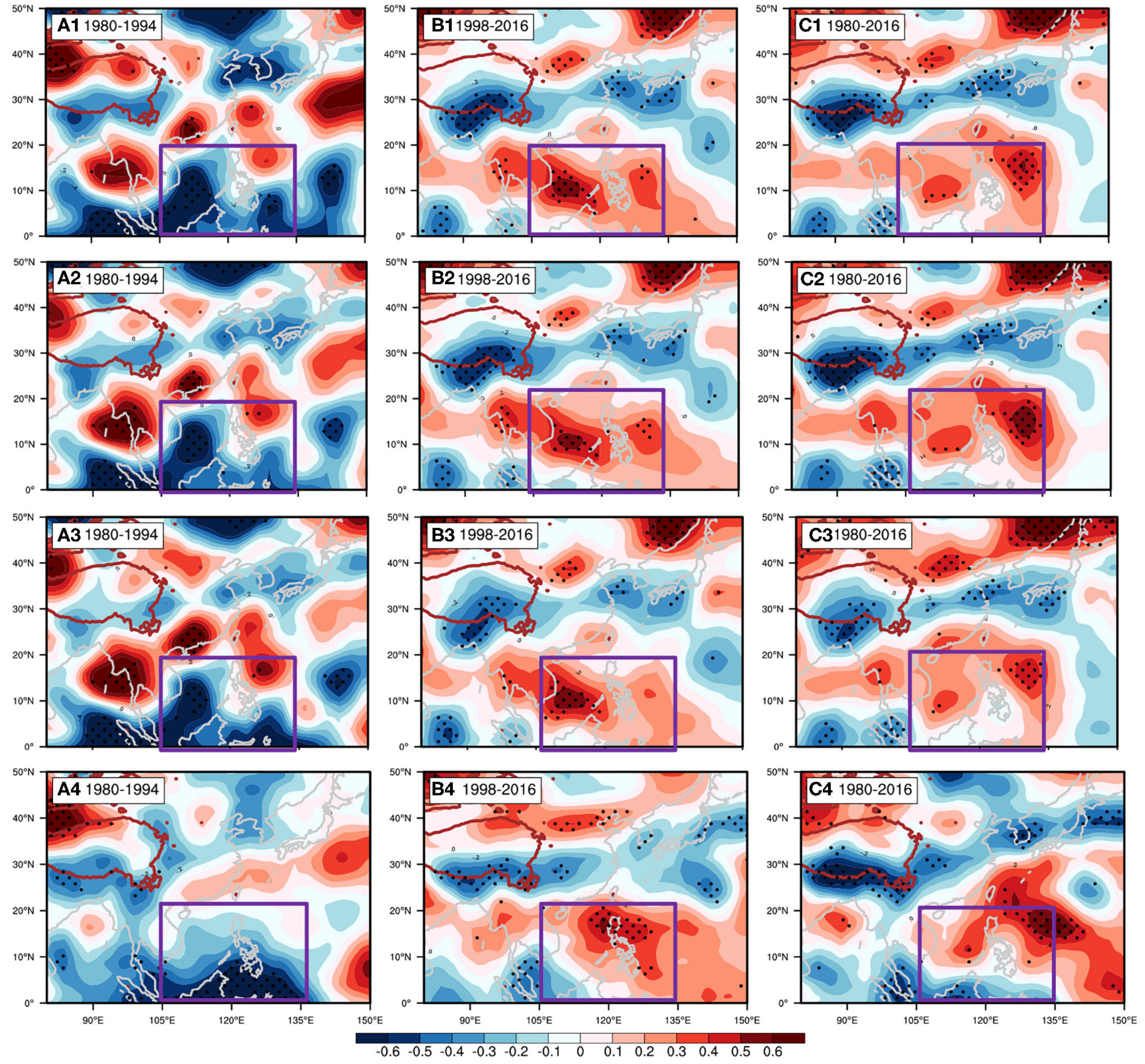

FIGURE 5 | Standardized partial regression coefficients between Tibetan Plateau temperature and summer precipitation (GPCP) during: **(A)** 1980–1994, **(B)** 1998–2016, and **(C)** 1980–2016. 1: station data, 2: JRA55, 3: ERA5, and 4: ERA–Interim data. The purple box areas represent the South China Sea. Black spots indicate significant differences above the 90% confidence level based on the Student's *t*–test.

To illustrate the changes of the TPST–SCSCM relationship, **Figure 6** displays the 13–year moving average of the partial regression coefficients between TPST and SCSCMP in the South China Sea during 1980–2016. During 1985–1994, the partial regression coefficients between TPST and SCSCMP are almost negative, but they stepwise increase in the late 1990s and, finally, they are all greater than 0 and they can reach 0.8 at the early 2010s. The variations in the correlation coefficients are relatively consistent in the station data and the three reanalysis data sets, with only small differences in the values, which also verify that the TPST–SCSCM relationship is changes in the late 1990s. It should be noted that similar results are also captured in other moving average window lengths (11 years and 15 years) and small change the region (100-135°E, 0-20°N; 100-135°E, 0-22°N;100-140°E, 5-20°N; 100-145°E, 0-22°N; not showed).

EFFECTS OF THE TPST INTERDECADAL VARIATION ON ATMOSPHERIC CIRCULATION

Since the normalized partial regression coefficient between TPST and SCSSMP is considered to be an isolated statistical

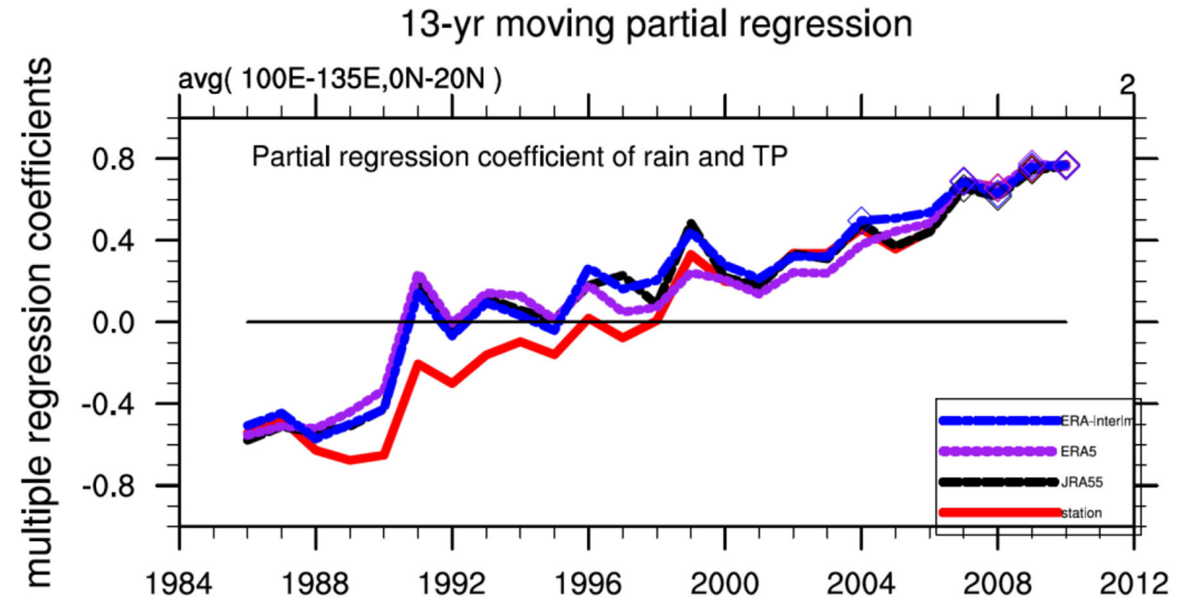

FIGURE 6 | The 13–year moving standardized partial regression coefficients between Tibetan Plateau temperature and precipitation in the South China Sea (Purple box in **Figure 5**) during JJA in 1986–2010 using different data sets (red line: station data; black line: JRA55; purple line: ERA5; yellow line: ERA–Interim). The x–axis indicates the middle year in the 13–year moving window (e.g., 1986 indicates the correlation coefficient for 1980–1992 and 1987 indicates the correlation coefficient for 1981–1993). Hollow rhombuses indicate significant differences above the 90% confidence level based on the Student's *t*–test.

relationship between them, TPST and other meteorological elements (VIMF, OLR et al.) can also show the influences of the decadal variation of TPST on other elements. Hence, we use the same reanalysis datasets (JRA55, EAR5, ERA–Interim) to conduct regression analyses of TPST and wind field to show the influence of decadal variation of TPST on atmospheric circulation over the South China Sea (**Figures 7**, **8**). During 1980–1994, an anticyclone appears at 700 hPa over the South China Sea (**Figures 7A–E**), which indicating that there is a negative correlation between the TPST and its wind field. In other words, the changes of TPST are more favorable for anticyclone enhance or for cyclone weaken at low–level over the South China Sea. At the same time, a strong anticyclone is also found over the Northern China and it also means the negative correlation between them. At 200 hPa, the South China Sea is dominated by the northerly wind, and the TPST is also negative correlated with the wind field (**Figures 8A–E**). The spatial pattern of this regression (TPST–wind field) is very similar to the regression pattern of TPST–SCSSMP from 1980 to 1994, which further confirms that changes in TPST deeply affect SCSSMP.

However, during 1998–2016, at 700 hPa, a wave–like structure in the low–latitude region moves easterly along the low–level monsoon flow (the red dotted line in **Figures 7B–F**). A strong cyclone exists in the southwestern part of the Tibetan Plateau and South China Sea. At 200 hPa, another wave train propagated downstream along the upper–level westerly jet stream and strong anticyclones appear over the South China Sea (**Figures 8B–F**). Combining the divergence at 200 hPa and convergence at 700 hPa over the South China Sea, strong convection is more likely to occurs and lead to water vapor converge, which means the likelihood of rain increase in the later period. By contrast, the region along the North China Plain across to the Korean Peninsula and to southern Japan is characterized by a northeasterly wind in the earlier period and anticyclonic circulation in the later period, thereby there is a negative correlation between the TPST and water vapor flux along the Meiyu front. It means less water vapor convergence here and the convection is suspended, leading to less rainfall in this area after the late 1990s. According to our results, during 1998–2016, the wave–like structure in the tropics moves westerly along the low–level monsoon and another wave train may propagate downstream along the upper–level westerly jet. Wang et al. (2008) has already conducted numerical experiments using the Max Planck Institute for Meteorology ECHAM4 to confirm that eastern Tibetan Plateau warming can excite or intensify these two Rossby wave trains. In this study, we confirm they results again by using the different reanalysis datasets.

To some extent, the partial regression coefficient pattern between TPST and SCSSMP is consistent with the SCSSM rainfall linear trend pattern (**Figure 4B**), which shows that the TPST is closely associated with the summer monsoon precipitation over the South China Sea, as also suggested in previous studies (Hsu and Liu, 2003; Wang et al., 2008). Consistent with the above mentioned (**Figure 6**), the relationship between the TPST and SCSSMP change when TPST underwent a shift that started around 1996. The TPST interdecadal variation may not only significantly affect the atmospheric circulation but also the water vapor transport and convective motion, and furtherly the SCSSMP. It is clearly that TPST is also negative

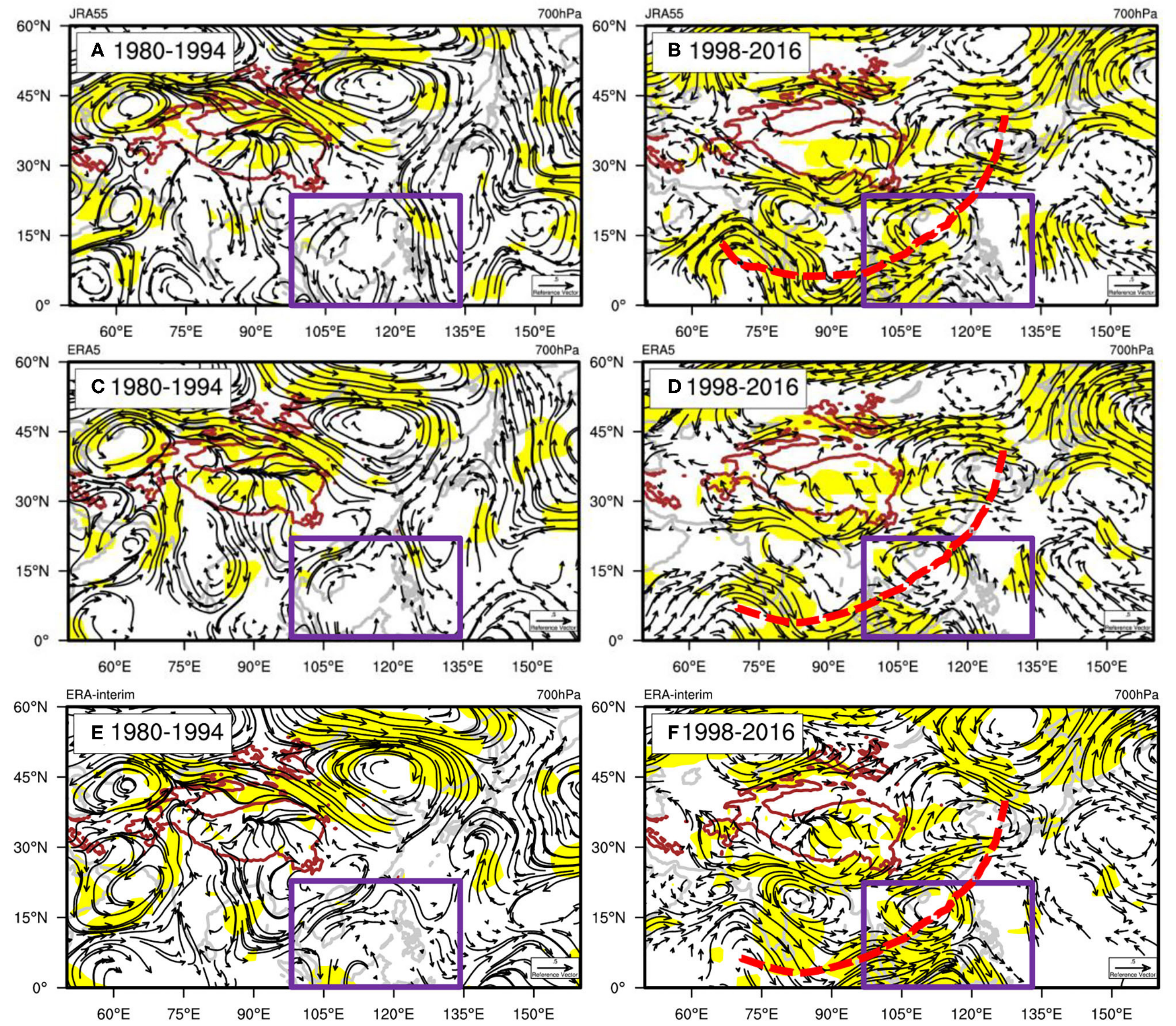

FIGURE 7 | Standardized partial regression coefficients between Tibetan Plateau temperature and wind field at 700 hPa in East Asia: **(A,C,E)** for the period from 1980 to 1994 and **(B,D,F)** for the period from 1998 to 2016. **(A,B)** Based on JRA55; **(C,D)** based on ERA5; and **(E,F)** based on ERA–Interim. Red solid line represents the Tibetan Plateau. The purple boxed areas represent the South China Sea. Red dashed lines represent wave–like structures. Hence, the area where the averaged altitude above 3,000 m is already masked. Vectors are ignored for values <0.20. Shading indicates significant differences above the 90% confidence level based on the Student's *t*–test.

correlated with VIMF over the South China Sea during 1980–1994 (**Figures 9A–E**), which meaning that it is much more dry air from the north Pacific gather here. Combining the regressions of wind field and water vapor flux, we are clearly understanding that the TPST change is not conducive to the SCSSMP. After the dramatic shift in TPST during 1998–2016, TPST is positive correlated with VIMF over the South China Sea (**Figures 9B–F**), which means that it is more favorable for water vapor convergence here. In other words, during 1998–2016, the area is more prone to precipitation when the convection conditions are suitable.

To further explore the changes in the convection motion after the interdecadal variation of the TPST, we study the changes in the TPST–OLR relationship to find the changes of the convection conditions. The regression coefficient between TPST at the observation sites and the OLR shows a positive correlation over the South China Sea during 1980–1994 (**Figure 10a**), while it is negative during 1998–2016 (**Figure 10b**). It is means that significant convection is likely to occur in the region during the latter period (**Figure 10b**), which also means that it is favorable for moisture convergence here. This change relationship is consistent with the results showed in **Figures 7**, **8**. In addition, the relationship is characterized by a positive correlation along the Yunnan–Guizhou Plateau passing through the middle and lower reaches of the Yangtze River to Japan, which suggests that convection weakens in this region during 1998–2016.

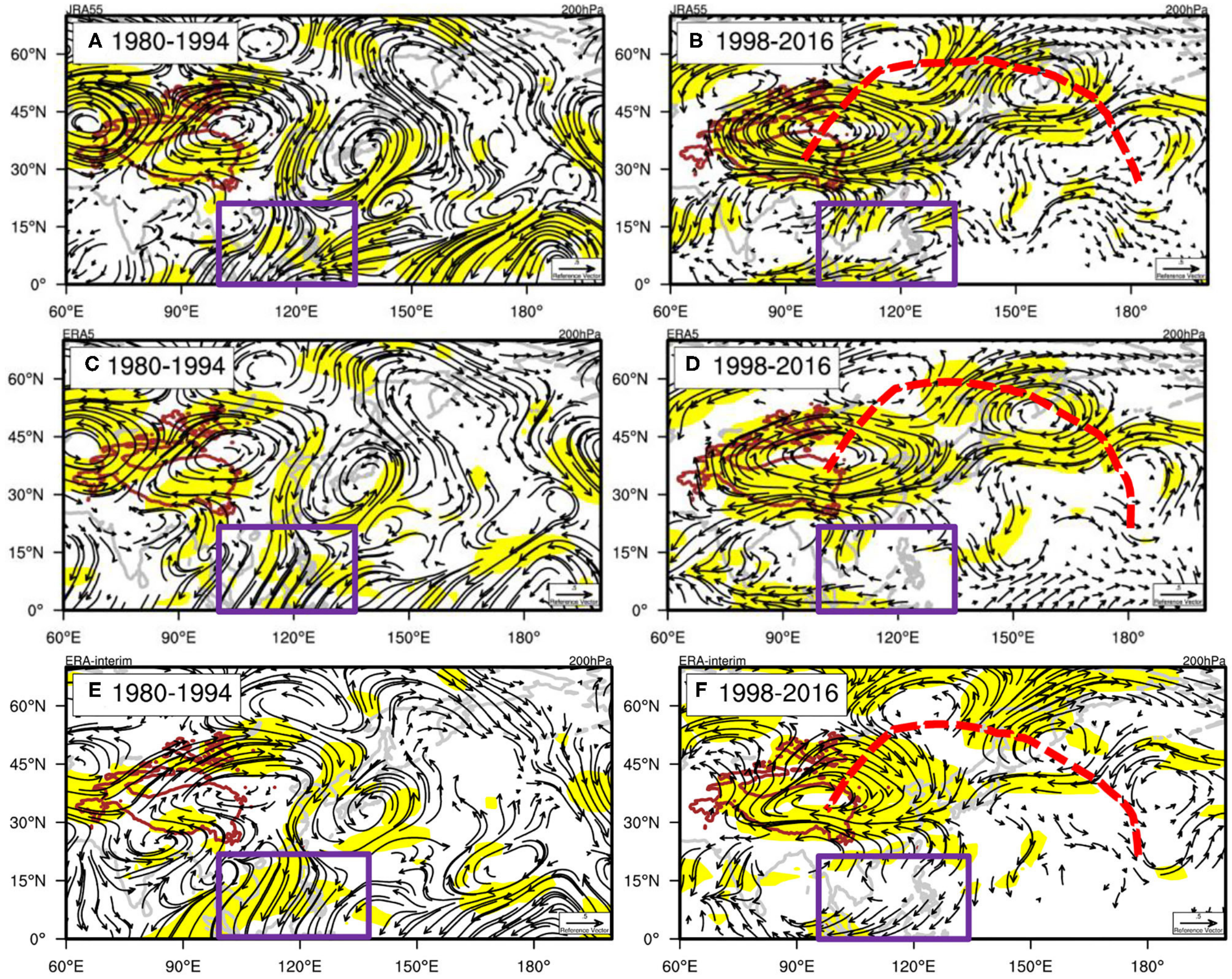

FIGURE 8 | Standardized partial regression coefficients between Tibetan Plateau temperature and wind field at 200 hPa in East Asia: **(A,C,E)** for the period from 1980 to 1994 and **(B,D,F)** for the period from 1998 to 2016. **(A,B)** Based on JRA55; **(C,D)** based on ERA5; and **(E,F)** based on ERA-Interim. Red solid line represents the Tibetan Plateau. The purple boxed areas represent the South China Sea. Red dashed lines represent wave-like structures. Vectors are ignored for values <0.20. Shading indicates significant differences above the 90% confidence level based on the Student's *t*–test.

During 1980–1994, the TPST is not conducive to convection in the South China Sea and water vapor could not gather there (**Figures 9A–E**), so the precipitation is lower in the early period. In the later period, TPST warming is conducive to convection in the South China Sea, and therefore the low–level moisture and precipitation increase (**Figures 4**, **9B–F**), and thus there is a positive relationship between the TPST and precipitation in the late 1990s. Our results suggest that in a changing climate, we should be cautious when using predictions with interdecadal variations (Piao et al., 2014; Zhang et al., 2019).

CONCLUSIONS AND DISCUSSIONS

Meteorological observation sites, JRA55, ERA5, and ERA–Interim datasets totally show that, between 1980 and 2016, the Tibetan Plateau summer surface temperature (TPST) increased rate (0.32°C/decade−0.42°C/decade) is far greater than the rate of global warming (0.15°C/decade). All datasets show that a regime shift in the TPST occurs around 1996 ($P < 0.05$), which means that a significant interdecadal variation exists in the TPST.

A stepwise regression model is conducted to explore global warming and natural internal variabilities, such as PDO, AMO, ENSO, and WNPSH, that can affect the changes in the relationship between the TPST and South China Sea summer monsoon precipitation (SCSSMP). We exclude the signals of ENSO, PDO, and AMO and finally set up a multiple regression equation between SCSSMP and TPST, WNPSH, global warming. The standardized partial regression coefficients between the TPST and SCSSMP is considered as the isolated statistical relationship the between them, which exclude the influences of

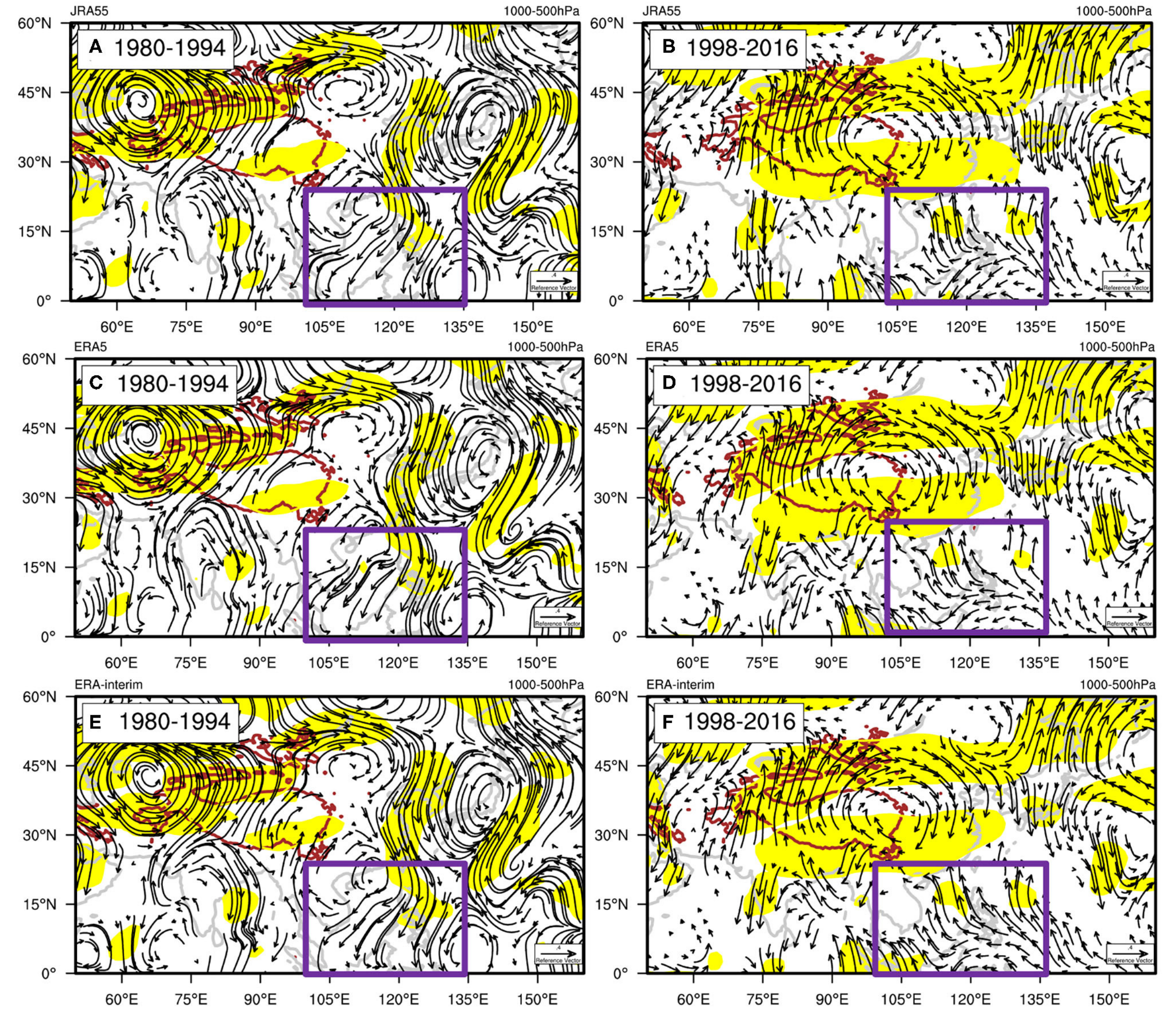

FIGURE 9 | Standardized partial regression coefficients between Tibetan Plateau temperature and vertically integrated moisture flux (VIMF) between 1000–500 hPa in East Asia: **(A,C,E)** for the period from 1980 to 1994 and **(B,D,F)** for the period from 1998 to 2016. **(A,B)** Based on JRA55; **(C,D)** based on ERA5; and **(E,F)** based on ERA-Interim. Vectors are ignored for values <0.15. Shading indicates significant differences above the 90% confidence level based on the Student's *t*–test.

other factors. These results showed that the correlation between the TPST and SCSSMP changes between 1980 and 2016. The TPST–SCSSMP relationship changes from a negative correlation to a positive correlation in the late 1990s.

The interdecadal variation of the TPST significantly affect the hemispheric atmospheric circulation, furtherly leading to the change of the SCSSMP. During 1980–1994, the anticyclone exists over the South China Sea is not conducive to convection (**Figure 10a**) and water vapor cannot gather there (**Figures 9A–E**), and therefore less precipitation occurs over the South China Sea. Hence, there is a negative relationship between the TPST and precipitation in the early period. In the later period, a wave–like structure in the low–latitude moves easterly along the low–level monsoon and a strong cyclonic circulation exists in the South China Sea, which is consistent with the negative correlation between the TPST–OLR. Hence, the TPST warming is conducive to convection over the South China Sea to increase the low–level moisture and precipitation, and thus there is a positive relationship between the TPST and precipitation in the late 1990s. Those results suggest that we should be cautious when using predictor with interdecadal variations in a changing climate.

Some issues still do not involve. Why there is a negative relationship between TPST and Meiyu front, extending from the

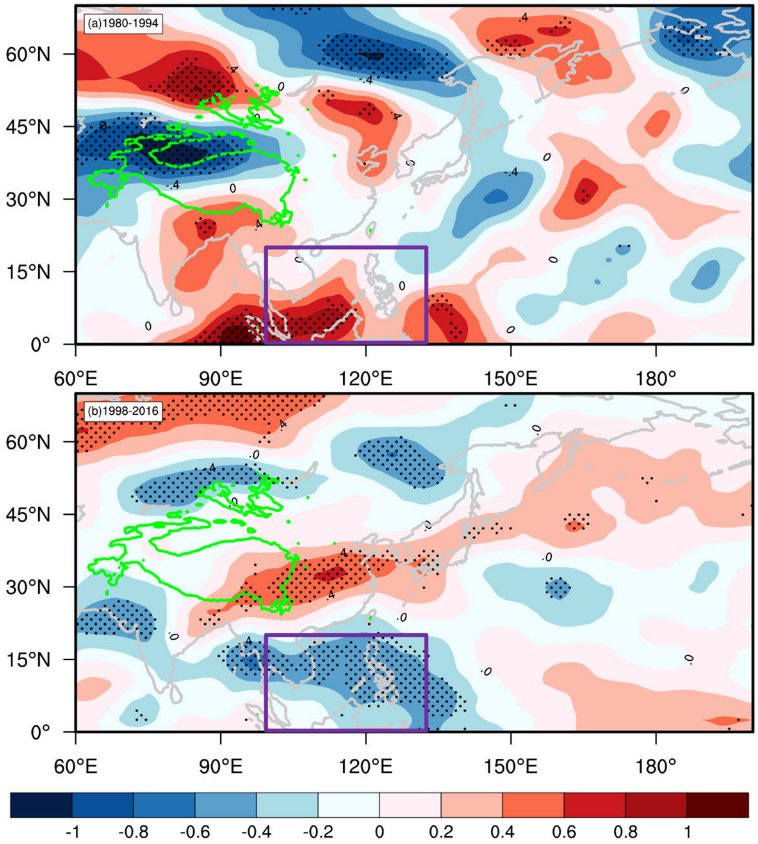

FIGURE 10 | Standardized partial regression coefficients between Tibetan Plateau temperature at station and OLR in East Asia: **(a)** for the period from 1980 to 1994 and **(b)** for the period from 1998 to 2016. The purple boxed areas represent the South China Sea. Black spots indicate significant differences above the 90% confidence level based on the Student's *t*–test.

southern of TP across the mid–lower reaches of the Yangtze River to the Korean Peninsula and Japan along the south–northeast trend. Hahn and Manabe (1975) suggested that the interannual variation of the TP heating likely modulated a Meiyu rain belt. Hsu and Liu (2003) further examined that he TP heating might impact the zonally elongated rainfall (Meiyu front) but not be the only dominant forcing. Recently, He et al. (2019) using the output of 30 models from CMIP5 provided further evidences that the enhanced latent heating maybe substantially increased precipitation over the southeastern TP. In other words, enhanced latent heat release (corresponding to the cooler temperature) might be responsible for the positive precipitation anomaly over the southeastern Tibetan Plateau. However, to what extent can TP heating or latent heat release explain the change of Meiyu. Further discussions are still needed.

According to **Figure 8**, it is likely that the summer diabatic heating over TP after 1998 is enhanced because there is a significant anticyclonic anomaly at 200 hPa. Does the increasing TPST denote an intensity surface heating source? Hoskins (1991) interpreted the atmospheric response to a given thermal forcing as the formation of lower layer cyclonic circulation and upper layer anticyclonic circulation. Wu and Liu (2000) furtherly developed the thermal adaptation theory (a prescribed deep/shallow convective-type heating). Wang et al. (2008) conducted the numerical experiments with atmospheric general circulation models by changing the albedo and showed that atmospheric heating would be enhanced after the TP temperatures rising. The reduction of albedo over the TP results in a local surface air temperature increase by more than 2°C. According to the thermal adaptation, the TP heating will result in a shallow cyclonic circulation at low-level and a deep anticyclonic circulation at high-level, which is consistent with the significant anticyclonic anomaly at 200 hPa (**Figure 8**). These results suggest that the summer diabatic heating over TP is likely enhance after 1998.

It should also be noted that, in this study, a simplified complex sea–land–gas interaction system is adopted, and these results are based on the assumption of a linear relationship between TPST and SCSSMP. In addition, many other factors could have affected the precipitation of South China Sea, such as the polar snow cover and snow depth. We only considered five other factors comprising global warming, ENSO, WNPSH, PDO, and AMO. Finally, uncertainties remain because our understanding of the linkage between the TPST and SCSSMP is based on statistical analyses. In the following study, we will use the ECHAM 6 numerical model to further verify our findings and understand the mechanism of the change relationship between TPST–SCSSMP.

DATA AVAILABILITY STATEMENT

The raw data supporting the conclusions of this article will be made available by the authors, without undue reservation.

AUTHOR CONTRIBUTIONS

JX and ML designed the experiments and ML conducted them. JC, LW, and XX provide some useful suggestions. ML prepared the manuscript with contributions from all of the co-authors. All authors contributed to the article and approved the submitted version.

FUNDING

This paper is supported by The Second Tibetan Plateau Scientific Expedition and Research (STEP) program (grant 2019QZKK0105) and the Funded by National Key R&D programs of China (grants 2018YFC1505705; 2018YFC1501706). It is also supported by the project of Enhancing School with Innovation of Guangdong Ocean University (230419053); Projects (Platforms) for Construction of Top-ranking Disciplines of Guangdong Ocean University (231419022); Special Funds of Central Finance Support the Development of Local Colleges and Universities (000041).

ACKNOWLEDGMENTS

We sincerely thank two reviewers whose comments allowed us to improve the manuscript substantially.

REFERENCES

Adler, R. F., Huffman, G. J., Chang, A., Ferraro, R., Xie, P., Janowiak, J., et al. (2003). The version 2 Global Precipitation Climatology Project (GPCP) monthly precipitation analysis (1979-present). *Hydrometeor J.* 4:1147–1167. doi: 10.1175/1525-7541(2003)004<1147:TVGPCP>2.0.CO;2

Annamalai, H., Hafner, J., Sooraj, K. P., and Pillai P. (2013). Global warming shifts the monsoon circulation, drying South Asia. *Climate J.* 26, 2701–2718. doi: 10.1175/JCLI-D-12-00208.1

Beniston, M. (2003). Climatic change in mountain regions: a review of possible impacts. *Clim. Change*. 59, 5–31. doi: 10.1007/978-94-015-1252-7_2

Beniston, M., Diaz, H., and Bradley, R. (1997). Climatic change at high elevation sites: an overview. *Clim. Change* 36, 233–251. doi: 10.1023/A:1005380714349

Berrisford, P., Dee, D., Poli, P., and Brugge, P. (2011). *The ERA-Interim Archive Version 2.0.* Berkshire: Reading.

Bollasina Massimo, A., and Gabriele, M. (2018). On the link between the subseasonal evolution of the North Atlantic Oscillation and East Asian climate. *Clim. Dyn.* 51, 3537-3557. doi: 10.1007/s00382-018-4095-5

Boos, W. R., and Kuang, Z. M. (2013). Sensitivity of the South Asian Monsoon to elevated heating. *Sci. Rep.* 3:1192. doi: 10.1038/srep01192

Burke, C., and Stott, P. (2017). Impact of anthropogenic climate change on the East Asian Summer Monsoon. *Clim. J.* 30, 5205–5220. doi: 10.1175/JCLI-D-16-0892.1

Ceppi, P., Scherrer, S., Fischer, A., and Appenzeller, C. (2010). Revisiting swiss temperature trends 1959-2008. *Int. J. Climatol.* 32, 203-213. doi: 10.1002/joc.2260

Ding, Y. H. (1992). Effects of the Qinghai-Xizang(Tibetan) Plateau on the circulation features over the plateau and its surrounding areas. *Adv. Atmos. Sci.* 9, 112-130. doi: 10.1007/BF02656935

Ding, Y. H., Sun, Y., Wang, Z., Zhu, Y., and Song, Y. (2009). Inter-decadal variation of the summer precipitation in China and its association with decreasing Asian summer monsoon. Part 507 II: possible causes. *Int. J. Climatol.* 28:508. doi: 10.1002/joc.1759

Draper, N., and Smith, H. (1981). *Applied Regression Analysis.* 2d Edition. New York, NY: John Wiley & Sons, Inc.

Duan, A. M., Li, F., Wang, M. R., and Wu, G. X. (2011). Persistent weakening trend in the spring sensible heat source over the Tibetan Plateau and its impact on the Asian summer monsoon, *Clim. J.* 24, 5671-5682. doi: 10.1175/JCLI-D-11-00052.1

Duan, A. M., Wang, M. R., Lei, Y. H., and Cui, Y. F. (2013). Trends in summer rainfall over China associated with the Tibetan Plateau sensible heat source during 1980-2008. *Clim. J.* 26, 261-275. doi: 10.1175/JCLI-D-11-00669.1

Duan, A. M., and Wu, G. X. (2005). Role of the Tibetan Plateau thermal forcing in the summer climate patterns over subtropical Asia. *Clim. Dyn*. 24, 793-807. doi: 10.1007/s00382-004-0488-8

Duan, A. M., and Wu, G. X. (2008). Weakening trend in the atmospheric heat source over the Tibetan Plateau during recent decades, Part I: Observations. *J. Clim.* 21, 3149-3164. doi: 10.1175/2007JCLI1912.1

Duan, A. M., Wu, G. X., Liu, Y. M., Ma, Y. M., and Zhao, P. (2012). Weather and climate effects of the Tibetan Plateau. *Adv. Atmos. Sci*. 29, 978-992. doi: 10.1007/s00376-012-1220-y

Efroymson, M. A. (1960). "Multiple regression analysis," *Mathematical Methods for Digital Computers*, eds A. Ralston and H. S. Wilf (New York, NY: Wiley), 191–203.

Fan, Y., Fan, K., Xu, Z., and Li, S. (2018). ENSO-South China Sea summer monsoon interaction modulated by the Atlantic Multidecadal Oscillation. *Clim. J.* 31, 3061-3076. doi: 10.1175/JCLI-D-17-0448.1

Feng, J., Wang, L., and Chen, W. (2014). How does the East Asian summer monsoon behave in the decaying phase of El Niño during different PDO phases? *Clim. J.* 27, 2682-2698. doi: 10.1175/JCLI-D-13-00015.1

Gao, K. L., Duan, A., De, M., Chen, G., and Wu, X. (2019). Surface energy budget diagnosis reveals possible mechanism for the different warming rate among Earth's three poles in recent decades. *Sci. Bull.* 64, 1140-1143. doi: 10.1016/j.scib.2019.06.023

Giorgi, F., Hurrel, J., Marinucci, M., and Beniston, M. (1997). Elevation dependency of the surface climate change signal: a model study. *Clim. J.* 10, 288–296. doi: 10.1175/1520-0442(1997)010<0288.EDOTSC>2.0.CO;2

Hahn, D. G., and Manabe, S. (1975). The role of mountains in the South Asian monsoon circulation. *J. Atmos. Sci.* 32, 1515-1541. doi: 10.1175/1520-0469(1975)032<1515.TROMIT>2.0.CO;2

He, C., Wang, Z., Zhou, T., and Li, T. (2019). Enhanced latent heating over the Tibetan Plateau as a key to the enhanced east Asian Summer Monsoon circulation under a warming climate. *Clim. J.* 32, 3373-3388. doi: 10.1175/JCLI-D-18-0427.1

Hoskins, B. (1991). Towards a PV-J view of the general circulation. *Tellus.* 43AB:27-35. doi: 10.1034/j.1600-0870.1991.t01-3-00005.x

Hsu, H. H., and Liu, X. (2003). Relationship between the Tibetan plateau heating and east Asian summer monsoon rainfall, Geophys. *Res. Lett*. 30:2066. doi: 10.1029/2003GL017909

Kobayashi, C., and Iwasaki, T. (2016). Brewer-Dobson circulation diagnosed from JRA-55. *J. Geophys. Res. Atmos.* 121:476. doi: 10.1002/2015JD023476

Lawrimore, J., Menne, M., Gleason, B., Williams, C., Wuertz, D., Vose, R., et al. (2011). An overview of the global historical climatology network monthly mean temperature data set, version 3. *J Geophys Res.* 116:D19121. doi: 10.1029/2011JD016187

Lee, S, Seo, Y., and Ha, K. (2013). Impact of the western North Pacific Subtropical High on the East Asian Monsoon precipitation and the Indian Ocean precipitation in the Boreal summertime. *Asia-Pacific J. Atmos. Sci*. 49, 171-182. doi: 10.1007/s13143-013-0018-x

Liu, X., and Chen, B. D. (2000). Climate warming in the Tibetan Plateau during recent decades. *Int. J. Climatol.* 20, 1729-1742. doi: 10.1002/1097-0088(20001130)20.14<1729.:AID-JOC556>3.0.CO;2-Y

Liu, X., Cheng, Z., Yan, L., and Yin, Z. (2009). Elevation dependency of recent and future minimum surface air temperature trends in the Tibetan Plateau and its surroundings. *Global Planet Chang*. 68, 164-174. doi: 10.1016/j.gloplacha.2009.03.017

Liu, Y. M., Wu, G. X., and Hong, J. L. (2012). Revisiting Asian monsoon formation and change associated with Tibetan Plateau forcing II. *Change. Climate Dyn.* 39, 1183–1195. doi: 10.1007/s00382-012-1335-y

Lu, C. X., Yu, G., and Xie, G. D. (2005). Tibetan Plateau serves as a water tower. *IEEE Trans. Geosci. Remote Sens*. 5, 1183–1195.

Malardel, S., Wedi, N., Deconinck, W., Diamantakis, M., Kuhnlein, C., Mozdzynski, G., et al. (2015). *A New Grid for the IFS*. Newsletter No. 146 - Winter 2015/16, ECMWF, 6.

Ohmura, A. (2012). Enhanced temperature variability in high-altitude climate change. *Theor. Appl. Climatol*. 110, 499-508. doi: 10.1007/s00704-012-0687-x

Pepin, N., Bradley, R. S., and Diaz, H. F. (2015). Elevation-dependent warming in mountain regions of the world. *Nat. Clim. Change* 5, 424-430. doi: 10.1038/nclimate2563

Pepin, N., and Lundquist, J. (2008). Temperature trends at high elevations: patterns across the globe. *Geophys. Res. Lett*. 35, L14701. doi: 10.1029/2008GL034026

Piao, S., Nan, H., and Chris, H. (2014). Evidence for a weakening relationship between interannual temperature variability and northern vegetation activity. *Nat. Commun.* 5:5018. doi: 10.1038/ncomms6018

Rangwala, I. (2013). Amplified water vapor feedback at high altitudes during winter. *Int. J. Climatol*. 33, 897-903. doi: 10.1002/joc.3477

Rangwala, I., and Miller, J. R. (2012). Climate change in mountains: a review of elevation-dependent warming and its possible causes. *Clim. Change* 114, 527-547. doi: 10.1007/s10584-012-0419-3

Seidel, D., and Free, M. (2003). Comparison of lower-tropospheric temperature climatologies and trends at low and high elevation radiosonde sites. *Clim. Change* 59, 53-74. doi: 10.1007/978-94-015-1252-7_4

Si, D., and Ding, Y. (2013). Decadal change in the correlation pattern between the Tibetan Plateau winter snow and the East Asian summer precipitation during 1979-2011. *J. Clim*. 26, 7622–7634. doi: 10.1175/JCLI-D-12-00587.1

Song, F., and Zhou, T. (2015). The Crucial role of internal variability in modulating the decadal variation of the East Asian Summer Monsoon-ENSO Relationship during the twentieth century. *Clim. J.* 28, 7093-7107. doi: 10.1175/JCLI-D-14-00783.1

Stanley, S. (2017). Summer rainfall patterns in east Asia shift with the wind. *Eos*. 98, 3011. doi: 10.1029/2017EO083011

Strong, G. S., Proctor, B., Wang, M., Soulis, E. D., Smith, C. D., Seglenieks, F., et al. (2002). Closing the Mackenzie Basin water budget, water years 1994/95 to 1996/97. *Atmos. Ocean* 40, 113-124. doi: 10.3137/ao.400203

Su, J., Duan, A., and Xu, H. (2017). Quantitative analysis of surface warming amplification over the Tibetan Plateau after the late 1990s using surface energy balance equation. *Atmos. Sci. Let.* 18, 112–117. doi: 10.1002/asl.732

Wang, B., Qing, B., and Hoskins, B. (2008). Tibetan Plateau warming and precipitation changes in East Asia. *Geo. Res. Let.* 35, L14702. doi: 10.1029/2008GL034330

Wang, Q., Fan, X., and Wang, M. (2014). Recent warming amplification over high elevation regions across the globe. *Clim. Dyn*. 43, 87-101. doi: 10.1007/s00382-013-1889-3

Wu, G. X., Duan, A. M., Liu, Y. M., Mao, J. Y., Ren, R. C., Bao, Q., et al. (2014). Tibetan Plateau climate dynamics: recent research progress and outlook. *Natl. Sci. Rev*. 2, 100-116. doi: 10.1093/nsr/nwu045

Wu, G. X., and Liu, Y. M. (2000). Thermal adaptation, overshooting, dispersion, and subtropical high. Part I: Thermal adaptation and overshooting (in Chinese). *Chin. J. Atmos. Sci*. 24, 433–436.

Wu, G. X., Liu, Y. M., Dong, B. W., Liang, X. Y., Duan, A. M., Bao, Q., et al. (2012b). Revisiting Asian monsoon formation and change associated with Tibetan Plateau forcing: Formation I. *Clim. Dyn*. 39, 1169-1181. doi: 10.1007/s00382-012-1334-z

Wu, G. X., Liu, Y. M., He, B., Bao, Q., Duan, A. M., and Jin, F. F. (2012a). Thermal controls on the Asian summer monsoon. *Sci Rep.* 2:404. doi: 10.1038/srep00404

Wu, L., Feng, X., and Liang, M. (2017). Insensitivity of the Summer South Asian High Intensity to a Warming Tibetan Plateau in Modern Reanalysis Datasets. *J. Clim.* 30, 3009-3024. doi: 10.1175/JCLI-D-16-0359.1

Wu, R., Hu, Z. Z., and Kirtman, B. (2003). Evolution of ENSO-related rainfall anomalies in East Asia. *J. Clim*. 16, 3742-3758. doi: 10.1175/1520-0442(2003)016<3742.EOERAI>2.0.CO;2

Xu, L., Xu, L., and He, S. (2018). Numerical simulation on the southern flood and northern drought in summer 2014 over Eastern China. *Theo. Appl. Climat.* 134, 1287-1299. doi: 10.1007/s00704-017-2341-0

Xu, X. D., Lu, C. G., Shi, X. H. (2010). Large-scale topography of China: a factor for the seasonal progression of the Meiyu rainband? *J. Geo. Res.* 115, D02110. doi: 10.1029/2009JD012444

Xu, X. D., Tao, S. Y., and Wang, J. Z. (2002). The relationship between water vapor transport features of Tibetan Plateau-monsoon "large triangle" affecting region and drought-flood abnormality of China (in Chinese). *Acta Meteorol. Sin.* 60, 257-266.

Xu, X. D., Zhao, T., and Shi, X. (2015). A study of the role of the Tibetan Plateau's thermal forcing in modulating rainband and moisture transport in eastern China (in Chinese). *Acta Meteorol. Sin.* 73, 20-35.

Yanai, M., Li, C. F., and Song, Z. S. (1992). Seasonal heating of the Tibetan Plateau and its effects on the evolution of the Asian summer monsoon. *J. Meteorol. Soc. Jpn*. 70, 319-351. doi: 10.2151/jmsj1965.70.1B_319

Ye, D. Z., and Gao, Y. (1992). *The Meteorology of the Qinghai-Xizang (Tibetan) Plateau*. Beijing: Science Press.

Ye, D. Z., and Gao, Y. X. (1979). *The Qinghai-Tibet Plateau Meteorology*. Beijing: Science Press.

Ye, D. Z., Luo, S. W., and Zhu, B. Z. (1957). The wind structure and heat balance in the lower troposphere over Tibetan Plateau and its surrounding, *Acta Meteorol. Sin.* 28, 108-121.

Ye, D. Z., and Wu, G. X. (1998). The role of the heat source of the Tibetan Plateau in the general circulation. *Meteorol. Atmos. Phys*. 67, 181-198. doi: 10.1007/BF01277509

Zhang, T., Wang, T., and Krinner, G. (2019). The weakening relationship between Eurasian spring snow cover and Indian summer monsoon rainfall. *Sci. Adv.* 5:eaau8932. doi: 10.1126/sciadv.aau8932

Zhang, Y., Li, T., and Wang, B. (2004). Decadal change of the spring snow depth over the Tibetan Plateau: the associated circulation and influence on the East Asian summer monsoon. *Clim. J.* 17, 2780–2793. doi: 10.1175/1520-0442(2004)017<2780.DCOTSS>2.0.CO;2

Zhao, S. R., Song, Z. S., and Ji, L. R. (2003). Heating Effect of the Tibetan Plateau on rainfall anomalies over North China during rainy season (in Chinese). *Chin. J. Atmos. Sci.* 27, 881–893.

Zhou, X. J., Zhao, P., and Chen, J. M. (2009). Impacts of thermodynamic processes over the Tibetan Plateau on the Northern Hemispheric climate. *Sci. China Ser.* 52, 1679–1693. doi: 10.1007/s11430-009-0194-9

Zhu, L. H, Huang, G., and Fan, G. Z. (2018). Elevation-dependent sensible heat flux trend over the Tibetan Plateau and its possible causes. *Clim. Dyn.* 52, 3997–4009. doi: 10.1007/s00382-018-4360-7

Conflict of Interest: The authors declare that the research was conducted in the absence of any commercial or financial relationships that could be construed as a potential conflict of interest.

frontiers
in Earth Science

ORIGINAL RESEARCH
published: 10 December 2020
doi: 10.3389/feart.2020.579442

Accumulated Effect of Intra-Seasonal Oscillation Convections over the Tropical Western North Pacific on the Meridional Location of Western Pacific Subtropical High

Zongci Huang, Wenjun Zhang, Xin Geng and Pang-Chi Hsu*

CIC-FEMD/ILCEC, Key Laboratory of Meteorological Disaster of Ministry of Education, Nanjing University of Information Science and Technology, Nanjing, China

An extreme northward displacement of the western Pacific subtropical high (WPSH) was detected during the boreal mid-late summer (July-August) of 2018, bringing record-breaking heat waves over northern East Asia. Negative sea surface temperature (SST) anomalies in the northern India Ocean (NIO) are usually accompanied with a northward shift of the WPSH. However, no prominent NIO SST anomalies were observed during the 2018 boreal summer. It is found that this extreme northward-shifted WPSH event is largely attributed to the accumulated effect of intra-seasonal oscillation (ISO) convection anomalies over the tropical western North Pacific (WNP). The accumulated effect on the WPSH meridional location is further supported by their significant correlation based on the data since 1979. While the relationship between the NIO SST anomalies and WPSH meridional location has substantially weakened since the late 1990s, the accumulated effect of the tropical WNP ISO convections keeps playing a crucial role in modulating the WPSH meridional displacement. The active WNP ISO activities can stimulates a poleward propagating Rossby wave train, which favors a northward shift of the WPSH. Our results suggest that the accumulated effect of the tropical WNP ISO convections should be considered when predicting the WPSH during the boreal mid-late summer season.

Keywords: east asian summer monsoon, northern India ocean, intra-seasonal oscillation, north-south location, western pacific subtropical high

Edited by:
Kyung-Ja Ha,
Pusan National University,
South Korea

Reviewed by:
Maoqiu Jian,
Sun Yat-sen University, China
Gang Huang,
Institute of Atmospheric Physics (CAS), China
Wen Zhou,
City University of Hong Kong,
Hong Kong

***Correspondence:**
Wenjun Zhang
zhangwj@nuist.edu.cn

Specialty section:
This article was submitted to Atmospheric Science, a section of the journal Frontiers in Earth Science

Received: *02 July 2020*
Accepted: *18 November 2020*
Published: *10 December 2020*

Citation:
Huang Z, Zhang W, Geng X and Hsu P-C (2020) Accumulated Effect of Intra-Seasonal Oscillation Convections over the Tropical Western North Pacific on the Meridional Location of Western Pacific Subtropical High. Front. Earth Sci. 8:579442. doi: 10.3389/feart.2020.579442

INTRODUCTION

As a crucial component of the East Asian summer monsoon circulation system (Rodwell and Hoskins, 2001), the western Pacific subtropical high (WPSH) has pronounced climate impacts over East Asia (e.g., Tao and Xu, 1962; Huang, 1963; Lau and Li, 1984; Tao and Chen, 1987; Ding, 1994; Zhao and Chen, 1995). The strength, shape, zonal and meridional displacements of the WPSH is closely associated with the intensity and distribution of precipitation and temperature over China (e.g., Tao and Zhu, 1964; Tao and Chen, 1987; Chang et al., 2000a; Chang et al., 2000b; Zhou and Yu, 2005). For example, when the WPSH strengthens and extends westward, abundant warm and moist air is brought from tropical seas to the land, which increases the precipitation over eastern China. On the contrary, a weak and eastward shifted WPSH generally leads to less precipitation there (e.g., Akiyama, 1973; Tao and Chen, 1987; Kodama, 1992; Chang, 2004; Wang et al., 2009; Fan et al., 2013).

The WPSH has prominent sub-seasonal variability with significant meridional movements. In general, the WPSH locates over the South China Sea from late-March to May, and then jumps northward to about 22°N around mid-June, resulting in the onset of plum rain (or Meiyu in China) over the middle-lower reaches of Yangtze River. After mid-July, the WPSH jumps northward again with its center around 30°N, leading to the end of plum rain and the onset of rainy season in northern China (e.g., Chen and Chang, 1980; Tao and Chen, 1987; Wang, 2002; Ding and Chan, 2005; Ninomiya and Shibagaki, 2007; Sampe and Xie, 2010).

The WPSH exhibits significant interannual and interdecadal variabilities, and great efforts have been devoted to investigate the possible mechanisms (e.g., Tao and Chen, 1987; Lu, 2001; Chung et al., 2011; Xu et al., 2015; Wang et al., 2017). On the interannual timescale, the variability of the WPSH is closely linked to the climate variability over the tropics. In particular, El Niño-Southern Oscillation (ENSO), the most prominent year-to-year climate fluctuation, exerts remarkable influence on the WPSH. During El Niño developing summers, the warm sea surface temperature (SST) anomalies in the central-eastern tropical Pacific can trigger an anomalous cyclonic circulation over the western North Pacific (WNP) (Wang and Zhang, 2002), and weaken the WPSH. In the subsequent autumn, an anomalous anticyclonic circulation forms and develops and can persist to the next summer via the local air-sea interaction (Wang et al., 2000; Wang and Zhang, 2002), the Indian Ocean (IO) capacitor effect (e.g., Xie et al., 2009), and the Combination-mode dynamics (e.g., Stuecker et al., 2015; Zhang et al., 2015; Zhang et al., 2016). Correspondingly, the WPSH tends to be intensified and maintains over the WNP during the El Niño decaying summer. On the decadal timescales, it is proposed that the WPSH experienced a prominent decadal change during the late 1970s (Gong and Ho, 2002). For example, the WPSH tends to be stronger and shifts southwestward due to the enhanced heating of the Indo-Pacific warm pool (Zhou et al., 2009). However, these arguments were challenged by other studies (e.g., He et al., 2015; Wu and Wang, 2015). They show that this decadal change cannot be observed when measuring the WPSH using dynamic factors such as vorticity, and the so-called decadal westward extension of the WPSH could be a manifestation of global warming.

Northern East Asia witnessed record-breaking heat waves during the 2018 boreal mid-late summer (July-August). The “2018 China Climate Bulletin”, released by the China Meteorological Administration (CMA), shows that the average temperature from July to August in northeastern China was 25.1 °C, 1.3 °C higher than normal, which recorded the highest temperature since 1961. 47 stations there experienced a record-breaking daily maximum temperature. It has been reported that these extreme heat waves are closely associated with the maintenance of the extreme northward-shifted WPSH (Ding et al., 2019; see **Figure 1**). This unexceptional phenomenon reminds us that investigations on the possible mechanisms for the WPSH meridional movement is of great importance for future prediction of the WPSH and associated summer heat waves. However, compared with the variability of WPSH intensity, little attention has been paid to investigate the variability and mechanisms of the WPSH meridional locations. Early studies proposed that the tropical WNP convection anomalies can modulate the WPSH meridional displacement through the Pacific-Japan (PJ) or the East Asia–Pacific pattern (Nitta, 1987; Huang and Li, 1987), which is featured by an atmospheric teleconnection with two centers respectively over the tropical WNP and mid-latitudinal region (Kosaka and Nakamura, 2006; Kosaka et al., 2011). The atmospheric circulation anomalies during 2018 mid-late summer also resembles the PJ teleconnection pattern (**Figures 1A**), which suggests a possible linkage between the extreme northward shift and the anomalous PJ pattern. The previous studies have shown that the PJ pattern is significantly correlated with ENSO in preceding winter (e.g., Xie et al., 2009; Kosaka et al., 2011; Kosaka et al., 2013). The El Niño-induced delayed warming in the tropical Indian Ocean anchors the WNP anticyclone through exciting an atmospheric Kelvin wave in the WNP, which comprises the tropical lobe of the PJ pattern (Xie et al., 2009). However, the observation shows a weak La Niña event in the preceding 2017/2018 winter. And the northern Indian Ocean (NIO) did not show prominent SST anomalies during 2018 summer. Thus, it seems that this weak La Niña event or the NIO SST anomalies is not the primary reason for the WPSH extreme northward displacement in 2018 boreal mid-late summer. One latest research suggested this heatwave event can be largely contributed by the abnormally enhanced Madden-Julian Oscillation (MJO; Madden and Julian, 1971) convections over the tropical WNP (Hsu et al., 2020).

It is compelling to expect that the western Pacific intra-seasonal oscillation (ISO) may have impacts on the meridional displacement of the WPSH, since it acts as a key factor for the extreme northward shift of the WPSH in 2018. We in this paper find that, on the interannual timescale, both the NIO SST anomalies and the accumulated effect of ISO convection anomalies over the tropical WNP play important roles in modifying the WPSH north-south location. While the contribution of the NIO SST anomalies has substantially weakened since the late 1990s, the accumulated effect of ISO convection anomalies exert a stable impact on the WPSH meridional displacement. The remainder of this paper is organized as follows. *Data and Methodology* introduces data, methodology and several definitions of climate indices. The interannual variability of the WPSH meridional displacement and the associated SST and convection anomalies are described in *Interannual Variability of the WPSH Meridional Displacement and Its Related Ocean-Atmospheric Features*. In *Importance of Two Factors on the WPSH Meridional Location*, an empirical model is established to forecast the WPSH meridional location based on the NIO SST anomalies and the accumulated intra-seasonal OLR (Accu-ISO) index defined to measure the accumulated effect of ISO convection anomalies. We also investigate the decadal change in relationship of the WPSH meridional movement with these two key factors. Finally, discussions and major conclusions are illustrated in *Summary and Discussion*.

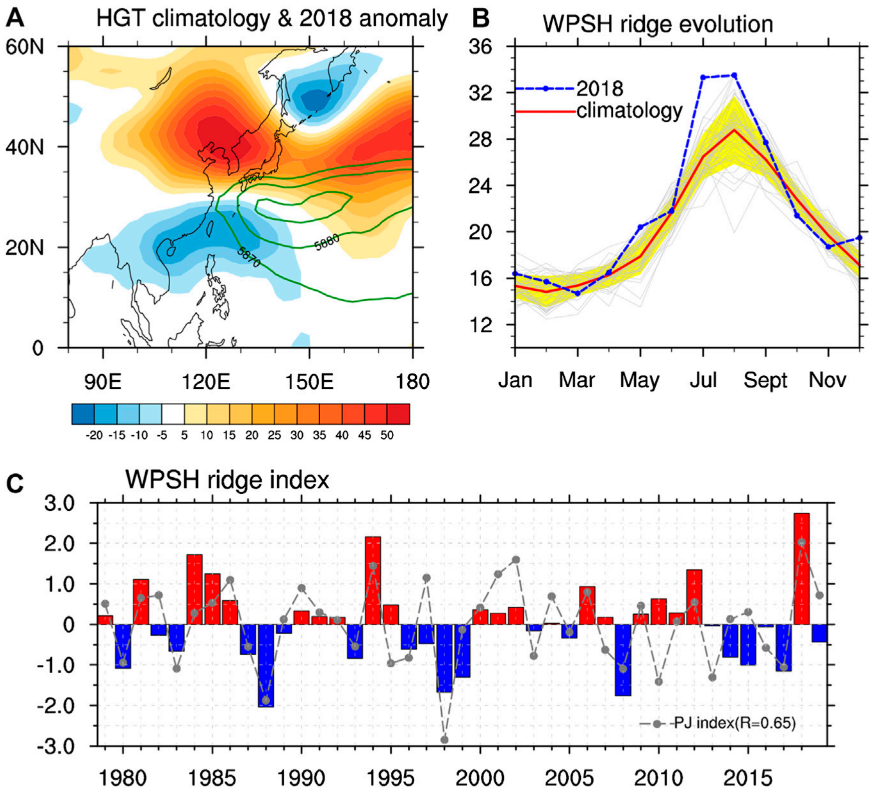

FIGURE 1 | (A) Distribution of the 500hPa geopotential height anomaly during the 2018 boreal mid-late summer (shading in m) and the climatological mean WPSH (contours in m). **(B)** Monthly evolution of the WPSH ridge index in 2018 (blue line), remaining years (gray line) and climatological mean (red line). The yellow shading denotes 1 standard deviation of the climatological mean WPSH ridge index. **(C)** Time evolution of the WPSH ridge index (bar) and PJ index (gray line) during the boreal mid-late summer from 1979 to 2019. The red/blue bars represent the northward/southward WPSH.

DATA AND METHODOLOGY

In this study, the monthly and daily mean atmospheric reanalysis datasets derived from the National Centers for the Environmental Prediction-Department of Energy (NCEP–DOE) Atmospheric Model Intercomparison Project-II reanalysis datasets (Kanamitsu et al., 2002) are utilized. The horizontal resolution is $2.5^\circ \times 2.5^\circ$. The global monthly SST anomalies are investigated based on the National Oceanic and Atmospheric Administration (NOAA) Extended Reconstructed SST analysis, version 5 (ERSSTv5, Huang et al., 2017) with the resolution of $2^\circ \times 2^\circ$. The interpolated daily mean outgoing longwave radiation (OLR) data on $2.5^\circ \times 2.5^\circ$ grids are provided by the NOAA (Liebmann and Smith, 1996). The precipitation data on $2.5^\circ \times 2.5^\circ$ grids are taken from Climate Prediction Center Merged Analysis of Precipitation (CMAP) (Xie and Arkin, 1997).

The mid-late summer (July-August) is our focus in this study. The WPSH ridge index, which is used to measure its meridional displacement, is defined by using the interface between the easterly and westerly of the subtropical high at the 500hPa geopotential height: the averaged latitudes satisfying both $u = 0$ and $\partial u/\partial y > 0$ conditions in a closed 5880 gpm contour over the area (10–60°N, 110–150°E) (Zhao, 1999; Liu et al., 2012). The boreal summer intra-seasonal oscillation (BSISO) index is used to describe the ISO activity. Following the previous studies (Lee et al., 2011; Lee et al., 2013), the BSISO index is measured as the multivariate (MV)-EOF analysis of daily OLR and 850 hPa zonal wind anomalies over the Asian summer monsoon (ASM) domain (10°S–40°N, 40°–160°E). BSISO1, comprised by the first and second MV-EOF modes, represents northward/northeastward propagating oscillations with an oscillating period of 30–60 days. BSISO2, comprised by the third and fourth MV-EOF modes, captures the northward/northeastward propagating oscillations with a 10–30-days oscillating period. The PJ pattern is defined as the leading empirical orthogonal function (EOF) mode of the mid-late summer mean 850-hPa relative vorticity over the western north Pacific (0°–60°N, 100°–160°E), and the PJ index is represented as the normalized PC1 time series (e.g., Kosaka and Nakamura 2010; Kosaka et al., 2013).

Anomalies were derived relative to the whole studying period (1979–2019) and the long-term linear trend is removed to avoid possible impacts of the global warming. The conclusions remain qualitatively the same even with the non-detrended data. To focus on the intra-seasonal variability when discussing the impact of ISO on the WPSH, the annual cycle (mean and first three harmonics of climatological annual variation) is removed from the daily mean OLR and 850 hPa zonal wind anomalies, and the running mean of the last 120 days is also subtracted to eliminate

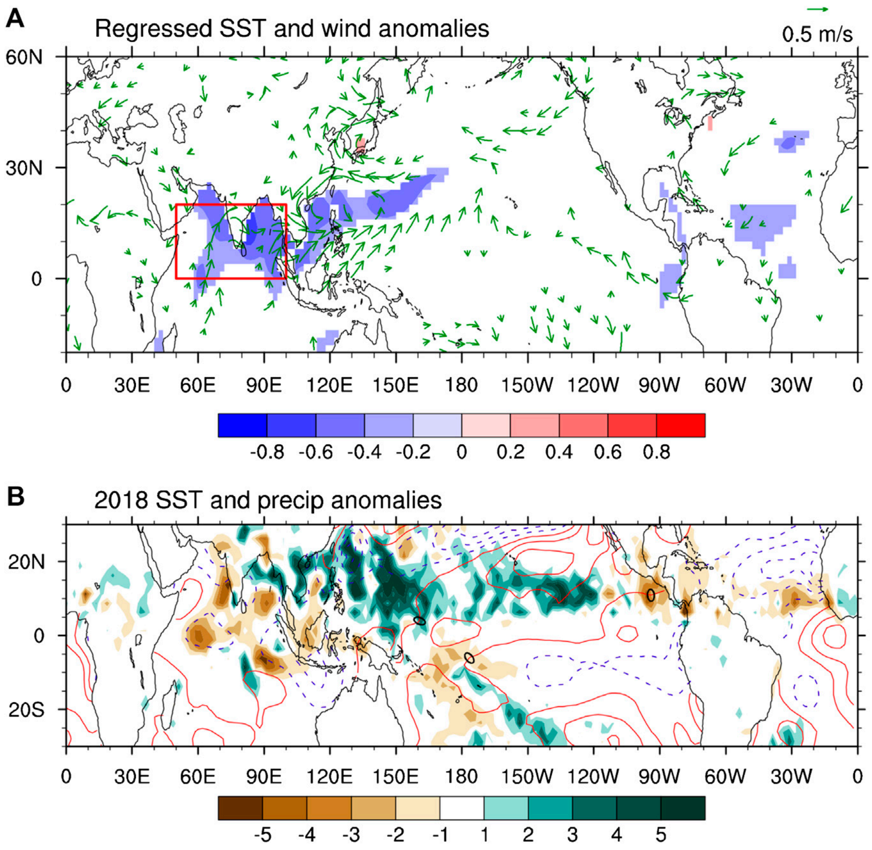

FIGURE 2 | (A) Regressed SST anomalies (shadings in °C) and 850 hPa wind anomalies (vectors in m/s) upon the WPSH ridge index during boreal mid-late summer of 1979–2017. Anomalies are shown only when they are significant at the 95% confidence level. The red box denotes the region where the NIO index is defined. **(B)** SST anomalies (contours in °C, from −1.5 to 1.5 by 0.3) and precipitation anomalies (shadings in mm/day) during boreal mid-late summer 2018. Solid and dashed lines in **(B)** denote positive and negative values, respectively.

the effects of the interannual variability (Wheeler and Hendon, 2004; Lee et al., 2013). All statistical significance tests are performed based on the two-tailed Student's t-test.

INTERANNUAL VARIABILITY OF THE WESTERN PACIFIC SUBTROPICAL HIGH MERIDIONAL DISPLACEMENT AND ITS RELATED OCEAN-ATMOSPHERIC FEATURES

As shown in **Figures 1B**, the WPSH ridge is usually located around 26.5°N in July and moves northward to near 29°N in August. However, an extreme northward shifted WPSH was detected during the 2018 summer. In June 2018, the WPSH was located at about 22°N, almost the same position as the climatological mean. Then the WPSH suddenly jumped from 22°N to about 33°N in July and maintained at this latitude through August. This meridional position is much more northward shifted than the climatological mean, especially for July. The WPSH ridge index during mid-late summer 2018 was far beyond one standard deviation (yellow shading) and was the most northward-shifted since 1979. We hereafter focus on the July-August averaged north-south location of the WPSH and try to investigate the possible reasons for this extreme event in 2018. It is clearly shown that the WPSH meridional location exhibits strong interannual variability with the largest value occurring in 2018 (**Figure 1C**), further confirming the extremity of the WPSH latitudinal location.

To examine the atmospheric circulation related to the WPSH latitudinal movement, the 850 hPa vorticity anomaly is regressed upon the WPSH ridge index (not shown). A poleward wave train-like atmospheric circulation pattern can be detected over East Asia and its adjacent oceans, with two opposite centers respectively over the subtropical WNP (10°–25°N) and mid-latitude region (30°–40°N). This meridional structure resembles the PJ pattern, and the WPSH ridge index is highly correlated with the PJ index (r = 0.65, statistically significant at 95% confidence level). Their high consistency (**Figures 1C**) suggests that they are possibly driven by same forcings. Since the PJ pattern acts as the bridge between the tropical and extra-tropical atmospheric circulation (e.g., Huang and Li, 1987; Nitta, 1987), we then consider the possible forcings from the tropics.

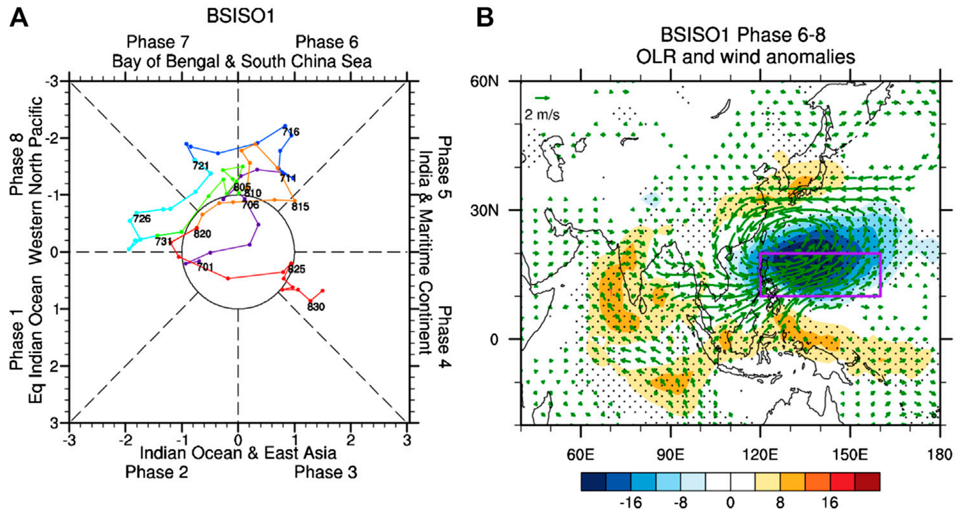

FIGURE 3 | (A) The phase space diagram of BSISO1 during the 2018 boreal mid-late summer. Each color represents ten days from July 1st to August 31st and the numbers correspond to the date. **(B)** Composite OLR (shading in W/m^2) and 850hPa wind anomalies (vectors in m/s) of active BSISO1 days in Phase 6–8 during boreal mid-late summer of 1979–2019. The days are selected when the ISO amplitude $(PC1^2 + PC2^2)^{1/2}$ exceeded 1. The stippled area and the green vectors denote the corresponding values are significant at the 95% significance level. The purple box in **(B)** denotes the key area (10°–20°N, 120°–160°E) of WNP region.

As illustrated in the introduction, the tropical SST is an important factor affecting the WPSH meridional movement. We here regress the simultaneous anomalous SST and horizontal wind onto the WPSH ridge index (**Figures 2A**). A northward-shifted WPSH is accompanied by significant negative SST anomalies in the northern Indian Ocean (NIO) and WNP. Correspondingly, an anomalous cyclone and anti-cyclone prevails over the WNP and near Japan, respectively. This result indicates that the NIO SST anomalies may exert a significant impact on the WPSH through modifying the WNP atmospheric anomalies. The warming NIO SST can suppress the convection over the WNP by inducing an anomalous anti-cyclone there as a response of a Kelvin wave response (Watanabe and Jin, 2002; Yang et al., 2007; Xie et al., 2009). The WNP atmospheric anomalies then influence the mid-latitudinal circulation through the PJ pattern, which tends to modulate the WPSH meridional location, consistent with the former study (Nitta, 1987). Along with the negative SST anomalies over the WNP during summer 2018, we observe positive precipitation anomalies there (**Figures 2B**), suggesting that the SST anomalies are possibly forced by the anomalous atmospheric circulation. Therefore, the SST anomalies may be not the ultimate reason for this meridional movement of the WPSH in summer. In the mid-late summer of 2018, weakly negative SST anomalies appear over the NIO (**Figures 2B**), which may have some impact on the WPSH north-south location anomaly. However, it is not strong enough to be used to explain the extreme northward shift of the WPSH in 2018.

Previous studies suggest that the ISO-associated convection activities can play an important role in the extreme temperature and precipitation anomalies over eastern China (e.g., Hong and Li, 2009; Hsu et al., 2016; Chen and Zhai, 2017; Hsu et al., 2017). The western tropical Pacific ISO has been recognized as an important forcing for the generation and maintenance of the abnormal northward shift of the WPSH in 2018 (Hsu et al., 2020). The BSISO1 index is used here to describe the ISO activity, since it can describe the ISO activities over the WNP more realistically compared with the MJO index (e.g., Lee et al., 2011; Chen and Zhai, 2017). The BSISO2 index showed a relatively weak evolution during the 2018 Northeast Asian heatwave period, suggesting a weak effect on the northward shift of WPSH in this case. In fact, Hsu et al. (2017) documented that the BSISO2 shows a closer relationship between heat waves over India and the Yangtze River basin, and the BSISO1 exerts significant influences over the Northeast Asia. The similar result can be found in **Figures 3A**, which shows the phase space diagram of BSISO1 from 1st July to 31st August. It can be observed that the BSISO1 is very active over the South China Sea (Phase 6–7) and WNP (Phase 8) area, especially from 7th July to 1st August and from 3rd August to 22nd August.

To verify the impacts of WNP ISO activities on the WPSH associated circulation, we composite the OLR and 850 hPa wind anomalies of the active ISO days in Phases 6–8 of BSISO1 during boreal mid-late summer from 1979 to 2019. The active ISO days are selected when the BSISO1 amplitude [represented by $(PC1^2 + PC2^2)^{1/2}$] exceeds one standard deviation. As shown in **Figures 3B**, during Phases 6–8 of the BSISO1, the anomalous convection is enhanced over the South China Sea and Philippine Sea, accompanying by prevailing cyclonic circulation anomalies over its northwestern part. Suppressed convection can be detected over the Indian Ocean and the Maritime Continent. Simultaneously, large-scale anticyclonic circulation anomalies are evident over northern China and Japan. It can be seen that the active BSISO1 over the South China Sea and WNP can influence the WPSH mid-latitudinal location by stimulating a poleward propagating Rossby wave train resembling the PJ teleconnection pattern.

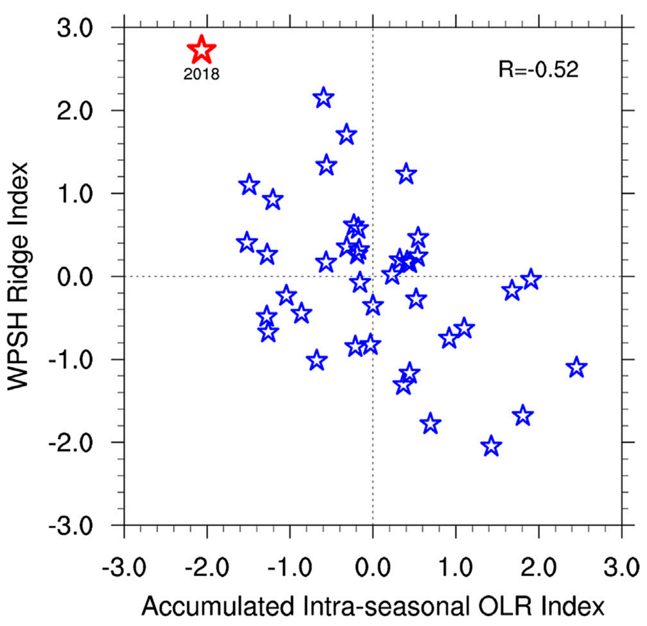

FIGURE 4 | Scatter plot of the WPSH ridge index as a function of the Accu-ISO anomalies over WNP (10°–20°N, 120°–160°E). The 2018 case is shown as the red star. The corresponding correlation coefficient between these two indices (R) is also displayed.

In order to explain the long-lasting extreme northward displacement of the WPSH in summer 2018, we then define an accumulated intra-seasonal OLR anomaly (Accu-ISO) index over the tropical WNP (10°–20°N, 120°–160°E) to investigate the importance of the accumulated effect of ISO convections on the WPSH meridional displacement. The Accu-ISO index is defined as the summation of tropical WNP-averaged intra-seasonal OLR anomalies from 1st July to 31st August in each year. This index may comprise both the amplitude and persistence of the ISO convective anomalies over the tropical WNP. It is shown in **Figure 4** that this Accu-ISO index is negatively correlated with the WPSH ridge index (r = -0.52, significant at the 95% confidence level). It suggests that the accumulated effect of ISO convections may also play a critical role on the north-south location of the WPSH during mid-late summer. During the summer of 1979 to 2019, the accumulated effect of ISO convections is the strongest in 2018, which may be responsible for the extreme northward shift of the WPSH and the associated summer heat waves during this summer.

IMPORTANCE OF TWO FACTORS ON THE WESTERN PACIFIC SUBTROPICAL HIGH MERIDIONAL LOCATION

To examine the performance of the two key processes in predicting the WPSH north-south location, we construct a multivariate linear regression model based on the NIO and the Accu-ISO indices. Following the previous study (Xie et al., 2009), the NIO index is defined as the area-averaged SST anomalies over the NIO region (**Figure 2**; red box). As shown in **Figure 5**, these two indices are not correlated with each other (r = 0.06, insignificant at the 95% confidence level), suggesting their linear statistical independence. **Figure 6** shows the time series of observed WPSH ridge index (blue line), and reconstructed WPSH ridge index based on the NIO index (purple line) and based on both the NIO and Accu-ISO indices (red line). The reconstructed WPSH index using both the NIO and Accu-ISO indices is highly correlated with the observed index (R = 0.68). The variance of the WPSH ridge index explained by both the NIO and Accu-ISO indices (R^2 = 47%) is much higher than that by the NIO index only (R^2 = 23%). It should be noted that the inclusion of the Accu-ISO index realistically captures the extreme WPSH

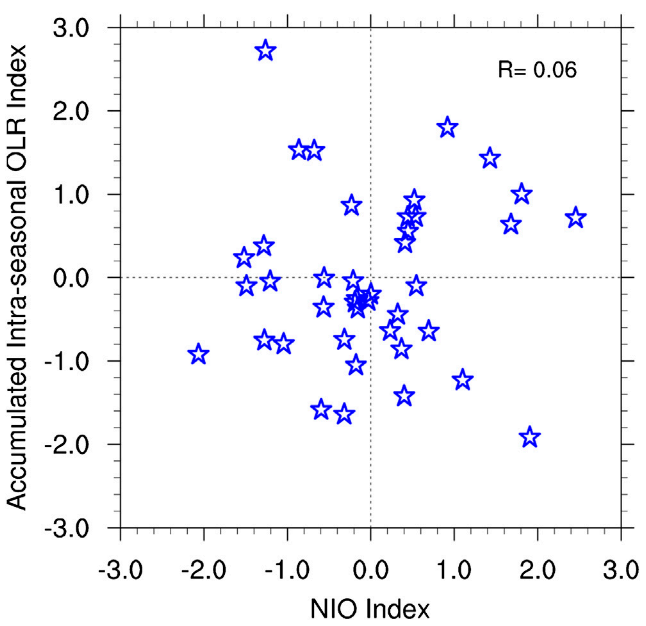

FIGURE 5 | Scatter plot of the Accu-ISO anomalies over WNP (10°–20°N, 120°–160°E) and the NIO index. The corresponding correlation coefficient between these two indices (R) is also displayed.

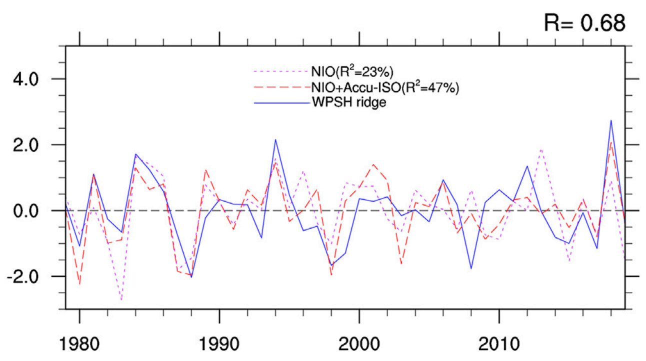

FIGURE 6 | Time series of the observed WPSH ridge index (blue line), the reconstructed WPSH ridge index based on the NIO index (purple line), and based on both the NIO and Accu-ISO indices (red line). The explained variances of the two regressed indices (R^2) are also displayed.

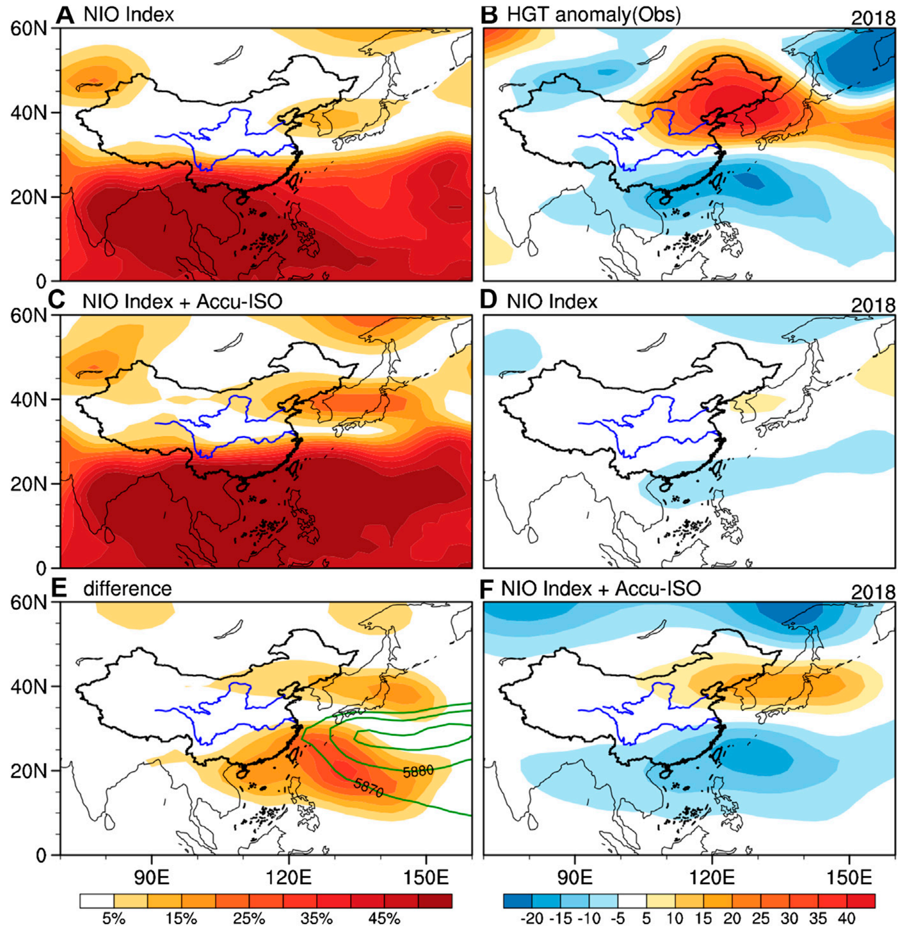

FIGURE 7 | Performance of linear regression models in capturing the boreal mid-late summer 500 hPa geopotential height anomaly. The explained variance for the anomalous 500 hPa geopotential height by the regression model with **(A)** the NIO index only, **(C)** both the NIO and Accu-ISO indices, and **(E)** their difference. Distribution of **(B)** the observed 500 hPa geopotential height anomaly (shading in m) in 2018 boreal mid-late summer, the reconstructed 500 hPa geopotential height anomaly based on the **(D)** NIO index predictor only and **(F)** both the NIO and Accu-ISO indices.

north-south movement in 1988, 1998 and 2018. These results suggest that the Accu-ISO index other than the NIO index provides an additional physical-based predictor for the WPSH north-south location.

We also calculate the variance pattern of 500 hPa geopotential height explained by the regression model with the NIO index only (**Figures 7A**) and with both the NIO and Accu-ISO indices (**Figures 7C**). It can be seen that the NIO index can explain more than 45% of the 500 hPa geopotential height variance over the tropical region, but only explain around 10% variance over the Korea peninsula (**Figures 7A**). When the Accu-ISO index is further considered in the regression model, the 500hPa geopotential height variance explained is significantly improved, especially in the widened part over the northeastern China and Korea peninsula (**Figures 7C**). The 500hPa geopotential height variance is increased by about 25% over the WNP and 15% over north East Asian, which largely reflects the variability of WPSH north-south location (**Figures 7E**). This point is also clearly verified by the comparison among the reconstructions of the 500hPa geopotential height anomalies in 2018 based on different regression models (**Figures 7B,D,F**). The reconstructed 500 hPa geopotential height anomalies based on both the NIO and Accu-ISO indices accurately captures two geopotential height anomalies centers over the WNP region and northern East Asia, which is much more realistic than those reconstructed by the NIO index alone.

To verify how well both the NIO SST anomalies and accumulated effect of ISO convections contribute to the prediction skill of the WPSH meridional displacement, an empirical prediction model is developed using the multiple linear regression method based on both the NIO and Accu-ISO indices:

$$\text{WPSH ridge index} = -0.37 \times \text{NIO} - 0.43 \times \text{Accu-ISO} \quad (1)$$

Due to the limited sample size, the first 36-years are used to act as a training period to estimate the regression coefficients and the residual 5-years are viewed as an independent testing period (**Figure 8**). It can be seen that during the training period, the empirical model can captures 39% variance of the observed

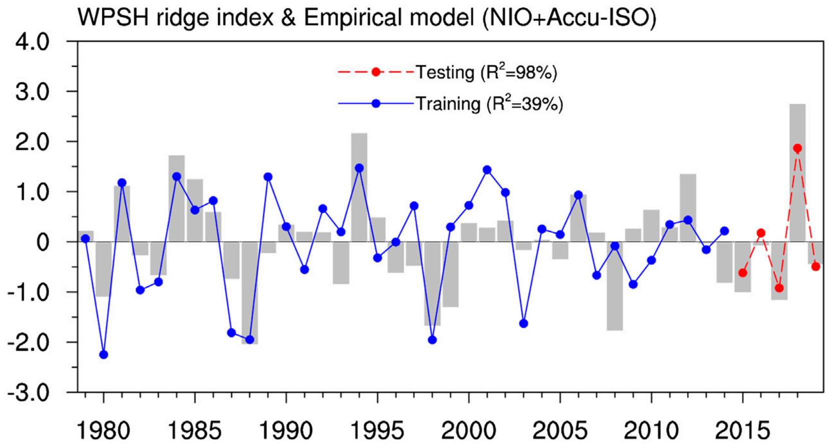

FIGURE 8 | Time evolution of the observed WPSH ridge index (bars) and the empirical model fitted values (lines) during the boreal mid-late summer from 1979 to 2019. The red and blue lines represent the training and testing results, respectively.

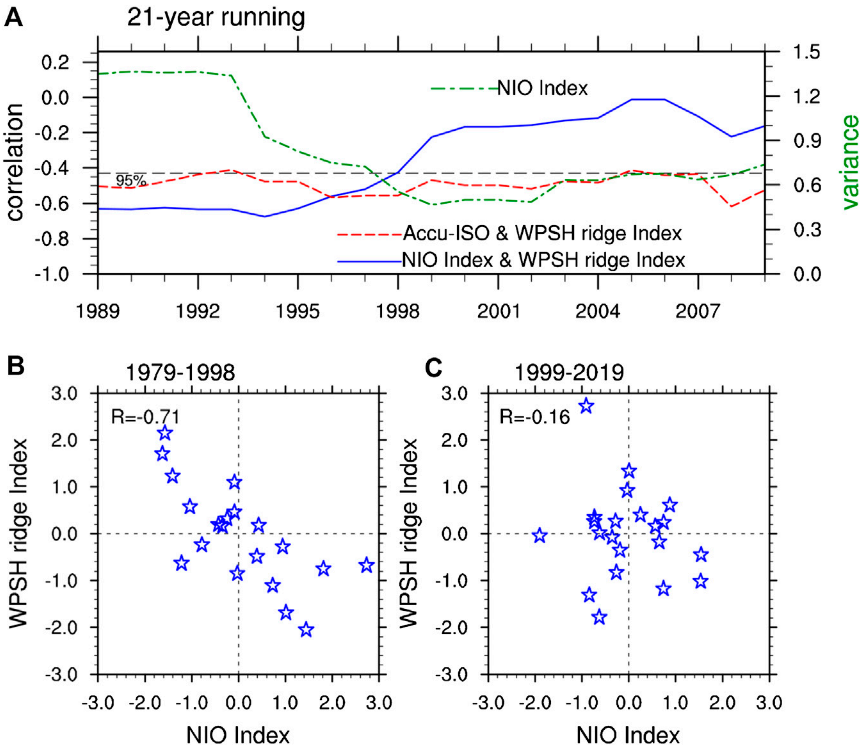

FIGURE 9 | (A) Time evolution of the 21-years running correlation coefficients of the WPSH ridge index with NIO index (blue line) and Accu-ISO index (red line). The green line denotes the 21-years running standard deviation of the NIO index. The black dashed line denotes the 95% confidence level based on the two-tailed Student's t test. Scatterplot of the WPSH ridge and NIO index during the mid-late summer of **(B)** 1979–1998 and **(C)** 1999–2019.

WPSH ridge index (R = 0.62; blue line). During the independent testing period, 98% variance of the WPSH meridional north-south movement is captured by the model (red line). Although there are only five cases in this period, the high correlation coefficient (R = 0.99) suggests that this empirical model offers a relatively accurate prediction of the WPSH meridional displacement.

Previous studies argued that the Indian Ocean SST has experienced a prominent decadal change around the late 1990s due to the Inter-decadal Pacific Oscillation (IPO)-induced

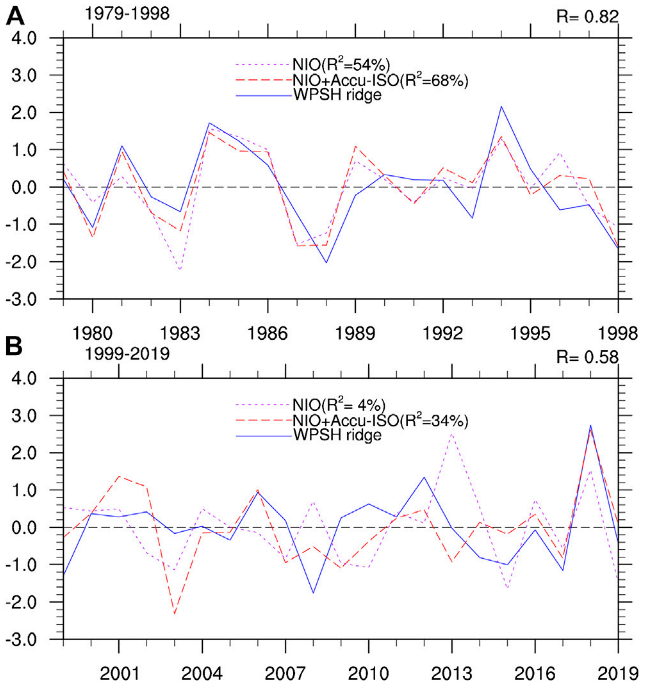

FIGURE 10 | (A) Time series of the observed WPSH ridge index (blue line), the reconstructed WPSH ridge index based on the NIO index (purple line), and the reconstructed WPSH ridge index based on both the NIO and Accu-ISO indices (red line) for the mid-late summer of 1979–1998. **(B)** Same as **(A)** but for 1999–2019. The explained variances of the two regressed indices (R^2) are also displayed.

atmospheric adjustment (e.g., Dong et al., 2016; Ummenhofer et al., 2017; Mohapatra et al., 2020). So, it deserves attention whether the impacts of the NIO SST anomalies on the WPSH north-south location displays decadal changes. We in **Figures 9A** show the 21-years-window running correlations of the WPSH ridge index with the NIO and Accu-ISO indices. It can be seen that the correlation coefficient between the WPSH ridge and NIO indices exhibits prominent decadal variations. While the NIO SST anomalies exhibit a strongly weakened association with the WPSH ridge after the late 1990s (blue line), the relationship between the Accu-ISO and WPSH ridge indices is consistently significant throughout the entire period (red line). We also display the different responses of the WPSH meridional displacement to the NIO SST anomalies before and after the late 1990s. Consistent with the results shown in **Figures 9A**, the WPSH ridge and NIO indices are significantly correlated during 1979–1998 (**Figures 9B**), while a non-significant relationship is found during 1999–2019 (**Figures 9C**). These results indicate that the NIO SST anomalies play relatively minor role on the WPSH north-south location after the late 1990s comparing with that of the accumulated effect of ISO convections. This point is further illustrated clearly in the time series of the observed and linearly regressed WPSH ridge indices (**Figure 10**). During 1979–1998, the WPSH meridional displacement is reconstructed well based on both the NIO and Accu-ISO indices with the major contribution from the NIO SST anomalies (R^2 = 54%). Since the impact of the NIO SST anomalies has weakened after the late 1990s (R^2 = 4%), the linear regression with both the NIO and Accu-ISO indices can only captures 34% variability of the north-south shift of the WPSH (R = 0.58) and the correlation is mainly contributed by the accumulated effect of ISO convections (R^2 = 30%). Considering the weakened relation of the NIO SST anomalies with the WPSH meridional locations in recent decades, we also examine the validity of **Eq. 1** but with only Accu-ISO index involved. In the last 5-years independent period, 72% variance is captured by the statistically model as a predictor of the Accu-ISO index. It suggests that the NIO SST anomalies play some contribution on the WPSH meridional locations despite that it is not a main predictor.

SUMMARY AND DISCUSSION

An extreme northward shift of WPSH was detected during the 2018 boreal mid-late summer, bringing record-breaking heat waves over northern East Asia region. Observed analyses show that the WPSH north-south location is statistically related to the NIO SST anomalies. However, weakly negative NIO SST anomalies in mid-late summer 2018 cannot explain the extreme northward shift of WPSH. The accumulated effect of ISO convections over the tropical WNP can also exert significant impacts on the WPSH north-south location, through exciting a poleward propagating Rossby wave train. During the mid-late summer from 1979 to 2019, the accumulated effect of ISO convections is the strongest in 2018, which is largely responsible for the extreme northward-shifted WPSH. While the modulation effect of the NIO SST anomalies has substantially weakened since the late 1990s, the accumulated effect of the WNP ISO convections exhibits a stationary relationship with the WPSH latitudinal movement.

At present, the reason for the weakened relationship between the NIO SST and the WPSH meridional displacement after the late 1990s is still unknown. We in **Figure 9A** display the 21-years-window running variance of the NIO index (green line). A remarkable decadal variation of NIO SST can also be observed around the late 1990s, which is consistent with the decadal change of the NIO-WPSH ridge relationship. It suggests that the variability of the NIO SST anomalies weakened in recent years, which possibly leads to a less modulation on the East Asian atmospheric circulation.

The BSISO1 during summer (July-August) 2018 exhibited very different propagation features from typical ISO events, with strong and quasi-stationary activities maintaining over the South China Sea and WNP (Phases 6–8) for up to 40 days. Many extreme climate events in recent years have been linked to similar abnormal ISO activities with relatively longer phase duration. For instance, the extreme drought during autumn and winter 2009/10 over southwestern China coincided with pro-longed suppressed MJO convection over the Bay of Bengal (Lv et al., 2012). However, the underlying mechanisms for these exceptional ISO events are not clear. During July-August 2018, remarkable moisture surpluses and strengthened cyclonic anomalies can be observed over the South China Sea and WNP (not shown), which could be the reason for the maintenance of the local enhanced BSISO1 activity (Hsu and Lee, 2005; Maloney 2009; Kim et al., 2014; Sobel et al., 2014).

In this study, we mainly focus on the important impacts of the accumulated effect of WNP ISO convections on the WPSH meridional movement and emphasize its role in capturing the extreme of northward shift of the WPSH in mid-late summer 2018. Contributions of other forcings, such as the anthropogenic forcing, should also be noted, since it has been reported to increase the probability of the extreme events (Imada et al., 2019; Qian et al., 2020).

DATA AVAILABILITY STATEMENT

The raw data supporting the conclusions of this article will be made available by the authors, without undue reservation.

AUTHOR CONTRIBUTIONS

WZ and ZH conceived the idea, conducted the data analysis and prepared the figures. ZH, WZ, and XG discussed the results and wrote the paper. P-CH helped perform the analysis with constructive discussions.

FUNDING

This work was supported by the National Key Research and Development Program (2018YFC1506002), and the National Nature Science Foundation of China (41675073, 41905073).

REFERENCES

Akiyama, T. (1973). The large-scale aspects of the characteristic features of the Baiu front. *Pap. Meteorol. Geophys.* 24 (2), 157–188. doi:10.2467/mripapers1950.24.2_157

Chang, C. P. (2004). East Asian monsoon. *World Scientific* 2, 572. doi:10.1142/5482

Chang, C. P., Zhang, Y., and Li, T. (2000a). Interannual and interdecadal variations of the East Asian summer monsoon and tropical Pacific SSTs. Part I: roles of the subtropical ridge. *J. Clim.* 13, 4310–4325. doi:10.1175/1520-0442(2000)013<4310:iaivot>2.0.co;2

Chang, C. P., Zhang, Y., and Li, T. (2000b). Interannual and interdecadal variations of the East Asian summer monsoon and tropical Pacific SSTs. Part II: meridional structure of the monsoon. *J. Clim.* 13, 4326–4340. doi:10.1175/1520-0442(2000)013<4326:iaivot>2.0.co;2

Chen, T. J. G., and Chang, C. P. (1980). The structure and vorticity budget of an early summer monsoon trough (mei-yu) over southeastern China and Japan. *Mon. Wea. Rev.* 108, 942. doi:10.1175/1520-0493(1980)108<0942:tsavbo>2.0.co;2

Chen, Y., and Zhai, P. (2017). Simultaneous modulations of precipitation and temperature extremes in Southern parts of China by the boreal summer intraseasonal oscillation. *Clim. Dynam.* 49, 3363–3381. doi:10.1007/s00382-016-3518-4

Chung, P., Sui, C., and Li, T. (2011). Interannual relationships between the tropical sea surface temperature and summertime subtropical anticyclone over the western North Pacific. *J. Geophys. Res. Atmos.* 116 (D13), D13111. doi:10.1029/2010JD015554

Ding, T., Gao, H., and Yuan, Y. (2019). The record-breaking northward shift of the western Pacific subtropical high in summer 2018 and the possible role of cross-equatorial flow over the Bay of Bengal. *Theor. Appl. Climatol.* 139, 1–10. doi:10.1007/s00704-019-02997-4

Ding, Y., and Chan, J. C. L. (2005). The East Asian summer monsoon: an overview. *Meteorol. Atmos. Phys.* 89, 117–142. doi:10.1007/s00703-005-0125-z

Ding, Y. (1994). "The summer monsoon in East Asia," in *Monsoons over China*. Dordrecht: Kluwer, 1–9.

Dong, L., Zhou, T., Dai, A., Song, F., Wu, B., and Chen, X. (2016). The footprint of the inter-decadal pacific oscillation in Indian ocean sea surface temperatures. *Sci. Rep.* 6, 21251. doi:10.1038/srep21251

Fan, L., Shin, S.-I., Liu, Q., and Liu, Z. (2013). Relative importance of tropical SST anomalies in forcing East Asian summer monsoon circulation: relative importance OF SSTA to EASM. *Geophys. Res. Lett.* 40, 2471–2477. doi:10.1002/grl.50494

Gong, D.-Y., and Ho, C.-H. (2002). Shift in the summer rainfall over the Yangtze River valley in the late 1970s: summer rainfall shift IN the late 1970s. *Geophys. Res. Lett.* 29, 78–1784. doi:10.1029/2001GL014523

He, C., Zhou, T., Lin, A., Wu, B., Gu, D., Li, C., et al. (2015). Enhanced or weakened western North pacific subtropical high under global warming? *Sci. Rep.* 5, 16771. doi:10.1038/srep16771

Hong, C.-C., and Li, T. (2009). The extreme cold anomaly over southeast Asia in february 2008: roles of ISO and ENSO. *J. Clim.* 22, 3786–3801. doi:10.1175/2009JCLI2864.1

Hsu, H.-H., and Lee, M.-Y. (2005). Topographic effects on the eastward propagation and initiation of the madden–julian oscillation. *J. Clim.* 18, 795–809. doi:10.1175/JCLI-3292.1

Hsu, P.-C., Lee, J.-Y., and Ha, K.-J. (2016). Influence of boreal summer intraseasonal oscillation on rainfall extremes in southern China: BSISO influences on rainfall extremes in southern China. *Int. J. Climatol.* 36, 1403–1412. doi:10.1002/joc.4433

Hsu, P.-C., Lee, J.-Y., Ha, K.-J., and Tsou, C.-H. (2017). Influences of boreal summer intraseasonal oscillation on heat waves in monsoon Asia. *J. Clim.* 30, 7191–7211. doi:10.1175/JCLI-D-16-0505.1

Hsu, P.-C., Qian, Y., Liu, Y., Murakami, H., and Gao, Y. (2020). Role of abnormally enhanced MJO over the western pacific in the formation and subseasonal predictability of the record-breaking Northeast Asian heatwave in the summer of 2018. *J. Clim.* 33, 3333–3349. doi:10.1175/JCLI-D-19-0337.1

Huang, B., Thorne, P. W., Banzon, V. F., Boyer, T., Chepurin, G., Lawrimore, J. H., et al. (2017). Extended reconstructed sea surface temperature, version 5 (ERSSTv5): upgrades, validations, and intercomparisons. *J. Clim.* 30, 8179–8205. doi:10.1175/jcli-d-16-0836.1

Huang, R. H., and Li, W. J. (1987). "Influence of the heat source anomaly over the western tropical Pacific onthe subtropical high over East Asia," in Proceedings of International Conference on the General Circulation of East Asia, Chengdu, China, April 10–15, 1987. 40–51.

Huang, S. (1963). Longitudinal movement of the subtropical anticyclone and its prediction. *Acta Meteorol. Sin.* 33, 320–332.

Imada, Y., Watanabe, M., Kawase, H., Shiogama, H., and Arai, M. (2019). The july 2018 high temperature event in Japan could not have happened without human-induced global warming. *Sola* 15A, 8–12. doi:10.2151/sola.15A-002

Kanamitsu, M., Ebisuzaki, W., Yang, S.-K., Hnilo, J. J., Fiorino, M., and Potter, G. L. (2002). NCEP-DOE AMIP-II reanalysis (R-2). *Bull. Am. Meteorol. Soc.* 83 (11), 1631–1643. doi:10.1175/bams-83-11-1631(2002)083<1631:nar>2.3.co;2

Kim, D., Kug, J.-S., and Sobel, A. H. (2014). Propagating versus nonpropagating madden–julian oscillation events. *J. Clim.* 27, 111–125. doi:10.1175/JCLI-D-13-00084.1

Kodama, Y.-M. (1992). Large-scale common features of subtropical precipitation zones (the Baiu frontal zone, the SPCZ, and the SACZ). Part I: characteristics of subtropical frontal zones. *J. Meteor. Soc. Jpn.* 70, 813–802. doi:10.2151/jmsj1965.70.4_813

Kosaka, Y., and Nakamura, H. (2010). Mechanisms of meridional teleconnection observed between a summer monsoon system and a subtropical anticyclone. Part I: the pacific–Japan pattern. *J. Clim.* 23, 5085–5108. doi:10.1175/2010JCLI3413.1

Kosaka, Y., and Nakamura, H. (2006). Structure and dynamics of the summertime Pacific–Japan teleconnection pattern. *Q. J. R. Meteorol. Soc.* 132, 2009–2030. doi:10.1256/qj.05.204

Kosaka, Y., Xie, S.-P., Lau, N.-C., and Vecchi, G. A. (2013). Origin of seasonal predictability for summer climate over the Northwestern Pacific. *Proc. Natl. Acad. Sci. U.S.A.* 110, 7574–7579. doi:10.1073/pnas.1215582110

Kosaka, Y., Xie, S.-P., and Nakamura, H. (2011). Dynamics of interannual variability in summer precipitation over east Asia. *J. Clim.* 24, 5435–5453. doi:10.1175/2011JCLI4099.1

Lau, K. M., and Li, M. T. (1984). The monsoon over East Asia and its global association-a survey. *Bull. Am. Meteorol. Soc.* 65, 116–125. doi:10.1175/1520-0477(1984)065<0114:tmoeaa>2.0.co;2

Lee, J.-Y., Wang, B., Wheeler, M. C., Fu, X., Waliser, D. E., and Kang, I.-S. (2013). Real-time multivariate indices for the boreal summer intraseasonal oscillation over the Asian summer monsoon region. *Clim. Dynam.* 40, 493–509. doi:10.1007/s00382-012-1544-4

Lee, J.-Y., Wang, B., Wheeler, M., Fu, X., and Waliser, D. (2011). "A metrics for boreal summer monsoon intraseasonal oscillation," in 36th NOAA Annual climate diagnostics and prediction workshop, Fort Worth, TX, October 3–6, 2011, 5.

Liebmann, B., and Smith, C. A. (1996). Description of a complete (interpolated) outgoing long wave radiation dataset. *Bull. Am. Meteorol. Soc.* 77, 1275–1277.

Liu, Y. Y., Li, W. J., Ai, W. X., and Li, Q. Q. (2012). Reconstruction and application of the monthly western Pacific subtropical high indices. *J. Appl. Meteorol. Sci.* 23, 414–423.

Lu, R. (2001). Interannual variability of the summertime North Pacific subtropical high and its relation to atmospheric convection over the warm pool. *J. Meteor. Soc. Jpn Ser. II* 79, 771–783.

Lv, J. M., Ju, J. H., Ren, J. Z., and Gan, W. W. (2012). The influence of the Madden-Julian Oscillation activity anomalies on Yunnan's extreme drought of 2009–2010. *Sci. China Earth Sci.* 55, 98–112. doi:10.1007/s11430-011-4348-1

Madden, R. A., and Julian, P. R. (1971). Detection of a 40–50 day oscillation in the zonal wind in the tropical Pacific. *J. Atmos. Sci.* 28, 702–708. doi:10.1175/1520-0469(1971)028<0702:DOADOI>2.0.CO;2

Maloney, E. D. (2009). The moist static Energy budget of a composite tropical intraseasonal oscillation in a climate model. *J. Clim.* 22, 711–729. doi:10.1175/2008JCLI2542.1

Mohapatra, S., Gnanaseelan, C., and Deepa, J. S. (2020). Multidecadal to decadal variability in the equatorial Indian Ocean subsurface temperature and the forcing mechanisms. *Clim. Dynam.* 54, 3475–3487. doi:10.1007/s00382-020-05185-7

Ninomiya, K., and Shibagaki, Y. (2007). Multi-scale features of the meiyu-baiu front and associated precipitation systems. *JMSJ* 85 (B), 103–122. doi:10.2151/jmsj.85B.103

Nitta, T. (1987). Convective activities in the tropical western pacific and their impact on the northern hemisphere summer circulation. *J. Meteorol. Soc. Jpn. Ser. II* 65, 373–390. doi:10.2151/jmsj1965.65.3_373

Qian, Y., Murakami, H., Hsu, P., and Kapnick, S. (2020). Effects of anthropogenic forcing and natural variability on the 2018 heatwave in northeast Asia. *Bull. Am. Meteorol. Soc.* 101, S77–S82. doi:10.1175/BAMS-D-19-0156.1

Rodwell, M. J., and Hoskins, B. J. (2001). Subtropical anticyclones and summer monsoons. *J. Clim.* 14, 3192–3211. doi:10.1175/1520-0442(2001)014<3192:SAASM>2.0.CO;2

Sampe, T., and Xie, S.-P. (2010). Large-scale dynamics of the meiyu-baiu rainband: environmental forcing by the westerly jet. *J. Clim.* 23, 113–134. doi:10.1175/2009JCLI3128.1

Sobel, A., Wang, S., and Kim, D. (2014). Moist static Energy budget of the MJO during DYNAMO. *J. Atmos. Sci.* 71, 4276–4291. doi:10.1175/JAS-D-14-0052.1

Stuecker, M. F., Jin, F.-F., Timmermann, A., and McGregor, S. (2015). Combination mode dynamics of the anomalous northwest pacific anticyclone. *J. Clim.* 28, 1093–1111. doi:10.1175/JCLI-D-14-00225.1

Tao, S., and Chen, L. (1987). "A review of recent research on the East Asian summer monsoon in China," in *Monsoon meteorology*. New York: Oxford University Press, Vol. 7, 60–92.

Tao, S., and Xu, S. (1962). Circulation characteristics in association with persistent summer drought and flood in the Yangtze-Huaihe River reaches. *Acta Meteorol. Sin.* 32, 1–18.

Tao, S., and Zhu, F. (1964). Variation of the 100 hPa flow pattern in South Asia in summer and the movement of the subtropical anticyclone over the western Pacific. *Acta Meteorol. Sin.* 34, 385–394. doi:10.11676/qxxb1964.039

Ummenhofer, C. C., Biastoch, A., and Böning, C. W. (2017). Multidecadal Indian ocean variability linked to the pacific and implications for preconditioning Indian ocean dipole events. *J. Clim.* 30, 1739–1751. doi:10.1175/JCLI-D-16-0200.1

Wang, B. (2002). Rainy season of the asian–pacific summer monsoon. *J. Clim.* 15 (4), 386–398. doi:10.1175/1520-0442(2002)015<0386:rsotap>2.0.co;2

Wang, B., Wu, R., and Fu, X. (2000). Pacific–east Asian teleconnection: how does ENSO affect east Asian climate? *J. Clim.* 13, 1517–1536. doi:10.1175/1520-0442(2000)013<1517:PEATHD>2.0.CO;2

Wang, B., and Zhang, Q. (2002). Pacific-east Asian teleconnection, Part II: how the Philippine Sea anomalous anticyclone is established during El Niño development. *J. Clim.* 15, 3252–3265. doi:10.1175/1520-0442(2002)015<3252:PEATPI>2.0.CO;2

Wang, B., Liu, J., Yang, J., Zhou, T., and Wu, Z. (2009). Distinct principal modes of early and late summer rainfall anomalies in east Asia*. *J. Clim.* 22, 3864–3875. doi:10.1175/2009JCLI2850.1

Wang, L., Yu, J., and Houk, P. (2017). Enhanced biennial variability in the Pacific due to Atlantic capacitor effect. *Nat. Commun.* 8, 14887. doi:10.1038/ncomms14887

Watanabe, M., and Jin, F. (2002). Role of Indian ocean warming in the development of Philippine Sea anticyclone during ENSO: philippine SEA anticyclone during ENSO. *Geophys. Res. Lett.* 29, 116-1–116-4. doi:10.1029/2001GL014318

Wheeler, M. C., and Hendon, H. H. (2004). An all-season real-time multivariate MJO index: development of an index for monitoring and prediction. *Mon. Weather Rev.* 132, 1917–1932. doi:10.1175/1520-0493(2004)132<1917:AARMMI>2.0.CO;2

Wu, L., and Wang, C. (2015). Has the western pacific subtropical high extended westward since the late 1970s? *J. Clim.* 28, 5406–5413. doi:10.1175/JCLI-D-14-00618.1

Xie, P., and Arkin, P. A. (1997). Global precipitation: a 17-year monthly analysis based on gauge observations, satellite estimates, and numerical model outputs. *Bull. Am. Meteorol. Soc.* 78, 20. doi:10.1175/1520-0477(1997)078<2539:GPAYMA>2.0.CO;2

Xie, S. P., Hu, K., Hafner, J., Tokinaga, H., Du, Y., Huang, G., et al. (2009). Indian Ocean capacitor effect on Indo-western Pacific climate during the summer following El Niño. *J. Clim.* 22, 730–747. doi:10.1175/2008JCLI2544.1

Xu, Z., Fan, K., and Wang, H. (2015). Decadal variation of summer precipitation over China and associated atmospheric circulation after the late 1990s. *J. Clim.* 28 (10), 4086–4106. doi:10.1175/jcli-d-14-00464.1

Yang, J., Liu, Q., Xie, S.-P., Liu, Z., and Wu, L. (2007). Impact of the Indian Ocean SST basin mode on the Asian summer monsoon. *Geophys. Res. Lett.* 34, L02708. doi:10.1029/2006GL028571

Zhang, W., Jin, F.-F., Stuecker, M. F., Wittenberg, A. T., Timmermann, A., Ren, H.-L., et al. (2016). Unraveling El niño's impact on the east asian monsoon and Yangtze River summer flooding: El niño's impact on the asian monsoon. *Geophys. Res. Lett.* 43 (11), 375–382. doi:10.1002/2016GL071190

Zhang, W., Li, H., Jin, F.-F., Stuecker, M. F., Turner, A. G., and Klingaman, N. P. (2015). The annual-cycle modulation of meridional asymmetry in ENSO's atmospheric response and its dependence on ENSO zonal structure. *J. Clim.* 28, 5795–5812. doi:10.1175/JCLI-D-14-00724.1

Zhao, Z., and Chen, G. (1995). The cause and forecast of long-term change of the latitudinal position of West Pacific Subtropical High in early summer. *J. Trop. Meteorol.* 11, 223–230.

Zhao, Z. G. (1999). *Summer drought and flood in China and the circulation patterns*. Beijing, China: China Meteorological Press.

Zhou, T., Yu, R., Zhang, J., Drange, H., Cassou, C., Deser, C., et al. (2009). Why the western pacific subtropical high has extended westward since the late 1970s. *J. Clim.* 22, 2199–2215. doi:10.1175/2008JCLI2527.1

Zhou, T., and Yu, R. C. (2005). Atmospheric water vapor transport associated with typical anomalous summer rainfall patterns in China. *J. Geophys. Res.* 110, D08104. doi:10.1029/2004JD005413

Conflict of Interest: The authors declare that the research was conducted in the absence of any commercial or financial relationships that could be construed as a potential conflict of interest.

frontiers
in Earth Science

ORIGINAL RESEARCH
published: 11 December 2020
doi: 10.3389/feart.2020.595548

Diversity of East China Summer Rainfall Change in Post-El Niño Summers

Wen Zhang[1]*, Xiaoye Zhou*[2]*, Pang-Chi Hsu*[1] *and Fei Liu*[3,4]*

[1]Earth System Modeling and Climate Dynamics Research Center, Nanjing University of Information Science and Technology, Nanjing, China, [2]Anhui Meteorological Observatory, Hefei, China, [3]School of Atmospheric Sciences and Guangdong Province Key Laboratory for Climate Change and Natural Disaster Studies, Sun Yat-sen University, Zhuhai, China, [4]Southern Marine Science and Engineering Guangdong Laboratory (Zhuhai), Zhuhai, China

East China has experienced positive precipitation anomalies in post-El Niño summers, mainly in the Yangtze-Huaihe River Valley. This kind of monsoonal rainfall change induced by El Niño, however, is not always the same due to El Niño diversity and mean state change. Here, we use cluster analysis on the post-El Niño (PE) East China summer precipitation anomalies to identify the diversity of this El Niño-induced monsoon change. The result shows that PE East China summer rainfall anomalies mainly display three different modes for all selected 20 El Niño events from 1957 to 2016. Cluster 1 shows the middle and lower reaches of the Yangtze River demonstrate strong wet anomalies, while South and North China are dominated by dry anomalies, similar to a sandwich mode. Cluster 2 is distinguished by dry anomalies over South China and wet anomalies over North China, exhibiting a dipole mode. Compared with Cluster 1, the change caused by Cluster 3 is different, showing negative anomalies over the Yangtze-Huaihe River Valley. The three clusters are correlated with successive events of El Niño, a quick transfer to a strong La Niña and a quick transfer to a weak La Niña respectively. The associated anomalous anticyclone (AAC) focuses on (120°E, 20°N) in Cluster 1, which expands southward for Cluster 2 and moves eastward for Cluster 3. The feedback of AAC-sea surface temperature (SST) mainly works for supporting the AAC in Cluster 1, but it is weak for Cluster 2; the strong easterly anomalies related to La Niña contribute to the AAC location change for Cluster 2. Both AAC-SST feedback and easterly anomalies support the AAC of Cluster 3. The CMIP5 output can capture these diverse responses in circulation except that their simulated AAC for Cluster 1 is significant to the east of the observed.

Keywords: summer rainfall, post-El niño, western north pacific, anomalous anticyclone, anomalous anticyclone-sea surface temperature feedback, equatorial easterly

Edited by:
Lin Wang,
Institute of Atmospheric Physics (CAS), China

Reviewed by:
Ashok Kumar Jaswal,
India Meteorological Department, India
Kaiming Hu,
Institute of Atmospheric Physics (CAS), China

***Correspondence:**
Fei Liu
liufei26@mail.sysu.edu.cn

Specialty section:
This article was submitted to Atmospheric Science, a section of the journal Frontiers in Earth Science.

Received: *17 August 2020*
Accepted: *11 November 2020*
Published: *11 December 2020*

Citation:
Zhang W, Zhou X, Hsu P-C and Liu F (2020) Diversity of East China Summer Rainfall Change in Post-El Niño Summers. Front. Earth Sci. 8:595548. doi: 10.3389/feart.2020.595548

INTRODUCTION

East Asian summer monsoon (EASM) plays a significant role in Asian monsoon system. The weather and climate in a large part of the East Asian region are affected by the variability and evolution of EASM (Chen et al., 1992; Wang et al., 2003). Rain bands distribution changes and a wide range of precipitation anomalies in China caused by the EASM often lead to floods, droughts and other meteorological disasters, damaging the ecological environment and GDP as well (Li, 2014; Xue et al., 2015). One of the most robust signals in air-sea coupling system over some tropics is the appearance of El Niño/Southern Oscillation (ENSO), which is of great importance in modulating the EASM change (Zhang et al., 1996; Tao and Zhang, 1998; Yang and Lau, 2006).

In the western North Pacific (WNP), the anomalous anticyclone (AAC) is a vital system connecting ENSO and climate changes in East Asia. With plenty of researches, it is indicated that the stable presence of WNP AAC in the decay years of El Niño suppresses the convective activity in the WNP, while EASM will be enhanced two seasons later (Zhang et al., 1996; Wang et al., 2000). Three mechanisms for maintaining anomalous WNP AAC have been proposed. The first mechanism reveals the importance of the AAC interacting with the WNP sea surface temperature (SST) cooling under the control of background average flow (Wang et al., 2000), which has been confirmed by coupled general circulation model (CGCM) experimental test (Wang et al., 2013). The northeast wind anomaly to the southeast of the AAC strengthens the average east wind. Besides, the upward latent heat flux (evaporation) there tends to be enhanced and SST, cooled. Conversely, the resultant ocean cooling will generate descending Rossby waves that reinforce the AAC and suppress local convection. The second mechanism is named the Indian Ocean capacitor effect, which indicates that the importance of SST anomalies in the tropical Indian Ocean (IO) is emphasized. It regards IO warming as a capacitor. The western North Pacific subtropical high (WNPSH) is enhanced by eastward propagation of Kelvin waves (Xie et al., 2009). This mechanism has been confirmed by numerical experiments, which include an atmospheric general circulation model (AGCM) (Huang et al., 2010) and a CGCM model (Chowdary et al., 2010; Chowdary et al., 2011). The coupling between the WNP AAC and ocean shifts from the WNP to the North Indian Ocean (NIO) as season changes. This influence which is named Indo-western Pacific ocean capacitor (IPOC) can further show the reason why the WNP AAC maintains (Kosaka et al., 2013; Wang et al., 2013). Besides, the two mechanisms are linked together and the feedback of AAC-SST is summarized, shown as a mode of coupled ocean-atmosphere, including WNP cooling and NIO warming (Xie et al., 2016).

SST cooling or warming's control over the central Pacific is the third mechanism for maintaining the WNP AAC. Xiang et al. (2013) found that a developing La Niña is associated with a stronger western Pacific subtropical high (WPSH) anomaly. Wang et al. (2013) also put forward that Walker circulation can be shifted by the central equatorial Pacific cooling, leading to convection over the Maritime Continent been reinforced while that over the WNP been suppressed. Therefore, AAC can be enhanced by descending Rossby waves and strengthened by the equatorial easterly winds, which pass over the western Pacific, with the former being stimulated by reduced convection around 160°E and the latter being induced by the increased Maritime Continent convection.

Atmospheric circulation at mid-to-high latitudes also affects changes in East Asian circulation. Thompson and Wallace (1998) found that the main mode of sea level pressure (SLP) variability to the 20°N in the North shows a "seesaw" structure. This mode is named the Arctic Oscillation (AO), existing not only near the ground, but also in the lower stratosphere. It has been shown that the AO is in linkage with the climate of East Asia (Gong et al., 2001; Park et al., 2011). With positive AO and strengthening polar vortex as well as the mid-latitude westerly, the cold air is confined to the polar region. But if AO appears in negative phase, the polar vortex weakens, and westerly weakens and moves southward. As a result, the Arctic cold air is prone to erupt to the south, affecting Asia (Wu et al., 2004). Furthermore, the spring AO can affect the EASM via influencing East Asian jet stream (Gong et al., 2002) and stimulating tropical air-sea feedback in the WNP (Gong et al., 2011). Gong et al. (2002) and other researchers, such as Gong and Ho (2003), Liu et al. (2019), pointed out that with positive phase of AO in May, WPSH moved northwest due to the northward movement of the East Asian jet stream, which enhanced EASM and reduced rainfall in the Yangtze River Basin in summer.

Many studies have shown that the circulation and precipitation of EASM are different under different categories of ENSO in their decaying phases, such as different intensity (Xue and Liu, 2008; Lee et al., 2014), onset location (Feng et al., 2011; Yuan and Yang, 2012), decay speed (Zhou et al., 2019), which all show the diversity of EASM. In addition, various kinds of El Niño cases correspond to different decaying speeds. For instance, in the decaying summer of eastern-Pacific type, the abnormal negative precipitation occurs in the north of Yangtze-Huaihe River region, while anomalous positive precipitation occurs in South China because El Niño decays slowly. However, opposite rainfall patterns are found in the decaying summer of central-Pacific type due to the quick decay (Feng et al., 2011). Moreover, El Niño cases are separated into four types in Wang et al. (2017): super, major, moderate, and minor ones, recognizing that the distributions of rainfall over East Asia are quite different due to various strength and evolution of El Niño. Zhou et al. (2019) divided El Niño decay into early stage and late stage. For an early transition, positive rainfall anomalies mainly emerge over East China with SST anomaly result over the middle-east Pacific transiting to the state analogous to La Niña during the decaying summer. For a late transition, a tripolar negative-positive-negative rainfall anomaly pattern appears over China with the SST anomalies remained.

The classifications are not only related to the complex ENSO properties, but also related to the average state. Compared with the negative Pacific decadal oscillation (PDO) phase, the EASM becomes more vigorous after a weak East Asian Winter Monsoon associated with ENSO during the positive PDO phases (Chen et al., 2013). Feng et al. (2014) focused on El Niño decadal modulation and pointed out that during the negative PDO phase, most regions in China are dominated by positive anomalies of rainfall because El Niño decays quickly. When PDO is in its positive phase, suppressed rainfall occurs over South and North China and reinforced rainfall occurs over Central China because El Niño decays slowly.

Seasonal evolution of the ENSO-EASM relationship is also of great importance since the rainfall responses may not be fully represented by June-August (JJA) mean rainfall anomalies (Ding, 2004; Ding and Chan, 2005). It is shown that the ENSO can affect the early stage and late stage of summer rainfall anomalies in a

TABLE 1 | Detail information in 38 CMIP5 models applied in this study.

Institute	Model	Resolution (latitude ×longitude)
Commonwealth scientific and industrial research organisation/Bureau of meteorology, CSIRO-BOM	ACCESS1-0	145 × 192
CSIRO-BOM	ACCESS1-3	145 × 192
Beijing climate center, BCC	Bcc-csm1-1	64 × 128
BCC	Bcc-csm1-1-m	160 × 320
Canadian center for climate modeling and analysis, CCCMA	CanESM2	64 × 128
National center for atmospheric research, NCAR	CCSM4	192 × 288
NCAR	CESM1-BGC	192 × 288
NCAR	CESM1-FASTCHEM	192 × 288
NCAR	CESM1-WACCM	96 × 144
Centro euro-mediterraneo sui cambiamenti climatici, CMCC	CMCC-CESM	48 × 96
CMCC	CMCC-CM	240 × 480
CMCC	CMCC-CMS	96 × 192
Center national de recherches météorologiques, center européen de recherche et formation avancée en calcul scientifique, CNRM-CERFACS	CNRM-CM5	128 × 256
CNRM-CERFACS	CNRM-CM5-2	128 × 256
Commonwealth scientific and industrial research organisation/Queensland climate change center of excellence, CSIRO-QCCCE	CSIRO-MK3-6–0	96 × 192
Geophysical fluid dynamics laboratory, NOAA-GFDL	GFDL-CM3	90 × 144
NOAA-GFDL	GFDL-ESM2G	90 × 144
NOAA-GFDL	GFDL-ESM2M	90 × 144
Goddard institute for space studies, NASA/GISS	GISS-E2-H-CC	90 × 144
NASA-GISS	GISS-E2-R	90 × 144
NASA-GISS	GISS-E2-R-CC	90 × 144
National institute of meteorological research, korea meteorological administration, NIMRKMA	HadGEM2-AO	145 × 192
UK met office hadley center, MOHC	HadGEM2-CC	145 × 192
MOHC	HadGEM2-ES	145 × 192
Institute for numerical mathematics, INM	inmcm4	120 × 180
Institut pierre simon laplace, IPSL	IPSL-CM5A-LR	96 × 96
IPSL	IPSL-CM5A-MR	143 × 144
IPSL	IPSL-CM5B-LR	96 × 96
Atmosphere and ocean research institute (university of tokyo), national institute for environmental studies, and Japan agency for marine-earth science and technology, MIROC	MIROC-ESM	64 × 128
MIROC	MIROC-ESM-CHEM	64 × 128
MIROC	MIROC5	128 × 256
Max planck institute for meteorology, MPI-M	MPI-ESM-LR	96 × 192
MPI-M	MPI-ESM-MR	96 × 192
MPI-M	MPI-ESM-P	96 × 192
Meteorological research institute, MRI	MRI-CGCM3	160 × 320
MRI	MRI-ESM1	160 × 320
Norwegian climate center, NCC	NorESM1-M	96 × 144
NCC	NorESM1-ME	96 × 144

different way in East Asia (Chang et al., 2000; Wang et al., 2009; Xing et al., 2016; Xing et al., 2017). From June to August, the rain belt conducts northward movement in El Niño decay stage (Ye and Lu, 2011; Wang et al., 2017). Feng et al. (2014) not only researched the EASM behaviors in PE summer, but also found the rainfall pattern has great subseasonal variation. From June to August, the northward migration of anomalous positive rainfall moves from South China to North China in the negative PDO phase due to two clearly northward shifts of the WPSH. Hu et al. (2017) put forward that the subseasonal variation of precipitation anomalies are attributed to the northward movement of the WNP AAC and subtropical jet anomalies in PE summer.

Previous studies all started from El Niño, while few attention was placed on El Niño-induced monsoon diversity itself. In this study, the goal is to identify the diversity of China summer rainfall change in PE summers first; then to analyze possible mechanisms related to the variations of the WNP AAC. The structure of this paper is arranged in the following way. The collection of data and research methods used in the study are depicted in *Data and Methods*. For *Results*, the precipitation over East China in PE summers is classified into three types, and the causes of different rainfall responses are explained. Subseasonal migration of rainfall anomalies in these three types are also discussed. Finally, whether model outputs support our discovery has been checked. In *Discussion and Conclusions*, the above conclusions are integrated together.

DATA AND METHODS

This study includes five datasets. For rainfall background information, 160 observational stations of the Chinese Meteorological Data Center ranging from 1951 to 2016 are used; and the data set of the Climatic Research Unit (CRU, TS4.01), which covers terrestrial rainfall data between 1901 and 2016 (Harris et al., 2014). Manual verification and correction were generally given to the suspicious and incorrect station rainfall data, and quality control codes were finally marked for them (Wang et al., 2007). Monthly wind and geopotential height fields come from the reanalysis data set of the National Centers of Environmental Prediction–National Center for Atmospheric Research (NCEP-NCAR), with the time range from January 1948 to the present (Kalnay et al., 1996). The monthly SST data comes from the data set of the Hadley Center Global Sea Ice and Sea Surface Temperature (HadISST), which is run by the UK Met Office's Hadley Center (Rayner et al., 2003) from 1870 to 2016. The years from 1957 to 2016 are chosen as the research period in this study, mainly to consider consistency and reliability. To eliminate possible effect of long-term trends, we detrended each field before analysis by removing the least squares linear trend of the dimension from all grid points.

Considering Taylor's et al. (2012) research, we also use the historical outputs from 38 coupled general circulation models (CGCMs) that took part in the Coupled Model Intercomparison Project phase 5 (CMIP5) during 1901–2004 (Taylor et al., 2012) to test if the findings based on observations are reproduced by these models. Only ensemble 1 of all the models is used. In **Table 1**, the model names, resolutions and organizations that provide the data are shown.

First, El Niño events from 1957 to 2016 are selected. The selection of the observed El Niño events is according to the Niño3.4 index, which is defined by the average SST anomalies in the region (120°–170°W, 5°S–5°N), which acquires anomalies through removing climatological average value and annual cycle for 1957–2016. When the normalized Niño3.4 index of an event exceeds 0.5 in the winter (DJF), the event is called an El Niño event. Following this definition, 20 events of El Niño are picked out, which include 1957/1958, 1963/1964, 1965/1966, 1968/1969, 1969/1970, 1972/1973, 1976/1977, 1977/1978, 1979/1980, 1982/1983, 1986/1987, 1987/1988, 1991/1992, 1994/1995, 1997/1998, 2002/2003, 2006/2007, 2009/2010, 2014/2015, and 2015/2016.

Then, the K-means cluster analysis (Wilks, 2011) is applied to classify these 20 events based on China rainfall anomalies in PE summer (JJA) during 1957–2016. Cluster analysis is a significant statistical method for pattern recognition. The operation process is simple, with high efficiency and scalability in data management; the time complexity is nearly linear, and it is suitable for mining large-scale datasets (Zhang et al., 2008). Compared with the symmetry characteristics of EOF analysis, this method can also realize the diversification of mode. In this method, for the purpose of evaluating how similar each member and the corresponding centroid, squared Euclidean distance is calculated. The silhouette clustering assessment criteria is applied to measure whether the skill of this statistical method is appropriate. The silhouette value ranging from −1 to +1 for each member can measure how similar a member is to the other members in its own cluster. When silhouette value is high, it means that the member matches with its own cluster well and is not a good match with its neighboring clusters (Kaufman et al., 2009). In general, we use the rainfall anomalies of these 20 events as the cluster analysis data, and as a result, these events are classified into three clusters. In this paper, composite analysis is used in analyzing different responses of these three types and the method of significance test is Student's *t*-test.

RESULTS

Rainfall Anomalies in China

This algorithm is sensitive to the selection of initial cluster centroid and the results can be influenced by it. To overcome this defect, we first estimate the range of k value and then find optimum value (Liu, 2016). Based on the stability and physical meanings, we found it is better to classify the selected events into three clusters, with six events (1968/1969, 1976/1977, 1977/1978, 1979/1980, 1982/1983, 1986/1987, and 2014/2015) in cluster 1, nine events (1963/1964, 1969/1970, 1977/1978, 1987/1988, 1997/1998, 2002/2003, 2006/2007, 2009/2010, and 2015/2016) in cluster 2, and five events (1957/1958, 1965/1966, 1972/1973, 1991/1992, and 1994/1995) in cluster 3.

The composite summer rainfall anomalies in China are shown in **Figure 1** for three clusters. For the average of 20 events, most regions are controlled by positive anomalies except for South and Northeast China, and for some eastern coastal areas (**Figure 1A**). In cluster 1, in the middle and lower reaches of the Yangtze River (MLRYR), there are positive anomalies of heavy rainfall and negative anomalies in South and North China, showing a tripolar pattern (**Figure 1B**). In cluster 2, the precipitation anomalies in South China and the lower reaches of the Yangtze River are negative. From the north of these areas to North China, the positive precipitation is abnormal (**Figure 1C**). In cluster 3, the Yangtze-Huaihe River Valley are dominated by negative rainfall anomalies; to the southern and northern area, it presents wet anomalies (**Figure 1D**). The strongest rainfall anomalies happen in the MLRYR in cluster 1.

Response of WNP AAC

The stable presence of the WNP AAC strongly influences East Asia monsoon in PE, especially in China (Zhang et al., 1999; Lin and Lu, 2009). **Figure 2** shows composite SST and wind anomalies of 850-hPa for three clusters. In cluster 1, the WNP AAC goes through the South China Sea and the Philippine Sea, while its center is located at (120°E, 20°N) (**Figure 2A**). The precipitation over South China is suppressed by the westward expansion of the AAC through Rossby wave propagation (Lin, 2008). Flows from the southwestern side of the WNP AAC transport moisture to MLRYR. The warm and moist air converges with the cool air from the high latitude, causing strong positive rainfall anomalies in this area. In cluster 2, the WNP AAC expands southward, which is associated with equatorial easterly wind anomaly, and Southeast China is controlled by the AAC (**Figure 2B**). The southwesterly wind anomaly, however, penetrates to North China and causes positive precipitation anomalies there. In cluster 3, the WNP AAC moves eastward and is centered at (150°E, 25°N) (**Figure 2C**), with its convergence center over Southeast China. These different AAC locations result in different types of rainfall responses.

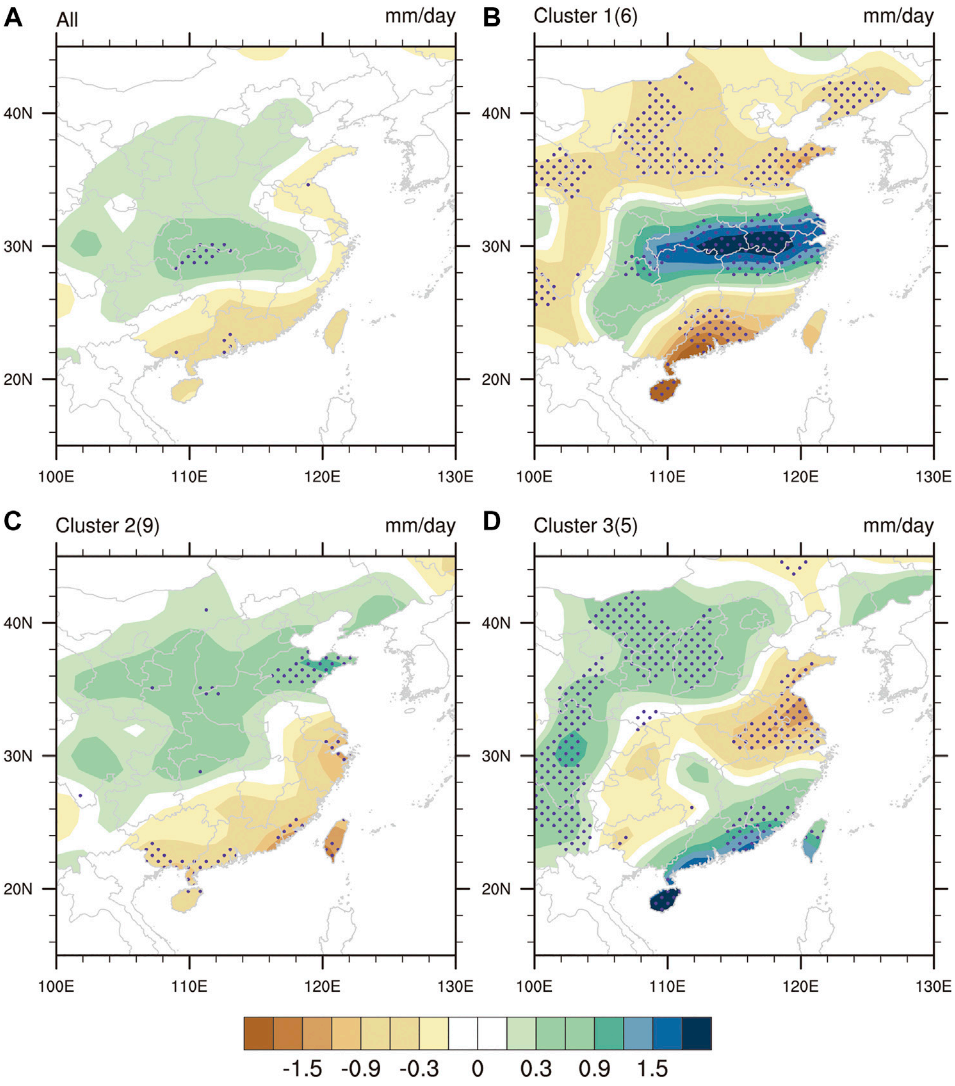

FIGURE 1 | Composite El Niño decaying summer rainfall (shading; mm/day) anomalies in East China which locates at 105°E to 140°E and 15°N to 55°N in **(A)** all 20 **(B)** cluster 1 **(C)** cluster 2, and **(D)** cluster 3 during 1957–2016. Number of events in each cluster is included in the parentheses. Stippling indicates that more than 2/3 of the events have the same sign in their own cluster.

Mechanisms to Maintain the WNP AAC

The local interaction of atmosphere-ocean has an impact on WNP AAC. In cluster 1, there are obvious positive SST anomalies in the middle-east equatorial Pacific and the whole IO. Westerly anomalies correlated with the SST anomalies exist in the central equatorial Pacific. Over the WNP, Northeasterly anomalies appear and the situ underlying SST anomalies are negative (**Figure 2A**). The anomalous northeasterlies strengthen the mean, resulting in SST cooling near the southeastern side of WNP AAC, thereby further increasing evaporation/entrainment (Wang et al., 2000). Deep convection can be suppressed by the cooling, which can generate atmospheric Rossby waves propagating westward, and strengthen the WNP AAC. The easterly anomaly over the NIO in the decaying summer weakens the southwest monsoon and maintains the NIO warming (Du et al., 2009). The Kelvin wave in the equatorial area is stimulated over the western Pacific by the warming of NIO to reinforce WNP AAC, which is called the "Indian Ocean capacitor" (Xie et al., 2009; Xie et al., 2016).

One of the unique features of cluster 2 events is that there is a remarkable strong La Nina phenomenon in the central-east Pacific, and there are anomalous easterlies over the Maritime Continent and the central equatorial Pacific. The NIO is occupied by easterly anomaly, and SST shows positive anomaly (**Figure 2B**). In terms of coupled NIO warming-WNP cooling mode, the WNP cooling is absent and only NIO warming exists. The strong easterly strengthens a convergence zone, thus positive rainfall anomaly extending westward and appearing over India. The intensive equatorial Pacific cooling leads to strong equatorial easterly anomalies, which help maintain the AAC and pull it southward.

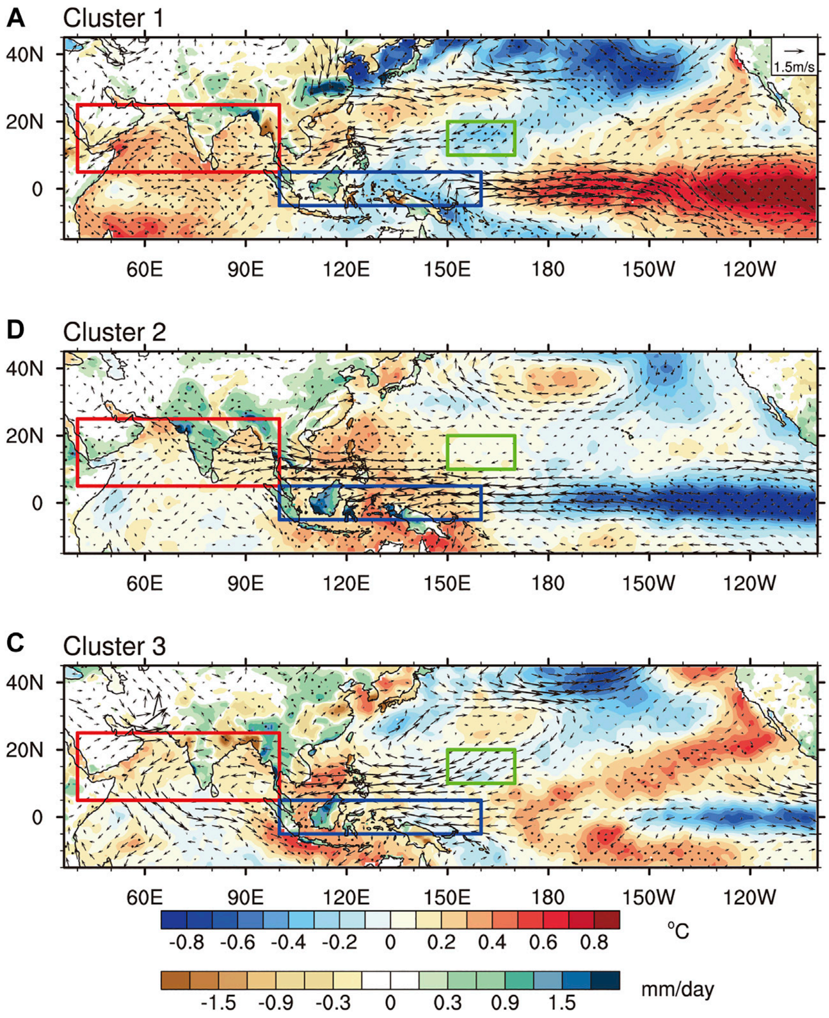

FIGURE 2 | Composite El Niño decaying summer land precipitation anomalies (shading; mm/day), SST anomalies (shading; °C), and wind anomalies of 850-hPa (vector; m/s) in **(A)** cluster 1 **(B)** cluster 2, and **(C)** cluster 3 during 1957–2016. The Northwest Pacific (150°–170°E, 10°–20°N), NIO (40°–100°E, 5°–25°N), and Indo-western equatorial Pacific (100°–160°E, 5°S–5°N) are represented by green, red, and blue boxes, respectively. The black dots indicate the anomalous SST and rainfall above confidence level of 90% in Student's *t*-test.

In the NIO, the warm SST is seen in cluster 3, and from central area to eastern Pacific, the cold one is shown. They are similar to cluster 2, but the La Niña-like cooling is weaker in cluster 3. Correspondingly, from central area of equatorial Pacific to the Maritime Continent, easterly anomaly is also weak. The resulted AAC is shifted eastward compared with that in cluster 2. The convergence zone is also shifted eastward and positive anomalies of the rainfall occur in the Maritime Continent and South China. A weak cold SST anomaly is found in the WNP, combined with northeasterly wind anomalies (**Figure 2C**).

Figure 3 shows seasonal development of Niño 3.4 index for these three clusters. For all 20 events, the central-eastern equatorial Pacific SST has peaked in developing winter; and for decaying summer, it decays to neutral condition. For cluster 1, the SST remains warm from the developing winter through the decaying summer. For cluster 2, this SST decays quickly to zero in the late spring and reaches a cold condition in

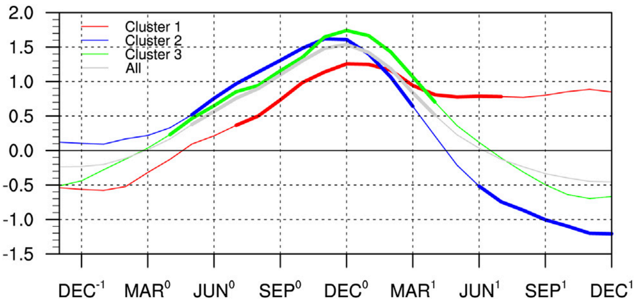

FIGURE 3 | Seasonal evolution of Niño3.4 index for the three clusters. The red, blue, green, and grey colors denote the composites of cluster 1, cluster 2, cluster 3, and all events, respectively. Thick lines indicate anomalies above the confidence level of 90% in Student's *t*-test. Superscripts −1, 0, 1 on the abscissa represent El Niños are in previous, developing, and decaying stages, respectively.

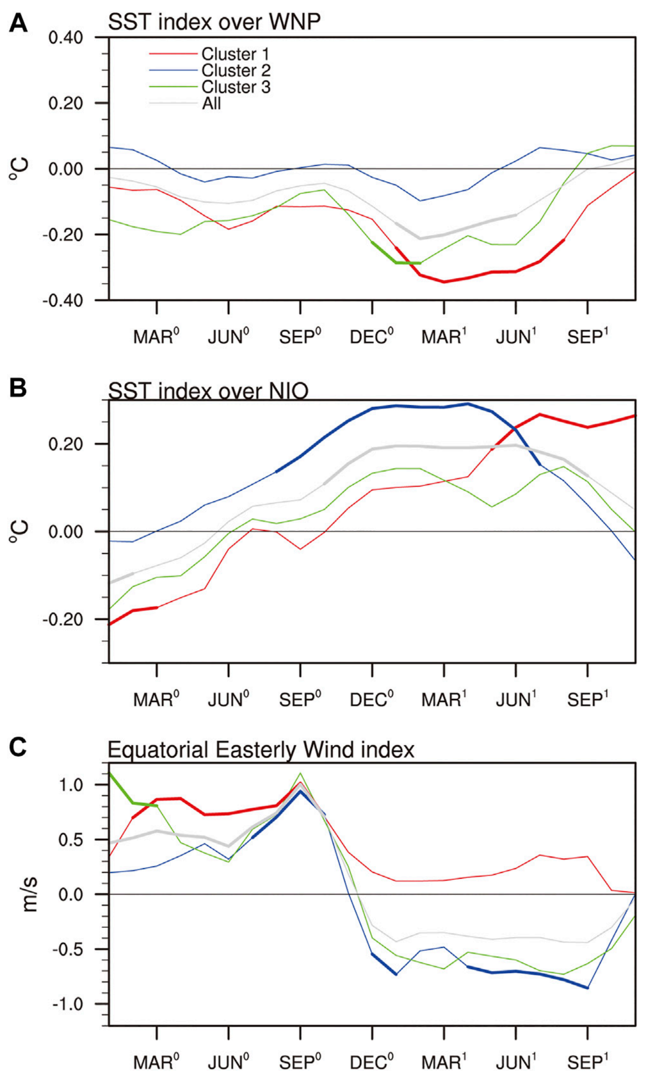

FIGURE 4 | Seasonal evolutions of three indices **(A)** WNP index **(B)** NIO index, and **(C)** Equatorial easterly wind index in three clusters. The WNP index and NIO index refer to the mean SST anomalies in the WNP (150°–170°E, 10°–20°N) and NIO (40°–100°E, 5°–25°N), respectively. The easterly index is represented by mean zonal wind anomalies in the equatorial area of western Pacific (100°–160°E, 5°S–5°N). The red, blue, green, and grey colors represent composite cluster 1, cluster 2, cluster 3, and all events, respectively. Thick lines indicate anomalies above the confidence level of 90% in Student's *t*-test. Superscripts 0 and 1 on the abscissa represent El Niños are in developing and decaying stages, respectively.

the following summer. For cluster 3, the overall trend is close to that in cluster 2, but the decay speed of SST is relatively slower and reaches zero in the early summer. Thus, we conclude that cluster 1 is related to successive El Niño, while clusters 2 and 3 are related to fast-decaying El Niño.

In summary, two feedbacks are found to maintain the WNP AAC in these three clusters, related to SST and atmospheric circulation contributions. One is the AAC-SST feedback, which means the mode of NIO warming coupling with WNP cooling; and second is the equatorial easterly feedback. To better illustrate two feedback mentioned above, we define three indices to represent them. For the AAC-SST feedback in the WNP section, the SST index refers to the WNP mean SST anomalies ranging (150°–170°E, 10°–20°N). For IO section of the dipole mode, the SST index refers to the averaged SST anomalies over the NIO, covering (40°–100°E, 5°–25°N). In addition, the mean easterly anomaly of the western equatorial Pacific (100°–160°E, 5°S–5°N), called the equatorial easterly index, is used to represent the equatorial easterly feedback. **Figure 4** shows the seasonal evolutions of the three indices for the three clusters respectively. In the decaying summer, the negative SST anomaly still exists in the WNP in clusters 1 and 3, while it disappears since the late spring in cluster 2 (**Figure 4A**). Furthermore, compared with cluster 1, the cold SST anomaly in cluster 3 is weaker. And SST anomalies for NIO are positive in the previous autumn and remain positive in the following summer in all three types (**Figure 4B**), meaning the AAC-feedback only exits in clusters 1 and 3. The equatorial easterly index reaches its peak in the previous autumn in all three types. The westerly anomaly remains positive in cluster 1 but the westerly anomalies turn to easterly anomalies from the late autumn in clusters 2 and 3. Additionally, the easterly anomaly is stronger in cluster 2 in the following summer (**Figure 4C**), meaning the easterly feedback in equatorial area only appears in clusters 2 and 3. In general, the WNP cooling and NIO warming are both notable in cluster 1 in the PE summer. In cluster 2, the NIO section of the AAC-SST feedback and the easterly feedback in equatorial are the main factors maintaining the WNP AAC. In cluster 3, the WNP cooling, NIO warming, and the equatorial easterly jointly support the WNP AAC; however, the feedbacks are relatively weak.

Middle-To-High-Latitude Response

Different rainfall responses are also affected by atmospheric circulation in the mid-to-high latitude. **Figure 5** presents the composite anomalous circulation field in upper troposphere for these clusters. In cluster 1, negative geopotential height anomaly appears at mid-high latitudes in Northern Hemisphere while positive anomaly appears over the polar region, similar to AO's negative phase (**Figure 5A**). The north-high and south-low situation is favorable for the polar cold air invading southward (Wu et al., 2004). The downward cold, dry air and the warm, moist air on west flank of the subtropical high encounter in MLRYR and bring heavy rainfall there. In clusters 2 and 3, the geopotential height anomaly is negative over the polar region and positive in mid and high latitude, which is in accordance with positive phase in the AO (**Figures 5B,C**). This south-high and north-low situation traps the cold air in the polar region by the high pressure, and it is difficult for the cold air to invade southward. Therefore, the southwesterly wind anomaly can penetrate to North China without the obstruction of the cold air, and causes rainfall in North China. In addition, westerly anomalies are found over the Tibetan Plateau in cluster 1 and cluster 3 (**Figures 5A,C**), which can transport warm advection to the lower reaches, causing ascending movement and enhancing precipitation over East China (Sampe and Xie, 2010; Hu et al., 2017). Role of subtropical front should be considered in the future (Wang et al., 2019).

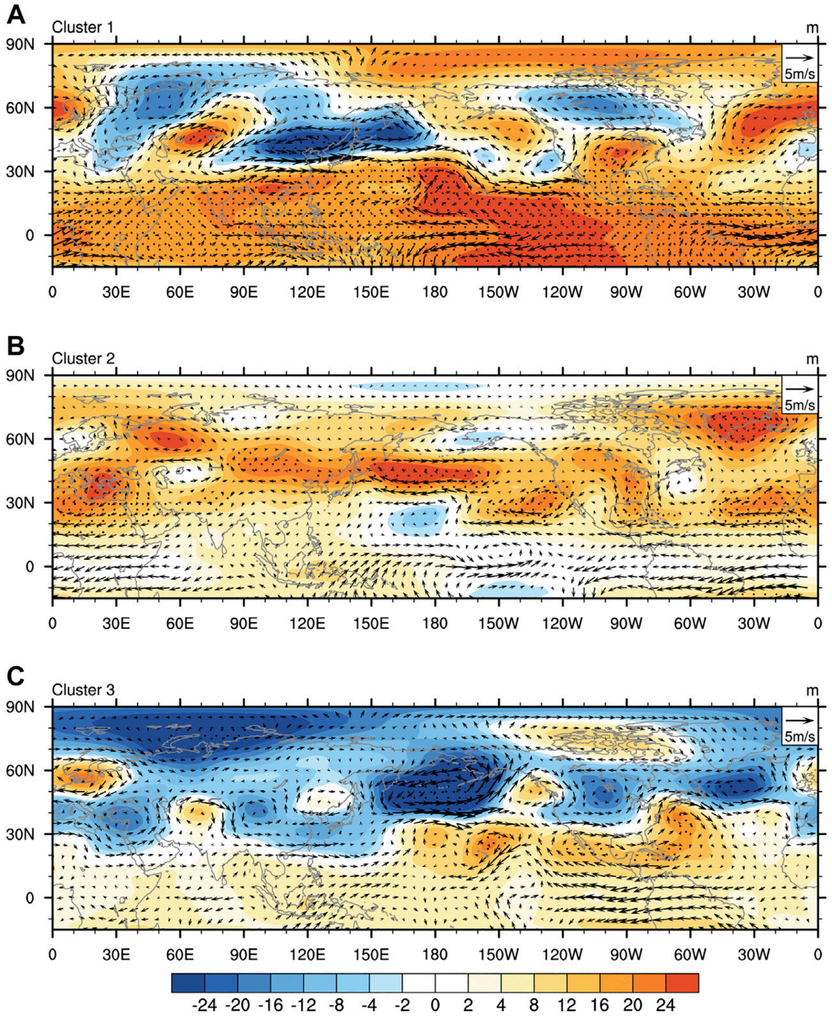

FIGURE 5 | Composite El Niño decaying summer geopotential height anomalies of 200-hPa (shading; m) and wind anomalies (vector; m/s) in **(A)** cluster 1 **(B)** cluster 2, and **(C)** cluster 3 during 1957–2016. The black dots indicate anomalous SST and rainfall above the confidence level of 90% in Student's *t*-test.

Subseasonal Migration of Rainfall

The diversity of China summer rainfall change may also be related to subseasonal migration of rainfall anomalies, because JJA averaged anomalies cannot completely represent the responses of precipitation. This is due to a northeast-southwest oriented subtropical front mainly controls the rainfall over China even the whole East Asia, which makes the region a distinct monsoon region. This convergence zone of the mean state migrates from southern part of China in June to northern part in August (Ding and Chan, 2005). For all 20 events (**Figures 6A,B,C**), the positive rainfall anomaly appears in parts of South China and southern part of the Yangtze River in June, and moves northward in next month to the Yangtze River Valley, and continues migrating to North China in August. The migration is similar to the northward movement in the mean state. At June, the AAC locates in the South China Sea, and after that moves toward north in July and August. For cluster 1 (**Figures 6D,E,F**), the positive rainfall anomalies remain in the MLRYR for the whole summer. The stabilization of the AAC around 22°N provides continuous rainfall in the mid-latitude region and leads to the JJA mean pattern in cluster 1. For cluster 2 (**Figures 6G,H,I**), the northward migration of rainfall anomalies is analogous to the observations in all events. The positive rainfall anomaly occurs in South China, and an AAC appears in the South China Sea at June for cluster 3 (**Figure 6J**). In July, the AAC moves to the east side, causing a tripolar rainfall mode distinguished by anomalous negative phase in the Yangtze-Huaihe River Valley while anomalous positive phases for the North and South (**Figure 6K**). In August, the AAC expands westward and the rainfall anomaly shows a dipole pattern (**Figure 6L**). These give rise to the positive-negative-positive sandwich rainfall pattern in JJA mean in cluster 3. The prominent subseasonal rainfall anomalies are caused by the rainfall concentrated in the subtropical frontal zone, and the

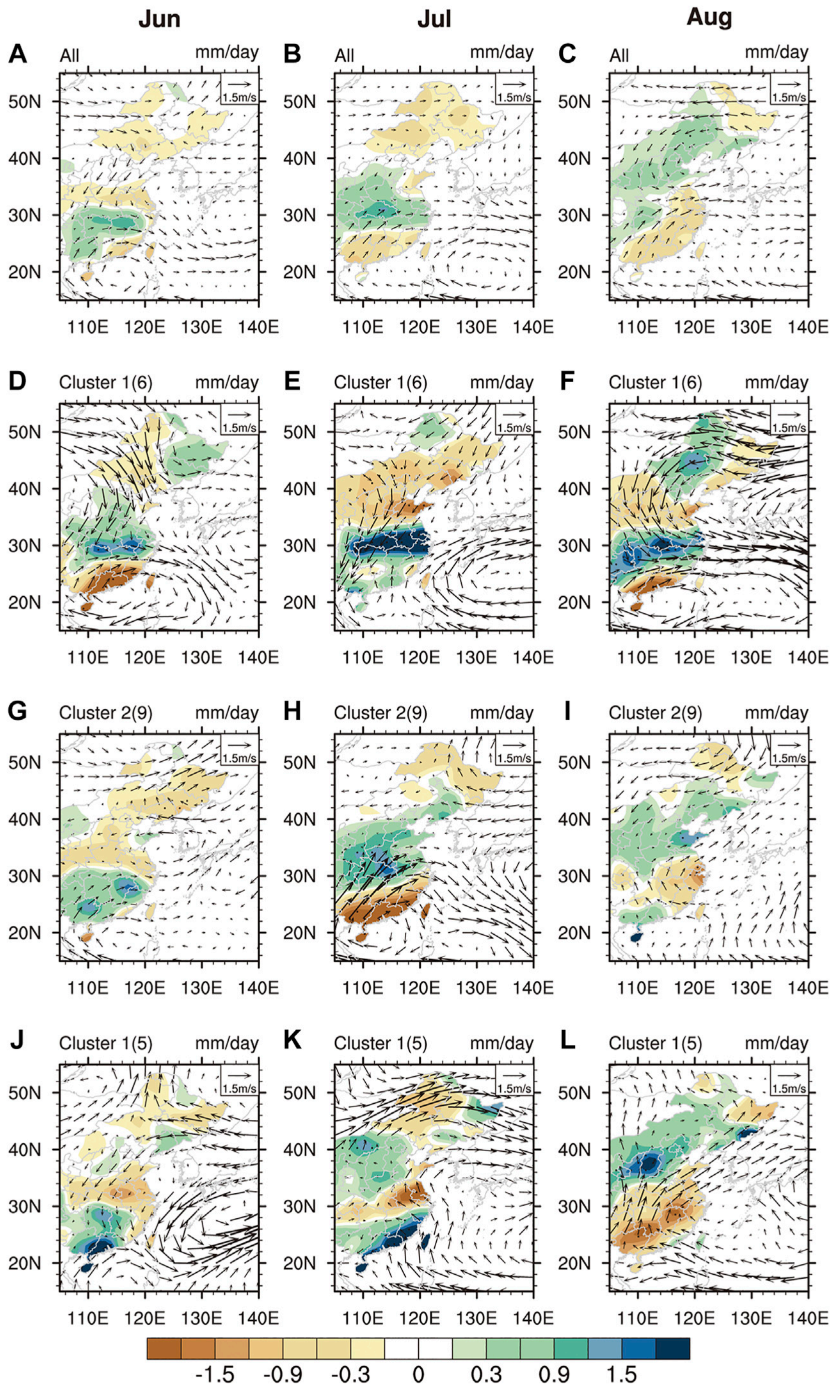

FIGURE 6 | Composite El Niño decaying summer rainfall anomalies (shading; mm/day) and wind anomalies of 850-hPa (vector; m/s) over East China in **(A)** June **(B)** July, and **(C)** August for all 20 events during 1957–2016 **(D) (E) (F)** and **(A) (B) (C)** are alike, respectively, but for cluster 1 **(G) (H)**, and **(I)** are for cluster 2; and **(J) (K)**, and **(L)** are for cluster 3. The number of events in each cluster is included in the parentheses. The black dots reveal anomalous rainfall above the confidence level of 90% in Student's *t*-test.

subtropical front migrates northward continuously. Correct prediction of this seasonal evolution is important to improve our subseasonal prediction of China summer rainfall (Liu et al., 2020), and the role of intraseasonal variability and synoptic perturbations over the monsoon trough should be studied in the future (Liu and Wang, 2013; Gao et al., 2018; Guan et al., 2019).

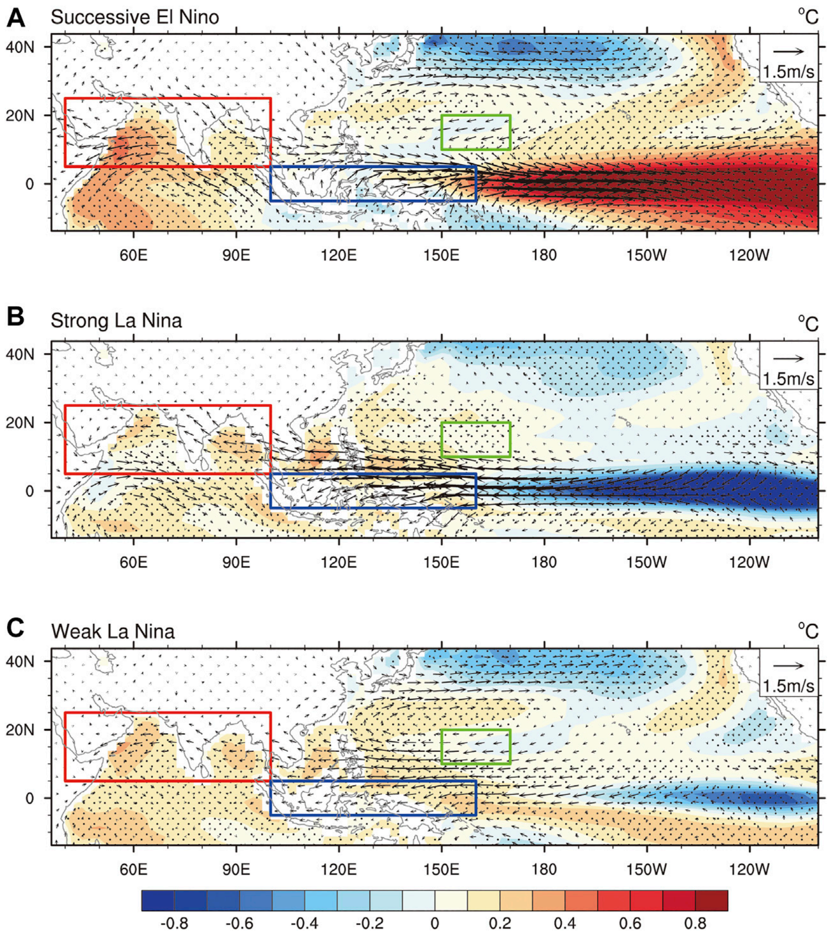

FIGURE 7 | Similar to **Figure 2**, but for **(A)** 490 successive El Niños **(B)** 289 strong La Niñas, and **(C)** 194 weak La Niñas during 1901–2004 in the selected 38 CMIP5 models.

Different Responses in CMIP5 Models

We use 38 CMIP5 model outputs during 1901–2004 to test if the responses exist in PE. Based on the above analysis results, clusters 1, 2, and 3 correspond to a successive El Niño, quick transition to a strong La Niña, and quick transition to the weak one in PE summers respectively. The successive El Niño means normalized Niño 3.4 index exceeding 0.5 in the preceding winter (DJF), as well as following summer (JJA). A quick transition to a strong La Niña refers to normalized Niño 3.4 index exceeding 0.5 in the preceding winter (DJF) and falling below −0.5 in the following summer (JJA). A quick transition to a weak La Niña refers to normalized Niño 3.4 index exceeding 0.5 in the preceding winter (DJF), and falling below 0 and exceeding −0.5 in the following summer (JJA). There are totally 490 successive El Niños, 289 strong La Niñas, and 194 weak La Niñas in these outputs.

In the PE summer of successive El Niños (**Figure 7A**), the NIO warming accompanied by the easterly wind anomaly is well stimulated while the WNP cooling is weaker than observed. The WNP AAC associated with subtropical, cold SST anomalies in the models, however, moves too far to the east compared with the observation, which locates at 150°E and 25°N.

For the quick transition to a strong La Niña (**Figure 7B**), the strong easterly wind anomaly connected with the cooling of SST over middle-east Pacific is simulated, as well as NIO warming. While WNP AAC's location is similar with that in the observations. Compared with the successive El Niño, the easterly wind anomalies also pull the AAC southward. For the quick transition to a weak La Niña (**Figure 7C**), the weak equatorial easterly wind anomaly and NIO warming are simulated. However, the SST cooling in the WNP is not significant. The WNP AAC also appears further to the east than in cluster 2.

The models can simulate different mechanisms associated with these three clusters (**Figure 8**). Consistent with observations, the models present stronger WNP cooling for successive El Niños and weak La Niñas than for strong La Niñas. Significant NIO warming is shown for all three clusters. The large equatorial easterly wind anomalies are also simulated for the quick transition.

In conclusion, the CMIP5 models can well capture the observed characteristics in three clusters of El Niños, which correspond to three clusters of rainfall respectively, except that

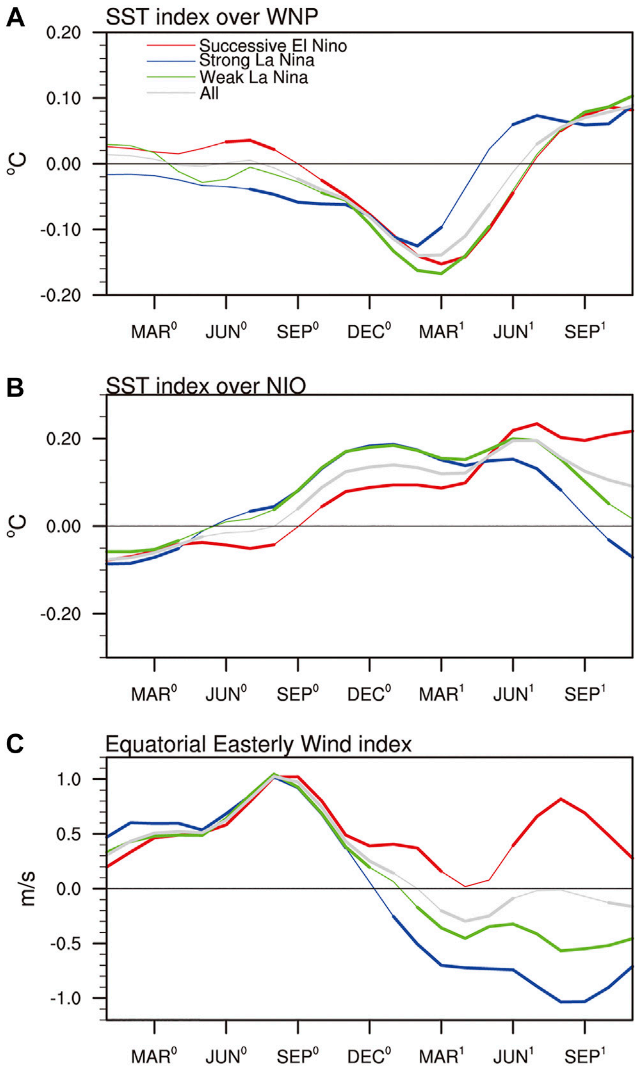

FIGURE 8 | Same as **Figure 5**, except that the red, blue, green, and grey colors denote the composites of 490 successive El Niños, 289 strong La Niñas, 194 weak La Niñas, and all events in the CMIP5 models, respectively.

they simulate an AAC too much to the east, compared with the observations for the successive El Niño.

DISCUSSION AND CONCLUSIONS

The study finds that East China summer rainfall changes can be divided into three types in PE summers, and that different mechanisms contribute to the diversity of the rainfall. **Figure 1B** indicates that cluster 1 is characterized by a tripolar pattern with distinct wet anomalies in the MLRYR, while dry anomalies in North and South China. Dry anomaly in the South and wet anomaly in the North are obvious for cluster 2, exhibiting a dipole pattern (**Figure 1C**). The rainfall pattern of cluster 3 is opposite to that of cluster 2 (**Figure 1D**).

The most important reason for these three different clusters of rainfall responses is the location of the WNP AAC. In cluster 1, the AAC locates at the Philippine Sea and South China Sea, transporting moisture to MLRYR (**Figure 2A**). In cluster 2, the AAC is pulled southward through the easterly wind anomalies in equatorial area, suppressing South China's rainfall and enhancing the rainfall in the northern part (**Figure 2B**). As for cluster 3, the WNP AAC is farther eastward but its convergence center is located in Southeast China (**Figure 2C**).

Two underlying mechanisms are responsible for the maintenance of the WNP AAC in the three clusters. For cluster 1, it is related to the successive El Niño (**Figures 2, 3**), and the WNP cooling and the NIO warming form an AAC-SST feedback to support the WNP AAC (**Figure 4**). For cluster 2, it transfers to strong La Niña in the decaying summer (**Figure 2, 3**), and easterly anomalies caused by SST cooling in the middle-east Pacific collaborate with NIO warming to contribute to the WNP AAC (**Figure 4**). For cluster 3, which transfers to weak La Niña in the decaying summer (**Figures 2, 3**), the AAC-SST feedback interacts with the easterly feedback in equator to support the WNP AAC (**Figure 4**).

We also find that the AO has an influence on the rainfall responses. The AO is negative for cluster 1, guiding cold air to the south (**Figure 5A**), while the AO is positive in clusters 2 and 3, blocking the cold air in the polar region (**Figure 5B,C**). The heavy precipitation in the MLRYR is partly due to the southward cold air reaching there.

Furthermore, subseasonal rainfall migration is quite variable in the three clusters. In cluster 1, the positive rainfall anomalies are stable in the MLRYR (**Figures 6D,E,F**). In cluster 2, from June to August, the anomalous positive precipitation move toward north (**Figures 6G,H,I**). In cluster 3, as for June and July, the wet anomalies remain in South China, and in August, they move toward north (**Figures 6J,K,L**).

The observed circulation responses could be reproduced by CMIP5 models in terms of the three clusters, but they stimulate an AAC farther to the east, compared with the observations for successive El Niños (**Figures 7, 8**).

DATA AVAILABILITY STATEMENT

The original contributions presented in the study are included in the article/Supplementary Material, further inquiries can be directed to the corresponding author/s.

AUTHOR CONTRIBUTIONS

The idea and manuscript writing are done by WZ and FL. WZ and XZ are responsible for data analysis and manuscript writing. P-CH and FL came up with the study design and the manuscript review.

FUNDING

This work was supported by the Natural Science Foundation of China (41975107).

REFERENCES

Chang, C.-P., Zhang, Y., and Li, T. (2000). Interannual and interdecadal variations of the East Asian summer monsoon and tropical Pacific SSTs. Part I: roles of the subtropical ridge. *J. Clim.* 13, 4310–4325. doi:10.1175/1520-0442(2000)013<4310:iaivot>2.0.co;2

Chen, L., Dong, M., and Shao, Y. (1992). The characteristics of interannual variations on the east asian monsoon. *J. Meteorol. Soc. Jpn.* 70, 397–421. doi:10.2151/jmsj1965.70.1b_397

Chen, W., Feng, J., and Wu, R. (2013). Roles of ENSO and PDO in the link of the East Asian winter monsoon to the following summer monsoon. *J. Clim.* 26, 622–635. doi:10.1175/jcli-d-12-00021.1

Chowdary, J. S., Xie, S.-P., Lee, J.-Y., Kosaka, Y., and Wang, B. (2010). Predictability of summer northwest Pacific climate in 11 coupled model hindcasts: local and remote forcing. *J. Geophys. Res.* 115, D22121. doi:10.1029/2010JD014595

Chowdary, J. S., Xie, S.-P., Luo, J.-J., Hafner, J., Behera, S., Masumoto, Y., et al. (2011). Predictability of Northwest Pacific climate during summer and the role of the tropical Indian Ocean. *Clim. Dynam.* 36, 607–621. doi:10.1007/s00382-009-0686-5

Ding, Y. H. (2004). Seasonal march of the East-Asian summer monsoon. in *East Asian monsoon*. Editor C. P. Chang (USA: World Scientific Series on Asia-Pacific Weather and Climate), 3–53

Ding, Y. H. and Chan, J. C. L. (2005). The East Asian summer monsoon: an overview. *Meteorol. Atmos. Phys.* 89, 117–142. doi:10.1007/s00703-005-0125-z

Du, Y., Xie, S.-P., Huang, G., and Hu, K. (2009). Role of air-sea interaction in the long persistence of El niño-induced north Indian ocean warming*. *J. Clim.* 22, 2023–2038. doi:10.1175/2008JCLI2590.1

Feng, J., Chen, W., Tam, C.-Y., and Zhou, W. (2011). Different impacts of El Niño and El Niño modoki on China rainfall in the decaying phases. *Int. J. Climatol.* 31, 2091–2101. doi:10.1002/joc.2217

Feng, J., Wang, L., and Chen, W. (2014). How does the east asian summer monsoon behave in the decaying phase of El Niño during different PDO phases?. *J. Clim.* 27, 2682–2698. doi:10.1175/JCLI-D-13-00015.1

Gao, S., Chen, Z., and Zhang, W. (2018). Impacts of tropical North Atlantic SST on western North Pacific landfalling tropical cyclones. *J. Clim.* 31, 853–862. doi:10.1175/jcli-d-17-0325.1

Gong, D.-Y. and Ho, C. H. (2003). Arctic oscillation signals in the East Asian summer monsoon. *J. Geophys. Res.* 108, 4066. doi:10.1029/2002JD002193

Gong, D.-Y., Wang, S.-W., and Zhu, J.-H. (2001). East Asian winter monsoon and Arctic oscillation. *Geophys. Res. Lett.* 28, 2073–2076. doi:10.1029/2000GL012311

Gong, D.-Y., Yang, J., Kim, S.-J., Gao, Y., Guo, D., Zhou, T., et al. (2011). Spring Arctic Oscillation-East Asian summer monsoon connection through circulation changes over the western North Pacific. *Clim. Dynam.* 37, 2199–2216. doi:10.1007/s00382-011-1041-1

Gong, D., Zhu, J. H., and Wang, S. W. (2002). Significant relationship between spring AO and the summer rainfall along the Yangtze River. *Chin. Sci. Bull.* 47, 948–952. doi:10.1360/csb2002-47-7-54610.1360/02tb9212 .(in Chinese)

Guan, W., Hu, H., Ren, X., and Yang, X. Q. (2019). Subseasonal zonal variability of the western Pacific subtropical high in summer: climate impacts and underlying mechanisms. *Clim. Dynam.* 53 (5-6), 3325–3344. doi:10.1007/s00382-019-04705-4

Harris, I., Jones, P. D., Osborn, T. J., and Lister, D. H. (2014). Updated high-resolution grids of monthly climatic observations - the CRU TS3.10 Dataset. *Int. J. Climatol.* 34, 623–642. doi:10.1002/joc.3711

Hu, K., Xie, S.-P., and Huang, G. (2017). Orographically anchored El Niño effect on summer rainfall in Central China. *J. Clim.* 30, 10037–10045. doi:10.1175/jcli-d-17-0312.1

Huang, G., Hu, K., and Xie, S.-P. (2010). Strengthening of tropical Indian ocean teleconnection to the Northwest Pacific since the mid-1970s: an atmospheric GCM study*. *J. Clim.* 23, 5294–5304. doi:10.1175/2010JCLI3577.1

Kalnay, E., Kanamitsu, M., Kistler, R., Collins, W., Deaven, D., au, L., et al. (1996). The NCEP/NCAR 40-year reanalysis Project. *Bull. Am. Meteorol. Soc.* 77, 437–471. doi:10.1175/1520-0477(1996)077<0437:TNYRP>2.0.CO;2

Kaufman, L. and Rousseeuw, P. J. (2009). *Finding groups in data: an introduction to cluster Analysis*. New York: Wiley

Kosaka, Y., Xie, S.-P., Lau, N.-C., and Vecchi, G. A. (2013). Origin of seasonal predictability for summer climate over the Northwestern Pacific. *Proc. Natl. Acad. Sci. Unit. States Am.* 110, 7574–7579. doi:10.1073/pnas.1215582110

Lee, S. K., DiNezio, P. N., Chung, E. S., Yeh, S. W., Wittenberg, A. T., and Wang, C. (2014). Spring persistence, transition, and resurgence of El Niño. *Geophys. Res. Lett.* 41, 8578–8585. doi:10.1002/2014gl062484

Li, Q. (2014). The evolution of east asian summer monsoon and Drought\Flood distribution on eastern China during the last 539yr. *AMR (Adv. Magn. Reson.)* 955-959, 3093–3097. doi:10.4028/www.scientific10.4028/www.scientific.net/amr.955-959.3093

Lin, H. (2009). Global extratropical response to diabatic heating variability of the Asian Summer Monsoon. *J. Atmos. Sci.* 66, 2697–2713. doi:10.1175/2009JAS3008.1

Lin, Z. and Lu, R. (2009). The ENSO's effect on eastern China rainfall in the following early summer. *Adv. Atmos. Sci.* 26, 333–342. doi:10.1007/s00376-009-0333-4

Liu, F., Ouyang, Y., Wang, B., Yang, J., Ling, J., and Hsu, P.-C. (2020). Seasonal evolution of the intraseasonal variability of China summer precipitation. *Clim. Dynam.* 54, 4641–4655. doi:10.1007/s00382-020-05251-0

Liu, F. and Wang, B. (2013). Mechanisms of global teleconnections associated with the asian summer monsoon: an intermediate model analysis*. *J. Clim.* 26, 1791–1806. doi:10.1175/jcli-d-12-00243.1

Liu, L., Zhou, T., Ning, L., Liu, J., Yan, M., Jin, C., et al. (2019). Linkage between the Arctic Oscillation and summer climate extreme events over the middle reaches of Yangtze River Valley. *Clim. Res.* 78, 237–247. doi:10.3354/cr01542

Liu, Q. Q. (2016). *Study on characteristics of the western North Pacific tropical cyclone types and its potential impact evaluation*. Tianjin, China: Tianjin University

Park, T.-W., Ho, C.-H., and Yang, S. (2011). Relationship between the arctic oscillation and cold surges over East Asia. *J. Clim.* 24, 68–83. doi:10.1175/2010JCLI3529.1

Rayner, N. A., Parker, D. E., Horton, E. B., Folland, C. K., AlexanderRowellKent, L. V. D. P. E. C., and Kaplan, A. (2003). Global analyses of sea surface temperature, sea ice, and night marine air temperature since the late nineteenth century. *J. Geophys. Res.* 108, 4407. doi:10.1029/2002JD002670

Sampe, T. and Xie, S.-P. (2010). Large-scale dynamics of the meiyu-baiu rainband: environmental forcing by the westerly jet*. *J. Clim.* 23, 113–134. doi:10.1175/2009jcli3128.1

Tao, S. Y. and Zhang, Q. Y. (1998). Response of asian winter and summer monsoon to ENSO events. (in Chinese). *Chin. J. Atmos. Sci.* 22, 399–407. doi:10.3878/j.issn.1006-9895.1998.04.02

Taylor, K. E., Ronald, J. S., and Meehl, G. A. (2012). An overview of CMIP5 and the experiment design. *Bull. Am. Meteorol. Soc.* 93, 14. doi:10.1175/BAMS-D-11-00094 .110.1175/bams-d-11-00094.1

Thompson, D. W. J. and Wallace, J. M. (1998). The Arctic Oscillation signature in the wintertime geopotential height and temperature fields. *Geophys. Res. Lett.* 25, 1297–1300. doi:10.1029/98GL00950

Wang, B., Li, J., and He, Q. (2017). Variable and robust East Asian monsoon rainfall response to El Niño over the past 60 years (1957-2016). *Adv. Atmos. Sci.* 34, 1235–1248. doi:10.1007/s00376-017-7016-3

Wang, B., Liu, J., Yang, J., Zhou, T., and Wu, Z. (2009). Distinct principal modes of early and late summer rainfall anomalies in East Asia*. *J. Clim.* 22, 3864–3875. doi:10.1175/2009JCLI2850.1

Wang, B., Xiang, B., and Lee, J.-Y. (2013). Subtropical high predictability establishes a promising way for monsoon and tropical storm predictions. *Proc. Natl. Acad. Sci. Unit. States Am.* 110, 2718. doi:10.1073/pnas.1214626110

Wang, H. J., Yang, Z. B., Yang, D. C., and Gong, X. C. (2007). Automatic quality control method and application of real-time data of automatic weather station (in Chinese). *Meteorol. Mon.* 33, 102–106. doi:10.3969/j.issn.1000-0526.2007.10.015

Wang, L., Hu, H., and Yang, X. (2019). The atmospheric responses to the intensity variability of subtropical front in the wintertime North Pacific. *Clim. Dynam.* 52 (9-10), 5623–5639. doi:10.1007/s00382-018-4468-9

Wang, B., Wu, R., and Fu, X. (2000). Pacific-East Asian teleconnection: how does ENSO affect East Asian climate?). pacific–East Asian teleconnection: how does ENSO affect East Asian climate?. *J. Clim.* 13, 1517–1536. doi:10.1175/1520-0442(2000)013<1517:PEATHD>2.0.CO;2

Wang, B., Wu, R., and Li, T. (2003). Atmosphere-warm ocean interaction and its impacts on asian-Australian monsoon variation*. *J. Clim.* 16, 1195–1211. doi:10.1175/1520-0442(2003)16<1195:AOIAII>2.0.CO;2

Wilks, D. S. (2011). *Statistical methods in the atmospheric sciences*. Cambridge, UK: Academic Press

Wu, B. Y., Bian, L. G., and Zhang, R. H. (2004). Effects of the winter AO and the arctic sea ice variations on climate variations over East Asia. *Chin. J. Polar Res.* 16, 211–220. doi:10.1007/BF02873097

Xiang, B., Wang, B., Yu, W., and Xu, S. (2013). How can anomalous western North Pacific subtropical high intensify in late summer?. *Geophys. Res. Lett.* 40, 2349–2354. doi:10.1002/grl.50431

Xie, S.-P., Hu, K., Hafner, J., Tokinaga, H., Du, Y., Huang, G., et al. (2009). Indian ocean capacitor effect on indo-western pacific climate during the summer following El Niño. *J. Clim.* 22, 730–747. doi:10.1175/2008JCLI2544.1

Xie, S.-P., Kosaka, Y., Du, Y., Hu, K., Chowdary, J. S., and Huang, G. (2016). Indo-western Pacific ocean capacitor and coherent climate anomalies in post-ENSO summer: a review. *Adv. Atmos. Sci.* 33, 411–432. doi:10.1007/s00376-015-5192-6

Xing, W., Wang, B., and Yim, S.-Y. (2016). Peak-summer East Asian rainfall predictability and prediction part I: southeast Asia. *Clim. Dynam.* 47, 1–13. doi:10.1007/s00382-014-2385-0

Xing, W., Wang, B., Yim, S. Y., and Ha, K. J. (2017). Predictable patterns of the may-june rainfall anomaly over East Asia. *J. Geophys. Res. Atmos.* 122, 2203–2217. doi:10.1002/2016JD025856

Xue, F. and Liu, C. (2008). The influence of moderate ENSO on summer rainfall in eastern China and its comparison with strong ENSO. *Chin. Sci. Bull.* 53, 791–800. doi:10.1007/s11434-008-0002-5

Xue, F., Zeng, Q., Huang, R., Li, C., Lu, R., and Zhou, T. (2015). Recent advances in monsoon studies in China. *Adv. Atmos. Sci.* 32, 206–229. doi:10.1007/s00376-014-0015-8

Yang, S. and Lau, K. M. (2006). "Interannual variability of the Asian monsoon," in *The asian monsoon*. Editor B. Wang (New York, USA: Springer), 259–293

Ye, H. and Lu, R. (2011). Subseasonal variation in ENSO-related East Asian rainfall anomalies during summer and its role in weakening the relationship between the ENSO and summer rainfall in eastern China since the late 1970s. *J. Clim.* 24, 2271–2284. doi:10.1175/2010jcli3747.1

Yuan, Y. and Yang, S. (2012). Impacts of different types of El Niño on the east asian climate: focus on ENSO cycles. *J. Clim.* 25, 7702–7722. doi:10.1175/jcli-d-11-00576.1

Zhang, R., Sumi, A., and Kimoto, M. (1999). A diagnostic study of the impact of El Niño on the precipitation in China. *Adv. Atmos. Sci.* 16, 229–241. doi:10.1007/BF02973084

Zhang, R., Sumi, A., and Kimoto, M. (1996). Impact of El Niño on the east asian monsoon. *J. Meteorol. Soc. Jpn.* 74, 49–62. doi:10.2151/jmsj1965.74.1_49

Zhang, Z., Zhang, J. X., and Xue, H. F. (2008). Improved K-means clustering algorithm. *Congress on Image and Signal Processing* 5, 169–172

Zhou, X., Liu, F., Wang, B., Xiangau, B., Xing, C., and Wang, H. Different responses of east asian summer rainfall to El Niño decays. *Clim. Dynam.* 53, 1497–1515. doi:10.1007/s00382-019-04684-6

Conflict of Interest: The authors declare that the research was conducted in the absence of any commercial or financial relationships that could be construed as a potential conflict of interest.

frontiers in Earth Science

ORIGINAL RESEARCH
published: 11 January 2021
doi: 10.3389/feart.2020.599447

Interdecadal Change of the Winter-Spring Tropospheric Temperature Over Asia and its Impact on the South China Sea Summer Monsoon Onset

Junli You[1,2], Maoqiu Jian[1,3]*, Si Gao[1,3]* and Jingjiu Cai[4]

[1]School of Atmospheric Sciences, Center for Monsoon and Environment Research and Guangdong Province Key Laboratory for Climate Change and Natural Disaster Studies, Sun Yat-Sen University, Zhuhai, China, [2]Lishui Meteorological Bureau, Lishui, China, [3]Southern Marine Science and Engineering Guangdong Laboratory (Zhuhai), Zhuhai, China, [4]Guangdong Meteorological Observatory, Guangzhou, China

Edited by:
Yoshiyuki Kajikawa,
RIKEN Center for Computational Science, Japan

Reviewed by:
Chao He,
Jinan University, China
Wen Chen,
Institute of Atmospheric Physics (CAS), China

***Correspondence:**
Maoqiu Jian
eesjmq@mail.sysu.edu.cn
Si Gao
gaosi5@mail.sysu.edu.cn

Specialty section:
This article was submitted to Atmospheric Science, a section of the journal Frontiers in Earth Science

Received: 27 August 2020
Accepted: 30 November 2020
Published: 11 January 2021

Citation:
You J, Jian M, Gao S and Cai J (2021) Interdecadal Change of the Winter-Spring Tropospheric Temperature Over Asia and its Impact on the South China Sea Summer Monsoon Onset. Front. Earth Sci. 8:599447. doi: 10.3389/feart.2020.599447

The interdecadal change of the winter-spring tropospheric temperature over Asia and its impact on the South China Sea summer monsoon (SCSSM) onset are investigated in this study. The SCSSM onset experiences a significant advance around the mid-1990s, which is attributed to the positive interdecadal anomaly of meridional temperature gradient in the mid-upper troposphere in May over the South China Sea monsoon region. This positive interdecadal anomaly can be traced back to the previous winter and spring, mainly associated with the mid-upper tropospheric warming in the East Asian subtropics. During the interdecadal anomalous seasonal evolution of the East Asian subtropical mid-upper tropospheric temperature, advection of the warm temperature anomaly by climatological mean wind overtakes the effects of anomalous adiabatic cooling and diabatic cooling, leading to a net interdecadal seasonal warming in winter. In spring, the adiabatic heating caused by the interdecadal anomalous subsidence flow cannot offset the effects of interdecadal anomalous cold advection and diabatic cooling, resulting in a net interdecadal seasonal cooling. However, the interdecadal seasonal cooling in spring is not strong enough to offset the interdecadal seasonal warming in winter, preserving an interdecadal mid-upper tropospheric warming over the subtropical East Asia in late spring. This interdecadal warming provides a favorable condition for the interdecadal advance of the SCSSM onset. Both observational analyses and numerical experiments suggest that the interdecadal change of atmospheric thermodynamic processes in winter–spring is related to the interdecadal warming in the tropical western Pacific. The enhanced convection and condensation heating over the regions from the South China Sea to the Philippines, forced by the tropical western Pacific warming, stimulates an anomalous anticyclone in the upper troposphere and warming in the whole troposphere over the subtropical East Asia.

Keywords: south China sea summer monsoon, onset, interdecadal change, tropospheric temperature, sea surface temperature

INTRODUCTION

The South China Sea (SCS) is located in the center of the Asian-Australian monsoon system, connecting the Indian Ocean and the Pacific. The SCS summer monsoon (SCSSM) affects not only the local climate, but also other areas through the energy and water cycle, and is closely associated with other monsoon systems (Murakami and Matsumoto, 1994; Wang et al., 2009; Jiang et al., 2018). The onset of SCSSM marks the end of the dry season in East Asia and the northwest Pacific, accompanied by the arrival of the summer rainy season. With the stepwise northward advance of the summer monsoon in East Asia, the monsoon rainband is established in South China, the Yangtze and Yellow River Basins in sequence, and Baiu in Japan and Changma in Korea occur at last (Tao and Chen, 1987; Ding, 1992; Qian et al., 2002; Wang and Lin, 2002; Ding and Chan, 2005). The abnormal onset timing of SCSSM has a great impact on the distribution of precipitation in eastern China, and even causes disasters such as floods and droughts. Some studies suggested that the relationship between the SCSSM onset and the precipitation over eastern China is regulated by the thermal state of the western Pacific warm pool. When the tropical western Pacific warm pool warms up, there is enhanced convection over the region from the Philippines across the SCS to the Indo-China peninsula, resulting in an early onset of SCSSM and more obvious northward jump of the western Pacific subtropical high, and eventually leading to less precipitation in the middle and lower reaches of the Yangtze River and more precipitation in the northern part of China, and vice versa (Huang and Sun, 1994; Huang et al., 2005). He and Zhu (2015) further pointed out that the positive (negative) SST anomaly in the tropical Indian Ocean in spring and summer can excite an anomalous anticyclone (cyclone) over the western Pacific via stimulating the Kelvin wave response, resulting in late (early) SCSSM onset and more (less) precipitation over lower reaches of the Yangtze River and the south of Japan from May to September. Actually, the SCSSM onset shows distinctive interannual and interdecadal variabilities (Wang et al., 2009; Kajikawa et al., 2012; Kajikawa and Wang, 2012; Xiang and Wang, 2013; Yuan and Chen, 2013; Luo and Lin, 2017). Therefore, it is of great significance to better understand the influence factors and physical mechanisms affecting the SCSSM onset.

Li and Yanai (1996) indicated that the Asian summer monsoon is first established in the Bay of Bengal, and then erupts successively in the Indo-China Peninsula and the SCS, and the Indian monsoon breaks out at last. Such sequence of the Asian summer monsoon onset is consistent with the seasonal reversal of the meridional temperature gradient (MTG) in the mid-upper troposphere south of Tibetan Plateau. As for climatological mean state, the SCSSM outbreaks in mid-May with the transition from easterlies to westerlies in the lower troposphere and from westerlies to easterlies in the upper troposphere, and MTG switches from negative to positive over the SCS. The positive mid-upper tropospheric MTG provides a favorable thermal condition for maintaining the circulation background of easterly vertical shear over the SCS and the SCSSM onset (Jian and Luo, 2001; Wu and Wang, 2001). The seasonal reversal of the MTG over the SCS is caused by a faster seasonal rising in the mid-upper tropospheric temperature over the northern SCS and surrounding area, which is primarily contributed by the warm advection process, than over the equatorial region (Jian and Luo, 2001). Mao et al. (2004) also suggested that the Asian summer monsoon onset is closely associated with the MTG overturning in the mid-upper troposphere.

Recently, many studies revealed that the SCSSM onset showed a significant interdecadal advance around 1993/94 (Kajikawa and Wang, 2012; Kajikawa et al., 2012; Xiang and Wang, 2013; Yuan and Chen, 2013; Luo and Lin, 2017). Kajikawa and Wang (2012) suggested the interdecadal warming of the western tropical Pacific accounts for the interdecadal advance of the SCSSM onset. Yuan and Chen (2013) further explained that the interdecadal warming of the tropical western Pacific leads to active convection over there and early eastward retreat of the western Pacific subtropical high, which favors the early onset of the SCSSM. Lin and Zhang (2020) suggested that the interdecadal warming over the western equatorial Pacific modulates the low-level zonal winds around the Kalimantan Island, which affects the subtropical high and the interdecadal advanced SCSSM onset. Xiang and Wang (2013) found more specific results that the early onset of the summer monsoon in the Arabian Sea and the Bay of Bengal is mainly regulated by the zonal sea surface temperature (SST) gradient in the equatorial Pacific, while the early onset of the SCSSM is mainly attributed to the positive SST anomaly near the Philippine Sea.

The previous studies mainly emphasize the influence of SST on the atmospheric circulation and the SCSSM onset, while the influence of the tropospheric temperature in the Asian monsoon region on the interdecadal advanced SCSSM onset around 1993/94 is less explored in terms of internal thermodynamic mechanisms and related external SST forcing. Specifically, the interdecadal change of the tropospheric temperature over the Asian monsoon region from winter to spring and its relationship with the interdecadal advanced SCSSM onset, as well as the responsible thermodynamic mechanisms and the influence of the interdecadal SST warming over the tropical Pacific are still unclear. It should be noted that not only the spring season but also the winter season have been concerned in this study, because the pronounced interdecadal warming in the winter troposphere over the subtropical East Asia plays a pivotal role on the interdecadal advanced SCSSM onset around 1993/94, which has been authenticated in this study. The aim of this study is to address the above issues. This paper is organized as follows. The datasets and methods are described in *Datasets and Methods*. *SCSSM Onset-Related Interdecadal Change of Mid-Upper Tropospheric Temperature over Asia in Winter-Spring* illustrates the SCSSM onset-related interdecadal change of the mid-upper tropospheric temperature over the Asian monsoon region in winter and spring. The seasonal evolution and the thermodynamic mechanisms of interdecadal change of the mid-upper tropospheric temperature over the East Asian subtropics are investigated in *Mechanisms for Interdecadal Warming over East Asian Subtropics*. Then, *Interdecadal Change of Tropical Western Pacific SST and its Impacts* discusses the effect of the interdecadal change in Indo-Pacific SST on the mid-upper tropospheric warming over the East Asian subtropics in winter and spring, based on diagnostic analyses. *Simulation of the Impacts of Diabatic Heating Anomalies Around the SCS and Philippines* presents the simulations of the impact of diabatic

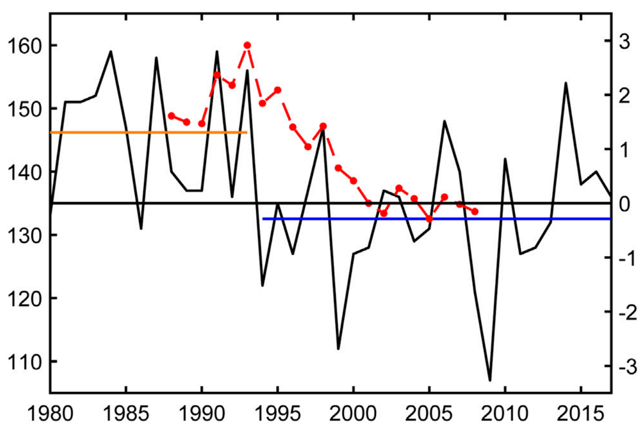

FIGURE 1 | Time series of the SCSSM onset date during 1980–2017. The left Y-axis is the sequence number of day for the SCSSM onset date from 1 January (day). Orange and blue lines denote the mean onset date in 1980–1993 and 1994–2017, respectively. Red dashed curve is the 9 years sliding *t*-test value (right Y-axis).

heating over the SCS-Philippines on the interdecadal advanced SCSSM onset. Finally, a summary and a discussion are presented in *Summary and Discussion*.

DATASETS AND METHODS

Datasets

The datasets used in this study are the European Center for Medium–Range Weather Forecasts (ECMWF) Interim reanalysis dataset (ERA-Interim; Dee et al., 2011) during the period 1979–2017, including four times daily (00, 06, 12 and 18 UTC) data and monthly mean data of wind, temperature and specific humidity at 18 standard pressure levels from 1,000 hPa to 100 hPa, with a horizontal resolution of 2.5 × 2.5°. In addition, the monthly mean SST data during 1979–2017 are from the Hadley Center (HadISST) with horizontal resolution of 1 × 1° (Rayner et al., 2003).

Definition of the SCSSM Onset Date

According to Lin et al. (2013), the SCSSM onset date is defined to be the first day when the steady westerlies at 850 hPa and easterlies at 250 hPa establish over the SCS region (5°–17.5°N, 110°–120°E) and last for at least 5 days.

Calculation of the Apparent Heat Source

The apparent heat source Q_1 (e.g., Yanai et al., 1973) in this paper is computed by the thermodynamic equation

$$c_p\left[\frac{\partial T}{\partial t} + V\cdot\nabla T + \left(\frac{p}{p_0}\right)^{\kappa}\omega\frac{\partial\theta}{\partial p}\right] = Q_1 \tag{1}$$

where T is air temperature, θ the potential temperature, V the horizontal wind, ω the vertical p-velocity, $\kappa = R/c_p$, R and c_p are the gas constant and the specific heat at constant pressure of dry air, and $p_0 = 1{,}000$ hPa.

For convenience, let

$$Q_{11} = c_p\frac{\partial T}{\partial t},\ Q_{12} = c_pV\cdot\nabla T,\ Q_{13} = c_p\left(\frac{p}{p_0}\right)^{\kappa}\omega\frac{\partial\theta}{\partial p} \tag{2}$$

Then, **Eq. 1** can be rewritten as

$$Q_{11} = -Q_{12} - Q_{13} + Q_1 \tag{3}$$

Where Q_{11}, $-Q_{12}$ and $-Q_{13}$ are the local temperature change, the horizontal temperature advection and the vertical adiabatic heating, respectively. The apparent heat source Q_1 is calculated with four times daily data, and then daily mean values are derived.

In addition, since this study will discuss the inter-monthly temperature change, it is necessary to give the thermodynamic expression for determining the monthly mean temperature change between two adjacent months as **Eq. 4**, and its derivation is shown in Appendix in detail, according to the thermodynamic equation and assuming each month has 30 days.

$$\begin{aligned}\left(\sum_{n=1}^{30}T_{i,n} - \sum_{n=1}^{30}T_{i-1,n}\right)\Big/30 = \Delta t\,\big[&\left(F_{i,29}+F_{i,28}\right) + 2\left(F_{i,27}+F_{i,26}\right)\\ &+ 3\left(F_{i,25}+F_{i,24}\right) + \cdots + 14\left(F_{i,3}\right.\\ &\left.+ F_{i,2}\right) + 15\left(F_{i,1}+F_{i-1,30}\right)\\ &+ 14\left(F_{i-1,29}+F_{i-1,28}\right) + \cdots\\ &+ 2\left(F_{i-1,5}+F_{i-1,4}\right)\\ &+ \left(F_{i-1,3}+F_{i-1,2}\right)\big]/15\end{aligned} \tag{4}$$

where $T_{i,n}$ is the daily mean temperature on the n-th day of the i-th calendar month, F the net effect of all thermal forcing terms on the right side of **Eq. 3**.

Linear Baroclinic Model

The linear baroclinic model (LBM; Watanabe and Kimoto, 2000) employed in this study is a linearized version of the atmospheric circulation model developed at the Center for Climate System Research, University of Tokyo, and the National Institute for Environmental Studies in Japan. In the numerical experiments, a horizontal resolution of T42 and 20 vertical levels in sigma coordinate system are applied. The climatology of the ERA-Interim data during 1979–2017 is adopted for the basic fields in the LBM simulations in winter and spring. The simulation experiments in this study are run for 30 days, and the mean values of the last 10 days are adopted.

SCSSM ONSET-RELATED INTERDECADAL CHANGE OF MID-UPPER TROPOSPHERIC TEMPERATURE OVER ASIA IN WINTER-SPRING

Figure 1 presents the time evolution of SCSSM onset date during the past 38 years from 1980 to 2017. It can be noticed that the SCSSM onset date shows a pronounced interdecadal shift around 1993/1994, with later onsets during the first epoch from 1980 to 1993 and earlier onsets during the

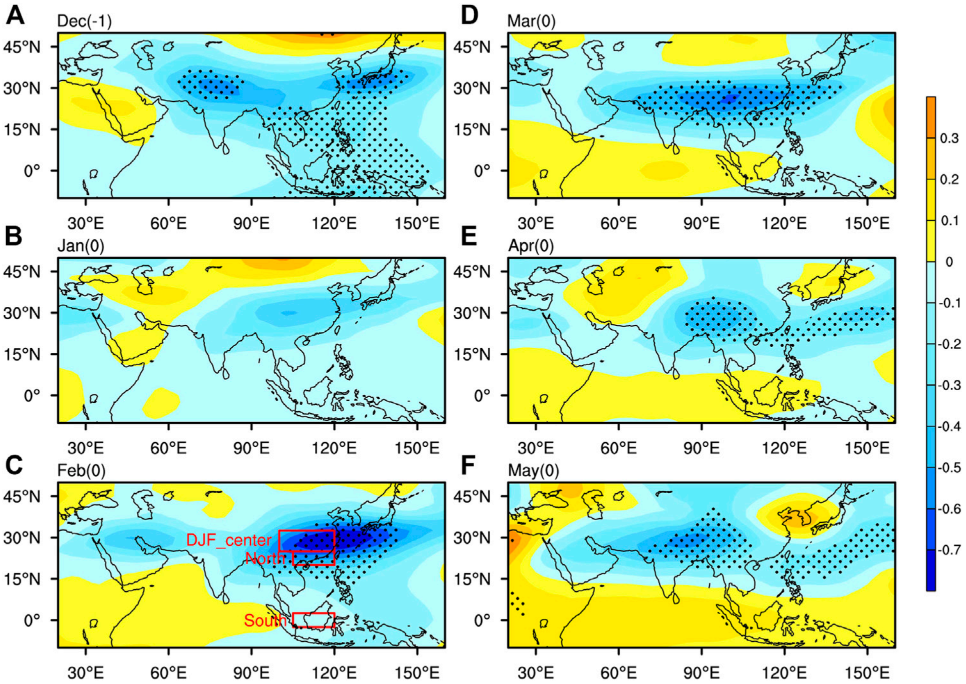

FIGURE 2 | Regressions of the monthly 500–200 hPa mean temperature against the SCSSM onset date from previous December to May. The regression coefficients significant at the 95% confidence level are stippled. The "DJF_center" is the demain (25°–32.5°N, 100°–120°E); "North" and "South" denote the northern domain (20°–25°N, 105°–120°E) and the southern domain (2.5°S–2.5°N, 105°–120°E) of the SCS, respectively.

second epoch from 1994 to 2017. The averaged onset dates are 26 May and 13 May during the two epochs, respectively. The interdecadal shift of SCSSM onset date around 1993/1994 is statistically significant at 95% confidence level according to the Student's *t* test, and this result is consistent with other studies (Kajikawa and Wang, 2012; Yuan and Chen, 2013; Lin and Zhang, 2020).

Climatologically, the reversal of vertical zonal wind shear and the MTG between 500–200 hPa are rapid over the SCS monsoon region during the SCSSM establishment, which can better evaluate the monsoon onset (Wu and Wang, 2001; Mao et al., 2004). Moreover, the seasonal evolution of the mid-upper tropospheric temperature difference between the subtropical continent and tropical ocean is the most striking. To reveal the SCSSM onset-related interdecadal change features of the mid-upper tropospheric (500–200 hPa) temperature change over East Asia, we conducted regression analysis on the 500–200 hPa mean temperature anomalies against the SCSSM onset date over the Asian monsoon region from winter to spring, and the results are shown in **Figure 2**. The spatial pattern mainly reflects the in-phase temperature variation in the Asian subtropics in winter and spring. In December (**Figure 2A**), two significant negative centers are located over the western part of Tibetan Plateau and East Asia, respectively. In January and February (**Figures 2B,C**), the main negative centers are over the East Asian subtropics. In spring (**Figures 2D–F**), the striking negative zones cover the subtropics of East Asia, with the centers over the eastern Tibetan Plateau. Considering the interdecadal advanced feature of the SCSSM onset, the abovementioned pronounced centers with negative regression coefficients over the East Asian subtropics imply that mid-upper temperature may also experience pronounced interdecadal warming in winter-spring. The SCSSM onset is closely related to the reversal of the MTG in the mid-upper troposphere over the SCS monsoon region. It is suggested that the positive temperature anomaly in the mid-upper troposphere over the East Asian subtropics in previous winter and following spring is conducive to an early seasonal reversal of the MTG over the SCS monsoon region, and then beneficial to the early onset of the SCSSM.

Figure 3 shows the normalized time series of the mid-upper tropospheric temperature in the winter center (25°–32.5°N, 100°–120°E) as shown in **Figure 2C**. It indeed presents a remarkable interdecadal warming trend. Both 1993 and 1998 were significant interdecadal shift points at 90% confidence level according to the 9 years sliding Student's *t*-test. Furthermore, the interdecadal advance of the SCSSM onset occurred around 1993/94, which is also the interdecadal turning point for the mid-upper tropospheric MTG anomalies over the South China Sea monsoon region in May (**Figure 4**), and the correlation of the MTG with the SCSSM onset date is −0.51 (over the 99% confidence level). These facts demonstrate that there exists an identical interdecadal shift point for the mid-upper tropospheric MTG over the SCS monsoon region and the SCSSM onset date. Therefore, we take 1993/94 as the interdecadal shift point in the following analyses for the two epochs, i.e., 1980–1993 and 1994–2017.

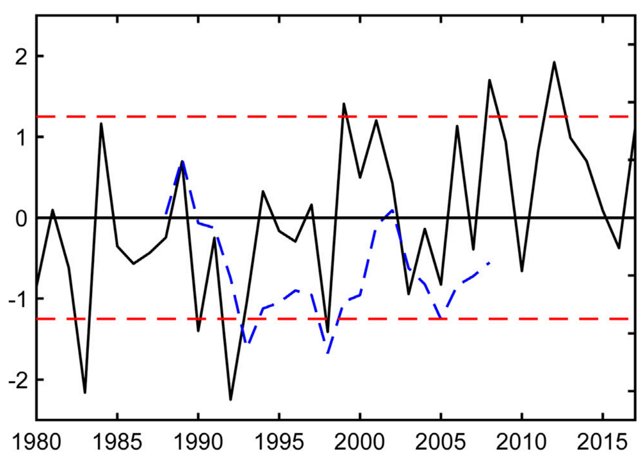

FIGURE 3 | Normalized time series (solid line) and its 9 years sliding t-test (blue dashed line) of 500–200 hPa mean temperature averaged in the winter center (25°–32.5°N, 100°–120°E) shown in **Figure 1C**. The red dashed lines denote the 90% confidence level of *t*-test.

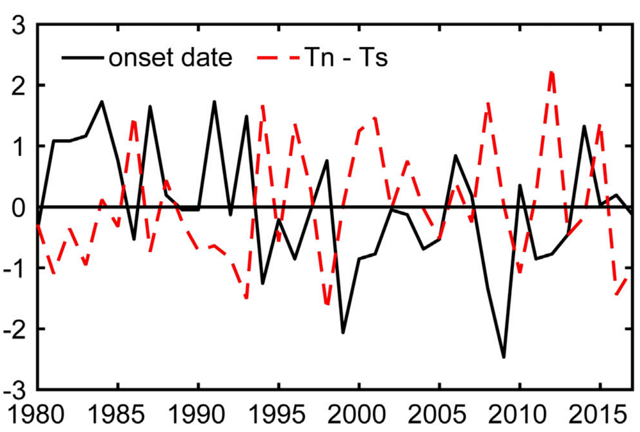

FIGURE 4 | Normalized time series of the 500–200 hPa mean MTG (TN–TS, red dashed line) between the northern domain (20°–25°N, 105–120°E) and the southern domain (2.5°S–2.5°N, 105°–120°E) of the SCS (as the boxes named "North" and "South" in **Figure 2C**, respectively) and the SCSSM onset date (black solid line) during 1980–2017.

MECHANISMS FOR INTERDECADAL WARMING OVER EAST ASIAN SUBTROPICS

Seasonal Evolution of the Interdecadal Change of Mid-upper Tropospheric Temperature

The interdecadal warming of the mid-upper troposphere around 1993/94 over the East Asian monsoon region is observed in all seasons, but the warming magnitudes vary with the seasons, which further leads to the season-dependent interdecadal change of the MTG. In autumn, the interdecadal warming in the mid-upper troposphere is more conspicuous over the tropics than over the subtropics of East Asia, resulting in weak negative MTG anomalies around the SCS monsoon region (**Figure 5A**). Conversely, the temperature increase is greater in the subtropics of East Asia than in the tropics in winter (**Figure 5B**), and therefore the interdecadal anomaly of the MTG over the SCS monsoon region turns from negative to positive. By comparing **Figures 5A,B**, the interdecadal warming magnitude over East Asia is larger in winter than in autumn, especially for southern China (**Figure 5D**). In spring (**Figure 5C**), the interdecadal warming pattern over the East Asian monsoon region is rather similar to that in winter, but the warming magnitude is significantly weakened. The seasonal evolution from winter to spring is characterized by relative cooling (**Figure 5E**). Since the interdecadal cooling of inter-seasonal change from winter to spring in the East Asian subtropics is less than the warming magnitude from autumn to winter, the East Asian subtropics eventually shows interdecadal warming of inter-seasonal change from autumn to spring, while the opposite occurs in the tropics (**Figure 5F**). Thus, an interdecadal pattern with positive MTG anomalies over the SCS monsoon region starts from winter and persists into spring (**Figures 5C,F**), which is conducive to the interdecadal advance of the SCSSM onset around 1993/94.

Based on **Figure 5**, it has been identified that the most prominent interdecadal warming in the mid-upper troposphere over the East Asian subtropics occurs in winter, which coincides well with the winter negative center in **Figure 1C**, and is accompanied by a pronounced interdecadal warming of inter-seasonal change from autumn to winter (**Figure 5D**). However, by examining the interdecadal temperature change month by month, it is verified that the warming over the East Asian subtropics is primarily attributed to the interdecadal warming of inter-monthly temperature changes from November to December and from January to February (see the red dashed line in **Figure 6**). On the contrary, an interdecadal cooling of the inter-seasonal temperature change is observed from December to January, and a more pronounced cooling is observed during February–March. The seasonal evolution of the interdecadal temperature change in the northern part of the SCS monsoon region is highly consistent with that in the winter center (**Figure 6**). Moreover, during July to November (except September), the interdecadal change of the mid-upper tropospheric temperature is larger over the southern part than the northern part of the SCS monsoon region, resulting in negative interdecadal MTG anomalies over the SCS. However, during the period of December to May, the interdecadal warming over the northern part of the SCS monsoon region is more pronounced than that over the southern part, therefore, the interdecadal MTG anomaly turns from negative to positive. The sustained positive interdecadal MTG anomalies over the SCS monsoon region during winter to spring, which is primarily attributed to the prominent interdecadal warming of inter-monthly temperature changes from November to December and from January to February over the East Asian subtropics,

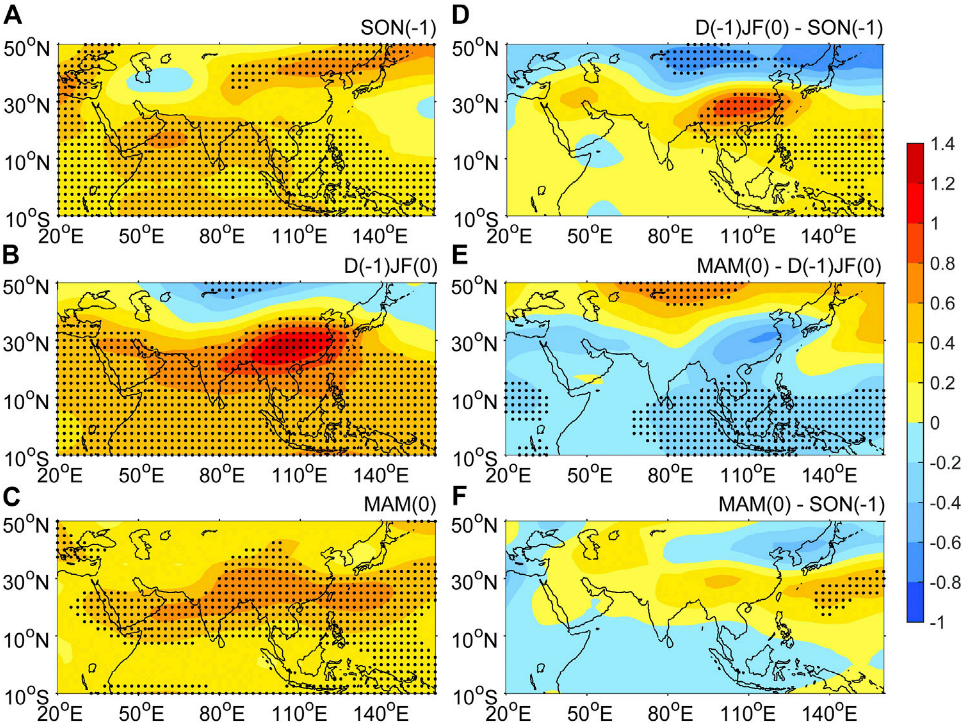

FIGURE 5 | Epochal differences (K) of the seasonal mean temperature **(left panel)** and the inter-seasonal change of temperature **(right panel)** in the 500–200 hPa layer. **Left panel: (A)** autumn (SON(−1)), **(B)** winter (DJF(0)), **(C)** spring (MAM(0)); **right panel: (D)** winter minus autumn, **(E)** spring minus winter, **(F)** spring minus autumn. Label "−1" denotes (1993–2016) minus (1979–1992), and "0" denotes (1994–2017) minus (1980–1993). The stippled areas denote the differences significant at the 95% confidence level.

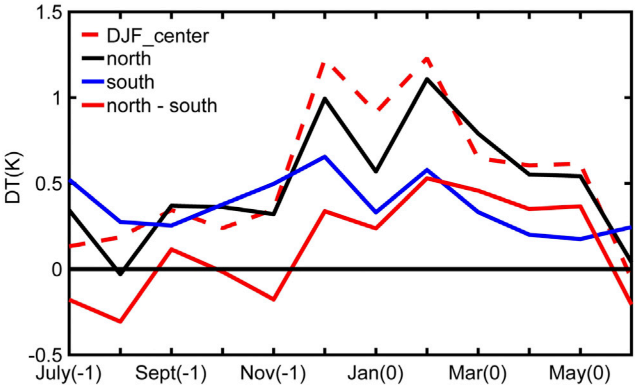

FIGURE 6 | Monthly evolution of the area-averaged 500–200 hPa temperature differences (K) between two epochs over the domain (DJF_center, 25°–32.5°N, 100°–120°E, red dashed line), the northern part (north, 20°–25°N, 105°–120°E, black solid line) and the southern part (south, 2.5°S–2.5°N, 105°–120°E, blue solid line) of the SCS monsoon region. The red solid line is epochal difference of the MTG (north–south). Numbers "−1" and "0" in brackets on the abscissa denote (1993–2016) minus (1979–1992) and (1994–2017) minus (1980–1993), respectively.

is pivotal to the interdecadal advance of the SCSSM onset around 1993/94.

Thermodynamic Mechanisms of Interdecadal Temperature Changes

The evolution of atmospheric temperature is attributed to various thermodynamic processes (e.g., horizontal temperature advection, vertical adiabatic heating, and diabatic heating) within the atmosphere. According to the relationship between the inter-monthly temperature change and the daily thermal forcing terms expressed as **Eq. 4**, we can clarify the specific thermodynamic processes and mechanisms responsible for the pronounced interdecadal change of the mid-upper tropospheric temperature over the East Asian subtropics during November to February and February to May.

Figure 7A shows the interdecadal differences of the inter-monthly temperature change rate in the mid-upper troposphere during November to February, and it is noticed that the pronounced warming center is located in the subtropical East Asia–northwestern Pacific. The warming center is formed with a primary contribution from the interdecadal enhancement of the horizontal advective heating (**Figure 7B**), and a slight positive contribution from the intensified diabatic heating along the East Asian coast and a small negative contribution in most areas within the range of 80°–100°E (**Figure 7C**). In contrast, the vertical adiabatic term shows a prominent cooling effect over the subtropical East Asia, indicating a negative contribution to the East Asian warming center (**Figure 7D**). Therefore, the

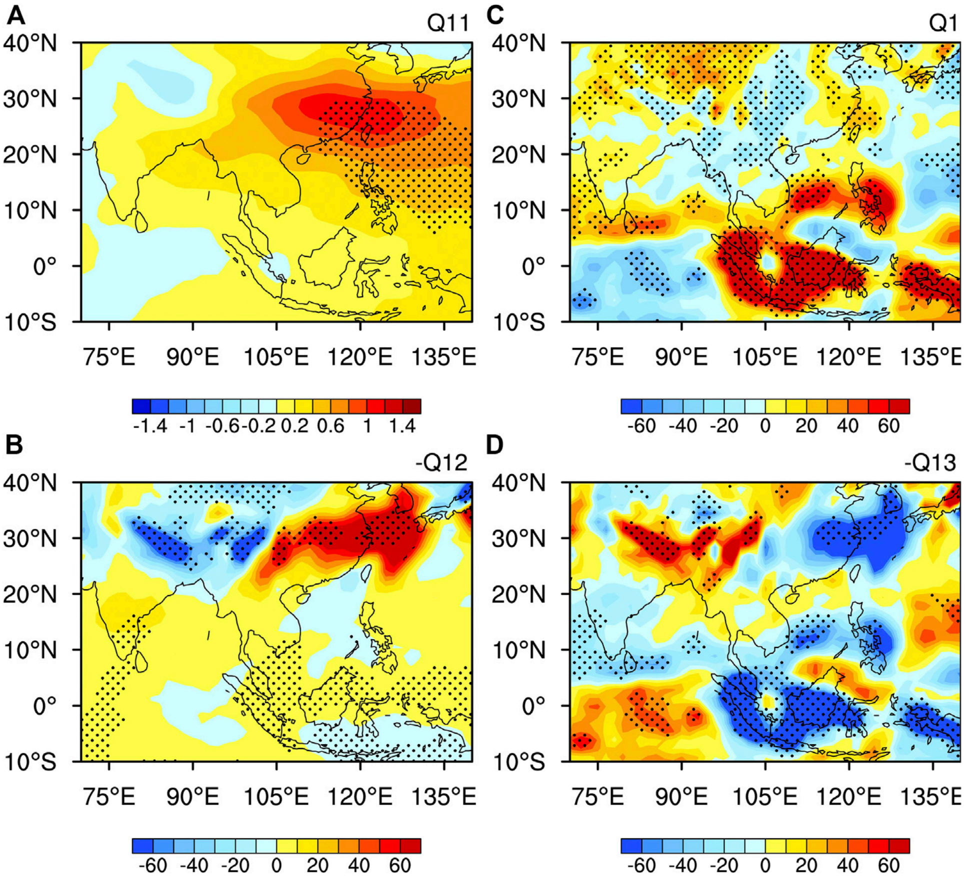

FIGURE 7 | Epochal differences (K) of the thermal forcing terms for the 500–200 h·Pa temperature change during November to February ((1994–2017) minus (1980–1993)). **(A)** Inter-monthly temperature change rate (Q11). **(B)** Temperature advection rate (–Q12). **(C)** Diabatic heating rate (Q1). **(D)** Adiabatic heating rate (–Q13). The stippled areas denote the difference significant at the 95% confidence level.

interdecadal warming center of inter-monthly temperature change in winter over the subtropical East Asia–northwestern Pacific is a result of significant abnormal horizontal advective heating, which could not be completely offset by abnormal adiabatic cooling and abnormal diabatic cooling. In addition, the warming over the northern SCS and South China is mainly caused by the interdecadal anomalous warm advection and diabatic heating. The tropical Indian Ocean within 5°–10°N, the SCS to the Philippines, and the Maritime Continent are mainly controlled by diabatic heating and adiabatic cooling associated with interdecadal anomalous ascending motion. The weak interdecadal warming due to inter-monthly temperature increment over the Maritime Continent from November to February is caused by abnormal diabatic heating and warm advection, partly counteracted by abnormal adiabatic cooling.

Further exploration indicates that the striking abnormal horizontal advective heating in the subtropical East Asia, as shown in **Figure 7B**, is mainly caused by the coordination of an interdecadal warming center over the eastern Tibetan Plateau and the climatologically prevailing westerlies over the subtropical region of Asia (**Figure 8A**). In contrast, the climatological mean temperature field together with the interdecadal wind anomalies leads to interdecadal cold advection over the East Asia (**Figure 8B**).

Figure 9A shows the interdecadal differences of inter-monthly temperature increment in the mid-upper troposphere from February to May. The evident cooling is observed over East Asia and the tropics of Asian-Australian monsoon region, with a cooling center over the East Asia.

The interdecadal cooling over East Asia is mainly attributed to a joint effect of anomalous cold advection and diabatic cooling over there (**Figures 9B,C**). Further examination indicates that the interdecadal cold advection over East Asia is a composite result of strong cold advection, induced by the interdecadal northerly wind and the climatologically negative MTG in the East Asian mid-upper troposphere, and a weak warm advection caused by the negative anomalies of zonal temperature gradient and the climatological westerlies (**Figures 8C,D**). Moreover, the aforementioned interdecadal diabatic cooling over East Asia is associated with interdecadal anomalous downdraft (**Figure 10C**). However, the adiabatic heating associated with the abnormal subsidence contributes positively to the warming over East Asia (**Figure 9D**), and its intensity cannot counteract the effects of

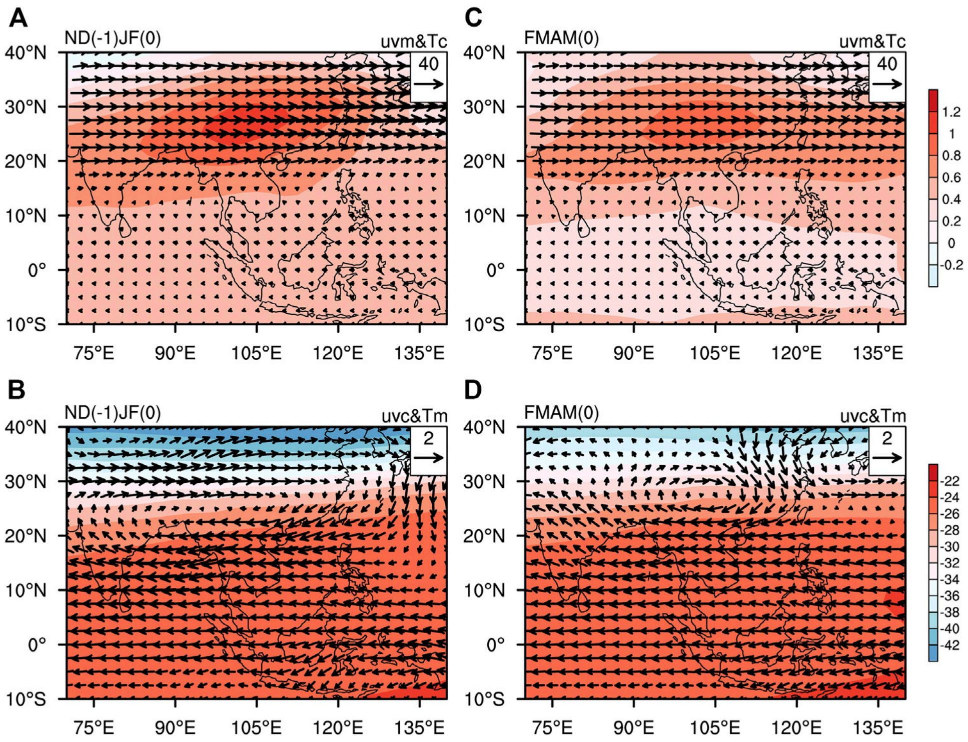

FIGURE 8 | (A) Climatologically mean 500–200 hPa wind (arrows, m/s) and the epochal differences of the 500–200 hPa temperature (color shading, K) in November–February. **(B)** Climatologically mean 500–200 hPa temperature (color shading, K) and the epochal differences of 500–200 hPa wind (arrow, m/s) in November–February. **(C)** Same as **(A)**, but for February–May. **(D)** Same as **(B)**, but for February–May. Climate-mean state: "(–1)" and " (0)" denote the mean state of 1979–2016 and 1980–2017, respectively. For the epochal difference, "(–1)" and "(0)" denote (1993–2016) minus (1979–1992), and (1994–2017) minus (1980–1993), respectively.

diabatic cooling and cold advection, thereby eventually leading to the cooling over East Asia.

In the tropics except the equatorial Indian Ocean, interdecadal cooling is mainly caused by the enhanced adiabatic cooling associated with the interdecadal enhancement of ascending motion (**Figures 9D**, **10C**), while the interdecadal cooling over the equatorial Indian Ocean results from the interdecadal weakening of diabatic heating caused by the weakened ascending motion (**Figures 9C**, **10C**).

INTERDECADAL CHANGE OF TROPICAL WESTERN PACIFIC SST AND ITS IMPACTS

In November-February, a horseshoe-shape pronounced interdecadal warming pattern appears in the tropical-subtropical western Pacific and a weak basin-wide warming in the tropical Indian Ocean. Meanwhile, the interdecadal change in the tropical central-eastern Pacific SST presents a wedge-type cooling pattern (**Figure 10B**). Corresponding to the above interdecadal SST change, interdecadal anomalous low-level cyclonic circulation exists over the SCS and the Bay of Bengal, anomalous low-level westerlies over the equatorial Indian Ocean, and anomalous low-level easterlies over the tropical central-western Pacific. Therefore, obvious interdecadal anomalous low-level convergence and upper-level divergence are observed over the Maritime Continent, the Philippines and nearby areas (**Figures 11A,B**), accompanied by interdecadal ascending motion (**Figure 10A**). Meanwhile, the interdecadal ascending motion over the East Asian coast to the Maritime Continent converges and sinks in north of the Bay of Bengal through vertical circulation, leading to vertical adiabatic warming over there. On the other hand, the enhanced convection over the regions from the SCS to the Philippines results in pronounced interdecadal intensified diabatic heating in the troposphere, resembling that shown in **Figure 7C**. Meanwhile, an interdecadal anomalous upper-level anticyclone is observed over the regions from the southern slope of the Tibetan Plateau to southern China (**Figure 10A**), which might be a response to the intensified diabatic heating forcing over the regions from the SCS to the Philippines (e.g., Liu et al., 1999); this is further demonstrated by model simulations in *Simulation of the Impacts of Diabatic Heating Anomalies Around the SCS and Philippines*. The above mentioned interdecadal anomalous upper-level anticyclone is accompanied by an interdecadal warming center in the mid-upper troposphere through hydrostatic balance (**Figure 5B**).

In February–May, the interdecadal change pattern of the tropical Indian Ocean-Pacific SST resembles that in November-February overall, indicating its long persistence

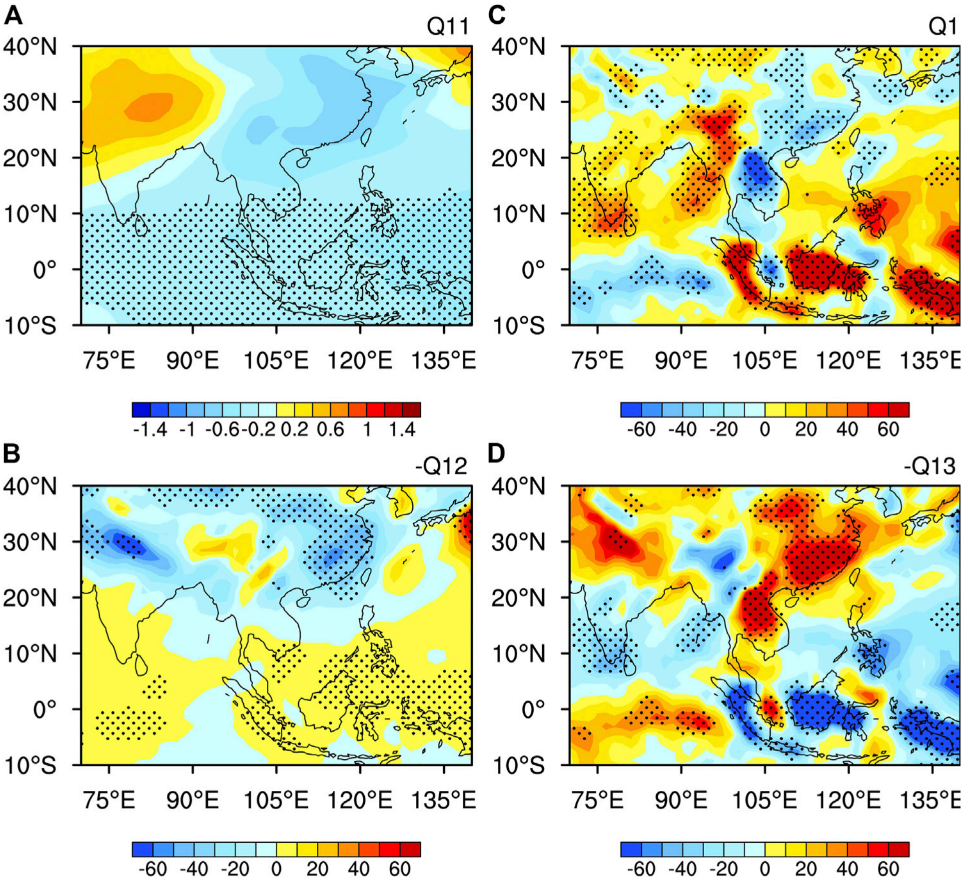

FIGURE 9 | As **Figure 7**, but for february-may.

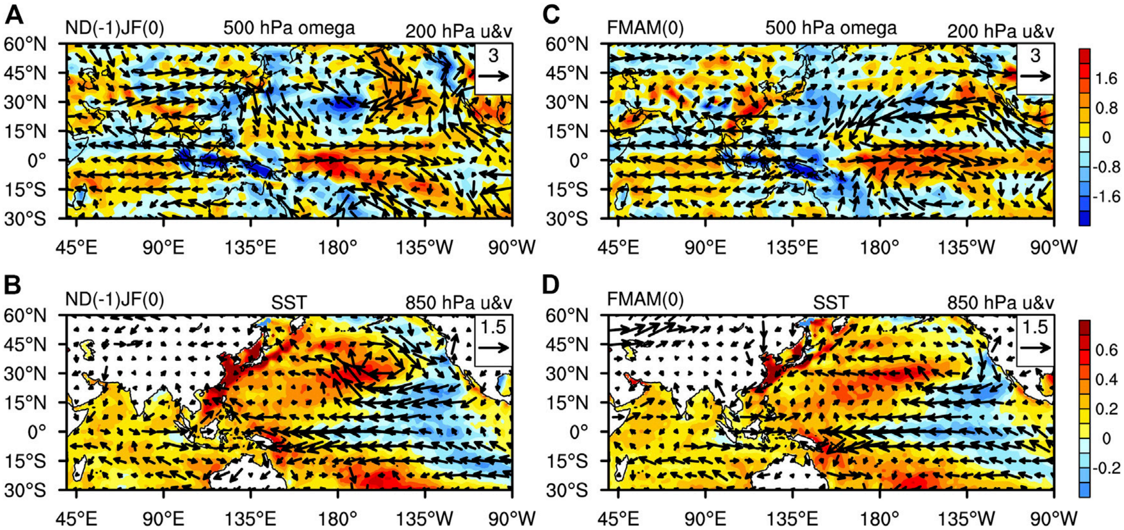

FIGURE 10 | Epochal differences of **(A)** 200 hPa wind (arrows, m/s) with 500 hPa p-velocity (shading, 10^{-2} Pa/s), and **(B)** 850 hPa wind (arrows, m/s) with SST (shading, K) for November–February. **(C)**, **(D)** same as **(A)**, **(B)** but for February–May. "(1)" denotes (1993–2016) minus (1979–1992), " (0)" denotes (1994–2017) minus (1980–1993).

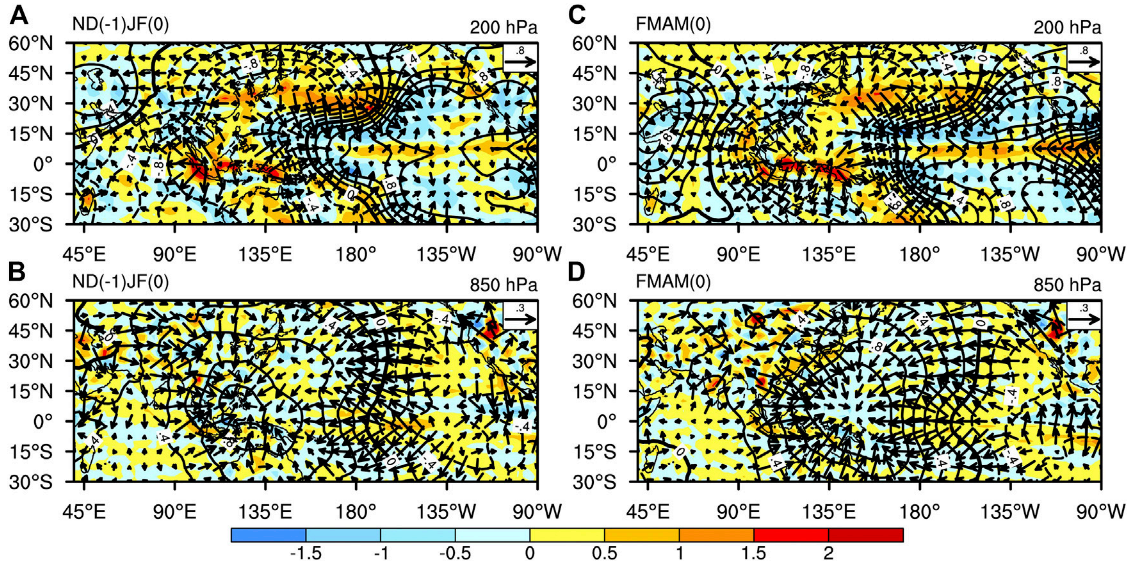

FIGURE 11 | (A) Epochal differences of divergent wind (arrows, m/s), divergence (shading, 10^{-6}/s) and velocity potential function (contours, 106 m^2/s) at 200 hPa and for November–February. **(B)** Same as **(A)**, but at 850 hPa and for November–February. **(C)** Same as **(A)**, but for February–May. **(D)** Same as **(B)**, but for February–May. "(1)" denotes (1993–2016) minus (1979–1992), and "(0)" denotes (1994–2017) minus (1980–1993).

(**Figure 10D**). However, the interdecadal warming center of the western Pacific SST has changed. Compared with the winter pattern, the positive SST anomalies in the East Asian coast and its adjacent areas weaken or even turn to be negative, and the positive SST anomaly center in the western equatorial Pacific weakens and moves southeastward to the tropical South Pacific Ocean northeast of Australia, and the interdecadal anomalous southwest–northeast-oriented warm center in the northwestern Pacific becomes significantly prominent. The pronounced interdecadal warming regions in the western Pacific induce an anomalous convergence center in the lower troposphere with an anomalous divergence center in the upper troposphere (**Figures 11C,D**), accompanied by interdecadal ascending motion (**Figure 10C**). The interdecadal intensified diabatic heating over the southern Philippines and the eastern Maritime Continent is caused by the obvious anomalous ascending motion (**Figure 9C**), and it stimulates an anomalous low-level cyclone over the SCS and the Philippine Sea through the Rossby-wave response (Gill, 1980). Such anomalous atmospheric circulation is conducive to the weakening and eastward retreat of the subtropical high over the SCS, beneficial to the early onset of the SCSSM. The anomalous updraft over the tropical western Pacific converges and sinks in southern China through vertical circulation (**Figure 11C**), resulting in adiabatic heating over there. In addition, similar to the situation in winter described above, the enhanced convection with the intensified condensation heating over the western Pacific may excite an anomalous upper-level anticyclone to the northwest side of the heating center, leading to the mid-upper tropospheric warming over this region (**Figures 5C, 10C**).

The above results demonstrate that in winter and spring, the interdecadal positive SST anomalies in the Maritime Continent-tropical western Pacific force enhanced convection and diabatic heating over there. The heterogeneous diabatic heating plays an important role in exciting an anomalous anticyclone and warming in the mid-upper troposphere over the East Asian subtropics.

SIMULATION OF THE IMPACTS OF DIABATIC HEATING ANOMALIES AROUND THE SCS AND PHILIPPINES

A simple baroclinic model (LBM, Watanabe and Kimoto, 2000) is applied to further verify the impacts of the western Pacific SST anomalies on the temperature and circulation change over the subtropical East Asian monsoon region mentioned in the previous section.

In order to achieve a better response of the atmosphere to the SST forcing, the prescribed forcing employs the atmospheric apparent heat source (Q_1) forcing rather than the SST forcing itself. Actually, the diabatic heating in the atmosphere over the Indio-Pacific Oceans is induced by the underlying SST forcing. Based on the horizontal distribution of interdecadal differences in the observed Q_1 (**Figures 7C, 9C**), we specified the horizontal structure of the Q_1 forcing field as shown in **Figures 12A,B** around the SCS and the Philippine Sea, which has been also confirmed by the regressions of the diabatic heating in November–February and February–May against the interdecadal component of the SCSSM onset date (not shown), and set the vertical structure of Q_1 to a gamma distribution with the peak at the 0.55 sigma level (**Figure 12C**). With the aforementioned settings of the Q_1 forcing field, sensitivity experiments were performed for the basic field of November–February and February–May, respectively.

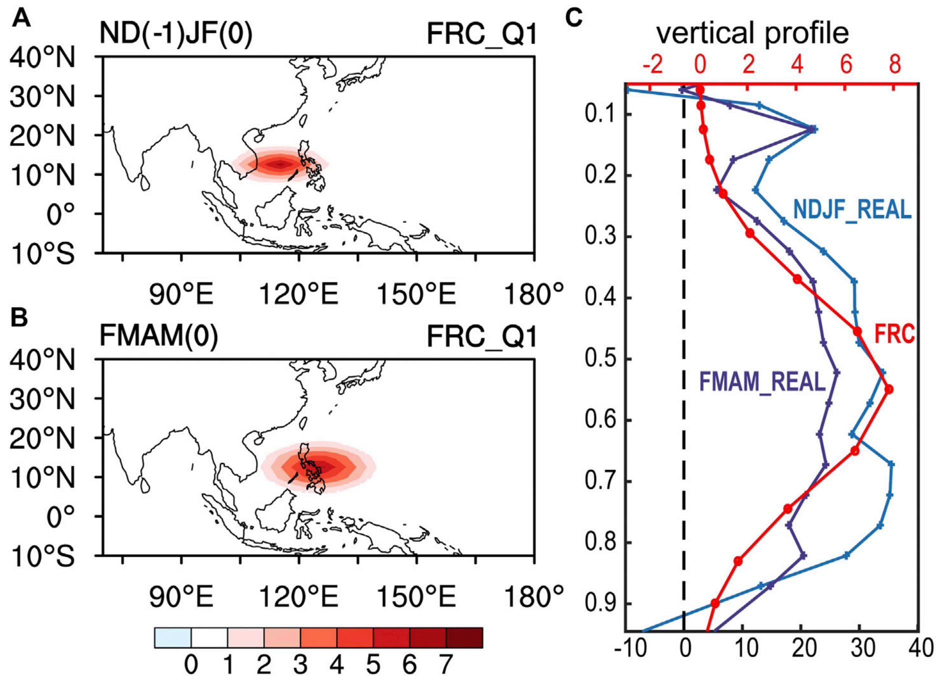

FIGURE 12 | Atmospheric heat source settings for the LBM numerical experiments. Horizontal distribution of the specified heat source (K/day) at the 0.55 sigma level in **(A)** November–February and **(B)** February–May. **(C)** Vertical profiles of the epochal differences of the area-averaged heat source observations (K, the lower abscissa) in the respective specified regions of **(A)** and **(B)** in November–February (NDJF_REAL, blue line) and February–May (FMAM_REAL, purple line), and the specified heat source at the forcing center (FRC, red line; K/day, the upper abscissa) in sigma coordinate.

Figure 13 shows the response of atmospheric circulation and the mid-upper tropospheric temperature to the atmosphere heating over the SCS-Philippines. Compared with the observations (left panel, **Figure 13**), the significant mid-upper tropospheric warming and upper-level anticyclone over the subtropical East Asian monsoon region can be well reproduced in both winter and spring (**Figures 13E,G**), although the simulated warming center in spring shifts slightly southward and the simulated warming magnitude in winter is larger compared to the observation. Especially, the distinct positive MTG anomalies in the mid-upper troposphere over the SCS monsoon region are well simulated qualitatively in winter and spring, with more obvious warming over the subtropical East Asia than over the Maritime Continent, which is beneficial to the interdecadal advance of the SCSSM onset. At low level, the anomalous cyclone near the SCS-Philippines has been also well simulated (**Figures 13H,F**). In general, the simulation results by the LBM in the East Asian monsoon region are quite similar to the observed interdecadal differences, indicating that the interdecadal SST warming in the tropical western Pacific have great impacts on the subtropical East Asian atmospheric circulation and tropospheric temperature through the convective heating. Here, we only consider the atmospheric heating over the SCS and the Philippines, and the influence of other ocean basins and other external forcings have not been taken into account. This may account for the differences between the simulation and the observation.

SUMMARY AND DISCUSSION

This study has examined the interdecadal change of the mid-upper tropospheric temperature over Asian monsoon region during winter and spring and its connection with the interdecadal advance of the SCSSM onset around 1993/94. We have further explored the specific physical processes and influence factors of the temperature change according to the interdecadal change of tropical Indo-Pacific SST and atmosphere circulation.

It is suggested that a significant interdecadal warming in the mid-upper troposphere over the subtropical East Asia in winter and spring is closely associated with the interdecadal advance of the SCSSM onset around 1993/94. The resulting enhanced MTG over the SCS monsoon region in winter and spring after 1994 provides a favorable thermal condition for the interdecadal early onset of the SCSSM.

In the mid-upper troposphere over the subtropical East Asia, there is an interdecadal warming due to the inter-monthly temperature increment during November–February, which is attributed to the striking anomalous horizontal advective heating in the subtropical East Asia caused by the coordination of an interdecadal warming center over the eastern Tibetan Plateau and the climatologically prevailing westerlies. While there is an interdecadal cooling due to the inter-monthly temperature reduction during February–May, which mainly results from the interdecadal anomalous cold advection, induced by the coordination of the interdecadal northerly wind anomalies and the climatologically negative

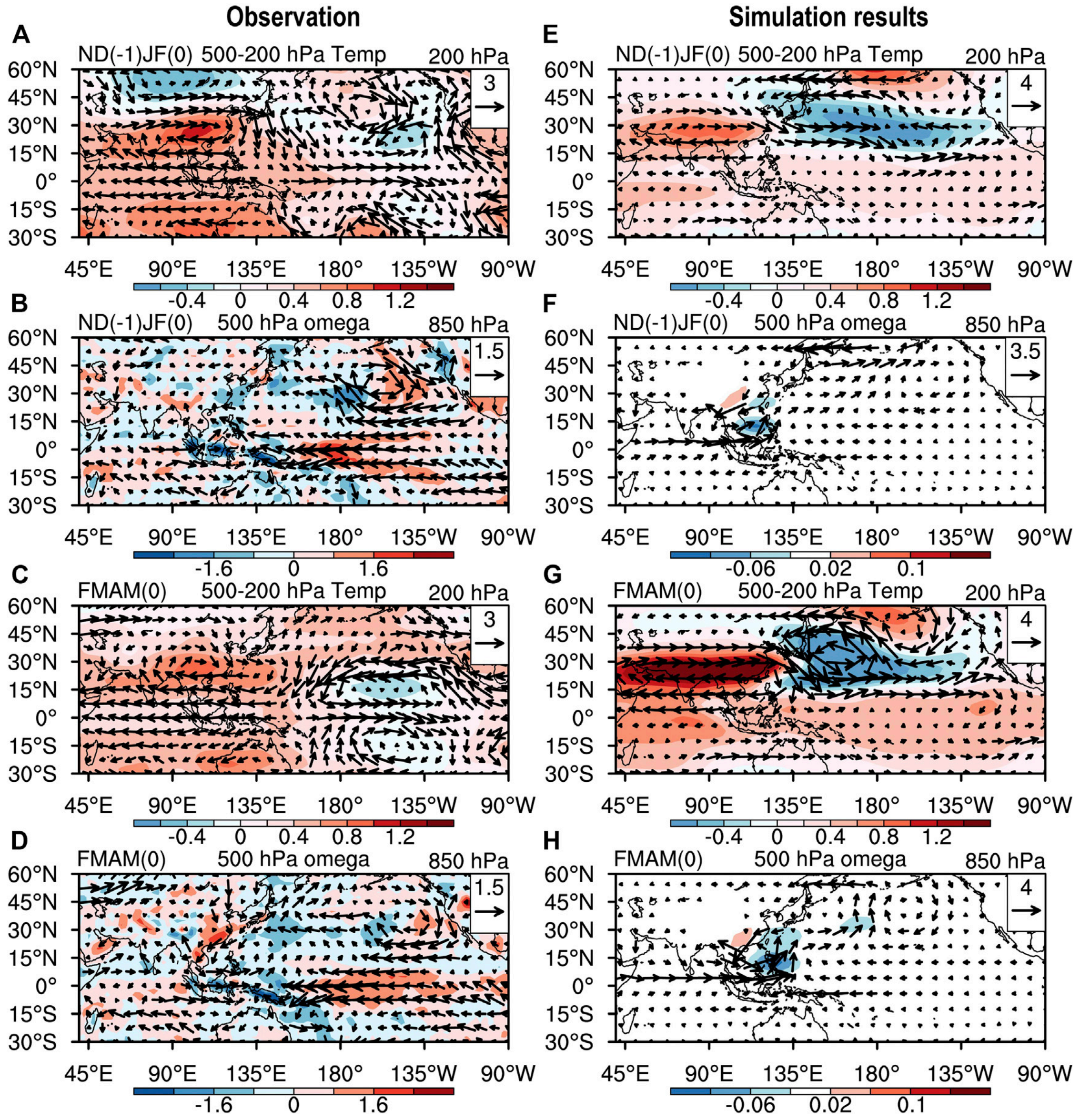

FIGURE 13 | Observation **(left panel)** and simulation **(right panel)** results of heat source forcing: **(A)**, **(E)** 200 hPa wind (vector, m/s) and mid-upper tropospheric temperature (shading, K) for November-February; **(B)**, **(F)** 850 hPa wind (vector, m/s) and 500 hPa *p*-velocity (shading, 10^{-2} Pa/s) for November-February. **(C)**, **(G)** same as **(A)**, **(E)** but for February–May. **(D)**, **(H)** same as **(B)**, **(F)** but for February–May.

MTG in the East Asian mid-upper troposphere, and diabatic cooling associated with interdecadal downdraft anomalies over East Asia. However, the interdecadal cooling during February–May is not intense enough to offset the interdecadal warming during November–February. Eventually, an interdecadal warming in the mid-upper troposphere remains over the subtropical East Asia at the end of spring, providing a favorable condition for the early onset of the SCSSM.

Furthermore, the interdecadal changes of tropical Indo-Pacific SST in winter and spring have great impacts on the interdecadal warming and atmospheric circulation anomalies over the East Asian subtropics. The interdecadal SST warming in the tropical western Pacific induces intensified convection and condensation heating over the SCS-the Philippine Sea and surrounding areas, exciting an anomalous anticyclone and a warming center in the mid-upper troposphere over the East Asian subtropics. These results are further confirmed by numerical experiments. There are some differences in the distribution of interdecadal tropical Indo-Pacific SST anomalies in winter and spring, leading to some differences in the interdecadal anomalies of atmospheric circulation and thermodynamic heating processes over the East Asian subtropics in two seasons. All the results provide a factual basis for understanding the thermodynamic origin of the interdecadal advance of the SCSSM onset around 1993/1994.

The variation of SST in different ocean basins may be related to each other. In addition to the interdecadal tropical Indo-Pacific warming, there also exists significant interdecadal warming in the North Atlantic. The Atlantic Multidecadal Oscillation (AMO) affects the tropical and regional SST through air-sea coupling (Lyu et al., 2017; Sun et al., 2017). As for interdecadal change, AMO can also influence the tropospheric temperature over Eurasia by adjusting the intensity and frequency of North Atlantic Oscillation (NAO) events (Goswami et al., 2006). This study mainly emphasizes the effects of the interdecadal change in tropical Indo-Pacific SST on the interdecadal warming of the East Asian troposphere, but the influence of the mid-high latitude signals and SST anomalies in other ocean basins on the interdecadal warming of the Asian subtropics in winter and spring remains to be further explored in the future.

It should be mentioned that the interdecadal change of the SCSSM onset around 1993/94 is not the sole turning point in recent 38 years. Another secondary turning point appeared around 1998/99 (**Figure 1**), which is also shown in the mid-upper temperature in winter over the subtropical East Asia as shown in **Figure 3**. This late 1990s shift has been detected by Huangfu et al. (2015), and they suggested that the large-scale atmospheric and oceanic change associated with this shift exhibits a more systematically significant interdecadal change signal around 1998/99. It was also emphasized that the late 1990s shift of the SCSSM onset was due to the interdecadal warming over the tropical western Pacific around late 1990s (Huangfu et al., 2015; Hu et al., 2018).

DATA AVAILABILITY STATEMENT

The original contributions presented in the study are included in the article/Supplementary Material, further inquiries can be directed to the corresponding authors.

AUTHOR CONTRIBUTIONS

JY contributed to analyzing the data, diagnostics and preparing the manuscript. MJ contributed to the conception of the study, interpretation of the results and preparing the manuscript. SG contributed to providing the comments and suggestions in the preparation of the manuscript, and helped edit the manuscript. JC contributed to calculating the apparent heat source data employed in the manuscript.

FUNDING

This work is jointly supported by the National Key Research and Development Program of China (Grant no. 2016YFA0600601), the National Natural Science Foundation of China (Grant no. 41530530, 41475049), Guangdong Province Key Laboratory for Climate Change and Natural Disaster Studies (Grant 2020B1212060025) and the Jiangsu Collaborative Innovation Center for Climate Change.

REFERENCES

Dee, D. P., Uppala, S. M., Simmons, A. J., Berrisford, P., Poli, P., Kobayashi, S., et al. (2011). The ERA-interim reanalysis: configuration and performance of the data assimilation system. *Q. J. R. Meteorol. Soc* 137, 553–597. doi:10.1002/qj.828

Ding, Y., and Chan, J. C. L. (2005). The East Asian summer monsoon: an overview. *Meteorol. Atmos. Phys* 89, 117–142. doi:10.1007/s00703-005-0125-z

Ding, Y. (1992). Summer monsoon rainfalls in China. *J. Meteorol. Soc. Jpn* 70, 373–396. doi:10.2151/jmsj1965.70.1B_373

Gill, A. E. (1980). Some simple solutions for heat-induced tropical circulation. *Q. J. R. Meteorol. Soc* 106, 447–462. doi:10.1002/qj.49710644905

Goswami, B. N., Madhusoodanan, M. S., Neema, C. P., and Sengupta, D. (2006). A physical mechanism for North Atlantic SST influence on the Indian summer monsoon. *Geophys. Res. Lett* 33, L02706. doi:10.1029/2005GL024803

He, J., and Zhu, Z. (2015). The relation of South China sea monsoon onset with the subsequent rainfall over the subtropical East Asia. *Int. J. Climatol* 35, 4547–4556. doi:10.1002/joc.4305

Hu, P., Chen, W., Huang, R. H., and Nath, D. (2018). On the weakening relationship between the South China sea summer monsoon onset and cross-equatorial flow after the late 1990s. *Int. J. Climatol* 38, 3202–3208. doi:10.1002/joc.5472

Huang, R. H., Gu, L., Xu, Y. H., Zhang, Q., Wu, S., and Cao, J. (2005). Characteristics of the interannual variations of onset and advance of the East Asian summer monsoon and their associations with thermal states of the tropical western Pacific. *Chin. J. Atmos. Sci* 29, 20–36 [in Chinese]. doi:10.3878/j.issn.1006-9895.2005.01.04

Huang, R. H., and Sun, F. Y. (1994). Impact of the thermal state and convective activities over the western Pacific warm pool on summer climate anomalies in East Asia. *Chin. J. Atmos. Sci* 18, 262–272 [in Chinese]

Huangfu, J., Huang, R. H., and Chen, W. (2015). Influence of tropical western pacific warm pool thermal state on the interdecadal change of the onset of the south China Sea summer monsoon in the late-1990s. *Atmos. Oceanic Sci. Lett* 8, 95–99. doi:10.1080/16742834.2015.11447244

Jian, M. Q., and Luo, H. B. (2001). Heat sources over Qinghai-xizang Plateau and surrounding areas and their relationships to onset of SCS summer monsoon. *Plateau Meteorol* 20, 381–387 [in Chinese]

Jiang, X., Wang, Z., and Li, Z. (2018). Signature of the South China Sea summer monsoon onset on spring-to-summer transition of rainfall in the middle and lower reaches of the Yangtze River basin. *Clim. Dynam* 51, 3785–3796. doi:10.1007/s00382-018-4110-x

Kajikawa, Y., and Wang, B. (2012). Interdecadal change of the South China Sea summer monsoon onset. *J. Clim* 25, 3207–3218. doi:10.1175/JCLI-D-11-00207.1

Kajikawa, Y., Yasunari, T., Yoshida, S., and Fujinami, H. (2012). Advanced Asian summer monsoon onset in recent decades. *Geophys. Res. Lett* 39, L03803. doi:10.1029/2011GL050540

Li, C., and Yanai, M. (1996). The onset and interannual variability of the Asian summer monsoon in relation to land-sea thermal contrast. *J. Clim* 9, 358–375. doi:10.1175/1520-0442(1996)009<0358:toaivo>2.0.co;2

Lin, A., Gu, D., Zheng, B., and Li, C. (2013). Relationship between South China sea summer monsoon onset and Southern Ocean sea surface temperature variation. *Chin. J. Geophys* 56, 383–391 [in Chinese]. doi:10.6038/cjg20130203

Lin, A., and Zhang, R. (2020). Climate shift of the South China sea summer monsoon onset in 1993/1994 and its physical causes. *Clim. Dynam* 54, 1819–1827. doi:10.1007/s00382-019-05086-4

Liu, Y., WuLiu, G. H., and Liu, P. (1999). The effect of spatially nonuniform heating on the formation and variation of subtropical high. Part III: condensation heating and South Asia high and western Pacific subtropical high. *Acta Meteorol. Sin* 57, 525–538 [in Chinese]

Luo, M., and Lin, L. J. (2017). Objective determination of the onset and withdrawal ofthe South China Sea summer monsoon. *Atmos. Sci. Lett* 18, 276–282. doi:10.1002/asl.753

Lyu, K., Yu, J., and Paek, H. (2017). The influences of the atlantic multidecadal oscillation on the mean strength of the north pacific subtropical high during boreal winter. *J. Clim* 30, 411–426. doi:10.1175/JCLI-D-16-0525.1

Mao, J. Y., Chan, J. C. L., and Wu, G. X. (2004). Relationship between the onset of the South China Sea summer monsoon and the structure of the Asian subtropical anticyclone. *J. Meteorol. Soc. Jpn* 82, 845–859. doi:10.2151/jmsj.2004.845

Murakami, T., and Matsumoto, J. (1994). Summer monsoon over the asian continent and western north pacific. *J. Meteorol. Soc. JPN* 72, 719–745. doi:10.2151/jmsj1965.72.5_719

Qian, W., Kang, H. S., and Lee, D. K. (2002). Distribution of seasonal rainfall in the East Asian monsoon region. *Theor. Appl. Climatol* 73, 151–168. doi:10.1007/s00704-002-0679-3

Rayner, N. A., Parker, D. E., Horton, E. B., Folland, C. K., Alexander, L. V., Rowell, D. P., et al. (2003). Global analyses of sea surface temperature, sea ice, and night marine air temperature since the late nineteenth century. *J. Geophys. Res* 108, 4407. doi:10.1029/2002JD002670

Sun, C., Kucharski, F., Li, J., Jin, F. F., Kang, I. S., and Ding, R. (2017). Western tropical Pacific multidecadal variability forced by the Atlantic multidecadal oscillation. *Nat. Commun* 8, 15998. doi:10.1038/ncomms15998

Tao, S. Y., and Chen, L. X. (1987). *A review of recent research on the East Asian summer monsoon in China monsoon meteorology*. Oxford, UK: Oxford University Press, 60–92.

Wang, B., Huang, F., Wu, Z. W., Yang, J., Fu, X. H., and Kikuchi, K. (2009). Multi-scale climate variability of the South China Sea monsoon: a review. *Dynam. Atmos. Oceans* 47, 15–37. doi:10.1016/j.dynatmoce.2008.09.004

Wang, B., and Lin, H. (2002). Rainy season of the Asian-Pacific summer monsoon. *J. Clim* 15, 386–398. doi:10.1175/1520-0442(2002)015<0386:RSOTAP>2.0.CO;2

Watanabe, M., and Kimoto, M. (2000). Atmosphere-ocean thermal coupling in the North Atlantic: a positive feedback. *Q. J. R. Meteorol. Soc* 126, 3343–3369. doi:10.1002/qj.49712657017

Wu, R., and Wang, B. (2001). Multi-stage onset of the summer monsoon over the western North Pacific. *Clim. Dynam* 17, 277–289. doi:10.1007/s003820000118

Xiang, B., and Wang, B. (2013). Mechanisms for the advanced asian summer monsoon onset since the mid-to-late 1990s. *J. Clim* 26, 1994–2009. doi:10.1175/JCLI-D-12-00445.1

Yanai, M., Esbenson, S., and Chu, J. (1973). Determination of bulk properties of tropical cloud clusters from large-scale heat and moisture budgets. *J. Atmos. Sci* 30, 611–627. doi:10.1175/1520-0469(1973)030<0611:dobpot>2.0.co;2

Yuan, F., and Chen, W. (2013). Roles of the tropical convective activities over different regions in the earlier onset of the South China Sea summer monsoon after 1993. *Theor. Appl. Climatol* 113, 175–185. doi:10.1007/s00704-012-0776-x

Conflict of Interest: The authors declare that the research was conducted in the absence of any commercial or financial relationships that could be construed as a potential conflict of interest.

Appendix

In this appendix, a thermodynamic expression that determines temperature change between two adjacent calendar months is derived. With the aid of **Eq. 2** , the thermodynamic energy **Eq. 1** can be simple written as

$$\frac{\partial T}{\partial t} = \frac{Q_1 - Q_{12} - Q_{13}}{c_p} = F(Q_1,\ Q_{12},\ Q_{13}) \tag{A1}$$

Where F is the forcing term, representing the net effect of all thermal heating processes, i.e. horizontal advection of temperature, vertical adiabatic heating and diabatic heating. Given $T_{i,n}$ represents the daily mean temperature on the n-th day of the i-th calendar month, and the local temperature change is calculated with the central difference scheme, then **Eq. 4** can be rewritten as

$$\frac{T_{i,n+1} - T_{i,n-1}}{2\Delta t} = F_{i,n} \tag{A2}$$

Where Δt is 1 day or 86,400 s. Given 30 days in a month and based on **Eq. A2**, we then have

$$\begin{cases} \dfrac{T_{i,1} - T_{i-1,29}}{2\Delta t} = F_{i-1,30} \\ \dfrac{T_{i,2} - T_{i-1,30}}{2\Delta t} = F_{i,1} \\ \dfrac{T_{i,3} - T_{i,1}}{2\Delta t} = F_{i,2} \\ \cdots\cdots\cdots \\ \dfrac{T_{i,30} - T_{i,28}}{2\Delta t} = F_{i,29} \end{cases} \tag{A3}$$

Adding the terms on the two sides of the formulas in **Eq. A3**, respectively, we get

$$\frac{T_{i,30} + T_{i,29} - T_{i-1,\,30} - T_{i-1,29}}{2\Delta t} = \sum_{n=1}^{29} F_{i,n} + F_{i-1,30} \tag{A4}$$

Applying the above procedures to a sliding window of time repeatedly, we obtain

$$\begin{cases} \dfrac{T_{i,28} + T_{i,27} - T_{i-1,\,28} - T_{i-1,27}}{2\Delta t} = \sum\limits_{n=1}^{27} F_{i,n} + F_{i-1,30} + F_{i-1,29} + F_{i-1,28} \\ \vdots \\ \dfrac{T_{i,4} + T_{i,3} - T_{i-1,4} - T_{i-1,3}}{2\Delta t} = F_{i,3} + F_{i,2} + F_{i,1} + \sum\limits_{n=4}^{29} F_{i-1,n} \\ \dfrac{T_{i,2} + T_{i,1} - T_{i-1,2} - T_{i-1,1}}{2\Delta t} = F_{i,1} + \sum\limits_{n=2}^{30} F_{i-1,n} \end{cases} \tag{A5}$$

Add the terms on the left and right sides of **Eqs A5, A6**, respectively, and get

$$\begin{aligned} \left(\sum_{n=1}^{30} T_{i,n} - \sum_{n=1}^{30} T_{i-1,n}\right)\Big/30 = \Delta \mathrm{t}\, \big[&\left(F_{i,29} + F_{i,28}\right) + 2\left(F_{i,27} + F_{i,26}\right) \\ &+ 3\left(F_{i,25} + F_{i,24}\right) + \cdots + 14\left(F_{i,3}\right. \\ &\left.+ F_{i,2}\right) + 15\left(F_{i,1} + F_{i-1,30}\right) \\ &+ 14\left(F_{i-1,29} + F_{i-1,28}\right) + \cdots \\ &+ 2\left(F_{i-1,5} + F_{i-1,4}\right) \\ &+ \left(F_{i-1,3} + F_{i-1,2}\right)\big]/15 \end{aligned} \tag{A6}$$

Equation A6 states that the inter-monthly change of monthly mean temperature is given by the sum of the weighted daily thermal forcing terms on the right within the two concerned months. For the convenience of calculation, we specify the number of days in each month as 30 days, and the first day or the last day of the month is omitted before calculation for the months with 31 days. When applying **Eq. A6** to January–February or February–March, we add the days in February up to 30 days by including the first two days in March or the last two days in January. Since the days of the calendar months are not all the same as 30 days, there are small biases when using the left side of **Eq. A6** to estimate the inter-monthly change of monthly mean temperature. However, the biases are generally very small and thus can be ignored.

frontiers in Earth Science

ORIGINAL RESEARCH
published: 13 January 2021
doi: 10.3389/feart.2020.610982

Interdecadal Change in the Relationship Between the Bay of Bengal Summer Monsoon and South China Sea Summer Monsoon Onset

*Zhenjie Zeng[1], Yuanyuan Guo[1] and Zhiping Wen[1,2,3]**

[1]Department of Atmospheric & Oceanic Sciences and Institute of Atmospheric Sciences, Fudan University, Shanghai, China, [2]Innovation Center of Ocean and Atmosphere System, Zhuhai, China, [3]Jiangsu Collaborative Innovation Center for Climate Change, Nanjing, China

The interdecadal change of the BOBSM–SCSSM relationship around the late 1970s is investigated in this paper. We found that the correlation between the BOBSM and SCSSM is 0.22 in 1958–1979, while it is 0.66 in 1980–2018. Further analyses showed that the strength of the South Asian High (SAH) at upper troposphere circulation experiences an interdecadal enhancement around the late 1970s; meanwhile its meridional shift exhibits a wider range in the second subperiod. Both the interdecadal change of the strength and meridional shift of the SAH contribute to a closer relationship of the BOBSM and SCSSM through modulating the divergent field at upper troposphere. As for the external forcing, the basin warming of the Indian Ocean after the late 1970s may serve as a relatively primary factor, which could induce a consistent background flow that may favor a closer BOBSM–SCSSM relationship in the second period. It is noted that the Indian Ocean warming is related to high pressure anomaly widely lying to the south of 20°N at upper troposphere, accompanied by the low pressure anomaly center to the north of 20°N. And this kind of upper-level circulation may result in strong westerly anomaly at the domain where the pressure gradient is large and then modulate the onset of the BOBSM and SCSSM in 1980–2018 through changing the upper-level divergent field. Besides, the low troposphere circulation associated with Indian Ocean warming is featured by the zonal-elongated high pressure anomaly spanning from the BOB and SCS to the northwest Pacific. The above coupling of the upper and lower troposphere, as a larger-scale consistent background flow controls the BOB and SCS, can modulate the interannual variation of the BOBSM and SCSSM synchronously and contributes to the closer relationship of the BOBSM and SCSSM in the second subperiod.

Keywords: Bay of Bengal summer monsoon, South China Sea summer monsoon, interdecadal change, South Asian High, Indian Ocean basin warming

OPEN ACCESS

Edited by:
Lin Wang,
Institute of Atmospheric Physics (CAS), China

Reviewed by:
Boqi Liu,
Chinese Academy of Meteorological Sciences, China
Maoqiu Jian,
Sun Yat-sen University, China

****Correspondence:***
Zhiping Wen
zpwen@fudan.edu.cn

Specialty section:
This article was submitted to Atmospheric Science, a section of the journal Frontiers in Earth Science

Received: *28 September 2020*
Accepted: *18 November 2020*
Published: *13 January 2021*

Citation:
Zeng Z, Guo Y and Wen Z (2021) Interdecadal Change in the Relationship Between the Bay of Bengal Summer Monsoon and South China Sea Summer Monsoon Onset. Front. Earth Sci. 8:610982. doi: 10.3389/feart.2020.610982

INTRODUCTION

The Asian summer monsoon (ASM), as the most active monsoon system, plays an important role on the spatial distribution and strength of rain belt in Asia. The onset of ASM, accompanied by an abrupt change in atmospheric circulation and energy, has great influences on the weather and climate of most Asian countries (Wu and Zhang, 1998; Wang et al., 2004; Mao and Wu, 2007; Zhou et al., 2018). In general, the onset of ASM can be divided into three successive processes: the onset of the Bay of Bengal summer monsoon (BOBSM) occurs in 25th pentad, followed by the onset of the South China Sea summer monsoon (SCSSM) in 28th pentad, and finally, the Indian summer monsoon (ISM) outbreaks in 31st pentad (Ding, 1992b; Xie and Saiki, 1999; Wang, 2006; Wu et al., 2013).

Substantive research studies have highlighted the pronounced variability of ASM systems both in the interannual and interdecadal time scale; meanwhile, many efforts have been devoted to figuring out possible causes which would contribute to the change in ASM systems. It has been noted that both local and remote sea surface temperature (SST) anomalous have a significant influence on the onset of ASM. Specifically, take the BOBSM, for example, it is attributed the interannual variations of BOBSM to either the local SST anomalous over Bay of Bengal or the intra-seasonal oscillation (ISO) (Wei-Dong et al., 2015). The remote forcing by El Niño-Southern Oscillation (ENSO) events can also result in the advanced or delayed onset of the BOBSM by modulating the ISO (Li et al., 2018). Except for the ISO, the ENSO-induced convection anomalous over southern Philippines can influence the upper-level divergence-pumping effect through altering the position of the SAH. And following the ENSO events, there is anomalous zonal gradient of SST over the Indian-western Pacific Ocean. Both the change of the upper-level divergence-pumping and zonal gradient of SST can affect the formation of monsoon convection during the onset process of the BOBSM (Liu et al., 2015b), while many other studies concluded that a warm (clod) ENSO event contributes to the late (early) SCSSM onset by modulating the Walker circulation (Webster and Yang, 1992; Chang and Chen, 1995; Wu and Meng, 1998; Luo et al., 2016). Furthermore, the anomalous SST over the tropical Indian Ocean (TIO) can prolong the effect of ENSO events on the SCSSM onset via changing the Philippine Sea anticyclone as well as the vertical velocity over SCS (Annamalai et al., 2007; Yang et al., 2007; Yuan et al., 2008; Xie et al., 2009; Hu and Duan, 2015).

In the interdecadal time scale, it is noted that there are significant decadal changes of ASM in the late 1970s and mid-1990s (Wang, 2001; Wu et al., 2010). Ensemble experiments point out that the decadal change of SST over the extratropical northern Pacific and tropical Pacific, especially over the tropical region, can qualitatively account for the ASM interdecadal climate shift around the late 1970s (Li et al., 2008; Fu et al., 2009). Furthermore, the combined impact of SST anomalies and the TP snow from winter and spring serves as a primary role in the decadal weakening of ASM in the late 1970s (Ding et al., 2008; Ding et al., 2009). While in the mid-1990s, an evident advance in the onset dates of the SCSSM is observed and studied from different angles. It is attributed to the earlier retreat of subtropical high, the increasing of the intraseasonal variability, and the tropical cyclone (Kajikawa et al., 2012; Kajikawa and Wang, 2012). Besides, the change of mean state over Pacific basin, which is characterized by a "grand" La Niña-like pattern, can advance the monsoon onset through the atmosphere wave (Ding et al., 2009; Yuan and Chen, 2013), and some studies noted that the interannual connection between the SCSSM and SST anomalies over the Indian Ocean and western Pacific performs significant shift around 1993/1994 (Yim et al., 2008; Xiang and Wang, 2013; Liu et al., 2016; Zhang et al., 2017). Overall, the interdecadal change of SST anomaly contributes to the interdecadal variation of ASM systems.

From the perspective of atmospheric circulation, the effects of the South Asian High (SAH) on ASM systems have been mentioned in accumulated studies, since the SAH helps to generate a favorable environment for the onset of both BOBSM and SCSSM. That is, a trumpet-shaped anomalous circulation lying in the southwestern part of the SAH at the upper troposphere leads to strong divergence pumping and then significant ascent movement over the BOB (Liu et al., 2013). Certainly, the SAH can also modulate the SCSSM through advecting anomalous potential vorticity by the northerly along the eastern SAH and enhanced convection over SCS (Liu and Zhu, 2016). These results suggest that the SAH may act as a bridge linking the BOBSM and SCSSM due to its continuous effect on the large-scale atmospheric circulation over the South Asia as well as the SCS. The location and strength of the SAH also exhibit an significant variation on the interdecadal time scale, which is linked to the SST anomalies over the SCS and western North Pacific (Zhang and Qian, 2000; Peng et al., 2018).

Apart from the forcing by tropical SST anomalies and modulation by the SAH, the air-sea interaction in the lower troposphere has been demonstrated as one of the essential factors that exert tremendous impact on the formation of monsoon vortex, which associates with the southerly and convection over BOB (Wu et al., 2011). Besides, some studies emphasize that the thermal and dynamical forcing of Tibetan Plateau (TP) may play an extremely important role on the onset of both BOBSM and SCSSM (He et al., 1987; Wu et al., 1998; Hu and Duan, 2015).

Given that many factors mentioned hereinbefore are linked to the onset of both SCSSM and BOBSM, the climatological onset date of the BOBSM is just 3 pentads before the SCSSM, and there might be a close connection between the BOBSM and SCSSM. For instance, Liu et al., 2002 pointed out that the immense latent heat released by the monsoon convection over the Bay of Bengal can enhance the southerly and convection over SCS based on observational evidence and numerical experiment. However, how the BOBSM correlates the SCSSM in the interannual time scale is not clear. Particularly, considering that the SCSSM exhibits significant variability in the interdecadal time scale (Wang, 2001; Wu et al., 2010), whether the connection changes in the interdecadal time scale remains unknown so far. These related research studies would advance our understanding of the mechanism responsible to the onset of the tropical monsoon and help to improve the prediction skill of monsoon onset.

The remainder of the paper is organized as follows: **Section 2** introduces the data and the method used in the present study. **Section 3** investigates the correlations of onset date between the BOBSM and SCSSM and shed light on a closer connection between these two monsoon systems after the late 1970s. **Section 4** focuses on the factors that result in the interdecadal shift of the linkage between the BOBSM and SCSSM. **Section 5** serves as a summary and discussion.

DATA AND METHODS

To lessen the uncertainty caused by any individual dataset, two sets of data, the National Centers for Environment Prediction (NCEP)–National Center for Atmospheric Research (NCAR) reanalysis data (NCEP1) (Kalnay et al., 1996), and the third version system of Twentieth Century Reanalysis (20CRv3) Project supported by the National Oceanic and Atmospheric (NOAA) (Slivinski et al., 2019), are used in this paper. The horizontal resolution of the NCEP reanalysis data and 20CRv3 data are 2.5° × 2.5° and 1.0° × 1.0°, respectively. Daily zonal wind (u), meridional wind (v), vertical velocity (ω), geopotential height (z), and temperature (t) are extracted from NCEP1 (20CRv3) during the period of 1958–2018 (1958–2015). The SST data ranged from 1958–2018 is from Met Office Hadley Center observations' datasets, with a horizontal resolution of 1.0° × 1.0° (Rayner et al., 2003).

In previous studies, various criteria are used to locate the onset date of ASM systems. Some studies identified the onset date based on the change of vertical shear of zonal wind which results from the seasonal transition of meridional temperature gradient (MTG), in the mid to upper troposphere (Webster and Yang, 1992; Li and Yanai, 1996; He et al., 2003). The MTG-based onset date has been used to investigate the interannual variability of the SCSSM in different decades (Liu et al., 2016) and interannual variation of the BOBSM (Mao and Wu, 2007). It was also found that the zonal wind at 850 hPa and the abrupt enhancement of rainfall over the monsoon regions perform well in depicting the year-to-year variation of the SCSSM onset (Wang et al., 2004; Luo et al., 2016). Even more, another definition only based on monsoon rainfall has been proposed to describe the rain band spanning from BOB to SCS (Wang and Linho, 2002; Wang et al., 2004). However, the criteria mentioned hereinbefore were usually used to identify either the onset date of the BOBSM or SCSSM. Considering that our focus is on the plausible connection between the BOBSM and SCSSM, a monsoon index, which was proposed by Wu et al., 2013, was used in the present work. The onset date of the BOBSM and SCSSM is identified by three criteria: (1) the vertical shear of zonal wind (200 hPa, −850 hPa) becomes negative, (2) the shift of surface wind direction is greater than 100°, and (3) daily precipitation is greater than 5 mm over each grid of the interested area, with precipitation over subtropical monsoon land greater than 3 mm. This monsoon index provides a more comprehensive way to describe the monsoon onset by combining the change of both wind and rainfall (Wu et al., 2013; Liu et al., 2015a), while it could reveal the successive process of ASM systems, which starts from the BOB and then develops to the SCS.

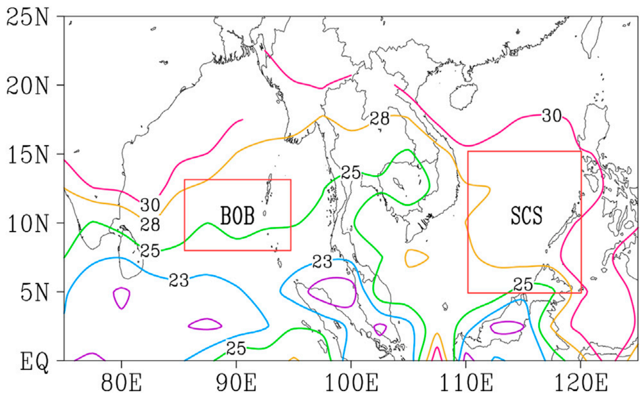

FIGURE 1 | The pentad-isochrones indicating the onset process of ASM for 1958–2018. The area encircled by red solid lines represents the selective BOBSM region and SCSSM region, respectively.

Besides, various monsoon indices were applied to be a supplement. The onset date of the BOBSM (Yan et al., 2018) is identified by three criteria: (1) the zonal wind (7.5°N–12.5°N, 85°E–95°E) at 850 hPa is higher than 3 m/s, (2) the zonal wind at 200 hPa is lower than −5 m/s, and (3) the above situation lasts five days. The onset date of the SCSSM (Ding et al., 2016) was defined as following: (1) the zonal wind (5°N–15°N, 110°E–120°E) at 850 hPa is higher than 0.5 m/s, and the averaged zonal wind in the next five days is higher than 0 m/s, (2) in 15 days after the onset date, there are 8 days at least when the westerly dominates the SCS monsoon region; meanwhile, the averaged zonal wind during the 15 days is required to be higher than 1 m/s, and (3) the onset date is supposed to be any date after 20th April.

INTERDECADAL CHANGE OF THE CONNECTION BETWEEN ONSET DATES OF BAY OF BENGAL SUMMER MONSOON AND SOUTH CHINA SEA SUMMER MONSOON

Figure 1 shows the climatological onset of ASM in different regions based on the method proposed by Wu et al., 2013. As is well known, ASM first outbreaks in pentad 25 over BOB, and then, it continually extends northward and eastward. In general, the SCSSM onsets in pentad 28, while the Indian summer monsoon onsets in pentad 30, approximately two pentads later than the SCSSM. The result is consistent with previous studies (Ding, 1992b; Xie and Saiki, 1999; Wang, 2006; Wu et al., 2013). The inconsistent outbreak among the BOBSM, Indian summer monsoon, and SCSSM may be attributed to the monsoon onset barrier that blocks the further westward advancement of the monsoon system after the ASM first outbreaks in the BOB (Liu et al., 2015a).

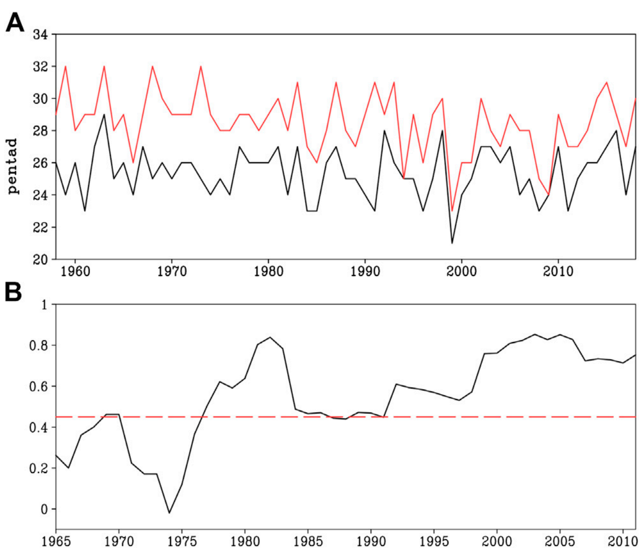

FIGURE 2 | (A) Time series of the monsoon onset pentad averaged over the selective BOBSM region (7.5°–12.5°N, 85°–95°E) and SCSSM region (5°–15°N, 110°–120°E). **(B)** A sliding correlation with a 15-years running window for the time series of the monsoon onset pentad of BOBSM and SCSSM, and the red dashed line denotes values reaching the 90% confidence level.

Since the focus in this research is on the onset of the BOBSM and SCSSM, two target domains (7.5°N–12.5°N, 85°E–95°E for the BOBSM and 5°N–15°N, 110°E–120°E for the SCSSM) were selected where the area-averaged onset pentad represents the monsoon onset in the BOB or SCS (**Figure 2A**). The onset dates of both BOBSM and SCSSM possess significant variability in the interannual time scale; moreover, both of them evidently oscillate in the interdecadal time scale. The results obtained from the power spectra analysis (figure not shown) show that the BOBSM onset has significant power in the 3-year, 5-year, and 12-year bands. The SCSSM onset is dominated by a major peak near 5-year band and a minor peak near 2.5-year band, while it also exhibits a 10-11 years periodicity which is insignificant at the 90% confidence level. However, many studies have addressed an interdecadal advance of the SCSSM onset around the late 1970s and mid-1990s (Wang, 2001; Ding et al., 2008; Wu et al., 2010; Xiang and Wang, 2013; Yuan and Chen, 2013; Liu et al., 2016). The inconsistence between our result and previous studies may be attributed to the different identification methods of the SCSSM.

Furthermore, it seems that the connection between the BOBSM and SCSSM becomes closer after the 1980s. To validate the possible linkage of onset between the BOBSM and SCSSM, a sliding correlation with a 15-year running window is applied (**Figure 2B**). The correlation coefficients between the BOBSM and SCSSM are below 0.47 before 1977, being mostly insignificant at the 90% confidence level. However, the sliding correlation dramatically rebounds since 1974 and then increases and sustains with the significance at the 90% confidence level after 1977. We calculated the correlation coefficients between the BOBSM and SCSSM during the period of 1958–1979 and 1980–2018, respectively (**Table 1**). The correlation increases from 0.21 to 0.67 based on the NCEP-1 reanalysis, which is also true based on 20CRv3 reanalysis, with correlation increasing from 0.21 to 0.66. Besides, whether the interdecadal change in the BOBSM–SCSSM relationship depends on the monsoon definition has been examined by virtue of different identifications mentioned in **Section 2**. The result shows that the BOBSM–SCSSM connection becomes closer with an increasing correlation from 0.15 to 0.69. These results suggest that the closer relationship between the BOBSM and SCSSM after the late 1970s was insensitive to the used reanalysis data and monsoon definition.

Due to the correction and improvement of datasets during the satellite era since the 1970s, there is a possibility that a closer BOBSM–SCSSM connection may be attributed to the quality of reanalysis data, which is, however, not easy to be overcome. To avoid the influence of unrealistic interdecadal change, all the variables used to identify the monsoon onset were subjected to a harmonic analysis to remove periods longer than 8 years. The correlation between the BOBSM and SCSSM onset is 0.31 in the first subperiod and 0.67 in the second subperiod, which is similar to the result shown in **Table 1**. Overall, the interdecadal change in the BOBSM–SCSSM relationship is robust.

Primarily, the evolutional processes of different monsoon systems in different periods were investigated by a lead-lag composite analysis (**Figures 3**, **4**), in which 0 pentad represents the monsoon onset pentad and −1 pentad represents the pentad before. During the first subperiod, the convection activities first appear over the Asian-Australian land bridge near the equator and in the eastern Indochina Peninsula in the −3 pentad (**Figure 3A**). Meanwhile, a weak convection center is observed to the south of the Indian Peninsula (namely, 0°–10°N, 70°E–85°E), which gradually enhances in the −2 pentad (**Figure 3C**) and then forms a zonal-elongated rain belt between the equator and 10°N in the −1 pentad (**Figure 3E**). With the breakdown of the ridge line of subtropical high over BOB, this zonal-elongated rain belt propagates northward to the north of 10°N and the westerly almost covers the BOB, leading to the onset of the BOBSM (**Figure 3G**). In the onset pentad, the northeast-southwest oriented rain belt remarkably enhances, in tandem with the further eastward retreat of the subtropical high and the building-up of the SAH at the upper troposphere (**Figure 3G**). From the perspective of the SCSSM, in −3 pentad, earlier than the SCSSM onset, the SAH solidly lies to the south of TP at the upper troposphere and the westerly controls the BOB (**Figure 3B**), suggesting that the BOBSM already outbreaks at the time. As time goes by, the SAH further strengthens and expands northeastward

TABLE 1 | Correlation coefficients between the BOBSM and SCSSM onsets during the period of 1958–1979 and 1980–2018, respectively.

	1958–1979	1980–2018
NCEP1	0.21	0.67[a]
20CRv3	0.21	0.66[a]

[a]*Indicates the significance at the 99% confidence level.*

The definition of the monsoon onset is based on Wu et al. (2013).

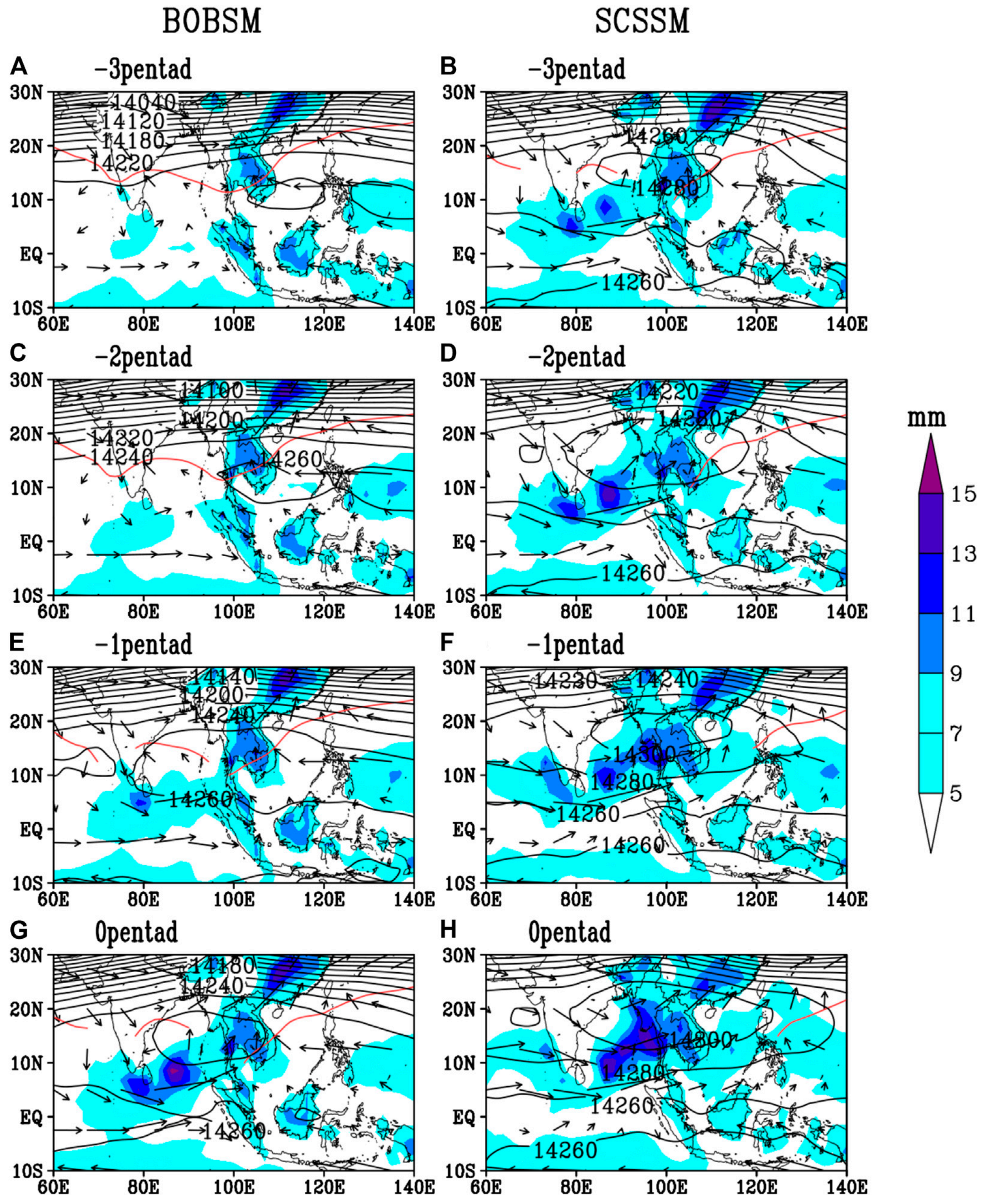

FIGURE 3 | Composite maps of precipitation (shaded; unit: mm), 850 hPa horizontal wind (vectors; unit: m/s), and geopotential height at 150 hPa (contour; unit: m) from −3 pentad to the onset pentad of **(left panel)** BOBSM and **(right panel)** SCSSM in the period of 1958–1979. The red line represents the ridge of western North subtropical high, which is defined by the zero zonal wind at 850 hPa (u = 0 m/s).

(**Figures 3D,F**), while the convection activity over the SCS becomes active after the eastward retreat of subtropical high in the -1 pentad (**Figure 3F**). In line with the abundant rainfall over the SCS and the strong and well-organized SAH covering the South Asian monsoon region in 0 pentad, the SCSSM eventually outbreaks (**Figure 3H**).

During the second subperiod, the convection activities were observed over the Asian-Australian land bridge near the equator in the −3 pentad (**Figure 4A**), with stronger amplitude compared with the counterpart during the first subperiod (**Figure 3A**). In the −1 pentad, there is a closed pressure high center appearing over the southern Indochina Peninsula and SCS (**Figure 4E**), which rapidly strengthens in the onset pentad of the BOBSM (**Figure 4G**). Compared with the first subperiod (**Figure 3G**), the SAH in onset pentad of the second subperiod (**Figure 4G**) is apparently stronger and lies more eastward, spanning from the BOB to the SCS. In term of the SCSSM, the SAH appears over the Indochina Peninsula and SCS

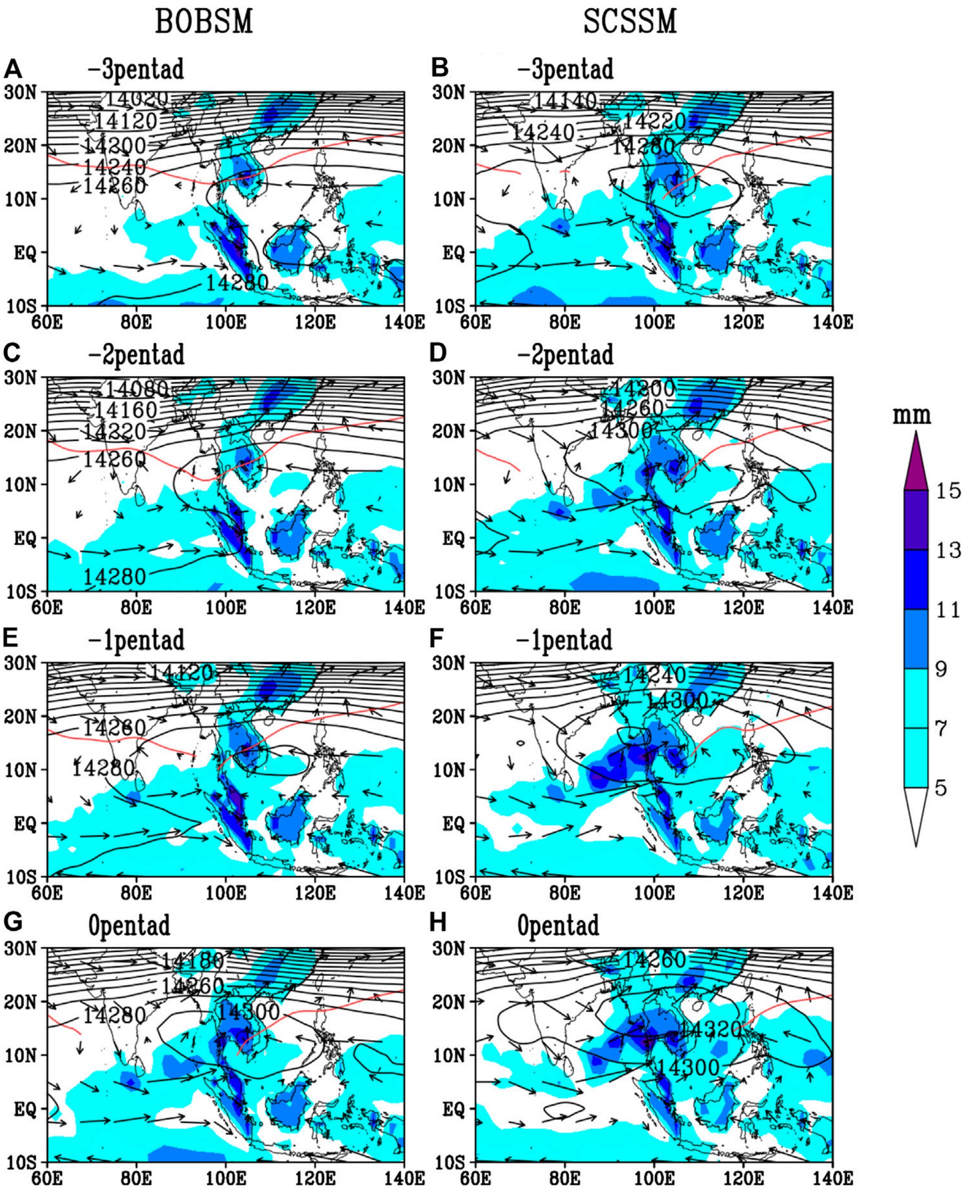

FIGURE 4 | Same as **Figure 3**, but in the period of 1980–2018.

in the −3 pentad (**Figure 4B**), lying more eastward compared with the SAH in the first subperiod (**Figure 3B**). Accompanied by the northward displacement of the SAH and significant enhancement of convection activities over the SCS, the southwesterly advances toward the SCS (**Figure 4H**), which indicates the outbreak of the SCSSM.

Overall, the spatial distribution and temporal evolution of the SAH before the SCSSM onset is distinguishable in different epochs. Specifically, the SAH already forms before the onset of both the BOBSM and SCSSM in the second subperiod, while a broader SAH spans from the BOB to the SCS, possibly providing a uniform background flow which may contribute to the closer connection between the BOBSM and SCSSM after the late 1970s.

PLAUSIBLE CAUSES OF INTERDECADAL CHANGE IN THE BAY OF BENGAL SUMMER MONSOON–SOUTH CHINA SEA SUMMER MONSOON RELATIONSHIP

Role of the South Asian High in May

Some studies indicate that the atmospheric circulation associated with the SAH can serve as divergence pumping over the BOB (Liu et al., 2012; Liu et al., 2013), while it can also provide positive potential vorticity, favoring the ascend movement over the SCS (Liu and Zhu, 2016). Hence, it was hypothesized that a stronger and boarder SAH may be an essential factor that jointly modulates the atmospheric circulation associated with the

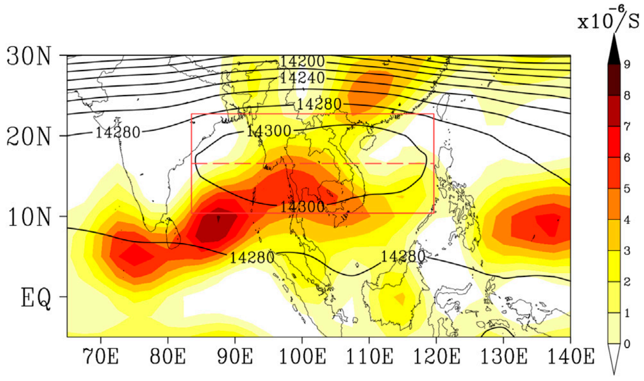

FIGURE 5 | Climatological geopotential height (contour; unit: m) and divergence (shaded; unit: s^{-1}) in May at 150 hPa from 1958 to 2018. Two regions (17.5°–22.5°N, 82.5°E–120°E and 10°–15°N, 82.5°E–120°E) are highlighted by red boxes, which were used to define the meridional displacement of the SAH.

TABLE 2 | Correlation coefficients between the first two EOF modes obtained from 150 hPa geopotential height in May (shown in **Figure 6**) and the onset of BOBSM and SCSSM during the period of 1958–1979 and 1980–2018, respectively.

		BOBSM	SCSSM
PC1	1958–1979	−0.06	−0.15
	1980–2018	0.43[a]	0.34[a]
PC2	1958–1979	0.50[a]	0.35
	1980–2018	0.51[a]	0.55[a]

[a] *Indicates the significance at the 90% confidence level.*

BOBSM and SCSSM onset. In general, the SAH first appears in early April (Liu et al., 2012; Liu et al., 2013; Wang et al., 2017), and then, the SAH solidly lies over the Indochina Peninsula between 10°N and 20°N in May, illustrated by the climatological geopotential height at the upper troposphere (**Figure 5**). Based on the onset pentads of different ASM systems identified by Wu et al., 2013, the BOBSM generally outbreaks in the 25th pentad and the SCSSM in the 28th pentad. Hence, the SAH variability in May (from the 25th to 30th pentad, approximately) was examined in this subsection in order to figure out the role of the SAH on the change of BOBSM–SCSSM relationship.

For the purpose of exhibiting the spatiotemporal variation of the SAH, we applied the empirical orthogonal function (EOF) analysis to the geopotential height field at 150hPa (**Figure 6**). As it can be seen in **Figure 6A**, the first EOF mode (EOF1), accounting for 84.0% of the total variance, displays a monopolar pattern with a center spanning from the Indochina Peninsula, BOB to SCS, which might represent a change in the strength of the SAH. The associated principle component (PC1) exhibits a significant interannual and interdecadal change. The running *t*-test was performed onto PC1 to determine the interdecadal shift time of PC1, which shows that the PC1 experiences a significant interdecadal shift around the late 1970s, that is, the SAH becomes stronger after then. This result is consistent with previous studies, for instance, it observed a stronger and boarder SAH in boreal summer after 1978 (Zhang et al., 2000; Peng et al., 2018). The correlation coefficients between PC1 and the BOBSM/SCSSM onset were calculated and are given in **Table 2**. Whether the BOBSM or SCSSM onset has a poor correlation with PC1 during the first subperiod, as the coefficients are −0.06 and −0.15, respectively. However, the correlations increase to 0.43 and 0.34 during the second subperiod, suggesting that a stronger SAH may play a more important role in connecting the BOBSM and SCSSM.

The upper tropospheric geopotential height and divergence flow associated with PC1 are shown in **Figure 7**. For the positive PC1 years in the first period, the composite 150 hPa height shows positive anomalies covering South Asia (**Figure 7C**), while the anomalous convergence is extremely weak, particularly over the BOB and SCS regions (**Figure 7A**), which indicates that a weak SAH seemly could not induce significant divergence flow at upper troposphere in the South Asia. In contrast, the positive anomalous cover larger scale of South Asia (**Figure 7D**), which means the SAH enhances significantly in the second period. And there are convergent anomalies covering the eastern BOB and SCS (**Figure 7B**), which may act as a larger-scale background flow that forms and sustains after the onset of the BOBSM. The pumping effect by the anomalous divergence/convergence flow at the upper troposphere over the BOB and SCS was supposed to be an important mechanism responsible to the closer BOBSM–SCSSM relationship after the late 1970s. However, the effect of advecting anomalous potential vorticity caused by the SAH on SCSSM (Liu and Zhu, 2016) is not significant in the interdecadal change (figures not shown).

The spatial pattern of the second EOF mode (EOF2), with a variance contribution of 6.7%, shows a meridional dipole pattern with out-of-phase signals to the north and south of 15°N, suggesting a meridional displacement of the SAH (**Figure 6B**). To further verify that the EOF2 reveals the meridional shift of the SAH, an index measuring the north-south displacement of the SAH (NSI) is defined by using the difference between the geopotential height at 150 hPa averaged over 10°–15°N, 82.5°–120°E and 17.5°–22.5°N, 82.5°–120°E (Wei et al., 2015). The principal component of EOF2 (PC2) is well related to the NSI with a correlation coefficient as high as 0.9, which implies the EOF2 can represent the north-south movement of the SAH in May to a large extent. Seemly, PC2 shifts from negative to positive phase around the late 1970s (**Figure 6D**), while the running *t*-test performed onto PC2 shows that it also experiences a significant interdecadal change in 1979. Overall, the EOF analysis suggests that the SAH may be stronger and more southward in the second subperiod.

Table 2 shows that the correlations of PC2 with the BOBSM (SCSSM) onset are 0.50 (0.35) in the first subperiod, while that increase to 0.51 (0.55) in the second subperiod. Note that the relationship between the meridional location of the SAH and SCSSM becomes tighter after 1979. In the first subperiod, there is a negative anomaly center of upper tropospheric geopotential height lying over South Asia (**Figure 8C**). Meanwhile, an anomalous convergence center locates at 150 hPa over the BOB, while the anomalous convergence over SCS is not significant (**Figure 8A**). When the SAH tends to displace

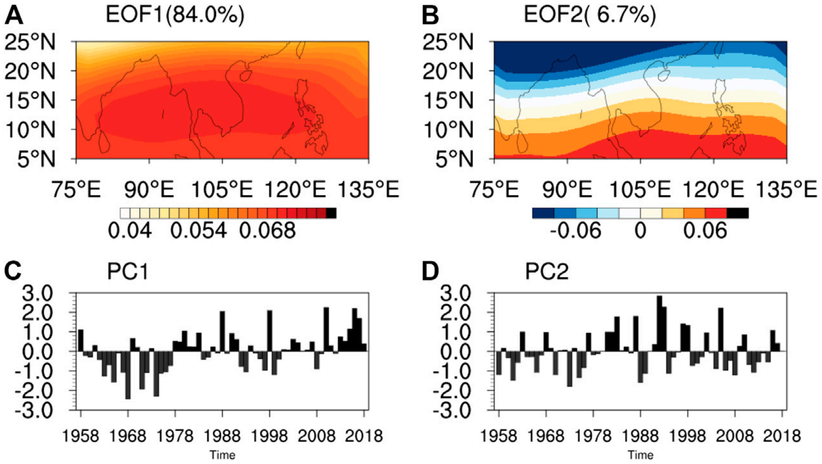

FIGURE 6 | Spatial distribution of **(A)** the first EOF mode (shaded), **(B)** the second EOF mode (shaded), and (bottom) the corresponding PCs of 150 hPa geopotential height anomalies in May from 1958–2018.

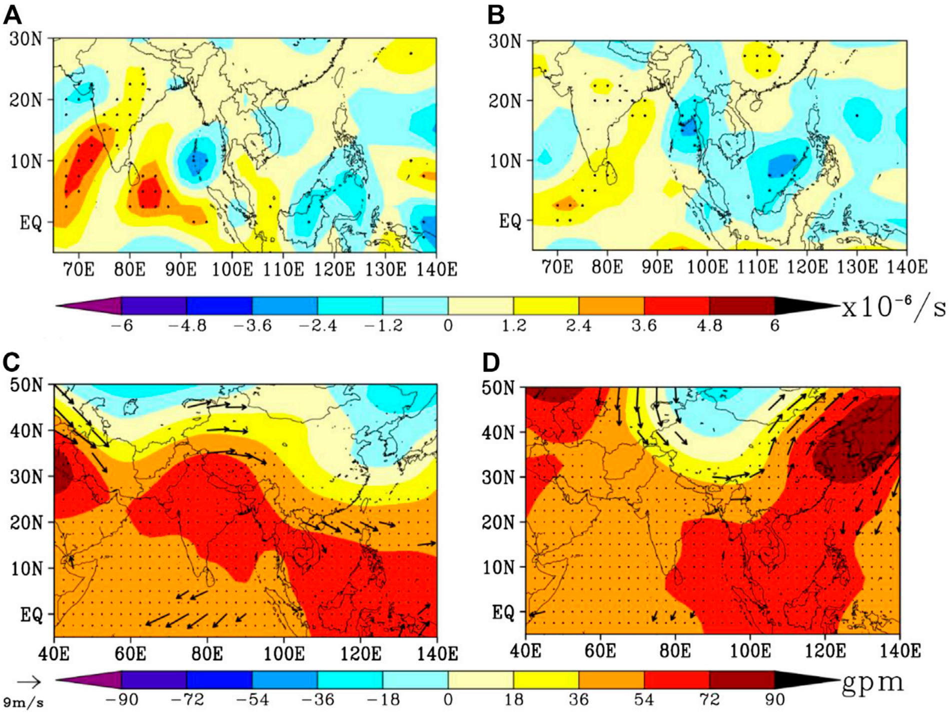

FIGURE 7 | Composite differences of **(upper)** the divergence anomaly (shaded; unit: s-1) and **(bottom)** geopotential height (shaded; unit: gpm) and horizontal wind (vector; unit: m/s) anomaly at 150 hPa in May between positive and negative years of PC1 for the period of **(left)** 1958–1979 and **(right)** 1980–2018. The positive (negative) years of PC1 are higher (lower) than 0.5 (−0.5). The stippling and black vectors denote values exceeding the 90% confidence level.

southward in the second subperiod, the composite divergence field shows significant anomalous convergence over both the BOB and SCS (**Figure 8B**), accompanied by a wider range of the meridional shift of the SAH. A larger amplitude of the north-south displacement of the SAH may be related to a larger range of the upper tropospheric divergent pumping, so it possibly has influence on the development of the monsoon-related convection over the eastern BOB and SCS, and then, it contributes to the increasing of the correlation between the SAH meridional shift and SCSSM onset in the 1980–2018 period.

Both the strength and the meridional swing patterns of the SAH exert impact on the onset of the monsoon, while Liu et al. 2017 demonstrated that the variations of the strength and the position of the SAH are linked to ENSO events. The evolution of

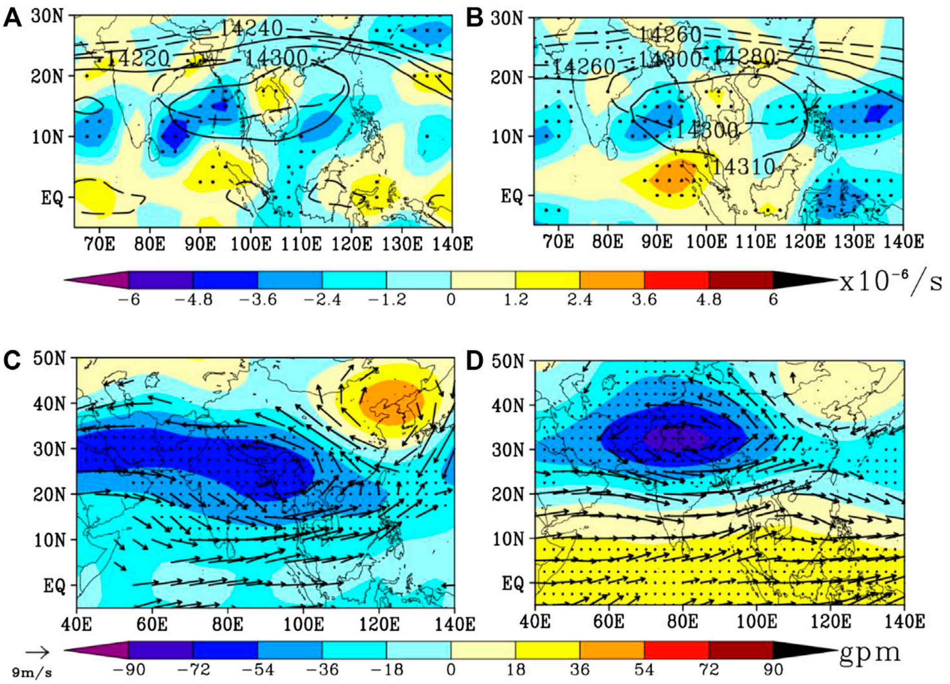

FIGURE 8 | Composite differences of **(upper)** the divergence anomaly (shaded; unit: s-1) and **(bottom)** geopotential height (shaded; unit: gpm) and horizontal wind (vector; unit: m/s) anomaly at 150 hPa in May between positive and negative years of PC2 for the period of **(left)** 1958–1979 and **(right)** 1980–2018. The positive (negative) years of PC1 are higher (lower) than 0.5 (−0.5). The black contour of **(A)** and **(B)** indicates the composites of 150 hPa geopotential height (contour; unit: m) for PC2 higher than 0.5 (solid line) or lower than −0.5 (dashed line). The stippling and black vectors denote values exceeding the 90% confidence level.

ENSO events in spring regulates the relative contribution of the SST over Indian and Pacific oceans to the SAH. Except for the SAH, the role of SST forcing plays an important role in the decadal variations of the relationship of monsoon onset via modulating the background flow, which is analyzed in the next part.

Role of Sea Surface Temperature Forcing

Many previous studies have demonstrated that the perturbation of SST may have pronounced influence on the Asian monsoon onset (Webster and Yang, 1992; Chang and Chen, 1995; Wu and Meng, 1998; Luo et al., 2016). For example, in the 1970s, the interdecadal warming over eastern Pacific weakens the ASM by enhancing the Hadley circulation over eastern Asia (Zeng et al., 2007). The anomalous SST over Indo-Pacific warm pool leads to the anomalous anticyclone over BOB and SCS which may contribute to the interdecadal change of ASM (Zhou et al., 2009). Hence, it is necessary to figure out what role the SST forcing plays on the interdecadal change of the BOBSM–SCSSM relationship around the late 1970s.

At first, the atmospheric circulation associated with different monsoon systems has been examined in different epochs. Considering that the SST forcing often affects the monsoon circulation by changing the background flow, the average was taken from April to May as the April-May mean includes the onset pentads of both BOBSM and SCSSM. **Figures 9**, **10** present the atmospheric circulation at the lower and upper troposphere associated with the BOBSM and SCSSM in different subperiods. When the BOBSM builds up late, a prominent anomalous low pressure is centered over the north of BOB and is accompanied by anomalous westerly over BOB in the upper troposphere (**Figure 9A**). In contrast, there is not evident system related to the BOBSM onset in the lower troposphere (**Figure 10A**). When the SCSSM onsets late, the upper troposphere over SCS is controlled by anomalous westerly wind (**Figure 9B**), while lower troposphere is taken place by an anomalous anticyclone (**Figure 10B**). Thus, in the first subperiod, there are distinguishable characteristics between the upper tropospheric circulation related to the BOBSM and SCSSM, respectively. However, in the second subperiod, the associated circulations with the BOBSM are similar to that with the SCSSM. Specifically, the location of anomalous low pressure at the upper troposphere presents a northeastward shift (**Figure 9C**), compared with that in the first subperiod (**Figure 9A**). The large-scale anomalous high pressure appears at 150 hPa from TIO to Arabian Sea, BOB and SCS, which cannot be seen in the first subperiod. The anomalous low pressure accompanied by large-scale anomalous high pressure at 150 hPa may contribute to a wider range westerly flow, which controls the upper troposphere of both BOB and SCS in the second subperiod (**Figures 9C,D**).

As term for the lower troposphere, when the BOBSM and SCSSM onset late in the 1980–2018 period, there is anomalous anticyclone accompanied by anomalous high pressure occurring in the BOB and SCS (**Figures 10C,D**), which is adverse to the development of the westerly flow and monsoon convection in lower troposphere (**Figure 4**). Except for the anomalous high

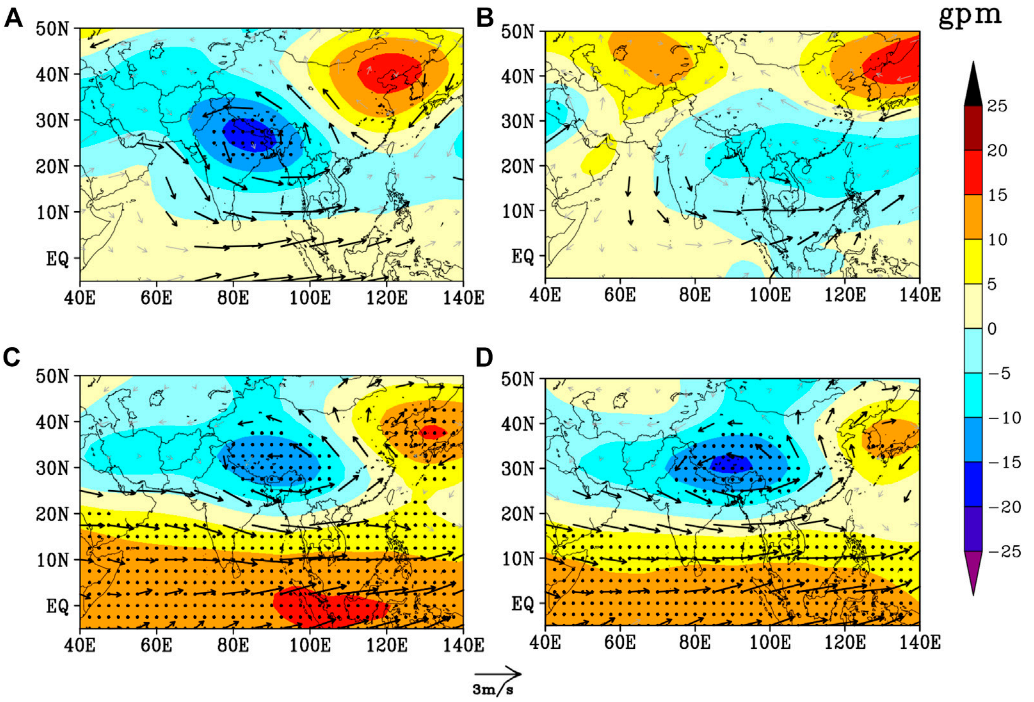

FIGURE 9 | Regression maps of the AM-mean wind anomaly (vectors; unit: m/s) and geopotential height anomaly (shaded; unit: m) at 150 hPa against the **(left)** BOBSM onset time and **(right)** SCSSM onset for **(upper)** 1958–1979 and **(bottom)** 1980–2018. The stippling and black vectors denote values exceeding the 90% confidence level.

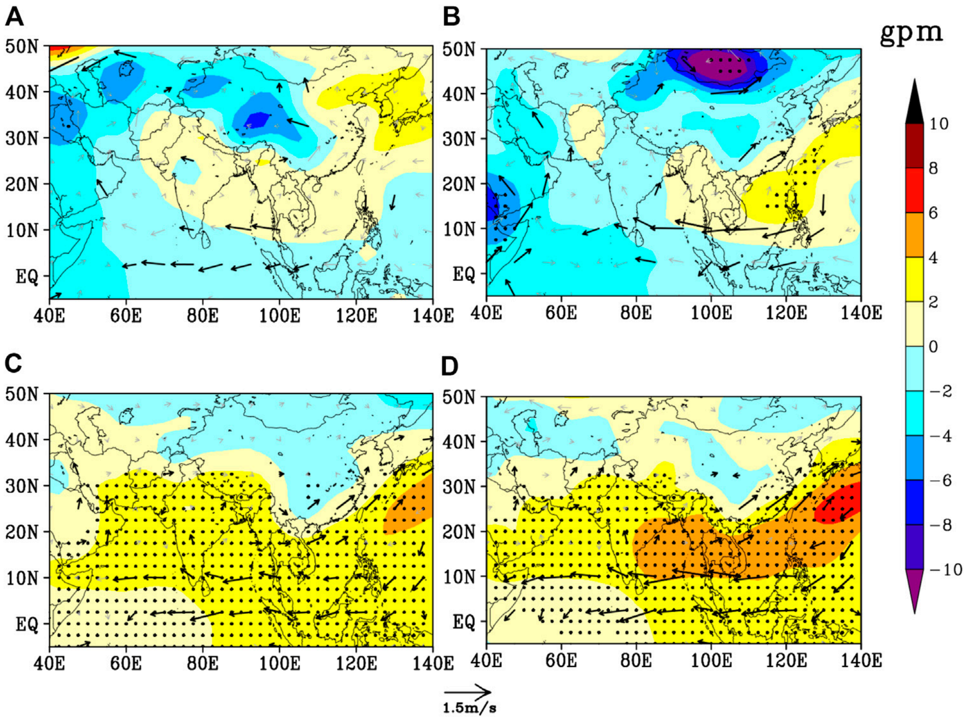

FIGURE 10 | Same as **Figure 9**, but for the variables at 850 hPa.

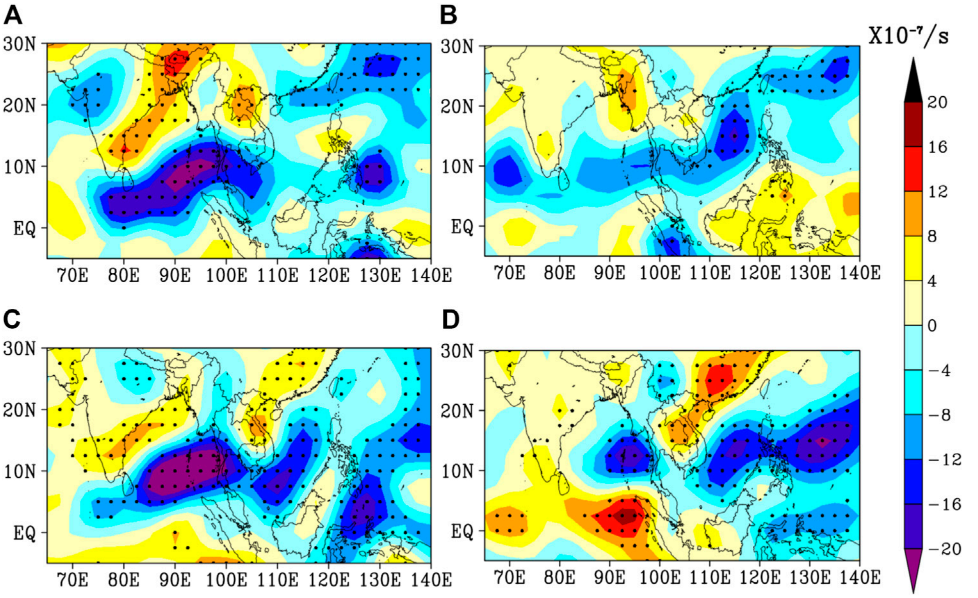

FIGURE 11 | Regression maps of the preonset divergence anomaly (shaded; unit: s^{-1}) at 150 hPa against the **(left)** BOBSM onset time and **(right)** SCSSM onset time for **(upper)** 1958–1979 and **(bottom)** 1980–2018. The stippling denotes values exceeding the 90% confidence level. The preonset stages of BOBSM and SCSSM are pentads 22–24 and 25–27, respectively.

pressure at 850 hPa over BOB and SCS coupling with the same anomalies at 150 hPa (**Figures 9C,D**), the vertical structure in the whole troposphere is occurred by the anomalous high pressure (figure not shown), which implies that it is a barotropic structure in the 1980–2018 period. In addition to the lower tropospheric circulation linked to the monsoon convection, Liu et al., 2013 showed that the trumpet-shaded easterly flow of the SAH forms divergence pumping and ascent movement, which are in favor of the monsoon outbreak. **Figure 11** demonstrates the divergence filed associated with the BOBSM and SCSSM in two periods, respectively. In the 1958–1979 period, the anomalous convergence over the south of BOB is relevant to the delayed BOBSM onset. But when the SCSSM builds up late, the related anomalous convergence only occurs over SCS where the development of convection contributes to the monsoon forming and some parts of tropical western North Pacific. In the 1980–2018 period, compared with the BOBSM (**Figure 11C**), although the SCSSM-related anomalous convergence is relatively weak (**Figure 11D**), the location of BOBSM-related anomalous convergence is similar to the SCSSM-related anomalous convergence. When the BOBSM and SCSSM onset late, the anomalous convergence ranging from the south of BOB and SCS to the east of Philippines modulates the monsoon convection in lower troposphere over BOB and SCS at the same pace. The larger scale of anomalous convergence may result from the anomalous westerly flow at 150 hPa (**Figures 9C,D**) because wider range of the anomalous westerly wind at 150 hPa in 1980–2018 weaken the trumpet-shaped easterly wind of the southern SAH, which results in the divergence pump for the formation of convection, and then contributes to the increasing correlation between the BOBSM and SCSSM in the 1980–2018 period.

As for the anomalies in lower troposphere, many research studies indicate that the SST anomaly can efficiently modulate the low-level circulations, leading to the change of the monsoon onset (Hu and Duan, 2015; Liu et al., 2016). According to **Figure 12**, the relevant SST anomalies are characterized by the anomalous cold SST in the SCS and western North Pacific in the 1958–1979 period. Besides, as for the onset of the BOBSM in the first subperiod, there is a positive SST anomaly over the western tropical Pacific (**Figure 12A**), and the negative SST anomalies (**Figure 12A**) are weaker than the SCSSM-related over SCS (**Figure 12B**). The difference of the relevant SST anomalies between the BOBSM and SCSSM indicates that the SST anomalies serving as the external forcing for the onset of the BOBSM and SCSSM are different. And the lack of synchronous SST anomalies over the whole northern Indian Ocean in the first period may be the reason why the anomalous anticyclone shrinks compared with the second period (Ding et al., 2010). In the 1980–2018 period, the warm SST anomalies over TIO, Arabian Sea, SCS, and the western North Pacific (**Figures 12C,D**) are resembling the basin warming mode of Indian Ocean after the 1980s which is noted by some studies (Saji et al., 2006; Zheng et al., 2011; Huang et al., 2015). This result is consistent with previous studies which demonstrated that the Indian Ocean basin warming mode serves as the main driver to the abnormal low-level anticyclone and the upper-level anomalous high pressure over South Asia (Yang et al., 2007; Yuan et al., 2008; Hu and Duan, 2015). However, the specific mechanism of the SSTA modulating the anomalous anticyclone at 850 hPa (**Figures 6C,D**) and the anomalous high pressure in upper troposphere (**Figures 5C,D**) remains unclear. And the contribution of the basin warming mode of the Indian Ocean to the variation of the

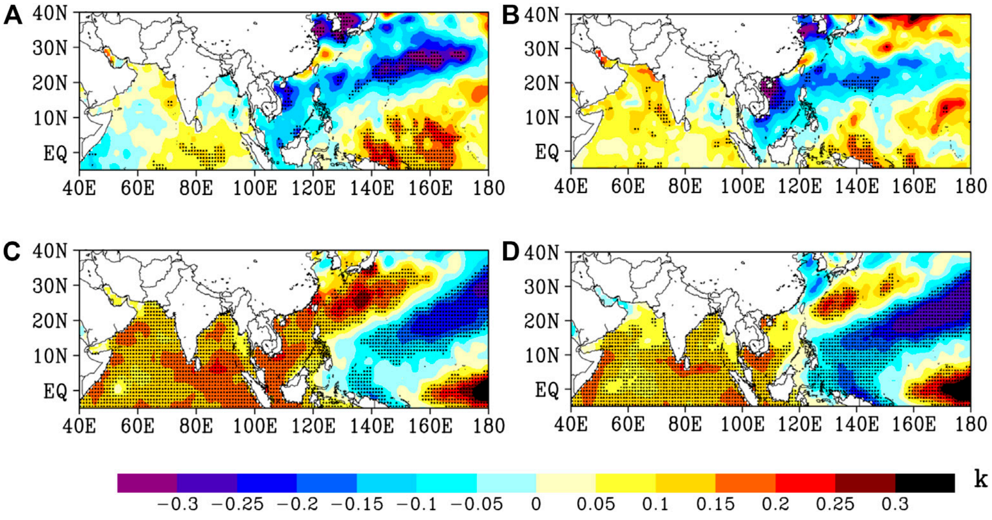

FIGURE 12 | Regression maps of the AM-mean SST (shaded; unit: K) against the **(left)** BOBSM onset time and **(right)** SCSSM onset time for **(upper)** 1958–1979 and **(bottom)** 1980–2018. The stippling denotes values exceeding the 90% confidence level.

BOBSM and SCSSM on the interdecadal time scale needs to be further analyzed.

SUMMARY AND DISCUSSION

In terms of onset, observations show that the BOBSM–SCSSM relationship experienced a significant interdecadal change around the late 1970s. In 1958–1979, the correlation between the BOBSM and SCSSM is 0.22, while it increases to 0.66 in 1980–2018, suggesting a closer connection between the BOBSM and SCSSM after the late 1970s. The evolution of the circulation at low troposphere and the SAH at upper troposphere during the monsoon onset shows interdecadal change as well. Through the analysis of upper troposphere circulation and the SAH, we found that the strength and the meridional shift of the SAH also experience a significant interdecadal change around the late 1970s. That is, the strength of the SAH experiences an interdecadal enhancement, while the meridional shift of the SAH exhibits a wider range in the second subperiod. Both interdecadal change of strength and the meridional shift of the SAH shed more influence in the monsoon onset by modulating the divergent field of upper troposphere in the second subperiod, which may contribute to the closer relationship of the BOBSM and SCSSM. Except for the internal variation of the atmospheric circulation, the external forcing from the SST cannot be ignored. It was found that the tropical Indian Ocean possesses a basin-scale warming after the late 1970s. The upper-level anomalous high pressure over the warming Indian Ocean is accompanied by an anomalous low-pressure center to its north, which is associated with strong westerly anomaly around 20°N, and then modulate the onset of the BOBSM and SCSSM in 1980–2018 through the upper-level divergent field. Furthermore, the zonal-elongated anomalous high pressure lying from the BOB and SCS to the western North Pacific at lower troposphere influences the outbreak of both BOBSM and SCSSM in the second subperiod. This coupling system between the upper and lower tropospheres can act as a large-scale background flow which may modulate the onset of the BOBSM and SCSSM synchronously.

In the present work, the role of SST forcing and the SAH in the BOBSM–SCSSM connection is investigated, respectively. However, the SAH can be influenced by the SST anomaly over the Indian Ocean via a heat-induced Matsuno–Gill pattern in upper troposphere according to previous studies (Yang et al., 2007; Wu et al., 2011; Hu and Duan, 2015). The linkage between SST forcing and the SAH and their relative contribution to the BOBSM–SCSSM relationship need more research. Except for the SST forcing, the interdecadal change of the BOBSM–SCSSM relationship may result from the thermal condition of upper tropospheric atmosphere to the north of BOB, which is plausibly linked to the thermal forcing of TP. According to the regressions of the 20°–30°N-averaged pressure-longitude cross-section of the air temperature in two subperiods, respectively (**Figure 13**), it was noted that there is an anomalous cold center to the north of BOB (80°–100°E) from the lower to upper troposphere (**Figure 13A**), which matches the location of the anomalous low pressure well (**Figure 9A**). In the 1980–2018 period, the prominent cold anomalies related to the BOBSM and SCSSM only extend from the middle to upper troposphere (**Figures 13C,D**), with a wider zonal range and shifting more eastward. It indicates that the difference of anomalous low pressure at upper troposphere in the two subperiods might be attributed to the discrepancies of atmospheric temperature. Besides, the solid existence of anomalous cold over the southern TP might be adverse to the reverse of meridional temperature gradient at the upper troposphere over the South Asia, which is concurrent with the onset of ASM (Webster and Yang, 1992; Li and Yanai, 1996; He et al., 2003). According to previous studies, the air temperature over the TP is significantly influenced by the TP through the

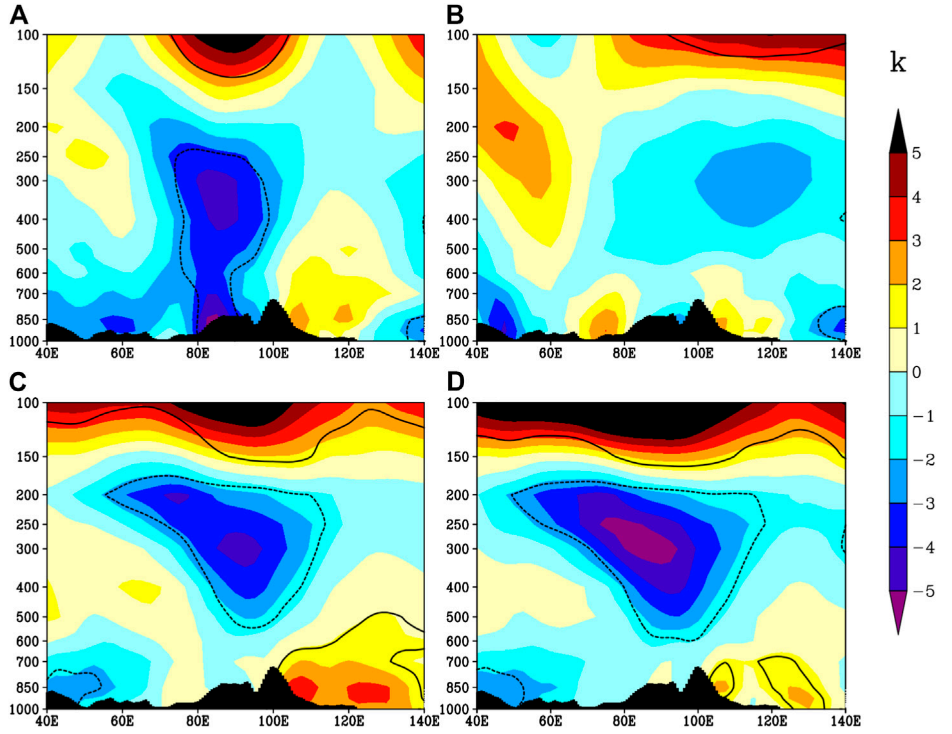

FIGURE 13 | Regression maps of the pressure–longitude cross-section of the AM-mean air temperature (shaded; unit: K) averaged between 20° and 30°N against the **(left)** BOBSM onset time and **(right)** SCSSM onset time for **(upper)** 1958–1979 and **(bottom)** 1980–2018. The area circled by black line denotes values exceeding the 90% confidence level.

sensible heating and vertical velocity (Ding, 1992a; Si and Ding, 2013). Hence, the role of TP forcing on the interdecadal change of the BOBSM–SCSSM relationship remains unknown which needs to be further investigated. Furthermore, the basin warming of the Indian Ocean can also affect the heat condition of TP through modulating the atmosphere circulation (Hu and Duan, 2015), the relative contribution of TP and SST on the monsoon onset remains unclear.

It is well-known that the ASM onset is a very complex issue, since it is linked to abundant climate systems on different timescale. For instance, the onset of the monsoon is related to the intraseasonal convection activity, the variability of the subtropical high over the western North Pacific, the cold-surge derived from the mid-latitude, and so on, which may be play a role on the change of the BOBSM–SCSSM relationship on the interdecadal time scale. Further analysis needs to be carried on to figure out what causes the closer connection between the BOBSM and SCSSM after the late 1970s.

DATA AVAILABILITY STATEMENT

Publicly available datasets were analyzed in this study. This data can be found here: NCEP1 [https://psl.noaa.gov/data/gridded/data.ncep.reanalysis.html]20CRv3 [https://psl.noaa.gov/data/gridded/data.20thC_ReanV3.html#detail]HadISST [https://www.metoffice.gov.uk/hadobs/index.html].

AUTHOR CONTRIBUTIONS

All authors have made a substantial, direct and intellectual contribution to the work, and approved it for publication.

FUNDING

This research is jointly supported by the National Key Research and Development Program of China (2016YFA0600601) and National Natural Science Foundation of China (41530530,41875087,41905072).

ACKNOWLEDGMENTS

The authors thank the reviewers for their valuable suggestions that helped improve this manuscript.

REFERENCES

Annamalai, H., Okajima, H., and Watanabe, M. (2007). Possible impact of the Indian ocean SST on the northern hemisphere circulation during El Niño*. *J. Clim*. 20, 3164–3189. doi:10.1175/JCLI4156.1

Chang, C.-P., and Chen, G. T.-J. (1995). Tropical circulations associated with southwest monsoon onset and westerly surges over the south China sea. *Mon. Weather Rev*. 123, 3254–3267. doi:10.1175/1520-0493(1995)123%3C3254:TCAWSM%3E2.0.CO;2

Ding, R., Ha, K. J., and Li, J. P. (2010). Interdecadal shift in the relationship between the East Asian summer monsoon and the tropical Indian Ocean. *Clim. Dynam*. 34, 1059–1071. doi:10.1007/s00382-009-0555-2

Ding, S., Wen, Z., and Chen, W. (2016). Interdecadal change in the relationship between the South China Sea summer monsoon onset and two types of pacific sea surface temperature anomaly. *Chin. J. Atmos. Sci*. 40, 243–256. doi:10.3878/j.issn.1006-9895.1507.15102

Ding, Y. (1992a). Effects of the Qinghai-Xizang (Tibetan) plateau on the circulation features over the plateau and its surrounding areas. *Adv. Atmos. Sci*. 9, 112–130. doi:10.1007/BF02656935

Ding, Y. H. (1992b). Summer monsoon rainfalls in China. *J. Meteorol. Soc. Japan Ser. II*. 70, 373–396. doi:10.2151/jmsj1965.70.1B_373

Ding, Y. H., Sun, Y., Wang, Z. Y., Zhu, Y. X., and Song, Y. F. (2009). Inter-decadal variation of the summer precipitation in China and its association with decreasing Asian summer monsoon Part II: possible causes. *Int. J. Climatol*. 29, 1926–1944. doi:10.1002/joc.1759

Ding, Y. H., Wang, Z. Y., and Sun, Y. (2008). Inter-decadal variation of the summer precipitation in East China and its association with decreasing Asian summer monsoon. Part I: observed evidences. *Int. J. Climatol*. 28, 1139–1161. doi:10.1002/joc.1615

Fu, J. J., Li, S. L., and Luo, D. H. (2009). Impact of global SST on decadal shift of east asian summer climate. *Adv. Atmos. Sci*. 26, 192–201. doi:10.1007/s00376-009-0192-z

He, H., Mcginnis, J. W., Song, Z., and Yanai, M. (1987). Onset of the asian summer monsoon in 1979 and the effect of the Tibetan plateau. *Mon. Weather Rev*. 115, 1966–1995. doi:10.1175/1520-0493(1987)115%3C1966:OOTASM%3E2.0.CO;2

He, H. Y., Sui, C. H., Jian, M. Q., Wen, Z. P., and Lan, G. D. (2003). The evolution of tropospheric temperature field and its relationship with the onset of Asian summer monsoon. *J. Meteorol. Soc. Jpn*. 81, 1201–1223. doi:10.2151/jmsj.81.1201

Hu, J., and Duan, A. (2015). Relative contributions of the Tibetan Plateau thermal forcing and the Indian Ocean Sea surface temperature basin mode to the interannual variability of the East Asian summer monsoon. *Clim. Dynam*. 45, 2697–2711. doi:10.1007/s00382-015-2503-7

Huang, G., Hu, K., Qu, X., Weichen, T., Shailei, Y., Guijie, Z., et al. (2015). A review about Indian Ocean basin mode and its impacts on east asian summer climate. *Chin. J. Atmos. Sci*. 40, 121–130. doi:10.3878/j.issn.1006-9895.1505.15143

Kajikawa, Y., and Wang, B. (2012). Interdecadal change of the south China Sea summer monsoon onset. *J. Clim*. 25, 3207–3218. doi:10.1175/JCLI-D-11-00207.1

Kajikawa, Y., Yasunari, T., Yoshida, S., and Fujinami, H. (2012). Advanced Asian summer monsoon onset in recent decades. *Geophys. Res. Lett*. 39, 1033. doi:10.1029/2011GL050540

Kalnay, E., Kanamitsu, M., Kistler, R., Collins, W., Deaven, D., Gandin, L., et al. (1996). The NCEP/NCAR 40-year reanalysis project. *Bull. Am. Meteorol. Soc*. 77, 437–471. doi:10.1175/1520-0477

Li, C., and Yanai, M. (1996). The onset and interannual variability of the asian summer monsoon in relation to land–sea thermal contrast. *J. Clim*. 9, 358–375. doi:10.1175/1520-0442(1996)009%3C0358:TOAIVO%3E2.0.CO;2

Li, H., Dai, A., Zhou, T., and Lu, J. (2008). Responses of East Asian summer monsoon to historical SST and atmospheric forcing during 1950–2000. *Clim. Dynam*. 34, 501–514. doi:10.1007/s00382-008-0482-7

Li, K. P., Liu, Y. L., Li, Z., Yang, Y., Feng, L., Khokiattiwong, S., et al. (2018). Impacts of ENSO on the Bay of bengal summer monsoon onset via modulating the intraseasonal oscillation. *Geophys. Res. Lett*. 45, 5220–5228. doi:10.1029/2018GL078109

Liu, B. Q., He, J. H., and Wang, L. J. (2012). On a possible mechanism for southern asian convection influencing the south asian high establishment during winter to summer transition. *J. Trop. Meteorol*. 18, 473–484. doi:10.16555/j.1006-8775.2012.04.007

Liu, B. Q., Liu, Y. M., Wu, G. X., Yan, J. H., He, J. H., and Ren, S. L. (2015a). Asian summer monsoon onset barrier and its formation mechanism. *Clim. Dynam*. 45, 711–726. doi:10.1007/s00382-014-2296-0

Liu, B. Q., Wu, G. X., Mao, J. Y., and He, J. H. (2013). Genesis of the south asian high and its impact on the asian summer monsoon onset. *J. Clim*. 26, 2976–2991. doi:10.1175/JCLI-D-12-00286.1

Liu, B. Q., Wu, G. X., and Ren, R. C. (2015b). Influences of ENSO on the vertical coupling of atmospheric circulation during the onset of South Asian summer monsoon. *Clim. Dynam*. 45, 1859–1875. doi:10.1007/s00382-014-2439-3

Liu, B. Q., and Zhu, C. W. (2016). A possible precursor of the south China Sea summer monsoon onset: effect of the south asian high. *Geophys. Res. Lett*. 43, 11072–11079. doi:10.1002/2016GL071083

Liu, B. Q., Zhu, C. W., and Yuan, Y. (2017). Two interannual dominant modes of the South Asian High in May and their linkage to the tropical SST anomalies. *Clim. Dynam*. 49, 2705–2720. doi:10.1007/s00382-016-3490-z

Liu, B. Q., Zhu, C. W., Yuan, Y., and Xu, K. (2016). Two types of interannual variability of South China Sea summer monsoon onset related to the SST anomalies before and after 1993/94. *J. Clim*. 29, 6957–6971. doi:10.1007/s00382-016-3490-z

Liu, Y. M., Chan, J. C. L., Mao, J. Y., and Wu, G. X. (2002). The role of Bay of Bengal convection in the onset of the 1998 South China Sea summer monsoon. *Mon. Weather Rev*. 130, 2731–2744. doi:10.1175/JCLI-D-16-0065.1

Luo, M., Leung, Y., Graf, H.-F., Herzog, M., and Zhang, W. (2016). Interannual variability of the onset of the South China Sea summer monsoon. *Int. J. Climatol*. 36, 550–562. doi:10.1175/1520-0493(2002)130%3C2731:TROBOB%3E2.0.CO;2

Mao, J., and Wu, G. (2007). Interannual variability in the onset of the summer monsoon over the Eastern Bay of Bengal. *Theor. Appl. Climatol*. 89, 155–170. doi:10.1002/joc.4364

Peng, L. X., Zhu, W. J., Li, Z. X., Ni, D. H., Chen, H. S., Pan, L. L., et al. (2018). The interdecadal variation of the south asian high and its association with the sea surface temperature of tropical and subtropical regions. *J. Trop. Meteorol*. 24, 111–122. doi:10.16555/j.1006-8775.2018.01.011

Rayner, N. A., Parker, D. E., Horton, E. B., Folland, C. K., Alexander, L. V., Rowell, D. P., et al. (2003). Global analyses of sea surface temperature, sea ice, and night marine air temperature since the late nineteenth century. *J. Geophys. Res. Atmos*. 108, 4407. doi:10.1029/2002JD002670

Saji, N. H., Xie, S. P., and Yamagata, T. (2006). Tropical Indian Ocean variability in the IPCC twentieth-century climate simulations. *J. Clim*. 19, 4397–4417. doi:10.1175/JCLI3847.1

Si, D., and Ding, Y. (2013). Decadal change in the correlation pattern between the Tibetan plateau winter snow and the east asian summer precipitation during 1979–2011. *J. Clim*. 26, 7622–7634. doi:10.1175/JCLI-D-12-00587.1

Slivinski, L. C., Compo, G. P., Whitaker, J. S., Sardeshmukh, P. D., Giese, B. S., Mccoll, C., et al. (2019). Towards a more reliable historical reanalysis: improvements for version 3 of the twentieth century reanalysis system. *Q. J. R. Meteorol. Soc*. 145, 2876–2908. doi:10.1002/qj.3598

Wang, B., and Linho (2002). Rainy season of the asian–pacific summer monsoon*. *J. Clim*. 15, 386–398. doi:10.1175/1520-0442(2002)015<0386:RSOTAP>2.0.CO;2

Wang, B., LinhoZhang, Y., and Lu, M.-M. (2004). Definition of South China sea monsoon onset and commencement of the east Asia summer monsoon*. *J. Clim*. 17, 699–710. doi:10.1175/2932.1

Wang, B. (2006). *The asian monsoon*. Berlin Heidelberg: Springer-Verlag, 845.

Wang, H. (2001). The weakening of the Asian monsoon circulation after the end of 1970's. *Adv. Atmos. Sci*. 18, 376–386.

Wang, L. J., Dai, A. G., Guo, S. H., and Ge, J. (2017). Establishment of the south asian high over the Indo-China Peninsula during late spring to summer. *Adv. Atmos. Sci*. 34, 169–180. doi:10.1007/s00376-016-6061-7

Webster, P. J., and Yang, S. (1992). Monsoon and enso - selectively interactive systems. *Q. J. R. Meteorol. Soc*. 118, 877–926. doi:10.1002/qj.49711850705

Wei, W., Zhang, R. H., Wen, M., Kim, B. J., and Nam, J. C. (2015). Interannual variation of the south asian high and its relation with Indian and east asian summer monsoon rainfall. *J. Clim*. 28, 2623–2634. doi:10.1175/JCLI-D-14-00454.1

Wei-Dong, Y., Kui-Ping, L., Jian-Wei, S., Lin, L., Hui-Wu, W., and Yan-Liang, L. (2015). The onset of the monsoon over the Bay of bengal: the year-to-year variations. *Atm. Ocean. Sci. Lett.* 5, 342–347. doi:10.1080/16742834.2012.11447011

Wu, G., Duan, A., Liu, Y., Yan, J., Liu, B., Ren, S., et al. (2013). Recent advances in the study on the dynamics of the Asian summer monsoon onset. *Chin. J. Atmos. Sci.* 37, 211–228. doi:10.1007/s00376-007-0972-2

Wu, G., Guan, Y., Liu, Y., Yan, J., and Mao, J. (2011). Air–sea interaction and formation of the Asian summer monsoon onset vortex over the Bay of Bengal. *Clim. Dynam.* 38, 261–279. doi:10.1007/s00382-010-0978-9

Wu, G. X., and Meng, W. (1998). Gearing between the indo-monsoon circulation and the pacific-walker circulation and the ENSO. Part I: Data analyses. *Chin. J. Atmos. Sci.* 22, 380.

Wu, G. X., and Zhang, Y. S. (1998). Tibetan plateau forcing and the timing of the monsoon onset over south Asia and the south China sea. *Mon. Weather Rev.* 126, 913–927. doi:10.1175/1520-0493(1998)126<0913:TPFATT>2.0.CO;2

Wu, R. G., Wen, Z. P., Yang, S., and Li, Y. Q. (2010). An interdecadal change in southern China summer rainfall around 1992/93. *J. Clim.* 23, 2389–2403. doi:10.1175/2009JCLI3336.1

Xiang, B. Q., and Wang, B. (2013). Mechanisms for the advanced asian summer monsoon onset since the mid-to-late 1990s. *J. Clim.* 26, 1993–2009. doi:10.1175/JCLI-D-12-00445.1

Xie, S.-P., Hu, K., Hafner, J., Tokinaga, H., Du, Y., Huang, G., et al. (2009). Indian ocean capacitor effect on indo–western pacific climate during the summer following El Niño. *J. Clim.* 22, 730–747. doi:10.1175/2008JCLI2544.1

Xie, S. P., and Saiki, N. (1999). Abrupt onset and slow seasonal evolution of summer monsoon in an idealized GCM simulation. *J. Meteorol. Soc. Jpn.* 77, 949–968. doi:10.2151/jmsj1965.77.4_949

Yan, H. M., Sun, C. H., Wang, L., Li, R., and Jin, Y. (2018). Studies on onset criterion and interannual characteristics of summer monsoon over Bay of Bengal. *Chin. J. Geophys.-Chin. Edit.* 61, 4356–4372. doi:10.1080/16742834.2012.11447011

Yang, J. L., Liu, Q. Y., Xie, S. P., Liu, Z. Y., and Wu, L. X. (2007). Impact of the Indian Ocean SST basin mode on the Asian summer monsoon. *Geophys. Res. Lett.* 34, L02708. doi:10.1029/2006GL028571

Yim, S.-Y., Jhun, J.-G., and Yeh, S.-W. (2008). Decadal change in the relationship between east Asian–western North Pacific summer monsoons and ENSO in the mid-1990s. *Geophys. Res. Lett.* 35. doi:10.1029/2008GL035751

Yuan, F., and Chen, W. (2013). Roles of the tropical convective activities over different regions in the earlier onset of the South China Sea summer monsoon after 1993. *Theor. Appl. Climatol.* 113, 175–185. doi:10.1007/s00704-012-0776-x

Yuan, Y., Zhou, W., Chan, J. C. L., and Li, C. Y. (2008). Impacts of the basin-wide Indian Ocean SSTA on the South China Sea summer monsoon onset. *Int. J. Climatol.* 28, 1579–1587. doi:10.1002/joc.1671

Zeng, G., Sun, Z., Wang, W. C., and Min, J. (2007). Interdecadal variability of the east Asian summer monsoon and associated atmospheric circulations. *Adv. Atmos. Sci.* 24, 915–926. doi:10.1007/s00376-007-0915-y

Zhang, H. Y., Wen, Z. P., Wu, R. G., Chen, Z. S., and Guo, Y. Y. (2017). Interdecadal changes in the East Asian summer monsoon and associations with sea surface temperature anomaly in the South Indian Ocean. *Clim. Dynam.* 48, 1125–1139. doi:10.1007/s00382-016-3131-6

Zhang, Q., Qian, Y., and Zhang, X. (2000). Interannual and interdecadal variations of the south Asia high. *Chin. J. Atmos. Sci.* 24, 67–78.

Zheng, X. T., Xie, S. P., and Liu, Q. Y. (2011). Response of the Indian Ocean basin mode and its capacitor effect to global warming. *J. Clim.* 24, 6146–6164. doi:10.1175/2011JCLI4169.1

Zhou, T. J., Yu, R. C., Zhang, J., Drange, H., Cassou, C., Deser, C., et al. (2009). Why the western pacific subtropical high has extended westward since the late 1970s. *J. Clim.* 22, 2199–2215. doi:10.1175/2008JCLI2527.1

Zhou, T., Wu, B., Guo, Z., He, C., Zhou, L., Chen, X., et al. (2018). A review of East Asian summer monsoon simulation and projection: achievements and problems, opportunities and challenges. *Chin. J. Atmos. Sci.* 42, 33. doi:10.3878/j.issn.1006-9895.1802.17306

Conflict of Interest: The authors declare that the research was conducted in the absence of any commercial or financial relationships that could be construed as a potential conflict of interest.

frontiers in Earth Science

ORIGINAL RESEARCH
published: 14 January 2021
doi: 10.3389/feart.2020.594656

Abnormal Change in Spring Snowmelt Over Eurasia and Its Linkage to the East Asian Summer Monsoon: The Hydrological Effect of Snow Cover

Bei Xu[1,2], Haishan Chen[1]*, Chujie Gao[3], Gang Zeng[1] and Qinghan Huang[4]

[1]Key Laboratory of Meteorological Disaster, Ministry of Education (KLME) and Collaborative Innovation Center on Forecast and Evaluation of Meteorological Disasters (CIC-FEMD), Nanjing University of Information Science and Technology (NUIST), Nanjing, China, [2]College of Intelligent Science and Control Engineering, Jingling Institute of Technology, Nanjing, China, [3]College of Oceanography, Hohai University, Nanjing, China, [4]Zhejiang Early Warning Center, Zhejiang Meteorological Bureau, Hangzhou, China

Edited by:
Wen Chen,
Institute of Atmospheric Physics (CAS), China

Reviewed by:
Anning Huang,
Nanjing University, China
Shangfeng Chen,
Institute of Atmospheric Physics (CAS), China

***Correspondence:**
Haishan Chen
haishan@nuist.edu.cn

Specialty section:
This article was submitted to Atmospheric Science, a section of the journal Frontiers in Earth Science

Received: *14 August 2020*
Accepted: *28 September 2020*
Published: *14 January 2021*

Citation:
Xu B, Chen H, Gao C, Zeng G and Huang Q (2021) Abnormal Change in Spring Snowmelt Over Eurasia and Its Linkage to the East Asian Summer Monsoon: The Hydrological Effect of Snow Cover.
Front. Earth Sci. 8:594656.
doi: 10.3389/feart.2020.594656

In this study, the relationship between Eurasian spring snowmelt and the East Asian summer monsoon (EASM), and its related mechanisms are investigated using observational and reanalysis data. Our analyses reveal that the interannual change of spring snowmelt over Eurasia is strongly linked to the EASM circulation variation and its corresponding summer precipitation in China. It is noteworthy that soil moisture anomaly caused by the snow hydrological effect (i.e., snowmelt) plays a bridging role in connecting the Eurasian snow cover and the EASM. The results show that increased spring snowmelt over Siberia induces anomalously higher soil moisture from spring to the following summer, thus continuously lowering the local temperature. Such a cooling effect leads to a weakened meridional temperature gradient and a decreased baroclinicity between north Eurasia and the Arctic Ocean. Consequently, the variation in atmospheric baroclinicity induced by the nonuniform heating of land surface exerts a significant impact on the synoptic eddy. The eddy forcing gives a positive feedback on intensification of the wave train over north Eurasia. Finally, the atmospheric circulation responses weaken the EASM and influence summer precipitation over China, producing excessive precipitation over most regions of South China and deficient rainfall over Northeast and North China. Our study emphasizes the hydrological effect of the sub-seasonal change of spring snow cover over Siberia, which has a significant linkage to the variation of the EASM intensity. The resultant changes in the EASM lead to an abnormal meridional dipole pattern of summer precipitation over China. These findings will contribute to the seasonal prediction of monsoon precipitation.

Keywords: snowmelt, snow hydrological effect, east asian summer monsoon, seasonal prediction, eurasian continent

INTRODUCTION

The weather and climate over China are evidently influenced by variations of the monsoon system. Previous studies have shown that large-scale summer drought and flood disasters over China, which can result in tremendous economic losses and human casualties (Wang, 2006; Ding et al., 2009), are closely associated with the onset and intensity of the East Asian summer monsoon (EASM). Therefore, it is essential to explore the nature and cause of the interannual variability of the EASM.

The interannual variability of the Asian monsoon system can be affected by anomalous variations of lower boundary layer properties such as sea surface temperature, snow cover/snow depth, and soil moisture (Wang et al., 2000; Wu et al., 2012; Xiao and Duan 2016; Moon and Ha 2019). Among them, snow cover exerts a great impact on the interannual variability of the monsoon owing to its abilities to alter surface albedo and regulate soil moisture (Xu and Dirmeyer 2011; Wu et al., 2014; Henderson et al., 2018). High albedo reflects more solar radiation, while melting snow absorbs heat and increases soil moisture. In addition, snow cover on the surface will also affect the release of sensible heat between land and atmosphere because of the low thermal conductivity of the snowpack. These local cooling effects, in turn, have been suggested to play a significant role in global-scale climate as well as region climate (Gong et al., 2003; Cohen et al., 2014). Eurasian snow cover has been revealed to significantly influence the Asian summer monsoon (Douville and Royer 1996; Liu and Yanai 2002; Souma and Wang 2010). For the Indian monsoon, numerous analyses have shown that there generally exists a negative correlation between the Eurasian snow cover and the subsequent Indian summer monsoon, indicating that excessive (deficient) Eurasian snow cover/snow depth from winter to spring is followed by weak (strong) Indian summer monsoon rainfall (Sankar-Rao et al., 1996; Fasullo 2004; Dash et al., 2006; Saha et al., 2012). A large amount of numerical simulations have suggested that the abnormal surface thermal states induced by such snow cover anomalies can affect the atmospheric circulation, consequently causing monsoonal precipitation anomalies (Barnett et al., 1989; Bamzai and Marx 2000; Xu and Dirmeyer 2013).

For the East Asia monsoon, previous studies showed that anomalies of Eurasian snow cover have a significant impact on the monsoon precipitation in different regions (Yang and Xu 1994; Kripalani et al., 2002; Wu et al., 2009; Zuo et al., 2014). For example, Wu and Kirtman (2007) found that the snow cover anomalies over western Siberia are associated with an obvious abnormal circulation pattern over the eastern Atlantic through Eurasia, which leads to anomalous spring rainfall in South China. By using snow cover data from National Oceanic and Atmospheric Administration (NOAA) satellites, Yim et al. (2010) noted that the variation of an abnormal dipole pattern of snow cover over Eurasia is closely related to the EASM precipitation over Korea and Japan. Shen et al. (2020) found that an anomalously lower snow water equivalent over Siberia leads to higher temperature from the surface to the mid-troposphere, forming a Rossby wave train response and then leading to below-normal summer rainfall in South-Central China.

Snow cover affects the monsoon circulation system/climate mainly through the albedo effect and snow hydrological effect (Groisman et al., 1994; Wang et al., 2015). Previous studies have emphasized a robust relationship between winter/spring Eurasian snow cover and the East Asian climate, and have attempted to illustrate the relative potential mechanism. However, whether the albedo effect or the snow hydrological effect is more important still remains unclear. Robock et al. (2003) concluded that the albedo of snow cover is more significant because the snow hydrological effect can last for only one to two months. To support this conclusion, Liu et al. (2004) performed regional climate simulations and showed that the effect of albedo dominates the process during which snow cover affects climate, while the effects of snowmelt and evaporation are relatively less important. Nevertheless, some other studies tended to show that the snow hydrological effect is more significant (Bamzai and Marx 2000; Dash et al., 2006), and the albedo effect of snow cover becomes dominant only at a certain stage or in a certain region (Ose 1996; Souma and Wang 2010). For example, Wu et al. (2014) and Zhang et al. (2008) suggested that soil moisture anomalies are likely to be caused by snowmelt in spring and then maintained to summer, finally producing abnormal variations in the summer precipitation. Halder and Dirmeyer (2017) showed that snow cover in Eurasia can affect soil moisture through the lagged hydrological effect, resulting in the abnormal Indian summer monsoon circulation and thus precipitation anomalies.

Previous studies mainly focus on the effects of snow cover on climate at the seasonal scale, while the sub-seasonal change of snow cover (i.e., snowmelt) and its influences are less investigated. It is worth mentioning that snow cover in Eurasia exhibits little change during the three months in winter but shows evident sub-seasonal variations in other seasons, especially in spring (Mu and Zhou 2010). During March, April, and May, snow cover variation can be characterized by a snowmelt starting from southern to northeastern Eurasia, and a large amount of snow cover has disappeared by May. Under such a condition, studies on spring snow cover in Eurasia relying on the seasonal averages may erase inter-monthly differences. For instance, Dey and Kummar (1982) found that an anomalously larger snow cover area in spring over Eurasia plays an important role in retarding the development of the Indian summer monsoon, while a similar change in the snowmelt area has stronger contrary effect. Thus, spring snowmelt may be more suitable to represent the sub-seasonal variation of snow cover.

Zhang et al. (2017) have already indicated that a decrease of spring snow water equivalent in Eurasia can affect the East Asian summer precipitation and its associated abnormal atmospheric circulation via triggering an anomalous midlatitude Eurasian wave train. However, its effects on the EASM circulation system, the dominant factor of summer precipitation over East Asia, still remain unclear. The purpose of the present study is to investigate the effect of spring snowmelt on the EASM system and discuss the possible physical mechanisms underlying it. The results show that a strong relationship exists between spring snowmelt over Eurasia and the EASM. To be more specific, when there is excessive snowmelt in spring over Siberia, the EASM weakens with more/less summer precipitations over southern/northern China, and vice versa. This is mainly due to the snow hydrological effect: The abnormally higher snowmelt changes the local soil moisture in spring, and such a soil moisture anomaly is sustained to summer. Consequently, a continuously cooling effect is induced over Siberia, which decreases the temperature gradient and baroclinicity between north Eurasia and the Arctic Ocean in summer. Therefore, the spring snowmelt exerts a great impact on the summer atmospheric states and the monsoon circulations.

The rest of this paper is arranged as follows. *Data and Methods* introduces the data and methods adopted in our study. *Climatologies of Observed Snow Water Equivalent and Snowmelt in Spring Over Eurasia* presents the basic features of spring snowmelt variations over Eurasia. *Relationships Between the Eurasian Spring Snowmelt and the East Asian Summer Monsoon* shows the relationship between the spring snowmelt over Eurasia and the EASM anomalies. The related mechanisms are investigated and demonstrated in *The Effect of Snowmelt Over Eurasia on the East Asian Summer Monsoon. Summary and Discussion* is the summary.

DATA AND METHODS

The data used in this study include: 1) The Finnish Meteorological Institute's monthly snow water equivalent (SWE) dataset (Takala et al., 2011) from 1979 to 2014 that has an original resolution of 25 km × 25 km; in this study, by adopting the method of bilinear interpolation, we produced uniform grids with a resolution of 1° × 1°. 2) Monthly soil moisture dataset provided by the Global Land Data Assimilation System (GLDAS) V2.0 for the period 1948–2012 (1° × 1°; Rodell et al., 2004), which has been used previously in studies related to East Asian land surface processes (Wu and Zhang 2013; Cheng et al., 2015). The soil moisture information for the surface layer (0–10 cm) was used in this study. 3) The monthly reanalysis data with a resolution of 1° × 1° provided by the European Center for Medium-Range Weather Forecasts (ECMWF) from 1979 to 2015, whose variables include soil moisture, 2-m surface temperature, geopotential height, temperature, and wind fields. 4) The monthly observed precipitation data with a resolution of 1° × 1° provided by the China Meteorological Administration.

In this study, the spring snowmelt amount was calculated by subtracting the SWE in May from that in March, and if the value of the defined difference is positive, it represents the spring snowmelt amount. The seasonal means of other variables were calculated by 3-months averages: spring (March to May) and summer (June to August). The study period was set to be 1981–2014.

The scheme adopted in this study to calculate the apparent heat source, Q_1 (Yanai et al., 1992), is shown as follows:

$$Q_1 = c_p\left[\frac{\partial\overline{T}}{\partial t} + \overrightarrow{V}\cdot\nabla\overline{T} + \overline{\omega}\left(\frac{p}{p_0}\right)^k\frac{\partial\overline{\theta}}{\partial p}\right]$$

in which $k = R/c_p$, R and c_p correspond to the gas constant of dry air and the specific heat at constant pressure, respectively, and θ is the potential temperature. Three terms are contained in the parentheses on the right side of the equation, corresponding to the local variation term, horizontal advection term, and vertical transport term. Q_1 represents the rate of air heating per unit mass per unit time.

CLIMATOLOGIES OF OBSERVED SNOW WATER EQUIVALENT AND SNOWMELT IN SPRING OVER EURASIA

Groisman et al. (1994) proposed that snow cover exhibits the greatest influence on the Earth's radiative balance in the spring period (especially April and May) when the incoming solar radiation is mainly concentrated in high-latitude regions (i.e., snow cover regions). **Figure 1** illustrates the multi-year mean SWE and snowmelt in spring, and their interannual standard deviations for the period of 1981–2014 over Eurasia.

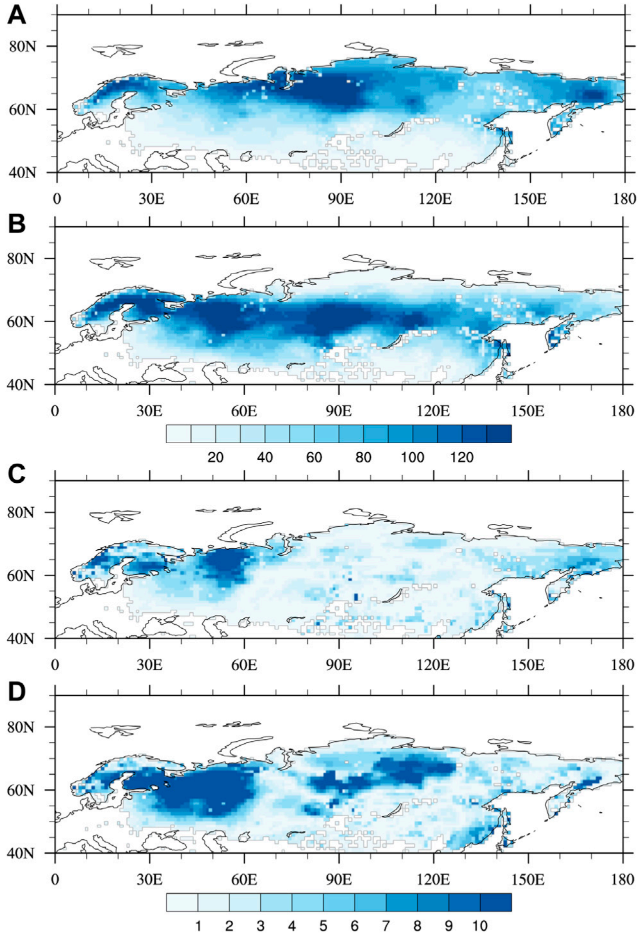

FIGURE 1 | The multi-year means of **(A)** SWE (mm) and **(B)** snowmelt (mm) in spring, and **(C,D)** their interannual standard deviations for the period of 1981–2014.

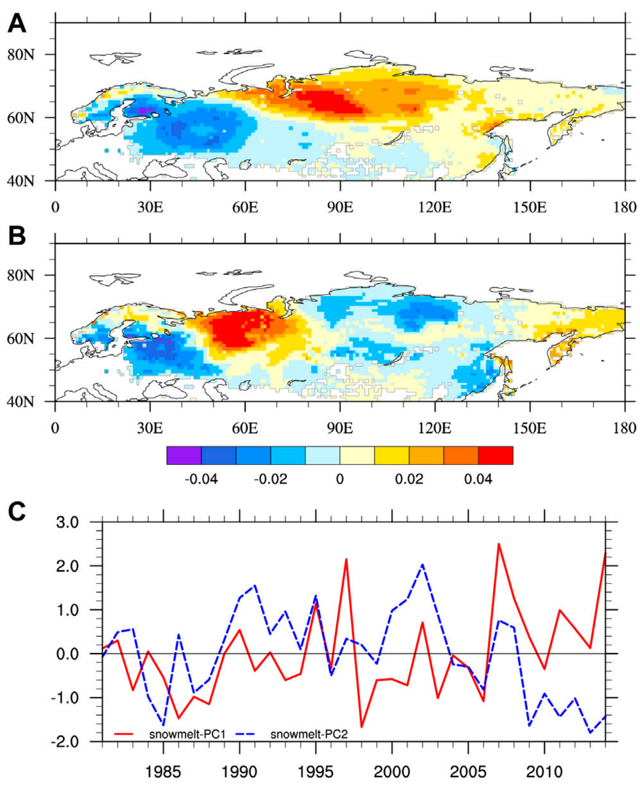

FIGURE 2 | Spatial pattern of **(A)** the first EOF mode, **(B)** the second EOF mode of spring snowmelt anomaly over Eurasia, **(C)** and time series of the two modes of spring snowmelt.

In spring, the northern part of Eurasia is almost completely covered by snow, and it is evident that the snow cover is relatively deeper over the region north of 60° N, with the maximal amount reaching 150 mm (**Figure 1A**). In addition, there is little interannual variability over Siberia, while northern Europe has a large interannual variability due to the freezing/thawing of snow, suggesting that there are evident changes in the speed of local snowmelt (**Figure 1C**). During the springtime, the mean snowmelt is mainly concentrated in Siberia, and the maximal snowmelt amount reaches 100 mm, which is comparable to the snow cover amount in spring (**Figure 1B**). In western Siberia and Europe, there are strong interannual variabilities of snowmelt (**Figure 1D**), which means there exists significant interaction between snow cover and atmospheric circulation and related surface air temperature changes (Chen et al., 2016; Wu and Chen 2016). Thus, spring snowmelt variation over Siberia and its potential influences are worthy of attention.

An empirical orthogonal function (EOF) analysis was further applied to investigate the Eurasian spring snowmelt variations. The first EOF mode (EOF1) of the spring snowmelt accounts for 20.5% of the total variance. According to North et al. (1982), this mode is well separated from others. **Figure 2** shows the spatiotemporal features of the first two EOF modes of Eurasian spring snowmelt. The spatial pattern of EOF1 is characterized by a west-east dipole pattern, with a negative center located in the East European Plain and a positive center in Siberia (**Figure 2A**). As shown by the principal component of EOF1 (PC1), the anomaly pattern exhibits significant interannual variations (**Figure 2B**) with a significant upward long-term trend (correlation between the time and PC1 is 0.38, $p < 0.05$). This further suggests that a relatively large variation center of spring snowmelt is located over Siberia. The second EOF mode (EOF2) of the spring snowmelt accounts for 15.2% of the total variance. As shown in **Figure 2B**, the EOF2 of Eurasian spring snowmelt shows the three-pole type, with a positive center in Northern Europe and two negative centers at Central Europe and Siberia.

RELATIONSHIPS BETWEEN THE EURASIAN SPRING SNOWMELT AND THE EAST ASIAN SUMMER MONSOON

Previous studies have presented that there are evident connections between snow cover over high-latitudes and the EASM (Wu and Kirtman 2007; Xiao and Duan 2016). Correspondingly, the East Asian summer precipitation and 850-hPa wind anomalies related to EOF1 of spring snowmelt were investigated with correlation analysis. As shown in **Figure 3**,

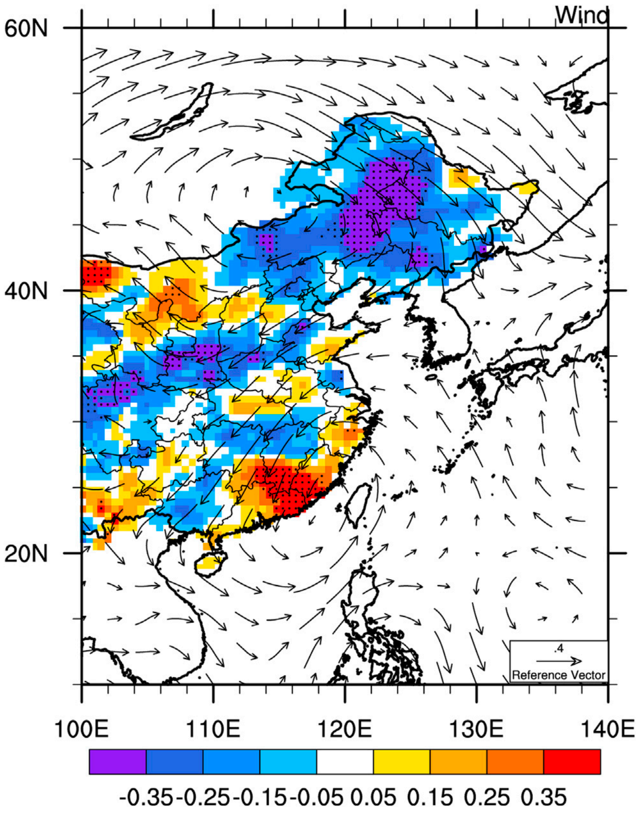

FIGURE 3 | The correlation coefficients between PC1 of the spring snowmelt over Eurasia and summer 850-hPa wind field (vector) over East Asia. The correlation coefficients between PC1 of the spring snowmelt over Eurasia and precipitation in eastern China are shaded. Dotted areas denote the correlation significant at the 95% confidence level.

the correlation coefficient pattern of wind filed with PC1 indicates that a weak cyclonic circulation exists in the south of 30° N in China, while the region around Lake Baikal is controlled by a strong anti-cyclonic circulation. When the PC1 phase is positive, there exist northeasterly (or northerly) wind anomalies from Northeast China, the Shandong Peninsula, the Bohai Gulf, and the middle to lower reaches of the Yangtze River to regions south of the Yangtze River, suggesting a weakened EASM activity. In contrast, when PC1 is negative, southwesterly wind anomalies become widely popular over East China and the Korean Peninsula, and the summer monsoon activity is strengthened. For the monsoon precipitation, the correlation distribution map of summer precipitation with PC1 shows a meridional dipole structure prevailing in the region between northern and southern China. When the snowmelt over Siberia is abnormally higher in spring, above-normal precipitation tends to be observed in south China and below-normal precipitation appears over north China, and vice versa. In addition, we recalculated our results based on the detrended data, and they are highly consistent with the results before removing the long-term trend.

According to Huang et al. (2015), the anomalous activity of the EASM has multi-spatial modes, and their results suggested that its second EOF mode (EOF2) shows consistent variation of summer wind over the extensive area extending from South China, across the middle-lower reaches of the Yangtze River, the Shangdong Peninsula, the Bay of Bohai Sea, to Northeast China and the Korean Peninsula, which represents the overall variation of EASM intensity. **Figure 4** shows EOF1 and EOF2 of the 850-hPa wind and summer precipitation over eastern China corresponding to the PCs of the EASM wind. The EOF1 mode of the 850-hPa wind is characterized by enhanced northeasterly wind from the middle and lower reaches of the Yangtze River to southern China and strengthened westerly wind between 10°N and 20°N. The anomalous precipitation pattern related to PC1 show negative anomalies over the middle and lower reaches of the Yangtze River, and positive anomalies over the east of northeast China, the southeast coastal area, and western Yunnan. (**Figure 4A**). The EOF2 mode of the 850-hPa wind is shown in **Figure 4B**, and it demonstrates a cyclonic circulation and an anti-cyclonic circulation over the south and north of East Asia, respectively, which is generally consistent with the anomalous wind related to PC1 of Eurasian snowmelt. The correlation coefficient between PC1 of spring snowmelt over Eurasia and PC2 of summer 850-hPa wind over East Asia reaches 0.38 (figure not shown), which is statistically significant at the 95% confidence level. **Figure 4B** further shows the summer precipitation over eastern China corresponding to PC2 of the EASM wind. The precipitation anomaly generally exhibits opposite phases between southern and northern China. The spatial correlation coefficient between the summer precipitation anomalies related to PC1 of spring snowmelt and PC2 of the EASM is as high as 0.65 ($p < 0.001$) (figure not shown). Those above findings further confirm that Eurasian spring snowmelt has evident effects on the EASM and its related precipitation.

To identify the key region of spring snowmelt affecting the EASM, **Figure 5** demonstrates the spatial distribution of the correlation coefficient between spring snowmelt and PC2 of the EASM. As expected, the key area is mainly located in Siberia (as shown by the black box in **Figure 5**), which has a large coverage of positive correlations. To quantify the Eurasian snowmelt variability and its relationship with the EASM, we defined a snowmelt index (I_{SM}) as the normalized area-averaged spring snowmelt over Siberia (55 –75 N and 60 –120 E). **Figure 6** shows the PC2 of the EASM and I_{SM} during 1981–2014. I_{SM} is highly

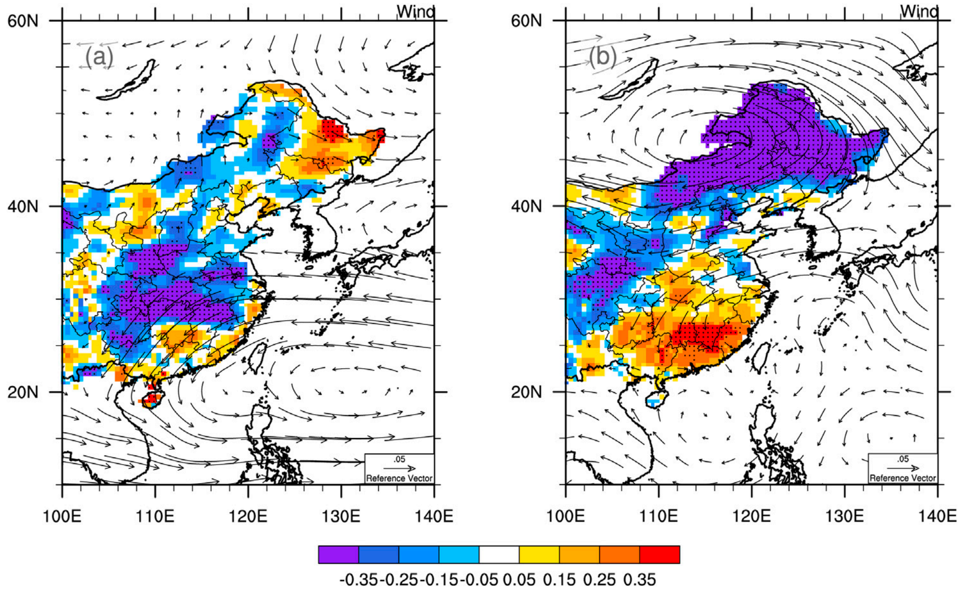

FIGURE 4 | Spatial patterns (vectors) of the **(A)** first and **(B)** second mode of EASM, whichare given by the first two modes of the summer 850-hPa wind EOF analysis over East Asia. The correlation coefficients between time series of PC1 (PC2) and precipitation in eastern China are shaded in a **(B)**. Dotted areas denote the correlation significant at the 95% confidence level.

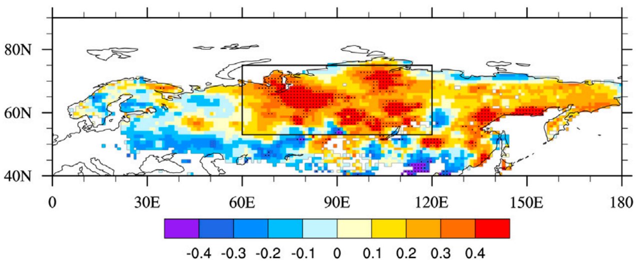

FIGURE 5 | Correlation coefficients between PC2 of the EASM and the spring snowmelt over Eurasia. Dotted areas denote the correlation significant at the 95% confidence level.

consistent with PC2 of the EASM, and their correlation coefficient is 0.55, which is statistically significant at $p < 0.001$. After removing their long-term trends, the correlation coefficient still reaches 0.45 ($p < 0.05$), verifying that the variation of EASM is distinctly associated with the spring snowmelt over Eurasia. Furthermore, the correlation distribution between I_{SM} and summer 850-hPa wind over East Asia as well as that between I_{SM} and rainfall in eastern China is shown in **Figure 7**. The correlation pattern more resembles the spatial distribution of EOF2 of the EASM and its corresponding precipitation anomalies, confirming that the key region where spring snowmelt affects the EASM lies over Siberia.

THE EFFECT OF SNOWMELT OVER EURASIA ON THE EAST ASIAN SUMMER MONSOON

SWE is a measure of water mass in the snowpack, and its characteristics determine the potential for the snow hydrological effect. In this study, we highlight the effect of spring snowmelt over Eurasia on the EASM circulation and precipitation, which can be attributed to the snow hydrological effect. It is found that the abnormal soil moisture over Eurasia induced by the spring snowmelt anomalies sustains itself to summer, affecting the local thermal state and thus the remote atmospheric circulation.

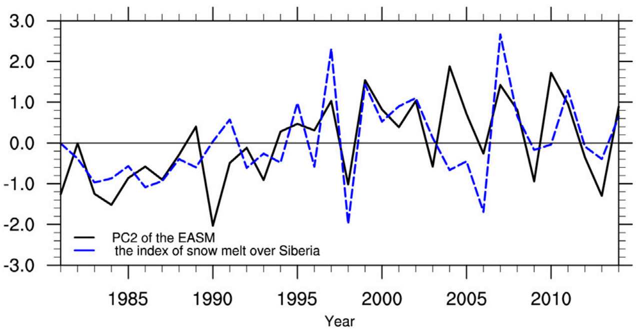

FIGURE 6 | The standardized time series of PC2 of the EASM over East Asia and the standardized time series of ISM during 1981–2014.

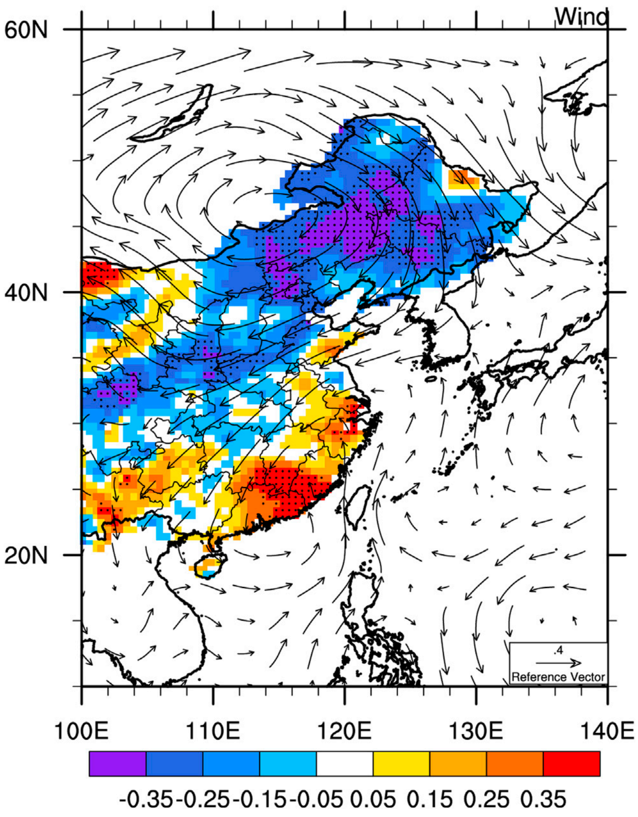

FIGURE 7 | The correlation coefficients between ISM and summer 850-hPa wind field (vector) over East Asia. The correlation coefficients between ISM and precipitation in eastern China are shaded. Dotted areas denote the correlation significant at the 95% confidence level.

Figure 8A displays the regressed 0–10-cm soil moisture anomalies during summer onto I_{SM}. Over Siberia, especially its western part, a significant increase in surface soil moisture occurs together with a large I_{SM}. The connection between snowmelt and soil moisture supports the clear snow hydrological effect during the warming season: Excessive (deficient) snowmelt leads to wetter (drier) soil. It is similar to the results of Quiring and Kluver (2009), who found that an increase in snowfall during winter shows a positive correlation with the soil moisture in the subsequent summer in the northern part of the Great Plains. Along with the anomalous surface evapotranspiration associated with such a moistening (drying) of soil (figure not shown), there is a significant cooling (warming) in local air temperature in summer (**Figure 8B**).

Soil moisture anomalies generated from snowmelt during spring can modulate land-atmosphere coupling (Xu and Dirmeyer 2011) and act as a delayed snow-driven feedback to the atmosphere in summer. To analyze the effect of snowmelt on the surface thermal conditions in spring and summer, we primarily investigated the apparent heating. **Figure 9** shows the height-latitude section (averaged over 40°–140° E) of the regression of spring and summer Q_1 anomalies onto I_{SM}. As

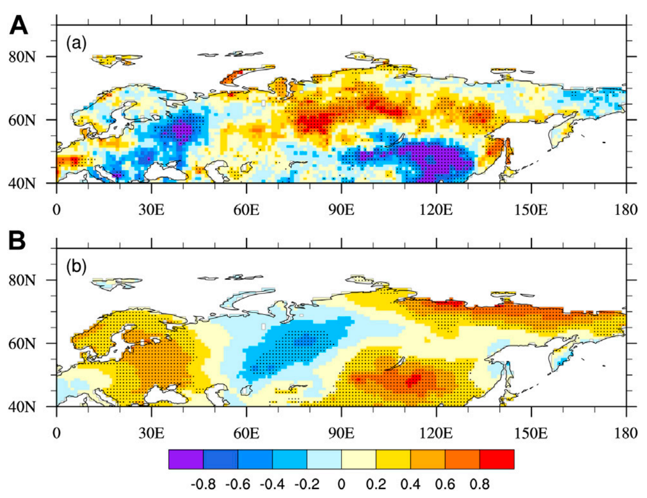

FIGURE 8 | Regression of **(A)** GLDAS-2.0 surface soil moisture (0–10 cm; mm), and **(B)** 2-m temperature (K) in summer onto ISM during 1981–2014. Dotted areas are significant at the 95% confidence level.

shown in **Figure 9A**, there exists a negative anomaly of Q_1 from the ground surface to the overlying atmospheric column in spring, resulting in a vertical temperature structure characterized by a "cold source" from the ground surface to the 500-hPa upper troposphere. In summer, the pattern of the apparent heating anomalies is quite similar to that in spring, but the corresponding strength in summer is only half of that in spring (**Figure 9B**). It is in agreement with previous studies which show that Eurasian snowmelt may directly increase soil moisture, and then affect soil temperature during warming seasons, thereby leading to the reduction of surface air temperature and tropospheric diabatic heating (Saito and Cohen 2003; Zuo et al., 2011).

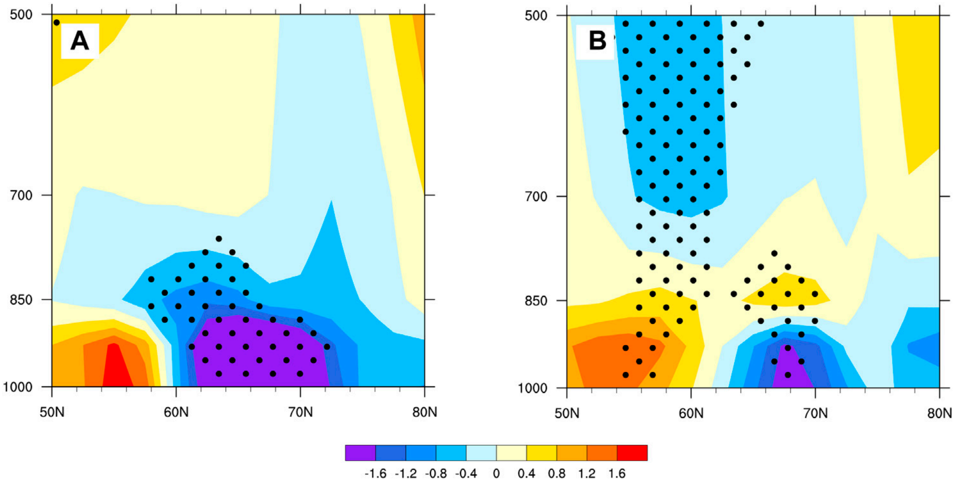

FIGURE 9 | Regression of the height-latitude section (averaged over 40°–140° E) in **(A)** spring and **(B)** summer Q1 (10 −6k/mon) anomalies onto ISM during 1981–2014. Dotted areas are significant at the 95% confidence level.

Figure 10A illustrates that the near-surface thermal conditions associated with snowmelt substantially change the local temperature thickness of the lower troposphere between 700 and 1,000 hPa, with a notable cooling centered over western Siberia. The decreased summer temperature over Siberia further reduces the meridional temperature gradient between northern Eurasia and the Arctic Ocean, and simultaneously strengthens the meridional temperature gradient between the mid-latitude regions to northern Eurasia. Lindzen et al. (1980) pointed out that the atmospheric baroclinicity is closely related to the meridional temperature gradient of the atmosphere. We calculated the maximum Eady growth rate σ_{BI} between 850 and 700 hPa, which was used to characterize the atmospheric baroclinicity, as follows: $\sigma_{BI} = 0.31f\,(\partial|\overline{V}|/\partial z)N^{-1}$ (where f is the Coriolis parameter, N is the Brunt–Väisälä frequency, $\overline{V}$ is the time-averaged horizontal wind speed, and z is the vertical height). **Figure 10B** shows the spatial distribution of the atmospheric baroclinicity index anomaly derived from the regression of I_{SM}. Based on the principle of thermal wind and the definition of atmospheric baroclinicity, if the north–south temperature gradient decreases to the north, then the atmospheric baroclinicity weakens; if the north–south temperature gradient increases to the south, then the atmospheric baroclinicity strengthens.

Further analysis indicates that the variation in the atmospheric baroclinicity induced by the nonuniform heating of the land surface can have a significant impact on the eddy kinetic energy. We used the eddy kinetic energy (EKE), $EKE = (u'^2 + v'^2/2)$, to represent the strength of a perturbation activity. u' and v' refer to the anomalous zonal and meridional wind, respectively. As shown in **Figure 10C**, when the Eurasian spring snowmelt increases, the high-latitude (60°–90° N) meridional temperature gradient becomes significantly weakened, and the corresponding high-latitude atmospheric baroclinicity also decreases (**Figure 10B**), leading to a weakened synoptic eddy activity in the middle troposphere. In addition, previous studies

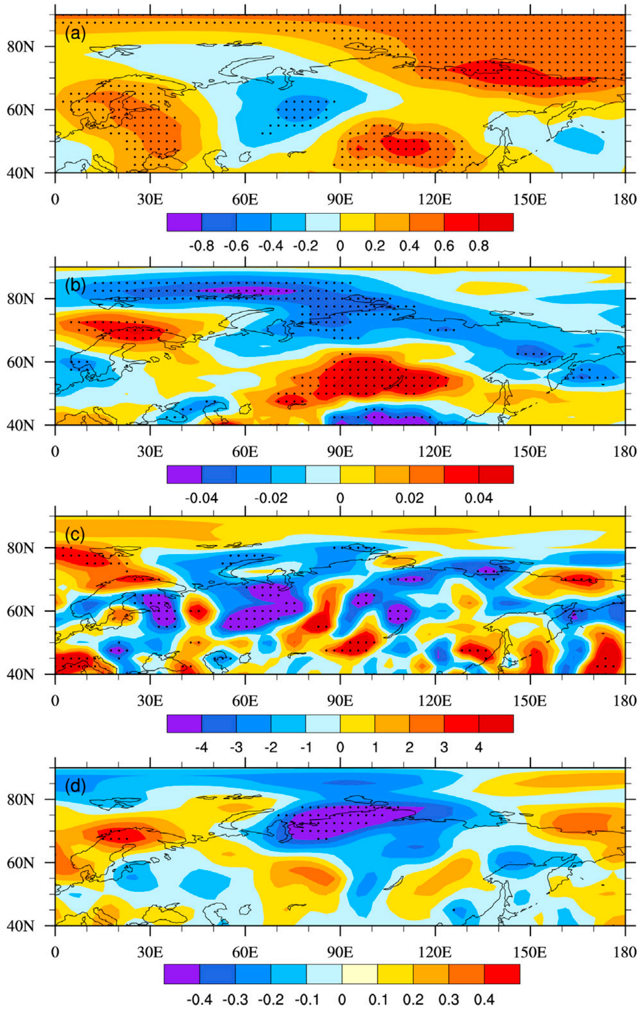

FIGURE 10 | Regression of **(A)** tropospheric temperature (K) averaged between 1,000 and 700 hPa, **(B)** atmospheric baroclinicity (day-1) at 700 hPa, **(C)** eddy kinetic energy ($m^2{\cdot}s^{-2}$), and **(D)** eddy forcing at 500 hPa (10–4 $m{\cdot}s^{-1}$) in summer onto ISM during 1981–2014. Dotted areas are significant at the 95% confidence level.

have demonstrated that the synoptic eddy feedback plays a key role in maintaining the low frequency flow (Hartmann and Lo 1998; Lorenz and Hartmann 2003). To examine changes in the synoptic eddy feedback on low frequency flow, the eddy forcing, i.e., the eddy-induced geopotential height tendency, is calculated based on the quasi-geostrophic potential vorticity equation (Lau and Holopainen 1984; Lau and Nath 1991). An eddy forcing is calculated as follows: $F = -\frac{f}{g}\nabla^{-2}(\nabla \cdot \overrightarrow{V}'\varsigma')$, in which $\overrightarrow{V}'$ and ς' represent the synoptic-scale zonal and meridional winds and vorticity, respectively, f is the Coriolis parameter, and g is the acceleration of gravity. **Figure 10D** illustrates the regression of the 500-hPa eddy forcing onto I_{SM}. It is evident that there is an eddy-induced cyclonic forcing over the high-latitude regions and an anticyclonic forcing over the middle and high latitudes. The summer eddy forcing anomaly associated with the spring I_{SM} plays a key role in intensifying the wave train in north Eurasia. According to the wave-mean flow interaction theory, the transient eddies can induce low frequency anomalies of the geopotential height, and the vorticity transfer can enhance the such anomaly (Song et al., 2016). **Figure 11** illustrates that at the 500-hPa geopotential height an evident midlatitude Eurasian wave train also prevails over the region from Scandinavia to East Asia, with a negative center located over the Central Siberian Plateau and a positive center over Mongolia. This anomaly pattern is similar to that in **Figure 10D**, which confirms a positive feedback of the eddy forcing anomaly to the atmospheric wave train over Eurasia. The eddy forcing-induced negative anomalies of geopotential field over high latitude regions further induce a positive geopotential height anomaly from Lake Baikal to the Northeastern China, contributing the weakening of the EASM (Song et al., 2016; Chen et al., 2017). These results imply that the anomalous snowmelt-induced upper-level thermal anomalies can provide favorable dynamic conditions for the development of wave train pattern over East Asia, which tends to act as the atmospheric bridge linking the surface thermal forcing and the EASM.

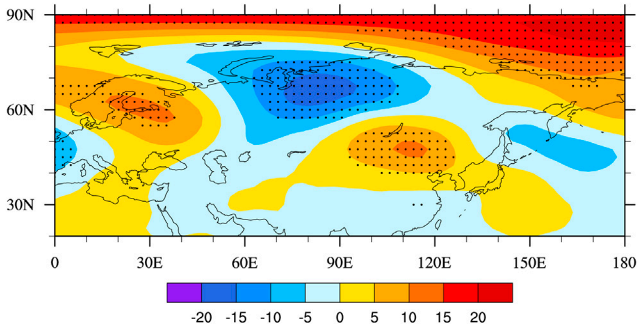

FIGURE 11 | Regression of 500-hPa geopotential height anomalies (gpm) in summer onto ISM during 1981–2014. Dotted areas are significant at the 95% confidence level.

To examine the EASM responses over East Asia, we further checked the summer wind anomalies associated with I_{SM}. **Figure 12A** shows the zonal wind anomalies at 200 hPa regressed onto I_{SM}. The Asian subtropical jet is normally located along the latitudinal band at 35°–45° N in summertime. The I_{SM} corresponds to significant positive anomalies to the north of the subtropical jet and negative anomalies over the jet zone. These zonal wind anomalies suggest that weakened westerly jet occurs in summer when there is excessive spring snowmelt over Siberia, and vice versa. Indeed, such an anomalous subtropical jet in summer over East Asia is closely linked to the strength of the EASM (Liao et al., 2004; Xie et al., 2015). Accordingly, **Figure 12B** demonstrates the summer meridional wind at 850 hPa regressed onto I_{SM}. With the increase of spring snowmelt over Siberia, eastern China mainly has a northerly wind anomaly, implying that the EASM is weakened. This prevents the northward moisture transportation in summer, causing precipitation surplus and deficit over southern and northern China (**Figure 7**),

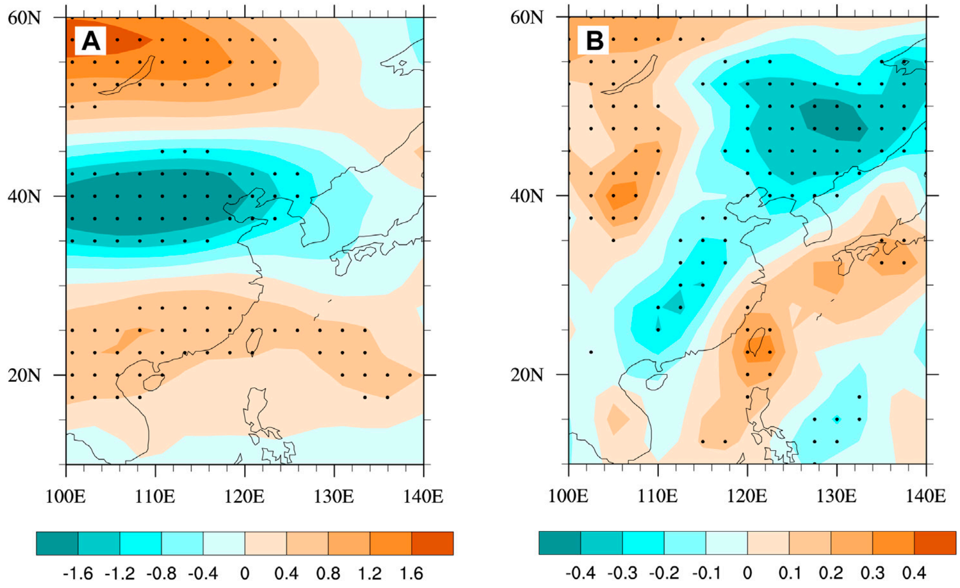

FIGURE 12 | Regression of **(A)** 200-hPa zonal wind (ms^{-1}) and **(B)** 850-hPa meridional wind (ms^{-1}) anomalies in summer onto ISM during 1981–2014. Dotted areas are significant at the 95% confidence level.

respectively. **Figure 13** shows the relationships of I_{SM} with summer precipitation over South China (20°–30° N and 110°–120° E) and North China (40°–55° N and 110°–135° E), respectively. In the period of 1981–2014, the spring snowmelt over Siberia has a strong positive relationship with summer precipitation over South China ($r = 0.35$, $p < 0.05$; **Figure 13A** significant negative correlation with summer precipitation over North China ($r = -0.56$, $p < 0.001$; **Figure 13B**). This indicates that when there is excessive snowmelt over Siberia, the summer rain band moves northward due to a weakened EASM. On the contrary, when there is abnormally deficient snowmelt over Siberia, the EASM will be intensified, consequently causing the monsoon precipitation to shift northward.

SUMMARY AND DISCUSSION

In the current study, we explored the Eurasian spring snowmelt anomaly and its linkages to the EASM and the related summer precipitation over eastern China. Using the monthly observed SWE dataset, we defined the spring snowmelt amount to reflect the sub-seasonal change of snow cover. The basic characteristics of the anomalous variations of spring snowmelt over Eurasia were analyzed, and the possible mechanisms behind the impact of the anomalous spring snowmelt on the EASM were explored from the perspective of snow hydrological effect over Eurasia.

Results show that EOF1 of Eurasian snowmelt exhibits a west–east dipole pattern, with a negative center located over the East European Plain and a positive center over Siberia. This anomalous snowmelt

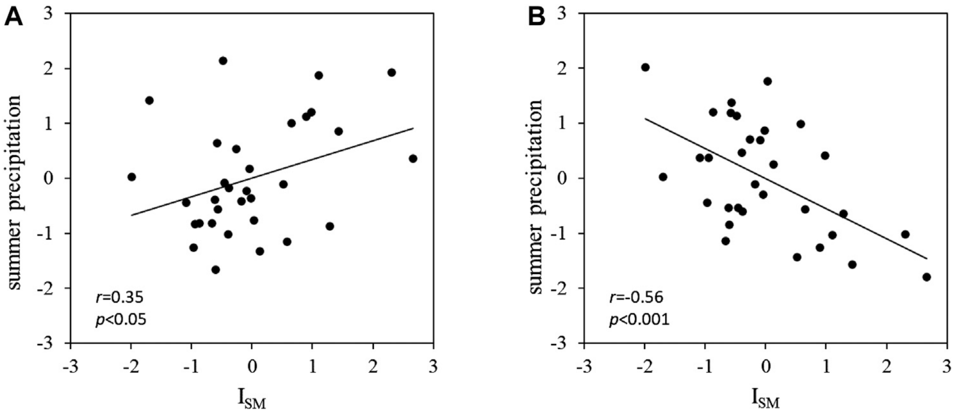

FIGURE 13 | Scatter plots **(A)** between ISM and the summer rainfall averaged over South China (20–30° N and 110–120° E), and **(B)** between ISM and the summer rainfall averaged over North China (40–55° N and 110–135° E) for the period of 1981–2014. All data were standardized for the correlation analysis.

pattern is significantly associated with EOF2 of the EASM, with the correlation coefficient between their principle components being 0.38. The further analysis verifies that the key region of spring snowmelt affecting the EASM is mainly located in Siberia. When there is more snowmelt in spring over Siberia, the summer monsoon activity generally becomes weakened, and there exists a dipole structure of summer precipitation in China (above-normal precipitation in the south and below-normal precipitation in the north). In contrast, associated with less spring snowmelt over Siberia, the overall summer monsoon activity becomes strengthened, and a northward movement of monsoon precipitation occurs.

Snowmelt is the major characteristic of the delayed hydrological effect, and the sub-seasonal snow melting process absorbs heat and increases soil moisture at the seasonal scale. The analysis in this study shows a robust positive correlation between snowmelt and the subsequent summer soil moisture. That is to say, the snow hydrological effect indeed exists and can hold a long-term memory via soil moisture anomaly persistency, which also plays an important role in connecting the snow cover over the mid-high latitudes and the EASM. The soil moisture is abnormally higher due to more snowmelt over Siberia in spring, and such a soil moisture anomaly is sustained to the following summer. Thus, the increased soil moisture can continuously lower the surface temperature and cool the atmosphere in summer. This cooling effect in Siberia leads to a weakened meridional temperature gradient and decreased baroclinicity between north Eurasia and the Arctic Ocean. Then, the variation in the atmospheric baroclinicity induced by the nonuniform heating of the land surface can produce a significant impact on the synoptic eddy. The synoptic eddy feedback further intensifies the wave train over north Eurasia.

The above factors create favorable physical conditions for the maintenance and enhancement of the anomalous Eurasian wave train prevailing over the region from Europe to Lake Baikal. The anomalous circulation patterns associated with an excessive snowmelt over Siberia ultimately weaken the EASM and influence the summer precipitation over China, with excessive precipitation occurring over most regions of South China and deficient precipitation over Northeast China and North China. Our findings demonstrate the role of anomalous snowmelt in triggering the Eurasian wave train, which is closely related to the EASM and summer precipitation over China. This study emphasizes the snow hydrological effect reflected by the spring snowmelt over Eurasia, and further contributes to the seasonal prediction of the EASM and summer precipitation over eastern China.

Previous studies indicate that spring Arctic Oscillation (AO) is the dominate driving factor for the spring surface air temperature and snow cover anomalies over the Eurasia (Chen et al., 2016). We adopt a spring AO index provided by the United States Climate Prediction Center (CPC) to denote the AO inter-annual variation. This index and its detailed information can be found at the following website: https://www.cpc.ncep.noaa.gov/products/precip/CWlink/daily_ao_index/ao.shtml. During our study period, the spring AO index exhibits an evident correlation with the PC1 of spring snowmelt over the Eurasia by a correlation coefficient of 0.33 ($p < 0.05$; Figure not shown). This suggests that the AO could also regulate the Eurasian snowmelt in spring. In addition, studies have shown that spring AO exerts evident impacts on the following EASM (Chen et al., 2015; Chen et al., 2020). Therefore, it is worth of attention that spring large-scale atmospheric circulation activities, such the AO, may contribute the Eurasian snowmelt affecting the EASM. This is beyond our current objective, which could be thoroughly investigated in the further.

DATA AVAILABILITY STATEMENT

The raw data supporting the conclusions of this article will be made available by the authors, without undue reservation.

AUTHOR CONTRIBUTIONS

HC designed the study, contributed to the idea, and revised manuscript writing. BX contributed to the data analysis and manuscript writing. CG and QH contributed to the data analysis. GZ contributed to the manuscript review.

FUNDING

This work was jointly supported by the National Science Fund for Distinguished Young Scholars (41625019), the National Natural Science Foundation of China (41230422, 41905054), the China Postdoctoral Science Foundation (2020T130168), the Joint Open Project of Key Laboratory of Meteorological Disaster, Ministry of Education/Collaborative Innovation Center on Forecast and Evaluation of Meteorological Disasters, Nanjing University of Information Science and Technology (KLME202006), and the Fifth "333 High Level Talents Training Project" of Jiangsu Province.

REFERENCES

Bamzai, A. S., and Marx, L. (2000). COLA AGCM simulation of the effect of anomalous spring snow over Eurasia on the Indian summer monsoon. *Q.J Royal Met. Soc.* 126, 2575–2584. doi:10.1002/qj.49712656811

Barnett, T. P., Dümenil, L., Schlese, U., Roeckner, E., and Latif, M. (1989). The effect of Eurasian snow cover on regional and global climate variations. *J. Atmos. Sci.* 46, 661–686. doi:10.1175/1520-0469(1989)046<0661:teoesc>2.0.co;2

Chen, H., Teng, F., Zhang, W., and Liao, H. (2017). Impacts of anomalous midlatitude cyclone activity over east Asia during summer on the decadal mode of East asian summer monsoon and its possible mechanism. *J. Clim.* 30, 739–753. doi:10.1175/jcli-d-16-0155.1

Chen, S., Chen, W., and Wu, R. (2015). An interdecadal change in the relationship between boreal spring arctic oscillation and the east asian summer monsoon around the early 1970s. *J. Clim.* 28, 1527–1542. doi:10.1175/jcli-d-14-00409.1

Chen, S., Chen, W., Wu, R., and Song, L. (2020). Impacts of the atlantic multidecadal oscillation on the spring arctic oscillation and the following East Asian summer monsoon relation. *J. Clim.* 33, 6651–6672. doi:10.1175/JCLI-D-19-0978.1

Cheng, S., Guan, X., Huang, J., Ji, F., and Guo, R. (2015). Long-term trend and variability of soil moisture over East Asia. *J. Geophys. Res. Atmos.* 120, 8658–8670. doi:10.1002/2015jd023206

Chen, S., Wu, R., and Liu, Y. (2016). Dominant modes of interannual variability in eurasian surface air temperature during boreal spring. *J. Clim.* 29, 1109–1125. doi:10.1175/jcli-d-15-0524.1

Cohen, J., Furtado, J. C., Jones, J., Barlow, M., Whittleston, D., and Entekhabi, D. (2014). Linking siberian snow cover to precursors of stratospheric variability. *J. Clim.* 27, 5422–5432. doi:10.1175/jcli-d-13-00779.1

Dash, S. K., Parth Sarthi, P., and Panda, S. K. (2006). A study on the effect of Eurasian snow on the summer monsoon circulation and rainfall using a spectral GCM. *Int. J. Climatol.* 26, 1017–1025. doi:10.1002/joc.1299

Dey, B., and Bhanu Kumar, O. S. R. U. (1982). An apparent relationship between Eurasian spring snow cover and the advance period of the Indian summer monsoon. *J. Appl. Meteorol.* 21, 1929–1932. doi:10.1175/1520-0450(1982)021<1929:aarbes>2.0.co;2

Ding, Y., Sun, Y., Wang, Z., Zhu, Y., and Song, Y. (2009). Inter-decadal variation of the summer precipitation in China and its association with decreasing Asian summer monsoon Part II: possible causes. *Int. J. Climatol.* 29, 1926–1944. doi:10.1002/joc.1759

Douville, H., and Royer, J.-F. (1996). Sensitivity of the Asian summer monsoon to an anomalous Eurasian snow cover within the Météo-France GCM. *Clim. Dynam.* 12, 449–466. doi:10.1007/bf02346818

Fasullo, J. (2004). A stratified diagnosis of the Indian monsoon-Eurasian snow cover relationship. *J. Clim.* 17, 1110–1122. doi:10.1175/1520-0442(2004)017<1110:asdoti>2.0.co;2

Gong, G., Entekhabi, D., and Cohen, J. (2003). Relative impacts of siberian and north American snow anomalies on the winter arctic oscillation. *Geophys. Res. Lett.* 30, 1848. doi:10.1029/2003gl017749

Groisman, P. Y., Karl, T. R., Knight, R. W., and Stenchikov, G. L. (1994). Changes of snow cover, temperature, and radiative heat balance over the northern hemisphere. *J. Clim.* 7, 1633–1656. doi:10.1175/1520-0442(1994)007<1633:coscta>2.0.co;2

Halder, S., and Dirmeyer, P. A. (2017). Relation of Eurasian snow cover and Indian summer monsoon rainfall: importance of the delayed hydrological effect. *J. Clim.* 30, 1273–1289. doi:10.1175/jcli-d-16-0033.1

Hartmann, D. L., and Lo, F. (1998). Wave-driven zonal flow vacillation in the southern hemisphere. *J. Atmos. Sci.* 55, 1303–1315. doi:10.1175/1520-0469(1998)055<1303:wdzfvi>2.0.co;2

Henderson, G. R., Peings, Y., Furtado, J. C., and Kushner, P. J. (2018). Snow-atmosphere coupling in the northern hemisphere. *Nat. Clim. Change.* 8, 954–963. doi:10.1038/s41558-018-0295-6

Huang, Y., Chen, H., Jiang, W., Xu, B., and Li, Z. (2015). Multi-spatial modes of East Asian summer monsoon activity: comparative analysis of various reanalysis data. *Chin. J. Atmos. Sci.* 39 (1), 145–160.

Kripalani, R. H., Kim, B.-J., Oh, J.-H., and Moon, S.-E. (2002). Relationship between Soviet snow and Korean rainfall. *Int. J. Climatol.* 22, 1313–1325. doi:10.1002/joc.809

Lau, N.-C., and Holopainen, E. O. (1984). Transient eddy forcing of the time-mean flow as identified by geopotential tendencies. *J. Atmos. Sci.* 41, 313–328. doi:10.1175/1520-0469(1984)041<0313:tefott>2.0.co;2

Lau, N.-C., and Nath, M. J. (1991). Variability of the baroclinic and barotropic transient eddy forcing associated with monthly changes in the midlatitude storm tracks. *J. Atmos. Sci.* 48, 2589–2613. doi:10.1175/1520-0469(1991)048<2589:votbab>2.0.co;2

Liao, Q.-H., Tao, S.-Y., and Wang, H.-J. (2004). Interannual variation of summer subtropical westerly jet in east Asia and its impacts on the climate anomalies of East Asia summer monsoon. *Chin. J. Geophys.* 47, 12–21. doi:10.1002/cjg2.449

Lindzen, R. S., Farrell, B., and Tung, K.-K. (1980). The concept of wave overreflection and its application to baroclinic instability. *J. Atmos. Sci.* 37, 44–63. doi:10.1175/1520-0469(1980)037<0044:tcowoa>2.0.co;2

Liu, H., Sun, Z., Wang, J., and Min, J. (2004). A modeling study of the effects of anomalous snow cover over the Tibetan Plateau upon the South Asian summer monsoon. *Adv. Atmos. Sci.* 21, 964–975.

Liu, X., and Yanai, M. (2002). Influence of Eurasian spring snow cover on Asian summer rainfall. *Int. J. Climatol.* 22, 1075–1089. doi:10.1002/joc.784

Lorenz, D. J., and Hartmann, D. L. (2003). Eddy-zonal flow feedback in the Northern Hemisphere winter. *J. Clim.* 16, 1212–1227. doi:10.1175/1520-0442(2003)16<1212:effitn>2.0.co;2

Moon, S., and Ha, K.-J. (2019). Early Indian summer monsoon onset driven by low soil moisture in the Iranian desert. *Geophys. Res. Lett.* 46, 10568. doi:10.1029/2019gl084520

Mu, S., and Zhou, G. (2010). Relationship between winter Northern Eurasian fresh snow extent and summer climate anomalies in China. *Chin. J. Atmos. Sci.* 34 (1), 213–226.

North, G. R., Bell, T. L., Cahalan, R. F., and Moeng, F. J. (1982). Sampling errors in the estimation of empirical orthogonal functions. *Mon. Weather Rev.* 110, 699–706. doi:10.1175/1520-0493(1982)110<0699:seiteo>2.0.co;2

Ose, T. (1996). The comparison of the simulated response to the regional snow mass anomalies over Tibet, Eastern Europe, and Siberia. *J. Meteorol. Soc. Jpn.* 74, 845–866. doi:10.2151/jmsj1965.74.6_845

Quiring, S., and Kluver, D. (2009). Relationship between winter/spring snowfall and summer precipitation in the Northern Great Plains of North America. *J. Hydrometeorol.* 10, 1203–1217. doi:10.1175/2009jhm1089.1

Robock, A., Mu, M., Vinnikov, K., and Robinson, D. (2003). Land surface conditions over Eurasia and Indian summer monsoon rainfall. *J. Geophys. Res.* 108, 4131. doi:10.1029/2002jd002286

Rodell, M., Houser, P. R., Jambor, U., Gottschalck, J., Mitchell, K., Meng, C.-J., et al. (2004). The global land data assimilation system. *Bull. Am. Meteorol. Soc.* 85, 381–394. doi:10.1175/bams-85-3-381

Saha, S. K., Pokhrel, S., and Chaudhari, H. S. (2012). Influence of Eurasian snow on Indian summer monsoon in NCEP CFSv2 freerun. *Clim. Dynam.* 41, 1801–1815. doi:10.1007/s00382-012-1617-4

Saito, K., and Cohen, J. (2003). The potential role of snow cover in forcing interannual variability of the major Northern Hemisphere mode. *Geophys. Res. Lett.* 30, 1302. doi:10.1029/2002gl016341

Sankar-Rao, M., Lau, K. M., and Yang, S. (1996). On the relationship between Eurasian snow cover and the Asian summer monsoon. *Int. J. Climatol.* 16, 605–616. doi:10.1002/(sici)1097-0088(199606)16:6<605::aid-joc41>3.0.co;2-p

Shen, H., Li, F., He, S., Orsolini, Y. J., and Li, J. (2020). Impact of late spring Siberian snow on summer rainfall in South-Central China. *Clim. Dynam.* 54, 3803–3818. doi:10.1007/s00382-020-05206-5

Song, L., Wang, L., Chen, W., and Zhang, Y. (2016). Intraseasonal variation of the strength of the east asian trough and its climatic impacts in boreal winter. *J. Clim.* 29, 2557–2577. doi:10.1175/jcli-d-14-00834.1

Souma, K., and Wang, Y. (2010). A comparison between the effects of snow albedo and infiltration of melting water of Eurasian snow on East Asian summer monsoon rainfall. *J. Geophys. Res.* 115, D02115. doi:10.1029/2009jd012189

Takala, M., Luojus, K., Pulliainen, J., Derksen, C., Lemmetyinen, J., Kärnä, J.-P., et al. (2011). Estimating northern hemisphere snow water equivalent for climate research through assimilation of space-borne radiometer data and ground-based measurements. *Remote Sensing of Environment.* 115, 3517–3529. doi:10.1016/j.rse.2011.08.014

Wang, B. (2006). *The asian monsoon*. Berlin Heidelberg: Springer.

Wang, B., Wu, R., and Fu, X. (2000). Pacific-East Asian teleconnection: how does ENSO affect East Asian climate? *J. Clim.* 13, 1517–1536. doi:10.1175/1520-0442(2000)013<1517:peathd>2.0.co;2

Wang, T., Peng, S., Ottlé, C., and Ciais, P. (2015). Spring snow cover deficit controlled by intraseasonal variability of the surface energy fluxes. *Environ. Res. Lett.* 10, 024018. doi:10.1088/1748-9326/10/2/024018

Wu, B., Yang, K., and Zhang, R. (2009). Eurasian snow cover variability and its association with summer rainfall in China. *Adv. Atmos. Sci.* 26, 31–44. doi:10.1007/s00376-009-0031-2

Wu, L., and Zhang, J. (2013). Asymmetric effects of soil moisture on mean daily maximum and minimum temperatures over eastern China. *Meteorol. Atmos. Phys.* 122, 199–213. doi:10.1007/s00703-013-0284-2

Wu, R., and Chen, S. (2016). Regional change in snow water equivalent-surface air temperature relationship over Eurasia during boreal spring. *Clim. Dynam.* 47, 2425–2442. doi:10.1007/s00382-015-2972-8

Wu, R., and Kirtman, B. P. (2007). Observed relationship of spring and summer East Asian rainfall with winter and spring Eurasian snow. *J. Clim.* 20, 1285–1304. doi:10.1175/jcli4068.1

Wu, R., Liu, G., and Ping, Z. (2014). Contrasting Eurasian spring and summer climate anomalies associated with western and eastern Eurasian spring snow cover changes. *J. Geophys. Res. Atmos.* 119, 7410–7424. doi:10.1002/2014jd021764

Wu, Z., Li, J., Jiang, Z., and Ma, T. (2012). Modulation of the Tibetan Plateau snow cover on the ENSO teleconnections: from the East Asian summer monsoon perspective. *J. Clim.* 25, 2481–2489. doi:10.1175/jcli-d-11-00135.1

Xiao, Z., and Duan, A. (2016). Impacts of Tibetan Plateau snow cover on the interannual variability of the East Asian summer monsoon. *J. Clim.* 29, 8495–8514. doi:10.1175/jcli-d-16-0029.1

Xie, Z., Du, Y., and Yang, S. (2015). Zonal extension and retraction of the subtropical westerly jet stream and evolution of precipitation over East Asia and the Western Pacific. *J. Clim.* 28, 6783–6798. doi:10.1175/jcli-d-14-00649.1

Xu, L., and Dirmeyer, P. (2011). Snow-atmosphere coupling strength in a global atmospheric model. *Geophys. Res. Lett.* 38, L13401. doi:10.1029/2011gl048049

Xu, L., and Dirmeyer, P. (2013). Snow-atmosphere coupling strength. Part II: albedo effect versus hydrological effect. *J. Hydrometeorol.* 14, 404–418. doi:10.1175/jhm-d-11-0103.1

Yanai, M., Chengfeng, L., and Zhengshan, S. (1992). Seasonal heating of the Tibetan Plateau and its effects on the evolution of the Asian summer monsoon. *J. Meteorol. Soc. Jpn.* 79, 419–434.

Yang, S., and Xu, L. (1994). Linkage between Eurasian winter snow cover and regional Chinese summer rainfall. *Int. J. Climatol.* 14, 739–750. doi:10.1002/joc.3370140704

Yim, S.-Y., Jhun, J.-G., Lu, R., and Wang, B. (2010). Two distinct patterns of spring Eurasian snow cover anomaly and their impacts on the East Asian summer monsoon. *J. Geophys. Res.* 115, D22113. doi:10.1029/2010jd013996

Zhang, J., Wang, W.-C., and Leung, L. R. (2008). Contribution of land-atmosphere coupling to summer climate variability over the contiguous United States. *J. Geophys. Res.* 113, D17119. doi:10.1029/2008jd009807

Zhang, R., Zhang, R., and Zuo, Z. (2017). Impact of Eurasian spring snow decrement on East Asian summer precipitation. *J. Clim.* 30, 3421–3437. doi:10.1175/jcli-d-16-0214.1

Zuo, Z., Yang, S., Wang, W., Kumar, A., Xue, Y., and Zhang, R. (2011). Relationship between anomalies of Eurasian snow and southern China rainfall in winter. *Environ. Res. Lett.* 6, 045402. doi:10.1088/1748-9326/6/4/045402

Zuo, Z., Yang, S., Zhang, R., Xiao, D., Guo, D., and Ma, L. (2014). Response of summer rainfall over China to spring snow anomalies over Siberia in the NCEP CFSv2 Reforecast. *Q. J. R. Meteorol. Soc.* 141, 939–944. doi:10.1002/qj.2413

Conflict of Interest: The authors declare that the research was conducted in the absence of any commercial or financial relationships that could be construed as a potential conflict of interest.

The reviewer (AH) declared a past co-authorship with one of the authors (HC) to the handling editor.

frontiers
in Earth Science

ORIGINAL RESEARCH
published: 20 January 2021
doi: 10.3389/feart.2020.599745

How Does Indian Monsoon Regulate the Northern Hemisphere Stationary Wave Pattern?

Jun-Hyeok Son[1,2], Kyong-Hwan Seo[1,2]*, Seok-Woo Son[3] and Dong-Hyun Cha[4]

[1]Department of Atmospheric Sciences, Division of Earth Environmental System, Pusan National University, Busan, South Korea, [2]Research Center for Climate Science, Pusan National University, Busan, South Korea, [3]School of Earth and Environmental Sciences, Seoul National University, Seoul, South Korea, [4]Department of Urban and Environmental Engineering, Ulsan National Institute of Science and Technology, Ulsan, South Korea

The Northern Hemisphere summer climate isstrongly affected by a circumglobal stationary Rossby wave train, which can be manifested by the first EOF mode of the geopotential height at 200 hPa. Interannual variation of this Northern Hemisphere wave (NHW) pattern has a significant impact on remarkably warm surface temperature anomalies over the North Atlantic, Northeast Europe, East Asia to Central-North Pacific, and America, particularly in 2018 and 2010. The NHW pattern is likely generated by atmospheric diabatic heating and vorticity forcing: diabatic heating is mainly confined in the Indian summer monsoon (ISM) precipitation region, whereas the anti-cyclonic vorticity forcing is distributed in the globe. The ISM is a well-known diabatic heat source; however, the main source of vorticity forcing has not been established. In general, the tropical vorticity anomaly comes from diabatic heating-induced atmospheric waves and randomly generated inherent internal waves. The linear baroclinic model experiment reveals that the NHW pattern can be generated by the westward propagating tropical waves generated by the ISM diabatic heat forcing.

Keywords: stationary Rossby waves, teleconnection, heat waves, Indian monsoon, linear baroclinic model

Edited by:
Jasti S. Chowdary,
Indian Institute of Tropical Meteorology (IITM), India

Reviewed by:
Wei Chen,
Institute of Atmospheric Physics (CAS), China
Ramesh Kumar Yadav,
IITM, India
Wei Wei,
Sun Yat-sen University, China

***Correspondence:**
Kyong-Hwan Seo
khseo@pusan.ac.kr

Specialty section:
This article was submitted to Atmospheric Science, a section of the journal Frontiers in Earth Science

Received: *28 August 2020*
Accepted: *06 November 2020*
Published: *20 January 2021*

Citation:
Son J-H, Seo K-H, Son S-W and Cha D-H (2021) How Does Indian Monsoon Regulate the Northern Hemisphere Stationary Wave Pattern?. Front. Earth Sci. 8:599745. doi: 10.3389/feart.2020.599745

INTRODUCTION

More than 90% of the world's population lives in the Northern Hemisphere, and the human life is significantly influenced by weather and climate variability. In summer, the occurrences of the heavy rainfall and heatwave are fatal to people's health and food production. These extremes are often caused by atmospheric Rossby waves, rather than randomly occurring (e.g., Feldstein and Dayan, 2008; Schubert et al., 2011; Harnik et al., 2016; Wirth et al., 2018). If the phase speed of the Rossby wave is zero, then the Rossby waves become stationary, and these waves have a tremendous impact on the climate system. The primary characteristic of the atmospheric Rossby waves is that waves propagate westward by the planetary vorticity advection; however, the Doppler effect of the westerly jet stream carries the waves eastward. In observations, planetary-scale small zonal wavenumber waves move westward, but large wavenumber waves propagate eastward by the Doppler effect. When the westward propagating phase speeds of the Rossby waves and the westerly wind speeds are the same, the waves become stationary relative to the ground.

Stationary Rossby wave trains over the Northern Hemisphere in summer are reported as the silk road pattern (SRP), circumglobal teleconnection (CGT), and the North Atlantic–Eurasian (AEA) teleconnection, and all these Rossby wave patterns significantly modulate the global climate system

(Lu et al., 2002; Ding and Wang, 2005; Wu et al., 2009). East–west elongated Eurasian wave train trapped in the subtropical jet stream is named the SRP (Lu et al., 2002; Enomoto et al., 2003). As an interannual component of the SRP (Chen and Huang, 2012), the CGT is the dominant circulation pattern over the midlatitude, and this wave train is known to be a result of diabatic heating in the Indian subcontinent or vorticity forcing around the exit of the jet stream over the North Atlantic (Ding and Wang, 2007; Ding et al., 2011). North Atlantic oscillation (NAO) related stationary Rossby waves penetrating across the Eurasian continent are explained as the North Atlantic–Eurasian (AEA) teleconnection in boreal summer (Wu et al., 2009; Seo et al., 2012; Seo and Son, 2012; Wu et al., 2012; Zheng et al., 2016; Li and Ruan, 2018).

In general, the phase-locking of the stationary Rossby waves is owing to stationary forcing such as a huge mountain, land–sea thermal contrast, slowly varying oceanic heat source, long-lasting atmospheric diabatic heating, and atmospheric vorticity forcing. The potential energy conversion from the baroclinic Asian jet to the kinetic energy of waves and the phase-locking effect of topographic boundary forcing are considered as the major mechanisms of the SRP (Sato and Takahashi, 2006; Kosaka et al., 2009). Hence, some portion of the SRP is regarded as the middle latitude-inherent internal mode in association with baroclinic instability; however, the CGT and AEA patterns may be generated by the stationary atmospheric diabatic heating and vorticity forcing.

The spatial structures of the CGT and SRP are almost the same over the Eurasian continent in monthly field (e.g., pattern correlation of geopotential height between CGT and SRP is above 0.80; not shown); however, a discrepancy is that the CGT is formed circumglobally, while the SRP phase is locked only in the Eurasian sector (Zhou et al., 2019). The source of the CGT is known to be related to the anomalous Indian summer monsoon (ISM) precipitation and the vorticity forcing around the Atlantic jet stream exit region, and the decadal variation of the CGT is linked to the Atlantic multidecadal oscillation (Lin et al., 2016; Stephan et al., 2019).

The ISM is one of the most intense convective systems over the globe, and the monsoon precipitation has a considerable variation on subseasonal to interdecadal timescale. The variability of atmospheric stationary waves is strongly tied with the temporal and spatial variations of forcing; however, the existence of inherent internal waves associated with the tropical convective random forcing or extratropical baroclinic instability is also related to the generation of a quasi-stationary wave train, and therefore it causes a lot of uncertainties in the stationary forcing-response causal relationship. Thus, a basic question arises here, "Does the ISM diabatic heat forcing generate the dominant stationary wave pattern in the Northern Hemisphere?" To answer this question, first, we defined the predominant mode of the Northern Hemisphere stationary Rossby waves. The EOF analysis using the geopotential height at 200 hPa in July reveals that the prominent Rossby wave train covers the entire Northern Hemisphere (**Figure 1**). For instance, if the EOF analysis is performed on the JJA average or other months, the space-time pattern is significantly different from using only in July (not shown). Interestingly, although the first EOF mode (EOF1) explains only ~16% of the total variance, overall anomaly pattern of the geopotential height in the Northern Hemisphere in July 2018 can be explained by the EOF1. In summer 2018, most countries in the Northern Hemisphere midlatitudes suffered severe heatwaves with long-lasting atmospheric stationary Rossby waves. Hereafter, we term this stationary Rossby wave pattern the Northern Hemisphere wave (NHW). The reason for using the new definition in this study is to intuitively express the dominant wave train that actually occurs, rather than understanding it based on the various and complex wave trains defined in previous studies. The principal component (PC) of NHW has substantial interannual variability, and it has a temporal correlation of 0.34 with CGT interannual time series, 0.41 with SRP index, and 0.51 with the AEA index. The CGT pattern is generally defined as an EOF1 of the meridional wind anomaly at 200 hPa over 100°W–100°E, 20°–80°N as suggested by Saeed et al. 2011; Saeed et al. 2014. On the other hand, the SRP index is calculated by the PC of the EOF1 using the meridional wind at 200 hPa in 30°–130°E, 30°–60°N (Chen et al., 2013), and the AEA teleconnection is represented in the EOF2 of the geopotential height anomaly at 500 hPa in 45°W–135°E, 15°–90°N (Li and Ruan, 2018). As shown in the previous studies, the CGT and SRP teleconnection patterns are formed in the midlatitude, whereas the AEA is situated in the high latitude. Therefore, it is considered that uniqueness of the NHW is that it is rather entire northern hemispheric pattern, as the name indicates. Furthermore, the entire NH pattern well represents the characteristic pattern appearing in the extreme heat wave events in July (**Figure 2**).

For the examination of the physical characteristics of the NHW, we analyzed the Rossby wave energy propagation pathway and demonstrated the trajectory using the Rossby wave ray-tracing method (Seo and Son, 2012; Zhao et al., 2015; Lee and Seo, 2019). The atmospheric responses to thermodynamical heat forcing or dynamical vorticity forcing are examined using the linear baroclinic model (LBM) (Watanabe and Kimoto, 2000). The steady-state LBM simulation shows the stationary wave response to prescribed diabatic heating or vorticity forcing. In this study, we investigate the source of the NHW pattern, and through this, the cause of the Northern Hemisphere temperature anomaly pattern is also elucidated. Finally, the decadal linear trend of the Northern Hemisphere circulation pattern and its possible mechanism are discussed.

DATA AND METHODS

The following monthly mean datasets (1979–2018) are used in this study: European Center for Medium-Range Weather Forecasts ERA-Interim reanalysis datasets in the pressure coordinate (Dee et al., 2011) and Global Precipitation Climatology Project precipitation version 2.3 (Adler et al., 2003).

Over the Northern Hemisphere in July, the EOF analysis is performed using the 200-hPa geopotential height anomaly, in

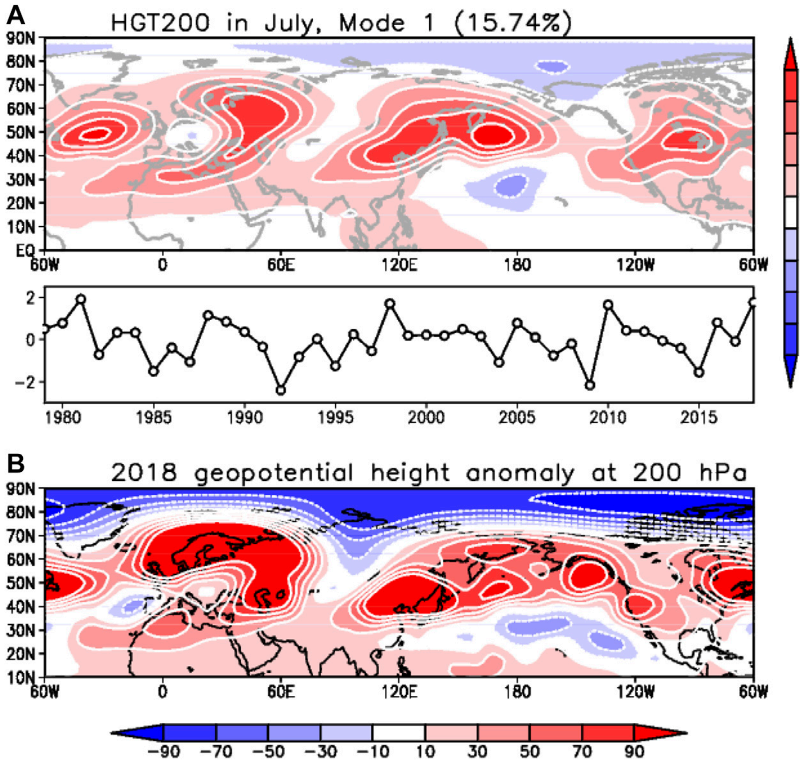

FIGURE 1 | (A) The EOF1 of geopotential height at 200 hPa in July and **(B)** the anomaly pattern in July 2018.

which the linear trend is removed at each grid point. For the statistical significance test in observational analysis, the Student *t*-test is used, and the Mann–Kendall significance test is performed for the linear trend analysis.

The apparent heat source ($Q1$) and apparent moisture sink ($Q2$) are calculated to illustrate tropical–subtropical diabatic heat forcing as follows (Yanai, 1961; Yanai et al., 1973):

$$Q1 \equiv \frac{\partial \bar{s}}{\partial t} + \overline{\nabla \cdot sV} + \frac{\partial}{\partial p}(\bar{s}\,\bar{\omega}) = Q_R + L(c-e) - \frac{\partial}{\partial p}\overline{s'\omega'}, \quad (1)$$

$$Q2 \equiv -L\left(\frac{\partial \bar{q}}{\partial t} + \overline{\nabla \cdot qV} + \frac{\partial}{\partial p}(\bar{q}\,\bar{\omega})\right) = L(c-e) + L\frac{\partial}{\partial p}\overline{q'\omega'}, \quad (2)$$

where $s \equiv c_p T + gz$ is the dry static energy; c_p is the specific heat capacity at constant pressure; T is the temperature; g is the gravitational acceleration; z is height; p is the pressure; q is the specific humidity; V is the horizontal velocity; ω is the vertical pressure velocity; Q_R is the radiative heating rate; L is the latent heat of vaporization; c is the rate of condensation per unit mass of air; and e is the rate of re-evaporation of cloud droplets. The horizontal averages are denoted by over bar, and primes denote deviations from the horizontal averages.

The $Q1$ is the heating resulting from convection, radiation, condensation, and eddy heat flux processes, and the $Q2$ is associated with the moisture sink due to net condensation and eddy moisture transport divergence. Note that the deep tropical convection and intense precipitation occurring during the ISM

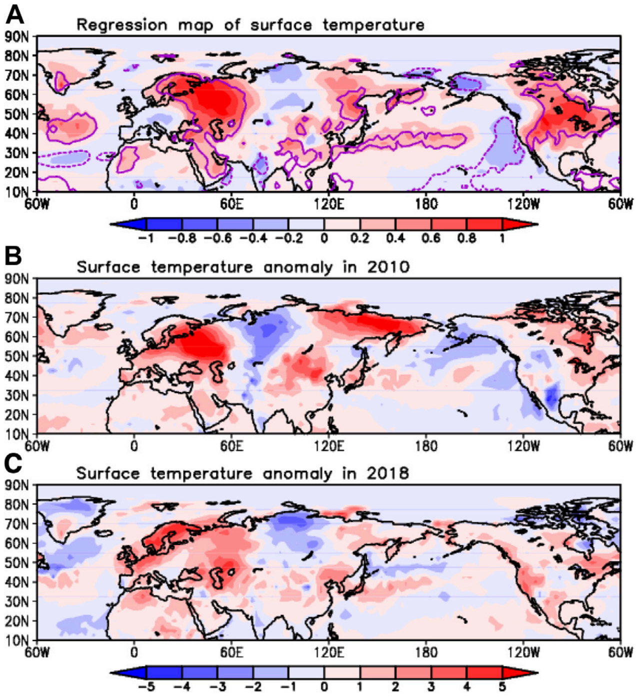

FIGURE 2 | (A) The surface temperature regression map (shading) in July against the PC, **(B)** 2010, and **(C)** 2018 anomaly pattern. Purple contours show 95% significant area.

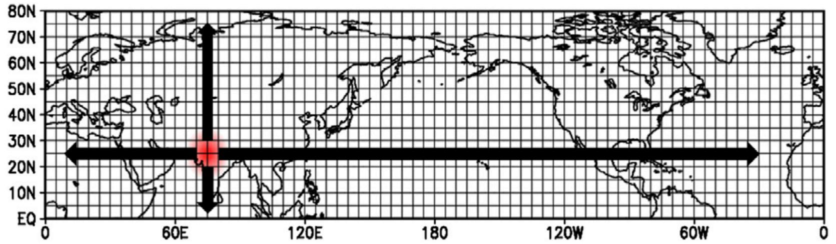

FIGURE 3 | Forcing centers for the LBM experiment. Red shading shows a prescribed forcing, and the forcing moves step by step to every grid on the Northern Hemisphere.

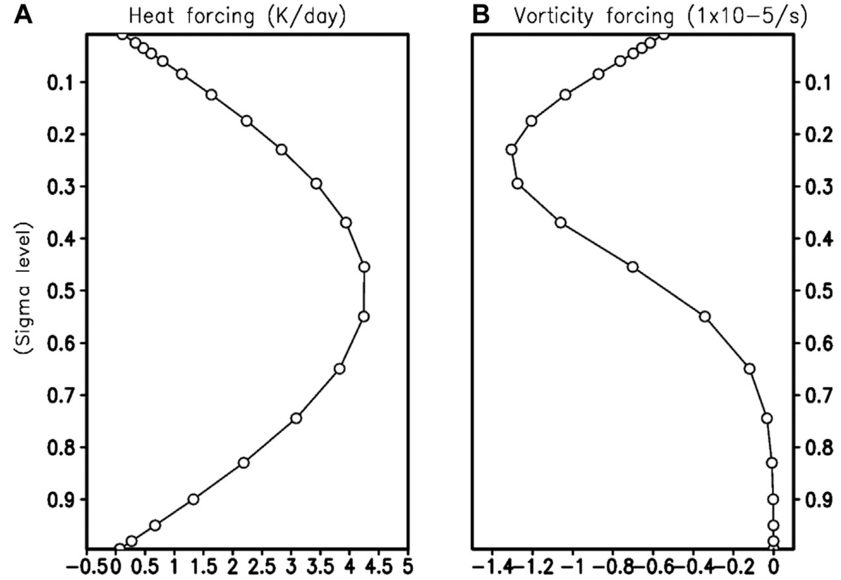

FIGURE 4 | Vertical profiles of individual heat and vorticity forcing for LBM experiments.

are accompanied by a significant amount of diabatic heating in the middle troposphere.

The LBM experiment is performed to verify whether the observed NHW circulation pattern is a primary linear response to direct diabatic heating or dynamical vorticity forcing. The model has a horizontal resolution of T42 and 20 vertical levels in the sigma coordinate, and the steady response to the prescribed diabatic heating or vorticity forcing is calculated (Watanabe and Kimoto, 2000). First, to search for potential forcing regions, arbitrary idealized heat forcing is applied to all grid points in the Northern Hemisphere, and the simulation results are compared with observations; then observational three-dimensional *Q1* forcing is applied to the LBM for the verification of the physical relationship between the ISM and NHW.

The trajectory of the Rossby wave energy propagation starting from diabatic heat and vorticity forcing is calculated by the ray-tracing method (Lighthill, 1978; Hoskins and Karoly, 1981; Hoskins and Ambrizzi, 1993; Seo and Son, 2012; Zheng et al., 2016; Lee and Seo, 2019). A detailed description of the ray-tracing method using the barotropic nondivergent vorticity equation in a horizontally nonuniform background flow can be found in Li et al. (2015) and Zhao et al. (2015). For the calculation of the ray, the initial zonal wavenumber is set to two to four, and the zonal and meridional wavenumbers are allowed to vary along the trajectory (Zhao et al., 2015).

Linkage Between the Northern Hemisphere Wave Pattern and the Northern Hemisphere Surface Temperature

In July 2018, the Northern Hemisphere climate was greatly influenced by stationary Rossby waves, and the peculiar geopotential height pattern can be described as the first mode of EOF (**Figure 1**). In the EOF1, the dominant zonal wave number in the midlatitudes is 4 or 5, and the positive anomaly centers are located in the North Atlantic, Northeast Europe, Northeast Asia, and America. The PC index shows strong interannual fluctuation, and the values for 1981, 1998, 2010, and 2018 are higher than +2 standard deviations. For example, the EOF1 and the 2018 anomaly patterns of geopotential height

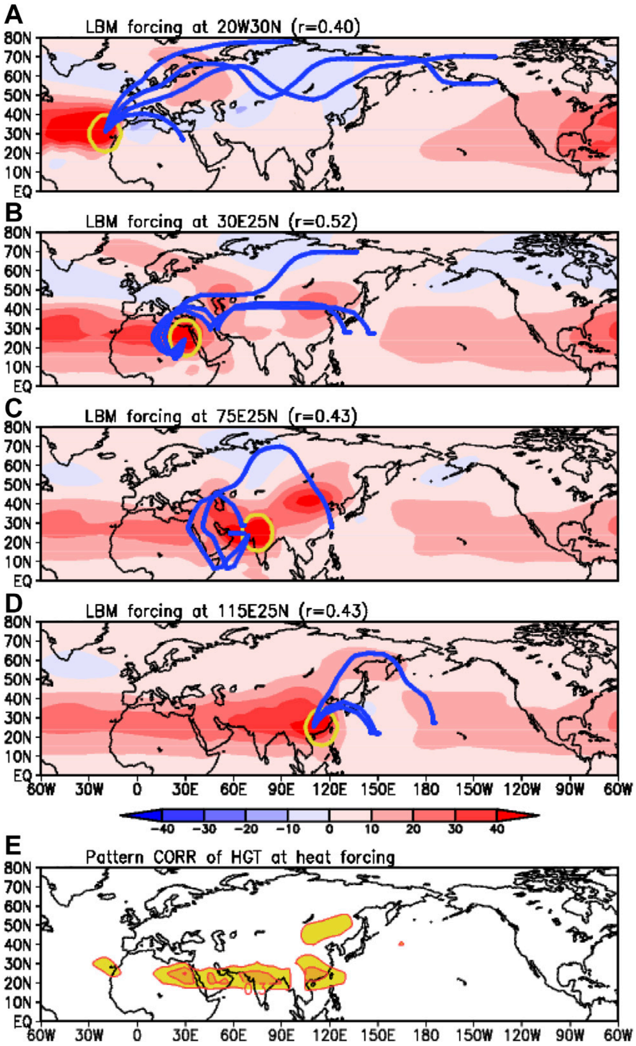

FIGURE 5 | The LBM experiment using diabatic heat forcing migrating in 5° interval over the Northern Hemisphere. The geopotential height anomaly at 200 hPa in the LBM experiment is shown for forcing of **(A)** 20°W 30°N, **(B)** 30°E 25°N, **(C)** 75°E 25°N, and **(D)** 115°E 25°N. The yellow circle denotes the heat forcing area, and the blue line shows the Rossby wave propagation path. The pattern correlation between the geopotential height anomaly in LBM experiments and EOF1 (**Figure 1A**) is calculated in **(E)**. The correlation is shown at each forcing center, and the contour interval is 0.1.

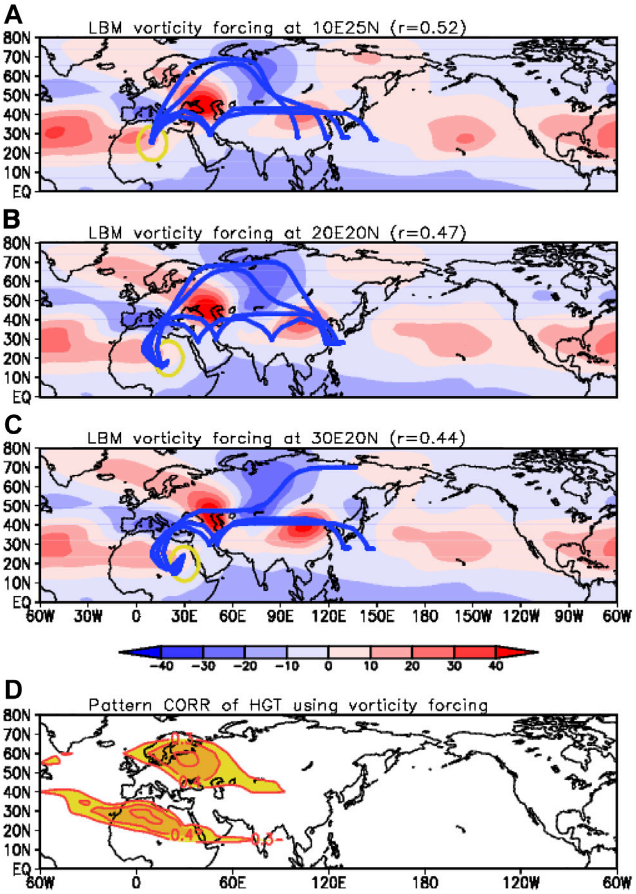

FIGURE 6 | The LBM experiment using vorticity forcing migrating in 5° interval over the Northern Hemisphere. Geopotential height anomaly at 200 hPa in LBM simulations using negative vorticity (anti-cyclonic) forcing **(A)** 10°E 25°N, **(B)** 20°E 20°N, and **(C)** 30°E 20°N is illustrated. The yellow circle denotes the vorticity forcing area, and the blue line shows the Rossby wave propagation path. The pattern correlation coefficient between EOF1 and LBM simulations is calculated at each forcing point **(D)**.

match well, but the detailed structures are not perfectly identical. The geopotential height fields over the Eurasian and African continent, and the Pacific look similar; however, the anomaly pattern in America and the North Atlantic is not correctly matched in **Figure 1**.

The regression map of surface temperature against the PC time series shows the corresponding surface temperature anomaly pattern with geopotential height anomaly (**Figure 2A**). Basically, the vertical structure of the midlatitude stationary Rossby waves is barotropic; this means that the upper tropospheric pressure anomaly is likely to modulate the surface pressure and accordingly temperature fields. In **Figure 2A**, warm temperature anomalies have formed in the North Atlantic, Northeast Europe, East Asia to Central-North Pacific, and America. It is interesting to see that the large-scale features of surface temperature in 2018 and 2010 are very similar to the regression map of surface temperature: the warm temperature over Northeastern Europe, East Asia, and Northeast America, and even cold anomaly in central Russia. From these shreds of evidence, now we can infer that the NHW significantly impact on the Northern Hemisphere pressure fields and temperature in July.

Potential Forcing for the Generation of the Northern Hemisphere Wave

Apparently thermodynamical or dynamical forcing may be required for the generation of the NHW; therefore, to examine the potential forcing of the NHW pattern, a suite of the LBM experiment is designed as follows: using prescribed steady forcing such as atmospheric diabatic heating and negative vorticity, respectively, experiments are conducted over the climatological (1979–2018) background state in July. The forcing having a diameter of 10° moves from 0° to 360°E and 0° to 80°N with 5° intervals as shown in **Figure 3**.

In general, deep atmospheric convection accompanies a huge amount of diabatic heating, and this thermodynamic forcing can generate the atmospheric Rossby wave teleconnection. Deep convection is usually characterized by middle heavy heating profile as shown in **Figure 4A** (if it is well organized so it has stratiform anvil clouds, then heating profile is top-heavy). Therefore, the middle-level (~500 hPa) heavy profile is prescribed as the idealized diabatic heat forcing structure, while the vorticity forcing has an upper troposphere (~250 hPa) heavy shape (**Figure 4**). In the tropics, the upper tropospheric negative relative vorticity or the positive geopotential height anomaly is physically linked to the lower-level cyclonic circulation by the vertical baroclinic structure. The strong baroclinicity of the pressure anomalies coincides with the occurrence of middle tropospheric diabatic heat forcing inside the organized large-scale convective system. However, in the mid and high latitude, the bottom heavy diabatic heat forcing directly induces atmospheric thickness change and drives vertically barotropic dynamic systems (Peng et al., 2003). For the consistency of the atmospheric response from diabatic heating and vorticity forcing, the negative vorticity forcing is prescribed in the upper troposphere. The upper troposphere heavy structure in vorticity forcing portrays the observational vorticity structure (not shown) (Lau and Nath, 1991; Li et al., 2007; Qian et al., 2019; Shi et al., 2019).

Diabatic heating is representative atmospheric thermodynamic forcing induced by the vigorous tropical convective activity and heavy precipitation. As a result of the LBM experiment by moving atmospheric diabatic heating horizontally, it seems that four forcing positions can make a meaningful contribution to the NHW. First, the NHW-like pattern (pattern correlation 0.40) can emerge from the diabatic heating situated over the Atlantic Ocean near Western Africa (**Figure 5A**). The geopotential height anomaly in the LBM simulation reveals that Rossby waves are generated from the Atlantic Ocean, and the Rossby wave energy propagates to the northeast across Russia. Meanwhile, the westward propagating tropical Rossby waves approach to Eastern America from the initial forcing region. Here, we note that the upper troposphere positive geopotential height anomalies and negative vorticity forcing over subtropical regions can be generated by westward propagating atmospheric waves. This means that the tropical–subtropical diabatic heat forcing generates the westward propagating Rossby waves, and again this anomalous vortex flow can be an additional vorticity forcing on the atmosphere. Second, the NHW pattern (correlation 0.52) can arise from Northeast Africa to the midlatitude (**Figure 5B**). In **Figure 5B**, the Rossby wave ray moves to the west initially, and then the path turns to the north across the Mediterranean, penetrating the critical latitude where the zonal wind is zero, by background southerly wind (Zhao et al., 2015).

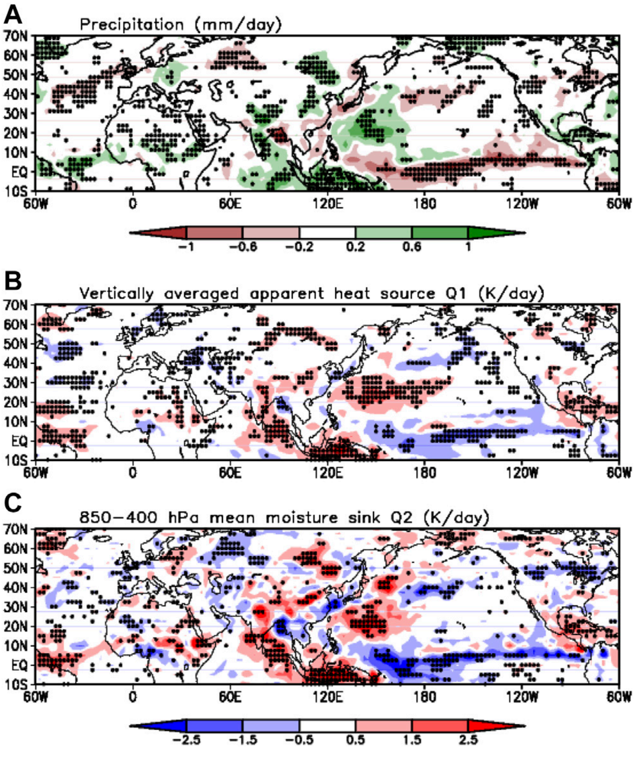

FIGURE 7 | Regression map of precipitation (GPCP), apparent heat source (Q1), and moisture sink (Q2) in July against PC time series. Dots denote significant area at the 95% level.

Third, the NHW can be generated (correlation 0.43) by Indian diabatic heat forcing (**Figure 5C**). Here, the Rossby wave trains pass through Turkey to the midlatitude by the southerly wind. Forth, forcing over South China (**Figure 5D**) also makes the NHW-like pattern (correlation 0.43). All those diabatic heating regions are potential forcing areas for the generation of the NHW (**Figure 5E**). The potential diabatic heat forcing regions, represented by forcing in LBM experiments inducing significant value of pattern correlation coefficient between geopotential height anomalies of EOF1 and LBM simulations, are shown in **Figure 5E**, where forcing lies along the subtropical regions from the Eastern Atlantic to South China.

The Rossby wave response forced by the negative (anti-cyclonic) vorticity is much different from the results of diabatic heat forcing. The vorticity forcing over North Africa has an important role in the formation of the NHW pattern (**Figure 6**). The negative vorticity forcing over North Africa can generate the NHW-like pattern (correlation above 0.40). Over the tropics, the stationary diabatic heating generates the westward propagating Rossby waves (**Figure 5**). The tropical vorticity forcing can be induced systematically by organized convective heat forcing, and the vorticity forcing can emerge randomly by the tropical internal wave dynamics. That means, the mechanism of the NHW pattern is classified into two categories as the

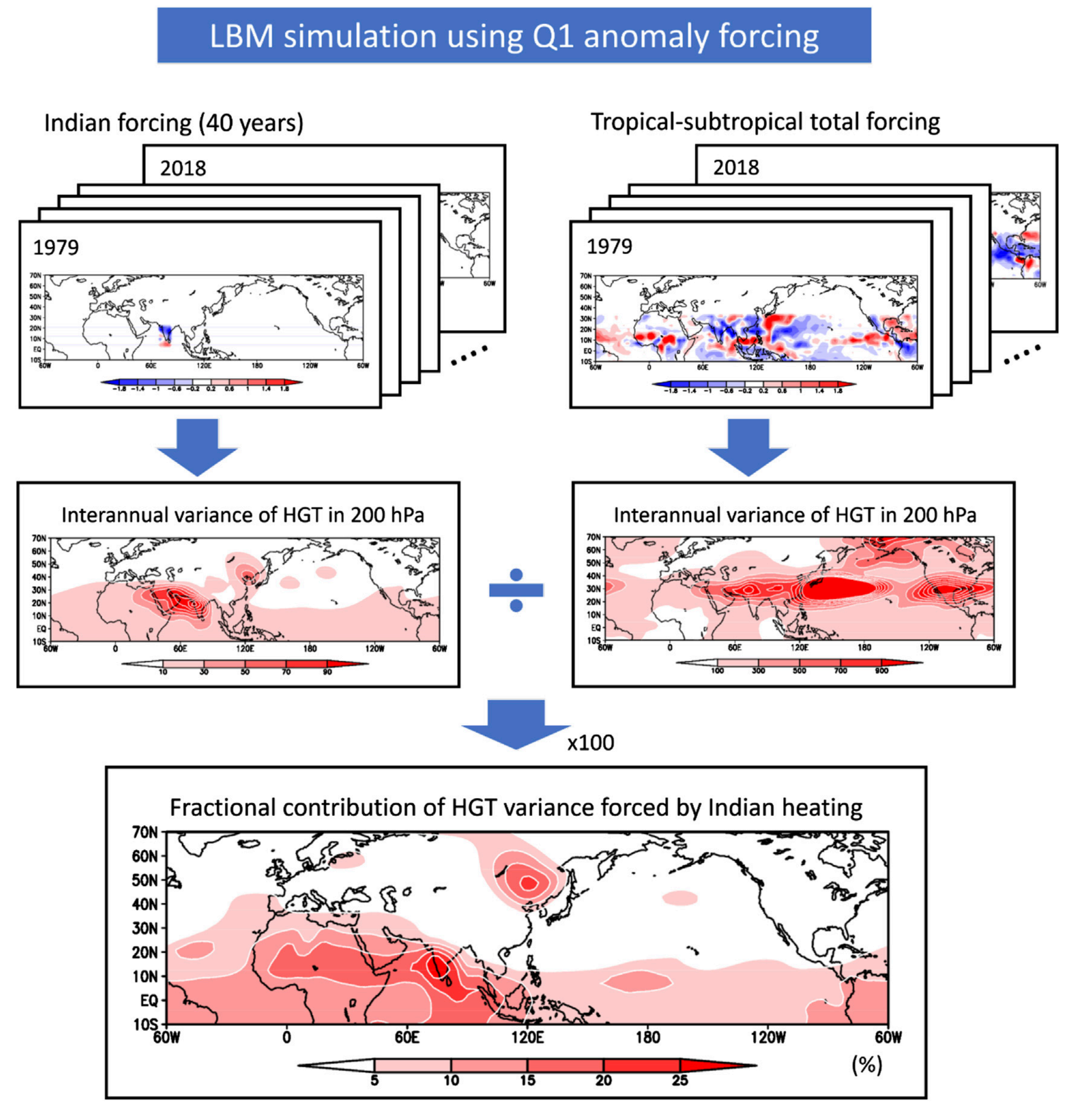

FIGURE 8 | LBM simulations to calculate a percentage contribution (%) of geopotential height in 200 hPa forced by Indian Q1 anomaly.

stationary convective heat forcing with westward propagating Rossby waves, and the atmospheric internal waves.

The LBM results do not guarantee that all potential forcing regions can be actual forcing for the NHW pattern in the real world, because the forcing in the LBM simulations is prescribed in arbitrary locations and vertical structures. Despite these limitations of the idealized experiment, relevant messages can be summarized as follows.

1. Diabatic heating in the Atlantic Ocean, Northeast Africa to India, and East China is a potential thermodynamic heat source inducing the NHW pattern.
2. Upper tropospheric negative vorticity over North Africa may be an important dynamical forcing for generating the NHW.
3. The westward propagating tropical waves emerging from the tropical and subtropical diabatic heat forcing can induce anomalous vorticity forcing for the NHW pattern.

The Generation of the Northern Hemisphere Wave Pattern Forced by Indian Summer Monsoon Precipitation

In observations, the NHW index is well correlated with the ISM precipitation, and the most prominent heat source region is the Indian subcontinent region (**Figure 7**). For reference, the extremely strong precipitation occurs over the Indian ocean and Indian subcontinent in 2010, and the strong positive

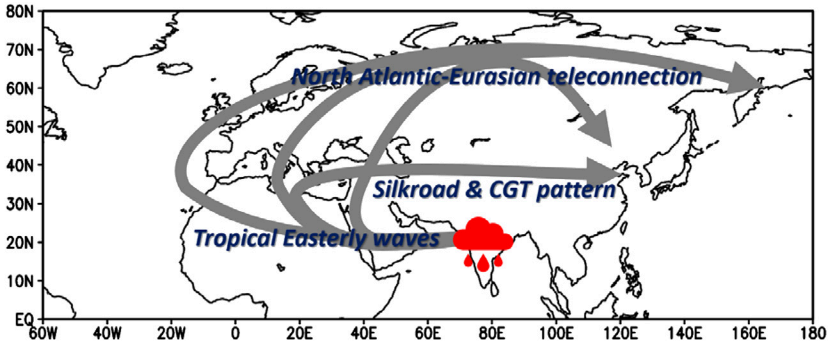

FIGURE 9 | Schematic diagram of the Northern Hemisphere teleconnection induced by the Indian monsoon. Gray lines show the teleconnection pathway generated from Indian diabatic heat forcing.

precipitation is formed over northern India in 2018 (not shown). The heavy rainfall or tropical-subtropical deep convection is accompanied with the atmospheric diabatic heating, which can be estimated by the apparent heat source *Q*1 and moisture sink *Q*2 (**Figures 7B**,C). When the intense precipitation appears, the *Q*1 shows the mid- and top-heavy vertical structure by the combination of condensation and radiation heating; however, the latent heat release in deep convection leads to a middle-level heavy vertical profile of *Q*2 (Seo and Wang, 2010).

According to the previous section, the NHW pattern is regulated by Indian diabatic heating itself and the related vorticity forcing; however, the quantitative contribution of the ISM to relevant vorticity forcing for the NHW pattern is still not elucidated. For the clarification on this point, the LBM experiments are performed using observational interannual *Q*1 anomaly forcing. In here, an essential assumption for the LBM experiment is that the climatological geopotential height pattern is related to climatological diabatic heat forcing, but the interannual variation of the geopotential height is constructed by anomalous atmospheric forcing. The LBM experiment using 3-dimensional Indian *Q*1 anomaly forcing (70°–85°E, 7.5°–25°N, 1,000–10 hPa) from 1979 to 2018 simulates interannual variation of the geopotential height, and thus we can calculate the interannual variance of the geopotential height anomaly as depicted by the procedure in **Figure 8**. The result shows that significant amount of geopotential height variance stretches out to North Africa from the Indian subcontinent diabatic heat forcing. Meanwhile, the tropical–subtropical total forcing explains a tremendous amount of geopotential height variability over the midlatitude. By the comparison of variances in two different experimental results (Total—Indian forcing), the fractional contribution of the Indian forcing is illustrated in **Figure 8**. The percentage contribution of geopotential height induced by Indian diabatic heating is 5–20% over the potential vorticity forcing regions shown in **Figure 6**.

The fractional variance of 5–20% seems small quantity; however, the Indian diabatic heating itself and sequential vorticity forcing over North African regions together generate the NHW pattern. Note that most of North African vorticity perturbations are induced by random tropical forcing with internal tropical easterly waves, and these waves are typically regarded as an atmospheric noise; therefore, the rigorous signal of 5–20% has a grateful meaning to understand the origin of the NHW pattern.

SUMMARY AND DISCUSSION

With dominant stationary wave pattern over the Northern Hemisphere in July, the NHW pattern is related to the anomalous ISM precipitation and sequential westward propagating tropical easterly waves. The tropical vorticity forcing comes from both the internal and forced atmospheric waves; here, the forced waves are primarily caused by the steady heat forcing, while atmospheric internal waves are regarded to exist randomly. The ISM precipitation and related stationary diabatic heating are responsible for the 5–20% of total geopotential height variability over North Africa. This result denotes that the ISM precipitation anomaly with westward propagating tropical waves contributes to the generation of NHW (**Figure 9**).

The midlatitude stationary Rossby waves can be generated from tropical forcing such as the ISM precipitation, but additional background environmental conditions are needed for the Rossby wave energy propagation from the tropics to the midlatitude. In **Figures 5**, **6**, and **9**, the tropical wave paths penetrate the critical latitude (zonal wind speed 0 m/s area) in relation to the distribution of southerly wind (not shown). In the future climate under the global warming, the vertical structures of forcing and background wind structure may change, and then detailed characteristics of the NHW will be changed, for example, by the zonal wavenumber change or individual location of the low- and high-pressure anomalies change by modification of background wind structures with brand new Rossby waves pathway.

For the discussion of a current decadal variability of the stationary wave patterns, the linear trend maps of geopotential height at 200 hPa, surface temperature, and precipitation are illustrated in **Figure 10**. Interestingly, the linear trend of the global geopotential height mimics the NHW pattern (pattern correlation is 0.60). Even at surface temperatures in **Figure 10B**,

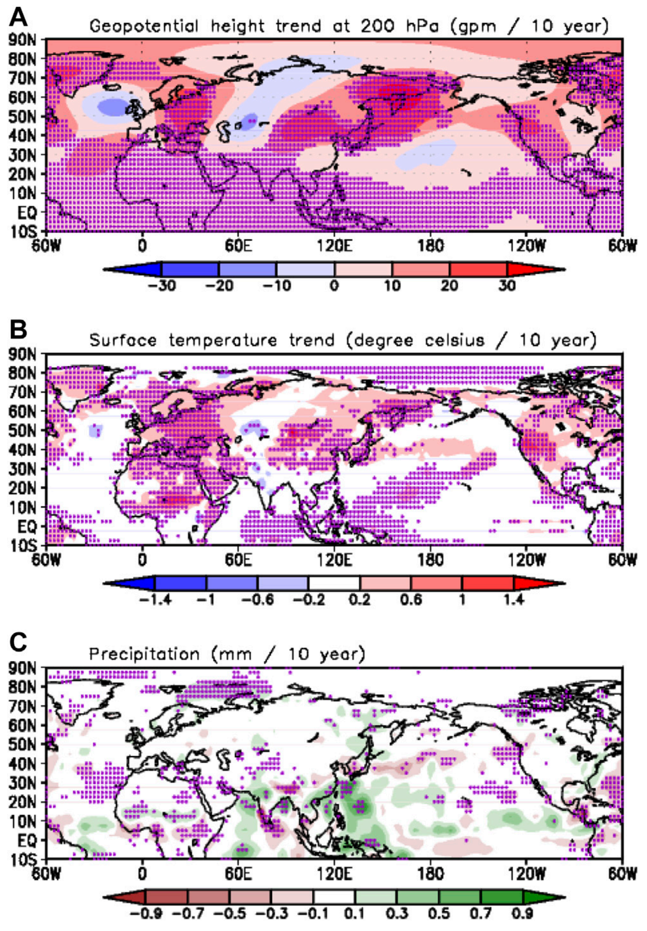

FIGURE 10 | Linear trend of **(A)** geopotential height at 200 hPa, **(B)** surface temperature, and **(C)** precipitation (1979–2018). The nonparametric Mann–Kendall test is used to evaluate whether there is a statistically significant linear trend in the time series at each grid point. Dots denote the significant regions at the 95% confidence level.

the pattern is nearly identical to the NHW related surface temperature shown in **Figure 3**. The interannual variability of NHW is owing to Indian precipitation (**Figure 7**), whereas the positive precipitation trend over Northern India, the Arabian Sea, and Eastern China is relevant to the positive decadal trend of the NHW (**Figure 10C**). Due to the global warming, the land heats more than the sea so moisture flux convergence is increasing over these monsoon areas. Those regions having the positive trend of precipitation are corresponding to the potential diabatic forcing regions shown in **Figure 5**, and this result implies that the long-term variation of the NHW also can be explained by tropical–subtropical diabatic heat forcing. However, the majority of forcing for the NHW can be changed with respect to the timescale; therefore, further analysis of the NHW pattern under the various timescale is needed.

With closing remarks, the occurrence of long-lasting stationary Rossby waves can change the global and regional climate, but the slow group velocity of transient eddies also has a significant role on the extreme temperature and precipitation (Feldstein and Dayan, 2008; Lau and Kim, 2012; Trenberth and Fasullo, 2012; Wirth et al., 2018). The phase speed means propagation of individual troughs and ridges, whereas the group velocity shows the speed of propagation of the entire wave packet. Therefore, integrated work needs to clarify the relative contribution of the stationary waves and transient eddies on the extraordinary midlatitude climate.

DATA AVAILABILITY STATEMENT

All original datasets used in this study are publicly available. The ERA-Interim data were taken from https://apps.ecmwf.int/datasets/. The GPCP precipitation data were downloaded from https://www.ncei.noaa.gov/data/global-precipitation-climatology-project-gpcp-daily/access/. The ETOPO5 topography data were taken from https://www.ngdc.noaa.gov/mgg/global/etopo5.HTML.

AUTHOR CONTRIBUTIONS

JS and KS conceived the study and wrote the manuscript. All authors provided critical feedback and helped shape the research and manuscript.

FUNDING

This study was supported by the National Research Foundation of Korea (NRF) grant funded by the Korea government (MSIP) (No. NRF-2020R1A2C2009414) and the KMA Research and Development Program under Grant KMI2018–01012.

REFERENCES

Adler, R. F., Huffman, G. J., Chang, A., Ferraro, R., Xie, P.-P., Janowiak, J., et al. (2003). The version-2 global precipitation Climatology Project (GPCP) monthly precipitation analysis (1979-present). *J. Hydrometeorol.* 4, 1147–1167. doi:10.1175/1525-7541(2003)004<1147:tvgpcp>2.0.co;2

Chen, G., and Huang, R. (2012). Excitation mechanisms of the teleconnection patterns affecting the July precipitation in northwest China. *J. Clim.* 25, 7834–7851. doi:10.1175/jcli-d-11-00684.1

Chen, G. S., Huang, H. R., and Zhou, T. L. (2013). Baroclinic instability of the Silk Road pattern induced by thermal damping. *J. Atmos. Sci.* 70, 2875–2893. doi:10.1175/JAS-D-12-0326.1

Dee, D., Uppala, S. M., Simmons, A. J., Berrisford, P., Poli, P., Kobayashi, S., et al. (2011). The ERA-Interim reanalysis: configuration and performance of the data assimilation system. *Q. J. Roy. Meteor. Soc.* 137, 553–597. doi:10.1002/qj.828

Ding, Q., and Wang, B. (2005). Circumglobal teleconnection in the northern hemisphere summer. *J. Clim.* 18, 3483–3505. doi:10.1175/jcli3473.1

Ding, Q., and Wang, B. (2007). Intraseasonal teleconnection between the summer Eurasian wave train and the Indian monsoon. *J. Clim.* 20, 3751–3767. doi:10.1175/jcli4221.1

Ding, Q., Wang, B., Wallace, J. M., and Branstator, G. (2011). Tropical-extratropical teleconnections in Boreal summer: observed interannual variability. *J. Clim.* 24, 1878–1896. doi:10.1175/2011jcli3621.1

Enomoto, T., Hoskins, B. J., and Matsuda, Y. (2003). The formation mechanism of the Bonin high in August. *Q. J. R. Meteorol. Soc.* 129, 157–178.doi:10.1256/qj.01.211

Feldstein, S. B., and Dayan, U. (2008). Circumglobal teleconnections and wave packets associated with Israeli winter precipitation. *Q. J. R. Meteorol. Soc.* 134, 455–467. doi:10.1002/qj.225

Harnik, N., Messori, G., Caballero, R., and Feldstein, S. (2016). The circumglobal North American wave pattern and its relation to cold events in eastern North America. *Geophys. Res. Lett.* 43, 11015–11023. doi:10.1002/2016gl070760

Hoskins, B. J., and Ambrizzi, T. (1993). Rossby wave propagation on a realistic longitudinally varying flow. *J. Atmos. Sci.* 50, 1661–1671. doi:10.1175/1520-0469(1993)050<1661:rwpoar>2.0.co;2

Hoskins, B. J., and Karoly, D. J. (1981). The steady linear response of a spherical atmosphere to thermal and orographic forcing. *J. Atmos. Sci.* 38, 1179–1196. doi:10.1175/1520-0469(1981)038<1179:tslroa>2.0.co;2

Kosaka, Y., Nakamura, H., Watanabe, M., and Kimoto, M. (2009). Analysis on the dynamics of a wave-like teleconnection pattern along the summertime Asian jet based on a reanalysis dataset and climate model simulations. *JMJS* 87, 561–580. doi:10.2151/jmsj.87.561

Lau, N.-C., and Nath, M. J. (1991). Variability of the baroclinic and barotropic transient eddy forcing associated with monthly changes in the midlatitude storm tracks. *J. Atmos. Sci.* 48, 2589–2613. doi:10.1175/1520-0469(1991)048<2589:votbab>2.0.co;2

Lau, W. K. M., and Kim, K.-M. (2012). The 2010 Pakistan flood and Russian heat wave: teleconnection of hydrometeorological extremes. *J. Hydrometeorol.* 13, 392–403. doi:10.1175/jhm-d-11-016.1

Lee, H.-J., and Seo, K.-H. (2019). Impact of the Madden-Julian oscillation on Antarctic sea ice and its dynamical mechanism. *Sci. Rep.* 9 (1). doi:10.1038/s41598-019-47150-3

Li, J. P., and Ruan, C. Q. (2018). The North Atlantic–Eurasian teleconnection in summer and its effects on Eurasian climates. *Environ. Res. Lett.* 13, 024007. doi:10.1088/1748-9326/aaeb56

Li, S., Robinson, W. A., Hoerling, M. P., and Weickmann, K. M. (2007). Dynamics of the extratropical response to a tropical Atlantic SST anomaly. *J. Clim.* 20, 560–574. doi:10.1175/jcli4014.1

Li, Y., Li, J., Jin, F. F., and Zhao, S. (2015). Interhemispheric propagation of stationary Rossby waves in a horizontally nonuniform background flow. *J. Atmos. Sci.* 72, 3233–3256. doi:10.1175/jas-d-14-0239.1

Lighthill, J. (1978). *Waves in fluids*. Cambridge: Cambridge University Press, 504. .

Lin, J.-S., Wu, B., and Zhou, T.-J. (2016). Is the interdecadal circumglobal teleconnection pattern excited by the Atlantic multidecadal oscillation?. *Atmos. Oceanic Sci. Lett.* 9, 451–457. doi:10.1080/16742834.2016.1233800

Lu, R.-Y., Oh, J.-H., and Kim, B.-J. (2002). A teleconnection pattern in upper-level meridional wind over the North African and Eurasian continent in summer. *Tellus* 54, 44–55. doi:10.1034/j.1600-0870.2002.00248.x

Peng, S., Robinson, W. A., and Li, S. (2003). Mechanisms for the NAO responses to the north Atlantic SST tripole. *J. Clim.* 16, 1987–2004. doi:10.1175/1520-0442(2003)016<1987:mftnrt>2.0.co;2

Qian, Q., Jia, X., and Wu, R. (2019). Changes in the impact of the Autumn Tibetan plateau snow cover on the winter temperature over North America in the mid-1990s. *J. Geophys. Res.: Atmosphere* 124, 343. doi:10.1029/2019jd030245

Saeed, S., Lipzig, N.V., Müller, W. A., Saeed, F., and Zanchettin, D. (2014). Influence of the circumglobal wave-train on European summer precipitation. *Clim. Dyn.* 43, 503–515. doi:10.1007/s00382-013-1871-0

Saeed, S., Müller, W.A., Hagemann, S., and Jacob, D. (2011). Circumglobal wave train and summer monsoon over northwestern India and Pakistan; the explicit role of the surface heat low. *Clim. Dyn.* 37, 1045–1060. doi:10.1007/s00382-010-0888-x

Sato, N., and Takahashi, M. (2006). Dynamical processes related to the appearance of quasi-stationary waves on the subtropical jet in the midsummer Northern Hemisphere. *J. Clim.* 19, 1531–1544. doi:10.1175/jcli3697.1

Schubert, S., Wang, H., and Suarez, M. (2011). Warm season subseasonal variability and climate extremes in the Northern Hemisphere: the role of stationary Rossby waves. *J. Clim.* 24, 4773–4792. doi:10.1175/jcli-d-10-05035.1

Seo, K.-H., Son, J.-H., Lee, S.-E., Tomita, T., and Park, H.-S. (2012). Mechanisms of an extraordinary East Asian summer monsoon event in July 2011. *Geophys. Res. Lett.* 39. doi:10.1029/2011gl050378

Seo, K.-H., and Son, S.-W. (2012). The global atmospheric circulation response to tropical diabatic heating associated with the Madden-Julian oscillation during northern winter. *J. Atmos. Sci.* 69, 79–96. doi:10.1175/2011jas3686.1

Seo, K.-H., and Wang, W. (2010). The Madden-Julian oscillation simulated in the NCEP climate forecast system model: the importance of stratiform heating. *J. Clim.* 23, 4770–4793. doi:10.1175/2010jcli2983.1

Shi, N., Tian, P., and Zhang, L. (2019). Simultaneous influence of the Southern Hemisphere annular mode on the atmospheric circulation of the Northern Hemisphere during the boreal winter. *Int. J. Climatol.* 39, 2685–2696. doi:10.1002/joc.5981

Stephan, C. C., Klingaman, N. P., and Turner, A. G. (2019). A mechanism for the recently increased interdecadal variability of the silk road pattern. *J. Clim.* 32, 717–736. doi:10.1175/jcli-d-18-0405.1

Trenberth, K. E., and Fasullo, J. T. (2012). Climate extremes and climate change: the Russian heat wave and other climate extremes of 2010. *J. Geophys. Res.* 117. doi:10.1029/2012jd018020

Watanabe, M., and Kimoto, M. (2000). Atmosphere-ocean thermal coupling in the North Atlantic: a positive feedback. *Q. J. Royal Met. Soc.* 126, 3343–3369. doi:10.1002/qj.49712657017

Wirth, V., Riemer, M., Chang, E. K. M., and Martius, O. (2018). Rossby wave packets on the midlatitude waveguide-A review. *Mon. Weather Rev.* 146, 1965–2001. doi:10.1175/mwr-d-16-0483.1

Wu, Z., Li, J., Jiang, Z., He, J., and Zhu, X. (2012). Possible effects of the north Atlantic oscillation on the strengthening relationship between the East Asian summer monsoon and ENSO. *Int. J. Climatol.* 32, 794–800. doi:10.1002/joc.2309

Wu, Z., Wang, B., Li, J., and Jin, F.-F. (2009). An empirical seasonal prediction model of the east Asian summer monsoon using ENSO and NAO. *J. Geophys. Res.* 114, D18120. doi:10.1029/2009jd011733

Yanai, M. (1961). A detailed analysis of typhoon formation. *J. Meteorol. Soc. Jpn.* 39, 187–214. doi:10.2151/jmsj1923.39.4_187

Yanai, M., Esbensen, S., and Chu, J.-H. (1973). Determination of bulk properties of tropical cloud clusters from large-scale heat and moisture budgets. *J. Atmos. Sci.* 30, 611–627. doi:10.1175/1520-0469(1973)030<0611:dobpot>2.0.co;2

Zhao, S., Li, J., and Li, Y. (2015). Dynamics of an interhemispheric teleconnection across the critical latitude through a southerly duct during boreal winter. *J. Clim.* 28, 7437–7456. doi:10.1175/jcli-d-14-00425.1

Zheng, F., Li, J., Li, Y., Zhao, S., and Deng, D. (2016). Influence of the summer NAO on the spring-NAO-based predictability of the East Asian summer monsoon. *J. Appl. Meteor. Climatol.* 55, 1459–1476 doi:10.1175/jamc-d-15-0199.1

Zhou, F., Zhang, R., and Han, J. (2019). Relationship between the circumglobal teleconnection and silk road pattern over eurasian continent. *Sci. Bull.* 64, 374–376. doi:10.1016/j.scib.2019.02.014

Conflict of Interest: The authors declare that the research was conducted in the absence of any commercial or financial relationships that could be construed as a potential conflict of interest.

frontiers in Earth Science

ORIGINAL RESEARCH
published: 19 February 2021
doi: 10.3389/feart.2021.642588

Asymmetric Relationship Between Mid-latitude Eurasian Circulation and Summer Rainfall in Hong Kong in Different Phases of ENSO

Yana Li[1†], *Ho-Nam Cheung*[2,3]* and *Wen Zhou*[4]

[1]Institute of Environment, Energy and Sustainability, The Chinese University of Hong Kong, Hong Kong, China, [2]School of Atmospheric Sciences and Guangdong Province Key Laboratory for Climate Change and Natural Disaster Studies, Sun Yat-sen University, Zhuhai, China, [3]Southern Marine Science and Engineering Guangdong Laboratory (Zhuhai), Zhuhai, China, [4]Center for Ocean Research in Hong Kong and Macau (CORE), School of Energy and Environment, City University of Hong Kong, Hong Kong, China

Edited by:
Lin Wang,
Institute of Atmospheric Physics (CAS), China

Reviewed by:
Juan Feng,
Institute of Atmospheric Physics (CAS), China
Boqi Liu,
Chinese Academy of Meteorological Sciences, China

***Correspondence:**
Ho-Nam Cheung
zhanghlan5@mail.sysu.edu.cn

†Present Address:
School of Energy and Environment, City University of Hong Kong, Hong Kong, China

Specialty section:
This article was submitted to Atmospheric Science, a section of the journal Frontiers in Earth Science

Received: 16 December 2020
Accepted: 18 January 2021
Published: 19 February 2021

Citation:
Li Y, Cheung H-N and Zhou W (2021) Asymmetric Relationship Between Mid-latitude Eurasian Circulation and Summer Rainfall in Hong Kong in Different Phases of ENSO. Front. Earth Sci. 9:642588. doi: 10.3389/feart.2021.642588

During the period 1979–2019, the interannual variation of summer rainfall in Hong Kong (HK), located on the South China coast, is weakly correlated with tropical forcing, including the El Niño/Southern Oscillation (ENSO). Instead, HK summer rainfall is strongly correlated with the mid-latitude circulation over the Urals and the preceding spring sea surface temperature (SST) over the North Atlantic (SST-Atl). The above relationship is stronger in negative ENSO summers, where the SST-Atl anomaly tends to persist from spring to summer. The persistence of the warm SST-Atl anomaly is associated with a Rossby wave train propagating from the North Atlantic to East Asia, with a low over the Urals and a high over the high latitudes of Asia. Correspondingly, the upper-tropospheric westerly jet in East Asia becomes stronger and shifts southward toward South China. The enhanced westerly wind over South China is accompanied by an anomalous Philippine Sea anticyclone, which transports more water vapor to the South China coast and causes more rainfall in HK. On the other hand, during positive ENSO summers, HK summer rainfall is affected by variation in the subtropical westerly jet over South China, which is related to water vapor transport from the Indian Ocean and Bay of Bengal. This is also associated with a height anomaly over northeastern China and the spring sub-polar North Atlantic SST. Therefore, it is important to investigate the impact of mid-latitude forcing on summer rainfall on the South China coast.

Keywords: Hong Kong rainfall, summer climate anomaly in China, spring North Atlantic SST, Ural high, extratropical wave train

INTRODUCTION

Hong Kong (HK) is a subtropical city with hot and humid weather in the boreal summer and cold and dry weather in the boreal winter. These characteristics are related to a seasonal reversal of wind direction associated with the East Asian monsoon, which arises from the land-sea thermal contrast and the topographic forcing exerted by the Tibetan Plateau (He et al., 1987; Tao and Chen, 1987; Wu et al., 2013). In HK, a coastal city adjacent to the South China Sea (SCS), summer rainfall is affected by tropical cyclone activity and the SCS summer monsoon (SCSSM), which marks the beginning of the rainy season. Li et al. (2015) showed that tropical cyclones account for around 20–25% of the rainfall in HK from July to October, and the percentage increases to about 40% for heavy rainfall (daily rainfall > 100 mm). South China, including HK, usually has more (less) rainfall during a strong (weak) SCSSM, which is likely preceded by an early (late) SCSSM onset (Zhou et al., 2005).

During the past few decades, the intensity of the SCSSM and the tropical cyclone activity over the western North Pacific have had strong interannual and interdecadal variation (Chan and Zhou, 2005; Kajikawa and Wang, 2012; Yuan, et al., 2012; Chen et al., 2013; Wang, et al., 2012; Li, et al., 2014; Li and Zhou, 2014; Liu and Chan, 2019). Concomitantly, summer rainfall in HK has had considerable interannual and interdecadal variation (Leung et al., 2004). Because HK is a densely populated city, seasonal forecasts of summer precipitation several months ahead are useful for government and policy makers to minimize loss due to flooding caused by extreme precipitation events. A strong and advanced SCSSM is usually linked to anomalous warming over the SCS and western tropical Pacific in spring (Zhu and Li, 2017; Li et al., 2019b). The El Niño-Southern Oscillation (ENSO, also known as El Niño and La Niña) is one of the most predictable phenomena over the tropical Pacific on interannual timescales, so it might be regarded as a potential predictor of the summer upper-tropospheric circulation in the Northern Hemisphere (Lee et al., 2011) and the summer rainfall in South China (Chan and Shi, 1999; Jiang and Zhu, 2021). Based on technical reports from the Hong Kong Observatory (HKO), ENSO and the intensity of the East Asian winter monsoon in the preceding winter are two important predictors of annual rainfall in HK (Chang and Yeung, 2003). A strong El Niño developing year (e.g., 1982 and 1997) tends to be wet, and a year following a strong La Niña onset (e.g., 1984 and 1999) tends to be dry. However, Zhou and Chan (2007) pinpointed that the SCSSM tends to have an early (late) onset and bring South China more (less) rainfall during a cold (warm) ENSO event. In general, El Niño does not have a significant impact on East Asian summer precipitation (Wang et al., 2017). The ENSO could better explain the autumn rainfall in South China (Wu et al., 2003). Compared to ENSO, other tropical forcing, such as sea surface temperature (SST) over the tropical central Pacific and a dipole sea surface temperature tendency in the Indo-Pacific warm pool in the previous winter, are more closely related to early summer rainfall over South China (He and Wu, 2014; Yim et al., 2014; Xing et al., 2016). We will show that the interannual variation of HK summer rainfall is not significantly correlated with tropical forcing.

The internal dynamics of the East Asian summer monsoon involves the tropical-midlatitude interactions (Tao and Chen, 1987; Lau et al., 2000). The summer rainfall over South China is also modulated by mid-latitude forcing other than tropical forcing. Following a weak winter monsoon, persistent cyclonic anomalies over the South China coast can enhance the East Asian summer monsoon (Chen et al., 2000; Wu and Chan, 2005; Chen et al., 2013). Prior to the SCSSM onset, frequent intrusion of synoptic disturbances from the midlatitudes into South China can trigger vigorous frontal precipitation and facilitate the SCSSM onset (Wang, 1992; Wang and Yasunari, 1994; Ding and Li, 1999; Ding and Chan, 2005; Zheng et al., 2006; Lin et al., 2010). The frontal precipitation over South China is related to the local lower-tropospheric meridional temperature gradient (Huang and Chen 2015). After the SCSSM onset, monsoonal fronts usually form at interfaces of tropical and extratropical forcing to bring frontal rainfall over South China. Such extratropical forcing is strongly modulated by blocking highs (Ninomiya and Shibagaki, 2007; Wu et al., 2009; Yim et al., 2014). The co-existence of blocking highs over the Ural Mountains and the Sea of Okhotsk, as well as a deep trough between the highs, can trigger persistent and intense subtropical frontal precipitation over East Asia (Ding and Chan, 2005; Chen and Zhai, 2014). A pronounced winter warming tendency from December to February over Siberia is associated with reduced snow cover over eastern Siberia in the subsequent summer, which favors warming and the occurrence of blocking highs over the Sea of Okhotsk, leading to increasing summer rainfall over South China (Yim et al., 2014).

On the other hand, Gong and Ho (2003) showed that the positive phase of the late spring Arctic Oscillation is related to a northward shift in the upper-tropospheric jet over East Asia in summer. This accompanies anomalous sinking motion over subtropical East Asia, which corresponds to less rainfall along the Meiyu-Baiu-Changma region and more rainfall in South China. Such an opposite precipitation anomaly is also be linked to the southeast-northwest movement of the South Asian high (Wei et al., 2015) and the meridional displacement of the subtropical jet stream over East Asia (Kim and Ha, 2021). Recently, Dai et al. (2020) proposed that a wave train propagating from Russia to China via the Tibetan Plateau affects the rain belts over Southeast China. Lin (2014) showed that the positive phase of the East Atlantic/Western Russia teleconnection pattern is accompanied by a southeastward propagation of a Rossby wave train over East Asia. This is related to a significant negative height anomaly and more rainfall over South China. We will show that the midlatitude forcing could strongly modulate HK summer rainfall.

The interannual variation of the East Asian summer monsoon is also linked to the pre-season sea surface temperature (SST) and the large-scale atmospheric circulation over the North Atlantic. Sung et al. (2006) found that the positive phase of the North Atlantic Oscillation (NAO), which is the dominant mode of the North Atlantic atmospheric circulation, in the preceding December could induce a northward shift in the westerly jet over East Asia in June and suppress summer rainfall in South China. Such a delayed impact is dynamically bridged by a Eurasian wave train trapped in the westerly waveguide, where the wave train is excited by anomalous upper-level convergence over the Mediterranean Sea after February (Watanabe, 2004). Moreover, following a positive winter NAO, the summer 500-hPa geopotential height anomaly over the Sea of Okhotsk tends to be positive (Ogi et al., 2004), which could affect summer rainfall over South China.

The spring NAO is also correlated with the East Asian summer monsoon, where the spring NAO influences the North Atlantic tripolar SST anomaly and the subsequent Rossby wave train response over Eurasia (Wu et al., 2009; Yim et al., 2014; Li et al., 2019a). The summer NAO or the North Atlantic tripolar SST can excite a wave train over Eurasia continent and influences diabatic heating over the Tibetan Plateau, which triggers a subtropical wave train. The midlatitude and subtropical wave trains jointly affect the extreme weather events in East Asia, such as the heatwave over northeastern China in 2018 and the extreme Meiyu season in 2020 (Wang et al., 2018; Liu et al., 2019; Liu et al., 2020). Chen et al. (2017) found that the interannual variation of NAO has a stronger relationship with the summer rainfall in south China after early 1990s. On interdecadal timescales, Chan and Zhou (2005) demonstrated that early summer monsoon rainfall over South China tends to be below or above normal when ENSO and the Pacific decadal oscillation are in phase. The Atlantic multidecadal oscillation also modulates summer rainfall over South China via a teleconnection pattern over Eurasia or via its impact on variation in the North Pacific (Si and Ding, 2016; Fan et al., 2018). We will show that the spring SST anomaly over the North Atlantic could be a potential predictor for HK summer rainfall.

The manuscript is organized as follows. Section *Data and Methods presents* the data used in this study. Seasonal forcing linked to HK summer rainfall is examined in Section *Seasonal Forcing of HK Summer Rainfall*. Then possible predictors are identified in Section *Dynamic Mechanisms in Different Summer ENSO Phases*. Section *Role of Spring North Atlantic SST Anomalies summarizes the results.*

DATA AND METHODS

Monthly precipitation data were extracted from the Hong Kong Observatory (HKO) Headquarters and the Climate Prediction Center Merged Analysis of Precipitation (CMAP) for the period 1979–2019. Atmospheric variables were extracted from the National Centers for Environmental Prediction-National Center for Atmospheric Research (NCEP-NCAR) global reanalysis datasets from the National Oceanic and Atmospheric Administration (NOAA) of the United States. These include the monthly fields of mean sea level pressure, multi-level wind (zonal and meridional components), omega (vertical velocity), specific humidity, and geopotential height for the period 1979–2019. The horizontal spatial resolution is 2.5°latitude × 2.5°longitude. The multi-level fields include 17 isobaric levels from 1,000 hPa to 10 hPa, except omega includes only 11 isobaric levels from 1,000 hPa to 100 hPa.

Monthly sea surface temperature data were extracted from the Hadley Centre sea ice and sea surface temperature dataset (HadISST) for the period 1979–2019, with a spatial resolution of 1°latitude × 1°longitude. The monthly Niño-3.4 index, obtained from the NOAA website (https://psl.noaa.gov/gcos_wgsp/Timeseries/Data/nino34.long.anom. data), is defined as the

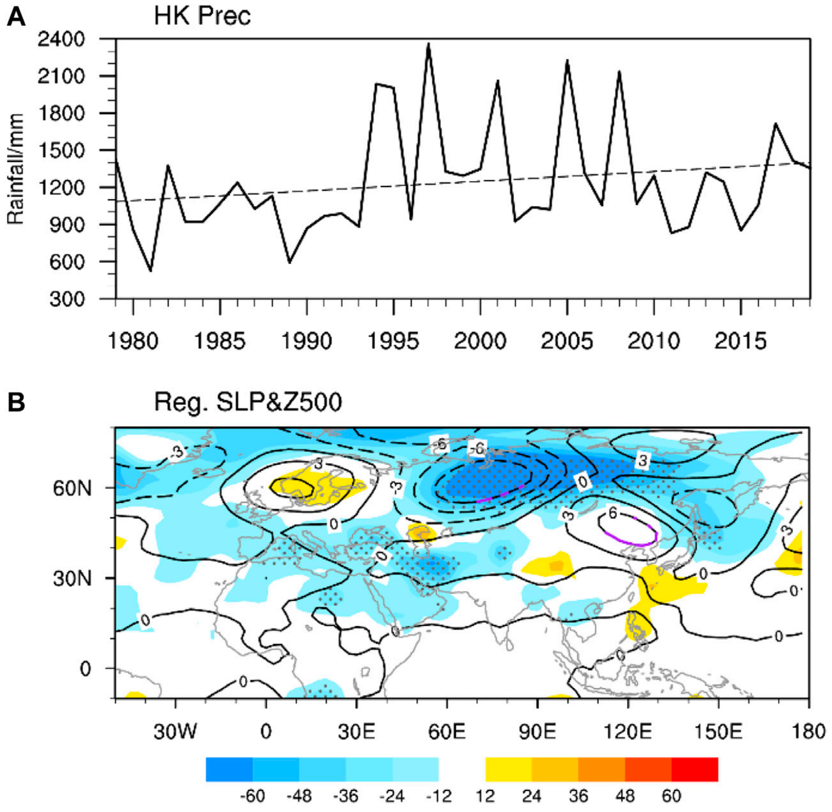

FIGURE 1 | (A) Time series of summer (June-July-August, JJA) rainfall at the HKO Headquarters (HK Prec, mm) for the period 1979–2019. **(B)** Regression of summer mean sea level pressure (shading, Pa) and 500-hPa geopotential height (contour intervals: 3 m) onto summer HK Prec. Stippling and purple contours are significant at the 95% confidence level.

area-averaged SST anomaly over 5°S–5°N and 170°–120°W with respect to the 1981–2010 climatology.

The vertically integrated water vapor flux over the 1,000–300 hPa layer (Q) is derived from the zonal and meridional components of the wind field (U, V) and the specific humidity (q):

$$Q = \frac{1}{g}\int_{1000\text{hPa}}^{300\text{hPa}} (Uq + Vq)\mathrm{d}p,$$

where g is the acceleration due to gravity.

The seasonal-mean water vapor flux ($\overline{Q}$) can be decomposed into its stationary $\overline{()}$ and transient $()'$ components, which represent the water vapor transport due to the seasonal-mean flow and the transient flow:

$$\overline{Q} = \underbrace{\frac{1}{g}\int_{1000\text{hPa}}^{300\text{hPa}} (\overline{U}\,\overline{q} + \overline{V}\,\overline{q})\mathrm{d}p}_{\text{stationary}} + \underbrace{\frac{1}{g}\int_{1000\text{hPa}}^{300\text{hPa}} (\overline{U'q'} + \overline{V'q'})\mathrm{d}p}_{\text{transient}}.$$

Because the contribution of the transient term to summer moisture transport in the tropics and South China is negligible (see Figure 5–6 in Li et al., 2013), this term can be approximated by the stationary term:

$$\overline{Q} \approx \frac{1}{g}\int_{1000\text{hPa}}^{300\text{hPa}} (\overline{U}\,\overline{q} + \overline{V}\,\overline{q})\mathrm{d}p,$$

where $\overline{Q}$ is derived by the monthly U, V and q.

The horizontal component of stationary wave activity fluxes at 250 hPa (W) is used to depict Rossby wave propagation, where the direction of wave activity fluxes is parallel to the group velocity (Takaya and Nakamura, 2001):

$$\boldsymbol{W} = \frac{p\cos\phi}{2|V|}\left\{\begin{array}{c} \dfrac{\overline{U}}{a^2\cos^2\phi}\left[\left(\dfrac{\partial\psi'}{\partial\lambda}\right)^2 - \psi'\dfrac{\partial^2\psi'}{\partial\lambda^2}\right] + \dfrac{\overline{V}}{a^2\cos\phi}\left(\dfrac{\partial\psi'}{\partial\lambda}\dfrac{\partial\psi'}{\partial\phi} - \psi'\dfrac{\partial^2\psi'}{\partial\lambda\partial\phi}\right) \\ \dfrac{\overline{U}}{a^2\cos^2\phi}\left(\dfrac{\partial\psi'}{\partial\lambda}\dfrac{\partial\psi'}{\partial\phi} - \psi'\dfrac{\partial^2\psi'}{\partial\lambda\partial\phi}\right) + \dfrac{\overline{V}}{a^2}\left[\left(\dfrac{\partial\psi'}{\partial\phi}\right)^2 - \psi'\dfrac{\partial^2\psi'}{\partial\phi^2}\right] \end{array}\right\},$$

where the overbar denotes the climatological mean, p is 250 hPa, and ψ' is the perturbation streamfunction derived from the regressed wind field.

SEASONAL FORCING OF HK SUMMER RAINFALL

Climatologically, the accumulated HK rainfall in boreal summer (June–July–August) is 1,235 mm during the period of 1979–2019, accounting for more than 50% of the total annual rainfall. The summer rainfall has strong interannual variation (**Figure 1A**), with two interdecadal turning points at 1993/1994 and 2009/2010. These interdecadal shifts are consistent with the SCSSM onset, which occurred earlier from 1993 to 1994 and became normal or occurred later in about 2010 (Wang et al., 2004; Wu et al., 2010; Kajikawa and Wang, 2012; Fan et al., 2014; Liu et al., 2016; Li et al., 2019b). Such a coincidence suggests a coherent relationship between the SCSSM onset and HK summer rainfall. Note that the slightly increasing trend of precipitation during the study period (the dashed line in **Figure 1A**) might indicate more precipitation in HK under global warming (Leung et al., 2004).

It is curious how strongly summer rainfall in HK is modulated by large-scale forcing from both the midlatitudes and the tropics. To identify the strongest seasonal large-scale forcing linearly related to summer rainfall in HK, a time series of normalized HK summer rainfall is regressed onto mean sea level pressure and 500-hPa geopotential height (**Figure 1B**). Although the strength of the western North Pacific subtropical high affects the intensity of the East Asian summer monsoon (e.g., Huang and Wu, 1989; Zhang et al., 1999; Chang et al., 2000), it is not statistically significant in relation to summer rainfall in HK. Instead, the year-to-year variation in summer rainfall in HK is significantly linearly correlated with the midlatitude circulation over central and East Asia. Specifically, more (less) summer rainfall in HK is associated with negative (positive) pressure anomalies centered over Ural-Siberia. It is also associated with positive (negative) pressure anomalies over Europe, but this signal is not significant. The linkage between summer rainfall in HK and the large-scale teleconnection over midlatitude Eurasia is noteworthy. It should be noted that the result is similar when the above analysis is repeated using the summer rainfall at stations along the South China coast.

In boreal summer, the Ural Mountains form one of the major blocking sectors in the Northern Hemisphere. The occurrence of a Ural blocking high advects more cold air from the high latitudes to Siberia. The associated cold air activity can enhance frontal precipitation when it meets warm and moist air from lower latitudes. The persistence of summer Ural blocking has been identified as one of the main dynamic causes of flooding near the

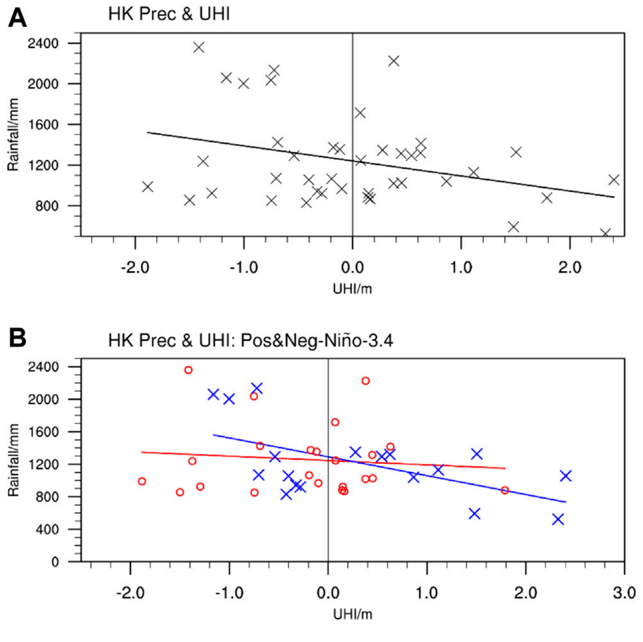

FIGURE 2 | (A) Scatterplot of HK Prec (mm) against the standardized Ural Height Index (UHI, m) in summer, where the straight line represents the least square fit. **(B)** Same as **(A)**, but for positive Niño-3.4 summers **(red)** and negative Niño-3.4 summers **(blue)**.

Yangtze River, as occurred in 1998 (Li et al., 2001), but a linkage between Ural blocking and summer rainfall in HK has not previously been revealed. Because we focus on seasonal-mean circulation, we define a Ural height index (UHI) as the standardized June-July-August (JJA) geopotential height averaged over 50°–70°N and 45°–90°E during 1979–2019. As shown in **Figure 2A**, the UHI against HK summer rainfall is significantly negatively correlated, where the correlation is −0.334 and exceeds the 95% confidence level. Such an inverse relationship suggests that more occurrence of Ural blocking is associated with less summer rainfall in HK. That means the relationship between Ural blocking and summer rainfall in the Yangtze River and HK (and the South China coast) is reversed. Before investigating the possible dynamic mechanism responsible for the above linkage, we would like to identify the pre-season signals of these circulation anomalies, which could be useful for seasonal forecasts.

Operationally, the seasonal prediction of HK summer rainfall has relied on SST, especially over the tropical Pacific (Chang and Yeung, 2003). However, we do not find a significant statistical relationship between the tropical SST and summer rainfall in HK. As shown in **Figures 3A,B**, summer rainfall in HK is also not significantly correlated with SST over the tropical Pacific during the concurrent summer and spring. The correlation between the Niño-3.4 index and HK summer rainfall is +0.109 during the period 1979–2019, where the average summer rainfall in positive and negative Niño-3.4 summers is 1,258 mm and 1,230 mm, respectively. It appears that Pacific SST cannot well predict summer rainfall in HK. Instead, the rainfall is moderated linked to SST over part of the North Atlantic in spring and summer. The lead–lag correlation (**Figure 3C**) between HK summer rainfall and North Atlantic SST over 30°–60°N and 45°–15°W in different seasons (SST-Atl, black boxes in **Figures 3A,B**) shows a significant positive correlation that peaks in spring. Therefore, the spring SST-Atl is a potential seasonal predictor for summer precipitation in HK.

It is also important to see whether the seasonal predictor of the UHI is the same as that of summer rainfall in HK, because the UHI and HK summer precipitation are moderately correlated. As shown in **Figures 3D–F**, the UHI is significantly correlated with SST in part of the North Atlantic and the tropical south Atlantic from spring to summer. It is also moderately correlated with SST in the Niño-3.4 region over the tropical Pacific during summer (**Figure 3E**). This is different from the insignificant correlation between summer rainfall in HK and SST over the tropical Pacific. When the summer UHI is correlated with SST in different seasons, we can observe the evolution of a La Niña-like pattern from the concurrent spring to the concurrent fall (figures not shown). This relationship can be depicted by a significant negative correlation between the UHI and the Niño-3.4 index (dotted dashed line in **Figure 3F**). In other words, a summer with a negative (positive) Niño-3.4 index is

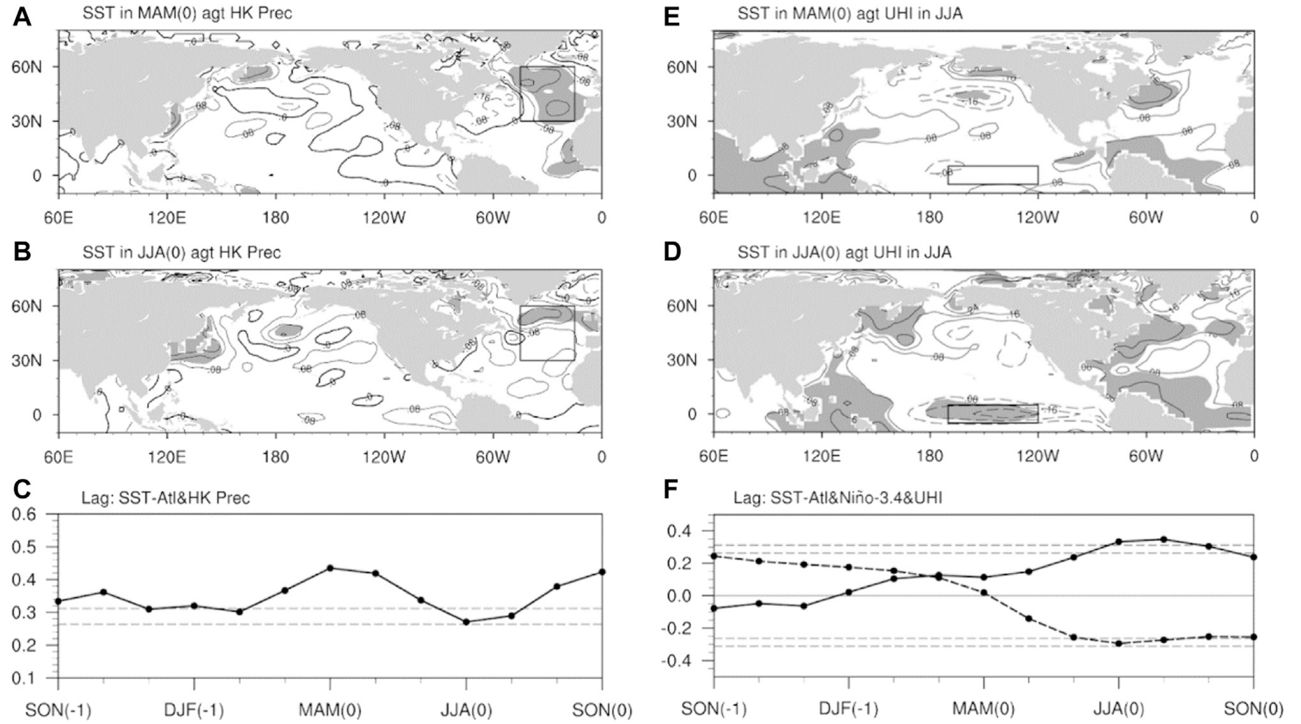

FIGURE 3 | Regression of **(A,B)** summer HK Prec and **(D,E)** summer UHI onto SST in **(A,D)** spring (March-April-May, MAM) and **(B,E)** summer. **(C)** Lead–lag correlation between HK Prec and seasonal mean SST in the North Atlantic enclosed by the black box (30°–60°N, 45°–15°W; SST-Atl) from the preceding autumn to the concurrent autumn. **(F)** Same as **(C)**, except for the lead–lag correlation between UHI and SST-Atl (dotted solid line) and the Niño 3.4 index (dotted dashed line). The Niño 3.4 region is denoted by the black box (5°S–5°N, 120°–170°W) in **(D,E)**. Dashed lines in **(C,F)** indicate the 90% and 95% confidence levels.

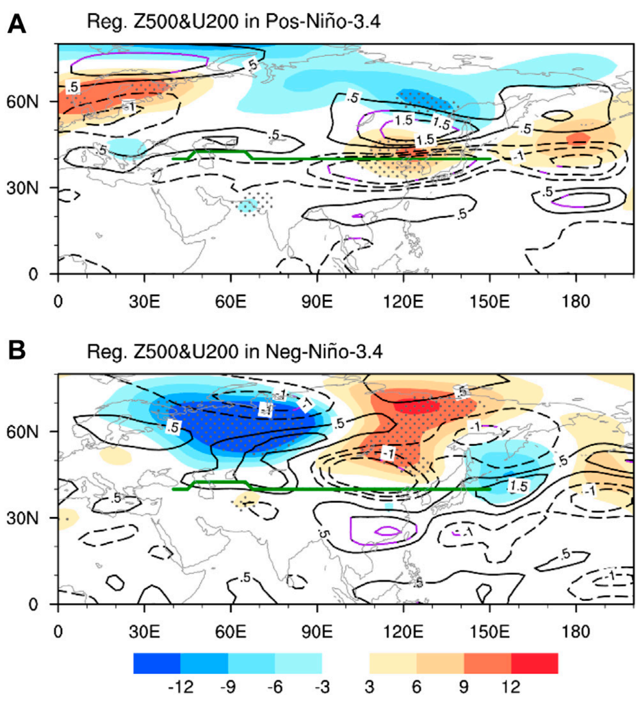

FIGURE 4 | Regression of summer 500-hPa geopotential height (shading, m) and 200-hPa zonal winds (contour interval: 0.5 m, zero contours are omitted) onto summer HK Prec for years with **(A)** a positive Niño 3.4 summer and **(B)** a negative Niño 3.4 summer. Stippling and purple contours indicate the 90% confidence level. The thick green line shows the climatological location of the westerly jet axis at 200 hPa.

more likely to have a positive (negative) UHI, which tends to be associated with less (more) summer rainfall in HK. However, while the UHI is significantly correlated with both the Niño-3.4 index and summer rainfall in HK, summer rainfall in HK is significantly correlated only with the UHI. The relationship between the UHI and summer rainfall in HK seems to be modulated by the phase of ENSO.

To examine the impact of ENSO, the study period is divided into positive (Niño-3.4 index > 0) and negative (Niño-3.4 index < 0) ENSO summers, specifically with 23 positive years and 18 negative years. **Figure 2B** shows that the linear relationship between the UHI and HK summer rainfall is strong (weak) in the negative (positive) phase of summer ENSO, where the linear correlation coefficient in the negative ENSO phase is −0.565 (exceeding the 95% confidence level). This asymmetric relationship suggests that the large-scale atmospheric forcing associated with HK summer rainfall is different in the two ENSO phases. Accordingly, in the following section the summer large-scale circulations are regressed against HK summer rainfall in positive and negative Niño-3.4 years separately.

DYNAMIC MECHANISMS IN DIFFERENT SUMMER ENSO PHASES

During positive Niño-3.4 years, HK summer rainfall is associated with a north-south oriented dipole-like height anomaly pattern over extratropical East Asia (**Figure 4A**). The negative anomalies at 60°N imply a weaker Okhotsk high and the positive anomalies at 40°N imply a weaker vortex over northeastern China. The positive height anomaly center is close to the climatological jet axis at 200 hPa. Correspondingly, the upper-tropospheric zonal winds south of the climatological jet location are weakened. The pronounced positive (negative) zonal wind anomalies at 50°N (35°N) suggest a northward (southward) shift of the westerly jet during positive Niño-3.4 years, with more (less) HK summer rainfall. The South China coast has slightly stronger zonal wind corresponding to more rainfall. These circulation anomalies are associated with the southward propagation of wave activity fluxes from North China to South China (**Figure 5A**). Besides the signal over East Asia, it is noticeable that HK summer rainfall in positive Niño-3.4 years is associated with positive height anomalies over Scandinavia (**Figure 4A**). However, its associated Rossby wave train propagates southeastward toward the Mediterranean and the Middle East, and it does not propagate farther toward East Asia. In short, the pronounced forcing of large-scale circulation related to HK summer rainfall in positive Niño-3.4 years is confined to East Asia.

During negative Niño-3.4 years, on the other hand, the large-scale circulation anomalies associated with HK summer rainfall indicate stronger tropical–midlatitude interactions (**Figure 4B**). The extratropical Eurasian continent has a strong zonal dipole pattern, with a center of action over the Urals and another center of action over the middle and high latitudes of Asia. The positive anomalies over Asia are associated with weaker zonal winds north of the climatological jet axis. The pronounced positive zonal wind anomalies over the South China coast suggest a southward shift of the westerly jet. The above results suggest that during negative Niño-3.4 years, the positive (negative) UHI tends to be accompanied by stronger (weaker) westerlies near the climatological jet and weaker (stronger) zonal wind over the

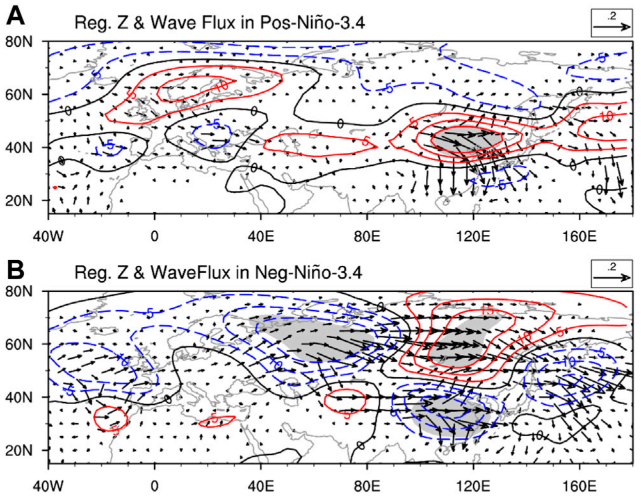

FIGURE 5 | Regression of summer 200-hPa geopotential height (contour, m) and wave activity flux (arrows, m) onto summer HK Prec for years with **(A)** a positive Niño-3.4 index and **(B)** a negative Niño-3.4 index. Shading indicates the 90% confidence level.

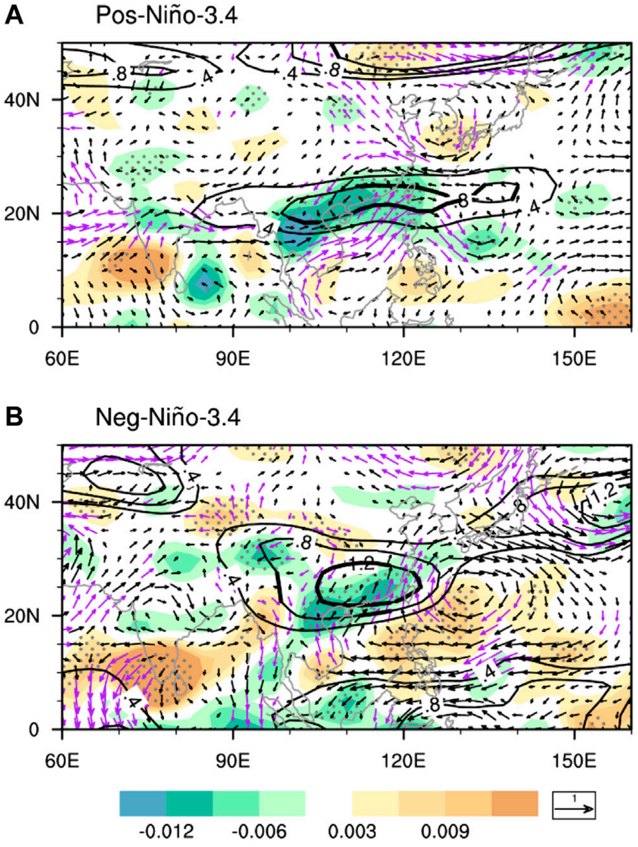

FIGURE 6 | Regression of summer 500-hPa vertical velocity (shading, Pa s^{-1}), 200-hPa zonal winds (black contours, m/s), and 850-hPa winds (arrows, m/s) onto summer HK Prec for years with **(A)** a positive Niño-3.4 index and **(B)** a negative Niño-3.4 index. Stippling, thick black contours, and purple arrows are significant at the 90% confidence level.

South China coast. This results in less (more) rainfall in HK. These circulation anomalies are associated with pronounced Rossby wave trains propagating from the Urals to East Asia (**Figure 5B**). One of the wave trains propagates toward the positive height anomalies over the high latitudes of Asia, where the wave train is split into two branches. One branch propagates southeastward toward the North Pacific, and the other branch propagates southward to East Asia via the Tibetan Plateau. Therefore, the HK summer rainfall anomalies in negative Niño-3.4 years are strongly influenced by large-scale forcing over the Urals.

Comparatively, the 500-hPa height regression pattern associated with HK summer rainfall in negative Niño-3.4 years (**Figure 4B**) strongly resembles the regression pattern associated with HK summer rainfall in all years (**Figure 1B**), including negative height anomalies over the Ural-Siberian region and positive height anomalies over the high latitudes of northern Asia. This is expected because of the much stronger linear correlation between the UHI and HK rainfall in negative Niño-3.4 years. However, the positive regressed height anomalies over northeastern China are captured only by positive Niño-3.4 years (**Figure 4A**); in negative Niño-3.4 years the positive regressed height anomalies are located at a higher latitude (**Figure 4B**). Corresponding to a distinct regressed height pattern, the upper-tropospheric zonal wind anomalies associated with HK rainfall in the two ENSO phases are different. Whereas the upper-tropospheric jet stream shifts meridionally over the midlatitudes of East Asia during positive Niño-3.4 years (**Figure 4A**), it shifts meridionally with a center over South China during negative Niño-3.4 years (**Figure 4B**). Apparently, the anomalies of HK summer rainfall in the two ENSO phases have different dynamics.

Besides the difference in large-scale circulations, the South China circulation anomalies associated with HK summer rainfall in the two ENSO phases are different (**Figure 6**). During positive Niño-3.4 years, strong lower-level convergence associated with enhanced HK summer rainfall is concentrated over southern China (**Figure 6A**). The associated southwesterlies extends from the Indian Ocean to the South China Sea, where the southwesterlies become more strengthened and zonally oriented, indicating a strong lower-level westerly jet. The corresponding upper-tropospheric jet stream is located northeast of the lower-tropospheric westerly jet stream, which extends zonally along 20°N from the Indochina Peninsula to the western North Pacific. The South China coast is located at the gap between the upper-tropospheric and lower-tropospheric jet streams, i.e., south of the upper-tropospheric jet and north of the lower-tropospheric jet. Correspondingly, this region has anticyclonic vorticity anomalies in the upper troposphere and cyclonic vorticity anomalies in the lower troposphere. These trigger stronger rising motion (shading in **Figure 6A**) and more precipitation over the South China coast. Specifically, the lower-tropospheric westerlies transport more water vapor from the Indian Ocean to the South China Sea. Therefore, HK rainfall anomalies during positive Niño-3.4 years are driven mainly by the local jet–precipitation dynamic processes and water vapor transport from the Indian Ocean.

During negative Niño-3.4 years, The upper-tropospheric zonal wind anomalies over South China are much stronger than their positive Niño-3.4 counterpart (**Figure 6A**), while the lower-tropospheric cyclonic anomalies are weak over the tropical Indo–Pacific Ocean and South China with weaker northerlies from mid-latitudes and enhanced southerlies associated with anticyclonic anomalies east of the Philippines (**Figure 6B**). As mentioned previously, the upper-tropospheric jet stream tends to shift southward associated with HK summer rainfall anomalies in negative Niño-3.4 years. Because the South China coast is located southwest of the maximum zonal wind anomalies (**Figure 6B**), the corresponding anomalous upper-tropospheric divergence ($\delta u/\delta x > 0$) can enhance anomalous rising motion over this region. On the other hand, the anomalous sinking motion over the Philippines is associated with less rainfall. This also accompanies an anomalous anticyclone transporting more water vapor toward the South China coast via the South China Sea. Therefore, the anomalies of HK summer rainfall in negative Niño-3.4 years are a result of the southward shift of a stronger or weaker upper-tropospheric jet stream toward South China and water vapor transport associated with the anomalous Philippine Sea anticyclone.

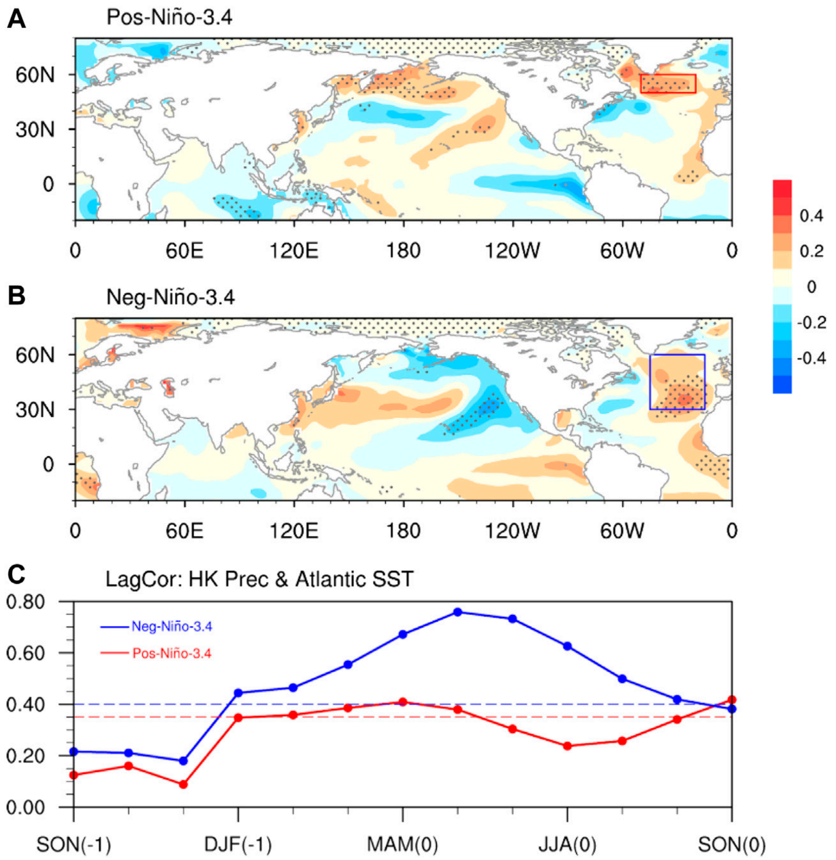

FIGURE 7 | Regression of spring SST (K) onto summer HK Prec for years with **(A)** a positive Niño-3.4 summer and **(B)** a negative Niño-3.4 summer. Stippling indicates the 90% confidence level. **(C)** Lead–lag correlation between HK Prec and seasonal mean SST-Atl-P for positive Niño-3.4 summers **(red)** and seasonal mean SST-Atl for negative Niño-3.4 summers **(blue)**. Dashed lines indicate the 90% confidence level.

ROLE OF SPRING NORTH ATLANTIC SST ANOMALIES

Now that we have identified the large-scale forcing responsible for HK summer rainfall anomalies in the two ENSO phases in Section *Dynamic Mechanisms in Different Summer ENSO Phases*, in this section we would like to further depict the precursory signals that could explain HK summer rainfall anomalies in these phases. As mentioned in Section *Seasonal Forcing of HK Summer Rainfall*, the spring SST-Atl is a potential precursor of HK summer rainfall (**Figure 3A**). However, this relationship is much stronger in negative Niño-3.4 summers (**Figure 7B**) and weaker during positive Niño-3.4 summers (**Figure 7A**). In negative Niño-3.4 years, the correlation between HK summer rainfall and SST-Atl in different months is significant from the preceding winter to the concurrent summer (**Figure 7C**). The above statistical analysis suggests that SST-Atl is a potential seasonal predictor of HK summer rainfall in negative Niño-3.4 years. Conversely, in positive Niño-3.4 years, HK summer rainfall is weakly correlated with SST-Atl because it is not correlated with the midlatitude North Atlantic SST captured by SST-Atl. Instead, HK summer rainfall in positive years is moderately correlated with the subpolar North Atlantic, which can be represented by an index called SST-Atl-P (50°–60°N, 50°–20°W; **Figure 7C**). In the following, we will show how the spring SST-Atl and SST-Atl-P can affect HK summer rainfall in negative Niño-3.4 years and positive Niño-3.4 years, respectively.

Negative ENSO Phase

Warmer spring and summer SST-Atl is associated with above-normal rainfall over South China (**Figures 8A,B**) and below-normal rainfall spreading from the eastern Indochina Peninsula to the western North Pacific. Such a dipole-like rainfall regression pattern resembles the regression pattern against HK summer rainfall (**Figure 5B**). Such a resemblance suggests an impact of the spring SST-Atl on HK summer rainfall. Moreover, the dipole-like rainfall regression pattern is associated with an anomalous anticyclonic circulation east of the Philippines. The southwesterly winds west of the anticyclonic anomaly convey abundant water vapor from the western North Pacific to South China. The convergence of water vapor over South China can enhance rainfall locally. Therefore, the anomalous Philippine Sea anticyclone is crucial for inducing stronger summer rainfall in HK. This anticyclone appears to be stronger when the warming of SST-Atl persists from spring to summer during negative Niño-3.4 years (**Figure 8B**).

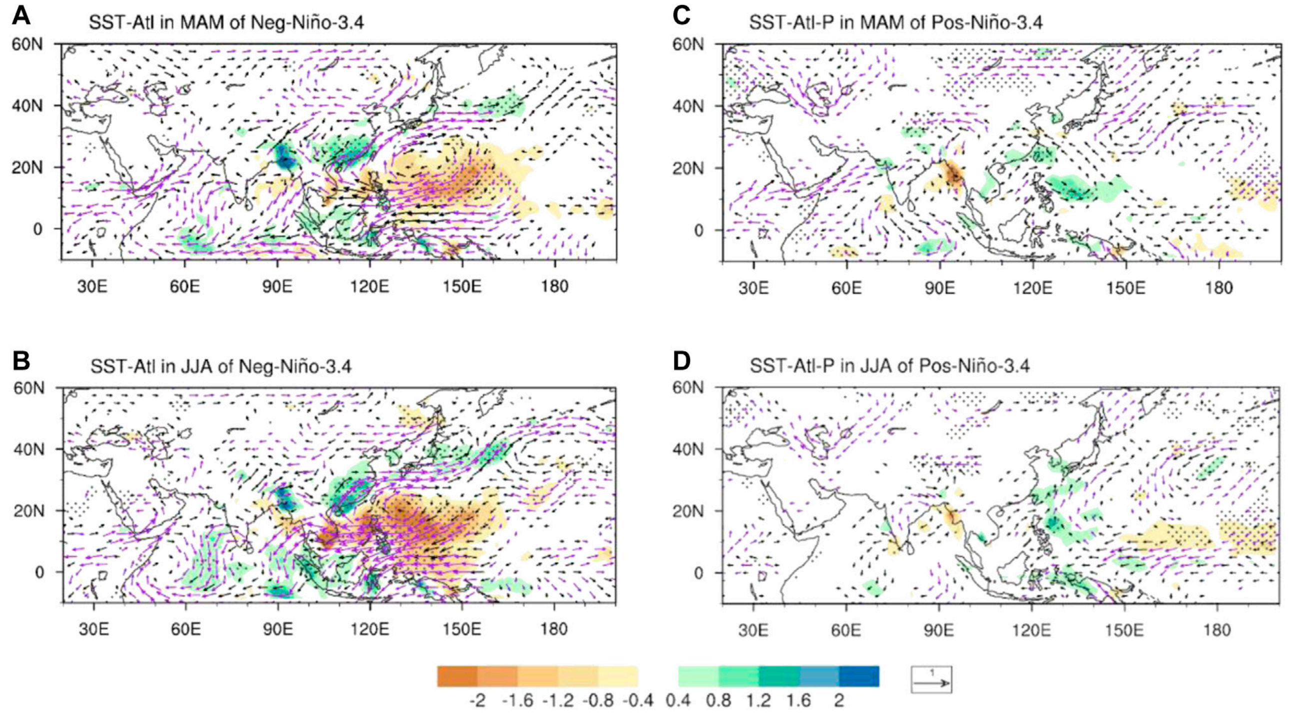

FIGURE 8 | Regression of summer precipitation (shading, mm day^{-1}) and integrated 1,000–300 hPa water vapor fluxes (vectors, kg m^{-1}s^{-1}) in JJA onto **(A,B)** the SST-Atl index in negative Niño-3.4 summers and **(C,D)** the SST-Atl-P index in positive Niño-3.4 summers. **(A,C)** spring and **(B,D)** summer. Stippling and purple vectors are significant at the 90% confidence level.

The time-lagged impact of the spring SST-Atl on the large-scale atmospheric circulation is further investigated in **Figures 9A–D**. In spring, warmer SST-Atl is associated with a "positive north–negative south" dipole anomaly over the North Atlantic (**Figure 9A**), which partly resembles the negative phase of the North Atlantic Oscillation. The dipole anomaly accompanies wave trains propagating eastward from the North Atlantic. The propagation is separated into two pathways over the eastern Atlantic (**Figure 9A**). The first wave train travels at the middle and high latitudes across Europe and the Barents Sea to the Ural Mountains. The second wave train travels across northern Africa to the Middle East. The northern wave train is more closely linked to the negative anomaly centered at 40°N over East Asia. From spring to summer, whereas the dipole anomaly over the North Atlantic associated with SST-Atl weakens and moves eastward, it persistently affects the East Asian circulation via the aforementioned two wave trains, especially the high-latitude wave train (**Figures 9B–D**). This corresponds to the persistence of a negative height anomaly near the Barents Sea and the Ural Mountains. The tropical-midlatitude interactions associated with the Ural height anomaly could explain the influence of SST-Atl on HK summer rainfall.

The summer Ural low (high) anomaly is associated with cyclonic flow (anticyclonic flow) over the southern part of the East Asian continent (figure not shown; can be deduced by **Figures 5B**, **9D**). This is accompanied by subtropical westerly (easterly) wind anomalies over South China. This is also linked to stronger (weaker) western North Pacific subtropical high because South China is located at the northern edge of the western North Pacific subtropical high. Such an influence can also be inferred by the southeastward propagation of the Rossby wave train toward the tropical western Pacific (**Figure 9D**). Accordingly, when SST-Atl is persistently warmer (cooler) from spring to summer during negative Niño-3.4 years, the summer Ural low (high) anomaly strengthens (weakens) the western North Pacific subtropical high. The associated southwesterly wind toward the South China coast (**Figures 8A,B**) enhances (reduces) HK summer rainfall.

In short, the summer in HK is expected to have more rainfall when the warming of SST-Atl persists from spring to summer in negative Niño-3.4 years. The SST-Atl anomaly influences HK summer rainfall via large-scale teleconnection with a center of action near the Ural Mountains.

Positive ENSO Phase

The spring and summer SST-Atl-P is not strongly linked with summer large-scale atmospheric circulation (**Figures 8C,D**). Although the spring SST-Atl-P is moderately correlated with HK summer rainfall (**Figure 7C**), it is only weakly correlated with rainfall over South China (**Figure 8C**). Moreover, warmer spring SST-Atl-P is associated with slightly above-normal rainfall east of the Philippine Sea and a weak cyclonic flow over the western North Pacific and the South China Sea (**Figure 8C**). This suggests that the spring North Atlantic SST in positive Niño-3.4 years does not modulate HK summer rainfall via enhancing water vapor transport associated with the Philippine Sea anticyclone.

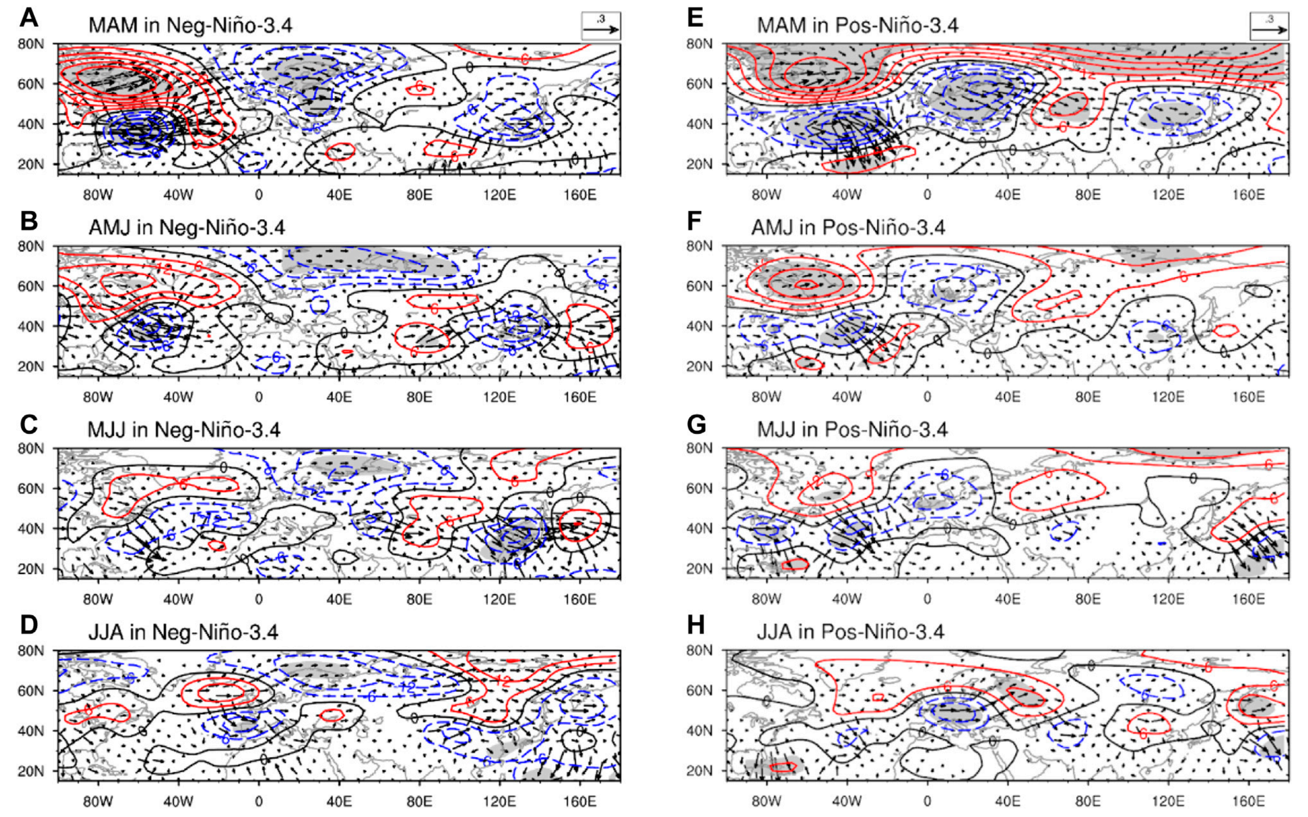

FIGURE 9 | Regression of spring to summer 200-hPa geopotential height (contours, m) and wave activity fluxes (arrows, m^2/s^2) onto **(left)** SST-Atl in negative Niño-3.4 summers and **(right)** SST-Atl-P in positive Niño-3.4 summers. Shading indicates the 90% confidence level. All variables are detrended during 1979–2019.

Indeed, the positive HK summer rainfall anomaly in positive Niño-3.4 years is associated with a remarkable high anomaly over northeastern China, a weak high anomaly over Scandinavia, and a weak low anomaly over central Europe (**Figure 4A**). To further depict how much the spring SST-Atl-P modulates the aforementioned large-scale circulation anomalies, the spring SST-Atl-P is regressed onto the spring-to-summer 200-hPa height and wave activity fluxes (**Figures 9E–H**). During spring, the large-scale circulation features associated with warmer SST-Atl-P during positive Niño-3.4 years (**Figure 9E**) is similar to those associated with warmer SST-Atl during negative Niño-3.4 years (**Figure 9A**). These features include a dipole-like anomaly over the North Atlantic and a midlatitude wave train across Eurasia (**Figure 9E**). The wave train in positive Niño-3.4 years (**Figure 9E**) is even stronger than its counterpart (**Figure 9A**), with pronounced centers of action over northeastern Europe (~30˚E), the Urals (~70˚E), and northeastern China (~120˚E). However, the low anomaly over northeastern China substantially weakens from spring to early summer (**Figures 9E–G**), and its sign is reversed in summer (**Figure 9H**). This is different from the progressive southward migration of the low anomaly over East Asia during negative Niño-3.4 years (**Figures 9A–C**). Meanwhile, the low anomaly over Europe moves southwestward from northeastern Europe in spring to central Europe in summer (**Figures 9E–H**), which accompanies a westward shift of the high anomaly over the Urals. The associated wave activity fluxes propagate southeastward from the Urals to East Asia via South Asia (**Figure 9H**). This partly explains the high anomaly over northeastern China associated with the HK summer rainfall anomaly (**Figure 5A**).

Therefore, the spring SST anomaly over the North Atlantic cannot well explain the HK summer rainfall anomaly during positive Niño-3.4 years. Besides the SST signal, it is noticeable that warmer SST-Atl-P in positive Niño-3.4 years is accompanied by positive height anomalies over the Arctic in spring (**Figure 9E**). This is related to weakening of the stratospheric polar vortex associated with a warmer North Atlantic. We found that HK summer rainfall is also significantly correlated with the 10-hPa geopotential height over the North Pacific in the preceding winter. However, the stratospheric signal also cannot well explain the large-scale circulation anomalies associated with the HK summer rainfall anomaly (figures not shown).

SUMMARY AND DISCUSSION

Although HK is located adjacent to the South China Sea, the interannual variation of HK summer rainfall during the period

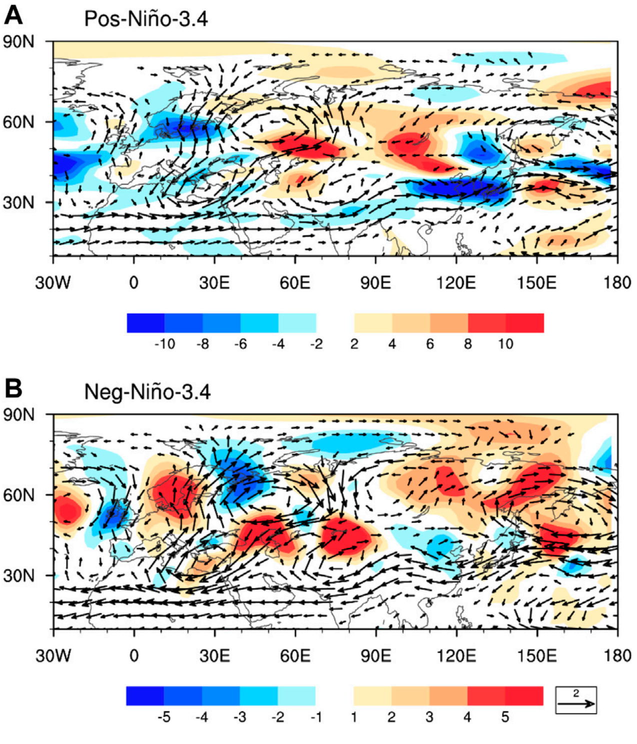

FIGURE 10 | Composite of the 200-hPa wind anomalies (arrows) in **(A)** positive and **(B)** negative Niño 3.4 summers (June-July-August). Difference in the interannual variance of the **(A)** 200-hPa zonal wind (shading) and **(B)** meridional wind (shading) between negative and positive Niño 3.4 summers (negative minus positive). Note that the scale of shading in **(A)** is two times that in **(B)**. Unit: m/s.

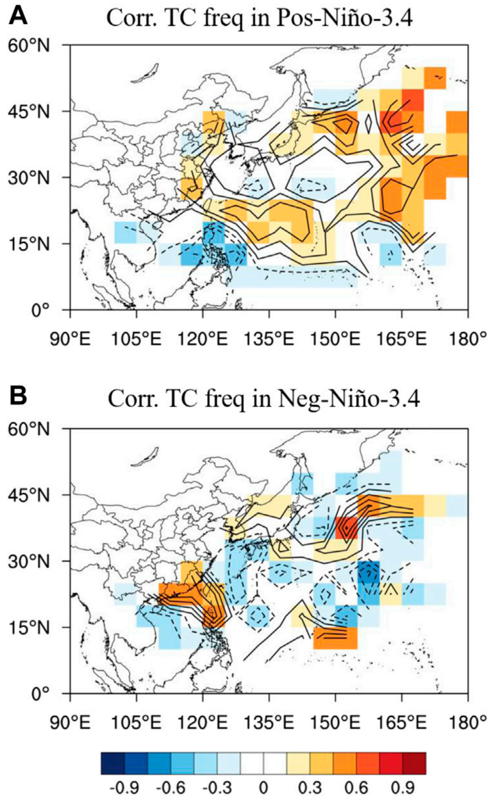

FIGURE 11 | Correlation between summer HK Prec and tropical cyclone track density in **(A)** positive Niño-3.4 summers and **(B)** negative Niño-3.4 summers. Tropical cyclone tracks were obtained from the Joint Typhoon Warning Center (https://www.metoc.navy.mil/jtwc/jtwc.html?western-pacific).

1979–2019 is not strongly correlated with tropical forcing, such as the intensity of the western North Pacific subtropical high and ENSO. Instead, HK summer rainfall is significantly correlated with summer circulation anomalies over the Ural–Siberian region (50°–70°N, 45°–90°E). Therefore, from a forecasting perspective, HK summer rainfall cannot be well predicted by the ENSO signal, which is an important precursor of East Asian summer monsoon intensity on interannual timescales. We have shown that the spring SST-Atl (North Atlantic SST) is a potential seasonal predictor for HK summer rainfall, where warmer spring North Atlantic SST tends to be followed by negative Ural height anomalies in summer and more HK summer rainfall. It should be noted that the relationship among SST-Atl, the summer Ural circulation, and HK summer rainfall is strong during negative Niño-3.4 summers and weak during positive Niño-3.4 summers.

In negative Niño-3.4 summers, HK summer rainfall is robustly correlated with SST-Atl from the preceding winter to the concurrent autumn. The persistent warming of SST-Atl from spring to summer is associated with a dipole-like pattern over the North Atlantic, where an anomalous high is located at high latitudes. This is associated with a Rossby wave train emanating from the North Atlantic and propagating to East Asia across the middle and high latitudes of Eurasia. Specifically, a low anomaly is located over the Barents Sea and a high anomaly is located over the high latitudes of Asia. This is associated with a southeastward propagation of a Rossby wavetrain toward subtropical East Asia and the tropical Pacific. This accompanies a stronger upper-tropospheric westerly jet shifting southward toward South China and a stronger Philippine Sea anticyclone. The latter enhances water vapor transport toward South China and contributes to more rainfall in HK. Hence, the HK summer rainfall anomaly in negative Niño-3.4 summers is associated with strong tropical–midlatitude interactions.

In positive Niño-3.4 summers, on the other hand, HK summer rainfall is moderately correlated with the spring North Atlantic SST over the subpolar region (SST-Atl-P). However, the significant correlation between HK summer rainfall and SST-Atl-P does not persist in other months. The spring SST-Atl-P is associated with a pronounced Rossby wave train across the middle and high latitudes of Eurasia in spring, but this wave train weakens substantially in early summer. The spring SST-Atl-P is associated with a Rossby wave train propagating southeastward from eastern Europe to East Asia via South Asia in summer. This partly explains the high anomaly over northeastern China. Indeed, HK summer rainfall in positive Niño-3.4 summers is associated with southward propagation of wave activity fluxes from midlatitude East Asia to South

China, which accompanies pronounced height anomalies confined to northeastern Asia. The rainfall anomaly in HK is largely modulated mainly by anomalies in westerly jets. This is related to enhanced upper-tropospheric and lower-tropospheric jet streams in subtropical Asia, where the lower-tropospheric wind anomaly is located south of the upper-tropospheric wind anomaly. The stronger westerly winds enhance the rising motion over HK and bring more water vapor from the Indian Ocean and Bay of Bengal to South China. Thus, tropical forcing may also play an important role in triggering rainfall anomalies in positive Niño-3.4 summers.

Why Does ENSO Modulate the Relationship Between the Mid-latitude Eurasian Circulation and HK Summer Rainfall?

We showed that HK summer rainfall is significantly correlated to mid-latitude Eurasian circulation, but it is unclear why this relationship is different in the two phases of ENSO. In order to address this issue, **Figure 10** shows the composite of the 200-hPa circulation anomalies in positive and negative Niño-3.4 summers, as well as the difference in the interannual variance between the two phases. While the wind anomalies in the two phases are opposite in sign, the magnitudes of these anomalies in negative Niño 3.4 cases are generally stronger than the positive cases, including the anomalies over the Ural Mountains, the East Asian jet region, and the northwestern Pacific. In the negative Niño 3.4 summers, the weaker subtropical jet over Eurasia is associated with a stronger interannual variation of wind over the midlatitude Eurasia. This can be depicted by stronger interannual variances of zonal wind south of the Ural Mountains and south of Lake Baikal (shading in **Figure 10A**), and stronger interannual variances of meridional wind over Scandinavia, central Asia and northeastern Asia (shading in **Figure 10B**). In other words, the weaker subtropical jet in the negative Niño 3.4 summers may favor a stronger impact of the midlatitude circulation on the East Asian circulation related to the HK summer rainfall.

Does Tropical Cyclone Activity Affect HK Summer Rainfall in the Two ENSO Phases?

As mentioned in the introduction, tropical cyclone (TC) activity is one of the factors contributing to HK summer rainfall. We have also correlated HK summer rainfall with summer TC track density in positive Niño-3.4 summers and negative Niño-3.4 summers separately. As shown in **Figure 11A**, more HK summer rainfall in positive Niño-3.4 summers is associated with fewer TCs over the Philippines and slightly more TCs passing across Taiwan and Fujian Province in southeastern China. However, it is not related to the TC track density along the South China coast. Conversely, more HK summer rainfall in negative Niño-3.4 summers is associated with more TCs making landfall over the South China coast (**Figure 11B**). Therefore, the HK summer rainfall anomaly in negative Niño-3.4 summers is also related to TC activity, while that in positive Niño-3.4 summers is not.

Overall, our results suggest that HK summer rainfall anomalies during the period 1979–2019 can be better predicted by the spring North Atlantic SST anomaly during negative Niño-3.4 summers. We also reveal a strong linkage between HK summer rainfall and circulation anomalies over the Urals and northeastern China in negative and positive Niño-3.4 summers. Because the persistence of height anomalies over these regions is related to the occurrence of Ural blocking and Okhotsk blocking, it is important to investigate the impact of blocking on rainfall in South China under different ENSO backgrounds in future.

DATA AVAILABILITY STATEMENT

The original contributions presented in the study are included in the article/Supplementary Material, further inquiries can be directed to the corresponding author.

AUTHOR CONTRIBUTIONS

Conceptualization: H-NC; methodology, and formal analysis: YL, and H-NC; original draft of the manuscript: YL; review and editing of the manuscript: H-NC, and WZ; validation: YL, H-NC, and WZ.

FUNDING

HNC is supported by the National Natural Science Foundation of China (Grant No. 42088101, 41905050), and Guangdong Province Key Laboratory for Climate Change and Natural Disaster Studies (Grant No. 2020B1212060025). ZW is supported by the Center for Ocean Research in Hong Kong and Macau (CORE).

REFERENCES

Chan, J. C. L., and Shi, J.-E. (1999). Prediction of the summer monsoon rainfall over South China. *Int. J. Climatol.* 19, 1255–1265. doi:10.1002/(sici)1097-0088(199909)19:11<1255::aid-joc430>3.0.co;2-k

Chan, J. C. L., and Zhou, W. (2005). PDO, ENSO and the early summer monsoon rainfall over south China. *Geophys. Res. Lett.* 32, L08810. doi:10.1029/2004GL022015

Chang, C.-P., Zhang, Y., and Li, T. (2000). Interannual and interdecadal variations of the East Asian summer monsoon and tropical Pacific SSTs. Part I: roles of the subtropical ridge. *J. Climate.* 13, 4310–4325. doi:10.1175/1520-0442(2000)013<4310:iaivot>2.0.co;2

Chang, W. L., and Yeung, K. H. (2003). Seasonal forecasting for Hong Kong-a pilot study. Hong Kong Observatory, Technical Paper 104.

Chen, J., Wen, Z., Wu, R., Wang, X., He, C., and Chen, Z. (2017). An interdecadal change in the intensity of interannual variability in summer rainfall over southern China around early 1990s. *Clim. Dyn.* 48, 191–207. doi:10.1007/s00382-016-3069-8

Chen, W., Feng, J., and Wu, R. (2013). Roles of ENSO and PDO in the link of the East Asian winter monsoon to the following summer monsoon. *J. Climate.* 26, 622–635. doi:10.1175/jcli-d-12-00021.1

Chen, W., Graf, H.-F., and Huang, R. (2000). The interannual variability of East Asian winter monsoon and its relation to the summer monsoon. *Adv. Atmos. Sci.* 17, 48–60. doi:10.1007/s00376-000-0042-5

Chen, Y., and Zhai, P. (2014). Two types of typical circulation pattern for persistent extreme precipitation in Central-Eastern China. *Q.J.R. Meteorol. Soc.* 140, 1467–1478. doi:10.1002/qj.2231

Dai, L., Cheng, T. F., and Lu, M. (2020). Summer monsoon rainfall patterns and predictability over southeast China. *Water Resour. Res.* 56, e2019WR025515. doi:10.1029/2019WR025515

Ding, Y., and Chan, J. C. L. (2005). The East Asian summer monsoon: an overview. *Meteorol. Atmos. Phys.* 89, 117–142. doi:10.1007/s00703-005-0125-z

Ding, Y. H., and Li, C. Y. (1999). *Onset and evolution of the South China Sea monsoon and its interaction with the ocean*. Beijing, China: China Meteorological Press, 423.

Fan, K., Xu, Z., and Tian, B. (2014). Has the intensity of the interannual variability in summer rainfall over South China remarkably increased?. *Meteorol. Atmos. Phys.* 124, 23–32. doi:10.1007/s00703-013-0301-5

Fan, Y., Fan, K., Xu, Z., and Li, S. (2018). ENSO-South China Sea summer monsoon interaction modulated by the Atlantic Multidecadal Oscillation. *J. Climate* 31, 3061–3076. doi:10.1175/JCLI-D-17-0448.1

Gong, D.-Y., and Ho, C.-H. (2003). Arctic oscillation signals in the East Asian summer monsoon. *J. Geophys. Res.* 108, 4066. doi:10.1029/2002JD002193

He, H., McGinnis, J., Song, Z., and Yanai, M. (1987). Onset of the asian monsoon in 1979 and the effect of the Tibetan plateau. *Mon. Wea. Rev.* 115, 1966–1995. doi:10.1175/1520-0493(1987)115<1966:ootasm>2.0.co;2

He, Z., and Wu, R. (2014). Indo-Pacific remote forcing in summer rainfall variability over the South China Sea. *Clim. Dyn.* 42, 2323–2337. doi:10.1007/s00382-014-2123-7

Huang, R., and Wu, Y. (1989). The influence of ENSO on the summer climate change in China and its mechanism. *Adv. Atmos. Sci.* 6, 21–32. doi:10.1007/BF02656915

Huang, W. R., and Chen, K. C. (2015). Trends in pre-summer frontal and diurnal rainfall activities during 1982-2012 over Taiwan and Southeast China: characteristics and possible causes. *Int. J. Climatol* 35, 2608–2619. doi:10.1002/joc.4159

Jiang, N., and Zhu, C. (2021). Seasonal forecast of south China sea summer monsoon onset disturbed by cold tongue La Niña in the past decade. *Adv. Atmos. Sci.* 38, 147–155. doi:10.1007/s00376-020-0090-y

Kajikawa, Y., and Wang, B. (2012). Interdecadal change of the South China Sea summer monsoon onset. *J. Climate* 25, 3207–3218. doi:10.1175/JCLI-D-11-00207.1

Kim, S., and Ha, K.-J. (2021). Interannual and decadal covariabilities in East Asian and western North Pacific summer rainfall for 1979–2016. *Clim. Dyn.* 56, 1017–1033. doi:10.1007/s00382-020-05517-7

Lau, K.-M., Kim, K.-M., and Yang, S. (2000). Dynamical and boundary forcing characteristics of regional components of the Asian summer monsoon. *J. Climate* 13, 2461–2482. doi:10.1175/1520-0442(2000)013<2461:dabfco>2.0.co;2

Lee, J.-Y., Wang, B., Ding, Q., Ha, K.-J., Ahn, J.-B., Kumar, A., et al. (2011). How predictable is the northern hemisphere summer upper-tropospheric circulation?. *Clim. Dyn.* 37, 1189–1203. doi:10.1007/s00382-010-0909-9

Leung, Y. K., Yeung, K. H., Ginn, E. W. L., and Leung, W. M. (2004). Climate change in Hong Kong. Hong Kong Observatory, Technical Paper 107.

Li, J., Zheng, F., Sun, C., Feng, J., and Wang, J. (2019a). Pathways of influence of the Northern Hemisphere mid-high latitudes on East Asian climate: a review. *Adv. Atmos. Sci.* 36, 902–921. doi:10.1007/s00376-019-8236-5

Li, Y., Yang, S., Deng, Y., and Zheng, B. (2020b). Signals of spring thermal contrast related to the interannual variations in the onset of the South China Sea summer monsoon. *J. Clim.* 33, 27–38. doi:10.1175/JCLI-D-19-0174.1

Li, R. C. Y., and Zhou, W. (2014). Interdecadal change in South China Sea tropical cyclone frequency in association with zonal sea surface temperature gradient. *J. Clim.* 27, 5468–5480. doi:10.1175/jcli-d-13-00744.1

Li, R. C. Y., Zhou, W., and Lee, T. C. (2015). Climatological characteristics and observed trends of tropical cyclone-induced rainfall and their influences on long-term rainfall variations in Hong Kong. *Mon. Wea. Rev.* 143, 2192–2206. doi:10.1175/MWR-D-14-00332.1

Li, S., Ji, L., Lin, W., and Ni, Y. (2001). The maintenance of the blocking over the ural mountains during the second meiyu period in the summer of 1998. *Adv. Atmos. Sci.* 18, 87–105. doi:10.1007/s00376-001-0006-4

Li, X., Zhou, W., Chen, D., Li, C., and Song, J. (2014). Water vapor transport and moisture budget over eastern China: remote forcing from the two types of El Niño. *J. Clim.* 27, 8778–8792. doi:10.1175/jcli-d-14-00049.1

Li, X., Zhou, W., Li, C., and Song, J. (2013). Comparison of the annual cycles of moisture supply over southwest and southeast China. *J. Clim.* 26, 10139–10158. doi:10.1175/JCLI-D-13-00057.1

Lin, A., Gu, D., Li, C., Zheng, B., and Liang, J. (2010). Relationship between the onset of the South China Sea summer monsoon and abnormal variations of frontal precipitation during the first rainy period in South China. *Acta Sci. Nat. Univ. Sunyatseni.* 49 (5), 136–143. [in Chinese].

Lin, Z. (2014). Intercomparison of the impacts of four summer teleconnections over Eurasia on East Asian rainfall. *Adv. Atmos. Sci.* 31, 1366–1376. doi:10.1007/s00376-014-3171-y

Liu, B., Yan, Y., Zhu, C., Ma, S., and Li, J. (2020). Record-breaking Meiyu rainfall around the Yangtze River in 2020 regulated by the subseasonal phase transition of the north atlantic oscillation. *Geophys. Res. Lett.* 47. e2020GL090342, doi:10.1029/2020GL090342

Liu, B., Zhu, C., Su, J., Ma, S., and Xu, K. (2019). Record-breaking northward shift of the western North Pacific subtropical high in July 2018. *J. Meteor. Soc. Japan.* 97, 913–925. doi:10.2151/jmsj.2019-047

Liu, B., Zhu, C., Yuan, Y., and Xu, K. (2016). Two types of interannual variability of South China Sea summer monsoon onset related to the SST anomalies before and after 1993/94. *J. Clim.* 29, 6957–6971. doi:10.1175/JCLI-D-16-0065.1

Liu, K. S., and Chan, J. C. L. (2019). Interdecadal variation of frequencies of tropical cyclones, intense typhoons and their ratio over the western North Pacific. *Int. J. Climatol.* 40, 3954–3970. doi:10.1002/joc.6438

Ninomiya, K., and Shibagaki, Y. (2007). Multi-scale features of the Meiyu-Baiu front and associated precipitation systems. *Jmsj.* 85B, 103–122. doi:10.2151/jmsj.85b.103

Ogi, M., Tachibana, Y., and Yamazaki, K. (2004). The connectivity of the winter North Atlantic oscillation (NAO) and the summer Okhotsk high. *J. Meteor. Soc. Japan.* 82, 905–913. doi:10.2151/jmsj.2004.905

Si, D., and Ding, Y. (2016). Oceanic forcings of the interdecadal variability in East Asian summer rainfall. *J. Clim.* 29, 7633–7649. doi:10.1175/JCLI-D-15-0792.1

Sung, M.-K., Kwon, W.-T., Baek, H.-J., Boo, K.-O., Lim, G.-H., and Kug, J.-S. (2006). A possible impact of the North Atlantic oscillation on the east Asian summer monsoon precipitation. *Geophys. Res. Lett.* 33, L21713. doi:10.1029/2006GL027253

Takaya, K., and Nakamura, H. (2001). A formulation of a phase-independent wave-activity flux for stationary and migratory quasigeostrophic eddies on a zonally varying basic flow. *J. Atmos. Sci.* 58, 608–627. doi:10.1175/1520-0469(2001)058<0608:afoapi>2.0.co;2

Tao, S., and Chen, L. (1987). "A review of recent research on the East Asian summer monsoon in China," in *Monsoon meteorology*. Editors C.-P. Chang and T. N. Krishnamurti (Oxford, United Kigdom: Oxford University Press), 60–92.

Wang, B., Li, J., and He, Q. (2017). Variable and robust East Asian monsoon rainfall response to El Niño over the past 60 years (1957-2016). *Adv. Atmos. Sci.* 34, 1235–1248. doi:10.1007/s00376-017-7016-3

Wang, B., LinHoZhang, Y., and Zhang, M.-M. (2004). Definition of south China sea monsoon onset and commencement of the east Asia summer monsoon*. *J. Clim.* 17, 699–710. doi:10.1175/2932.1

Wang, X., Wang, D., Zhou, W., and Li, C. (2012). Interdecadal modulation of the influence of La Niña events on mei-yu rainfall over the Yangtze River valley. *Adv. Atmos. Sci.* 29, 157–168. doi:10.1007/s00376-011-1021-8

Wang, Y. (1992). Effects of blocking anticyclones in Eurasia in the rainy season (Meiyu/Baiu season). *J. Meteor. Soc. Japan.* 70, 929–951. doi:10.2151/jmsj1965.70.5_929

Wang, Y., and Yasunari, T. (1994). A diagnostic analysis of the wave train propagating from high-latitudes to low-latitudes in early summer. *J. Meteor. Soc. Japan.* 72, 269–279. doi:10.2151/jmsj1965.72.2_269

Wang, Z., Yang, S., Lau, N.-C., and Duan, A. (2018). Teleconnection between summer NAO and East China rainfall variations: a bridge effect of the Tibetan Plateau. *J. Climate* 31, 6433–6444. doi:10.1175/JCLI-D-17-0413.1

Watanabe, M. (2004). Asian jet waveguide and a downstream extension of the North Atlantic Oscillation. *J. Clim.* 17, 4674–4691. doi:10.1175/JCLI-3228.1

Wei, W., Zhang, R., and Wen, M. (2015). Interannual variation of the South Asian high and its relation with Indian and East Asian summer monsoon rainfall. *J. Clim.* 28, 2623–2634. doi:10.1175/JCLI-D-14-00454.1

Wu, G., Duan, A., Liu, Y., Yan, J., Liu, B., Ren, S., et al. (2013). Recent advances in the study on the dynamics of the Asian summer monsoon onset. *Chin. J. Atmos. Sci.* 37, 211–228 [in Chinese]. doi:10.3878/j.issn.1006-9895.2012.12312

Wu, M. C., and Chan, J. C. L. (2005). Observational relationships between summer and winter monsoons over East Asia. Part II: results. *Int. J. Climatol.* 25, 453–468. doi:10.1002/joc.1153

Wu, R., Hu, Z.-Z., and Kirtman, B. P. (2003). Evolution of ENSO-related rainfall anomalies in East Asia. *J. Climate.* 16, 3742–3758. doi:10.1175/1520-0442(2003)016<3742:eoerai>2.0.co;2

Wu, R., Wen, Z., Yang, S., and Li, Y. (2010). An interdecadal change in southern China summer rainfall around 1992/93. *J. Clim.* 23, 2389–2403. doi:10.1175/2009jcli3336.1

Wu, Z., Wang, B., Li, J., and Jin, F.-F. (2009). An empirical seasonal prediction model of the East Asian summer monsoon using ENSO and NAO. *J. Geophys. Res.* 114, D18120. doi:10.1029/2009JD011733

Xing, W., Wang, B., and Yim, S.-Y. (2016). Peak-summer East Asian rainfall predictability and prediction part I: southeast Asia. *Clim. Dyn.* 47, 1–13. doi:10.1007/s00382-014-2385-0

Yim, S.-Y., Wang, B., and Xing, W. (2014). Prediction of early summer rainfall over South China by a physical-empirical model. *Clim. Dyn.* 43, 1883–1891. doi:10.1007/s00382-013-2014-3

Yuan, F., Chen, W., and Zhou, W. (2012). Analysis of the role played by circulation in the persistent precipitation over South China in June 2010. *Adv. Atmos. Sci.* 29, 769–781. doi:10.1007/s00376-012-2018-7

Zhang, R., Sumi, A., and Kimoto, M. (1999). A diagnostic study of the impact of El Niño on the precipitation in China. *Adv. Atmos. Sci.* 16, 229–241. doi:10.1007/bf02973084

Zheng, B., Liang, J., Lin, A., Li, C., and Gu, D. (2006). Frontal rain and summer monsoon rain during pre-rainy season in South China. Part I: determination of the division dates. *Chin. J. Atmos. Sci.* 30, 1207–1216. doi:10.3878/j.issn.1006-9895.2006.06.15

Zhou, W., and Chan, J. C. L. (2007). ENSO and the South China Sea summer monsoon onset. *Int. J. Climatol.* 27, 157–167. doi:10.1002/joc.1380

Zhou, W., Chan, J. C. L., and Li, C. (2005). South China Sea summer monsoon onset in relation to the off-equatorial ITCZ. *Adv. Atmos. Sci.* 22, 665–676. doi:10.1007/BF02918710

Zhu, Z., and Li, T. (2017). Empirical prediction of the onset dates of South China Sea summer monsoon. *Clim. Dyn.* 48, 1633–1645. doi:10.1007/s00382-016-3164-x

Conflict of Interest: The authors declare that the research was conducted in the absence of any commercial or financial relationships that could be construed as a potential conflict of interest.

frontiers in Earth Science

ORIGINAL RESEARCH
published: 10 March 2021
doi: 10.3389/feart.2020.568365

Impacts of Indian Ocean Dipole–Like SST on Rice Yield Anomalies in Jiangsu Province

Jingwei Xu[1,2]*, *Nikolay V. Koldunov*[3]*, *Min Xu*[4]*, *Xiuhua Zhu*[5], *Klaus Fraedrich*[1,2], *Xi Jiang*[1], *Shoupeng Zhu*[1] and *Xiefei Zhi*[1]

[1]Key Laboratory of Meteorological Disaster, Ministry of Education (KLME)/Joint International Research Laboratory of Climate and Environment Change (ILCEC)/Collaborative Innovation Center on Forecast and Evaluation of Meteorological Disasters (CIC-FEMD)/Joint Center for Data Assimilation Research and Applications, Nanjing University of Information Sciences and Technology (NUIST), Nanjing, China, [2]Max Planck Institute for Meteorology, Hamburg, Germany, [3]Alfred Wegener Institute (AWI), Bremerhaven, Germany, [4]Meteorological Bureau of Jiangsu Province, Nanjing, China, [5]Center for Earth System Research and Sustainability, CliSAP, University of Hamburg, Hamburg, Germany

Edited by:
Kyung-Ja Ha,
Pusan National University,
South Korea

Reviewed by:
Bijoy Vengasseril Thampi,
Science Systems and Applications,
Inc., United States
Renguang Wu,
Zhejiang University, China

***Correspondence:**
Jingwei Xu
xu_jw@sina.cn
Nikolay V. Koldunov
koldunovn@gmail.com
Min Xu
amin0506@163.com

Specialty section:
This article was submitted to
Atmospheric Science,
a section of the journal
Frontiers in Earth Science

Received: *01 June 2020*
Accepted: *10 December 2020*
Published: *10 March 2021*

Citation:
Xu J, Koldunov NV, Xu M, Zhu X, Fraedrich K, Jiang X, Zhu S and Zhi X (2021) Impacts of Indian Ocean Dipole–Like SST on Rice Yield Anomalies in Jiangsu Province. Front. Earth Sci. 8:568365. doi: 10.3389/feart.2020.568365

One of the main water vapor sources of eastern China is the Bay of Bengal, over which the circulation is influenced by the Tropical Indian Ocean Dipole (TIOD). The TIOD has a long-lasting effect on weather patterns, which in turn influence the rice yield and quality in eastern China, such as in Jiangsu Province. To identify the main mechanism involved, we perform a detailed investigation of the connections between the TIOD-like sea surface temperature (SST) and the climatic suitability for growing rice, and the subsequent rice yield anomalies, in Jiangsu Province. In particular, we compare the relationships, and identify the underlying mechanisms, of TIOD SST with suitable sunshine duration, temperature and precipitation during the period of rice culture in the province. Singular Value Decomposition (SVD) results show that the TIOD-like SST has a close correlation with the rice yield anomalies, with a temporal correlation coefficient of 0.43 for 53 years, passing the 99% significance level. Furthermore, in the negative TIOD-like SST years, the background circulation weakens the transport effect of the atmospheric river through which water vapor is transported from the Bay of Bengal to eastern China. This decreased amount of transported water vapor decreases the precipitation and total cloud cover in the province. In turn, this significantly increases the sunshine duration, which plays a key role in rice yield anomalies. The increased sunshine duration and higher temperatures lead to positive rice yield anomalies, and vice versa. Our findings highlight that climatic factors, such as TIOD-like SST, have a far-reaching influence on agricultural production (in this case, rice yield), and thus special attention should be paid to interdisciplinary research in the fields of climate and agriculture.

Keywords: rice yield anomalies, climatic suitability, East Asian summer monsoon, Jangsu, Indian ocean dipole, sea surfce temperature

INTRODUCTION

Weather patterns during periods of crop culture have an influence on crop yield and quality. Climatic factors can tune these weather patterns and thus have a far-reaching effect on crop yield. The most consumed crop in southern China is rice (Xu et al., 2018). It was the first and most widely cultivated crop in Jiangsu Province, and over the past 30 years has had a relatively stable annual planting area of about 2.2 million hectares, accounting for 40% of the province's grain area. Establishing a rice yield forecast method based on climatic factors is therefore critical for agricultural management, food security and food trade policy in this region.

Although rice shows notable adaptability to climate, specific climatic conditions are still required for successful ripening and to ensure a high quality product (Huang et al., 2018). The climate background also has a remarkable influence on agricultural yield (Lobell and Asner, 2003; Xu et al., 2018). There are many methods available to predict rice yields, including statistical meteorological models, rice growth models, and field sampling (Lai et al., 2009; Ju et al., 2010; Guo et al., 2017; Huang et al., 2017; Xu et al., 2018). Among these methods, studies have shown that statistical meteorological models based on climate indices can be effective at predicting crop yield (Lobell and Asner, 2003; Ju et al., 2010; Holzkämper et al., 2013; Iizumi et al., 2014; Yuan et al., 2014; Guo et al., 2017; Huang et al., 2017; Huang et al., 2018).

Recent studies have shown that the Indian monsoon shows strong correlation with the southern trough over the Bay of Bengal (Guan and Yamagata, 2003), which controls the amount of total precipitable water transported to eastern China. Greater total precipitable water transport from the Indian monsoon is usually associated with a weaker western Pacific subtropical high in the southwestern part of this subtropical high (Zhang, 2001), which leads to greater westerly wind anomalies instead of dominant southwesterly winds in the southwestern part of this subtropical high. These southwesterly winds would normally transport water vapor to eastern China. Thus, without them, conditions are unfavorable for the transport of water vapor into eastern China, therefore leading to less rainfall over the middle and lower reaches of the Yangtze River valley. Hence, there is a link between the Indian monsoon and weather patterns in eastern China. The Tropical Indian Ocean Dipole (TIOD), a climate index, can represent the circulation over the Indian Ocean, which can influence the transported water vapor and in particular have an effect on the western Pacific subtropical high. However, accounting for the weather patterns in a specific area (i.e., in Jiangsu Province) the target sea surface temperature (SST) area is the TIOD-like SST. The TIOD-like SST can indicate the circulation which affects the temperature and sunshine duration in Jiangsu Province, which are key factors for rice yield.

The extent of the far-reaching influence of the TIOD-like SST on agricultural industry in eastern China is still uncertain. Accordingly, the aim of this study is to clarify the relationship between the TIOD-like SST, climatic suitability and rice yield anomalies. In this paper, we suggest a mechanism by which the background circulation characterized by the climate index can tune the weather patterns, affect the crop-specific climatic suitability and, consequently, the rice yield response. Our approach can improve the ability to forecast rice yield evolution based on climate indices for a particular year or under a given climate scenario. Moreover, this approach can provide a scientific basis for shaping food security warning systems and food trade policy, as well as improve the management of rice cultivation.

To investigate the connection between the TIOD-like SST and rice yield anomalies, we focus on the following topics:

- Establishing whether the TIOD-like SST has a close connection with rice yield anomalies in Jiangsu Province;
- Describing the possible mechanism involved in the influence of the TIOD-like SST on the proposed variables that affect the climatic suitability; and
- Analyzing the link between the climatic suitability and the rice yield anomalies.

The rest of the paper is structured as follows: *Data and Methods* section describes the observational datasets, rice yield data, and the method used to calculate the climatic suitability. In *Results* section we describe the connection between the TIOD-like SST and the rice yield anomalies, the possible mechanism involved in the influence of the TIOD-like SST on the climatic suitability, and the link between the climatic suitability and rice yield anomalies. Discussion and conclusions are presented in *Conclusion and Discussion* section.

DATA AND METHODS

Weather Observations and Rice Yield Data

We used a county-level rice yield dataset for the period 1961–2017 (from the Jiangsu Provincial Bureau of Statistics). The daily observations from 70 weather stations in Jiangsu Province, including 2-m air temperature, sunshine duration and precipitation, provided a high spatial and temporal resolution. These daily observations were used to calculate the daily suitability and then the monthly means, which were used to calculate the climatic suitability during the rice-growing period (June–October) from 1961 to 2017. We also used a dataset called the China Daily Gridded Precipitation dataset, version 5.1 (CN05.1; Wu and Gao, 2013; Xu et al., 2009), which has a spatial resolution of $0.25^{\circ} \times 0.25^{\circ}$.

We also collected data on rice-growth stages in Jiangsu for the 1984–2018 from 19 agrometeorological observation stations, which is the longest set of agrometeorological observation data available in Jiangsu. The observations include the start and end dates of each rice stage in every year: the seedling, regreening, tillering, jointing—boot, heading—flowering, and milking—maturity periods. These observations were used to determine the average rice-growth-stage dates and parameters in the suitability equations, which are the key factors for calculating the climatic suitability.

Reanalysis Data

In order to analyze the transported water vapor in the entire air column, we employed the water vapor flux and total Precipitable

Water (PW). The water vapor flux data were from ERA-Interim: https://apps.ecmwf.int/datasets/data/interim-full-moda/levtype=sfc/. The PW data were taken from the NCEP/DOE AMIP-II Reanalysis (Reanalysis-2): http://www.cpc.ncep.noaa.gov/products/wesley/reanalysis2/. The Total Cloud Cover (TCC) was the vertical integral of high-cloud cover, medium-cloud cover and low-cloud cove. The SST is Hadley Center Global Sea Ice and Sea Surface Temperature (HadISST), (Rayner et al., 2003).

Calculation of Annual Rice Yield Anomalies

We followed the approach of Iizumi et al. (2014) to calculate the annual rice yield anomalies. For a given year, t, and county, c, the percentage yield anomaly deviating from a normal yield, $\overline{Y_{t,c}}$ (defined as the 5-year running mean for the interval $t-2$ to $t+2$) was calculated as follows:

$$Y'_{t,c} = \frac{Y_{t,c} - \overline{Y_{t,c}}}{\overline{Y_{t,c}}} \times 100 \tag{1}$$

where $Y_{t,c}$ denotes the real yield. The calculation of the percentage yield anomaly emphasizes the yield changes caused by short-term, primarily climate-related factors, although demand, prices, technology and other factors may also affect year-to-year variations. Due to the 5-year running window, the first 2 years (1961 and 1962) and last 2 years (2016 and 2017) were not calculated. The values of the percentage yield anomalies are likely to be sensitive to the methods used to calculate normal yield. Among the methods for calculating normal yields (e.g., Kucharik and Ramankutty, 2005; Xu et al., 2018), we used the 5-year running mean method because of its simplicity. Although the yield anomalies are sensitive to the number of years used to calculate normal yield, the results based on different calculation methods are similar.

Precipitation Anomaly Percentage

The precipitation anomaly percentage is calculated as follows: $P'_t = \frac{P_t - \overline{P}}{\overline{P}} \times 100\%$, where $\overline{P}$ is the mean precipitation for the research period in Jiangsu, P_t is the precipitation amount in a particular month, and P'_t is the precipitation anomaly percentage in a particular month.

Climatic Suitability Based on Temperature

Previous studies (Geerts et al., 2006; Läderach et al., 2013; Fraga et al., 2016) have shown that climatic suitability has a close relationship with crop yield. Identification of climatic suitability is therefore an effective way to predict crop yields in a particular year or under a specific climate scenario (Teixeira et al., 2013). Most studies analyze three types of climatic suitability, based on temperature, sunshine duration and precipitation.

Fuzzy mathematics is applied to calculate the temperature response of rice (Cutforth and Shaykewich, 1990). The β-function can reasonably well reflect the nonlinear relationship between crop growth and temperature. The effect of temperature on rice differs above and below the optimum temperature range. The temperature suitability (S_T) ranges between 0 and 1, and is calculated as:

$$S_T = \begin{cases} \dfrac{\left[(T - T_1) \times (T_2 - T)^B\right]}{\left[(T_0 - T_1) \times (T_2 - T_0)^B\right]} & (T_1 < T < T_2) \\ B = \dfrac{T_2 - T_0}{T_0 - T_1} & \\ 0 & (T \leq T_1 \text{ or } T \geq T_2) \end{cases} \tag{2}$$

The parameters in this formula vary in different rice-growth periods based on agrometeorological observations, where B is the temperature-dependent factor, T_0 (°C) is a time-dependent optimum temperature for rice in different growth stages, and T_1 (°C) and T_2 (°C) are the physiological lower and upper temperature limits of rice development, respectively. When $T \leq T_1$ or $T \geq T_2$, the plants stop growing and $S_T = 0$.

Many studies (e.g., Zhao et al., 2003; Lai et al., 2009) have shown that, during the growth process, the daily sunshine duration (Shaw, 1964) has a critical value of 70% of the required sunshine duration. When the sunshine duration exceeds this critical value, the response of the crop to sunlight reaches a suitable state, and the suitability value is one when the crop then reaches a suitable state for its growth; otherwise, the sunshine duration suitability rises with the increasing number of hours of sunshine. The suitability based on sunshine duration (S_S) (Oury, 1965) is calculated as:

$$S_S = \begin{cases} e^{-\left[\frac{S - S_0}{b}\right]^2} & (S < S_0) \\ 1 & (S \geq S_0) \end{cases} \tag{3}$$

As the temperature suitability, the parameters S and S_0 are also obtained from the 30 years of agrometeorological observations in Jiangsu, where S is sunshine duration in hours, S_0 is 70% of the required sunshine duration, which varies with the rice growth stage, and b is an empirical parameter that also varies with the growth stage.

Precipitation is the main source of water and soil moisture for the crop. The degree of rice suitability regarding precipitation is characterized by the ratio of incoming and required water (Doll, 1967). Incoming water is mainly provided by natural precipitation and artificial irrigation. Expenditure of plant water is mainly due to the evapotranspiration during the crop's own physiological and ecological processes. The crop suitability based on precipitation S_p, without considering artificial irrigation, is calculated as (Xu et al., 2018):

$$S_p = \begin{cases} P/P_0 & (P < P_0) \\ P_0/P & (P \geq P_0) \end{cases} \tag{4}$$

As with the temperature and sunshine duration, the parameter P_0 is based on the agrometeorological observations during the period of rice culture. Where this suitability is based on 10 days of precipitation, P_0 is the 10-days physiological water requirement of the crop (unit: mm) and P is the actual 10-days precipitation (unit: mm). It is worth noting that when precipitation is excessive, it will harm the crop. So, in water vapor–enhanced years, the precipitation suitability sometimes decreases.

In a relatively recent review paper, Holzkämper et al. (2013) commented that there have not been many international publications on the topic of climatic suitability, for the key parameters are based on local agrometeorological field observations. The rice growth conditions depend on the local climate conditions and rice type. The climatic suitability estimates are obtained through field experiments and control experiments, but many of the publications relevant to the climate suitability for rice are not often available in English. Although **Eqs 2–4** came from the Chinese literature, climatic suitability is a relatively common methodology for cultivation yield research. There have, for example, been relationships reported between corn yield variance and temperature and precipitation in North America (Lobell and Asner, 2003; Almaraz et al., 2008).

Improvement in Climatic Suitability Model Parameters

Based on the rice growth period in Jiangsu Province (Lai et al., 2009; Xu et al., 2018), we observed the key parameters for the climatic suitability model during the different stages of growth, which were determined by *in-situ* observation (**Table 1**). The crop growth and development parameters and meteorological indicators have been fixed for each growth stage of rice. Therefore, there is a "jump" between two successive stages. In reality, the meteorological conditions over the rice growth areas are continuous. To solve this "jumping" issue, data corresponding to the rice growth and development stages (**Table 1**) were obtained for the most recent 30 years. Then, using polynomial fitting, the temperature parameters and parameter b were fitted to the day of the rice growth in stages from *in-situ* observation (X). Finally, a continuous curve was established, with which the daily optimum temperature and the temperature range in which the rice can grow were calculated. The polynomial fitting equations are as follows:

$$T_0 = 7\times10^{-8}X^4 - 2\times10^{-5}X^3 + 0.0003X^2 + 0.1952X + 18.915 \tag{5}$$

$$T_1 = 3\times10^{-8}X^4 - 7\times10^{-6}X^3 - 0.0009X^2 + 0.2306X + 8.587 \tag{6}$$

$$T_2 = 10^{-5}X^3 - 0.0042X^2 + 0.4026X + 27.768 \tag{7}$$

$$b = 2\times10^{-7}X^3 - 9\times10^{-5}X^2 + 0.0023X + 5.1233 \tag{8}$$

Other Methods

In this paper, most variables and observations have been calculated based on the corresponding climate mean and standard deviation for the period 1963–2015. The relative bias denotes the yearly deviation from the climate mean divided by the standard deviation. This normalized bias indicates not only the sign of the anomaly but also how far the value is from the climate state.

To acquire the possible connections between the climate background and the annual rice yield anomalies, the Singular Value Decomposition (SVD) method (Bretherton et al., 1992) is employed. In addition, the climatic suitability, estimated from weather-station daily observations and agrometeorological observation data, is calculated to quantify the cumulative effects of the climate conditions.

RESULTS

Relationship Between the TIOD-Like SST and Rice Yield Anomalies

In order to obtain the connection between rice yield and the SST in the Indian Ocean, the statistical method of SVD (Bretherton et al., 1992) was employed, which is a powerful method for identifying the dominant coupling modes between two data fields. The leading SVD mode shows the heterogeneous pattern maps, which are the amplitude of variation from SST and rice yield anomalies (**Figure 1a, b**). The time series of the first leading mode (SVD1) shows the temporal evolution of the amplitude and polarity of the characteristic patterns, which indicates that SVD1 describes 70.97% of the variability in total anomalies. This time series of SVD1 illustrates that the SST pattern has a strong temporal relationship with the rice yield anomaly pattern, with a temporal correlation coefficient (TCC) of 0.43, passing the 99% significance level, for the 53-years sample. The TIOD index is defined based on the SST anomaly difference between the western (10°S–10°N, 50–70°E) and southeastern (10°S to the equator, 90–110°E) regions. For the tropical Indian Ocean SST, it is a TIOD-like SST pattern, which shows the key SST areas are in the 30–15°S, in the south of the traditional TIOD SST regions. The rice yield anomaly pattern shows a jigsaw-like distribution, which has been documented in many previous studies (Ju et al., 2010; Guo et al., 2017; Huang et al., 2017; Xu et al., 2018).

To ensure that the obtained SVD patterns are not spurious results, we also performed EOF analysis separately for the two fields, which display the leading EOF structures (not shown here), and are very similar to the leading SVD structures. Considering the relative levels of rice cultivation in Jiangsu Province (**Figure 2**), special attention should be paid to central and southern Jiangsu, since more rice is planted there. This means these areas have a greater weight in the total Jiangsu rice yield anomaly.

The Indian monsoon affects rainfall in the middle and lower reaches of the Yangtze River valley (Zhang, 2001), such as Jiangsu Province, *via* modulation of transported water vapor. Atmospheric circulation can affect the rice yield by influencing rainfall, duration of sunlight hours, and temperature (**Figure 3**) (Lai et al., 2009; Huang et al., 2017; Huang et al., 2018; Xu et al., 2018). We found that the TIOD-like SST has a close relationship with rice yield anomalies, with a TCC of 0.43 in 1963–2015, especially in the periods 1970–1990 and 2002–2012 (**Figure 1C**). This TCC is greater than the TCC of a single suitability with rice anomalies. Furthermore, lots of extreme TIOD-like SST events coincide with the rice yield anomalies.

TABLE 1 | Parameters used to determine the suitability of climatic variables, S_T, S_S, and S_P, during rice growth and development stages, determined by the 19 longest agrometeorological observation datasets available in Jiangsu.

Stages	S_T (daily temperature)				S_P (10 days mean precipitation)	S_S (daily sunshine hours)
	T_1/°C	T_0/°C	T_2/°C	B	P_0/mm	S_0/h
Seedling	10	20	30	5.14	38	9.53
Regreening	15	25	37	5.14	38	9.53
Tillering	17	27	38	5.04	45	9.53
Jointing—boot	18	28	40	4.83	66	8.95
Heading—flowering	20	30	35	4.5	64	8.35
Milking—maturity	15	22	32	4.1	29	7.61

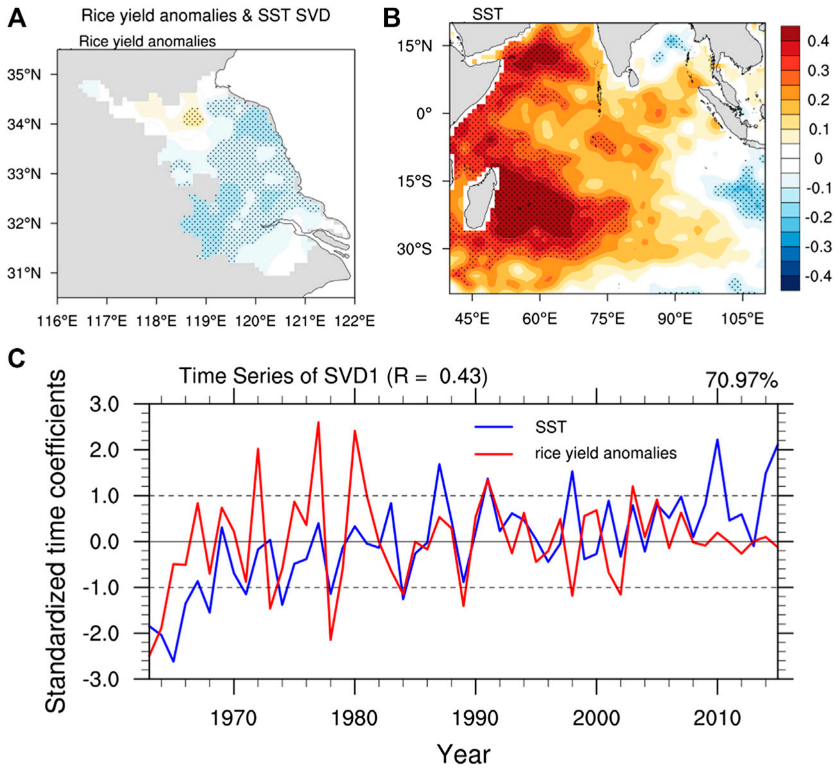

FIGURE 1 | The first leading SVD modes for **(A)** the rice yield anomaly pattern, **(B)** the TIOD-like SST pattern, and **(C)** the expanded time coefficients. The temporal correlation coefficient of rice yield anomalies (red line) and TIOD-like SST (blue line) is 0.43, which is significant at the 0.01% confidence level based on the two-tailed *t*-test. The first leading SVD describes 70.97% of the variability.

Possible Mechanism of Impact of the TIOD-Like SST With the Proposed Variables of Climatic Suitability

To study the possible mechanisms through which the positive TIOD-like SST anomalies lead to negative sunshine duration, we analyze the total PW for the entire atmosphere during the extreme high or low TIOD-like SST years (**Figure 4**). Because reliable reanalysis circulation data are only available for the period after 1979, the composited circulation in the five extremely positive TIOD-like SST years (1987, 1998, 2010, 2014, and 2015) and the five extremely negative TIOD-like SST years (1984, 1989, 1996, 1999, and 2002) are studied. A high positive relationship with the transported water vapor means that, during the positive TIOD-like SST years, the transported water vapor usually increases in Jiangsu Province and vice versa, which passed the 95% level of statistical significance (**Figure 4**).

One of the main sources of total PW transport over eastern China is the southwesterly winds from the Bay of Bengal (Xu et al., 2019b). In positive TIOD years (**Figure 5**), the TIOD has a positive connection with the amount of water vapor transported to China *via* the Bay of Bengal (Guan and Yamagata, 2003; Xu et al., 2019a). When the TIOD is in its positive phase, the total PW

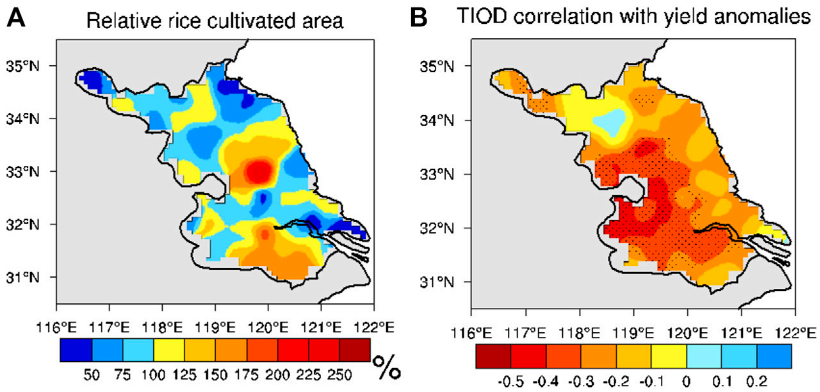

FIGURE 2 | Relative rice cultivation areas **(A)** and the temporal correlation of the TIOD and rice yield anomalies **(B)**. Similar to the relative bias, the value is calculated by the actual area minus the Jiangsu mean of 70 county-level-based rice cultivation areas, and then divided by the standard deviation of the 70 county-level-based rice cultivation areas, as explained in *Improvement in Climatic Suitability Model Parameters* section. Dotted areas in **(B)** are statistically significant at the 95% confidence level in the period 1963–2015.

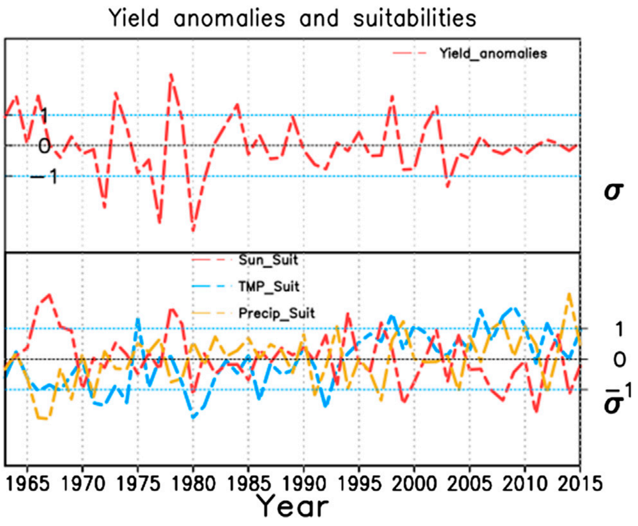

FIGURE 3 | Time series of yield anomalies (upper panel, red line), and the climatic variables S_T (lower panel, blue line), S_S (lower panel, red line) and S_P (lower panel, yellow line).

TABLE 2 | Relative bias of S_T, S_S, S_P and TIOD-like SST from SVD1 during the lifetime of rice (June–October) in the years of extreme rice yield anomalies.

Extreme years	Yield	S_T	S_S	S_P	TIOD like SST
1964	1.6	0.2	0.3	0.2	2.0
1966	1.6	−1.1	1.8	−1.9	1.3
1984	1.3	−0.5	−0.2	0.3	1.2
2002	1.3	0.3	1.0	−0.1	0.5
1978	2.3	0.1	1.7	−0.8	1.1
1998	1.6	1.5	0.3	0.6	−1.5
1972	−2.0	−1.5	−0.3	0.3	1.1
1980	−2.8	−1.9	−1.2	0.6	−0.4
1981	−1.1	−1.5	−0.1	−0.2	−0.2
1977	−2.6	0.0	−0.4	0.7	−0.4
2003	−1.3	0.1	−0.7	0.1	−0.8

is increased almost 50% compared with the standard deviation in the same grid box, which causes an increase in the transported water vapor convergence, TCC, and extremely low sunshine duration (**Figure 6**). Under this weather situation, sunshine duration is reduced over Jiangsu Province. Meanwhile, the precipitation in the rice-growth period is usually excessive in water vapor–enhanced years, which leads to a low precipitation suitability. Therefore, it is not as strong as that with sunshine duration (**Figure 6**). The sunshine duration suitability and precipitation anomaly appear in almost all extreme rice yield years. The spatial correlation coefficient of the sunshine duration suitability pattern and the SVD1 rice yield anomaly pattern is 0.71 in positive TIOD-like SST years and −0.63 in negative TIOD-like SST years, whereas the other two spatial correlation coefficients of suitability are around 0.3.

However, during the negative TIOD-like SST years, the enhanced water vapor flux path disappears in the background circulation in positive TIOD years (**Figure 5**). In these years, relatively dry conditions are shown over the vast area of central and eastern China; the total PW is decreased by about 50% compared with the standard deviation in the grid box, indicating a connection between the TIOD-like SST and precipitation in the lower reaches of the Yangtze River (Zhang, 2001). In these dry conditions, there is relatively less water vapor convergence and precipitation. This reduction in water vapor convergence and TCC lead to an increase in sunshine duration—a key factor in increasing rice yields.

As mentioned above, the TIOD-like SST has a high TCC with sunshine duration and yield anomalies. The TIOD-like SST can indicate the background circulation by itself. In TIOD-like SST negative years, the circulation over Southwest China blocks the transported vertical integral of water vapor from the Bay of Bengal to East China (Guan and Yamagata, 2003). Relatively dry conditions are shown throughout the vast area of China. In

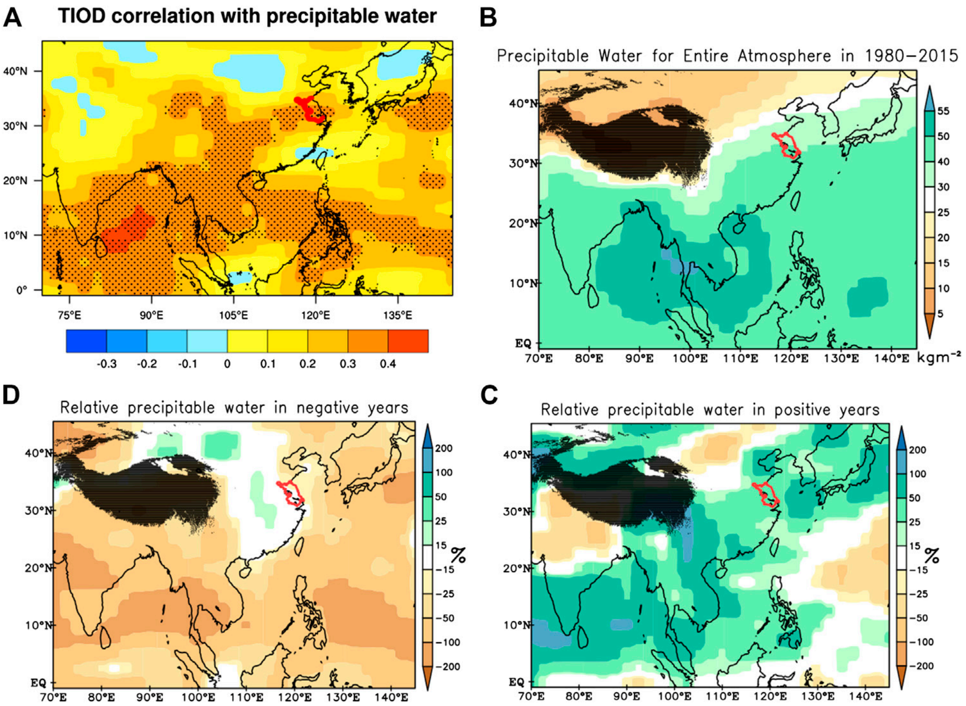

FIGURE 4 | Correlation of TIOD with the amount of precipitable water for the entire atmosphere **(A)** during the rice-growing period (June–October). Dotted areas passed the two-tailed *t*-test at the 95% level of statistical significance. **(B)** The mean precipitable water for the entire atmosphere in 1980–2015, **(C)** precipitable water for the entire atmosphere in positive TIOD years, and **(D)** precipitable water for the entire atmosphere in negative TIOD years. Black shading indicates regions with an elevation exceeding 3,000 m above sea level.

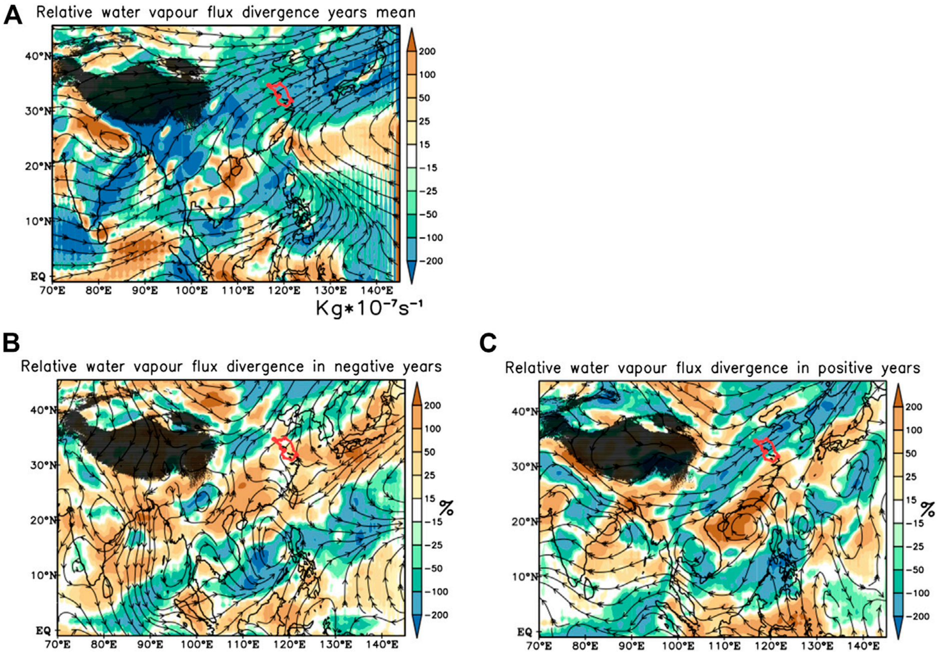

FIGURE 5 | (A) Mean water vapor flux divergence in 1963–2015, **(B)** the relative bias of water vapor flux divergence in positive TIOD-like SST years, and **(C)** negative TIOD-like SST years. Colors indicate the water vapor flux divergence; vectors indicate the water vapor flux.

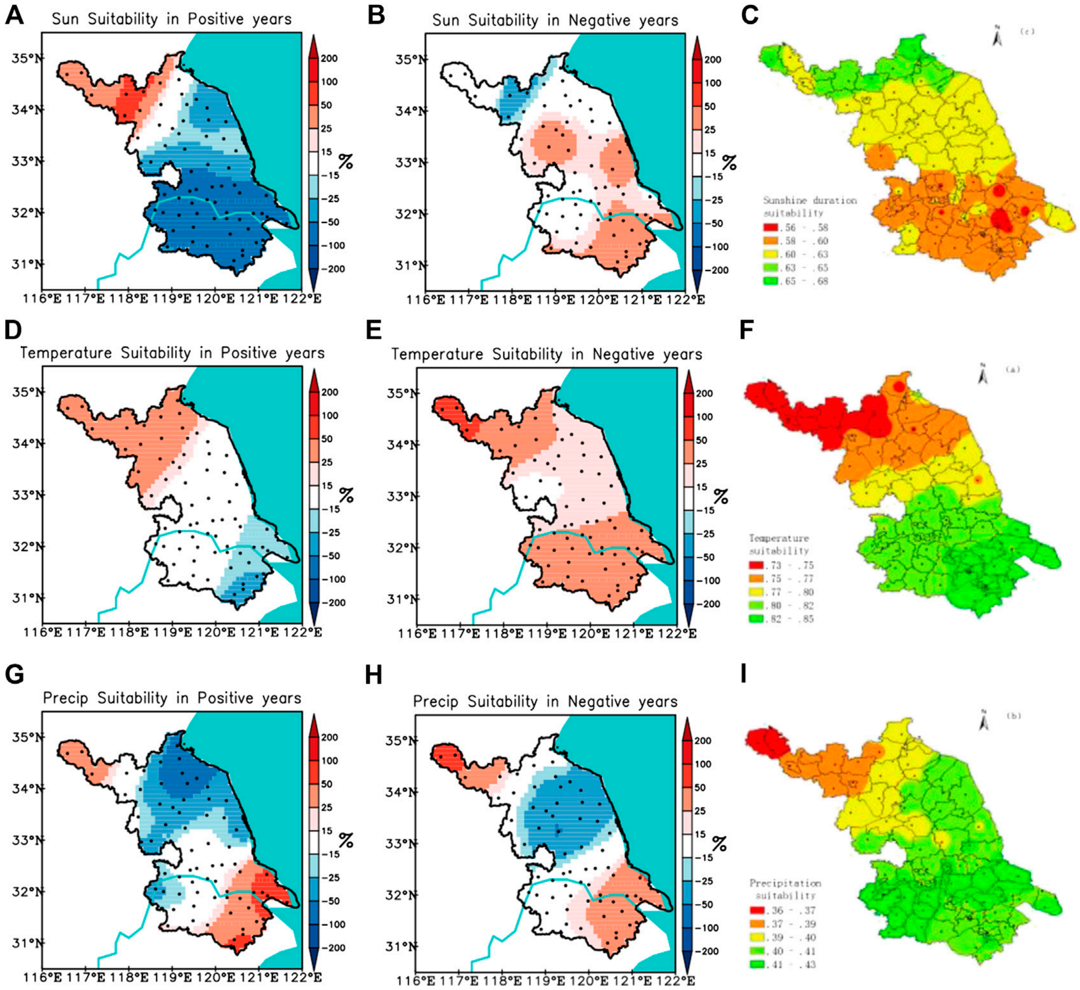

FIGURE 6 | (A) Relative bias of sunshine duration suitability in positive TIOD-like SST years, **(B)** negative TIOD-like SST and **(C)** mean sunshine duration suitability in June–October in 1963–2015 . Panels **(D–F)** are the same as **(A–C)** but for temperature suitability. Panels **(G–I)** are the same as **(A–C)** but for precipitation suitability. The Yangtze River is shown as a blue line and the blue shaded area indicates the sea. Black points indicate the weather observation stations. The sunshine duration suitability pattern has a close relationship with the SVD1 rice yield anomaly pattern, with a spatial correlation coefficient of 0.71 in positive TIOD-like SST years and −0.63 in negative TIOD-like SST years.

these dry conditions, there is probably a low water vapor convergence, TCC, and usually less precipitation. These reductions in TCC and precipitation, however, lead to increases in sunshine duration and sometimes temperature—key factors that improve rice yields. In positive phases of the TIOD, the circulation over Southwest China is suitable for water vapor transport to Jiangsu Province, which causes a greater water vapor convergence, TCC and precipitation, and reduced sunshine duration. The precipitation in Jiangsu is usually exceeds the upper limit of water requirement of rice, leading to a lower precipitation suitability in TIOD-like SST positive years, and the precipitation suitability is nonlinear with the TIOD-like SST.

Connection Between Rice Yield Anomalies and Variables of Climatic Suitability

To explore the cumulative effect of the climate on annual rice yields, we calculated the variables contributing to climatic suitability throughout the rice growth period for the extreme yield anomaly years, based on daily observations (**Table 2**). The correlation coefficients of temperature, sunshine and precipitation suitability to relative meteorological yield during the whole growing period of rice from 1961 to 2014, were 0.12, 0.36, and −0.30, respectively (Xu et al., 2018), which is less than the TCC from the TIOD-like SST with rice yield anomalies.

The sunshine duration suitability pattern has a close relationship with the SVD1 rice yield anomaly pattern, with a spatial correlation coefficient of 0.71 in positive TIOD-like SST years and −0.63 in negative TIOD-like SST years. The spatial correlation coefficient for the temperature suitability pattern is about 0.44 in positive and negative TIOD-like SST years, while for the precipitation suitability pattern it is 0.12 and 0.31 in positive and negative TIOD-like SST years, respectively.

Comparing the three main contributors to climatic suitability in the extremely high rice yield anomaly years, sunshine duration matches the major part of them (**Figure 6**). The extreme sunshine

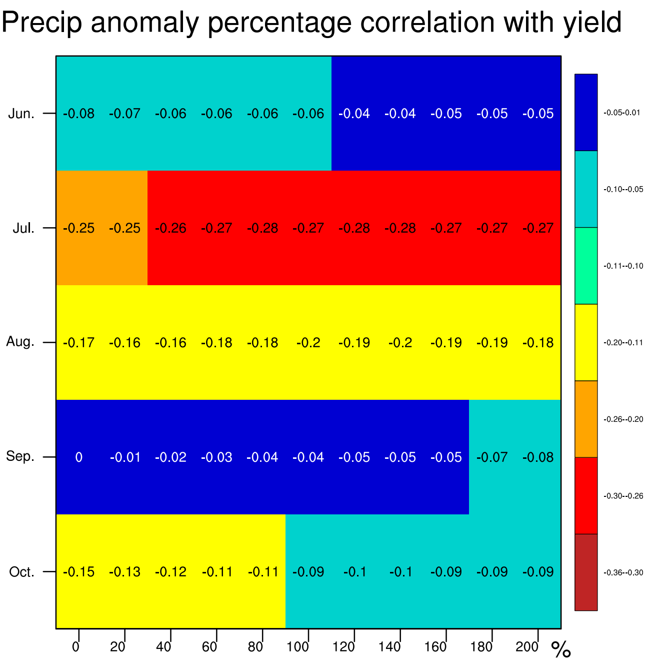

Precip anomaly percentage correlation with yield

	0	20	40	60	80	100	120	140	160	180	200
Jun.	-0.08	-0.07	-0.06	-0.06	-0.06	-0.06	-0.04	-0.04	-0.05	-0.05	-0.05
Jul.	-0.25	-0.25	-0.26	-0.27	-0.28	-0.27	-0.28	-0.28	-0.27	-0.27	-0.27
Aug.	-0.17	-0.16	-0.16	-0.18	-0.18	-0.2	-0.19	-0.2	-0.19	-0.19	-0.18
Sep.	0	-0.01	-0.02	-0.03	-0.04	-0.04	-0.05	-0.05	-0.05	-0.07	-0.08
Oct.	-0.15	-0.13	-0.12	-0.11	-0.11	-0.09	-0.1	-0.1	-0.09	-0.09	-0.09

FIGURE 7 | The yearly precipitation anomaly percentage in June–October, respectively, with yearly rice yield anomalies. Red boxes are statistically significant at the 90% confidence level.

duration suitability events coincide with the greatest rice yield anomalies in Jiangsu Province. Since rice cultivation in Jiangsu Province can use water from other resources, including the Yangtze River, the Huaihe River and even underground water, precipitation is not the only water supply; hence, farm irrigation can reduce the potential damage caused by low rainfall (Xu et al., 2018). For extreme heavy precipitation events, only when the precipitation anomaly exceeds 40% in July can it affect rice yield, which is statistically significant at the 90% confidence level (**Figure 7**). Except in some extreme dry years, the irrigation condition is sufficient for rice cultivation (Xu et al., 2018). Rice yield does not show any great connection with temperature suitability, with a temporal correlation coefficient of 0.12. Among the historical rice-crop disasters in Jiangsu Province between 1949 and 2019, damage was caused by temperature only twice—in the extreme high temperature years of 2003 and 2013 (Huang et al., 2018).

CONCLUSION AND DISCUSSION

The Indian monsoon and East Asian summer monsoon are relatively isolated systems, although recent findings have demonstrated that the Indian monsoon influences rainfall over the middle and lower reaches of the Yangtze River valley, such as in Jiangsu Province in eastern China, *via* its control over the transport of water vapor (Zhang, 2001). In this work, we identified the main connections between the TIOD-like SST and rice yield anomalies in Jiangsu Province. The results show that background circulation anomalies, indicated by the TIOD-like SST, can directly lead to anomalies in transported water vapor over Jiangsu Province. Precipitable water and water vapor flux convergence cause TCC anomalies that lead to sunshine duration and temperature anomalies. Sunshine duration—the variable that is least influenced by human activity in rice cultivation—plays a major part in rice yield anomalies. Although we identify the main mechanism connecting the TIOD-like SST with rice yield anomalies in Jiangsu Province, further detailed simulations with a rice yield model are needed to identify the magnitude of the effect of certain climate indices. Our results can be summarized as follows:

1. The time series of SVD1 describes 70.97% of the variability in total variations. The time series of SVD1 illustrates the SST pattern has a strong temporal relationship with the rice yield anomaly pattern, with a temporal correlation coefficient of 0.43, passing the 99% significance level, for the 53-years sample.
2. The transport of total PW over eastern China can be blocked or enhanced by the circulation in Southwest China, accompanied by TIOD-like SST anomalies (Xu et al., 2019b). On the one hand, in the negative phase of the TIOD, the circulation over Southwest China blocks the transported water vapor and leads to relatively dry conditions over the vast area of eastern China. Under these dry conditions, there is probably a low water vapor flux convergence, TCC, and usually less precipitation. These conditions can lead to increased sunshine duration, which is a key factor in increasing rice yields. On the other hand, in the positive phase of the TIOD-like SST, the circulation over Southwest China is suitable for the transport of water vapor over Jiangsu Province, which causes an increased water vapor convergence, TCC, and precipitation. In turn, this significantly decreases the sunshine duration. Therefore, usually, the negative TIOD-like SST accompanies positive sunshine duration and positive rice yield anomalies, and vice versa.
3. In Jiangsu Province, the most important variable for climatic suitability is sunshine duration. It was found to be a factor in most years that recorded rice yield anomalies, with the greatest spatial correlation coefficients of 0.71 and −0.63, for positive and negative TIOD like years, respectively, with the SVD1 rice anomaly pattern among the three suitabilities. This is because precipitation is not the only water supply for rice cultivation in Jiangsu Province. Moreover, rice can also survive under a wide range of temperatures. It is therefore worth noting that sunshine duration plays a key role in rice yield anomalies in Jiangsu Province.

To sustain a clear focus in this study, we have mainly discussed the impact and mechanism of the TIOD-like SST on rice yield anomalies in Jiangsu Province. The climatic suitability based on observations is so far the closest approach to the actual growth of rice. Since 2010, this climatic suitability method has been used to characterize the quantitative impacts of sunshine, temperature and rainfall on crops growth in Jiangsu Meteorological Bureau. The operational agrometeorological services during these years prove that the climatic suitability method is an effective method to describe the accumulate effect of weather on crops. Nonetheless, irrigation data are not available for every cultivation area in Jiangsu Province. The effect of irrigation on rice yield is thus far still uncertain. Other climatic factors, such as the western Pacific subtropical high, different rice varieties, and human activity (e.g., irrigation or agriculture policy), all have an impact on climatic suitability and rice yield anomalies. The climate has cumulative influences on the various stages of rice growth and development. The primary focus of this work has been the connection between the TIOD-like SST, sunshine duration and rice yield anomalies. This study emphasizes again the connection between the TIOD-like SST and eastern China, which has a far-reaching influence on agricultural industry. Special attention should be paid to climatic circulation and its influence on crop yield. Future work should investigate the relationship between climate factors and climatic suitability for the other major crops in the region (e.g., wheat, maize and soybean).

DATA AVAILABILITY STATEMENT

The datasets generated for this study are available on request to the corresponding author.

AUTHOR CONTRIBUTIONS

JX initiated and coordinated the work. JX and MX provided the calculation and analysis of rice yield anomalies. JX, NK, and MX wrote the manuscript. XZ, KF, and XJ gave valuable suggestions for revisions. SZ and XZ revised the basic flow anomalies analysis.

FUNDING

This work was jointly supported by a project entitled "Relationships between glacier changes and atmospheric circulation in High Mountain Asia," supported by the National Natural Science Foundation of China (Grant Nos. 41871053, 41371095, and 91337218), the China Special Fund for Meteorological Research in the Public Interest (Grant No. GYHY 201406008), project S1 (Diagnosis and Metrics in Climate Models) of the Collaborative Research Centre TRR 181 Energy Transfer in Atmosphere and Ocean program funded by the German Research Foundation (project 274762653). This study was also funded by "the Priority Academic Program Development of Jiangsu Higher Education Institutions" (PAPD).

ACKNOWLEDGMENTS

We thank reviewers for comments and suggestions that helped to improve the manuscript. Also, we thank the ECMWF NCEP and CMA for providing the gridded data. We also thank the Jiangsu Provincial Bureau of Statistics for providing the rice yield data.

REFERENCES

Almaraz, J. J., Mabood, F., Zhou, X., Gregorich, E. G., and Smith, D. L. (2008). Weather variability and corn yield at a higher latitude locale: south-western Quebec. *Clim. Change.* 88 (2), 187–197. doi:10.1007/s10584-008-9408-y

Bretherton, C. S., Smith, C., and Wallace, J. M. (1992). An intercomparison of methods for finding coupled patterns in climate data. *J. Clim.* 5, 541–560. doi:10.1175/1520-0442(1992)005<0541:AIOMFF>2.0.CO;2

Cutforth, H. W., and Shaykewich, C. F. (1990). A temperature response function for corn development. *Agric. For. Meteorol.* 50, 159–171. doi:10.1016/0168-1923(90)90051-7

Doll, J. P. (1967). An analytical technique for estimating weather indexes from meteorological measurements. *J. Farm Econ.* 49, 79–88. doi:10.2307/1237069

Fraga, H., Santos, J. A., Malheiro, A. C., Oliveira, A. A., Moutinho-Pereira, J., and Jones, G. V. (2016). Climatic suitability of portuguese grapevine varieties and climate change adaptation. *Int. J. Climatol.* 36, 1–12. doi:10.1002/joc.4325

Geerts, S., Raes, D., Garcia, M., Del Castillo, C., and Buytaert, W. (2006). Agro-climatic suitability mapping for crop production in the Bolivian Altiplano: a case study for quinoa. *Agric. For. Meteorol.* 139, 399–412. doi:10.1016/j.agrformet.2006.08.018

Guan, Z., and Yamagata, T. (2003). The unusual summer of 1994 in East Asia: IOD teleconnections. *Geophys. Res. Lett.* 30, 1544. doi:10.1029/2002GL016831

Guo, J., Hu, X., Gao, L., Xie, K., Ling, N., Shen, Q., et al. (2017). The rice production practices of high yield and high nitrogen use efficiency in Jiangsu, China. *Sci. Rep.* 7, 2101. doi:10.1038/s41598-017-02338-3

Holzkämper, A., Calanca, P., and Fuhrer, J. (2013). Identifying climatic limitations to grain maize yield potentials using a suitability evaluation approach. *Agric. For. Meteorol.* 168, 149–159. doi:10.1016/j.agrformet.2012.09.004

Huang, J., Islam, A. R. M. T., Zhang, F., and Hu, Z. (2017). Spatiotemporal analysis the precipitation extremes affecting rice yield in Jiangsu province, southeast China. *Int. J. Biometeorol.* 61, 1863–1872. doi:10.1007/s00484-017-1372-7

Huang, J., Zhang, F., Zhou, L., Hu, Z., and Li, Y. (2018). Regional changes of climate extremes and its effect on rice yield in Jiangsu province, southeast China. *Environ. Earth Sci.* 77, 106. doi:10.1007/s12665-018-7295-8

Iizumi, T., Luo, J., Challinor, A. J., Sakurai, G., Yokozawa, M., Sakuma, H., et al. (2014). Impacts of el niño southern oscillation on the global yields of major crops. *Nat. Commun.* 5, 3712. doi:10.1038/ncomms4712

Ju, W., Gao, P., Zhou, Y., Chen, J. M., Chen, S., and Li, X. (2010). Prediction of summer grain crop yield with a process-based ecosystem model and remote sensing data for the northern area of the Jiangsu Province, China. *Int. J. Rem. Sens.* 31, 1573–1587. doi:10.1080/01431160903475357

Kucharik, C. J., and Ramankutty, N. (2005). Trends and variability in US corn yields over the twentieth century. *Earth Interact.* 9, 1–29. doi:10.1175/EI098.1

Läderach, P., Martinez-Valle, A., Schroth, G., and Castro, N. (2013). Predicting the future climatic suitability for cocoa farming of the world's leading producer countries, Ghana and Côte d'Ivoire. *Clim. Change.* 119, 841–854. doi:10.1007/s10584-013-0774-8

Lai, C., Qian, H., Duan, H., and Song, Q. (2009). Climate suitabiltiy and its change trend of double cropping rice in Huaihe River Basin. *Chin. J. Ecol.* 28, 2339–2346. doi:10.13292/j.1000-4890.2009.0382 [in Chinese].

Lobell, D. B., and Asner, G. P. (2003). Climate and management contributions to recent trends in U.S. agricultural yields. *Science* 299, 1032. doi:10.1126/science.1077838

Oury, B. (1965). Allowing for weather in crop production model building. *Am. J. Agric. Econ.* 47, 270–283. doi:10.2307/1236574

Rayner, N. A., Parker, D. E., Horton, E. B., Folland, C. K., Alexander, L. V., Rowell, D. P., et al. (2003). Global analyses of sea surface temperature, sea ice, and night marine air temperature since the late nineteenth century. *J. Geophys. Res. Atmos* 108, 4407. doi:10.1029/2002JD002670

Shaw, L. H. (1964). The effect of weather on agricultural output: a look at methodology. *Am. J. Agric. Econ.* 46, 218–230. doi:10.2307/1236485

Teixeira, E. I., Fischer, G., Van Velthuizen, H., Walter, C., and Ewert, F. (2013). Global hot-spots of heat stress on agricultural crops due to climate change. *Agric. For. Meteorol.* 170, 206–215. doi:10.1016/j.agrformet.2011.09.002

Wu, J., and Gao, X. (2013). A gridded daily observation dataset over China region and comparison with the other datasets. *Chin. J. Geophys.* 56, 1102–1111.

Xu, J., Koldunov, N., Remedio, A. R. C., Sein, D. V., Zhi, X., Jiang, X., et al. (2019a). On the role of horizontal resolution over the Tibetan Plateau in the REMO regional climate model. *Clim. Dynam.* 51, 4525–4542. doi:10.1007/s00382-018-4085-7

Xu, J., Koldunov, N. V., Remedio, A. R. C., Sein, D. V., Rechid, D., Zhi, X., et al. (2019b). Downstream effect of Hengduan Mountains on East China in the REMO regional climate model. *Theor. Appl. Climatol.* 135, 1641–1658. doi:10.1007/s00704-018-2721-0

Xu, M., Wu, H., Zhang, P., Gao, P., and Xu, J. (2018). Long-term prediction method of rice annual agricultural climate status in Jiangsu Province based on climatic suitability. *Meteorol. Mon.* 44, 1220–1227. doi:10.7519/j.issn.1000-0526.2018.09.008 [in Chinese].

Xu, Y., Gao, X., Shen, Y., Xu, C., Shi, Y., and Giorgi, F. (2009). A daily temperature dataset over China and its application in validating a RCM simulation. *Adv. Atmos. Sci.* 26, 763–772.

Yuan, L., Yang, X., Wang, E., and Xue, C. (2014). Climate and crop yields impacted by ENSO episodes on the North China Plain: 1956–2006. *Reg. Environ. Change.* 14, 49–59. doi:10.1007/s10113-013-0455-1

Zhang, R. (2001). Relations of water vapor transport from Indian monsoon with that over East Asia and the summer rainfall in China. *Adv. Atmos. Sci.* 18, 1005–1017. doi:10.1007/BF03403519

Zhao, F., Qian, H., and Jiao, S. (2003). The climatic suitability model of crop: a case study of winter wheat in Henan Province. [in Chinese]. *Resour. Sci.* 25, 77–82.

Conflict of Interest: The authors declare that the research was conducted in the absence of any commercial or financial relationships that could be construed as a potential conflict of interest.

frontiers
in Earth Science

ORIGINAL RESEARCH
published: 19 March 2021
doi: 10.3389/feart.2021.622889

Changes in Slight and Extreme Precipitation Events From 1963 to 2017 Over Northern Xinjiang, China

Minggang Li, Yong Zhao*, Yang Li, Xin Zhou and Shaobo Zhang

Plateau Atmosphere and Environment Key Laboratory of Sichuan Province, Chengdu University of Information Technology, Chengdu, China

Based on daily measured data from 25 stations in Xinjiang Province from 1963 to 2017, we discuss the statistical characteristics, linear trends, and temporal concentration of slight precipitation (SP) and extreme precipitation (EP) events, and consider relationships between SP and EP events and daily mean temperature. The results show that SP events contribute strongly to the total annual number of wet days, and that EP events contribute strongly to the total annual precipitation amount. In consist with the decrease in SP events and the increase in EP events over the 55-year period, the contribution of SP events to total annual number of wet days has decreased significantly while the contribution of EP events to total annual precipitation amount has increased significantly. SP event usually distributes through most months of the year, whereas EP event usually concentrates in summer (JJA). Influenced by the negative trends for SP events frequency and positive trends of EP events frequency during recent decades, the concentration degree for SP and EP events have significantly increased and decreased, respectively. Distinct differences are found between the relationships of SP events and EP events to daily mean temperature. The daily mean temperature recorded at the stations in Northern Xinjiang on days with SP events was between –35°C and +34°C, and for EP events ranged from –21°C to +30°C. Regionally averaged curves for the change in SP and EP event frequency with temperature have bimodal and unimodal distributions, respectively. Trends for daily mean temperatures and for the frequency of SP events at different temperatures agree well over nearly the entire temperature range, while trends for daily mean temperatures and for the frequency of EP events at different temperatures are not always consistent. These results will help to improve our understanding of the characteristics and variability of precipitation in arid regions within the context of climate warming.

Keywords: slight precipitation, extreme precipitation, Northern Xinjiang, temporal concentration, precipitation response to warming

Edited by:
Lin Wang,
Institute of Atmospheric Physics (CAS), China

Reviewed by:
Xiaojian Zhang,
Nanjing University, China
Xingwen Jiang,
China Meteorological Administration, China
Ruidan Chen,
Sun Yat-sen University, China

****Correspondence:***
Yong Zhao
zhaoy608@cuit.edu.cn

Specialty section:
This article was submitted to Atmospheric Science, a section of the journal Frontiers in Earth Science

Received: *29 October 2020*
Accepted: *24 February 2021*
Published: *19 March 2021*

Citation:
Li M, Zhao Y, Li Y, Zhou X and Zhang S (2021) Changes in Slight and Extreme Precipitation Events From 1963 to 2017 Over Northern Xinjiang, China. Front. Earth Sci. 9:622889. doi: 10.3389/feart.2021.622889

INTRODUCTION

Significant climate responses to global warming have been observed in arid and semi-arid areas. In eastern hemisphere, a drier climate response and dryland expansion existed are in most part of the arid lands, including Central Asia, and Northwest China (Chen et al., 2009; Li et al., 2013; Huang et al., 2016a,b, 2019; Zhang et al., 2020). There was a century-long course of warm and dry over the arid region of Northwest China, until the abrupt climate shift occurred in its west part (particularly in Xinjiang Province) around 1987 (Shi et al., 2002, 2003). As a special phenomenon among the arid lands (Zhang et al., 2010; Li et al., 2015), this warm and humid climate tendency in Xinjiang Province is attached with complex mechanism and enormous impacts on regional climate and ecosystem (Yao et al., 2013; Chen et al., 2016; Zhao et al., 2017). In order to have a better understand of the warm and humid climate change and to counter the extreme climate issues in Xinjiang, such as drought in spring while flood in summer, and the coexistence of drought and flood, many studies for precipitation response to the rising temperature were conducted (Wang et al., 2012, 2013, 2017; Jiang et al., 2013; Deng et al., 2014; Yao et al., 2015). Most of these works emphasized the significant increase in extreme precipitation (EP) events and discussed its potential impacts, but less well understood and insufficient studies have been carried out regarding the slight precipitation (SP) events, a precipitation type that account for large proportions in total annual wet days in Xinjiang province (Fu et al., 2008; Liao et al., 2012) and have large importance in arid lands. Zhang et al. (2012) suggested an increasing risk of both flood and drought are expected with the observed upward trend of concurrent strong and weak precipitation extremes in Tianshan Mountains. These all indicate that a comprehensive investigation of SP and EP events will not only help to better understand the response of precipitation to temperature rise, but also help to better understand the current extreme climate issues in Xinjiang.

For the issue of how the precipitation response to a warming background, researchers have proposed many important theories. Based on the Clausius-Clapeyron relation (C-C relation), Trenberth et al. (2003) suggested that, as the moisture in the air column increases with rising temperature, the intensity of precipitation will increase. While on the other hand, the condition for formulation of precipitation will be more difficult to reach, resulting in a decrease of precipitation frequency, especially for light and moderate precipitation events. Other theories, such as "wet-get-wetter" and "warmer-get-wetter" help to understand why the response of precipitation to the warming background varies from region to region (Held and Soden, 2006; Xie et al., 2010; Huang et al., 2013). For instance, the "wet-get-wetter" theory suggested that, the surface evaporation and moisture in the air column both increase in the context of temperature rising, and the accelerated water cycle may eventually make the dry areas drier and wet areas wetter. Many different precipitation responses to the warming climate have been observed in China over recent decades. In addition to increases or decreases in total annual precipitation, the persistence and phase of precipitation may change, and the proportions of precipitation events in different levels (e.g., small rain, moderate rain, and heavy rain) may be affected (Liu et al., 2005; Qian and Lin, 2005; Huang et al., 2011; Zhai et al., 2017). With the rapid warming in the second half of 20th century, generally, precipitation events with relatively large intensities (e.g., heavy rain, extreme rain) increased and precipitation events with small intensities (e.g., slight rain, small rain) decreased significantly in China (Zhai et al., 2005; Qian et al., 2007; Fu et al., 2008). This is largely in consist with the conclusion in Trenberth et al. (2003). However, there are many dynamic and thermodynamic factors that can bring impacts on precipitation, which makes it complicated to assess the effect of rising temperatures on precipitation in different regions.

Accompanied with the warm and humid climate tendency in Xinjiang Province, apart from the significant upward trends for the frequency of extreme precipitation events, obvious increase in small precipitation events and total number of annual wet days were also observed in both the relatively earlier works (Zhai et al., 2005; Qian et al., 2007; Fu et al., 2008) and those recent ones (Jiang et al., 2013; Wang et al., 2013; Deng et al., 2014; Zhou et al., 2015). Apparently, these changes conflict with the "wet-get-wetter" (dry-get-drier) theory, and cannot be well explained by the conclusion in Trenberth et al. (2003) too. As for SP events, the earlier studies reported opposite results for the trend of SP events in Xinjiang province during the second half of 20th century (e.g., Qian et al., 2007; Xin et al., 2008), while the recent studies on changes of precipitation in Xinjiang Province usually based on the indicators defined by Expert Team for Climate Change Detection Monitoring and Indices (ETCCDMI), which contains no indicator for SP events (Jiang et al., 2013; Wang et al., 2013; Deng et al., 2014; Zhou et al., 2015). Moreover, although there is an expected increase in extreme precipitation with temperature rising, the understanding of the relationship between precipitation and temperature remains insufficient at present. Recently, Utsumi et al. (2011) show that the relationship between extreme daily precipitation and daily mean surface temperature are not monotonous in the midlatitudes, and Xiao et al. (2017) found a piece-wise linear relationship between daily surface temperature and extreme precipitation in Central and Eastern China, and showed that the relationship changed from a positive to a negative relationship at approximately 25°C.

Based on the previous analyses, there are several questions need to be addressed. For examples, during recent few decades, particularly the last two decades, how the SP events changes in Northern Xinjiang? Are changes in SP and EP events reflected in their relative contributions to annual totals, and can these lead to changes in the structure of annual precipitation? Over recent decades, no clear trends have been observed in precipitation concentration in Xinjiang Province (Li et al., 2011), but these have not been broken down and explained in terms of changes to SP and EP events. To what extent can these changes explain the current status of extreme climate issues in Northern Xinjiang? How closely are the changes in precipitation connected to the warming climate in Xinjiang? Specifically, are there any connections between changes in SP and EP events and the rising temperature? To address the questions above, the content of this paper is organized as follows: data and methods are introduced in section 2, trends and characteristics observed for SP and EP events in Northern Xinjiang are described in section 3, and section 4 presents a statistical analysis of SP and EP event concentration. Connections between precipitation distribution and daily mean temperature are discussed in section 5, and section 6 summarizes the paper and presents some discussion and conclusions.

DATA AND METHODS

Data

We used daily precipitation and mean temperature measurements from 25 stations across Northern Xinjiang covering 55 years from 1963 to 2017, which we obtained from the China Meteorological Data Service Center. Prior to analysis, this dataset was pre-processed using a quality control procedure that excluded data from stations where more than 30 days of data were missing over the study period, or where the recorded station position had changed by more than 20 km. Two more stations were removed after quality control because the total number of annual wet days that they recorded was extremely low, which study of EP events show to be statistically unlikely. The topography of Northern Xinjiang and the locations of the 25 stations are shown in **Figure 1A**. The Tianshan and Altai mountains dominate the topography of Northern Xinjiang and are located in the south and north of the region, respectively, with the Junggar Basin between them.

It is also worth noting that the observation of liquid precipitation at Xinjiang stations changed from manual observation to automatic observation in 2007, and the observation of solid precipitation changed in 2012. Although the homogeneity of precipitation data can be affected by factors such as location change or changes in rain gauge type (Jiang et al., 2008; Yang and Li, 2014), no evidence of the influence of automatic observation on the identification of SP has been found so far. However, it is worth considering whether the transition from manual to automatic observations in Xinjiang could be a cause of inhomogeneity in the precipitation data, especially for SP.

Methods

The SP events discussed in this study were wet days (daily precipitation ≥0.1 mm) with precipitation between 0.1 and 0.9 mm, and EP events were defined using a threshold method. Wet days were classified as EP events when the precipitation amount exceeded the 95th percentile threshold. We followed Bonsal et al. (2001) to calculate the 95th percentile threshold. In detail, wet days were identified in the data from each station and all wet days from 1963 to 2017 were arranged in order of ascending precipitation amount for each individual station. The 95th percentile threshold was calculated from the resulting distribution and wet days with a precipitation amount exceeding this threshold were considered to be EP events for that station. See **Table 1** for more details.

The intra-annual frequency distributions for SP and EP events were analyzed by calculating the concentration degree

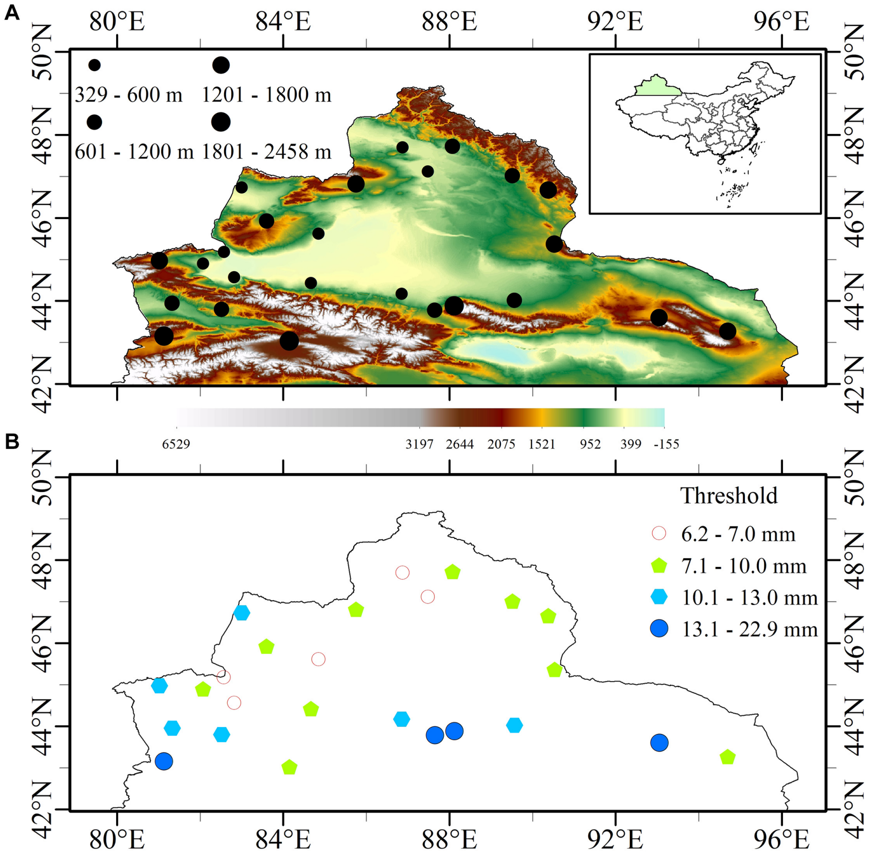

FIGURE 1 | (A) Topography for Northern Xinjiang and location of the 25 stations. **(B)** The 95th percentile thresholds used to define extreme precipitation events.

TABLE 1 | Definitions of precipitation indices and comparison with other works.

Indices	Definition	Agree with	Differ from
Wet days	daily precipitation ≧ 0.1 mm	(Liu et al., 2005; Li et al., 2011; Jiang et al., 2013; Wang et al., 2013; Zheng et al., 2014)	(Qian and Lin, 2005; Zhou et al., 2015; exceeds 1.0 mm) (Wang et al., 2012; Zhang et al., 2012; ≧ 1.0 mm)
SP events	daily precipitation between 0.1 and 0.9 mm		(Qian et al., 2007; Fu et al., 2008; between 0.1 and 1.0 mm). (Xin et al., 2008; Zheng et al., 2014; between 0.0 and 0.2 mm).
EP events	daily precipitation exceeds 95th threshold	(Qian and Lin, 2005; Zhai et al., 2005; Wang et al., 2012, 2013; Jiang et al., 2013; Zhou et al., 2015)	[Qian et al., 2007; (exceeds 50 mm); Xin et al., 2008; (exceeds 99th threshold)]

(CD) and concentration period (CP), which are widely used to investigate the concentration of daily precipitation and dust storm events. The calculation of CD and CP was based on the assumptions that the monthly occurrences of an event could be treated as a vector quantity, and the direction for a year can be seen as a circle (Zhang and Qian, 2003; Li et al., 2011; Zhao et al., 2017). Hence, CD and CP were calculated as follows:

$$R_i = \sum r_{ij}$$

$$R_{xi} = \sum r_{ij} \bullet \sin \theta_j$$

$$R_{yi} = \sum r_{ij} \bullet \cos \theta_j$$

$$CD_i = \frac{\sqrt{R_{xi}^2 + R_{yi}^2}}{R_i}$$

$$CP_i = \arctan \left(\frac{R_{xi}}{R_{yi}} \right)$$

Where i represents the ith year, j represents the jth month of the year, r_{ij} is the total number of events (for SP or EP events in this study) in the jth month of the ith year, R_i represents the total number of events over all 12 months of the ith year, and θ_j is the azimuth for the jth month. R_x and R_y donate the horizontal and vertical components of the vector. The value for CD ranges from 0 to 1 and reflects how concentrated in time events were within a given year. If there were no events in a year, or if events were distributed evenly through the year, then the CD value is 0. If events are wholly concentrated in a single month, then the CD value is 1. In all other cases, a larger value for CD indicates a higher concentration of events in time. The value for CP reflects the month when the events were most intense, taking into account the frequency of events within the month, and the start and end months for individual events. Values for CP range from 0 to 360°, where 0–30° corresponds to January, 30–60° corresponds to February, and so on with 330°–360° corresponding to December.

STATISTICAL PROPERTIES OF SP AND EP EVENTS IN NORTHERN XINJIANG

Xinjiang is far from the Pacific Ocean, and the Tibetan Plateau prevents significant moisture from the Indian Ocean from reaching the region. Precipitation in Xinjiang is therefore characterized by a low annual precipitation amount, few annual wet days, and low precipitation intensity. The threshold used to identify EP events in Xinjiang is much lower than for monsoon region in Eastern China (Zhai et al., 2005). The 95th percentile for daily precipitation amount gives a threshold of between 7 and 13 mm for defining EP events at the most Northern Xinjiang stations, as shown in **Figure 1B**. There are five stations with thresholds below 7 mm, but the threshold is above 6 mm for all stations. Although there are four stations with thresholds greater than 13 mm, three of these thresholds are below 14 mm and there is only one station where the threshold is much greater (22.9 mm). Relatively high thresholds were evident at stations in the south and west of Northern Xinjiang, and most thresholds exceed 10 mm in these areas. The thresholds at stations on the north and west sides of the Junggar Basin are generally below 10 mm, which is relatively small, and three of the five stations in Northern Xinjiang with thresholds below 7 mm are located in these regions. The mean threshold used to define EP events across Northern Xinjiang is small, at 10.1 mm, but the numbers above show that there are large differences across the region.

The mean annual occurrence of SP and EP events and the mean annual precipitation amounts that are attributed to SP and EP events are shown in **Figure 2**. The annual occurrence of SP events at most stations across Northern Xinjiang ranges from 30 to 50 days (**Figure 2A**), and the average across all 25 stations is 41.7 days. Most stations where the occurrence of SP events exceeds the average are in the west part of Northern Xinjiang, and there are fewer stations with frequent SP events in the east part of the region. The station where SP events are most infrequent is at the eastern edge of Northern Xinjiang, where SP events occur for 24.8 days per year on average; this is the only station where the average frequency for SP events is below 30 days per year. There are five stations where SP events occur with an average frequency of more than 50 days per year. These are all in the western part of Northern Xinjiang, where the highest SP event frequency is 62 days per year, which is nearly 10 days more than the average at any other station. The spatial pattern of mean annual SP amount (**Figure 2B**) is similar to that for SP occurrence (**Figure 2A**), which is also higher in the west and lower in the east. The mean annual precipitation amount attributable to SP events is between 12 and 18 mm at most stations across Northern Xinjiang. The station for which this is lowest, at 8.9 mm, is also where SP events occur most infrequently. The station where the total precipitation

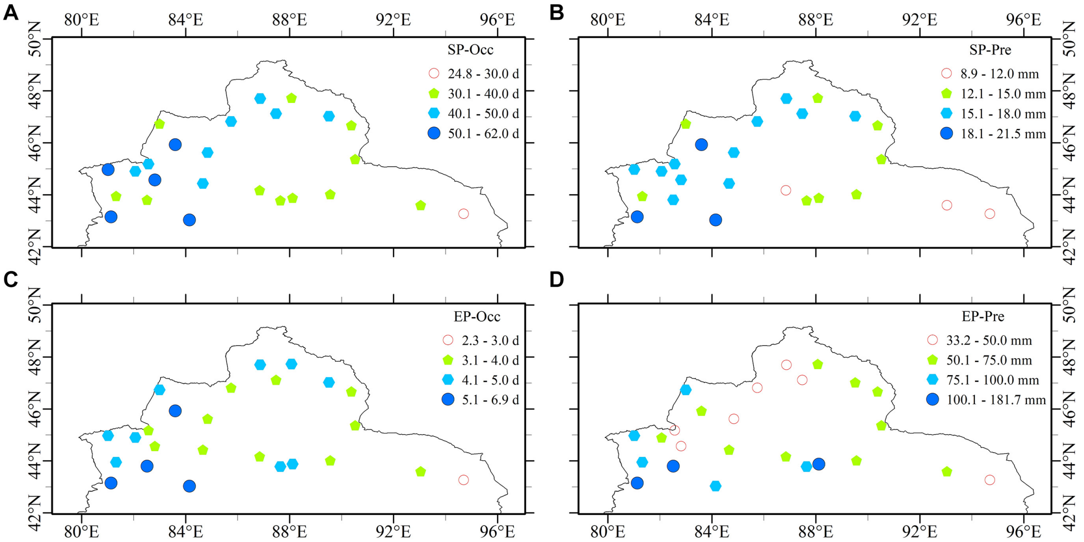

FIGURE 2 | (A) Mean number of slight precipitation (SP) events per year, **(B)** mean total annual precipitation amount attributed to SP events, **(C)** mean number of extreme precipitation (EP) events per year, and **(D)** mean total annual precipitation amount attributed to EP events.

attributable to SP events is highest, at 21.5 mm, is the station where SP events occur most frequently.

Slight precipitation events occur approximately 10 times more frequently than EP events at most stations across Northern Xinjiang, and there are some similarities between the spatial distributions for the different events (**Figures 2A,C**). For example, stations in the west experience more frequent EP and SP events than stations in the east, and the stations where EP events are most frequent are also the stations where SP events are most frequent. It is clear that EP events occur infrequently in Northern Xinjiang. **Figure 2C** shows that EP events occur fewer than five times per year at most stations, and the mean occurrence across all 25 stations is 4.2 days per year. This low frequency for EP events is consistent with the arid climate, which makes the annual number of wet days low in Xinjiang. The spatial pattern for event frequency, which shows EP and SP events to be more frequent in the west than in the east, is not apparent in the distribution of total precipitation amount attributable to EP events (**Figure 2D**) because the amount of precipitation from EP events in northwest parts of the Junggar Basin is low. The relatively higher annual precipitation amounts attributable to EP events occur at stations in southwest areas of Northern Xinjiang. The average annual precipitation amount attributable to EP events is between 50 and 100 mm at most stations, and the mean across all 25 stations is 69.3 mm, which suggests that EP events account for a large proportion of the total annual precipitation over Northern Xinjiang, and highlights potential risks that may arise from EP events. Note that there are three stations where the annual precipitation amount from EP events exceeds 100 mm, and that at one (Tianchi station) of these stations, it reaches 181.7 mm, showing that these areas are more strongly affected by EP events than other areas.

To better understand changes in SP and EP events at stations across Northern Xinjiang, we looked at linear trends in the contribution of SP and EP events to the total number of wet days and total annual precipitation amounts. The annual number of wet days that correspond to SP events is shown as a proportion of the total number of annual wet days in **Figure 3A** for each station. In agreement with previous research (Liao et al., 2012), the contribution of SP events to the total number of annual wet days is relatively high in Xinjiang; the regional mean is 49.5%, indicating that nearly half of all wet days in Xinjiang are SP events. The proportion of wet days that are accounted for by SP events is below 40% at only five stations, and the smallest proportion is 33.5%, meaning that SP events account for more than a third of the total number of wet days at all stations, as shown in **Figure 3A**. However, the linear trends show that the proportion of total wet days that are accounted for by SP events has decreased significantly over recent decades at most stations (**Figure 3B**). The trend is negative at all stations except one, and is statistically significant for two thirds of the stations. The decrease is particularly noticeable at stations around the Junggar Basin. The low intensity of SP events means that their contribution to the total annual precipitation amount is small (**Figure 3C**), despite the fact that they account for a large proportion of the total number of wet days. The mean contribution of SP events to the total precipitation amount across all 25 stations is 8.5%. The contribution is less than 10% at more than half of the stations across Northern Xinjiang, and is less than 15% at nearly all stations, with the exception of one station where the contribution is 16.5%. Trends in the contribution of SP events to the total number of wet days (**Figure 3B**) are similar to the trends in the contribution of SP events to total precipitation amount (**Figure 3D**). Both trends are positive for the same single station and negative at all other stations, and both trends are strongly decreasing at most stations around the Junggar Basin.

The contribution of EP events to the total annual precipitation amount ranges from 24.3 to 32.8% at stations across Northern

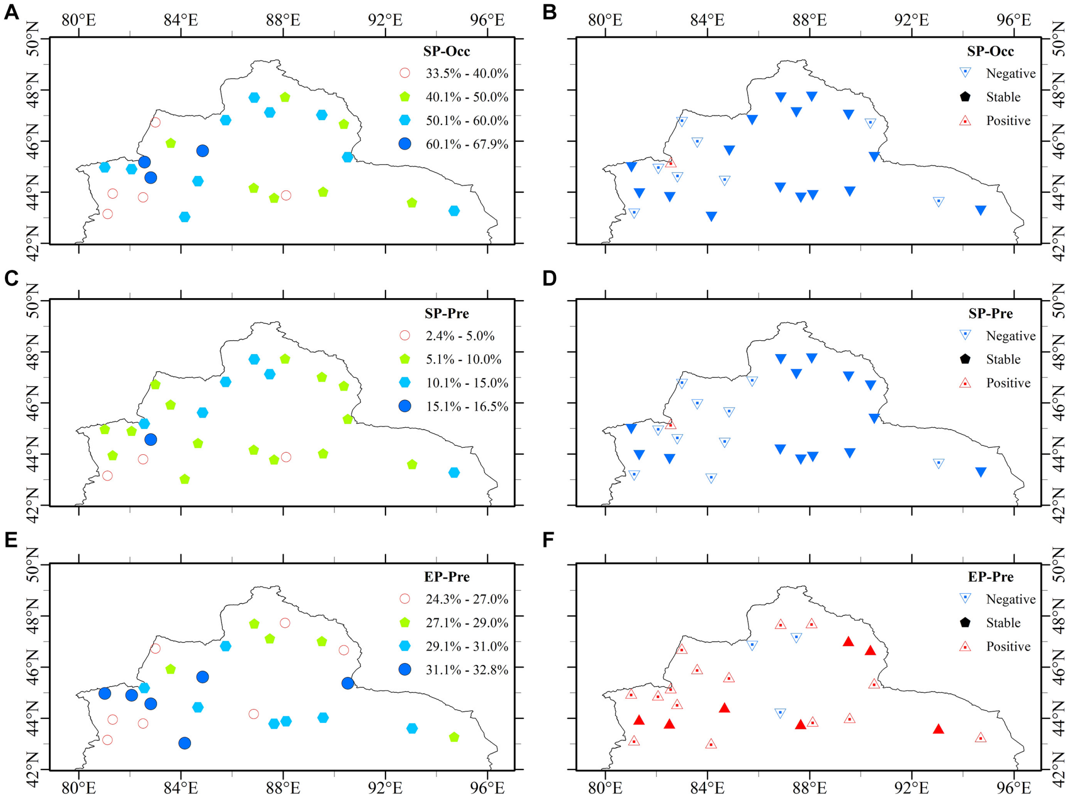

FIGURE 3 | (A) The average contribution of SP events to the total annual number of wet days, **(B)** linear trends in the contribution of SP events to the total annual number of wet days over 55 years, **(C)** the contribution of SP events to the total annual precipitation amount, **(D)** linear trends in the contribution of SP events to the total annual precipitation amount over 55 years, **(E)** the contribution of EP events to the total annual precipitation amount, and **(F)** linear trends in the contribution of EP events to the total annual precipitation amount over 55 years. Solid triangles mark where the linear trends are significant at the 95% confidence level.

Xinjiang (**Figure 3E**), and the average across all 25 stations is 28.8%. EP events typically have high intensity and therefore their contribution to the total annual precipitation amount generally exceeds the contribution of SP events, despite the fact that EP events account for only 5% of the total number of wet days at every station, which is much lower than for SP events. There existed a contrast in the contribution of EP events to the total precipitation amount at stations in the southwest of Northern Xinjiang; at three stations in this area, EP events account for less than 27% of total annual precipitation amount, while at four stations in this same area, EP events account for more than 31% of total annual precipitation amount. There are also differences in the Junggar Basin, where the contribution of EP events to the total precipitation amount is higher at stations in southern parts of the basin than at stations in northern parts of the basin. There are clear differences between the trends for the contributions of SP and EP events to the total annual precipitation amount (**Figures 3D,F**), and this is reflected in both the magnitude of the trends and in the degree to which they are significant. There is an increasing trend in the contribution of EP events to the total annual precipitation amount at most stations and it is negative at only three stations (**Figure 3F**). By contrast, the negative trend of the contribution of SP events to the total annual precipitation amount is observed at almost all the stations (**Figure 3D**). Moreover, the trends are significant with a confidence level of 95% at only seven stations (**Figure 3F**), while the trends for the contribution of SP events to the total annual precipitation amount are statistically significant at most stations (**Figure 3D**). The difference is particularly noticeable at stations around the Junggar Basin.

Figure 4 shows the proportion of the total number of annual wet days and total annual precipitation amount accounted for by SP and EP events averaged across all 25 stations, as well as the mean anomalies for the number of annual wet days and for the total annual precipitation amount. In agreement with **Figures 3B,D**, the regional averages for the proportion of annual wet days accounted for by SP events (**Figure 4A**), and for the contribution of SP events to the total annual precipitation amount (**Figure 4B**) decreased over the period from 1963 to 2017. Notably, both of these negative trends reflect a dramatic decline that began in the late 1990s and that there were no discernible trends between the early 1960s and the mid-1990s. Between 1963 and 1995, SP events accounted for 49.96% of wet days, and 7.23% of the total precipitation amount, which exceeds the 48.66 and 6.81% calculated for between 1963 and 2017. Most years where SP events accounted for an extremely low proportion of both wet days and the total precipitation amount were between 2000 and 2017. Over this period, the regional mean for the proportion of

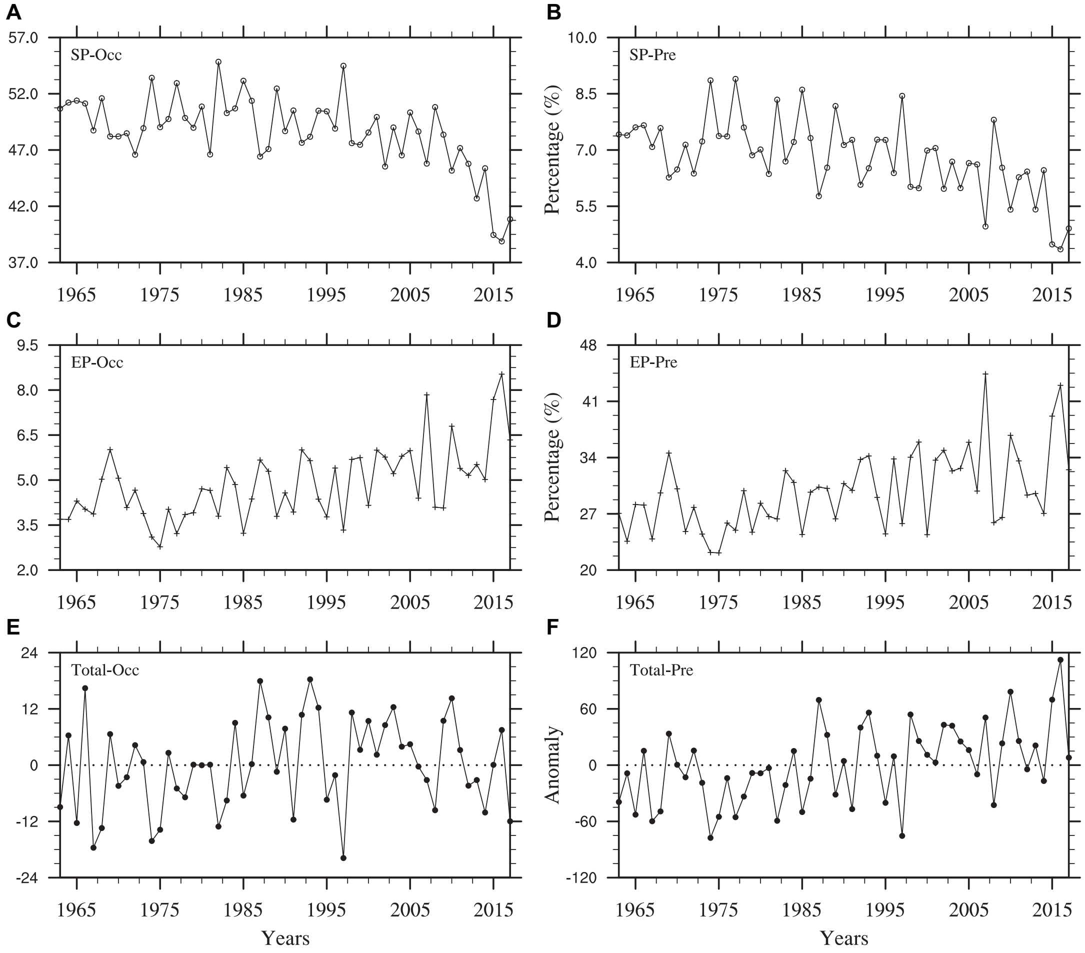

FIGURE 4 | The regionally averaged contribution of SP and EP events **(A,C)** to the total number of annual wet days: **(A)** SP, and **(C)** EP; and **(B,D)** to the total annual precipitation amount: **(B)** SP, and **(D)** EP; **(E)** anomalies in the regionally averaged total number of annual wet days; **(F)** anomalies in the regionally averaged total annual precipitation amount. Plotted data are the means calculated over all 25 stations across Northern Xinjiang from 1963 to 2017.

wet days accounted for by SP events was 46.05%, and the regional mean contribution of SP events to total precipitation amount was 6.05%, which are both relatively low.

In contrast, there were increasing trends over the study period for the proportion of annual wet days accounted for by EP events (**Figure 4C**), and for the contribution of EP events to the total annual precipitation amount (**Figure 4D**). Both of these measures gradually increased from a minimum in 1975, and the rate of increase for both measures increased over the study period, particularly after the early 2000s. The 3 years in which EP events made the greatest contribution to the total precipitation amount, and accounted for the greatest proportion of wet days, were 2007, 2015, and 2016. Between 2005 and 2017, EP events accounted for the largest proportions of both annual number of wet days and total precipitation amount (5.91 and 33.34%, respectively), which exceeds the mean contributions over both the whole study period (4.86 and 29.83%, respectively), and the period from 1963 to 2000 (4.41 and 28.25%, respectively). In addition to the opposing trends, there are further contrasts between the contributions of SP and EP events to the number of wet days and to the total precipitation amount. Both the correlation coefficient between the contribution of SP and EP events to total annual number of wet days and the correlation coefficient between the contribution of SP and EP events to total annual precipitation amount are −0.76. Particularly, in some years, when the proportional contribution of EP events was particularly high, the proportional contribution from SP events was usually low, and vice versa. For example, the proportion of wet days accounted for by EP events was extremely low in 1974, 1985, and 1997 (**Figure 4C**), when the proportion of wet days accounted for by SP events was very high (**Figure 4A**). As a further example, the contribution of EP events to the total precipitation amount was very high in 2007, 2015, and 2016 (**Figure 4D**), when the contribution from SP events was extremely low (**Figure 4B**).

There was a significant shift at around 1987 in the time series of both the total annual number of wet days (**Figure 4E**) and for the total precipitation amount (**Figure 4F**). The annual number of wet days in Northern Xinjiang typically oscillates on a decadal scale rather than following an upwards trend; there were relatively few wet days in the years before the mid-1980s, relatively more wet days in the years following the late 1990s, and a high number of wet days in the years between the mid-1980s and mid-1990s (**Figure 4E**). The increasing trend in the annual precipitation amount (**Figure 4F**) is more obvious than the trend in the number of annual wet days because the two quantities followed opposing trends from the early 2000s, which the annual number of wet days began a slight decline in the early 2000s, while the total annual precipitation amount continued to rise.

The impact of SP events on the number of wet days and EP events on the total annual precipitation amount was assessed for each station using the coefficient of determination, shown in **Figure 5**. The coefficient of determination between the annual number of SP events and the number of annual wet days ranges from 0.15 to 0.87 and the mean value across all 25 stations is 0.53 (**Figure 5A**). The coefficient of determination between the precipitation amount attributable to SP events and the total precipitation amount ranges from 0 to 0.21 (not shown). The coefficient of determination between the annual number of EP events and the total annual number of wet days ranges from 0.02 to 0.34 (not shown), and the coefficient of determination between the precipitation amount attributable to EP events and the total annual precipitation amount ranges from 0.46 to 0.81 (**Figure 5B**). In agreement with our earlier findings in **Figures 3**, **4**, SP events influence the annual number of wet days more strongly than the total precipitation amount, while the converse is true for EP events.

Slight precipitation events occur frequently and contribute strongly to the total number of wet days, but they have a low intensity and so the annual precipitation amount attributable to SP events, and the proportion of the total annual precipitation amount that this accounts for, is therefore small. The situation is reversed for EP events. Since EP events are intense, the annual precipitation amount from EP events, and the contribution of this to the total annual precipitation amount, is high, despite the infrequent occurrence of EP events and their small contribution to the total number of wet days. Notice that the annual number of wet days increased in Northern Xinjiang over recent decades, means that the decrease in frequency of SP event was offset by the increase in frequency of other precipitation events. Especially in the period before the late 1990s, when the decrease of SP events is not very fast.

A few previous studies have focused on the changes in the precipitation for different grades at some Xinjiang stations, and they show that the constant decline in slight precipitation

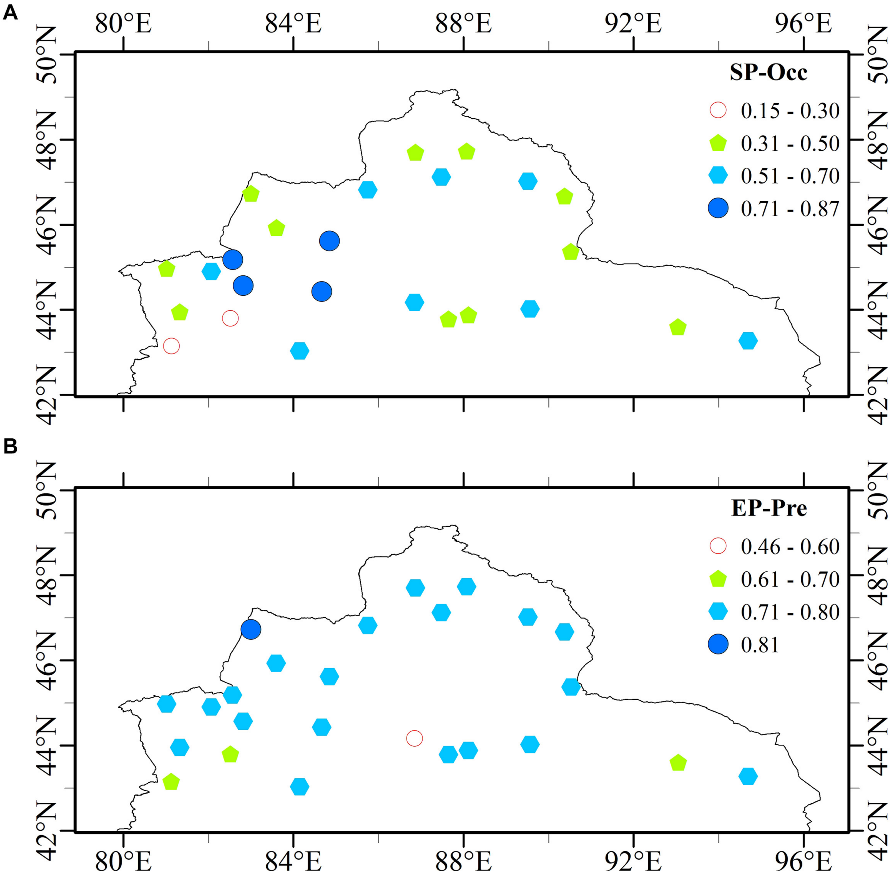

FIGURE 5 | The coefficient of determination at each station in Northern Xinjiang for: **(A)** the annual occurrence of SP events and the annual number of wet days, and **(B)** the annual precipitation amount attributable to EP events and the total annual precipitation amount.

frequency at Urumchi station and stations in the Bole region (on the southwest side of the Junggar Basin) was well-defined between the 1960s and 2000s (Xin et al., 2008; Zheng et al., 2014), and a significantly lower frequency was also found in the 2000s. This is consistent with our results and proves the importance of changes in precipitation events with lower intensity in Xinjiang.

CONCENTRATION OF SP AND EP EVENTS OVER NORTHERN XINJIANG

We investigated the intra-annual features of the characteristics of the SP and EP events, and of the long-term changes to these, using the measures of CD and CP described in see section "Methods." The CD and CP values for the SP and EP events at each station in Northern Xinjiang are shown in **Figure 6**, with all of the values from the study period being classified into different categories. The CD values for SP are typically <0.3 at most stations (**Figure 6A**), which implies that the concentration of SP events is generally low in Northern Xinjiang. The number of years for which CD is less than 0.3 ranges from 29 to 54 across the stations, which means that CD is relatively small for more than half the study period at all stations in Northern Xinjiang; in fact, CD is rarely greater than 0.5 at any station for any year in the study period. This suggests that SP events are generally spaced over several months in Northern Xinjiang, and the distribution of CP for SP events in **Figure 6B** supports this conclusion. CP for SP events includes three or four seasons for most stations, with a significant peak for one season. At some stations, the probability is nearly equal for all four seasons, showing that SP events occur in all months with nearly equal frequency at these stations. The CP for SP events from all 55 years occurred primarily in winter (DJF), and secondly in autumn (SON), particularly for stations around the Junggar Basin. Overall, CP varies between regions and winter is the dominant CP for most, but not all, stations in Northern Xinjiang. For example, the CP for SP events occurred mainly in spring (MAM) at some stations in the southwest.

There are some years in which CD is 1 (or 0) for EP events (**Figure 6C**), reflecting the fact that only one EP event occurred (or none). Apart from these two cases, CD for EP events is greater than 0.5 for most years at most stations, suggesting that EP events are concentrated in time on an intra-annual scale. However, it should be noted that at some stations, CD is less than 0.5 for more than a quarter of the years included in the study period, indicating that EP events were spaced further apart in time in those years. The most common CP for EP events between 1963 and 2017 was in summer (JJA; **Figure 6D**), but MAM is the second most probable season for EP event occurrence. The mean number of years for which the CP was in MAM, averaged across all 25 stations, is 11.8, which is nearly a third of the number of years for which it was in JJA, and twice the number of years for which most EP events occur in SON. The low annual frequency and high CD values for EP events imply that EP events in Northern Xinjiang are most likely to occur in the warmer seasons, which is very different to the timing of SP events.

There are clear inter-annual and long-term variations in SP and EP events (**Figure 4**), and both exhibit notable intra-annual variability. The inter-annual variability of CD for EP and SP events is shown at a regional scale in **Figure 7** and suggests that the concentration of both SP and EP events has changed in recent decades. Moreover, the changes to CD for SP and EP events are related to long-term trends in SP and EP events. There is a significant upward trend in regionally averaged CD values for SP events (**Figure 7A**), which results from a marked shift from lower to higher values around the late 1990s that is clearly related to changes in the frequency of SP events (**Figure 4A**). In contrast, there is notable decline in the regionally averaged CD values for EP events (**Figure 7B**). This decrease is clearly relevant

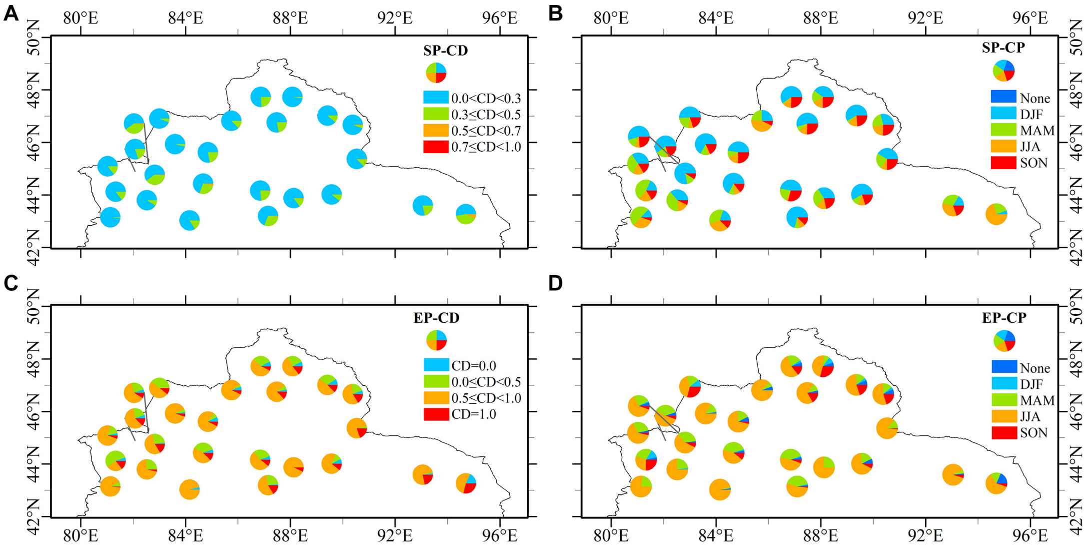

FIGURE 6 | Annual values of **(A)** CD, and **(B)** CP for SP events at each station in Northern Xinjiang from 1963 to 2017; **(C,D)** are as **(A,B)**, but for EP events. (Values of 55 years were classified into different categories).

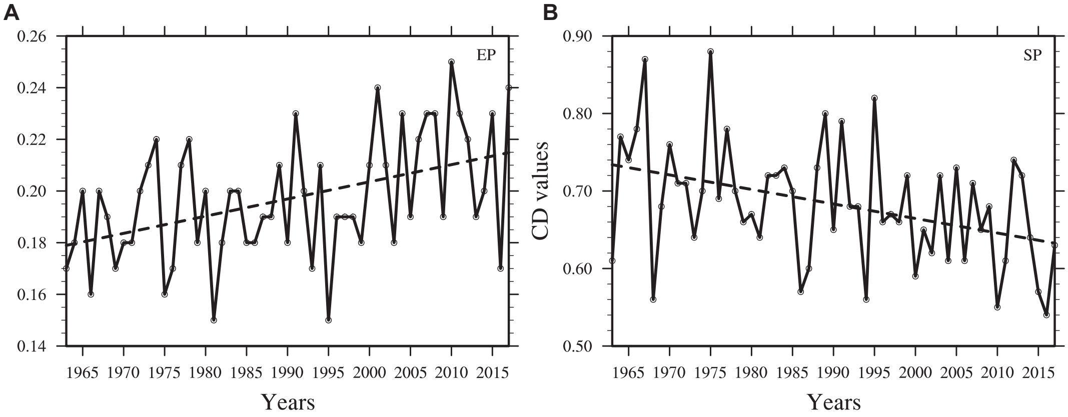

FIGURE 7 | Regionally averaged CD for: **(A)** SP, and **(B)** EP events over Northern Xinjiang from 1963 to 2017.

to the increased frequency of EP events over recent decades (**Figure 4C**) because an increase in event frequency can easily lead to a decrease in event concentration, particularly when the increase does not occur in the main season.

The large difference between the concentration of SP and EP events originates from the significant differences in the statistical characteristics of SP and EP events, including in their mean annual frequency and the trends they have followed over recent decades. The annual frequency for SP events is high and they may occur in almost any month in a year, while EP events are less frequent and usually occur in the warmer months, when the air column is warmer and can hold more water vapor. As a result, EP events are more concentrated than SP events over the course of a year. In addition, due to the opposing trends for SP and EP event frequency, trends in the concentration of SP and EP events are also opposing.

CONNECTIONS BETWEEN PRECIPITATION DISTRIBUTION AND DAILY MEAN TEMPERATURE

The seasonal variations in the frequency of SP and EP events suggests that air temperature may also influence their occurrence. We used the empirical orthogonal function (EOF) method to assess how the spatial distribution of precipitation varies with daily mean temperature. To be specific, the occurrence of SP and EP events at each daily mean temperature were checked for every Northern Xinjiang station, then the temperature range of SP and EP occurrence for the whole region was calculated. At each station, for each degree in the temperature range covering the SP events, the number of SP events was counted and we then calculated the mean intensity of these SP events. The frequency (or intensity) of the SP events from the 25 stations varied with the different daily mean temperatures and can be seen as a spatiotemporal field, as can that of EP event frequency and EP event intensity. The EOF analysis was then performed on the original values of these four fields, and four first modes were obtained. These first modes for the variations in SP and EP events with temperature are shown in **Figures 8**, **9**, and the variance contributions of EOF1 from SP event frequency, SP event intensity, EP event frequency, and EP event intensity were 81.3, 91.8, 70.9, and 81.2%, respectively. All of the first eigenvectors are positive over the whole of Northern Xinjiang (**Figure 8**), and the differences between them reflect the distribution of areas where their individual values are high. The first eigenvector from the EOF analysis of the variability in the frequency of SP events with temperature has a high value in western areas, including the northwest part of the Junggar Basin and the western part of the Tianshan mountains (**Figure 8A**). The region where the first eigenvector for the EOF analysis of the variability in SP event intensity with temperature has high values is the northeastern area of Junggar Basin (**Figure 8B**). For the analysis of EP event frequency with temperature, the first eigenvector has a positive maximum in the western part of the Tianshan mountains (**Figure 8C**), and the first eigenvector for the analysis of variability in EP event intensity with temperature is in the southern part of the Junggar Basin (**Figure 8D**).

Although the locations of the maxima for the eigenvectors differ between the analysis of the SP and EP events, there are some similarities in the spatial distribution of the first eigenvector for the analysis of both events. However, the time coefficient from the EOF analysis of changes in SP and EP events with temperature is very different for the SP and EP events (**Figure 9**). SP events occur within a daily mean temperature range of −35 to +34°C and EP events occur within −21 to +30°C. There are two maxima for the variability of SP event frequency within the daily mean temperature range of −35 to +34°C: one from −14 to −5°C, and one from 14 to 22°C (**Figure 9A**). There is a temperature interval between these two peaks that corresponds to relatively low variability for the occurrence of SP events, but the variabilities in this interval is still larger than that in the intervals between −18 and −35°C and between 25 and 34°C. The variability of the intensity of SP events varies slowly with temperature, gradually increasing between −35 and +18°C, then dropping notably (**Figure 9B**). Apart from differences in the temperature range, the most obvious difference between the distributions of variability for SP

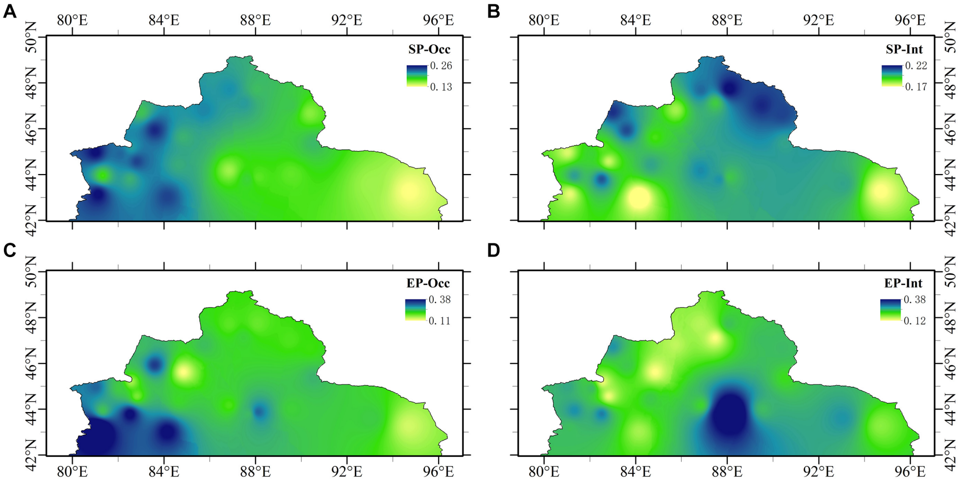

FIGURE 8 | The first eigenvectors from the EOF analysis of variations in **(A)** SP event frequency, **(B)** SP event intensity, **(C)** EP event frequency, and **(D)** EP event intensity with daily mean temperature change.

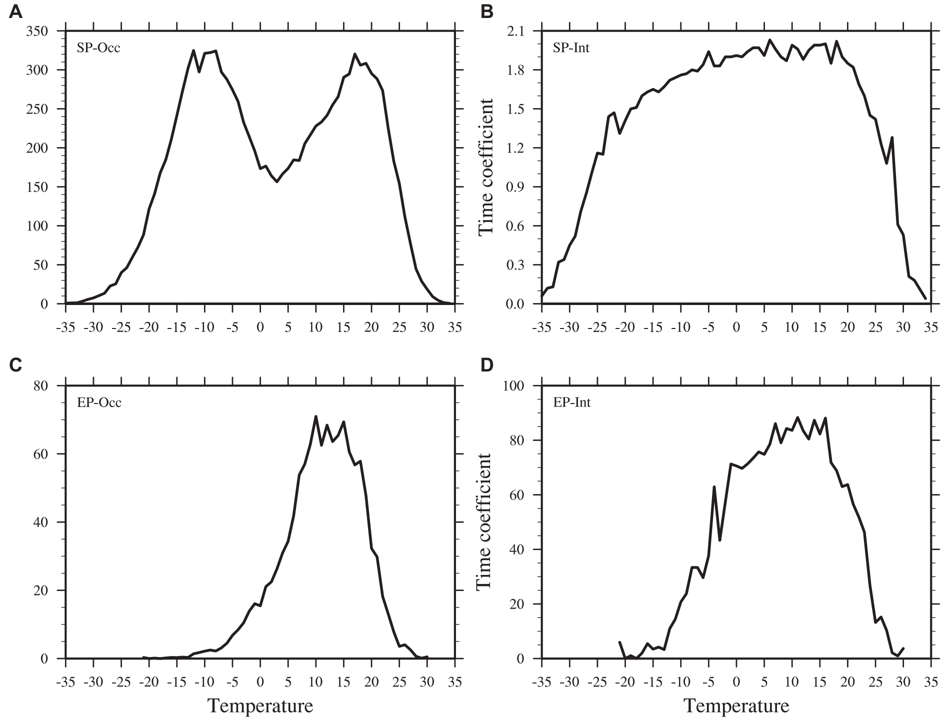

FIGURE 9 | The time coefficient of the first modes from the EOF analysis of variations in **(A)** SP event frequency, **(B)** SP event intensity, **(C)** EP event frequency, and **(D)** EP event intensity with daily mean temperature change.

and EP event frequency with temperature is that there is only one maximum for EP event frequency with temperature (**Figure 9C**). As shown in **Figure 9C**, EP events occur more frequently in the temperature interval 7 to 18°C, and less frequently below 2°C and above 21°C. Compared with the results for SP events, changes in the intensity of EP events with temperature are more dramatic and there is a peak at temperatures between 6 and 16°C, where EP event intensity is clearly higher, while the intensity of EP events quickly drops at temperatures above 16°C (**Figure 9D**).

Precipitation in many areas around the world has changed strikingly in response to the warming climate (IPCC, 2013). To understand the connections between changes in temperature and SP and EP events in Northern Xinjiang, we calculated the trends for the annual frequency of different daily mean temperatures and that of SP and EP events at different daily mean temperatures; these trends are shown in **Figure 10** alongside their climatic averages. The daily mean temperature in Northern Xinjiang generally ranges from −35 to +34°C, and has a distribution with two peaks, and the mean number of days each year that fall within each 1° division of this range is 5.21 (**Figure 10A**). The first peak is low and flat and ranges from −9 to −6°C, within which temperature range the average annual frequency remains above 7 days. The second peak is more prominent and ranges from 9 to 23°C, within which range the average annual frequency remains above 8 days. Consistent with the warming climate over recent decades, the frequency of warm daily mean temperatures (above 18°C) has increased, and the frequency of cold daily mean temperatures (below −15°C) has decreased. There is no significant trend in the frequency of days where the mean temperature is between −15 and 18°C, but there are continuous upward and downward trends for daily mean temperatures within smaller ranges inside this interval, for example there is a negative trend in the frequency of daily mean temperatures between 0 and 17°C (**Figure 10A**).

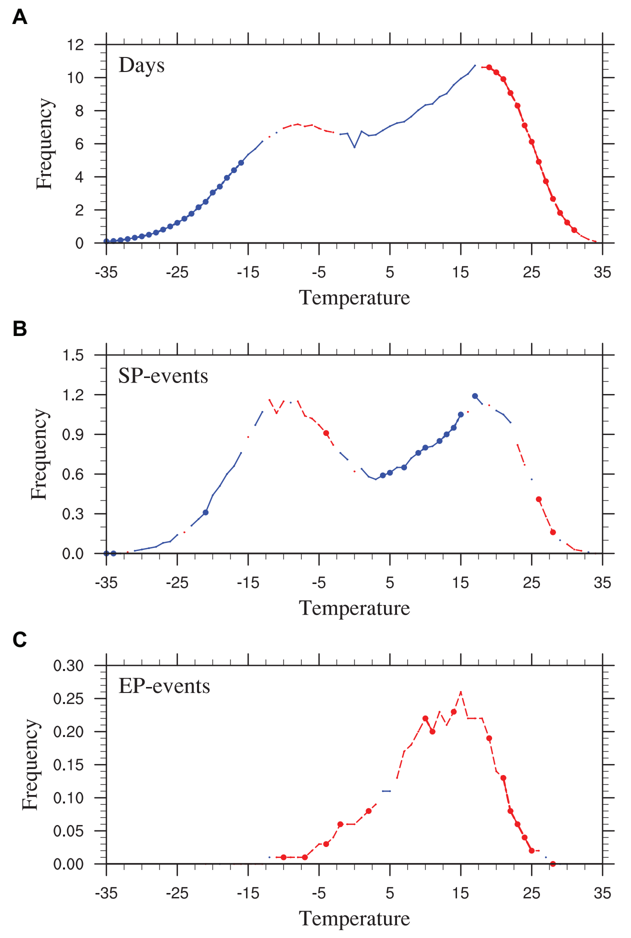

FIGURE 10 | (A) Average annual frequency of days with different daily mean temperatures. **(B)** Average annual frequency of SP events on days with different daily mean temperatures. **(C)** Average annual frequency of EP events on days with different daily mean temperatures. Plotted data represent the mean across all stations, calculated from data covering 1963–2017. Red (blue) lines indicate a positive (negative) linear trend over the 55 years; lines marked with dots show trends that are significant at the 95% confidence level.

As shown in **Figures 10B,C**, the distributions of SP and EP event frequency with temperature have a bimodal and a unimodal distribution, respectively, which agrees with the results of the EOF analysis in **Figure 9**. For some temperatures, there are similarities between the trends for the number of days with that temperature (**Figure 10A**) and for the frequency of SP events (**Figure 10B**). For example, there are negative trends for SP event frequency, and for the average number of days with temperatures between 1 and 15°C, or below −16°C, and there is a positive trend in both the average number of days and SP event frequency for temperatures around −5°C (**Figure 10B**). From inspection of the changes in daily mean temperature and SP event frequency, it is clear that there is a positive relationship between temperature and SP event occurrence over most time intervals. When daily mean temperatures within a certain temperature range become more frequent, then the occurrence of SP events within that temperature range generally also increases, and vice versa. There are significant decreases in SP event frequency between 4 and 15°C. In contrast, EP events occur more frequently at most temperatures over recent decades, with the exception of a few narrow intervals, such as between 4 and 5°C (**Figure 10C**), which suggests that the relationship between temperature and EP event frequency is more complicated. Although the trends for number of days with different daily mean temperatures (**Figure 10A**) and EP event frequency (**Figure 10C**) have the same sign at temperatures above 18°C and at around −5°C, the trends are opposite between 6 and 17°C.

There are differences between the distributions and trends for the frequency of SP and EP events at different mean daily temperatures. Firstly, the temperature range for days when SP events occur is from −35 to +34°C, which is broader than the range for EP events, which is from −21 to 30°C. Secondly, there are differences between the frequency distribution for SP and EP events with temperature: there are two peaks in the SP event frequency distribution, and one for the EP event frequency distribution. Lastly, the trends for the number of days and for SP event frequency agree better over different temperatures than the trends for the number of days and for EP event frequency. The trends for the number of days and for the frequency of SP events are the same over nearly the entire temperature range, but the trends for the number of days and for the frequency of EP events do not always agree, and are opposite for temperatures between 6 and 17°C.

CONCLUSION AND DISCUSSION

We used daily precipitation and mean temperature data from 25 stations from 1963 to 2017, to compare statistical features and changes for SP and EP events over various timescales, and to investigate and compare relationships between SP and EP events and daily mean temperature. Our main conclusions are as follows:

(1) In Northern Xinjiang, from a regional perspective, SP events contribute strongly to and account for 49.5% of the total annual number of wet days, and contribute weakly to and account for 8.5% of the total annual precipitation amount. By contrast, EP events contribute strongly to and account for 28.8% of the total annual precipitation amount, and contribute weakly to and account for 5% of the total annual number of wet days.

(2) Over recent decades, in consist with the negative trend in SP events, the contribution of SP events to the total annual precipitation amount and the total annual number of wet days decreased significantly. Meanwhile, the contribution of EP events to the total annual precipitation amount increased significantly with the positive trend in EP events.

(3) The CD and CP values for SP event over the past 55 years show that SP events generally occur spaced through all months of the year, while EP events are generally concentrated in JJA. Regionally averaged CD values for SP and EP events have significantly increased and decreased, respectively, over Northern Xinjiang during the past 55 years, and this is related to the frequency of SP and EP events, which have experienced significant negative and positive trends, respectively.

(4) There are distinct differences between the relationships of SP and EP events to daily mean temperature. The daily mean temperatures at which SP events occur range from –35 to +34°C at the stations across Northern Xinjiang, while the temperature range for EP events is from –21 to +30°C. There are two peaks in the regionally averaged curve between SP event frequency and temperature and only one peak in the curve for EP events. Trends for daily mean temperatures and for the frequency of SP events at different temperatures agree well over nearly the entire temperature range, while trends for daily mean temperatures and for the frequency of EP events at different temperatures are not always consistent.

Long-term changes to precipitation characteristics that vary on a decadal scale are often related to changes in sea surface temperature (Wang et al., 2014; Ning and Bradley, 2015; Yan et al., 2019). For example, an increase in the daily variability of precipitation from the Indian monsoon was caused by a warming trend in the tropical Indian Ocean, which resulted in more heavy precipitation events and fewer moderate precipitation events (Goswami et al., 2006). Signals such as the basin mode (IOBM) and the dipole mode (IOD) in the tropical Indian Ocean have an important influence on precipitation in East China (Guan and Yamagata, 2003; Yang et al., 2007; Xie et al., 2009). There may also be links between IOBM and precipitation in Xinjiang indicated from recent studies. For example, Zhao et al. (2014, 2018) suggested that the weakened Indian monsoon is conducive to cooling of the middle and upper troposphere over central Asia in summer, and to increased water vapor transport from the tropical Indian Ocean to Central Asia, which may both contribute to increased precipitation in southern Xinjiang. Similar relationships between the Indian Ocean and Central Asia are also suggested by the results of climate projections from the CMIP5 experiment (Zhao and Zhang, 2015). In future work, we intend to study the impacts of signals from the Indian Ocean on SP and EP events in Northern Xinjiang, and the mechanisms that connect them.

DATA AVAILABILITY STATEMENT

Publicly available datasets were analyzed in this study. This data can be found here: http://data.cma.cn/data/cdcdetail/dataCode/SURF_CLI_CHN_MUL_DAY_V3.0.html.

AUTHOR CONTRIBUTIONS

YZ contributed to the development and planning of the study. ML performed the data analysis and wrote the manuscript. YL assisted with data analysis and figures. XZ helped perform the precipitation concentration analysis. SZ helped perform the analysis of precipitation response to the rise in temperature. All authors contributed to the article and approved the submitted version.

FUNDING

This work was jointly supported by the National Key R&D Program of China (Grant No. 2018YFC1507103), Sichuan Science and Technology Program (Grant No. 2020JDJQ0050), National Natural Science Foundation of China (Grant Nos. 41971026 and 41805054), and the Scientific Research Foundation of CUIT (Grant No. KYTZ201727).

REFERENCES

Bonsal, B. R., Zhang, X., Vincent, L. A., and Hogg, W. D. (2001). Characteristics of daily and extreme temperatures over Canada. *J. Clim.* 14, 1959–1976. doi: 10.1175/1520-0442(2001)014<1959:CODAET>2.0.CO;2

Chen, F. H., Wang, J. S., Jin, L. Y., Zhang, Q., Li, J., and Chen, J. H. (2009). Rapid warming in mid-latitude central Asia for the past 100 years. *Front. Earth Sci. China* 3:42–50. doi: 10.1007/s11707-009-0013-9

Chen, Y. N., Li, W. H., Deng, H. J., Fang, G. Z., and Li, Z. (2016). Changes in central Asia's water tower: past, present and future. *Sci. Rep.* 6:35458. doi: 10.1038/srep39364

Deng, H. J., Chen, Y. N., Shi, X., Li, W. H., Wang, H. J., Zhang, S. H., et al. (2014). Dynamics of temperature and precipitation extremes and their spatial variation in the arid region of northwest China. *Atmos. Res.* 138, 346–355. doi: 10.1016/j.atmosres.2013.12.001

Fu, J. L., Qian, W. H., Lin, X., and Chen, D. L. (2008). Trends in graded precipitation in China from 1961 to 2000. *Adv. Atmos. Sci.* 25, 267–278. doi: 10.1007/s00376-008-0267-2

Goswami, B. N., Venugopal, V., Sengupta, D., Madhusoodanan, M. S., and Xavier, P. K. (2006). Increasing trend of extreme rain events over India in a warming environment. *Science* 314, 1442–1445. doi: 10.1126/science.1132027

Guan, Z. Y., and Yamagata, T. (2003). The unusual summer of 1994 in East Asia: IOD teleconnections. *Geophys. Res. Lett.* 30:1544. doi: 10.1029/2002GL016831

Held, I. M., and Soden, B. J. (2006). Robust responses of the hydrological cycle to global warming. *J. Clim.* 19, 5686–5699. doi: 10.1175/JCLI3990.1

Huang, D. Q., Zhu, J., and Kuang, X. Y. (2011). Decadal variation of different durations of continuous Meiyu precipitation and the possible cause. *Chin. Sci. Bull.* 56, 424–431. doi: 10.1007/s11434-010-4241-x

Huang, J. P., Ji, M. X., Xie, Y. K., Wang, S. S., He, Y. L., and Ran, J. Q. (2016a). Global semi-arid climate change over last 60 years. *Clim. Dyn.* 46, 1131–1150. doi: 10.1007/s00382-015-2636-8

Huang, J. P., Ma, J. R., Guan, X. D., Li, Y., and He, Y. L. (2019). Progress in semi-arid climate change studies in China. *Adv. Atmos. Sci.* 36, 922–937. doi: 10.1007/s00376-018-8200-9

Huang, J. P., Yu, H. P., Guan, X. D., Wang, G. Y., and Guo, R. X. (2016b). Accelerated dryland expansion under climate change. *Nat. Clim. Chang.* 6, 166–171. doi: 10.1038/nclimate2837

Huang, P., Xie, S.-P., Hu, K., Huang, G., and Huang, R. (2013). Patterns of the seasonal response of tropical rainfall to global warming. *Nat. Geosci.* 6, 357–361. doi: 10.1038/ngeo1792

IPCC (2013). *Climate Change 2013: The Physical Science Basis. Contribution of Working Group I to the Fifth Assessment Report of the Intergovernmental Panel on Climate Change*. Cambridge: Cambridge Univ. Press.

Jiang, F. Q., Hu, R. J., Wang, S. P., Zhang, Y. W., and Tong, L. (2013). Trends of precipitation extremes during 1960–2008 in Xinjiang, the northwest China. *Theor. Appl. Climatol.* 111, 133–148. doi: 10.1007/s00704-012-0657-3

Jiang, Z. H., Huang, Q., and Li, Q. X. (2008). Study of precipitation series homogeneous adjustment and their correction over China in the last 50 years. *Clim. Environ. Res.* 13, 67–74.

Li, B. F., Chen, Y. N., Li, W. H., Chen, Z. S., Zhang, B. H., and Guo, B. (2013). Spatial and temporal variations of temperature and precipitation in the arid region of northwest China from 1960-2010. *Fresenius Environ. Bull.* 22, 362–371.

Li, X. M., Jiang, F. Q., Li, L. H., and Wang, G. G. (2011). Spatial and temporal variability of precipitation concentration index, concentration degree and concentration period in Xinjiang, China. *Int. J. Climatol.* 31, 1679–1693. doi: 10.1002/joc.2181

Li, Y., Huang, J. P., Ji, M. X., and Ran, J. J. (2015). Dryland expansion in northern China from 1948 to 2008. *Adv. Atmos. Sci.* 32, 870–876. doi: 10.1007/s00376-014-4106-3

Liao, X. M., Chen, D. L., and Xie, Y. (2012). Spatial and temporal distribution of dry spells in China. *Acta Meteor. Sin.* 67, 321–336.

Liu, B. H., Xu, M., Henderson, M., and Qi, Y. (2005). Observed trends of precipitation amount, frequency, and intensity in China, 1960-2000. *J. Geophys. Res.* 110:D08103. doi: 10.1029/2004JD004864

Ning, L., and Bradley, R. S. (2015). Winter climate extremes over the northeastern United States and southeastern Canada and teleconnections with large-scale modes of climate variability. *J. Clim.* 28, 2475–2493. doi: 10.1175/JCLI-D-13-00750.1

Qian, W., and Lin, X. (2005). Regional trends in recent precipitation indices in China. *Meteor. Atmos. Phys.* 90, 193–207. doi: 10.1007/s00703-004-0101-z

Qian, W. H., Fu, J. L., and Yan, Z. W. (2007). Decrease of light rain events in summer associated with a warming environment in China during 1961–2005. *Geophys. Res. Lett.* 34:L11705. doi: 10.1029/2007GL029631

Shi, Y. F., Shen, Y. P., and Hu, R. J. (2002). Preliminary study on signal, impact and foreground of climatic shift from warm-dry to warm-humid in northwest China. *J. Glaciol. Geocryol.* 24, 219–226.

Shi, Y. F., Shen, Y. P., Li, D. L., Zhang, G. W., Ding, Y. J., Hu, R. J., et al. (2003). Discussion on the present climate change from warm-dry to warm-wet in northwest China. *Quat. Sci.* 23, 152–164.

Trenberth, K. E., Dai, A. G., Rasmussen, R. M., and Parsons, D. B. (2003). The changing character of precipitation. *Bull. Amer. Meteor. Soc.* 84, 1205–1217. doi: 10.1175/BAMS-84-9-1205

Utsumi, N., Seto, S., Kanae, S., Maeda, E. E., and Oki, T. (2011). Does higher surface temperature intensify extreme precipitation? *Geophys. Res. Lett.* 38:L16708. doi: 10.1029/2011GL048426

Wang, F., Yang, S., Higgins, W., Li, Q. P., and Zuo, Z. Y. (2014). Long-term changes in total and extreme precipitation over China and the United States and their links to oceanic–atmospheric features. *Int. J. Climatol.* 34, 286–302. doi: 10.1002/joc.3685

Wang, H. J., Chen, Y. N., and Chen, Z. S. (2013). Spatial distribution and temporal trends of mean precipitation and extremes in the arid region, northwest of China, during 1960-2010. *Hydrol. Process.* 27, 1807–1818. doi: 10.1002/hyp.9339

Wang, H. J., Chen, Y. N., Xun, S., Lai, D. M., Fan, Y. T., and Li, Z. (2012). Changes in daily climate extremes in the arid area of northwestern China. *Theor. Appl. Climatol.* 112, 15–28. doi: 10.1007/s00704-012-0698-7

Wang, Y. J., Zhou, B. T., Qin, D. H., Wu, J., Gao, R., and Song, L. C. (2017). Changes in mean and extreme temperature and precipitation over the arid region of northwestern China: observation and projection. *Adv. Atmos. Sci.* 34, 289–305. doi: 10.1007/s00376-016-6160-5

Xiao, C., Wu, P. L., Zhang, L. X., and Song, L. C. (2017). Robust increase in extreme summer precipitation intensity during the past four decades observed in China. *Sci. Rep.* 6:38506. doi: 10.1038/srep38506

Xie, S. P., Deser, C., Vecchi, G. A., Ma, J., Teng, H., and Wittenberg, A. T. (2010). Global warming pattern formation: sea surface temperature and rainfall. *J. Clim.* 23, 966–986. doi: 10.1175/2009JCLI3329.1

Xie, S. P., Hu, K. M., Hafner, J., Tokinaga, H., Du, Y., Huang, G., et al. (2009). Indian ocean capacitor effect on Indo-Western Pacific climate during the summer following El Niño. *J. Clim.* 22, 730–747. doi: 10.1175/2008JCLI2544.1

Xin, Y., Cui, C. X., Zhang, G. X., Zhang, X., Liu, X. W., and Sheng, X. Q. (2008). Spatial-temporal variation of precipitation for different grade and the events of extreme precipitation over Bole, Xinjiang. *J. Desert Res.* 28, 362–369.

Yan, P. W., Huang, D. Q., Zhu, J., Kuang, X. Y., and Huang, Y. (2019). The decadal shift of the long persistent precipitation over the northern part of China and the associated ocean conditions. *Int. J. Climatol.* 39, 3043–3056. doi: 10.1002/joc.6001

Yang, J. L., Liu, Q. Y., Xie, S. P., Liu, Z. Y., and Wu, L. X. (2007). Impact of the Indian Ocean SST basin mode on the Asian summer monsoon. *Geophys. Res. Lett.* 34:L02708. doi: 10.1029/2006GL028571

Yang, S., and Li, Q. X. (2014). Improvement in homogeneity analysis method and update of China precipitation data. *Adv. Clim. Chang. Res.* 10, 276–281. doi:

Yao, J. Q., Yang, Q., Chen, Y. N., Hu, W. F., Liu, Z. H., and Zhao, L. (2013). Climate change in arid areas of northwest China in past 50 years and its effects on the local ecological environment. *Chin. J. Ecol.* 32, 1283–1291.

Yao, J. Q., Yang, Q., Liu, Z. H., and Li, C. Z. (2015). Spatio-temporal change of precipitation in arid region of the northwest China. *Acta Ecol. Sin.* 35, 5846–5855. doi: 10.5846/stxb201310242567

Zhai, P. M., Liao, Z., Chen, Y., Yu, R., Yuan, Y. F., and Lu, H. (2017). A review on changes in precipitation persistence and phase under the background of global warming. *Acta Meteor. Sin.* 75, 527–538. (in Chinese)

Zhai, P. M., Zhang, X. B., Wan, H., and Pan, X. H. (2005). Trends in total precipitation and frequency of daily precipitation extremes over China. *J. Clim.* 18, 1096–1108. doi: 10.1175/JCLI-3318.1

Zhang, L. J., and Qian, Y. F. (2003). Annual distribution features of precipitation in China and their interannual variations. *Acta Meteor. Sin.* 17, 146–163.

Zhang, Q., Singh, V. P., Li, J. F., Jiang, F. Q., and Bai, Y. G. (2012). Spatio-temporal variations of precipitation extremes in Xinjiang, China. *J. Hydrol.* 434–435, 7–18. doi: 10.1016/j.jhydrol.2012.02.038.

Zhang, Q., Yao, Y. B., Li, Y. H., Huang, J. P., Ma, Z. G., Wang, Z. L., et al. (2020). Causes and changes of drought in China: research progress and prospects. *J. Meteor. Res.* 34, 460–481. doi: 10.1007/s13351-020-9829-8

Zhang, Q., Zhang, C. J., Bai, H. Z., Li, L., Sun, L. D., Liu, D. X., et al. (2010). New development of climate change in northwest China and its impact on arid environment. *J. Arid Meteorol.* 28, 1–7.

Zhao, Y., Huang, A. N., Zhou, Y., Huang, D. Q., Yang, Q., Ma, Y. F., et al. (2014). Impact of the middle and upper tropospheric cooling over central Asia on the summer precipitation in the Tarim Basin, China. *J. Clim.* 27, 4721–4732. doi: 10.1175/JCLI-D-13-00456.1

Zhao, Y., Yu, X. J., Yao, J. Q., Dong, X. X., and Li, H. J. (2018). The concurrent effects of the South Asian monsoon and the plateau monsoon over the Tibetan Plateau on summer rainfall in the Tarim Basin of China. *Int. J. Climatol.* 39, 74–88. doi: 10.1002/joc.5783

Zhao, Y., and Zhang, H. Q. (2015). Impacts of SST warming in tropical Indian ocean on CMIP5 model projected summer rainfall changes over central Asia. *Clim. Dyn.* 46, 3223–3238. doi: 10.1007/s00382-015-2765-0

Zhao, Y., Zhou, Y., Wang, M. Z., Huo, W., Huang, A. N., Yang, X. H., et al. (2017). Annual distributions and variations of dust weather occurrence over the Tarim Basin, China. *Theor. Appl. Climatol.* 132, 209–217. doi: 10.1007/s00704-017-2081-1

Zheng, X. Q., Li, X. J., Yang, Fan, Sang, C. Q., and Gu, R. (2014). Changing features of precipitation in Urumqi during 1961-2010. *J. Arid Land Resour. Environ.* 28, 178–184.

Zhou, B. T., Xu, Y., Wu, J., Dong, S. Y., and Shi, Y. (2015). Changes in temperature and precipitation extreme indices over China analysis of a high-resolution grid dataset. *Int. J. Climatol.* 36, 1051–1066. doi: 10.1002/joc.4400

Conflict of Interest: The authors declare that the research was conducted in the absence of any commercial or financial relationships that could be construed as a potential conflict of interest.

frontiers in Earth Science

ORIGINAL RESEARCH
published: 05 April 2021
doi: 10.3389/feart.2020.599785

Nonlinear Forced Change and Nonergodicity: The Case of ENSO-Indian Monsoon and Global Precipitation Teleconnections

Tamás Bódai[1,2]*, *Gábor Drótos*[3,4,5], *Kyung-Ja Ha*[1,6,7], *June-Yi Lee*[1,7] *and Eui-Seok Chung*[1,2]

[1]*Center for Climate Physics, Institute for Basic Science, Busan, South Korea,* [2]*Pusan National University, Busan, South Korea,* [3]*Instituto de Física Interdisciplinary Sistemas Complejos, CSIC-UIB, Palma de Mallorca, Spain,* [4]*MTA–ELTE Theoretical Physics Research Group, Eötvös University, Budapest, Hungary,* [5]*Institute for Theoretical Physics, Eötvös University, Budapest, Hungary,* [6]*BK21 School of Earth and Environmental System, Pusan National University, Busan, South Korea,* [7]*Research Center for Climate Sciences, Pusan National University, Busan, South Korea*

We study the forced response of the teleconnection between the El Niño–Southern Oscillation (ENSO) and the Indian summer monsoon (IM) in the Max Planck Institute Grand Ensemble, a set of Earth system ensemble simulations under historical and Representative Concentration Pathway (RCP) forcing. The forced response of the teleconnection, or a characteristic of it, is defined as the time dependence of a correlation coefficient evaluated over the ensemble. We consider the temporal variability of spatial averages and that with respect to dominant spatial modes in the sense of Maximal Covariance Analysis, Canonical Correlation Analysis and Empirical Orthogonal Function analysis across the ensemble. A further representation of the teleconnection that we define here takes the point of view of the predictability of the spatiotemporal variability of the Indian summer monsoon. We find that the strengthening of the ENSO-IM teleconnection is robustly or consistently featured in view of various teleconnection representations, whether sea surface temperature (SST) or sea level pressure (SLP) is used to characterize ENSO, and both in the historical period and under the RCP8.5 forcing scenario. It is found to be associated dominantly with the principal mode of ENSO variability. Concerning representations that involve an autonomous characterisation of the Pacific, in terms of a linear regression model, the main contributor to the strengthening is the regression coefficient, which can outcompete even a declining ENSO variability when it is represented by SLP. We also find that the forced change of the teleconnection is typically nonlinear by 1) formally rejecting the hypothesis that ergodicity holds, i.e., that expected values of temporal correlation coefficients with respect to the ensemble equal the ensemble-wise correlation coefficient itself, and also showing that 2) the trivial contributions of the forced changes in means and standard deviations are insignificant here. We also provide, in terms of the test statistics, global maps of the degree of nonlinearity/nonergodicity of the forced change of the teleconnection between local precipitation and ENSO.

Keywords: ENSO-Indian monsoon teleconnection, forced response, ensemble, ergodicity, snapshot attractor, maximum covariance analysis, canonical correclation analysis

Edited by:
Wen Chen,
Institute of Atmospheric Physics (CAS), China

Reviewed by:
Debashis Nath,
Sun Yat-sen University, China
Eduardo Zorita,
Helmholtz Centre for Materials and Coastal Research (HZG), Germany

***Correspondence:**
Tamás Bódai
bodai@pusan.ac.kr

Specialty section:
This article was submitted to Atmospheric Science, a section of the journal Frontiers in Earth Science

Received: *28 August 2020*
Accepted: *22 December 2020*
Published: *05 April 2021*

Citation:
Bódai T, Drótos G, Ha K-J, Lee J-Y and Chung E-S (2021) Nonlinear Forced Change and Nonergodicity: The Case of ENSO-Indian Monsoon and Global Precipitation Teleconnections. Front. Earth Sci. 8:599785. doi: 10.3389/feart.2020.599785

1 INTRODUCTION

ENSO teleconnections are widely studied, but their changes resulting from external forcing, such as an increasing concentration of greenhouse gases, remain to be further explored and understood. Power and Delage (2018) provide a multi-model assessment of ENSO-precipitation teleconnection changes based on the fifth phase of the Coupled Model Intercomparison Project (CMIP5) archive. They consider, in particular, ENSO-driven precipitation anomalies in tropical regions around the globe, and assess them jointly with changes of mean precipitation. Haszpra et al. (2020a) have evaluated only the trend in the strength of ENSO-precipitation teleconnection, however, not in a multimodel ensemble but the so-called "single model initial condition large ensemble" (SMILE) CESM1-LE (Kay et al., 2015). Working with a SMILE has the advantages that the response to forcing is correctly represented in that model at least (Bódai and Tél, 2012; Drótos et al., 2015; Tél et al., 2019), and seeking a physical interpretation of changes is not faced with confusion at the outset, even if the physics depicted in that model is inaccurate or unrealistic.

The forced response is the time evolution of some ensemble-wise statistics, or, most generically, that of the probability measure carried by the climate snapshot attractor (Bódai and Tél, 2012; Drótos et al., 2015; Tél et al., 2019). The ensemble-wise statistics evaluated over the converged ensemble (Drótos et al., 2017) is in a one-to-one correspondence with the external forcing of the nonautonomous dynamical system, hence the term 'forced response.' For specific observables, this translates to the time evolution of any statistics evaluated with respect to an ensemble, e.g., that of mean values, standard deviations, correlation coefficients, empirical orthogonal functions (EOFs). Note that quantifiers of internal variability exhibit a forced response just as well as quantifiers of the "mean state." The ensemble must have converged to the time-evolving snapshot attractor (Drótos et al., 2017); in the terminology of climate research, this means the correct representation of the full ensemble spread along with the absence of any drift. External forcing is defined as an explicit dependence on time of any parameter of the system (Ghil and Lucarini, 2020), which in historical and RCP runs corresponds to changes in the atmospheric composition (including greenhouse gases, anthropogenic aerosols and volcanic aerosols), land use, and solar activity (Meinshausen et al., 2011).

Without convergence, or considering a single realization, which may even correspond to observations, the state depends also on initial conditions, so that forced changes cannot be precisely disentangled from changes brought about by internal variability. In an attempt of doing this nevertheless, concerning a single realization, the standard practice is that a trend, linear or not (Franzke, 2014), is simply identified as a forced change, before possibly "anomalies," i.e., (what is assumed to be) the internal variability is analyzed. Identifying the principal component (PC) of the leading or first empirical orthogonal function (EOF1) (Storch and Zwiers, 1999) obtained without detrending with the forced response (Kim and Ha, 2015; Pandey et al., 2020) is still somewhat arbitrary. It certainly leads to biases (Drótos et al., 2016). Yet, even with SMILEs available, it is very common to see that authors evaluate temporal statistics first–unnecessarily involving a subjective factor—and ensemble statistics afterward (Vega-Westhoff and Sriver, 2017; Carréric et al., 2020). The biases of all these approaches are certainly controlled by the magnitude of the climate change signal relative to the intensity of internal variability—a kind of signal-to-noise ratio. Computing the PC1 of EOF1 without detrending, as mentioned just above, is in fact meant to maximize the signal at least, and the EOF1 is referred to (Santer et al., 2019) as a "fingerprint" of the forced change—the spatial pattern that is supposed to be distorted by internal variability, in any single realization, the least. See (Timmermann, 1999) which is concerned rather with the minimization of the "noise."

It is not pertinent to talk about "advantages" of temporal or ensemble methods over one another, because no situation arises when we need to decide between them. When an ensemble is available, the correct, conceptually sound ensemble method is to be applied if the forced response (including that of internal variability) is concerned. However, certainly we can make statements only about the given model.[1] Therefore, we should speak only about limitations in the respective situations of analyzing observational or modeled ensemble data.

We should note that the finite-size estimators of some statistics of basic interest are not generally unbiased—an example to appear in this work—and there might not be a universally applicable correction to the estimator to make it unbiased [unlike, e.g., the fortunate cases of the central moments (Heffernan, 1997)]. Therefore, even an ensemble-wise approach could suffer from biases in practice with the ensemble size being always finite. Some extreme value statistics are likely other examples.

Concerning teleconnections, in particular, the forced response can be identified as the time evolution of the ensemble-wise Pearson correlation coefficient (Herein et al., 2016; Yettella et al., 2018) (in a simple linear approach) between some quantities representing anomalies. The anomaly can correspond to a simple spatial (mean of a temporal) mean (Bódai et al., 2020b), but also the PC of an EOF concerning variability across the ensemble, called a snapshot EOF (SEOF) (Haszpra et al., 2020c). Haszpra et al. (2020a) take the latter approach; however, this can be extended to obtaining anomalies observing the "mutual variability," e.g., in the sense of Maximal Covariance Analysis (MCA) (Storch and Zwiers, 1999) or Canonical Correlation Analysis (CCA) (Storch and Zwiers, 1999; Härdle and Simar, 2007). That is, with an interest in a teleconnection and its forced response, MCA and CCA—just like EOF analysis—can also be pursued concerning the variability across the ensemble, whereby we can refer to these methods as SMCA and SCCA. This is perhaps best suited to teleconnection analyses concerning two extended, possibly disconnected, regions. See an application of SMCA to studying the forced change of the coupling of JJA 200 hPa geopotential height and September sea ice concentration in (Haszpra et al., 2020b; Topál et al., 2020).

An other important example would be the relationship of the summer monsoon precipitation on the Indian subcontinent with

---

[1] It is, therefore, instructive to study a multimodel ensemble of SMILEs.

the ENSO phenomenon which extends over the whole of the Equatorial Pacific (Wang, 2006; Mishra et al., 2012; Wang et al., 2015). In a previous publication (Bódai et al., 2020b) we examined the forced response of the ENSO-Indian monsoon teleconnection in the Max Planck Institute Grand Ensemble (MPI-GE) (Maher et al., 2019) representing the monsoon by the average JJAS precipitation over India and the ENSO by either the gridpoint- and SLP-based SOI (Southern Oscillation Index), or the areal mean of the SST in some extended area in the Equatorial Pacific. Standard choices for the latter are the Niño3, Niño4, and Niño3.4 regions. For the first time we established, via a formal hypothesis test, that standard representations of the teleconnection[2] strengthened in this model, both in the historical period and under the high-emission RCP8.5 forcing scenario, although not necessarily monotonically. In fact, using the SOI it was the historical period only when an increase could be detected, and, using the Niño3 index, it was rather the RCP8.5 scenario under which an increase could be detected. This raises the question whether the discrepancy is down more to 1) the physical difference between the SOI and Niño3 indices, or 2) rather that–one based on two distant gridpoints while the other on a limited region of the Equatorial Pacific–they "take somewhat different slices" of the whole ENSO phenomenon. This question is especially relevant when spatial characteristics of ENSO may also have a forced response besides the amplitude. In fact, using the Niño3.4 index, instead of Niño3, the result is closer to that using the SOI or the so-called box-SOI. With all these representations, one is able to detect the same nonmonotonicity: a temporary weakening around the turn of the millennium. In addition, both with Niño3.4 and the box-SOI changes are detected both under the historical and scenario forcing. On the one hand (I), this seems to rule out that using SST versus SLP makes much difference. We will see below that this is actually not precisely the case. On the other hand (II), it is still a question whether spatial characteristics of ENSO (in terms of SEOFs) or the whole teleconnection (in terms of SMCA or SCCA) would also change, or only the variance as reflected in the magnitudes of the PCs belonging to either of the said instantaneous (snapshot) spatial modes. These are the two basic questions that we set out here to investigate.

Furthermore, this study identifies, in terms of a regression model, three controlling factors driving the forced change of the ENSO-IM teleconnection strength. These are the ENSO variability, the coupling (i.e., the regression coefficient), and the intensity of other influences—which include but are not restricted to internal influences from the IM region and can be viewed as noise. We find that the changes of the ENSO-IM teleconnection are not driven only or dominantly by the change of ENSO variability. Nevertheless, it imprints its nonlinearity onto the teleconnection change, which might be an important source of biases (besides using a biased estimator). In particular, any nonlinearity prompts that the system should be nonergodic[3] with respect to correlations, i.e., biases should exist (Drótos et al., 2016) in the temporal correlation coefficient evaluated in, say, multi-decadal time windows. Such a bias is something to bear in mind besides the ample statistical fluctuations of finite-size statistics even under a stationary climate (Bódai et al., 2020b). Nonlinearity is implied in our case by a nonmonotonic change in the ENSO variability: after a seemingly monotonic change, a decline follows in the second half of the 21st c. under RCP8.5.[4] Given that the ensemble size is finite and not so large from the point of view of teleconnections, we develop here a statistical test whereby we can detect nonergodicity, and, subsequently, map out regions of the world where such a nonergodicity can be detected in the MPI-GE in the context of the relationship of local precipitation with ENSO.

The rest of the paper is organized as follows. In **Section 2** we provide details about our methodology of analyzing the forced response of teleconnections, such as the way we pursue EOF, MCA, CCA, the definitions of a host of teleconnection representations, as well as the idea of decomposing the change of the teleconnection strength in terms of a simple regression model. In **Section 3** we provide results both on spatial aspects of the forced change of the ENSO-IM teleconnections and those concerning magnitudes. **Section 4** provides a comparison of the MPI-ESM with observational and reanalysis data. In **Section 5** we outline our method of detecting nonergodicity and map out the world with respect to the degree of nonergodicity concerning the synoptic relationship of the local JJA precipitation with ENSO. In **Section 6** we discuss and summarize our results.

2 DATA AND METHODS

2.1 Data

The analysis is restricted to the historical and RCP8.5 simulations of the Max Planck Institute Grand Ensemble (MPI-GE, Maher et al., 2019), which is a collection of initial-condition ensemble simulations of the Max Planck Institute Earth System Model (MPI-ESM) under various forcing. The MPI-ESM is a fully coupled Earth system model, and its version 1.1.00p2, between phases 5 and 6 of the CMIP, was used to generate the MPI-GE from initial conditions that sample a long pre-industrial control run. See Maher et al. (2019) for further details. We make use of the same 63 of the 100 ensemble members as done in (Bódai et al., 2020b), due to concerns that the discarded members have not converged to the climate attractor of the model (Drótos et al., 2017).

To characterize the ENSO we make use of the 2D fields of either the Sea Level Pressure (SLP) or the Sea Surface Temperature (SST). The Indian Summer Monsoon Rain (ISMR) was calculated from the total (convective and large-scale) precipitation rate. The variable

---

[2] We do not regard the co-evolution of the ensemble means of e.g., Niño3 and the Indian summer monsoon rain to be part of the teleconnection, unlike Pandey et al. (2020), as these responses could be largely unrelated. Yet, using an infinite ensemble, the rank correlation coefficient with respect to the temporal variability, i.e., evolution, of the ensemble means is trivially 1. The prediction or projection of the Indian summer monsoon rain does not even need to rely on the Equatorial Pacific SST, but could be just facilitated by e.g., some extrapolation of the observed response of its own. That is, if there was reason to believe that we have a reliable estimate of the forced response.

[3] We emphasize that the bias that defines "nonergodicity" is based on the ideal ensemble mean, not a sample mean for a finite-size ensemble.

[4] Such a feature is absent in the CESM1-LE (Haszpra et al., 2020a).

codes for SLP, SST and total precipitation rate are 134, 12 and 4, respectively. Monthly mean SLP is accessible publicly at `https://esgf-data.dkrz.de/projects/mpi-ge/`under variable name "psl." The SST can be derived from the top layer of the 3D potential temperature field, whose variable is "thetao." Alternatively, one can use the surface air temperature variable, as e.g., the monthly mean approximates the SST very well over the ocean. Instead of the total precipitation rate [km/s], one can use the precipitation flux [kg/s/m^2], whose variable name is "pr."

2.2 Representations of the ENSO-IM Teleconnection

The scalar quantity of the ISMR, averaged over JJAS and over India, is the same as that calculated in (Bódai et al., 2020b), in order to secure a correspondence with the so-called AISMR rain gauge data set (Parthasarathy et al., 1994) (excluding some states of India; see their Figure 1). We will refer to the model ISMR corresponding to the observational AISMR region also as AISMR. Scalar quantities to represent ENSO variability are also the same as in (Bódai et al., 2020b), as follows. 1. Average SST in the standard Niño3 region represented by the box (5°S, 5°N, 210°E, 270°E); 2. average SST in the standard Niño3.4 region (5°S, 5°N, 190°E, 240°E); 3. SLP difference, $p_{\text{diff}} = p_{\text{Tahiti}} - p_{\text{Darwin}}$, between the closest gridpoints to Tahiti and Darwin; 4. the difference of the average SLPs in the boxes (5°S, 5°N, 80°E, 160°E) and (5°S, 5°N, 200°E, 280°E). We will refer to these quantities as the 1. Niño3 index, the 2. Niño3.4 index, the 3. SOI and the 4. box-SOI, respectively (SOI being short for the Southern Oscillation Index). See a discussion on them in Section 4.a of (Bódai et al., 2020b).

We investigate the correlation of the "near-synoptic" JJA mean of any of Niño3, Niño3.4, SOI and box-SOI with the JJAS AISMR. The correlation coefficient r is evaluated across the ensemble, as done in (Bódai et al., 2020b), which results in time series with one data point from each year. These time series are representations of the forced response of the ENSO-IM teleconnection. However, the finite ensemble size entails a relatively large sampling error, and the corresponding fluctuations in the estimated signal, $\hat{r}(t)$, badly mask the true forced response signal, $r(t)$. Therefore, in the first round, we do not aspire to draw conclusions about the shape of $r(t)$, but only to detect if there is any monotonic time dependence in a given time period. For this, we employ the Mann–Kendall test (Mann, 1945) in the same way as done in (Bódai et al., 2020b), aiming to reject the hypothesis of stationarity against the alternative hypothesis of a monotonic trend masked by serially uncorrelated stationary noise. In fact, the Pearson correlation coefficient, or rather its Fisher-transform, is likely an exceptional quantity in that such a test of nonstationarity is rather straightforward to apply to it[5]. To study some characteristics of the time dependence, we take all possible subintervals of the simulation period, and apply the hypothesis test separately for each of them (Bódai et al., 2020b).

We will evaluate correlation coefficients of the AISMR also with the PCs belonging to EOFs. PCs and EOFs can be also defined and constructed with respect to (wrt.) the ensemble, as a "snapshot"[6], hence the name SEOF, as proposed by Haszpra et al. (2020a,c).[7] The SEOFs concerning SST are evaluated here wrt. the Equatorial Pacific box (30°S, 30°N, 150°E, 295°E), and, concerning SLP, wrt. the narrower box (10°S, 10°N, 150°E, 295°E). Traditional EOFs are decomposing spatio-temporal variability as a sum of independent standing waves, i.e., spatial patterns, orthogonal in the N-dimensional gridpoint space, modulated by arbitrary but uncorrelated temporal signals, the PCs. Snapshot EOFs are computed in the same way but different time steps are replaced by different ensemble members (i.e., realizations of the dynamics).

Besides the requirement of ("spatial") orthogonality, each new EOF is defined such that the corresponding PC has the largest possible variance, leading to an eigen-problem. The variances of the PCs σ_n^2, $n = 1,...,N$, are singular values of the covariance matrix and belong to the EOFs being the corresponding singular vectors[8]. We find them by using Matlab's `svd` as done in (Björnsson and Venegas, 1997). The ordering of the singular values wrt. magnitude, $\sigma_N^2 < \ldots < \sigma_1^2$, provides a natural ordering of the EOFs, which are denoted as EOF1, EOF2, etc., and likewise we write PC1, PC2, etc. PCn is said to explain a fraction of the total variance:

$$\text{FVE} = \sigma_n^2 \bigg/ \sum_{n=1}^{N} \sigma_n^2. \tag{1}$$

PC1s of the SLP and the SST fields in the same box have more in common than, e.g., Niño3 and SOI, because Niño3 and SOI do not derive from a mathematical definition of dominance[9]; and one could think that more similar representations yield more similar results[10]. Therefore, firstly, we wish to see if we can establish a robust representation of the ENSO-IM teleconnection by having possibly a better match between the forced response signals belonging to the SLP and SST than between those using the classic indices 1.-4. Secondly, the

---

[5] The case of the standard deviation, a statistic of basic interest giving a primary representation of internal variability, is already nontrivial, as nonstationarity would imply heteroscedasticity, in which case the reliable detection of nonstationarity is not straightforward. Assuming homoscedasticity wrongly, the estimates of standard errors could be either negatively or positively biased, and, therefore, a type II error can be made: not rejecting stationarity at a certain confidence level when the process is actually nonstationary.

[6] The quotation marks are used because the concept of a "snapshot" makes the best sense concerning a time-continuous evolution, whereas here we consider the discrete-time annual progression of a seasonal mean.

[7] Ensemble-wise EOFs, SEOFs, were used earlier in the context of probabilistic ensemble forecasting in e.g., (Zheng et al., 2013; Zheng et al., 2017; Zheng et al., 2019), in which case the concern was certainly not the forced response.

[8] It is also common to redefine PCs to be normalized and EOFs to be multiplied by the corresponding standard deviations.

[9] Although, the rationale behind defining simple indices is such that we want to work with a simple-to-compute quantity (e.g., an areal average or difference between two locations) that correlates very strongly with the dominant variability in terms of EOFs, which latter can be seen to represent a more natural method of decomposing the variability of a field.

[10] If the same wider box is used with the SLP as with the SST, the "weight" of the EOF1 is concentrated on parts of the perimeter of the box. Despite the dissimilarity of the EOF1s with the SLP in the two different boxes, the time dependence of the corresponding correlation coefficients r(PC1,AISMR) are actually very similar.

teleconnection strength can possibly change because of a shift in the "center of action" of the ENSO phenomenon, something that can have a different impact on the teleconnection representations given by one of indices 1.-4. and the AISMR. Thirdly, including higher EOF modes can reveal more predictive power of the full field compared with a simple index alone. In this regard we are interested in whether the correlations to do with the higher modes are more susceptible to the anthropogenic forcing. We will only show results for the second modes. Traditionally, only the first two or three EOFs are regarded to describe ENSO[11], and we should distinguish between ENSO-related and full Pacific variability, but EOFs beyond the third will be found to have negligible importance, we will thus usually drop this distinction.

The pursual of the listed three points of inquiry can be supported by MCA and CCA. MCA and CCA are similar to the EOF analysis, but consider two fields, and find paired modes recursively whose paired PCs are respectively uncorrelated with the readily determined PCs belonging to the other modes of the same kind (or "side") and have the maximal covariance and correlation, respectively, between them[12]. Note that these modes do not capture in general the locally dominant modes of variability in the given regions (which may be represented e.g., by EOFs); this is the situation only in the uninteresting case: for fields that are not related at all. Instead, they highlight parts of the variability in the two regions that are interrelated the most. These are not additive "parts" of the variability for CCA though; only the MCA modes are independent being spatially orthogonal, but not the CCA modes. By comparing these patterns and their changes to those locally defined in the given regions and thus characterizing ENSO and the IM in our case, we might possibly obtain some hints about how much spatial rearrangements of the relevant areas contribute to changes in the teleconnection strength, but confirmations by further analyses would be necessary.

Similarly to ENSO, we may carry out an EOF analysis on the Indian precipitation field, as represented by M gridpoints, to identify dominant modes of variability from a local point of view, for which we can use the box of (5°S, 40°N, 65°E, 100°E). However, an arbitrarily selected box may not provide a good representation. In fact, the comparison of the time dependence of correlation coefficients belonging to teleconnection representations or characteristics involving the scalar AISMR, on the one hand, and involving the full spatio-temporal monsoon variability, on the other hand, would make most sense if the domain for the latter were the same as for AISMR. We make this choice for our main exposition, and provide the results with the choice of the box given above for comparison in the **Supplementary Material**, including those obtained by replacing AISMR by the box summer precipitation (BOXSR).

CCA yields the correlation coefficients between the paired PCs by definition; as for the MCA, besides the covariance of the paired PCs yielded by the definition, the correlation coefficient is straightforward to compute. The correlations of these PCs are not analogous to those between the AISMR and the PCs of EOFs of ENSO. We anticipate that the SMCA and SCCA lead to higher correlations than the SEOF analysis, stemming from their very definition. In this regard, as the fourth point of inquiry, we want to see if higher correlations are more susceptible to anthropogenic forcing. A comparison of the correlation coefficients yielded by the MCA or CCA can be made with those between the PCs of the EOFs of the same order on the two sides. Although, in contrast with MCA and CCA, PCs mismatched wrt. the EOF order will in general feature a nonzero r.

On the side where $M > N$, the MCA modes form an orthogonal basis. The covariance matrix in this basis is diagonal, with entries conveniently denoted by σ_m^2, $m = 1,...,M$, and, therefore, MCA modes can also be associated with a fraction of variance explained, FVE, according to **Eq. 1**. Because of the nonorthogonality of the CCA modes, the fraction of variability that each of them explains would not sum up to 1. Nevertheless, we can still evaluate the FVE wrt. to the "target" side of the IM in the context of CCA if we simply retain the areal mean scalar AISMR to represent that side. This way, we have only a single nontrivial Equatorial Pacific SST/SLP CCA mode. We consider this as a further representation of the ENSO- or Equatorial Pacific-IM teleconnection.

From the point of view of predictability, in view of the regression model

$$\Psi = a\Phi + \xi, \tag{2}$$

where Φ, Ψ and ξ represent the ENSO (or ENSO-related) signal, the IM (or IM-related) signal and random noise, the square of the correlation coefficient r^2 gives in fact the fraction of the variance of the predictand Ψ that the predictor Φ can deterministically predict ("explain" in what follows), since

$$r = \frac{a\sigma_\Phi}{\sigma_\Psi}. \tag{3}$$

In the case of multiple predictors, $\Phi_1, \ldots, \Phi_N$, in terms of a multi-dimensional linear regression model, the square of the coefficient of multiple correlation or determination (Storch and Zwiers, 1999)

$$R^2 = \mathbf{r}^{\mathrm{T}}\mathbf{C}_{\Phi\Phi}^{-1}\mathbf{r},$$

$$\mathbf{r} = [r(\Phi_1, \Psi), \ldots, r(\Phi_N, \Psi)]^{\mathrm{T}}, \qquad \mathbf{C}_{\Phi\Phi} = [C_{\Phi\Phi,nn'}] = [r(\Phi_n, \Phi_{n'})],$$

can likewise quantify predictability, and a teleconnection strength (by the same token as with the one-dimensional case). When the predictors are uncorrelated, $\mathbf{C}_{\Phi\Phi}^{-1}$ is the identity matrix, and, so,

$$R^2 = \mathbf{r}^2 = \sum_{n=1}^{N} r^2(\Phi_n, \Psi). \tag{4}$$

This concept can be further generalized considering multiple scalar predictands, $\Psi_1, \ldots, \Psi_M$, when they provide a decomposition of the spatio-temporal variability of the ultimate predictand. Such a decomposition of the IM can be given by the orthogonal basis of the EOFs or the MCA modes (if $M < N$) on the IM side (but not the CCA modes) and the corresponding PCs. In contrast, on the side of the predictor, which is the ENSO or Equatorial Pacific in our case,

---

[11] Strictly speaking, each mode should be tested if it can be distinguished from noise and if it features characteristics associated with ENSO.

[12] As for the MCA, maximizing the unexplained covariance implies that the PCs are uncorrelated as reflected by the SVD decomposition.

the independence of the scalar predictors Φ_n is not required. Concerning the same predictors Φ_n, one can associate a coefficient R_m of multiple correlation to each independent IM mode. As each IM mode explains only a fraction of the total variance (**Eq. 1**), this factor needs to multiply R_m^2 to provide the fraction of the spatio-temporal IM variability explained (FSTVE) by the predictors Φ_n via that one IM mode. Thanks to the independence of these modes, by analogy with **Eq. 4**, these fractions can be summed up over the modes to give the total FSTVE:

$$\mathrm{TFSTVE} = \frac{\sum_{m=1}^{M} \sigma_m^2 R_m^2}{\sum_{m=1}^{M} \sigma_m^2}. \tag{5}$$

In the natural case when Φ_n are the PCs belonging to the ENSO-side MCA modes, which is our choice for calculations, R_m reduces to be just $r(\Phi_m, \Psi_n)$, $n{=}m$. One can take the square root of TFSTVE in order to have something comparable to the correlation coefficient r associated with the one-dimensional setting of e.g., spatial averages. Nevertheless, they are not comparable from the point of view that the same fraction of AISMR variability explained as the TFSTVE provides much less information given that it overlooks the spatial part of the variability. Furthermore, concerning the detection of nonstationarity potentially by the MK-test, it is not clear to us whether the Fisher transform can be applied to TFSTVE to produce residuals described by independent identically distributed random variables—a requirement by the MK-test—the same way as it does in the case of the Pearson correlation coefficient (Fisher, 1915; Bódai et al., 2020b). We pursue this analysis in the belief that it does to a reasonable approximation.

We carry out the MCA and CCA over the same domains as the EOF analyses, whether it is the AISMR domain or a box, by applying Matlab's `svd` and `canoncorr`, respectively. Before pursuing MCA and EOF analysis, we regrid the SST data using Matlab's `griddata`, mapping the irregular ocean grid onto a regular one of 2° latitude-longitude resolution. With this, a weighting by the grid cell area as proposed by Baldwin et al. (2009) is straightforward (although it makes hardly any difference in these tropical regions). Instead of the complete field, the SCCA is performed on the PCs corresponding to the first 10 SEOFs, since it is ill-defined on the full fields as a result of the number of gridpoints on any considered domain being larger than the number of ensemble members used. MCA could also be restricted to the first 10 SEOFs, presumably without much influence on the results. In fact, it turns out that on the Equatorial Pacific side, as few as 3 EOFs capture most of the variance (see **Supplementary Figures S2, S3**). Therefore, we can regard the TFSTVE to represent the ENSO-IM teleconnection even if we are prepared to regard only the first 3 EOFs to constitute the ENSO phenomenon. On the other side, 10 EOFs are also sufficient to represent the IM variability. We will speak about SCCA modes as the linear combination of the SEOF modes in terms of the coefficients defining the so-called canonical variables. Indeed, thanks to the orthogonality of the SEOFs, the projection of the full fields onto these modes yields the SCCA PCs whose correlations were maximized by the SCCA.

The finite size of the data set (the number of the ensemble members, or the length of the time series if evaluation is carried out wrt. time) introduces errors in the estimates of the spatial modes of the various kinds mentioned. The relative errors are increasing with the order of the mode (North et al., 1982; Quadrelli et al., 2005). In our experience, these errors seem to lead to a negative bias in estimating r involving some EOF (e.g., r(PC1, AISMR) or r(PC1, PC1)), but to a positive bias of r to do with MCA or CCA. In fact, with a high enough dimensionality of the spatial representation, given the number of ensemble members fixed to be 63, $r = 1$ can result for the first CCA mode, or even for a number of leading CCA modes. (We can reproduce this even with completely unrelated fields both characterized by spatially and temporally uncorrelated noise.)

The biases of r can be reduced by pooling data within a relatively short time window. We use a moving window of a length of 11 years. The anomaly for each data point in such a time window could be calculated by subtracting the combined temporal and ensemble mean (i.e., the mean over all the pooled data points). Alternatively, which is what we choose to rather do, one can pool data for determining only the modes more accurately. Such a smoothed MCA or CCA mode (or even an EOF) calculated from the pooled anomaly data as described is ordered to the middle of the time window. The correlation coefficient r is then estimated wrt. ensemble-wise variability only, from the subset of the pooled anomaly data belonging only to the mid-window single year. One can go further, as we do, by leaving out the mid-window data for the first part of this process of determining smoothed modes. This should lead to a negative bias, just like with r(PC1, AISMR), etc. We will refer to these estimates of r as "conservative." From the point of view of detecting nonstationarity, however, our conclusions rely on the assumption that the bias depends only on the ensemble size, but not e.g., the true value of r. As for the simple representations involving indices like Niño3, one can also apply pooling to determine the ensemble means, and, so, anomalies, more precisely.

The statistical errors of the numerically determined modes can pose a problem in studying the forced response of the modes, however. It is so because the `svd` algorithm returns the mode estimates with an arbitrary orientation. Before looking at the year-to-year time dependence, or possibly taking temporal means in time windows to compare, one needs to make sure that all the mode estimates corresponding to different years have the same orientation. We do this by picking a reference year and flip modes in other years if they do not have the same orientation as the one in the reference year. We check whether they do by checking the sign of the cross-correlation with the mode in the reference year. However, if modes are corrupted too much, then we are in fact checking the agreement of the orientation of mostly the random components, not those of the underlying true modes. In our experience, mistakes of wrongly flipping modes are made already in the case of the second modes. Nevertheless, the fewer the mistakes, the less error is made in determining the forced response. Furthermore, this problem should affect the smoothed modes to a lesser degree.

In conclusion, to represent the teleconnection, we shall use r of Niño3–AISMR, Niño3.4–AISMR, CCA-AISMR, R, and TFSTVE. We provide results separately for the constituents of R including r

of PC1-AISMR and PC2-AISMR in association with EOFs on the Pacific side. Furthermore, we show in the **Supplementary Material** that r of CCA-AISMR and R are one and the same thing. We shall not consider as a representation any individual $r(\mathrm{PC}n,\mathrm{PC}n)$ for EOF, MCA, CCA, but the latter quantities also characterize some aspect of the teleconnection and will support our analysis.

We will explain some findings about these r's by comparing spatial patterns of different modes. Nevertheless, we show in the **Supplementary Material** that forced changes of spatial patterns do not necessarily have robust implications for the change of the teleconnection strength: r of CCA-AISMR may be dominated by r of EOF1–AISMR even if the spatial pattern of CCA-AISMR in the Pacific has a large weight from EOFi, $i > 1$, thanks to the small variability that is associated with that given EOFi compared to EOF1. This also means that we may not want to refer to CCA-AISMR as a representation of the ENSO–IM teleconnection from the point of view of the weights of Pacific EOFs in this CCA mode, but only as a representation of an Equatorial Pacific–IM teleconnection, whereas we may do regarding the weight of r's associated with those EOFs. As a further point of reference, we shall also consider the map displaying the correlation coefficient of the precipitation at each grid point with EOF1 or EOF2 on the Pacific side.

2.3 Decomposition of the Forced Change of the Teleconnection Strength

Once the $r(t)$ signal is established, we can ask about the origin of the observed time dependence. Instead of trying to find physical mechanisms, here we pursue only a statistical attribution. We consider the linear regression model (**Eq. 2**) which underpins the correlation coefficient r. In this model, we can attribute changes in r to three factors, via considering the relationship

$$r = \frac{1}{\sqrt{1 + \left((\sigma_\xi/\mathrm{a})/\sigma_\Phi\right)^2}}. \tag{6}$$

These three factors are:

- The ENSO variability $\sigma_\Phi = \mathrm{std}[\Phi]$;
- The ENSO-IM coupling a, being the regression coefficient;
- The noise strength $\sigma_\xi = \mathrm{std}[\xi]$.

Note that, like r, both σ_Φ and σ_ξ are defined in terms of the variability wrt. the ensemble, for every year separately. That is, like $r(t)$, we have time series $\sigma_\Phi(t)$ and $\sigma_\xi(t)$, and also $a(t)$. Attribution is then based on a simple comparison of these time series. For instance, we can say that a change in $r(t)$ is due to a change in $\sigma_\Phi(t)$ in a time period if no change is seen in $a(t)$ and $\sigma_\xi(t)$ in the given time period. Note that we can already say the same if σ_ξ/a shows no change. In fact, what is outlined in this example has been suggested to us as a plausible explanation: "perhaps the strengthening of the ENSO-IM teleconnection is due to an increasing ENSO variability in this model." Although apriori this possibility is hard to exclude, we note that it would be rather specific and could be seen accidental to the ENSO-IM teleconnection given that ENSO-precipitation teleconnections can either strengthen or weaken in different places on Earth (Power and Delage, 2018). This is shown in Figure 2 of (Haszpra et al., 2020a) for the CESM1-LE; and the MPI-GE dataset shows a rather similar picture as seen in our **Supplementary Figure S1** in the **Supplementary Material**.

Concerning the numerical evaluation of the quantities in question, the first step is to evaluate σ_Φ directly, i.e., we compute the standard deviation of Φ over the ensemble. Then we compute σ_ξ/a by inverting **Eq. 6**, as r is already available. Note that with this calculation, the sign of a remains undetermined; however, it can be easily recovered being the same as that of r. Anticipating that σ_ξ/a is not constant in time, we can evaluate a by, first, directly evaluating the IM variability σ_Ψ, and, subsequently, using the textbook equation **Eq. 3**. (We could, of course, evaluate a directly by linear regression, but calculating the standard deviation is easier, and we already have r on hand.) In turn, having now also a on hand, σ_ξ can be obtained by multiplying σ_ξ/a by a.

For a quantitative assessment of which factor dominates the change in r out of the ENSO-related variability (σ_Φ) and the combination of the noise strength and the coupling (σ_ξ/a) in a time period $[t_1, t_2]$, we set up a simplified framework. We assume that the ENSO-related variability increases; in particular, it increases as $\sigma_\Phi(t_2) = \beta\sigma_\Phi(t_1)$, $\beta > 1$, and that we also have a decrease $\sigma_\xi(t_2)/a(t_2) = \alpha\sigma_\xi(t_1)/a(t_1)$, $\alpha < 1$. From **Eq. 6** we see that $\alpha\beta > 1$ would mean that the increase in ENSO-related variability has a larger effect on the increase of $r(t)$ than the decrease in σ_ξ/a. Given the very noisy time series, the appropriate approach would be a statistical test attempting to reject the null hypothesis of $\alpha\beta = 1$. However, it is not clear to us how this can be done. As for a preliminary analysis, we simply estimate $\alpha\beta$ by estimating α and β separately before taking their product. E.g., α is estimated from a least-squares linear fit of the time series of $\sigma_\xi(t)/a(t)$ in a time period $[t_1, t_2]$, obtaining the ordinates at the beginning and end of the period, $\sigma_\xi(t_1)/a(t_1)$ and $\sigma_\xi(t_2)/a(t_2)$, respectively. β is estimated similarly from the time series of $\sigma_\Phi(t)$. We estimate $\alpha\beta$ in all possible time periods $[t_1, t_2]$, similarly as done with the MK-test. Note that the results are not robust in situations when r is near zero and estimates change sign with time. This is the case typically already with PC2's, as well as with the use of BOXSR instead of AISMR, and, so, we provide results only for unaffected representations/characteristics. When r is small, so is a, resulting occasionally in large spikes of $\sigma_\xi(t)/a(t)$, therefore, we will instead plot the reciprocal $a(t)/\sigma_\xi(t)$.

Note that such an attribution proposed here is not generically applicable to representations or characteristics of the teleconnection based on MCA and CCA. This is because the signal $\sigma_\Phi(t)$ typically cannot be attributed solely to the ENSO/Equatorial Pacific when the associated mode also changes, which latter is determined by the mutual relationship of the ENSO and IM, not just the ENSO alone.

3 THE FORCED RESPONSE OF THE ENSO-IM TELECONNECTION

3.1 Spatial Aspects

We start by inspecting spatial characteristics of the ENSO and IM variability by means of SEOFs and by comparing them to those corresponding to largest covariances and correlations defined through SMCA and SCCA whereby on the IM side the domain of

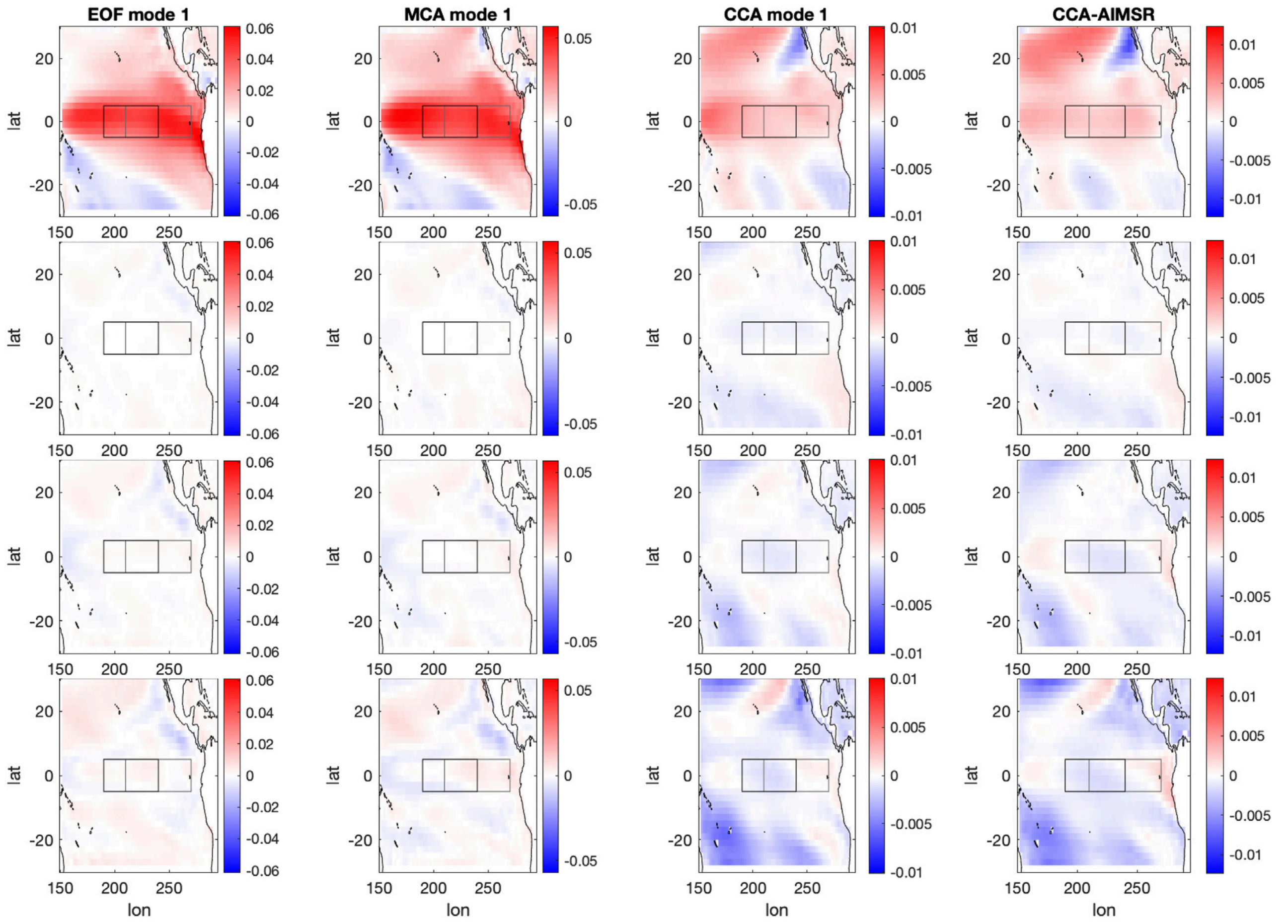

FIGURE 1 | Forced change of the first modes of JJA-mean SST variability in the Equatorial Pacific. Temporal means are taken in four consecutive 50-year periods starting from 1900. The top row displays the temporal mean in the first period, and the subsequent rows display the difference with respect to that in the following periods. Leftmost column: EOF-, 2nd column: MCA-, third column: CCA first mode, last column: the only mode of CCA-AISMR. For the MCA and CCA analysis the domain on the side of the Indian monsoon is the area associated with the AISMR, as seen in **Figure 2**. The Niño3 and Niño3.4 boxes are marked in gray and black, respectively.

the AISMR is considered only. We pay particular attention to the forced changes of these patterns.

Figure 1 shows the first modes of these analyses on the side of the ENSO based on the SST, averaged within four subsequent 50-year periods starting from 1900. We only show these temporal means of the smoothed modes, which were described in **Section 2.2**. The year-to-year changes of the modes are presented in Supplementary Videos[13].

At the beginning of the simulations, EOF1, which is the most important pattern associated with ENSO variability, looks very similar to results in the literature, featuring its main "bump" in the central Pacific. Furthermore, hardly any forced change is visible in it even upon the strong RCP8.5 forcing. In comparison, Carréric et al. (2020) suggests that the maximum of the EOF1 mode shifts to the east in the CESM1-LE by showing that some center (C) mode (Takahashi et al., 2011) shifts to the east more in comparison with the westward shift of some east (E) mode[14]. This does not appear to be so here.

The first SST MCA mode looks practically the same when evaluated with respect to the full field and to the first three SST EOFs as seen in **Supplementary Figure S2**, and it is very similar to EOF1 in both cases. This suggests that MCA1 mainly reflects ENSO variability, which is further supported by the similarity in the forced changes of these patterns. We recall that these changes are minor.

---

[13] SST mask mode 1: https://youtu.be/2AVETrcfBVU
SST mask mode 2: https://youtu.be/EZQ7r2v7-zk
SST box mode 1: https://youtu.be/C62BKGVDQvQ
SST box mode 2: https://youtu.be/QgLQCbS3ZRU
SLP mask mode 1: https://youtu.be/HbxJjOz1RUA
SLP mask mode 2: https://youtu.be/fahPv_fLgx0
SLP box mode 1: https://youtu.be/PQHv7B8B2sw.
SLP box mode 2: https://youtu.be/74_ltkeOiqg.

[14] This situation is not shown conclusively in (Haszpra et al., 2020a) because only three snapshots are shown belonging to single years, and it is not clear how much statistical error is associated with them, leaving an uncertainty about the locations of the peaks.

In contrast to the MCA1 modes, the first CCA modes, evaluated with respect to the first 10 SST EOFs, once with the full Indian precipitation field and once with AISMR (in which case CCA1 is the only CCA mode), show considerable differences when compared to EOF1. Perhaps the main difference is a much weaker weight of the central Pacific (with more weight being concentrated to the west, perhaps because it is geographically close to India), and this might give even more importance to the observation that variability in some off-equatorial regions seems to have an opposite contribution to the teleconnection than to the main ENSO mode (EOF1). (Although, recall that the relative weights of EOFs in CCA-AISMR do not imply a similar relationship concerning the corresponding correlation coefficients.) One such region is next to South America, and another is to the east of Australia, at least at the beginning of the simulations.

The contrast in spatial features persists for the forced changes. The first CCA modes do undergo a considerable change by the late 21st century. It is even more interesting to observe this change to have a different sign in the middle of the ENSO domain (highlighted by the Niño3 and Niño3.4 boxes) compared to the sign of the minor change in the EOF1 and the MCA1 mode. On the other hand, the region to the east of Australia seems to revert its sign, finally conforming with that in EOF1.

Although each panel of **Figure 1** blends 50 separate entities, the mostly monotonic emergence of the changes in consecutive rows suggests that we can see meaningful signals. Otherwise, the Supplementary Video https://youtu.be/2AVETrcfBVU shows ample year-to-year change in the form of a flickering. Given that the forcing is rather smooth and gradual (except for volcanic eruptions), this is likely just a fluctuation stemming from the error of sampling by a finite-size ensemble.

EOF2 for SST also exhibits a well-known pattern, which is practically a dipole or tripole, see **Supplementary Figure S12**. Its central part undergoes some degree of attenuation until 2100, except perhaps in the very middle, which can be regarded as a westward shift of one "pole" of the tripole. At the same time, areas in the north of the box gain importance. However, all changes are moderate.

CCA2, which is likely not orthogonal to CCA1, seems to be also shaped—beside EOF1—by higher-order EOFs other than EOF2 or even EOF3, which is prompted by **Supplementary Figure S2**. MCA2 is just in between EOF2 and CCA2, which is not surprising given that an association between MCAi and EOFi and also between MCAi and CCAi is expected. The strength of the association is determined by the regions' own variances, on the one hand, and their interrelation, on the other.

We would like to remind though that the temporal means of the second modes are less reliable than those of the first modes, as discussed in **Section 2.2**, which can be seen in the Supplementary Videos https://youtu.be/EZQ7r2v7-zk and https://youtu.be/fahPv_fLgx0.

The **Supplementary Figures S6, S14** suggest very similar conclusions for the first two modes in the SLP-based representations and characteristics as for SST on the side of the Pacific, except that the patterns look rather trivial for the EOFs and the MCA modes.

On the side of the IM, **Figure 2** shows that the leading mode of precipitation variability (EOF1) is concentrated to the middle of the AISMR region. The MCA1 mode is somewhat different in putting more weight on the foothills of the Himalayas. This is consistent with the *r* map featuring the strongest correlations over land at this region; and it is epitomized by the CCA1 mode putting an overwhelming part of its weight here. CCA1 misses practically any similarity with EOF1. At the same time, the similarity of the patterns of the forced changes of the four fields shown (rows 2–4) is remarkable, even though these changes are minor over the land.

EOF2 for the precipitation is also very different from CCA2, see **Supplementary Figure S16**. EOF2 is a dipole, with an emphasis on the northeast of India but not yet at its edge. CCA2 also features important areas in the southern part of India, not coinciding with the peaks of EOF2 or EOF1. Interestingly, MCA2 is very similar to CCA2 and is thus very different from EOF2. The *r* map computed for the subleading mode, EOF2, of the Pacific SST field is also very different from any of these patterns. Surprisingly, it is quite similar to that computed for EOF1 (seen in **Figure 2**). Note that the second modes presented in **Supplementary Figure S16** undergo moderate changes in time, which do not affect the conclusions of this paragraph.

Recognizing the importance of areas off the AISMR region, we repeat all computations of this section based on the precipitation field of the complete Indian box instead of the AISMR region. Surprisingly, there is hardly any alteration on the Pacific side (**Supplementary Figures S5, S13**). On the Indian side, as expected, CCA1 (**Supplementary Figure S10**) features peaks where the *r* maps also do, with a special emphasis on the Himalayas. Regions over the Indian Ocean lose importance with time. Interestingly, EOF1 and MCA1 (in the same figure) become similar to CCA1, although with the stronger peak appearing over the ocean (but also weakening with time).

The second modes of the complete Indian box (**Supplementary Figure S18**) are mainly concentrated on the sea. While CCA2 exhibits considerable similarity with the *r* map corresponding to EOF2 of the Pacific SST field, there are major differences with MCA2 and EOF2 in the same figure, not attenuated over time either.

So far, all joint modes presented in the analysis of the Indian patterns were based on SST on the Pacific side. **Supplementary Figures S9, S11, S17, S19** illustrate that almost identical results are obtained with SLP. We thus conclude that the patterns on the Indian side are very much insensitive to the representation of variability on the Pacific side.

3.2 The Forced Evolution of Correlation Coefficients

The time evolution of the quantifiers defined in **Section 2.2** is given in **Figure 3** for the SST-based representations of the ENSO-side variability and applying the AISMR mask on the IM side. Concerning the affected representations involving MCA and CCA, the Mann–Kendall test statistics corresponding to the

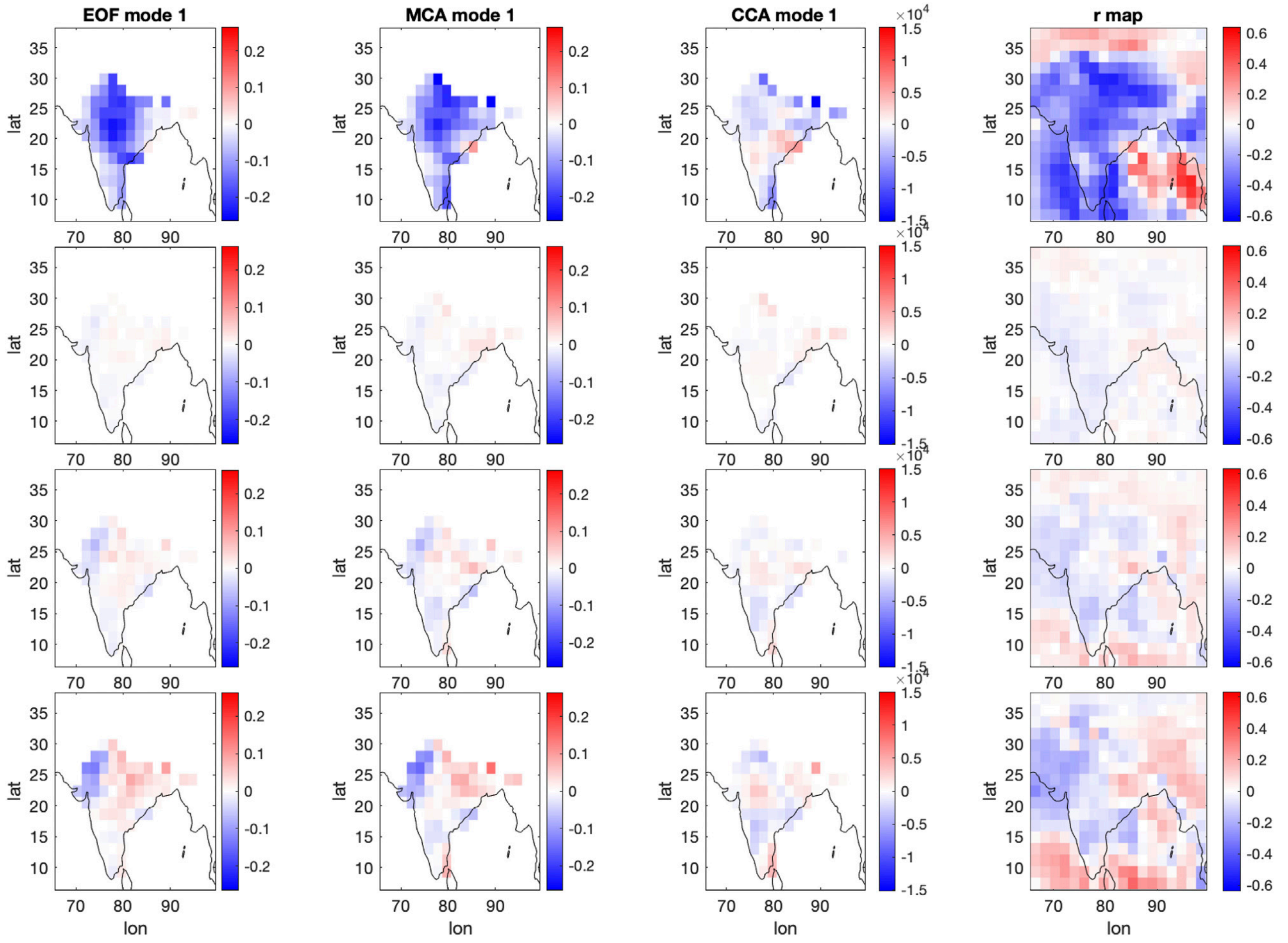

FIGURE 2 | Same as **Figure 1** wrt. the first three columns, but concerning the Indian summer monsoon. In the fourth column a correlation map and its changes are shown concerning the gridpoint-wise JJAS precipitation and the PC1 of the EOF1 of the SST in the box seen in **Figure 1**.

meaningful conservative r estimates are plotted for every subinterval in **Figure 4**, etc.

From a technical point of view, the different estimates of r featuring a positive (blue curves) and a negative bias (brown curves) are further apart for the more erroneous MCA2 and CCA2 modes in **Figure 3**, as can be expected. Furthermore, even their nonstationarity is likely considerably corrupted by the positive biases. From the point of view of detectability, however, the positive bias goes with smaller statistical fluctuations. It is interesting to note that the result with positive bias does not feature much nonstationarity for either CCA1 or CCA2, while it does with CCA-AISMR. As for the result with negative bias, the nonstationarity for CCA-AISMR is in between those of CCA1 and CCA2.

A very distinct separation of the results with positive and negative bias is also seen for TFSTVE which quantifies the predictability of also the spatial variation. Furthermore, performing MCA using PC1-3 of the SST field (yellow line) is hardly different from using the full fields (brown line), which underlines that TFSTVE does represent an ENSO-IM variability. This result could perhaps be expected considering the rapid decay of the variance explained by higher-order Pacific EOFs as presented in **Figure 5**. Furthermore, in fact, TFSTVE is dominated overwhelmingly by MCA1, which latter on the Pacific side is in turn dominated by EOF1 (**Figure 1**). This is prompted by the decay of the variance explained by higher-order IM EOFs, on the one hand, and those of $r_i\,(\mathrm{PC}_i, \mathrm{PC}_i)$ with the mode number i, on the other, seen also in **Figure 5**. In this regard we note that a further source of bias originates from taking the square of $R_m = r_m$ in **Eq. 5** in conjunction with statistical errors of a near-zero r_m. This bias amounts to a systematic error of about 0.02, as will be indicated in **Section 4**.

Having said these, we conclude that TFSTVE is reasonably high to represent a strong teleconnection, and its time evolution is detected to be a long-term increase in **Figure 4G**. An increase is, however, not detected in shorter intervals around 1900, 2000, and in the very late 21st c.; instead, slight drops are suggested by the test statistics.

The PCs of MCA1, the leading contributor to TFSTVE, exhibit a relatively high r (MCA1 in **Figure 3**) with a time dependence very similar to that of TFSTVE, which carries over to the MK-test results in **Figures 4E,G**. r of the PCs of MCA2 is lower; in fact, it is relatively close to zero in the lower estimate (MCA2 in **Figure 3**). The

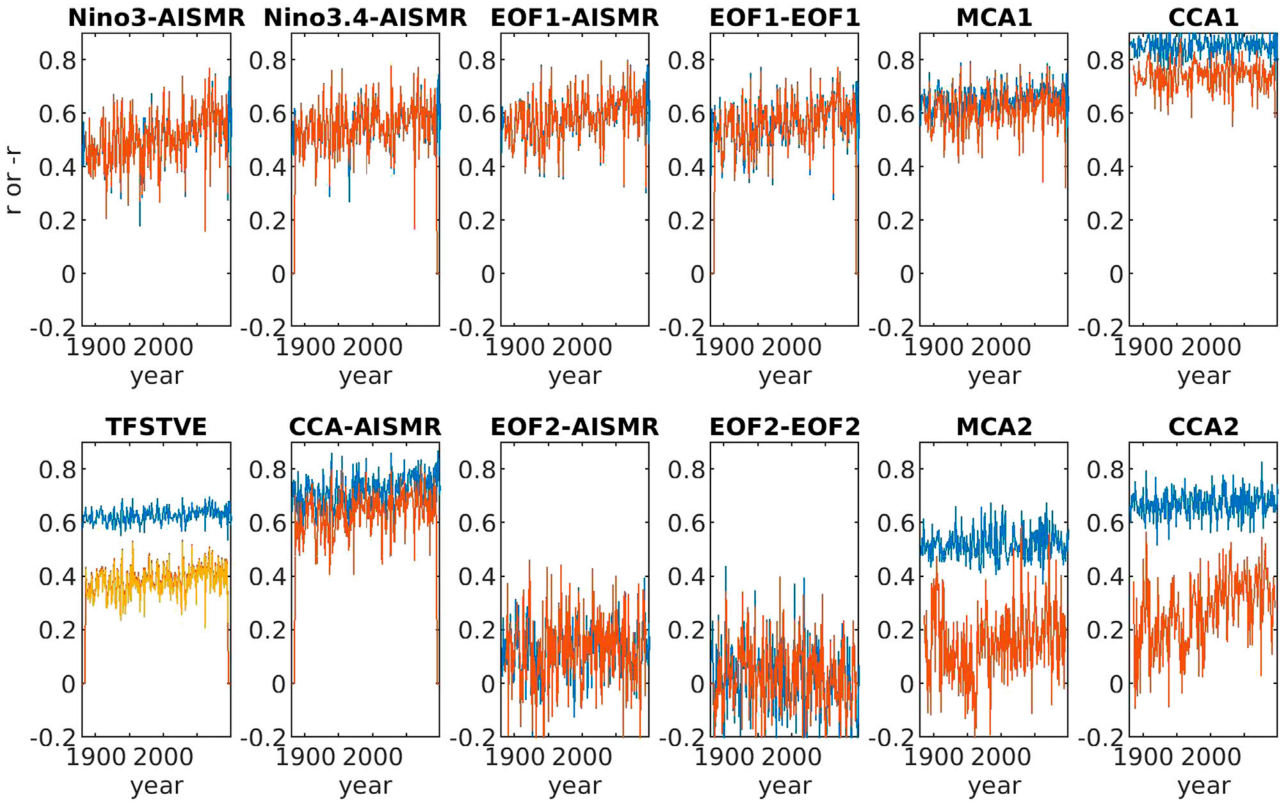

FIGURE 3 | Time-evolution of the ensemble-wise correlation coefficients *r* associated with different representations of the ENSO-IM teleconnection or some relationship between the two domains seen in color in **Figures 1**, **2**. In addition, in the bottom left corner we show the (square-root of the) total fraction of spatio-temporal IM variability explained, TFSTVE (**Eq. 5**), by PCs of the ENSO-side SMCA modes, as a further represenation of the ENSO-IM teleconnection. Blue curves show the straightforward naive estimates, and brown curves show the "conservative" estimates (see **Section 2.2**). In the case of TFSTVE, the yellow curve shows the estimate obtained by performing SMCA based on only 3 Equatorial Pacific SEOFs.

dominant feature in its time dependence is also a long-term increase (**Supplementary Figure S38C**).

We recall here from the previous section that MCA modes have a similar pattern to EOFs, which may suggest that the relationship expressed by the MCA modes should be observable between the EOFs, characterizing variability of local importance, of either side. Indeed, *r* between the PCs of EOF1s (EOF1-EOF1 in **Figure 3**) is only slightly smaller than for MCA1. It undergoes a more pronounced long-term increase (**Figure 4D**). At the same time, *r* between the PCs of EOF2s (EOF2-EOF2 in **Figure 3**) is practically zero and is not detected to change at all (**Supplementary Figure S38B**). This suggests that the phenomena expressed by EOF1s are quite important for the teleconnection, but the same is not true for EOF2s.

Correlation is preserved for EOF1 and somewhat regained for EOF2 on the Pacific side when the IM side is chosen to be respresented by AISMR instead of EOFs, see EOF1-AISMR and EOF2-AISMR in **Figure 3**. AISMR is thus more strongly correlated with the Pacific variability than PCs of individual EOFs of the AISMR region. Temporal changes are generally also a bit more pronounced (**Figure 4C**; **Supplementary Figure S38A**).

One can then go further and take the coefficient of multiple correlation, *R*, of all Pacific EOFs with AISMR, which is the same as *r* corresponding to the single CCA-AISMR mode, a full representation of the ENSO-IM teleconnection. It is very high (see CCA-AISMR in **Figure 3**). It undergoes a relatively strong increase in the 20th c. with a more definite stop in the late 21st c. (**Figure 4H**), especially in comparison with the time evolution of TFSTVE (**Figure 4G**), but also with other MCA- or EOF-based characteristics (**Figures 4C–E**). Such differences may be related to the differences in the changes of the corresponding patterns as described in **Section 3.1**. Nevertheless, all main features are shared by these representations or charactersistics.

This is also true for the Niño3-AISMR and Niño3.4-AISMR representations (**Figures 4A,B**, both showing a high correlation in **Figure 3**). On the level of details, the increase of *r* of Niño3-AISMR extends very late to the 21st c. For *r* of Niño3.4-AISMR, the increase is more moderate, and a drop is undoubtedly detected after 2000, which is exceptional among the representations and characteristics discussed so far. The relative suppression of the overall increase for *r* of Niño3.4-AISMR may be related to the opposing changes of EOF1 and CCA-AISMR in the Niño3.4 region as discussed in **Section 3.1**.

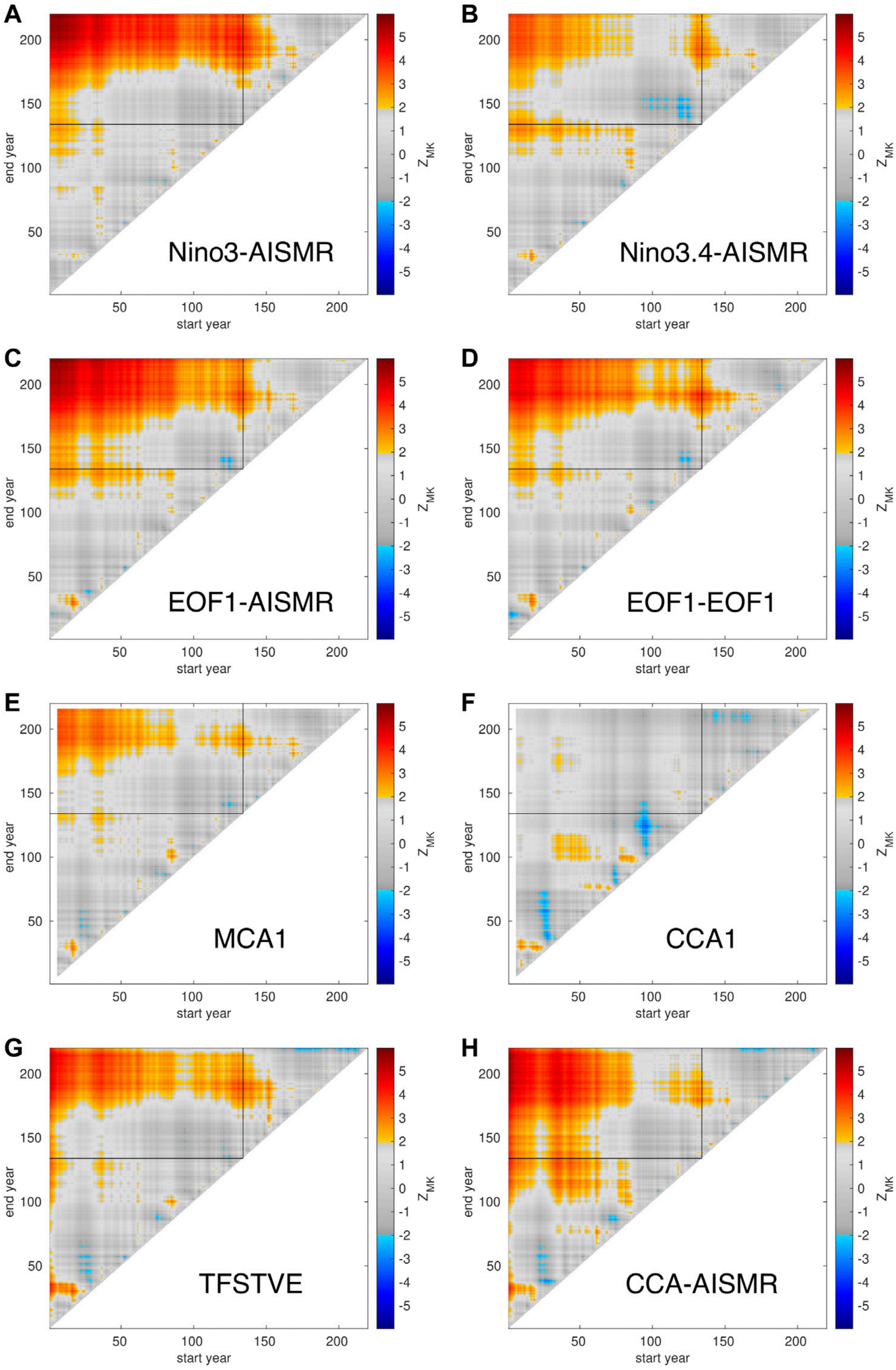

FIGURE 4 | Test statistics of the Mann-Kendall test for the stationarity of (the "conservative estimates" of) $r(t)$ or $-r(t)$ (shown by the brown curves in **Figure 3**), depending on which of these gives an overall positive value. The diagrams correspond to panels of **Figure 3** as: **(A)** Niño3-AISMR; **(B)** Niño3.4-AISMR; **(C)** EOF1-AISMR; **(D)** EOF1-EOF1; **(E)** MCA1; **(F)** CCA1; **(G)** TFSTVE; **(H)** CCA-AISMR. Red and blue shades correspond to $p < 0.05$, i.e., a detection of nonstationarity at that significance level.

CCA1 and CCA2 evaluated with the precipitation field within the AISMR region do not fit the picture outlined so far. Remember from **Section 3.1** that their spatial patterns look very different from EOFs and MCA modes on the IM side and are concentrated on the very edges of the AISMR region, so that moderate importance should be associated with the corresponding results from the point

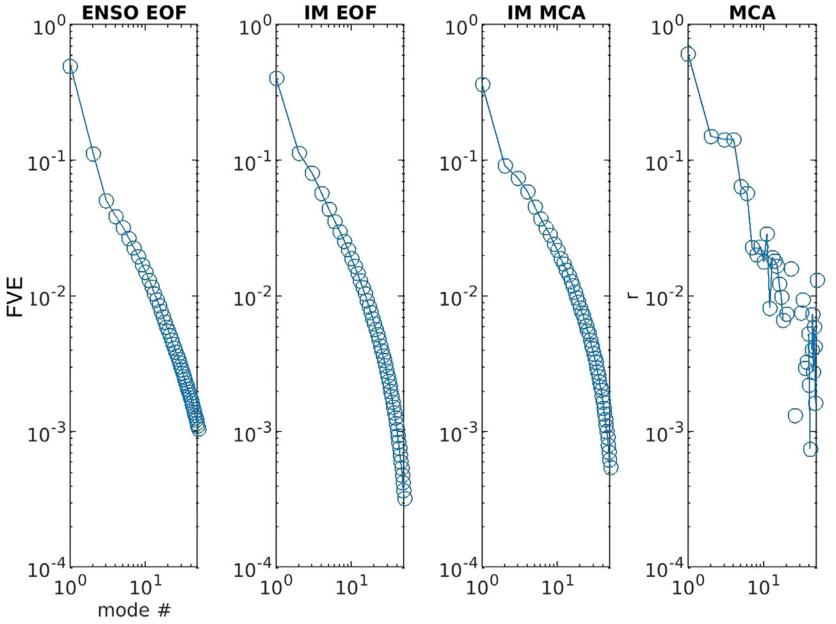

FIGURE 5 | Fraction of variance explained FVE by ("raw"/"unsmoothed") SEOF and SMCA modes. In addition, the rightmost diagram shows the "conservative" estimate of the correlation coefficients for the paired PCs of SMCA modes. Results of temporal averages for the full data span of 1880–2100 are shown in log-log diagrams.

of view of the teleconnection, in spite of the high correlations (CCA1 and CCA2 in **Figure 3**).

The shape of CCA1 and CCA2 on the IM side, together with the r maps, suggests that important areas for the teleconnection fall outside of the AISMR region and prompts to evaluate modes of spatiotemporal variability in the complete Indian box. As mentioned in **Section 3.1**, this brings modes of the same order similar to each other and to the r maps of the Pacific EOFs, reveals the importance of the bulk of the Himalayas and of oceanic areas, and a loss of this importance with time. This importance loss might imply that characteristics of the teleconnection might strengthen more when they are based solely on the AISMR region rather than the complete box.

We do observe in **Supplementary Figures S26, S34** that results for TFSTVE, the MCA modes and the paired EOFs are very similar for the complete box as for the AISMR region except that the signal of strengthening is much weaker (and turns to a pronounced weakening for EOF2-EOF2). At the same time, CCA1 and CCA2 now exhibit strengthening (with the previously described intermittent periods), even stronger than the other characteristics. However, for characteristics for which AISMR is replaced by the mean box precipitation (BOXSR), the correlation becomes unreasonably low. These characteristics do not deserve further analysis and illustrate that applying appropriate techniques to select IM-related precipitation within the box is essential.

Using SLP instead of SST in a suitable subset of the Pacific box does not yield any difference that would be worth mentioning (**Figure 6**; **Supplementary Figures S25, S27, S33, S35, S39, S41,** except for SOI and box-SOI). This means that SLP reflects the same phenomenology as SST in the respective domains. The results with SOI and box-SOI are similar to the rest, and differences in the details are not possible to interpret without extending the currently used domain to the west.

3.3 The Drivers of Changes in Correlation Coefficients

Having established the observable changes, we can now ask about their drivers in terms of the linear regression model as introduced in **Section 2.3**. We emphasize again that attribution in the case of characteristics involving MCA and CCA is in general not possible. Furthermore, we do not perform statistical tests here regarding these drivers. Therefore, the attribution of a change in r to different factors is not rigorous but rather tentative.

Figure 7 suggests that ENSO-side variability, σ_Φ, first stagnates then increases with time in the early 21st c. irrespective of which dominant mode is taken. This seems to be followed by an equally fast decrease starting from the mid 21st c., with seemingly all of the gain lost by the end of the century in view of Niño3 and PC1. The decrease is a bit more moderate with Niño3.4, which should contribute to the result that ENSO variability can dominate changes in the correlation coefficient by the late 21st c. as seen in **Figure 8B**. Although, no doubt another reason is that in this representation the coupling a increases less and σ_ξ increases more than for other characteristics. Beside the decrease of σ_Φ in the second half of the 21st c., a continued increase of a/σ_ξ might still make r continue to increase. However, a/σ_ξ might also experience a nonmonotonicity, although likely starting to decrease later than σ_Φ. If that happens, clearly $r(t)$ would be also nonmonotonic. However, this is not detected (**Figure 6**),

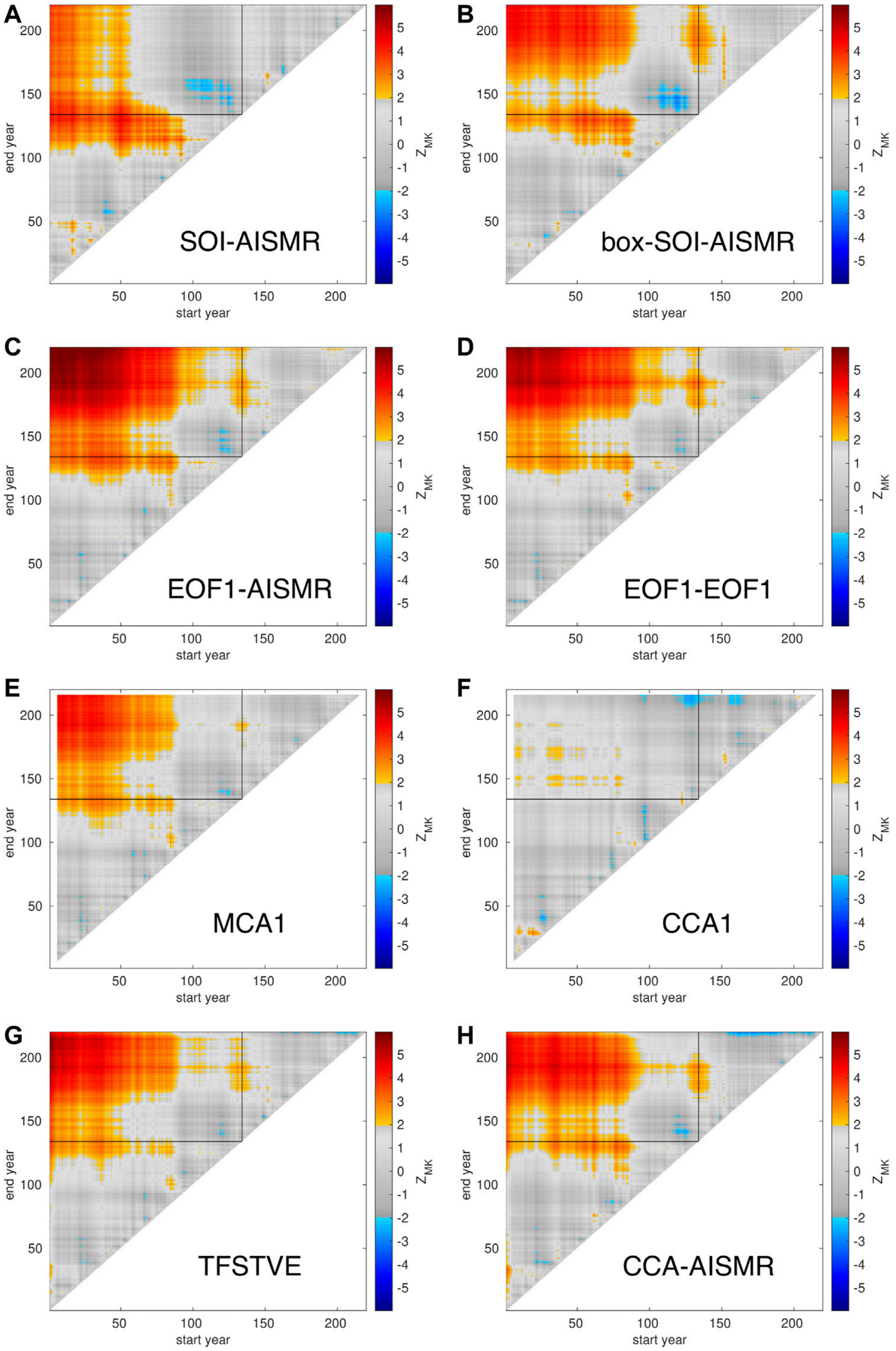

FIGURE 6 | Same as **Figure 4** but the ENSO side is characterized based on the SLP.

perhaps because of the shortness of the time period when this happens. Another important nontriviality in the time evolution of a/σ_ξ is a drop at the turn of the 20th–21st centuries. This drop is related to a drop in the time evolution of a and serves as a possible explanation for the drop in the correlation coefficient at the same time. It turns out from **Figure 7** that both a and σ_ξ typically undergo a considerable increase otherwise, with a "winning," but only slightly.

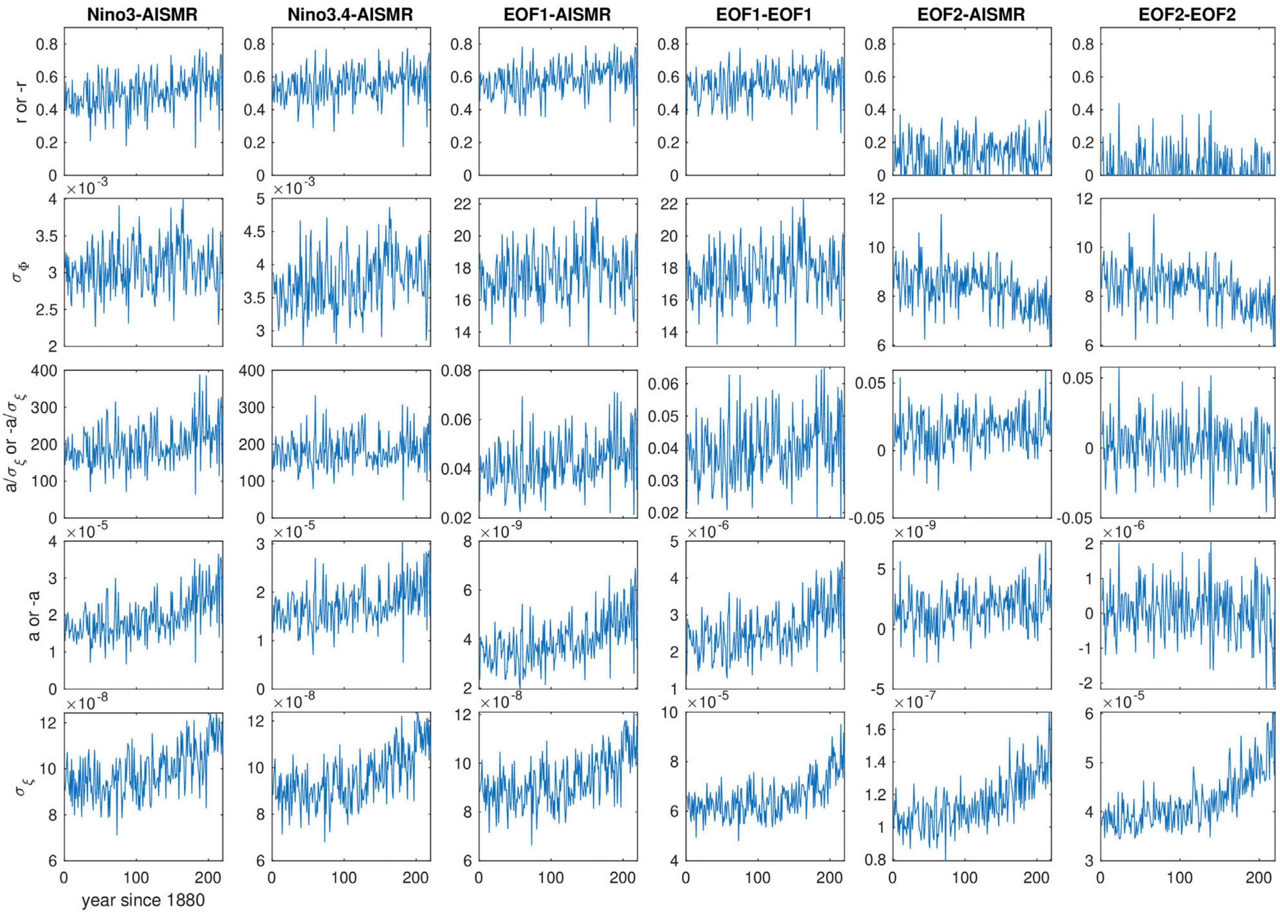

FIGURE 7 | The forced evolution of correlation coefficients $r(t)$ and the drivers of change; see **Section 2.3**. The different columns correspond to different representations of the relationship between the variability in the regions of ENSO and the IM. For columns 1–3 and 5 the IM is represented by the average monsoon rain AISMR. Columns 1–4 concern the dominant modes of variability, and columns 5–6 concern the next-to-dominant modes of variability.

Making use of the SLP mostly agrees with the findings obtained with the SST, see **Figures 6**, **9**. The only but important exception is a decreasing ENSO-side variability in view of PC1. We note that the same domain as used for the SST is not suited for the SLP: the corresponding principal modes (whether SEOFs, SMCA and SCCA modes) are unrelated to the essence of the ENSO phenomenon, as a concentration of the high-amplitude areas on the edges of the domain indicates (Bódai et al., 2020a).

Although second modes were found to be relatively unimportant for the teleconnection, there seems to be considerable nonstationarity in σ_Φ for EOF2, which might still have an impact on an other important teleconnection representation, CCA-AISMR.

4 COMPARISON OF THE MPI-GE TO OBSERVATIONS AND REANALYSIS

Results and conclusion that derive from a large ensemble apply only to the model that generated the data. However, the ultimate enquiry pertains to the actual Earth system, and, in that regard, one should perform some comparison of the model with observations. Clearly, it has its limitations given that the observational record corresponds to a single realization, and, so, it provides proportionally less information about the system. In (Bódai et al., 2020b) we compared long-term means and trends of the SST fields and precipitation in South Asia, as well as temporal correlation coefficients pertaining to areal means like e.g. the AISMR and Niño3. Our conclusion was, however, that it is not possible to detect nonstationarity from single realisations. In terms of spatial modes of variability and associated correlations, it is likewise doubtful to be able to establish the forced response from observational data. What we can compare here are modes and correlations that are in a way overall "representative of a time period."

Calculations are carried out with respect to temporal variability, not only for observations, but also for each member of the ensemble, so as to make a comparison meaningful. In turn, the different realisations for the model will provide some statistics for the finite-size temporal estimates. As proper anomalies cannot be obtained for observations, we instead feed the calculations with data that represent "high-frequency variability." It is obtained by

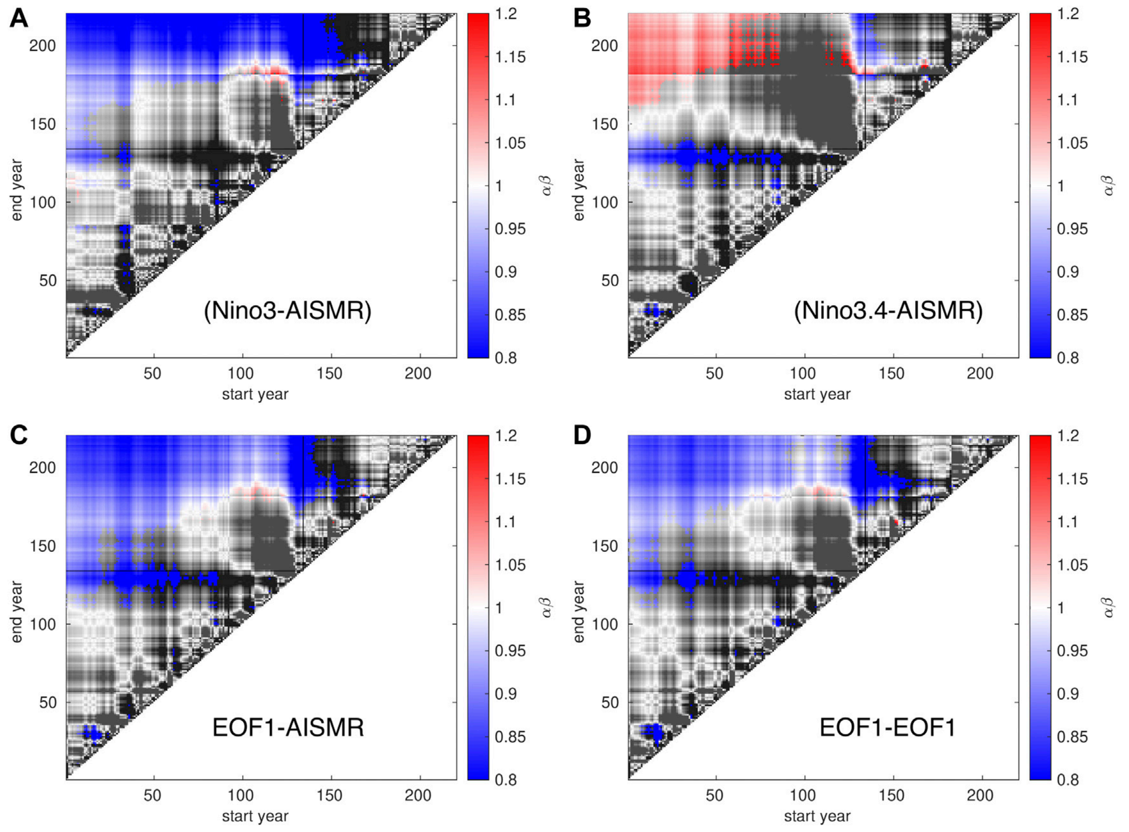

FIGURE 8 | Relative importance of σ_Φ versus a/σ_ξ to the change of $r(t)$. The diagrams correspond to those of **Figure 4** showing the Mann–Kendall test statistics for $r(t)$. Color is applied only where $r(t)$ changes significantly. The color saturates where $\alpha\beta$ is outside of the range indicated in the colorbars.

subtracting a low-frequency component from every data point, which is approximately a 21 years moving window mean. We use the same method as in (Bódai et al., 2020b), applying a Savitzky–Golay filter of order 3 to the running window means. We obtain conservative estimates e.g. for r associated with PCs belonging to modes by parting the data into two consecutive periods of equal length, computing the modes from the first part, and computing PCs by projecting the fields given by the second part onto those modes.

The data representing observations are obtained from the 20th century CERA 20C reanalysis product (Laloyaux et al., 2018) for Pacific SST, and the CRU PRE v4.03 gridded precipitation data (Harris, 2019a; Harris, 2019b) for the Indian summer monsoon rain. We analyze the time period of 1901–2010. Precipitation variables are not available for CERA 20C, hence, we can make a comparison with the model only with respect to the representation where the AISMR domain is used. This is not a problem from the point of view that only land areas have a practical relevance. The precipitation data of the 20th Century Reanalysis V2 data (Compo et al., 2011) is not so faithful to reality; it does not reproduce the AISMR time series (Parthasarathy et al., 1994) well, and yields only an r(Niño3, AISMR) = −0.2.

The results for the SST principal modes are displayed in **Figure 10**. The ensemble means of the temporal modes in the top row are hard to distinguish from the temporal means of the snapshot modes as seen in **Figure 1**. In the second row the ensemble standard deviations reveal that the sampling error is much bigger to do with the CCA compared to the MCA and EOF. The observational EOF1 is more concentrated on the Eastern Equatorial Pacific, or, at least, it does not feature a second peak in the Western Equatorial Pacific like the model does. The weight of the observational MCA1 mode is somewhat shifted to the west wrt. EOF1. The observational CCA1 and CCA-AISMR modes are similar to one another, just like those of the models, but the respective observational modes are much less similar to the model modes as compared to EOF1 and MCA1. The observational CCA1 and CCA-AISMR modes are concentrated to the middle of the Equatorial Pacific while the model modes on the westernmost of the Equatorial Pacific and even on off-equatorial areas. Yet, the associated correlation coefficients match very closely (**Figure 11F**).

As for the IM side, the modes are shown in **Figure 12**. Again, regarding the model, the resemblance of the ensemble means of the temporal modes in the top row and the temporal means of the snapshot modes as seen in **Figure 2** is uncanny. It is rather surprising that the CCA1 modes on the IM side match rather well between observation and model. Otherwise, so do the r maps

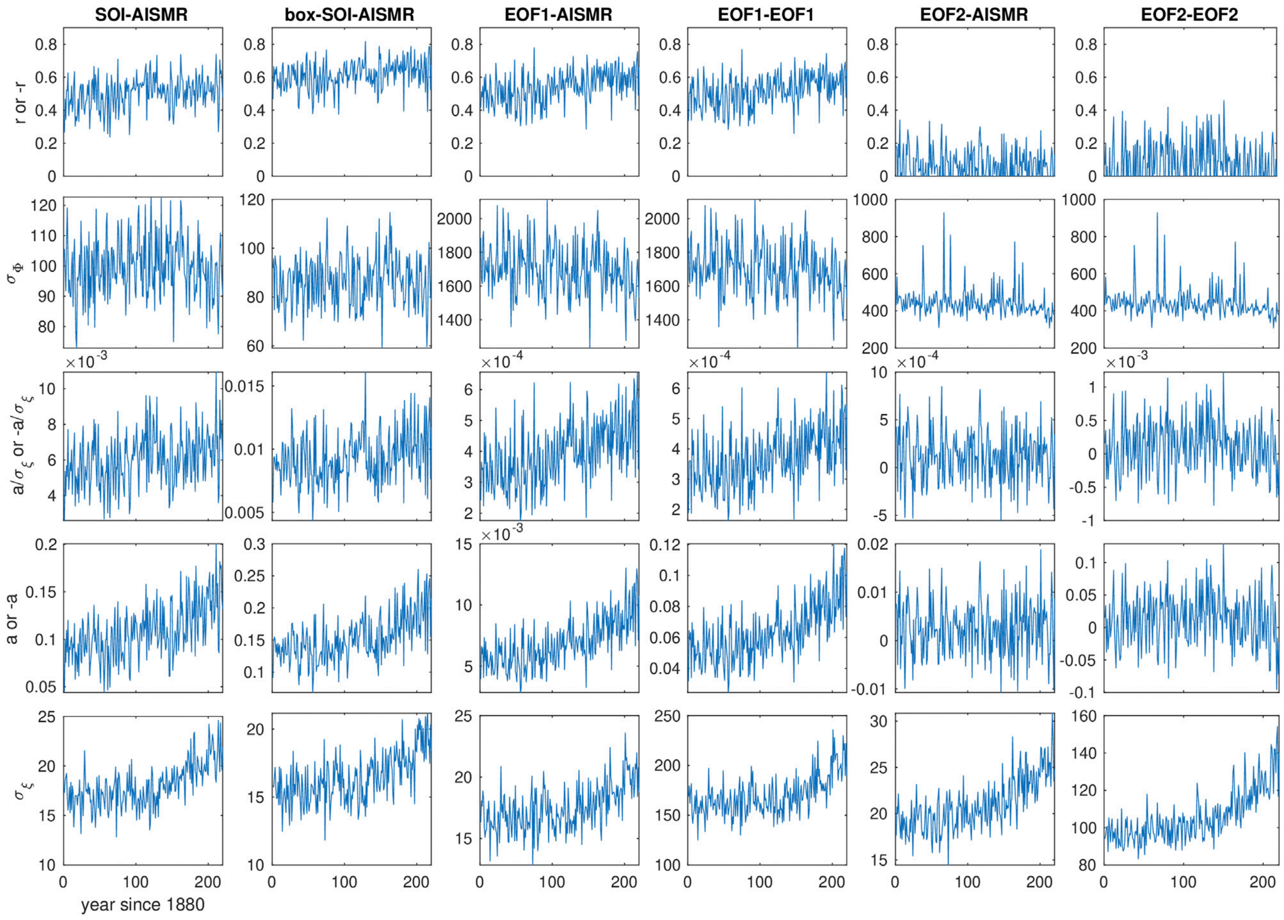

FIGURE 9 | Same as **Figure 7** but the ENSO side is characterized based on the SLP.

and the MCA1 modes match rather well. The observational EOF1, however, does not appear to closely resemble the observational MCA1 mode, unlike for the model, which might have only to do with the fact that the model does not resolve the very wet climatology over the Western Ghats. The fact that the observational MCA1 mode does not have a strong weight over the Western Ghats despite the high resolution should have to do with the weak correlations with PC1 of the Equatorial Pacific SST in this area, as shown by the r maps.

Some of these observations apply also to the second modes. It is particularly surprising how the observational and model CCA2 modes both on the Pacific (**Supplementary Figure S42**) and IM side (**Supplementary Figure S43**) resemble one another, even despite the large sampling fluctuations as shown in the middle rows.

As for the correlation coefficients r and TFSTVE, seen in **Figure 11**, the estimate from observations is always smaller, except for the Ninõ3-AISMR representation [in panel (A)]. It is not clear how this exception could be explained by the restriction of the observational EOF1 to the east (**Figure 10**, bottom left), if it could be at all. It is the CCA-AISMR representation (F) that yields the largest (conservative estimate of) r also for observations, very slightly below the figure for the model. In contrast, the TFSTVE (E) is considerably smaller for observations, which is prompted by both r (C) and FVE (D) being smaller for the observational MCA1 mode. Nevertheless, these diagrams suggest that this can be just a statistical fluctuation of the single observational realization. Note also that r for the higher-order MCA modes is practically zero; that is, only MCA1 contributes to the TFSTVE.

We emphasize once again that the above comparison cannot confirm confidence that the MPI-GE correctly features a strengthening ENSO-IM teleconnection. Neither can it undermine the confidence thanks to the fairly close match in most aspects, the observational results falling seemingly within the ensemble-wise variation of the MPI-GE estimates.

5 NONERGODICITY

Whenever the forced change is nonlinear, whether due to a nonlinear progression of the forcing or a nonlinear response characteristic, an estimation of the momentary ensemble-mean

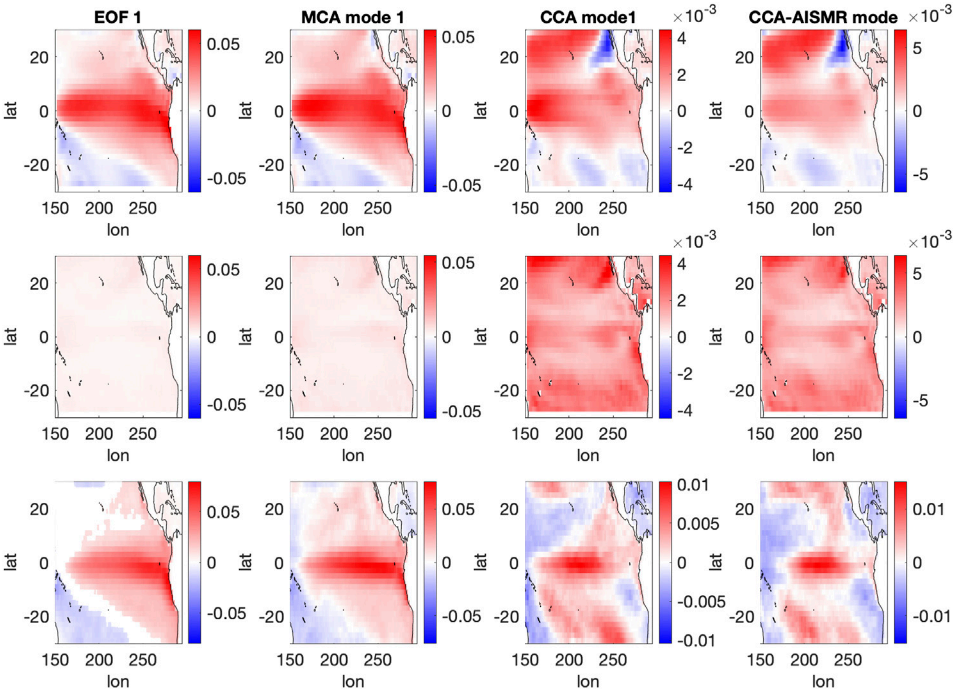

FIGURE 10 | Comparison of principal SST modes obtained by temporal EOF analysis, MCA, CCA (the columns corresponding to those of **Figure 1**) between the MPI-ESM (top row) and observation (bottom row). In the middle row the ensemble-wise standard deviations are shown in the same color range as the modes themselves.

climatology by a temporal mean in a finite window should be biased (Drótos et al., 2016). That is, the ensemble mean of the temporal mean would not be equal to the ensemble mean itself (say, at the middle of the time window), which is termed nonergodicity. Higher-order statistics should be biased even in the unlikely case that the forced change of the ensemble mean is linear and the internal variability would not feature a forced change. The linear Pearson correlation coefficient is no exception, i.e., its time-based evaluation (the traditional choice) will be biased even if the ensemble means of the correlated quantities exhibit a temporally linear forced response. Notwithstanding, a linear time evolution of the Pearson correlation coefficient $r(t)$ itself may lead to a vanishing bias, and this is what we will elaborate on in this section.

In fact, $r(t)$ clearly features a nonlinear change in various representations and characteristics of the ENSO-IM teleconnection and related quantifiers in the MPI-GE, whether it is a monotonic but degressive change (represented by a concave graph) or a nonmonotonic one, as seen in **Figures 4**, **6**, **7**, **9**. However, the evaluation of the bias or the degree of nonergodicity is not straightforward in this case since the "signal-to-noize ratio" is rather poor thanks to the relatively small ensemble size. Nevertheless, we can attempt to at least detect the presence of nonergodicity by performing a statistical test. The quantity of the so-called test statistics can in turn serve as some quantifier of the degree of nonergodicity.

To the end of constructing a suitable test, we observe that the Fisher transform $\hat{z} = \operatorname{arctanh}(\hat{r})$ ($\hat{r}$ distinguishes the finite-N sample estimate of r) provides approximately normally distributed independent identically distributed random variables (wrt. the different years) with a standard deviation $\approx 1/\sqrt{N-3}$ for large enough N and any true value r of the correlation coefficient.[15] The same applies, of course, to the finite-τ-window sample correlation coefficient r_τ when $\Phi(t)$, $\Psi(t)$ are not auto-correlated and their ensemble means and standard deviations remain constant in time. In such a case, the only reason that the expectation

$$\langle (\hat{z}_\tau - z)^2 \rangle \tag{7}$$

at any time does not match the theoretical value $(\tau - 3)^{-1}$ is the existence of a bias:

$$\langle \hat{z}_\tau \rangle \neq z, \tag{8}$$

i.e., nonergodicity.

We have four issues to consider. First, z is not available because of the finite N ensemble size. Therefore, we cannot evaluate nonergodicity at any time (every year). Instead, we can consider nonergodicity overall in an interval of length T calculating

$$v = \sum_{t=1}^{T} \sum_{n=1}^{N} (\hat{z}_{\tau,t,n} - \hat{z}_t)^2. \tag{9}$$

Second, had $\hat{z}_\tau$ and $\hat{z}$ in the above been computed from combinations from the same sample of size $T = N$ (without

---

[15] This approximation assumes the correlated variables to follow a Gaussian distribution, but non-Gaussianity has been checked to have a farly negligible effect for some basic ENSO-quantifiers and AISMR in (Bódai et al., 2020b).

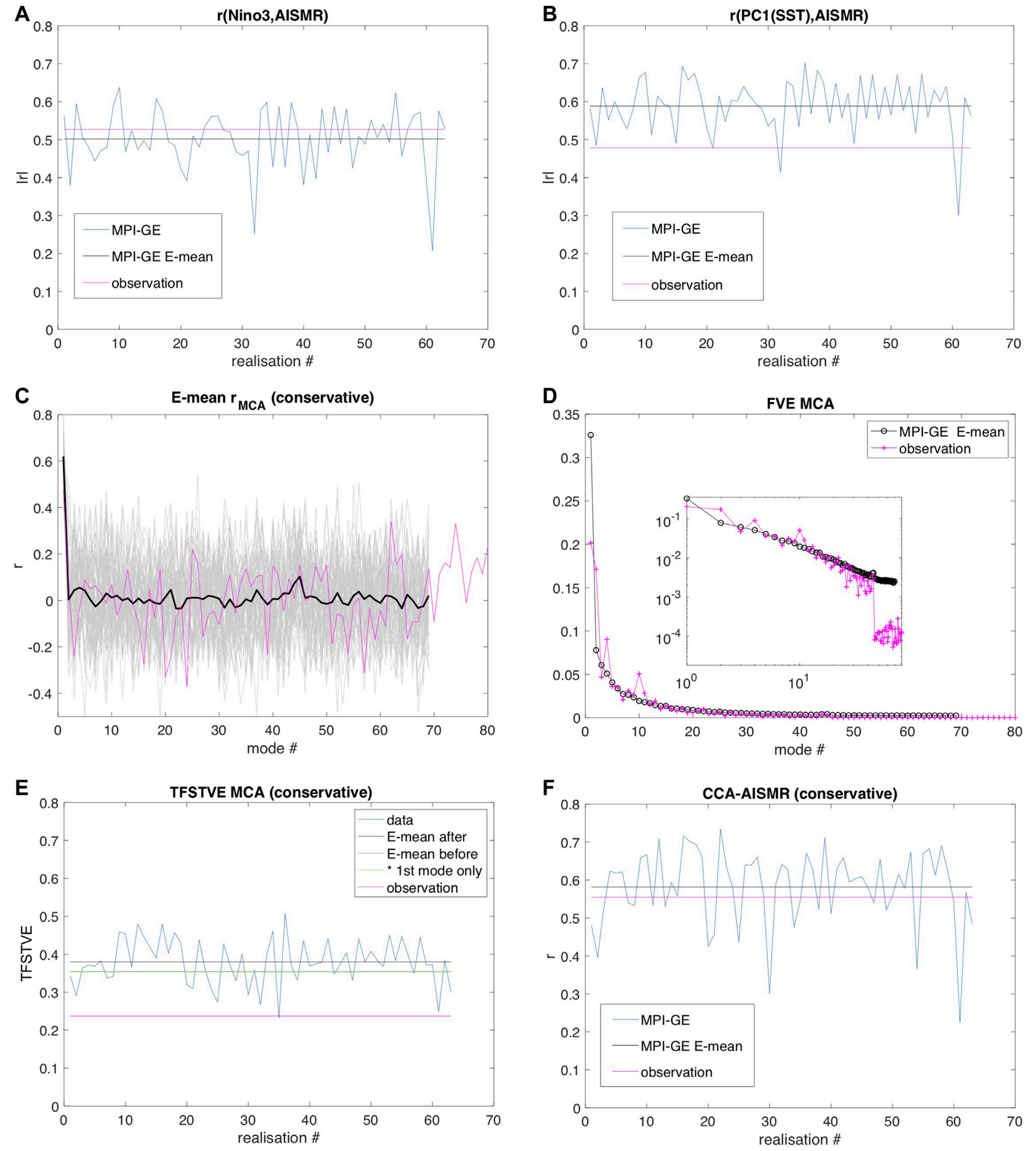

FIGURE 11 | Comparison of temporal correlation coefficients *r* **(A-C,F)**, FVE **(D)**, TFSTVE **(E)**, between the MPI-ESM (blue, black, gray, green curves) and observation (magenta curve) for various representations of the ENSO-IM teleconnection. Panel **(E)** indicates that the systematic error for the conservative estimate of TFSTVE (brown curve) in **Figure 3** is about 0.02.

repetition), Cochran's theorem (Cochran, 1934) would dictate that *cv* (where *c* is an appropriate constant factor) would be distributed according to a χ^2-distribution. This would allow for calculating the p-value in the usual way by evaluating the χ^2-distribution at the level given by the calculated test statistics. However, our setting is somewhat different $T = N$, which might not be possible to tackle

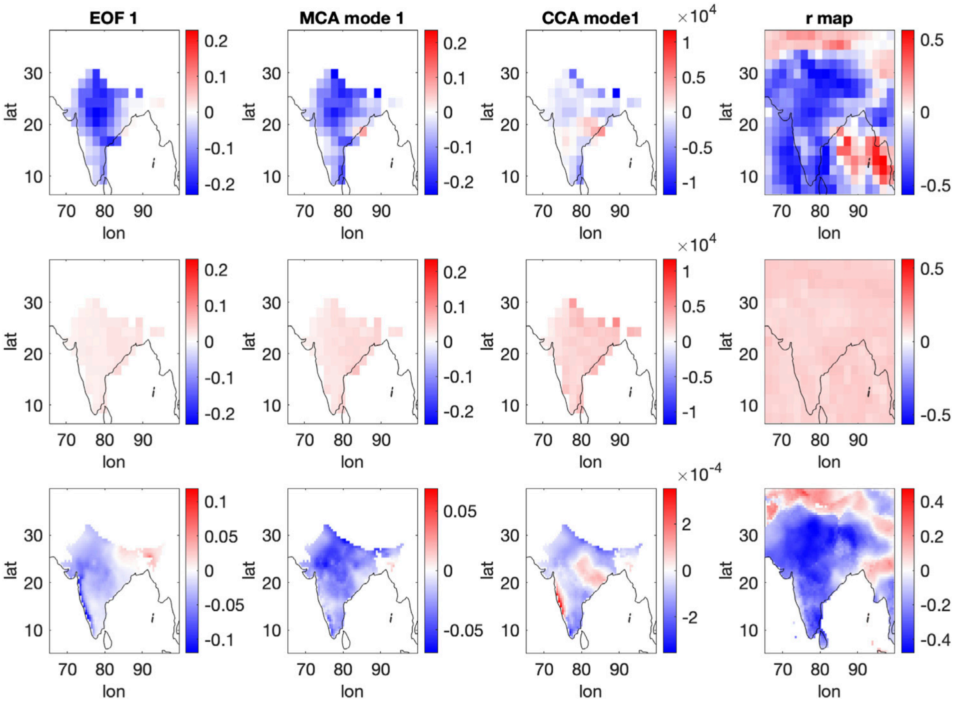

FIGURE 12 | Same as **Figure 10**, but for the Indian summer monsoon precipitation (the columns corresponding to those of **Figure 2**).

analytically. Nevertheless, one can sample the test statistics and, therefore, determine its quantiles to arbitrary precision. We have performed this sampling simply by generating sample correlation realisations by generating realisations of correlated random variables X and Y, where $Y = aX + \xi$, and X and ξ are normally distributed independent random variables. This is a further assumption for the nature of our variables, from which deviations certainly exist but which are presumably moderate enough to have a secondary effect for the results. Note that the moving-window temporal correlation coefficient $\hat{r}_{\tau,t}$ is calculated upon pregenerating x_t and y_t, $t = 1, \ldots, T$. We have checked that cv does seem to follow a χ^2-distribution even in our setting, but we do not utilize it.

Third, Φ is in fact auto-correlated, regardless of the choice to represent ENSO-related variability. As a simple test, we took X to be governed by an auto-regressive process of order 1, $X_{t+1} = \phi X_t + \xi_t$, such that the lag-1 autocorrelation is 0.3, and we have found only little shift in the distribution of v wrt. its standard deviation. We also took this value of 0.3, and calculated the 0.95 quantile of v, obtaining about 670 using the parameters $T = 220$, $\tau = 31$, $N = 63$; while it is 667 with a serially uncorrelated X_t.

As a fourth issue, there might be a low-frequency influence on the teleconnection, say, via a time-dependent a (Gershunov and Barnett, 1998; Torrence and Webster, 1999; Krishnamurthy and Goswami, 2000; Krishnamurthy and Krishnamurthy, 2014; Watanabe and Yamazaki, 2014). This should increase the width of the distribution of the sample temporal correlation coefficient, i.e., it should be larger than $1/\sqrt{N-3}$. We tested the effect of this by introducing an additive perturbation, $a_t = a_0 + \delta a_t$, where δa_t is modeled again as an AR(1) process, setting $\phi = 0.8$ and such a noise strength that $\mathrm{std}[\delta a_t] = 0.05$. With this the 0.95 quantile is 674; that is, the effect is rather small. This corroborates well with the findings of (Gershunov et al., 2001; Yun and Timmermann, 2018), namely, that even if there was a low-frequency modulation of the ENSO-IM teleconnection strength, it would be too weak to detect from century-long observations. The cancellation effect described by Krishnamurthy and Goswami (2000) may be an alternative view of this.

Turning to our application, the test statistics is found to be 756 for the ENSO-IM teleconnection representation given by the Niño3-AISMR pair. That is, it is well above the 0.95 quantile, corresponding to a minuscule p-value, so that the hypothesis of ergodicity can be rejected with extremely high confidence. We also evaluate the test statistics corresponding to the global correlation maps seen in **Supplementary Figure S1**. The result of this can be presented as a global map, too (**Figure 13**), in which a contour for the 0.95 quantile, 670, encloses regions where ergodicity can be rejected at the usual significance level of 0.05. We can see such regions not just in the tropics or in the Equatorial Pacific, but all over the world. Nevertheless, the highest levels of bias/nonergodicity is indeed found at the center of ENSO variability and elsewhere in the Equatorial Pacific.

We note that even if $r(t)$ changes linearly, or not at all, there could be a trivial source of the bias, namely, a changing ensemble mean or standard deviation of Φ or Ψ. We redo the calculation of the test statistics in order to exclude the former trivial source. In particular, we subtract the respective ensemble-mean time series from the Φ and Ψ time series, separately for each ensemble

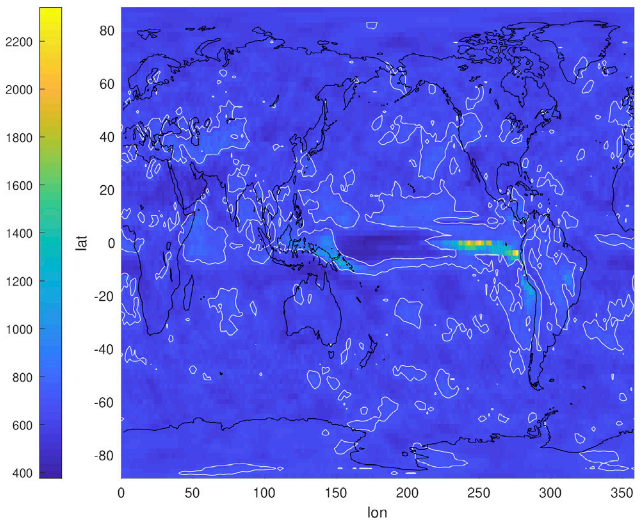

FIGURE 13 | Test statistics of our ad hoc test of nonergodicity regarding the Pearson correlation coefficient. The contours mark the 0.95 quantile. Here, ENSO is represented by PC1 of EOF1.

member, before calculating the temporal correlation coefficient $\hat{r}_\tau$. The result (**Supplementary Figure S44**) is hardly distinguishable from the original one (**Figure 13**) with respect to the patterns, only the values of v are slightly off. That is, in this case the change of the mean state hardly contributes to the bias. As mentioned, the forced change of the standard deviation can also be a source of bias. We believe that, just as the ensemble-mean change, this is also a negligible effect, considering especially that in windows of $\tau = 30$ yr the changes of the σ_Φ time series seem unlikely to be detectable in **Figures 7**, **9**. For this reason, nonergodicity should robustly imply the nonlinearity of $r(t)$.

6 DISCUSSION AND CONCLUSION

We have re-examined the forced response of the ENSO-Indian monsoon (IM) teleconnection as conveyed by the MPI-GE data. One main increment taken by the new analysis is the consideration of spatial aspects of any forced change. This was achieved by determining empirical orthogonal functions (EOFs) and modes of Maximum Covariance Analysis (MCA) and Canonical Correlation Analysis (CCA), and considering various characteristics and representations of the teleconnection defined through these tools. Beyond individual correlation coefficients, we defined the total fraction of the spatio-temporal IM variability explained (TFSTVE) by the Pacific variability, and interpreted results in the spirit of the coefficient of multiple correlation, R. We found that both TFSTVE and R are dominated by the first-order modes, both wrt. their magnitude and forced changes. Characterizing different aspects of the relationship between the variability of the two regions allowed us to build a robust picture of forced changes.

We have found almost all characteristics and representations to convey a picture of a strengthening teleconnection in terms of a statistical test, confirming earlier findings. One or two slight drops around the turn of the 20th–21st centuries have also been detected, and the increase in strength has been found to slow down in the late-21st c. The latter aspect is more prominent when spatial variability is taken into account on a wider region around India, including the Himalayas and surrounding oceanic areas. We have found indications that using such a region may be more suited to analyzing and understanding the teleconnection between ENSO and the IM, but aspects specific to the traditional observational product of all-Indian summer monsoon rainfall (AISMR) may be underrepresented and overlooked in this way.

The late-21st c. slowdown mostly has to do with a curious nonmonotonicity in the change of the ENSO variability: in most representations of ENSO variability, about midway in the 21st c. rather suddenly it starts to decline. In terms of a linear regression model that can be associated with evaluating the (linear) Pearson correlation coefficient, the typically increasing regression coefficient—which can be viewed as an ENSO-IM coupling strength—also plays a strong role. Although the model's noise strength undergoes a similar increase, which has an opposing role, the change of the coupling is found to dominate. The latter turns out to be the central piece of the robust or consistent picture of the strengthening ENSO-IM teleconnection. We conjecture that the temporary drop or drops in the teleconnection strength at the turn of the 20th–21st centuries are also related to corresponding changes in the coupling strength.

We leave it for future work to attribute these features to physical effects. In any case, the change of both the coupling and noise strength should involve both thermodynamic and dynamic factors.

Some differences between different characterstics and representations are due to changes in the relevant spatial patterns. The most interesting finding is that the pattern of maximal ENSO variability and that of maximal correlation with the IM precipitation undergo opposing trends in the middle of the ENSO domain: the middle becomes more important for ENSO itself, while it loses importance for the teleconnection. On the side of the IM, the AISMR region gains relative importance for local variability and even more for the teleconnection with ENSO.

It is essential to note that based on observations the ENSO-IM teleconnection appears to have weakened since about 1980 (Kumar et al., 1999; Bódai et al., 2020b). In (Bódai et al., 2020b) we argued that several reasons could be responsible for this mismatch. Among them one is that the MPI-ESM associated with the MPI-GE is not consistent with the observations of the 20th c. Indian Ocean (IO) warming and IM precipitation decline: in terms of the long-term trend, the ranges of simulated realisations, wrt. both the IO temperature and ISMR, do not contain the observations as respective single realisations–by far [see Figures 12, 13 of (Bódai et al., 2020b)]. See (Aneesh and Sijikumar, 2018), for example, for the role of the IO warming regarding the decline of ISMR, concerning La Niña years, in particular. However, it is a question yet to be answered if the decline of precipitation does actually translate into a weakening of the ENSO-IM teleconnection in the precise sense of a forced change.

Another possibility for the reason for the said mismatch was posited in (Bódai et al., 2020b) to be the very considerable fluctuations of temporal correlation coefficients—the larger in magnitude the shorter the time window—even under stationary unforced conditions, and even without decadal variability of the correlated signals. Evaluating temporal correlations is troubled by further problems when there is a forced change, namely, that 1) when the forced change is nonlinear, the temporal correlations are biased (**Section 5**), and that 2) the forced signal is not known, and, therefore, the anomalies that are meant to be correlated cannot even be constructed. A detrending, say, removing a linear slope in a time window, does not seem to be a good fix, as even under stationary conditions one would find spurious trends due merely to internal variability, and, so, we would remove a signal that should not be removed.

When an ensemble is available, concerning a single model at least, the biases to do with point 1) above can be detected and, to a certain extent, quantified. We have developed an ad hoc statistical test to do just that, and applied it to the ENSO-IM teleconnection as well as the relationship of global precipitation and ENSO. We have found many regions of the world where a bias could be detected. The reasons for the nonlinearities that such biases imply can be manifold, not only driven by the nonlinearity of the change of ENSO variability, and it should be carefully examined in the future.

Our methodology indeed ensures that the detected biases imply nonlinearity (i.e., not only nonlinearity implies biases, but also the other way round). In our context of the historical and scenario change of ENSO-precipitation teleconnections, robust nonlinearity has been found. Given that nonlinearity implies (presupposes) a forced change, we turn out to have on hand a statistical test for the nonstationarity of teleconnections (linear correlations). This can be seen to complement the Mann-Kendall test (in the special case of the nonstationarity of the correlation coefficient), because the latter takes the alternative hypothesis of a monotonic change, while our test includes nonmonotonic changes too.

DATA AVAILABILITY STATEMENT

The data generated and analysed for this study are available upon reasonable request. For reproducing purposes, one can make use of the MPI-GE data available at https://esgf-data.dkrz.de/projects/mpi-ge/, as suggested in **Section 2**. Observational/reanalysis data sets analysed in **Section 4** are available at the webpages whose URL's are included in the bibliographic entries.

AUTHOR CONTRIBUTIONS

TB developed any new code, including those implementing SMCA and SCCA, carried out all the numerical analyses and created all the figures for the paper. GD and subsequently TB originated the ideas of SMCA and SCCA, respectively. TB proved the equivalence of the correlation coefficient of CCA with a scalar target and the coefficient of multiple correlation. TB proposed the breaking down of the change of the correlation coefficients into three constituents according to the linear regression model. TB devised the statistical test for nonergodicity of correlations motivated by Axel Timmermann's enquiry. GD, J-YL, E-SC suggested to calculate the differences as e.g., in **Figure 1**; and to evaluate the relative importance of ENSO variability as seen in **Figure 8** developed and implemented by TB. TB and GD lead the interpretation of results and the writing of the manuscript. K-JH, J-YL, E-SC contributed to the manuscript.

FUNDING

TB was supported by the Institute for Basic Science (IBS), under IBS-R028-D1. G.D. acknowledges financial support from the Spanish State Research Agency through the María de Maeztu Program for Units of Excellence in R&D under grant no. MDM-2017-0711, from the National Research, Development and Innovation Office (NKFIH, Hungary) under grant nos. K125171 and FK-124256, and from the European Social Fund through the fellowship no. PD/020/2018 under the postdoctoral program of the Government of the Balearic Islands (CAIB, Spain). Support for the Twentieth Century Reanalysis Project dataset is provided by the U.S. Department of Energy, Office of Science Innovative and Novel Computational Impact on Theory and Experiment (DOE INCITE) program, and Office of Biological and Environmental Research (BER), by the National Oceanic and Atmospheric Administration Climate Program Office, and by the National Oceanic and Atmospheric Administration Climate Program Office, and by the NOAA Physical Sciences Laboratory.

ACKNOWLEDGMENTS

TB thanks Tímea Haszpra, Malte Stuecker, Kyung-Sook Yun for useful discussions regarding applying spatial weighting according to Baldwin et al. (2009), an appropriate domain for modal analysis using the SLP, using gridded observational precipitation data (CRU PRE) only but not unreliable reanalysis data, respectively, and Axel Timmermann for his interest in nonergodicity including a discussion on whether nonergodicity implies the nonlinear change of correlations and vice versa. GD thanks Claudia E. Wieners for useful discussions about the relationship between ENSO and the total variability of the Equatorial Pacific. TB thanks Keith Rodgers for informing him about the volume of Variations that includes (Haszpra et al., 2020b). GD is thankful to B. Stevens, T. Mauritsen, Y. Takano, and N. Maher for providing access to the output of the MPI-ESM ensembles. 20th Century Reanalysis V2 data provided by the NOAA/OAR/ESRL PSL, Boulder, Colorado, United States, from their Web site at https://psl.noaa.gov/. Free access to the CRU PRE data and the CERA 20C reanalysis product is gratefully acknowledged. The preprint of this paper (Bódai et al., 2020a) can be found at https://arxiv.org/abs/2009.02155. The authors acknowledge the constructive comments by the two reviewers, one of whom prompted the definition of TFSTVE.

SUPPLEMENTARY MATERIAL

The Supplementary Material for this article can be found online at: https://www.frontiersin.org/articles/10.3389/feart.2020.599785/full#supplementary-material.

REFERENCES

Aneesh, S., and Sijikumar, S. (2018). Changes in the La Niña teleconnection to the Indian summer monsoon during recent period. *J. Atmos. Sol. Terr. Phys.* 167, 74–79. doi:10.1016/j.jastp.2017.11.009

Baldwin, M. P., Stephenson, D. B., and Jolliffe, I. T. (2009). Spatial weighting and iterative projection methods for EOFs. *J. Clim.* 22, 234–243. doi:10.1175/2008JCLI2147.1

Björnsson, H., and Venegas, S. A. (1997). A manual for EOF and SVD analyses of climatic data. *Tech. rep.* 97 (1), 112–134.

Bódai, T., Drótos, G., Ha, K.-J., Lee, J.-Y., Haszpra, T., and Chung, E.-S. (2020a). Nonlinear forced change and nonergodicity: the case of ENSO-Indian monsoon and global precipitation teleconnections arXiv.2009.02155. *Atmos. Oceanic Phys.* Available at: https://arxiv.org/abs/2009.02155

Bódai, T., Drótos, G., Herein, M., Lunkeit, F., and Lucarini, V. (2020b). The forced response of the El niño–southern oscillation–Indian monsoon teleconnection in ensembles of earth system models. *J. Clim.* 33, 2163–2182. doi:10.1175/JCLI-D-19-0341.1

Bódai, T., and Tél, T. (2012). Annual variability in a conceptual climate model: snapshot attractors, hysteresis in extreme events, and climate sensitivity. *Chaos: An Interdisciplinary J. Nonlinear Sci.* 22, 023110. doi:10.1063/1.3697984

Carréric, A., Dewitte, B., Cai, W., Capotondi, A., Takahashi, K., Yeh, S.-W., et al. (2020). Change in strong Eastern Pacific El Niño events dynamics in the warming climate. *Clim. Dynam.* 54, 901–918. doi:10.1007/s00382-019-05036-0

Cochran, W. G. (1934). The distribution of quadratic forms in a normal system, with applications to the analysis of covariance. *Math. Proc. Camb. Phil. Soc.* 30, 178–191. doi:10.1017/S0305004100016595

Compo, G. P., Whitaker, J. S., Sardeshmukh, P. D., Matsui, N., Allan, R. J., Yin, X., et al. (2011). The Twentieth century reanalysis Project. *Q. J. R. Meteorol. Soc.* 137, 1–28. doi:10.1002/qj.776

Drótos, G., Bódai, T., and Tél, T. (2015). Probabilistic concepts in a changing climate: a snapshot attractor picture. *J. Clim.* 28, 3275–3288. doi:10.1175/JCLI-D-14-00459.1

Drótos, G., Bódai, T., and Tél, T. (2016). Quantifying nonergodicity in nonautonomous dissipative dynamical systems: an application to climate change. *Phys. Rev. E* 94, 022214. doi:10.1103/PhysRevE.94.022214

Drótos, G., Bódai, T., and Tél, T. (2017). On the importance of the convergence to climate attractors. *Eur. Phys. J. Spec. Top.* 226, 2031–2038. doi:10.1140/epjst/e2017-70045-7

Fisher, R. A. (1915). Frequency distribution of the values of the correlation coefficient in samples from an indefinitely large population. *Biometrika* 10, 507–521.

Franzke, C. L. E. (2014). Nonlinear climate change. *Nat. Clim. Change* 4, 423–424. doi:10.1038/nclimate2245

Gershunov, A., and Barnett, T. P. (1998). Interdecadal modulation of ENSO teleconnections. *Bull. Am. Meteorol. Soc.* 79, 2715–2726. doi:10.1175/1520-0477(1998)079<2715:IMOET>2.0.CO;2

Gershunov, A., Schneider, N., and Barnett, T. (2001). Low-frequency modulation of the ENSO–Indian monsoon rainfall relationship: signal or noise? *J. Clim.* 14, 2486–2492. doi:10.1175/1520-0442(2001)014<2486:LFMOTE>2.0.CO;2

Ghil, M., and Lucarini, V. (2020). The physics of climate variability and climate change. *Rev. Mod. Phys.* 92, 035002. doi:10.1103/RevModPhys.92.035002

Härdle, W., and Simar, L. (2007). *Canonical correlation analysis*. Berlin, Heidelberg: Springer Berlin Heidelberg, 321–330. doi:10.1007/978-3-540-72244-1_14

Harris, I. (2019a). [Dataset]: CRUTS v4.03 data variables: PRE. https://crudata.uea.ac.uk/cru/data/hrg/cru_ts_4.03/cruts.1905011326.Ωv4.03/pre/

Harris, I. (2019b). [Dataset]: Release notes for CRU TS v4.03. https://crudata.uea.ac.uk/cru/data/Ωhrg/cru_ts_4.03/Release_Notes_CRU_TS4.03.txt

Haszpra, T., Herein, M., and Bódai, T. (2020a). Investigating ENSO and its teleconnections under climate change in an ensemble view—a new perspective. *Earth Syst Dyn.* 11, 267–280. doi:10.5194/esd-11-267-2020

Haszpra, T., Topál, D., and Herein, M. (2020b). "Detecting forced changes in internal variability using Large Ensembles: on the use of methods based on the "snapshot view." *New research on climate variability and change using initial-condition Large Ensembles. Variations*. Editors C. Deser and K. Rodgers (Washington: UCAR), Vol. 18, 36–43.

Haszpra, T., Topál, D., and Herein, M. (2020c). On the time evolution of the arctic oscillation and related wintertime phenomena under different forcing scenarios in an ensemble approach. *J. Clim.* 33, 3107–3124. doi:10.1175/JCLI-D-19-0004.1

Heffernan, P. M. (1997). Unbiased estimation of central moments by using U-statistics. *J. Roy. Stat. Soc. B* 59, 861–863.

Herein, M., Márfy, J., Drótos, G., and Tél, T. (2016). Probabilistic concepts in intermediate-complexity climate models: a snapshot attractor picture. *J. Clim.* 29, 259–272. doi:10.1175/JCLI-D-15-0353.1

Kay, J. E., Deser, C., Phillips, A., Mai, A., Hannay, C., Strand, G., et al. (2015). The community Earth system model (CESM) large ensemble project: a community resource for studying climate change in the presence of internal climate variability. *Bull. Am. Meteorol. Soc.* 96, 1333–1349. doi:10.1175/BAMS-D-13-00255.1

Kim, B.-H., and Ha, K.-J. (2015). Observed changes of global and western Pacific precipitation associated with global warming SST mode and mega-ENSO SST mode. *Clim. Dynam.* 45, 3067–3075. doi:10.1007/s00382-015-2524-2

Krishnamurthy, L., and Krishnamurthy, V. (2014). Influence of PDO on South Asian summer monsoon and monsoon–ENSO relation. *Clim. Dynam.* 42, 2397–2410. doi:10.1007/s00382-013-1856-z

Krishnamurthy, V., and Goswami, B. N. (2000). Indian monsoon–ENSO relationship on interdecadal timescale. *J. Clim.* 13, 579–595. doi:10.1175/1520-0442(2000)013<0579:IMEROI>2.0.CO;2

Kumar, K. K., Rajagopalan, B., and Cane, M. A. (1999). On the weakening relationship between the Indian monsoon and ENSO. *Science* 284, 2156–2159. doi:10.1126/science.284.5423.2156

Laloyaux, P., de Boisseson, E., Balmaseda, M., Bidlot, J. R., Broennimann, S., Buizza, R., et al. (2018). CERA-20C: a coupled reanalysis of the twentieth century. *J. Adv. Model. Earth Sys.* 10 (5), 1172–1195. doi:10.1029/2018MS001273

Maher, N., Milinski, S., Suarez-Gutierrez, L., Botzet, M., Dobrynin, M., Kornblueh, L., et al. (2019). The Max Planck Institute Grand ensemble: enabling the exploration of climate system variability. *J. Adv. Model. Earth Syst.* 11, 2050–2069. doi:10.1029/2019MS001639

Mann, H. B. (1945). Nonparametric tests against trend. *Econometrica* 13, 245–259.

Meinshausen, M., Smith, S. J., Calvin, K., Daniel, J. S., Kainuma, M. L. T., Lamarque, J.-F., et al. (2011). The RCP greenhouse gas concentrations and their extensions from 1765 to 2300. *Climatic Change* 109, 213. doi:10.1007/s10584-011-0156-z

Mishra, V., Smoliak, B. V., Lettenmaier, D. P., and Wallace, J. M. (2012). A prominent pattern of year-to-year variability in Indian Summer Monsoon Rainfall. *Proc. Natl. Acad. Sci. Unit. States Am.* 109, 7213–7217. doi:10.1073/pnas.1119150109

North, G. R., Bell, T. L., Cahalan, R. F., and Moeng, F. J. (1982). Sampling errors in the estimation of empirical orthogonal functions. *Mon. Weather Rev.* 110, 699–706. doi:10.1175/1520-0493(1982)110<0699:SEITEO>2.0.CO;2

Pandey, P., Dwivedi, S., Goswami, B. N., and Kucharski, F. (2020). A new perspective on ENSO-Indian summer monsoon rainfall relationship in a warming environment. *Clim. Dynam.* 55, 3307–3326. doi:10.1007/s00382-020-05452-7

Parthasarathy, B., Munot, A. A., and Kothawale, D. R. (1994). All-India monthly and seasonal rainfall series: 1871–1993. *Theor. Appl. Climatol.* 49, 217–224. doi:10.1007/BF00867461

Power, S. B., and Delage, F. P. D. (2018). El Niño–Southern Oscillation and associated climatic conditions around the world during the latter half of the twenty-first century. *J. Clim.* 31, 6189–6207. doi:10.1175/JCLI-D-18-0138.1

Quadrelli, R., Bretherton, C. S., and Wallace, J. M. (2005). On sampling errors in empirical orthogonal functions. *J. Clim.* 18, 3704–3710. doi:10.1175/JCLI3500.1

Santer, B. D., Fyfe, J. C., Solomon, S., Painter, J. F., Bonfils, C., Pallotta, G., et al. (2019). Quantifying stochastic uncertainty in detection time of human-caused climate signals. *Proc. Natl. Acad. Sci. Unit. States Am.* 116, 19821–19827. doi:10.1073/pnas.1904586116

Storch, H. V., and Zwiers, F. W. (1999). *Statistical analysis in climate research*. Cambridge, United Kingdom: Cambridge University Press. doi:10.1017/CBO9780511612336

Takahashi, K., Montecinos, A., Goubanova, K., and Dewitte, B. (2011). ENSO regimes: reinterpreting the canonical and modoki El Niño. *Geophys. Res. Lett.* 38. doi:10.1029/2011GL047364

Tél, T., Bódai, T., Drótos, G., Haszpra, T., Herein, M., Kaszás, B., et al. (2019). The theory of parallel climate realizations. *J. Stat. Phys.* 179 (5–6), 1496–1530. doi:10.1007/s10955-019-02445-7

Timmermann, A. (1999). Detecting the nonstationary response of ENSO to greenhouse warming. *J. Atmos. Sci.* 56, 2313–2325. doi:10.1175/1520-0469(1999)056<2313:DTNROE>2.0.CO;2

Topál, D., Ding, Q., Mitchell, J., Baxter, I., Herein, M., Haszpra, T., et al. (2020). An internal atmospheric process determining summertime arctic sea ice melting in the next three decades: lessons learned from five large ensembles and multiple CMIP5 climate simulations. *J. Clim.* 33, 7431–7454. doi:10.1175/JCLI-D-19-0803.1

Torrence, C., and Webster, P. J. (1999). Interdecadal changes in the ENSO–monsoon system. *J. Clim.* 12, 2679–2690. doi:10.1175/1520-0442(1999)012<2679:ICITEM>2.0.CO;2

Vega-Westhoff, B., and Sriver, R. L. (2017). Analysis of ENSO's response to unforced variability and anthropogenic forcing using CESM. *Sci. Rep.* 7, 18047. doi:10.1038/s41598-017-18459-8

Wang, B. (2006). *The Asian Monsoon*. Berlin, Germany: Springer-Verlag. doi:10.1007/3-540-37722-0

Wang, B., Xiang, B., Li, J., Webster, P. J., Rajeevan, M. N., Liu, J., et al. (2015). Rethinking Indian monsoon rainfall prediction in the context of recent global warming. *Nat. Commun.* 6, 7154. doi:10.1038/ncomms8154

Watanabe, T., and Yamazaki, K. (2014). Decadal-scale variation of South Asian summer monsoon onset and its relationship with the pacific decadal oscillation. *J. Clim.* 27, 5163–5173. doi:10.1175/JCLI-D-13-00541.1

Yettella, V., Weiss, J. B., Kay, J. E., and Pendergrass, A. G. (2018). An ensemble covariance framework for quantifying forced climate variability and its time of emergence. *J. Clim.* 31, 4117–4133. doi:10.1175/JCLI-D-17-0719.1

Yun, K.-S., and Timmermann, A. (2018). Decadal monsoon-ENSO relationships reexamined. *Geophys. Res. Lett.* 45, 2014–2021. doi:10.1002/2017GL076912

Zheng, M., Chang, E. K. M., and Colle, B. A. (2013). Ensemble sensitivity tools for assessing extratropical cyclone intensity and track predictability. *Weather Forecast.* 28, 1133–1156. doi:10.1175/WAF-D-12-00132.1

Zheng, M., Chang, E. K. M., Colle, B. A., Luo, Y., and Zhu, Y. (2017). Applying fuzzy clustering to a multimodel ensemble for U.S. East coast winter storms: scenario identification and forecast verification. *Weather Forecast.* 32, 881–903. doi:10.1175/WAF-D-16-0112.1

Zheng, M., Chang, E. K. M., and Colle, B. A. (2019). Evaluating U.S. East coast winter storms in a multimodel ensemble using EOF and clustering approaches. *Mon. Weather Rev.* 147, 1967–1987. doi:10.1175/MWR-D-18-0052.1

Conflict of Interest: The authors declare that the research was conducted in the absence of any commercial or financial relationships that could be construed as a potential conflict of interest.

frontiers in Earth Science

ORIGINAL RESEARCH
published: 08 April 2021
doi: 10.3389/feart.2021.615325

Connection of Quasi-Resonant Amplification to the Delay in Atmospheric Residence Times Over India

T. V. Lakshmi Kumar[1], *G. Purna Durga*[1], *K. Koteswara Rao*[2]*, *Humberto Barbosa*[3], *Ashwini Kulkarni*[4], *Savita Patwardhan*[4], *R. K. Mall*[5] and *V. Brahmananda Rao*[6]

[1]Atmospheric Science Research Laboratory, SRM Institute of Science and Technology, Kattankulathur, India, [2]Centre for Climate Change and Sustainability, Azim Premji University, Bengaluru, India, [3]Laboratório de Análise e Processamento de Imagens de Satélites-LAPIS, Instituto de Ciências Atmosféricas-ICAT, Universidade Federal de Alagoas, UFAL, Maceió, Brazil, [4]Indian Institute of Tropical Meteorology, Ministry of Earth Sciences, Pune, India, [5]DST-Mahamana Center of Excellence in Climate Change Research, Banaras Hindu University, Varanasi, India, [6]Instituto de Pesquisas Espaciais, São José Dos Campos, Brazil

Mean monthly Atmospheric Residence Times (ART), deduced from the global climate models of Coupled Model Intercomparison Project 5 (CMIP5) under RCP4.5 and RCP8.5 emission scenarios over Indian landmass, show a perceptible increase by the end of the 21st century. India, being a tropical country, faces prolonged ART, particularly during the June month of Southwest monsoon season (June to September) which will be an indicative measure of the increased frequency of extreme weather events. Here we show a possible connection of quasi-resonant amplification (QRA) to the recent (August 2018) Kerala heavy rains that resulted in severe floods and claimed more than 400 mortalities. Remarkable delay in residence times over India during June is shown to have an association with QRA evidenced by the higher magnitudes of amplitudes at the wavenumbers six and seven from the 19 global climate models of CMIP5 under the RCP4.5 and RCP8.5 scenarios.

Keywords: atmospheric residence times, southwest monsoon, QRA, CMIP5, extreme events

Edited by:
Kyung-Ja Ha,
Pusan National University, South Korea

Reviewed by:
Gen Li,
Hohai University, China
Subimal Ghosh,
Indian Institute of Technology Bombay, India

***Correspondence:**
K. Koteswara Rao
koti.meteo@gmail.com

Specialty section:
This article was submitted to Atmospheric Science, a section of the journal Frontiers in Earth Science

Received: *08 October 2020*
Accepted: *15 February 2021*
Published: *08 April 2021*

Citation:
Lakshmi Kumar TV, Durga GP, Rao KK, Barbosa H, Kulkarni A, Patwardhan S, Mall RK and Rao VB (2021) Connection of Quasi-Resonant Amplification to the Delay in Atmospheric Residence Times Over India.
Front. Earth Sci. 9:615325.
doi: 10.3389/feart.2021.615325

INTRODUCTION

The atmospheric residence times (ART) are defined as the time that the moisture stays in the atmosphere before it precipitates (Chahine, 1992). The spatiotemporal variability of residence times characterizes the regional and global hydrological cycle (Van Der Ent and Tuinenburg, 2017). Chahine (1992) reported residence times as the ratio of precipitable water vapor to the precipitation rate. Later, Trenberth (1998) studied the same over the globe and termed them as the *e–folding* residence times and reported the atmosphere's depletion and restoration rates of moistening and drying. Van Der Ent and Tuinenburg (2017) studied the ART using atmospheric moisture tracking models and reported the global average residence times as 8.9 ± 0.4 days Van Der Ent and Tuinenburg (2017) used the method to estimate the residence times is slightly different by Chahine (1992), Trenberth (1998) where they have not considered the horizontal transport of water vapor in estimating the residence time. Hence, Van Der Ent and Tuinenburg (2017) termed the residence times obtained by Chahine (1992), Trenberth (1998) as the residence times for moisture recycling (Wang et al., 2018). It is worth mentioning that moisture recycling is a diagnostic measure for local evaporation contribution in turning the moisture into rainfall over the same region (Brubakar et al., 1993; Lakshmi Kumar et al., 2021). Moisture recycling over India has been studied by Lakshmi Kumar et al. (2014), Pathak et al. (2014), Sujit et al. (2017). We can find more details on

TABLE. 1 | List of CMIP 5 Models used for the analysis.

S.No	Modeling Center	Model Name	Atmospheric resolution (lat × lon)
1.	Commonwealth Scientific and Industrial Research Organization (CSIRO) and Bureau of Meteorology (BOM), Australia	ACCESS1.0	1.25° × 1.875°
2.	Beijing Climate Center	BCC-CSM1-1	2.8° × 2.8°
3.	College of Global Change and Earth System Science, Beijing, Normal University.	BNU-ESM	2.8° × 2.8°
4.	National Center for Atmospheric Research	CCSM4	0.9° ×1.25°
5.	Centro Euro-Mediterraneo per I Cambiamenti Climatici	CMCC-CM	0.75° × 0.75°
6.	Centre National de Recherches Météorologiques	CNRM-CM5	1.406° × 1.406°
7.	Commonwealth Scientific and Industrial Research Organization	CSIRO-Mk3.6.0	1.875° × 1.895°
8.	NOAA Geophysical Fluid Dynamics Laboratory	GFDL-CM3	2.0° × 2.5°
9.	NASA Goddard Institute for Space Studies	GISS-E2-R	2.0° × 2.5°
10.	Institute for Numerical Mathematics	INM-CM4	1.5° × 2.0°
11.	Institute Pierre-Simon Laplace	IPSL-CM5A-LR	1.89° × 3.75°
12.	Institute Pierre-Simon Laplace	IPSL-CM5A-MR	1.26° × 2.5°
13.	Japan Agency for Marine-Earth Science and Technology, Atmosphere and Ocean Research Institute (The University of Tokyo), and National Institute for Environmental Studies	MIROC-ESM	2.8° × 2.8°
14.	Japan Agency for Marine-Earth Science and Technology, Atmosphere and Ocean Research Institute (The University of Tokyo), and National Institute for Environmental Studies	MIROC-ESM-CHEM	2.8° × 2.8°
15.	Max Planck Institute for Meteorology	MPI-ESM-LR	1.9° × 1.9°
16.	Max Planck Institute for Meteorology	MPI-ESM-MR	1.875° × 1.9°
17.	The University of Tokyo, National Institute for Environmental Studies, and Japan Agency for Marine–Earth Science and Technology	MIROC5	1.417° × 1.406°
18.	Meteorological Research Institute	MRI-CGCM3	1.1° × 1.1°
19.	Norwegian Climate Centre	NorESM1-M	1.89° × 2.5°

moisture recycling over the Indian monsoon region using CMIP5 models in Lakshmi Kumar et al. (2021). Li et al. (2011) used the Special Sensor Microwave Imager (SSMI) water vapor, and Global Precipitation Climatology Project (GPCP) rainfall data sets to study the global moisture recycling and reported the decrease/increase of moisture recycling in lower/higher precipitation zones, which strengthens the concept of "rich get richer and the poor get poorer" as the societies are more vulnerable to the perturbations in water cycle than the temperature alone (http://blogs.nature.com/news/2012/04/global-water-cycle-is-revving-up.html). As the inverse of cycling rate is the residence time (Chahine, 1992), the global decrease of cycling of moisture indicates the increase in ART. However, ART is the indicator of the atmospheric water holding capacity that combines the role of evaporation and water vapor. The spatial variability of residence times throws challenges in understanding the atmospheric dynamics and thermodynamics in terms of its motion and moisture content. Also, it has great potential to realize the intensity of local and regional hydrological cycles over the oceans and the landmass.

Recent studies of Kornhuber et al. (2019), Mann et al. (2018) and Coumou et al. (2014) reported that extreme events such as droughts, floods in different parts of the globe are having a connection with the slow-moving amplified Rossby waves, known as quasi-resonant amplification (QRA). Severe damage in Bosnia, Herzegovina, Serbia, and Croatia due to the floods caused by the cyclone during the 14th and May 19, 2014 have been explained by the dynamic processes such as planetary wave resonance (Stadtherr et al., 2016). These Rossby waves move eastward, carrying the moisture from tropics to poles, creating lows and highs worldwide. As the jet streams meander with these waves, these mid-latitude waves become slow and cause the wave resonance, resulting in extreme weather events worldwide. The amplification of quasi-resonant Rossby waves can be seen in the amplitude of zonal wavenumber from six to 8. These QRA favorable conditions are linked to increase Arctic warming that happened due to climate change (Mann et al., 2017). Mann et al. (2018) stressed the increase of QRA events resulting in more extreme weather events across the globe under business as usual conditions using the CMIP five model simulations. As the increased residence times manifest extreme weather events, associated changes in residence times can be in future QRA events.

The studies on ART over India are very sparse. Lakshmi Kumar et al. (2014) studied the residence times based on the formula of Chahine (1992) on all Indian time scale. They reported the ART to vary from 10 to 2 days during the pre-monsoon (March to May) and southwest monsoon (June to September) seasons over India. Pathak et al. (2014) limited their studies to precipitation recycling to infer the source and sinks of moisture over India. In the present work, the time series of mean monthly ART for the southwest monsoon has been obtained from 1986 to 2,100 under RCP 4.5 and 8.5 emission scenarios. Attempts are made to see QRA's possible connection with the Kerala heavy rains in Aug 2018 by studying the zonal wave spectra and other associated methods. Further, the delay in residence times has been focused on India during the southwest monsoon season. This delay is studied concerning the QRA for future climate change scenarios.

METHODS AND DATA SETS USED

The main data source for the present study is the global climate models' outputs from CMIP5 for the period 1986 to 2,100. Nineteen (19) models have been considered in the present study to estimate the ART. List of the models used along with

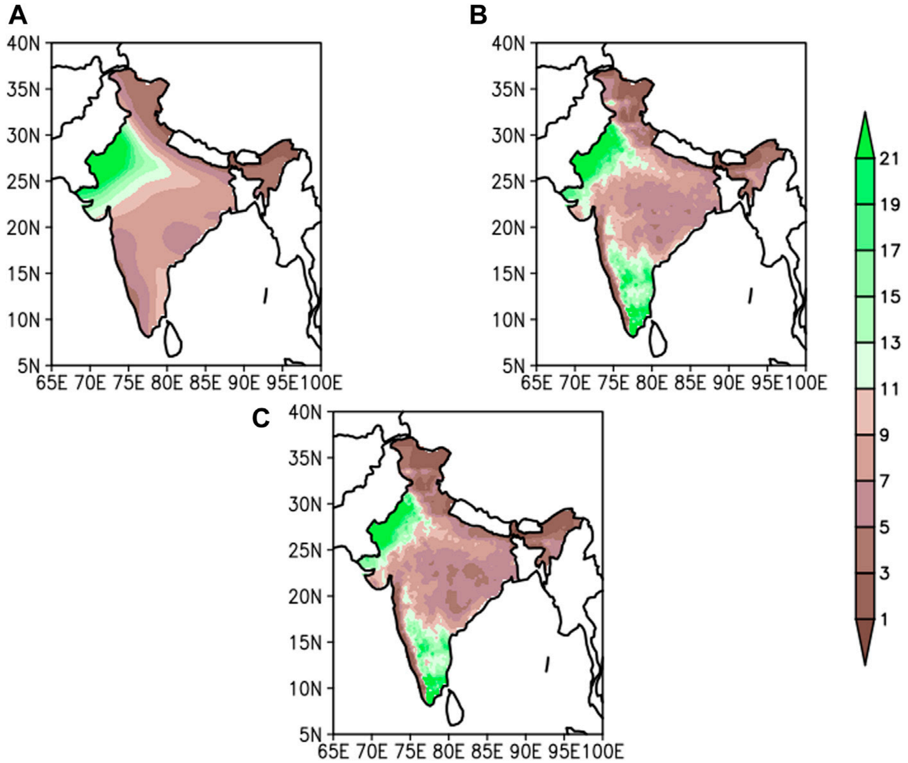

FIGURE 1 | Spatial pattern of mean monthly atmospheric residence times (ART) over India obtained from **(A)** CMIP5 MMM data sets, **(B)** water vapor of ERA and rainfall of IMD and **(C)** water vapor of NCEP and rainfall of IMD for the south west monsoon season of 1986–2005.

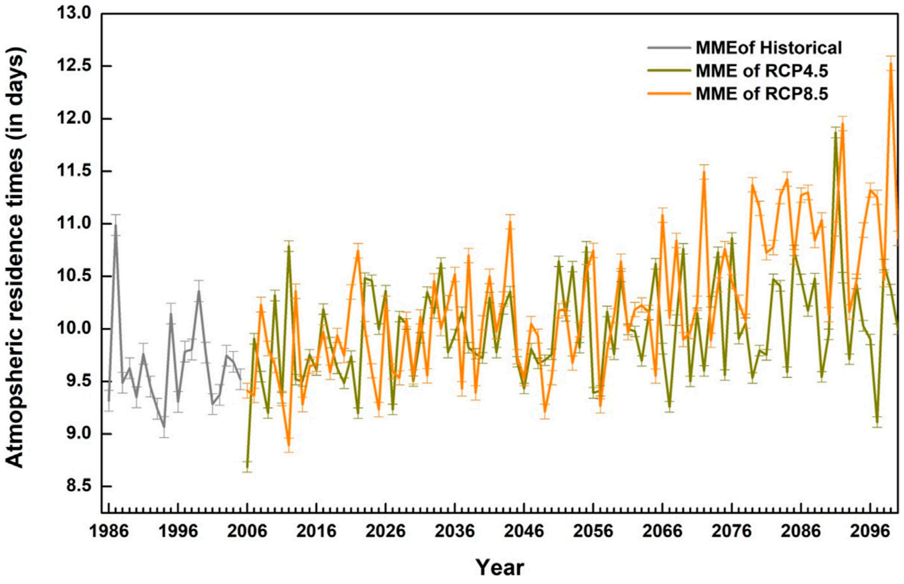

FIGURE 2 | Mean monthly atmospheric residence times over Indian landmass for the SW monsoon from 1986 to 2,100 obtained from the multi model ensemble of CMIP 5 (vertical bars represent the standard error from the 19 global climate models).

the details are given in **Table.1** (Taylor et al., 2012). We estimated the residence times in the historical period of 1986–2005 and also for the three future epochs 2016–2035, 2046–2065, and 2080–2099, which are treated as near, mid, and far future (Stocker et al., 2013) under the two emission scenarios of RCP 4.5 and RCP 8.5. All the models are with monthly temporal resolution and brought to the 1°

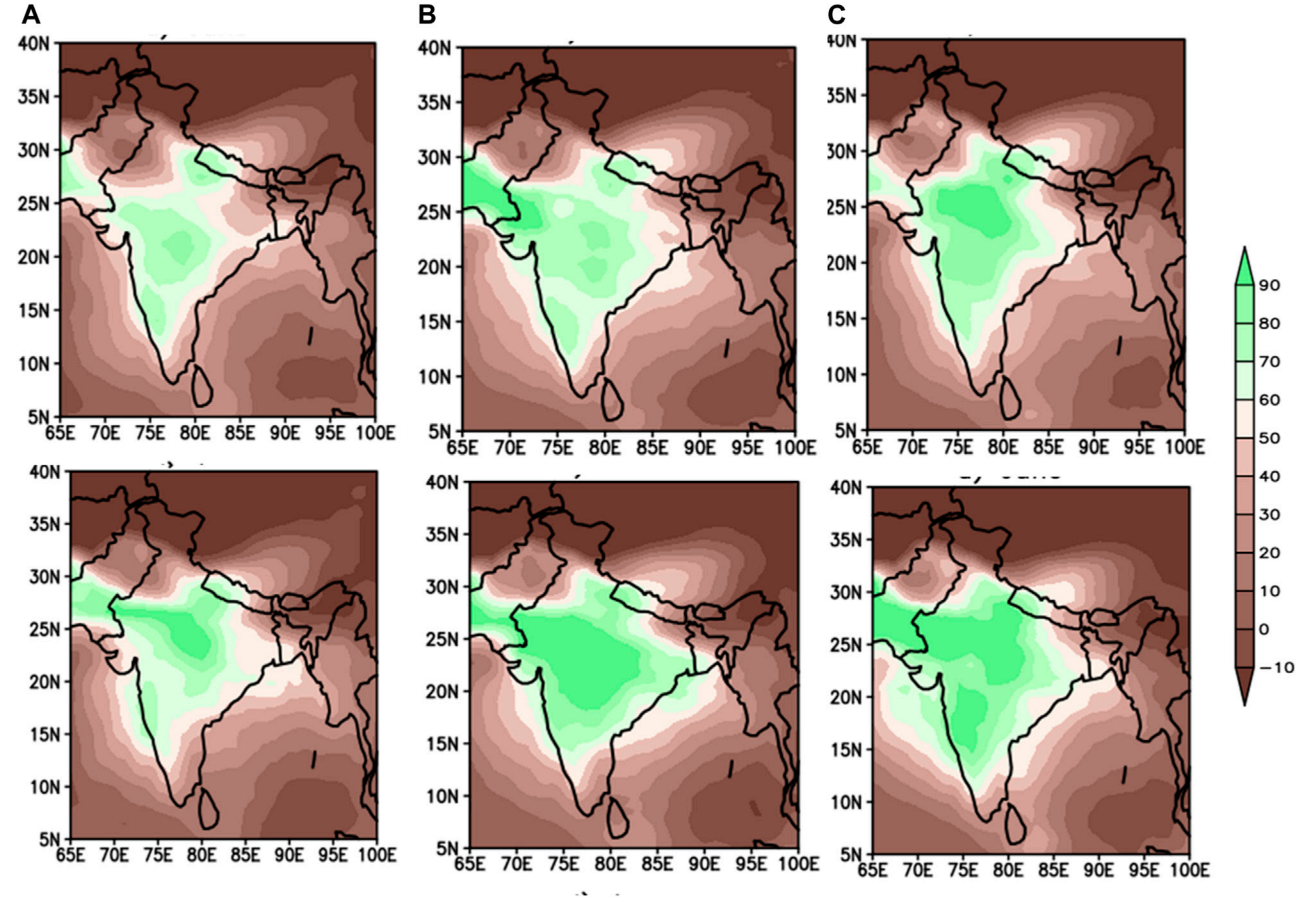

FIGURE 3 | Anomalies in ART for June over India for the periods **(A)** 2016–2035, **(B)** 2046–2065 and **(C)** 2080–2099 under RCP 4.5 (top panel) and 8.5 (bottom panel) emission scenarios.

× 1° spatial resolution by the bilinear interpolation technique (Mishra et al., 2018) for obtaining the Multi-Model Mean (MMM) (mean of the all models) which will help to study the explicit diagnosis of residence times on space and time scale. In the present work, we used the method of Chahine (1992) to estimate the atmospheric residence times (ART) by taking the ratio of the precipitable water vapor to the precipitation rate. Time series of ART have been obtained by averaging the respective grids over different regions under consideration. We also estimated the ART using the gridded rainfall data developed by India Meteorological Department (IMD) based on the wide rain gauge network (Pai et al., 2014) and the precipitable water vapor data from European Center for Medium-Range Weather Forecasting Reanalysis (ERA) and National Center for Environmental Protection (NCEP) gridded data set. These are used to compare with the CMIP5 model derived ART to understand the agreement between them.

Meridional wind at 300 hPa for June month has been obtained for different CMIP five models and subjected to the one-dimensional simple harmonic oscillator problem to get the zonal wavenumber spectra for different years. The meridional wind fields have been averaged zonally for each 10° box for the latitudinal region 37.5°N to 57.5°N and are used in the present study. The QRA mechanism can be understood from the phase speed equation of Rossby waves, which is given below,

$$C = U - \frac{\beta}{(K^2 + l^2)} \tag{1}$$

Where c is the phase speed, U is the zonal wind, $ß$ are the Rossby parameter, and K and l are meridional and zonal wave numbers, respectively. From **Eq. 1**, it can be inferred that the phase speed of stationary Rossby waves dependent on the magnitude of zonal wavenumber. Since the wind speeds are high in the southern hemispheric region, the QRA can apply to lower wavenumbers, i.e., above 4. But in the case of the northern hemisphere, similar QRA can be seen for higher wavenumbers i.e., above six or 7 (Kornhuber et al., 2017). Important steps in the aforementioned methodology are also provided in the flowchart given below.

RESULTS AND DISCUSSION

The space scale variations of ART over India obtained from the CMIP5 MMM and the water vapor of ERA and NCEP with the rainfall of IMD for the SW monsoon season of 1986–2005 are

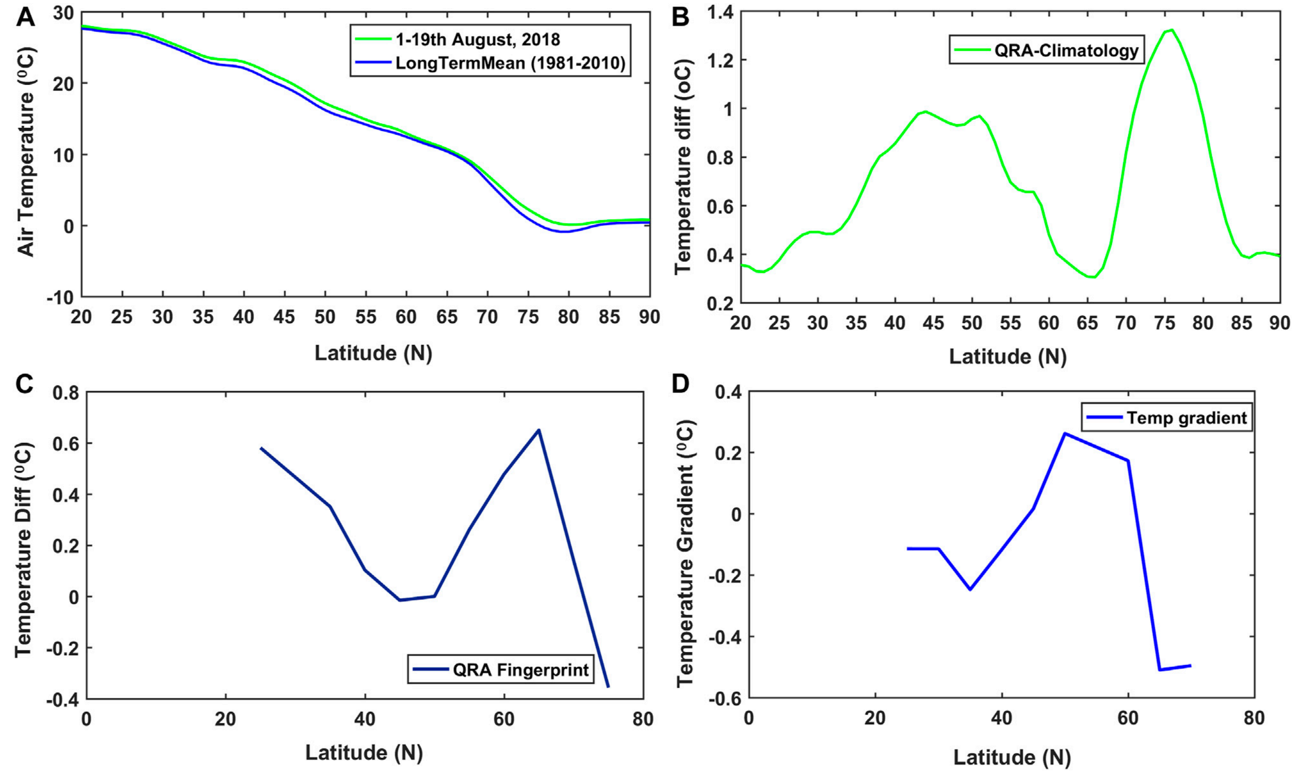

FIGURE 4 | (A) Meridional variations of zonal mean surface temperatures over NH **(B)** the difference between zonal mean temperatures associated with QRA favorable conditions **(C)** The QRA fingerprint and **(D)** Temperature gradient for each 5 over NH during 1–19th August 2018.

shown in **Figures 1A–C**. The ART pattern obtained from the model and reanalysis data sets shows similar features over the monsoon core region of India. Mean monthly ART show less than 11 days over the MCI. However, the ART are much higher over India's other regions, such as peninsular India and northwestern parts of India, which might be due to the low SW monsoon activity. Mean monthly ART over Indian landmass for the SW monsoon season under RCP 4.5 and 8.5 emission scenarios from 1986 to 2,100 showed a steady increase from 9.32 ± 0.44 to 10 ± 0.26 10.86 ± 0.21, respectively (**Figure 2**). These regional ART are analogous to the global atmospheric lifetimes of water vapor reported varying from 8 to 10 days (Chahine, 1992; Trenberth, 1998; Bosilovich and Schubert, 2002; Van Der Ent et al., 2014). The increase in ART is generally attributed to the increased radiative forcing that enhances the atmospheric water holding capacity, which is mainly driven by the rise in temperature (Trenberth, 1998) and the low exchange of moisture flux from surface to free troposphere (Allan and Liepert, 2010). Higher and lower residence times over oceans and land regions and the variability of residence times regionally are also connected to different reasons such as the land-sea patterns, stable stratification of the atmosphere in desert areas, intense coupling of evaporation and precipitation within the extratropical cyclones of the mid latitudinal regions, quasi-continuous evaporation over tropical regions respectively. The delay in the ART over the Indian landmass indicates the long span regional hydrological cycle over India. This delay also resembles the Indian hydrological cycle's intensification, resulting in more frequent extreme weather events. The estimated spatial ART for the southwest monsoon months June, July, August, and September show a remarkable delay in June month compared to other months (**Supplementary Figure S1**). A delay of 50–90% from its mean has been observed with peak activity in the Western Ghats and core monsoon region (**Figure 3**). The delay in residence times gradually focused on the core monsoon region during the epochs 2046–2065 and 2080–2099, extending to the Western Ghats during the later epoch. The rest of the months have shown a slight delay in residence times along with the oceanic part. Since the SW monsoon is active over the Western Ghats and central Indian regions, the delay may conspicuous in these regions. The observed delay of ART in June may affect the agriculture sector, as Findell et al. (2019) reported. The reduction in global recycling might impact the crop yields to make them increasingly soil moisture limited. As the reduction in recycling is an indication of delay in residence times (Chahine, 1992), this will also impact the crop yields. Also, the reported delay of ART in the monsoon core region covering the geographical regions of Indo-Gangetic plains will play a crucial role as this region is prone to continuous droughts (Nath et al., 2017). The possible reasons one may think for the delay in ART during June month could be due to the increasing pre-monsoon rainfall and the changes in the monsoon onset dates. But, Sinha et al. (2019) reported that India's pre-monsoon rainfall had shown a

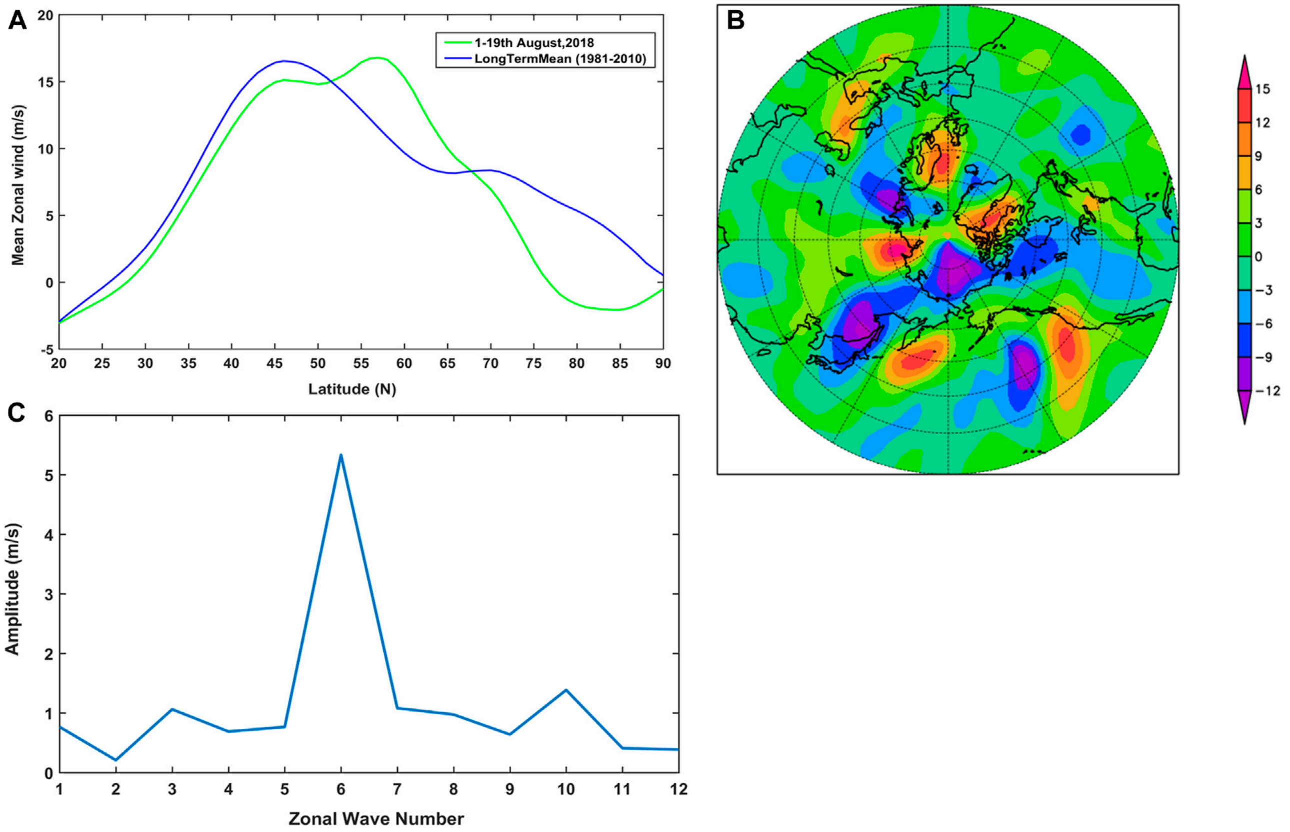

FIGURE 5 | (A) Meridional variations of upper-troposphere (300hPa) zonal mean zonal winds over NH **(B)** Circumglobal variations of upper-troposphere (300hPa) meridional wind fields over NH and **(C)** Zonally averaged zonal wave number spectra for the meridional wind fields at 300 hPa over 37.5° to 57.5°N for the period 1st to August 19, 2018.

significant decreasing trend. This trend is attributed to the precipitation over China and temperature over the South China Sea, which will impact the Indian southwest monsoon rainfall. Secondly, southwest monsoon's onset dates over the core monsoon India are slightly advanced from 1979 to 2014 (**Supplementary Figure S2**). Also, Rai et al. (2015) reported that the early onset of monsoon over India's northwest parts would decrease the rainfall amounts during the June and July months of southwest monsoon. Further, our analysis on the increasing number of heavy rainfall events (rainfall greater than 64 mm per day) (**Supplementary Figure S3**) and the number of dry days (All India rainfall less than 2 mm per day) (**Supplementary Figure S4**) in June for the period 1986 to 2005 over India confirmed that there is an increment of aforementioned which could be due to delayed residence times. Unlike the temperature, the computed rainfall trend over the monsoon season for the future emission scenarios also does not yield any significantly increasing or decreasing (**Supplementary Figure S5**). The trend in water vapor shows a perceptible increase as it is mainly dependent on temperature (**Supplementary Figure S6**). Past studies of Goswami and Xavier (2005) reported that though the trend of summer monsoon rainfall over Central India is not increasing, the frequency of heavy rainfall events shows a remarkable increase. This remarkable increase is offset by the decreasing number of moderate rainy days, which compensate for rainfall, not increasing, and keeping steady. Hence, the ratio of precipitable water vapor to the rainfall (residence times) provides a good understanding of extreme weather events' increasing frequency. This work's main objective is to examine the QRA during the June month to show the delayed residence times, causing the increased frequency of extreme weather events associated with the Rossby wave resonance. As reported, the southward incursion of upper tropospheric westerlies associated with mid-latitude troughs can severely affect the Indian summer monsoon. This interaction depends on the phase of Rossby waves (Joseph et al., 2014). It is also worth mentioning that the CMIP five models project increased Indian summer monsoon rainfall due to its strong negative feedback of cloud-radiation in the western Pacific and reduced surface warming over the eastern equatorial Indian Ocean (Li et al., 2015; Li et al., 2016; Li et al., 2017). Here, we first show QRA's indication during the recent Kerala floods, which is the result of heavy rainfall over the regions of Kerala during August 2018. Hunt and Menon (2020) attributed Kerala heavy rainfall events in 2018 to climate change, which weakened the synoptic activity of the Indian monsoon and increased tropical tropospheric moisture. The rainfall over Kerala from 1st to August 19, 2018 is 758.6 mm against the normal rainfall amount of 287.6 mm (The organisation, H. S., 2018). Using the

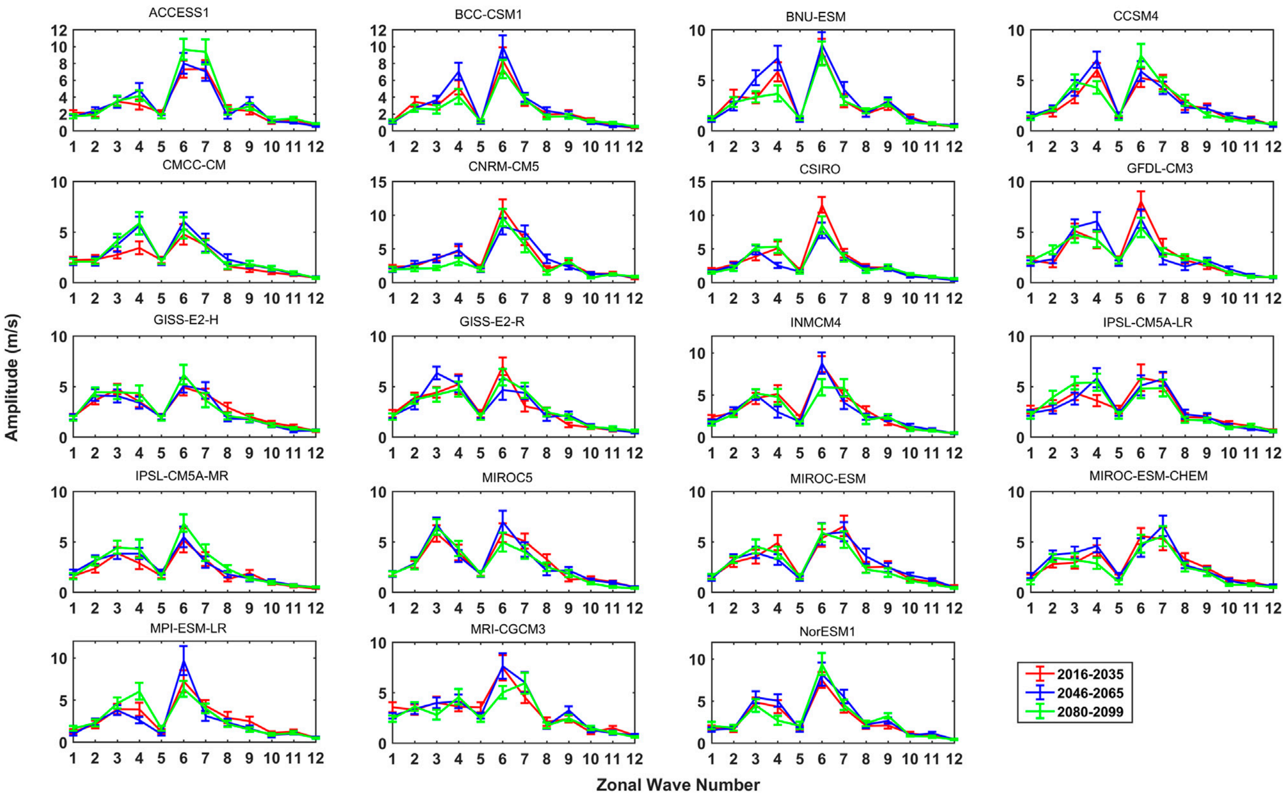

FIGURE 6 | Zonal wave number spectra for the meridional wind fields at 300 hPa over 37.5° to 57.5°N for the June month for the near, mid and far future terms under RCP4.5 scenario.

National Centers for Environmental Prediction (NCEP) reanalysis data, the QRA detection scheme suggested by Kornhuber et al. (2017) has been carried out. **Figures 4A–D** shows the meridional variations of seasonal mean surface temperature from 1st to Aug 19, 2018 and its corresponding climatology. **Figure 4B** reveals the difference between the temperature of QRA time and its climatology. QRA fingerprint has been obtained (**Figure 4C**) by restricting profiles to the mid latitudinal region (25 N-75 N) and calculated the associated variation in temperature associated with QRA (**Figure 4D**). The corresponding temperature gradient and the temperature decrease the near-neutral values around 40̊ N and positive values through 50 N and peak in subpolar latitudes. The temporal gradient **Figure 4D** shows the positive values in the mid latitudinal region and poleward reduction. These temperature gradient variations resemble the minimum zonal wind and strong westerlies over mid and polar latitudes, which are the favorable conditions of QRA.

The zonal mean zonal wind fields at 300 hPa from 1st to Aug 19, 2018 and the climatology (1981–2010) (**Figure 5A**) show the double jet structure by slowing down in mid latitudinal regions, amplification in sub-Polar Regions. **Figure 5B** shows the corresponding variations in surface temperature during the observational period and climatological period. **Figure 5B** is the zonal mean of meridional wind at 300 hPa showing a wavy pattern symbolizing the highs and lows across the poles and tropics. The zonal wavenumber spectra for the period 1st to August 19, 2018 for the zonally averaged meridional wind from 37.5°N to 57.5°N latitudes show the peak amplitude, the wave number six and is high compared to that of the same for the normal period (**Figure 5C**). As the floods caused by heavy downpours are not connected to human-induced climate change, the reasons are the short term variability in natural climate change induced by the anomalous large scale circulation features (Mishra and Shah, 2018). As the stationary waves influence the hydrological cycle by showing the changes in a vertical motion and the divergent circulations in the zonal variations of moisture, these can be related to the Asian monsoon (Wills et al., 2019). These stationary Rossby waves influencing the extreme weather persists longer than the synoptic scales, and hence these can be detected with sizable data less than the seasonal scale (Screen 2014). As the amplification in the Rossby waves has been seen at wave number six for the Kerala floods, we apply a similar technique to detect the Rossby wave influence on the future climate change scenarios of delayed residence times in June over India. Zonal wavenumber spectra for 19 global climate models show the peak at the wavenumbers six or seven during the three epochs of RCP 4.5 climate scenarios (**Figure 6**). The vertical bars in **Figure 6** denote the standard error. Most of the models show a higher amplitude at wave number more than 5. The standard error of the amplitude of wave numbers six and seven is high compared to other

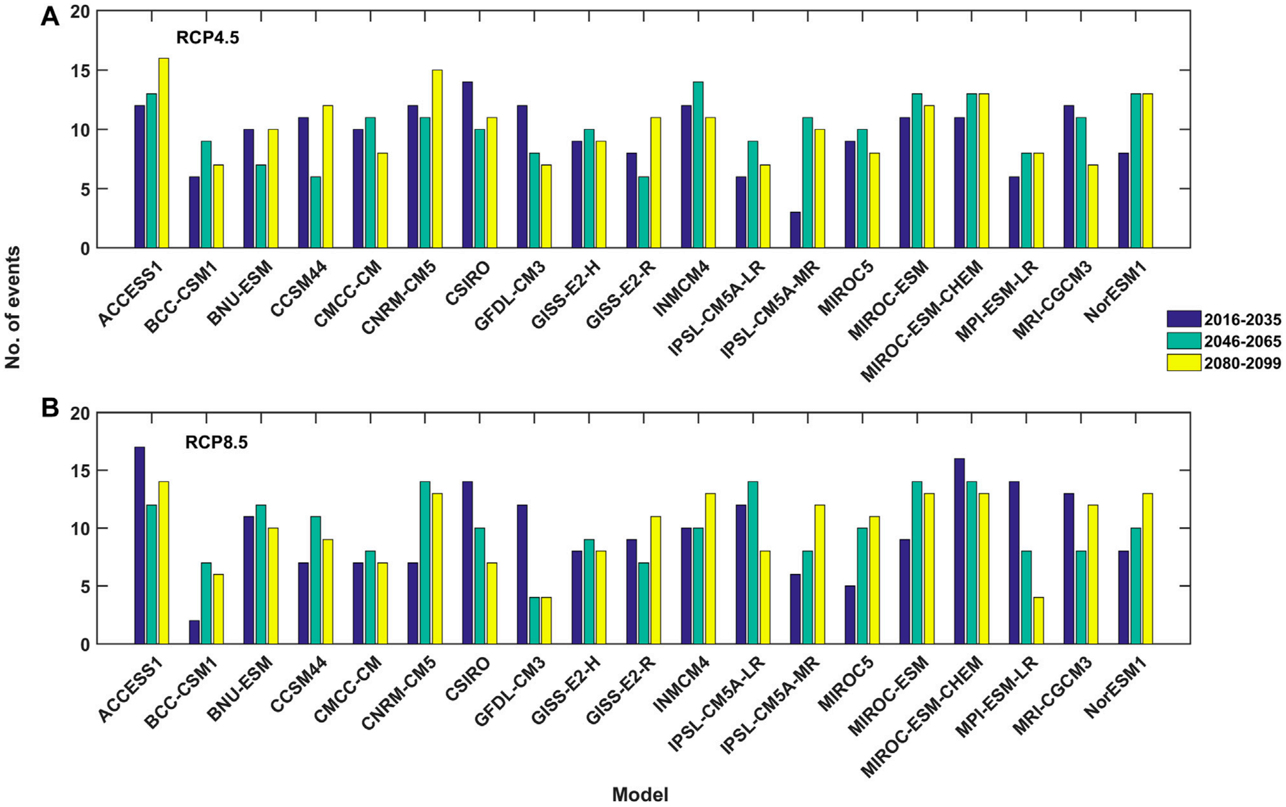

FIGURE 7 | Number of QRA events with 1.5 of standard deviation obtained from all models during June for the near, mid and far future terms under **(A)** RCP4.5 **(B)** RCP8.5 emission scenarios.

wavenumbers, indicating the higher variability with the higher wavenumbers representing the favorable conditions for the QRA occurrence over the Indian region. Kornhuber et al. (2017), in their work on the QRA during the summertime Rossby wave resonance in the northern and southern hemispheres for the period 1979 to 2015, using the reanalysis data, found that the duration of the QRA events in the NH for wave number 7 as 6 days duration and the average duration for the wavenumbers 6–8 as 4.6 days. This duration is shorter than that of over the SH, observed at the wavenumber four and 5. However, from **Figure 6**, it can learn that the amplitude peaks change randomly for the near-century (2016–2035), mid-century (2046–2065), and far-century (2080–2099) future terms. We also show the number of QRA events for all the models during the above-mentioned periods (**Figure 7**). The events are calculated based on the wavenumber amplitude is higher than 1.5 of its standard deviation. All the models witnessed the occurrence of QRA with a distinguished number of events. An average of 10 years among the 20 years is found to be with extreme QRA from all models under RCP4.5 and 8.5 emission scenarios. Models such as ACCESS1, BNU-ESM, CCSM4, CNRM-CM5, GISS-E2-R, and MIROC-ESM-CHEM show the highest number of QRA events during the far future period in the RCP4.5 scenario, while models like GISS-E2-R, INMCM4, IPSL-CM5A-MR, MIROC5, and NorESM1 shows the highest number of QRA events during the far future period in the RCP8.5 scenario. As reported by Mann et al. (2018), some of the CMIP five models, which show the Arctic warming only could indicate the increase in QRA occurrence in the future while the rest yield to a potential decrease. In the present study, we could also see similar results of increasing and decreasing QRA events in different epochs. Nevertheless, India's residence times could show a continuous increase for future scenarios, showing that QRA is a primary component that influences the delay in ART over India. As the association of QRA is evidenced over the Indian region for different years of the study period, higher amplitude observed from the wave numbers six and seven and the number of QRA events from all the models indicate the intense and heavy rainfall events resulting from longer prolonged dry spells during the June month of Southwest monsoon season over India.

CONCLUSIONS

Based on the analysis performed in the present study, we draw the following main conclusions.

i. June month over India witnessed a great delay in ART in near, mid, and far-future scenarios of RCP 4.5 and 8.5 pathways. This delay is concentrated in the regions of the Western Ghats and the core monsoon region of India.
ii. The association of QRA has been shown to have a connection with recent Kerala heavy rains in the year 2018.

iii. The delay in ART during June over India is associated with the occurrence of QRA events in near, mid, and future climate change scenarios.

DATA AVAILABILITY STATEMENT

The original contributions presented in the study are included in the article/**Supplementary Material**, further inquiries can be directed to the corresponding author.

AUTHOR CONTRIBUTIONS

TK conceived the idea, written the draft paper. GD analyzed the data. KR developed the idea and made the draft paper as a fair one. HB, RM, and VR are helped in interpreting the results and correction of manuscript. AK and SP helped in the interpretation of the results.

ACKNOWLEDGMENTS

The authors are thankful to the Science Engineering Research Board (SERB), Govt. of India, for funding this work.

SUPPLEMENTARY MATERIAL

The Supplementary Material for this article can be found online at: https://www.frontiersin.org/articles/10.3389/feart.2021.615325/full#supplementary-material.

REFERENCES

Allan, R. P., and Liepert, B. G. (2010). Anticipated changes in the global atmospheric water cycle. *Environ. Res. Lett.* 5, 025201–025203. doi:10.1088/1748-9326/5/2/025201

Bosilovich, M. G., and Schubert, S. D. (2002). Water vapor tracers as diagnostics of the regional hydrologic cycle. *J. Hydrometeor* 3, 149–165. doi:10.1175/1525-7541(2002)003<0149:wvtado>2.0.co;2

Brubaker, K. L., Entekhabi, D., and Eagleson, P. S. (1993). Estimation of continental precipitation recycling. *J. Clim.* 6, 1077–1089. doi:10.1175/1520-0442(1993)006<1077:EOCPR>2.0.CO;2

Chahine, M. T. (1992). The hydrological cycle and its influence on climate. *Nature* 359, 359–379. doi:10.1038/359373a0

Coumou, D., Petoukhov, V., Rahmstorf, S., Petri, S., and Schellnhuber, H. J. (2014). Quasi-resonant circulation regimes and hemispheric synchronization of extreme weather in boreal summer. *Proc. Natl. Acad. Sci.* 111, 12331–12336. doi:10.1073/pnas.1412797111

Findell, K. L., Keys, P. W., van der Ent, R. J., Lintner, B. R., Berg, A., and Krasting, J. P. (2019). Rising temperatures increase importance of oceanic evaporation as a source for continental precipitation. *J. Clim.* 32, 7713–7726. doi:10.1175/jcli-d-19-0145.1

Goswami, B. N., and Xavier, P. K. (2005). Dynamics of "internal" interannual variability of the Indian summer monsoon in a GCM. *J. Geophys. Res. Atmos.* 110, 1–17. doi:10.1029/2005jd006042

Hunt, K. M. R., and Menon, A. (2020). The 2018 Kerala floods: a climate change perspective. *Clim. Dyn.* 54, 2433–2446. doi:10.1007/s00382-020-05123-7

Joseph, S., Sahai, A. K., Chattopadhyay, R., Sharmila, S., Abhilash, S., and Rajeevan, M. (2014). *Contrasting progression phase of Indian summer monsoon during June 2013 and 2014 : observational diagnostics*. Pune: Indian Institute of Tropical Meteorology.

Kornhuber, K., Osprey, S., Coumou, D., Petri, S., Petoukhov, V., Rahmstorf, S., et al. (2019). Extreme weather events in early summer 2018 connected by a recurrent hemispheric wave-7 pattern. *Environ. Res. Lett.* 14. doi:10.1088/1748-9326/ab13bf

Kornhuber, K., Petoukhov, V., Karoly, D., Petri, S., Rahmstorf, S., and Coumou, D. (2017). Summertime planetary wave resonance in the Northern and Southern hemispheres. *J. Clim.* 30, 6133–6150. doi:10.1175/jcli-d-16-0703.1

Lakshmi Kumar, T. V., Purnadurga, G., Koteswara Rao, K., and Mall, R. K. (2021). *Moisture recycing over monsoon core region of India in response to global warming from CMIP 5 model data sets, Book, Asian monsoon—beyond teleconnections*, Editor C. Gnannaseelan, A. Parekh, and J. S. Chowdary (Amsterdam, NL: Elsevier Publications) Under Review.

Lakshmi Kumar, T. V., Rao, K. K., Uma, R., and Aruna, K. (2014). The role of El Niño Southern Oscillation on the patterns of cycling rates observed over India during the monsoon season. *J. Water Clim. Chang.* 5, 696. doi:10.2166/wcc.2014.128

Li, G., Xie, S.-P., and Du, Y. (2016). A robust but spurious pattern of climate change in model projections over the tropical Indian ocean. *J. Clim.* 29 (15), 5589–5608. doi:10.1175/jcli-d-15-0565.1

Li, G., Xie, S.-P., and Du, Y. (2015). Monsoon-induced biases of climate models over the tropical Indian ocean*. *J. Clim.* 28, 3058–3072. doi:10.1175/jcli-d-14-00740.1

Li, G., Xie, S.-P., He, C., and Chen, Z. (2017). Western Pacific emergent constraint lowers projected increase in Indian summer monsoon rainfall. *Nat. Clim Change* 7, 708. doi:10.1038/NCLIMATE3387

Li, L., Jiang, X., Chahine, M. T., Olsen, E. T., Fetzer, E. J., Chen, L., et al. (2011). The recycling rate of atmospheric moisture over the past two decades (1988-2009). *Environ. Res. Lett.* 6, 034018. doi:10.1088/1748-9326/6/3/034018

Mann, M. E., Rahmstorf, S., Kornhuber, K., Steinman, B. A., Miller, S. K., and Coumou, D. (2017). Influence of anthropogenic climate change on planetary wave resonance and extreme weather events. *Sci. Rep.* 7, 4682. doi:10.1038/srep46822

Mann, M. E., Rahmstorf, S., Kornhuber, K., Steinman, B. A., Miller, S. K., Petri, S., et al. (2018). Projected changes in persistent extreme summer weather events: the role of quasi-resonant amplification. *Sci. Adv.* 4, eaat3272. doi:10.1126/sciadv.aat3272

Mishra, S. K., Sahany, S., Salunke, P., Kang, I.-S., and Jain, S. (2018). Fidelity of CMIP5 multi-model mean in assessing Indian monsoon simulations. *Npj Clim. Atmos. Sci.* 1, 1–8. doi:10.1038/s41612-018-0049-1

Mishra, V., and Shah, H. L. (2018). Hydroclimatological perspective of the Kerala flood of 2018. *J. Geol. Soc. India* 92, 645–650. doi:10.1007/s12594-018-1079-3

Nath, R., Nath, D., Li, Q., Chen, W., and Cui, X. (2017). Impact of drought on agriculture in the Indo-Gangetic plain, India. *Adv. Atmos. Sci.* 34, 335–346. doi:10.1007/s00376-016-6102-2

Pai, D. S., Latha, S., Rajeevan, M., Sreejith, O. P., Satbhai, N. S., and Mukhopadhyay, B. (2014). Development of a new high spatial resolution (0.25×0.25) long period (1901–2010) daily gridded rainfall data set over India and its comparison with existing data sets over the region. *Mausam* 65, 1–18.

Pathak, A., Ghosh, S., and Kumar, P. (2014). Precipitation recycling in the Indian subcontinent during summer monsoon. *J. Hydrometeorol.* 15, 2050–2066. doi:10.1175/jhm-d-13-0172.1

Rai, A., Saha, S. K., Pokhrel, S., Sujith, K., and Halder, S. (2015). Influence of preonset land atmospheric conditions on the Indian summer monsoon rainfall variability. *J. Geophys. Res. Atmos.* 120, 4551–4563. doi:10.1002/2015JD023159

Screen, J. A. (2014). Arctic amplification decreases temperature variance in northern mid- to high-latitudes. *Nat. Clim Change* 4, 577–582. doi:10.1038/nclimate2268

Sinha, P., Nageswararao, M. M., Dash, G. P., Nair, A., and Mohanty, U. C. (2019). Pre-monsoon rainfall and surface air temperature trends over India and its global linkages. *Meteorol. Atmos. Phys.* 131, 1005–1018. doi:10.1007/s00703-018-0621-6

Stadtherr, L., Coumou, D., Petoukhov, V., Petri, S., and Rahmstorf, S. (2016). Record Balkan floods of 2014 linked to planetary wave resonance. *Sci. Adv.* 2, e1501428. doi:10.1126/sciadv.1501428

Stocker, T. F., Qin, D., Plattner, G.-K., Tignor, M. M. B., Allen, S. K., and Boschung, J. (2013). *Climate change 2013: the physical science basis. Contribution of Working Group I to the Fifth Assessment Report of the Intergovernmental Panel on Climate Change*. Cambridge, UK and New York, NY. Cambridge University Press, 1535

Sujit, K., Saha, S. K., Pokhrel, S., Hazra, A., and Chaudhari, H. S. (2017). The dominant modes of recycled monsoon rainfall over India. *J. Hydrometeorol* 18, 2647–2657. doi:10.1175/JHM-D-17-0082.1

Taylor, K. E., Stouffer, R. J., and Meehl, G. A. (2012). An overview of CMIP5 and the experiment design. *Bull. Am. Meteorol. Soc.* 93, 485–498. doi:10.1175/bams-d-11-00094.1

The organisation, H. S. (2018). *Hydrology (S) directorate STUDY REPORT Kerala FLOODS OF AUGUST 2018*New Delhi: Central Water Comission.

Trenberth, K. E. (1998). Atmospheric moisture residence times and cycling: implications for rainfall rates and climate change. *Clim. Change* 39, 667–694. doi:10.1023/a:1005319109110

Van Der Ent, R. J., and Tuinenburg, O. A. (2017). The residence time of water in the atmosphere revisited. *Hydrol. Earth Syst. Sci.* 21, 779–790. doi:10.5194/hess-21-779-2017

Van Der Ent, R. J., Wang-Erlandsson, L., Keys, P. W., and Savenije, H. H. G. (2014). Contrasting roles of interception and transpiration in the hydrological cycle – Part 2: moisture recycling. *Earth Syst. Dyn.* 5, 471–489. doi:10.5194/esd-5-471-2014

Wang, N., Zeng, X.-M., Zheng, Y., Zhu, J., and Jiang, S. (2018). The atmospheric moisture residence time and reference time for moisture tracking over China. *J. Hydrometeorol.* 19, 1131–1147. doi:10.1175/jhm-d-17-0204.1

Wills, R. C. J., White, R. H., and Levine, X. J. (2019). Northern hemisphere stationary waves in a changing climate. *Curr. Clim. Change Rep.* 5, 372–389. doi:10.1007/s40641-019-00147-6

Conflict of Interest: The authors declare that the research was conducted in the absence of any commercial or financial relationships that could be construed as a potential conflict of interest.

Advantages of publishing in Frontiers

OPEN ACCESS
Articles are free to read
for greatest visibility
and readership

FAST PUBLICATION
Around 90 days
from submission
to decision

HIGH QUALITY PEER-REVIEW
Rigorous, collaborative,
and constructive
peer-review

TRANSPARENT PEER-REVIEW
Editors and reviewers
acknowledged by name
on published articles

Frontiers
Avenue du Tribunal-Fédéral 34
1005 Lausanne | Switzerland

Visit us: www.frontiersin.org
Contact us: frontiersin.org/about/contact

REPRODUCIBILITY OF RESEARCH
Support open data
and methods to enhance
research reproducibility

DIGITAL PUBLISHING
Articles designed
for optimal readership
across devices

FOLLOW US
@frontiersin

IMPACT METRICS
Advanced article metrics
track visibility across
digital media

EXTENSIVE PROMOTION
Marketing
and promotion
of impactful research

LOOP RESEARCH NETWORK
Our network
increases your
article's readership